Structural Chemistry of Glasses

by [K. J. Rao]

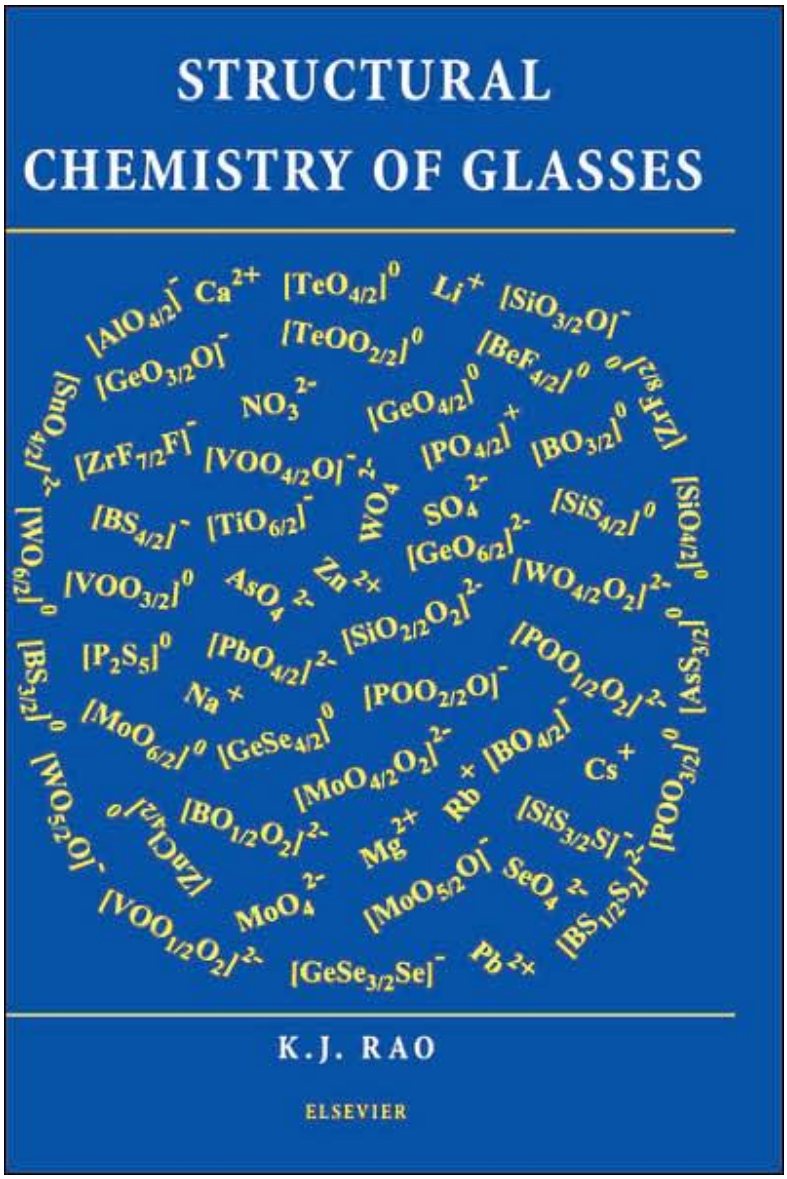

- ISBN: 0080439586
- Publisher: Elsevier Science & Technology Books
- Pub. Date: August 2002

Preface and acknowledgements

It is for two good reasons that I have endeavoured to write this book. First, I have found that there is a real need for a new book, particularly for beginners in glass research, which gives a fair account of a variety of exciting new knowledge in this branch of science. The book should also expose the readers to the veritable stock of concepts found useful all along in glass science, many of which were drawn especially from chemistry. Second is that, for a long time my students and post-doctoral associates have been urging me to write such a book in view of my interest in a variety of glasses. Therefore, when I was asked by my teacher, Professor C.N.R. Rao (many thanks to him, right away) to write this book, I found it a welcome opportunity. I am particularly delighted that Elsevier has come forward to publish it.

Regarding the scope of the book, I have been largely guided by my own experience in teaching and research. This book deals mainly with inorganic glasses, albeit examples are drawn from polymer and organic glasses for illustration. There is an emphasis on the physical chemistry aspects of glass science.

Two of my students, Mr. Sundeep Kumar and Mr. Harish Bhat have assisted me in writing and have been careful student critics of this book. I hope my interaction with them has helped improve clarity of presentation. Long discussions, I held with Harish and Sundeep on many concepts, experiments, etc. in glass research, not all of which are reflected in this book, have been a rewarding experience.

An unconventional start is made in this book. The first chapter is a brief essay which is intended to remind the reader that there is a long and historical relation between glasses and mankind. Glasses are the first truly man-made materials and have served eminently in fulfilling many of our everyday needs. Also, glasses have a transcendental beauty to which I feel we should pay homage in the first place. My hope is that the essay evokes a well-founded curiosity in the minds of the reader regarding the subject of glasses. Another unconventional feature of this brief chapter is to give the outline of what is in the book, a matter usually the preserve of the preface.

I have gained much by reading several excellent books already in print, some of them dated, but precious. I am indebted to all these authors; their books are listed in references. A large number of the original papers and reviews in the field have been cited. Even so, I suspect that a few important references may have been missed. I regret the unintentional omission and solicit forgiveness.

Professor C. A. Angell, then at Purdue Universtiy, introduced me to glass science. (Late) Professor A. R. Cooper, at Case Western Reserve kindled my hopes for a research career. I am most grateful to both of them. Two other fine scientists I collaborated with in glass science are Professor Joe Wong (Lawrence Livermore) and Professor S. R. Elliott (Cambridge). To both of them I express my gratitude. Professor J. M. Thomas (Royal Institution) made a lasting influence on my ways of thinking. I wish to record my gratefulness for the encouragement I received from Sir John.

I have benefited greatly by my collaboration with Professor A. Levasseur and Professor J. Etourneau (ENSCPB and ICMCB) of the University of Bordeaux. I wish to express my gratitude to these extraordinarily fine friends.

Several excellent students and post-doctoral fellows have worked with me at SSCU. They have not only helped me sustain my interest in glass science, but also given much happiness in the rather demanding academic life I have had. To all of them, my sincerest best wishes. I make a special mention of my best wishes to Sundeep, Harish, Dr. (Mrs.) Munia Ganguli and Mr. Panneerselvam for all their help in writing this book.

IISc in general and SSCU in particular has been the best thing to happen to me in my life. My interactions with the highly accomplished and friendly colleagues at SSCU will be remembered for all times. To all these colleagues I am much beholden.

Writing this book meant working with students in the office, at home, inside coffee shops and on the lawns of IISc for long hours. My wife, Sudha, and my son, Vijay, not only put up with my neglect of the household, but also offered support during all the extra hours of work I had to put in. I record my warmest and deeply personal appreciation of their help and cooperation.

English is not my mother tongue. There are bound to be mismatches between my intentions and expressions. Hopefully the scientific content has not suffered. Readers sensitive to language may please forgive me for the lapses.

I hope the book serves the objectives which motivated me to write it and will be found useful by the researchers in glass science.

December 21, 2001. K. J. Rao.

Acknowledgements to Publishers

I am very grateful to the following publishers for giving permission to reproduce various figures and tables in the book. The authors and the sources are individually acknowledged at relevant places.

American Association for the Advancement of Science, New York; Academic Press, Harcourt, Inc., Florida; The American Ceramic Society, Ohio; American Chemical Society, Washington D.C.; American Institute of Physics, New York; American Physical Society, Maryland; Cambridge University Press, Cambridge; Chapman and Hall/CRC, Florida; The Electrochemical Society, Inc., New Jersey; Society of Glass Technology, Sheffield; The McGraw-Hill Companies, New York; Institute of Physics Publishing, Bristol; John Wiley & Sons, Ltd., Chichester; Aoba,Aramaki, Sendai; Allyn and Bacon/Longman, New York; Macmillan Publishers Ltd, U.K.; Materials Research Society, Pennsylvania; Oxford University Press Inc., New York; Kluwer Academic /Plenum Publishers, London; Indian Academy of Sciences, Bangalore; The Royal Society, London; Royal Society of Chemistry, Cambridge; Springer-Verlag, Heidelberg; Taylor and Francis, Oxfordshire (http://www.tandf.co.uk/journals); Wiley-VCH, Weinheim; Society of Photo-optical Instrumentation Engineers, Bellingham; Deutsche Glastechnische Gessellschaft, Frankfurt; Editions de Physique, France; Deutsche Bunsen-Gesellschaft fur Physikalische Chemie, Frankfurt.

Table of Contents

	Dedication	
	Preface and Acknowledgements	
	Acknowledgements to Publishers	
Ch. 1	The World of Inorganic Glasses	1
Ch. 2	The Glassy State	13
Ch. 3	The Glass Transition Phenomenon	77
Ch. 4	Structural Techniques	137
Ch. 5	Theoretical Studies	185
Ch. 6	D.C. Conductivity	203
Ch. 7	A.C. Conductivity	263
Ch. 8	Semiconducting Glasses	307

Ch. 9	Relaxation Phenomena	375
Ch. 10	Elastic Properties and Pressure Effects	401
Ch. 11	Optical Properties	429
Ch. 12	Oxide Glasses	463
Ch. 13	Chalcogenide Glasses	513
Ch. 14	Other Glasses	535
	Subject Index	559

Praising what is lost makes the remembrance dear.
- W. Shakespeare

CHAPTER 1

THE WORLD OF INORGANIC GLASSES

In her most fascinating work on glasses, titled "Glass Source Book", Jo Marshall (1990) captures mankind's long and intimate association with glasses, 'It is only when one tries to imagine a world without glass that one realizes in how many ways it is used and the extent of our unthinking acceptance of it'. In today's world, starting from drinking goblets to the dressing mirrors, from the electric bulbs to the communication cables, from the window glasses to the wine bottles, from the decorative vases to the vast variety of chemical glassware, a whole range of everyday human requirements is met by glasses. In those magnificent collections of the world's best museums, history of millenniums of the bygone cultures of the world is held in captive animation in the great works of glass art. The boundless and inexorable human spirit has been expressed by many a master artist through the medium of glass. The colours, the curves and the leaps of imagination are combined with the luster and ductility of glass in creating those timeless objects of art. In the words of Leopald Rochowansky, "...snatched from the unending stream of time, they (glasses) unfold the limpid purity of a festive day". They are a lofty record of the ingenuity and the illimitable creativity of the human mind.

Natural glasses

While man has made glasses by design to meet his needs and to express his emotions, nature has also made them (Pye et al., 1984), but in violent fury. The volcanic outflow of the molten magma from the bowels of the earth get cooled and form glasses. Huge meteoric impacts have been known to dent the earth's surface and create molten pools out of the crust material, which in subsequent impacts spill over and form smaller bits of glasses. *Obsidian* is a volcanic alumino-silicate glass containing oxides of Na, K, Ca, Fe and traces of Mn. These are millions of years old and most of the obsidian glasses must have crystallized during the history of earth's harsh and changing weather. *Impactites* are natural glasses formed from crystalline materials rendered amorphous by the shock of meteoric impact. Glasses formed from impacted melts are known as *tektites*. Tektites have

been recovered from all parts of the world, from Australia, from the deep-sea deposits of the Indian ocean, from central Europe, from Libyan desert etc. These are again alumino-silicate glasses, except for the presence of MgO and small quantities of TiO_2, as in Australian and Asian tektites. Tektites are at least 700,000 years old. Small tektite pieces of less than a millimeter in diameter, known as *micro-tektites*, are very widespread on earth's surface and they are generally light yellow-brown in colour. The composition and homogeneity of some of the tektites from Australia indicate that they may be of lunar origin. Glass specimens recovered from the Libyan desert are pale yellow to yellowish green in colour and contain 97% or more of SiO_2.

Glasses through the centuries: a historical perspective

The art and technology of glass long preceded their scientific understanding. Investigations of ancient glasses take us to the very dawn of civilization. It appears that glass was first made in Mesopotamia in western Asia. Objects dated to 4000 B.C. have been found which are covered with coloured glazes containing copper compounds. The glass vessels recovered in Egypt were made between 14^{th} and 16^{th} century B.C. The method adopted seems to have been to melt the glasses, draw out threads, wind them around a sand or clay core which was itself held on an iron rod and re-melt the glass threads. Many chemical agents were used by Egyptians to colour the glasses. Patterns used to be made by assembling pieces of coloured glass and re-melting them. Egyptian glass making declined around 11^{th} century B.C., by which time it had spread to Syria, Cyprus and other eastern Mediterranean regions. Syria and Palestine emerged as major glass making centers after 1000 B.C. Syrians and Palestinians made core-formed vessels using the same techniques and colours as Egyptians, but in different shapes. They also developed the technique of glass blowing. Macedonia and Greece also emerged as centers of glass making around 400 B.C. At this time, the techniques of making glass tableware such as bowls, use of brilliant colours and use of lathes and grinding wheels for making decorations had been developed. Also, Greeks developed sandwiching techniques by which gold layers were trapped between clear glass parts. Mosaic forming technique was also developed to impart special colour effects.

The emergence of Roman Empire between 3^{rd} and 2^{nd} century B.C. led to glass making in Rome and other parts of Italy. Both the methods of imparting different colours and of glass blowing had become quite popular

by this time. One of the great techniques bequeathed from this era is the making of *cameo* glasses. These are made by super-imposing a white opaque glass on a base of coloured glass. Portions of white layer are cut away in places to expose the colour of the base glass and the remaining white glass is now carved by the gem cutting technique to provide a relief of the art in mind. The next major developments were in the regions of Byzantine (Greek Empire) and the countries that came under Islam. Till about 7^{th} century A.D., glass making seems to have thrived in Syria and Palestine. The so-called *Hedwig* glasses belong to this period and are characterized by high relief created by diamond cutting. The Arab invasion spread to most parts of Asia and Europe adjacent to Mediterranean including Spain. In the 9^{th} century A.D., Baghdad emerged as a center of glass making. During following two centuries, Persia became a major producer of fine glassware and the technique of grinding the glass surfaces was developed. Extensive use of enamels and making of gilted inscriptions are the important developments of this period. After the conquest of Persia by Chengis Khan, Syria again became a prominent glass making center in 13^{th} century A.D. This is the period when decorated mosque lamps from Damascus became very famous. But at the end of 14^{th} century A.D., fall of Damascus to the armies of Timur led to emigration of Syrian workers to Samarkand (present Uzbekistan).

By this time, in Europe, the independent republic of Venice had emerged as a great center for glass making. Its supremacy in glass is reflected in such expressions as *facon de Venice*, which was the hallmark of elegance, beauty and taste. This remarkable development is apparently due to the extraordinary patronage the glass workers received from the government in the form of tax reliefs and social recognition. Also, all the glass makers of Venice at that time were made to settle down in the island of Murano and encouraged to develop in professional privacy their prosperous art of glass making. There were two significant developments during this time. One is the discovery that addition of calcia gives rise very bright and shiny glasses; the glasses could be worked to remarkable thinness and feather-light and (crystal-like) clear glasses could be made. These were known as *crystallo* glasses. The second was the technique of forming *ice glasses* in which the hot *metal* (molten glass) gathered at the end of an iron pipe was first plunged into ice cold water momentarily and then blown so that the exterior surface appeared like an enlarged web of tiny cracks. This process gave a sparkling frosted appearance to the objects. Other technical developments in Venice included the formation of *lattimo* (milky white) glasses by the addition of tin oxide and making of

calcedonio glasses as imitations of precious and semi-precious stones, which was in great fashion in Renaissance Europe. It is said that there was no kind of precious stone, which could not be imitated by the industry of glass-workers – "a sweet contest of nature and of man". Towards the end of the 16^{th} century, glass making flourished in other parts of Europe due to the emigration of many catholic glass workers from Italy. It may be noted that the patronage of the Church by way of encouraging the making of stained glasses was a very powerful factor in retaining glassmakers in parts of Europe. It was as influential as those given by the rulers in Islamic world to their glass workers. In this period workers in England developed the technique of making *waldglas* (green or amber tinted glasses). Developments during the following years in Europe were more in terms of techniques, development of local and popular designs and making glass articles affordable by the middle classes. Use of water-power mill to engrave glasses was developed in Germany and the use of cutting wheel became popular for doing *intaglio* work. Also, in Germany, potash-lime glass was developed, which was harder than *crystallo*, and was therefore better suited for working with engraving wheels. There were continued improvements by the Dutch in the use of diamond point engraving. The development of the "glass of lead" (lead containing glasses) in Britain by G. Ravencroft which could compete with the brilliance of the *crystallo* also belongs to this period. The lead containing glasses were heavier and could not be made as thin as *crystallo*. But the presence of lead, gave better light dispersing character which enabled lead glasses to compete with *crystallo*. Also, lead-containing glasses were especially suited for deep cutting, which gave rise to a whole new class of utility glasses (cut glass). This period also witnessed gradual emergence of the use of machines in glass making. J. Wedgewood summarized this period most thoughtfully as the one when glass making gradually moved from the craftsman to the draftsman.

19^{th} century gave birth to industries with mechanized glasswork, both in Europe and in the United States across the Atlantic. It also spread eastwards to Bohemia and other countries where making of the crystal glass became quite popular. New coloured glazes were developed to paint the glassware. Glasses with fluorescent colours of the greenish yellow kind were made by the addition of uranium salts. Translucent milky-white glass known as *Opaline* was developed in France around 1810 by the addition of metallic oxides to glass. By 1851, during which year the Great Exhibition was held in London, there was a tremendous flourish in glass industry and glass had come to be established, not only as an adorable art

medium but also as an affordable part of household throughout Europe. Advances were made in working with glass objects such as etching with HF, which helped the revival of *cameo* art in Britain. This is exemplified in the replication of the celebrated *Portland Vase* by John Northwood using a cobalt blue glass covered with a white glass casing. This period also saw the emergence of making pressed glass. Among the notable developments in United States were making glasses which had orange, blue or green iridescence and glasses which are heat sensitive and changed their colours when heated. By the end of the 19th century, the modern methods of glass making had come to stay in most countries of Europe, America and far east like Japan, India and China.

The finest products of this period also were associated with great names such as Antonio Salviati of Venice (Murano), Henry Powell of England – famed for his sweeping curves of *Art Noveau*, Archibald Knox of England, Emile Galle of France, Louis Tiffany of USA (immortalized for his lamp-shades), Karl Kopping of Germany, Almeric Walter of France known for his work with *pate-de-verre* (glass paste; itself re-discovered by Henri Cros in 1885), F. Egermann credited with the discovery of staining glass with yellow colour using silver chloride, D. Biemann famed for wheel engraved decoration etc. The period between the world wars also witnessed rapid growth of the science of glasses in addition to the glass art. Morris Merionot and Rene Lalique of France and Joseph Hoffmann of Vienna belong to this period. Rene Lalique revived the method of *cire-perdue* (lost wax) method of making glass objects. The period following world war II has been dominated by scientific developments, although new dimensions to the glass art has been provided by artists all over the world (Cousins, 1989). Mention may be made of Eino Maelt of USSR, Gunter Knye, Klaus Moje and E. Eisch (all from Germany), B. Sipec of Czechoslovakia, Dale Chihuly of USA, Timo Sarpaneva of Finland and Lino Tagliapietra of Italy for their breath taking creations.

The history of glass making in China and India (Sen and Chaudhuri, 1985) is somewhat shrouded in unclear chronology. There are evidences from glass objects recovered from graves in Japan, Korea and China that glass was in use as early as 6th century. Analysis of the Chinese glass reveals that they contained lead and barium, which were evidently in use in the 2nd and 3rd century B.C., at the time when the use of either lead or barium was not yet known in the Mediterranean region. Several excavations at historical sites in India reveal that there was widespread use of glass objects as early as 5th century B.C. These glasses also contain

lead. Literary evidences reveal that the antiquity of Indian glass should be as old as *Vedic* period (use of the sanskrit word *Kacha* for glass is found in *Yajurveda* dated ~1200 B.C. and in *Shathapatha and Taithriya Brahmanas* dated ~1000 B.C.). Analysis of glasses from Takshashila reveals that addition of Ca and Mg oxides and also of alumina was widely known even in 6^{th} century B.C. It is interesting to note that glass bangles have been an essential ornamental wear of Hindu women even in the pre-Buddhistic period.

Making of glasses in large quantities must have been known even during the times when Syria and Palestine enjoyed supremacy in glass making. A giant glass slab (3.4m×1.95m×0.5m) was discovered in an ancient Jewish site near Haifa, which has been attributed to Roman times. Its weight - 8.8 tons - is more than half the weight of glass block made for the 200 inch reflector at Mt. Palomar (14.5 tons), which belongs to the 20^{th} century.

20^{th} century not only witnessed the emergence of glass as an integral part of human life but also the evolution of manufacturing techniques and a deeper scientific understanding of glasses. Growth of glass science is evidently connected with the growth of chemistry and physics, particularly of inorganic materials. The inherent characteristic of this growth is a strong empiricism born out of keen observation of the effects of addition of a variety of oxides and other materials to an essentially silica glass. We have already noted the development of brilliance through the addition of CaO, of increased dispersive power through the addition of PbO and of formation of a whole range of colours through the addition of oxides like CoO, all of which were found empirically by the master glass workers. These effects are now more clearly understood because of the better understanding of chemistry and physics of these materials – largely a development of the 20^{th} century. Once it was understood that glass is amorphous in its structure as opposed to the periodic structure of crystalline materials, the importance of local structures and of chemical bonding became evident. The high degree of chemical inertness of the surface of silicate glasses and the workability of glass into large and desired shapes of any complexity made them a natural choice for use in chemical laboratories. The optical transparency and the ability to be shaped, ground etc. of glasses led to far reaching applications of them in making components like lenses to optical fibers.

Till the emergence of the use of machines in making glass objects, which transformed glass making into a factory business, glass making units consisted of groups of very few people (3 to 6) (Wymer, 1964). An

expert and leader known as *gaffer*, assisted by a *servitor*, a *foot-maker* and a *taker-in*, down the line, constituted a team. Glass melting and annealing furnaces (*lehrs*), characteristically long armed chair of the *gaffer*, long iron pipes at the end of which *metal* (glass melt) was gathered, a variety of cutting tools like scissors, shapers like pincers and an iron topped table (marvering table) constituted their main equipment. The transformation of such units into factories resulted in the production of more numbers of the same with greater accuracy and speed, but took away something very vital from the craft itself, which Morris lamented, "...the machine was the willing lackey of the greedy businessman sacrificing design quality for more monetary gain" and John Ruskin deplored, "all very neat, finished and perfect form in glass is barbarous."

Glass in modern times

Nevertheless, following the industrial revolution, glass making did become the business of factories. 20th century saw the development of twin roller technique to make sheet glass, a few mm in thickness, couple of meters in width and of any desired length (Tooley, 1974). Machines have been developed where blobs of glass are blown into moulds using compressed air and shaped into bottles. Machines have been built to make fibers by extruding melts through metal orifices and rolled on to large diameter spindles or are gathered as (fibrous) glass-wool. Thick sheets of flat glass – plate glass – are made by a special float process where melts are made to settle and freeze on molten tin pools, which provide optically smooth and parallel surfaces. Glasses are coloured with added oxides or halides and made to change their colours or become darker on exposure to light or heat. Glasses are doped with rare-earth ions for use as lasers. Blocks of glasses are ground, polished and coated to serve as mirrors in telescopes to gaze at the celestial objects and as lenses in powerful microscopes to look into the amazing world of cellular biology. Many are the uses of glasses and correspondingly the techniques to make them in the required form. Glass-fibers are used in large quantities as insulating materials and now the high quality fine silica fibers put together as cables thousands of kilometers long are used for information transmission across the globe. Thick slabs of clear lead glass are used as radiation shields in nuclear power plants. It would be difficult for us to imagine a world without electric bulbs, which constitutes one of the major uses of glass. The largest products of glass industry are bottles used to store beverages and perfumes. Fiber reinforced plastics have found immense use as

modern lightweight structural materials. Borosilicate glasses are used in the extremely important area of nuclear waste disposal. Bio-glasses such as those based on calcium phosphate and silica are employed in bone repair and replacements.

More than 90% of the glass in use is based on oxides and in particular silica, which justifies the sobriquet that glass is essentially 'sand-and-ashes'. But many specialized glasses in use are not based on silica. For example, phosphate and fluro-phosphate glasses, used as hosts for lasers, zinc phosphate and lead borate glasses used as solders. A whole variety of chalcogenide glasses are used for their switching behavior – the material switches from a resistive to a conducting state when a critical voltage is applied across or current is passed through. Memory panels are made from such glasses. Glassy Se has been at the heart of reprographic machines, which form today an integral part of all modern business. Halide glasses are being currently developed to substitute the silica fibers in information technology due to their superior transparency. Amorphous Si and InCuSe are materials used in photo-voltaics. A variety of ionically conducting glasses, particularly those based on Li and Ag, are being used in the making of batteries. Glassy metals have found a number of applications, particularly in transformer cores, magneto-optic discs, magnetic heads and sensors (Sakurai et al., 1993). An emerging application of metallic glasses is in storing hydrogen for forming electrodes in Nickel-metal hydride batteries (Ovshinsky, 2000).

Glass manufacturing processes came into existence at the turn of the 20^{th} century, notably as a result of American ingenuity. Today, industrial glass worldwide is a significant component of national economies. In 1993, USA alone manufactured ~300 million container units (bottles). Although glass used for making bottles constitute the largest percentage of glass products, flat glass and electric bulbs are not far behind. They also form a significant part of glass products and they command higher prices weight per weight compared to containers. In 1995, USA and Japan produced roughly 10 million metric tons of glass each. In many emerging economies such as India and China, glass industry has been growing at a very high rate (reportedly increasing at the rate of 160% p.a.).

In this book

Therefore, we live in a world in which glasses play a very important role in all aspects of our daily life and this is enough reason for

us to study the science of these glasses. This book is intended to explore the physico-chemical principles of inorganic glasses. The second chapter addresses questions like what are these glasses, under what conditions are they formed, what type of materials can be obtained in the glassy state, what techniques are generally available for making glasses and what general principles govern the glass structure etc. Although it appears as if the success in forming a glass is simply a question of how fast one can quench a melt, we are keenly aware that some materials form glasses and some do not. In other words there is a glass forming ability, which distinguishes the materials. Many efforts have been made to understand the basis of this ability to form glasses. Those thoughtful approaches are also discussed in chapter 2. The glassy state is governed by a unique thermal event known as *glass transition*. When a glass forming melt is cooled to a temperature known as glass transition temperature, an already metastable supercooled liquid transforms into a metastable solid. Understanding the glassy state, therefore, is critically dependent on an understanding of this phenomenon. Many approaches have been made to comprehend the glass transition phenomena. When considered together these approaches have been found to be helpful in providing a better understanding glasses but none of them singly appears to be a successful theory of glass transition. These approaches are presented and discussed in Chapter 3. In recent times, detailed investigation of the viscosities of glass forming liquids have revealed patterns of behavior in the supercooled region which are intimately connected to the nature of glass transition. The patterns are described in terms of *fragile* and *strong* liquid behaviors. The concept of fragility is also discussed in chapter 3.

Unlike in crystalline materials, in glasses, the structure needs to be understood at three different levels; local or short-range structures, intermediate range structures and long range structures. However, there is no long range order because there is no periodicity in the structure of glasses. Also, there is no requirement of stoichiometry in glasses. Therefore in order to determine the structure of a glass, it is not enough to do one good diffraction experiment like in crystalline materials. Both diffraction and other spectroscopic techniques are needed to arrive at meaningful structural information in glasses. In chapter 4, some of the important techniques such as diffraction (X-ray, neutron and electron), Extended X-ray Absorption Fine Structure (EXAFS), X-ray Absorption Near Edge Structure (XANES), high resolution magic angle spinning nuclear magnetic resonance (HR MAS NMR, vibrational (IR and Raman) spectroscopies and X-ray photoelectron spectroscopy (XPS) are discussed.

Several other characterization techniques related to optical, mechanical and thermal properties are also useful as secondary structural techniques. They have been discussed but in different chapters because of the appropriateness of the context. Even when diffraction and spectroscopic data are available, structure elucidation requires modelling and theoretical evaluation of the energies of the structural entities present in glasses. Modelling is accomplished in several ways. There are hand built (Chapter 2) models and computer simulated models. Two widely used computer based techniques are molecular dynamics (MD) and Monte Carlo (MC) simulations. MD simulation, as the name itself indicates, provides direct information on the dynamics of the constituent particles both in super-cooled and glassy regions. These techniques of simulation require the use of interaction potentials of several types. *Ab initio* calculations of interaction energies of small groups of atoms are performed using quantum chemical methods. In chapter 5, we discuss these methodologies, which complement experimental structural techniques.

Cations present in glasses diffuse through the glass structure, some of the smaller cations do so relatively easily. This motion is the origin of ionic conductivities of glasses. Conductivities are very high in the so-called fast ion conducting (FIC) glasses. When more than one type of cation, such as two alkali ions, are present in the glass, they affect each other's motion and this phenomena is described as the mixed ion effect. The most widely studied is the mixed alkali effect (MAE). In chapter 6, d.c. conductivity, FIC and MAE phenomena have been presented. In alternating electric field (a.c.) ionically conducting glasses exhibit very interesting universal phenomena. At ordinary temperatures, and in applied fields of MHz frequencies, most glasses show conductivity divergences, which follow power laws. The a.c. conductivities have been studied in great detail because of the challenging nature of the observed behavior. This is the subject matter of Chapter 7.

Chalcogenide glasses are typically semiconducting, because their resistivites are generally high and decrease with increasing temperature. The understanding of the origin of semiconducting behavior itself has been an exciting chapter in glass science (and led to the award of the only Nobel prize on a subject related to glass science to Sir Nevil F. Mott and Prof. P. W. Anderson in 1972). In Chapter 8, we discuss a whole range of phenomena associated with electron transport in glasses. Glass transition involves slowing down of atomic motions in the super-cooled region and eventual freezing in of certain modes. But the local motions continue to exist in glasses, although their frequencies decrease to low values. The

metastable state of the glass and its structure supports a variety of motions in the glassy state, all of which can be probed by imposing a suitable perturbation (an electrical field or a mechanical stress) and examining how the perturbations decay after the removal of the fields. The manner of dissipation of the perturbation is the relaxation. The relaxation phenomena as a whole have certain very interesting features and have been discussed in Chapter 9. Glasses are inherently brittle and below their annealing temperatures, catastrophically fail under applied stress. The strength of a glass, and the nature of the failure are discussed in Chapter 10. The relation of mechanical properties to the structure are also discussed. The most important and symbolic characteristics of glasses are their transparency and colour. These are optical properties. In chapter 11, the optical properties, their determination, colour and constitution, and the basis of some advanced applications of glasses such as laser glasses and optical communication fibers are discussed.

The last three chapters summarize unique structural and chemical features of a variety of glasses. They also provide an overview of the important aspects of the glass systems. Chapters 12 and 13 discuss respectively oxide and chalcogenide glasses particularly in view of their chemistry, structure and a number of special phenomena associated with them. In chapter 14, synthesis, structure and properties of halide, oxyhalide, oxynitride and metallic glasses are discussed. Some aspects of glass-like carbon have also been presented.

References:

Jo Marshall, 1990, Glass Source Book (Chartwell Books Inc., New Jersey).

Pye, L.D., J.G. O'Keeefe and V.D. Frechette, eds., 1984, Natural Glasses (North-Holland, Amsterdam).

Cousins, M., 1989, 20th Century Glass (Chartwell Books Inc., New Jersey).

Sen, S.N., and M. Chaudhuri, 1985, Ancient glass and India (Indian National Science Academy, New Delhi).

Wymer, N., 1964, Its Made Like This : Glass (Johm Baker, London).

Tooley, F.V., 1974, The Handbook of Glass Manufacture, vol. 1 (Books for Industry, Inc., New York).

Sakurai, Y., Y. Hamakawa, T. Masumoto, K. Shirae and K. Suzuki, 1993, Current topics in Amorphous Materials: Physics and Technology (North Holland, Amsterdam).

Ovshinsky, 2000, in Insulating and Semiconducting Glasses, ed. P. Boolchand (World Scientific, Singapore) p. 729.

The important thing in science is not so much to obtain new facts as to discover new ways of thinking about them.
- Sir William Bragg

CHAPTER 2

THE GLASSY STATE

The first question we need to address is 'what is a glass?' The traditional view is that glass is a solid obtained by supercooling a liquid and that it is X-ray amorphous. Additionally a glass, when heated, should also exhibit a thermal characteristic known as the "glass transition" at a temperature, T_g. At T_g, second derivative thermodynamic properties, namely heat capacity, thermal expansivity and compressibility undergo more or less sudden changes. Therefore all amorphous materials are not necessarily glasses. For example materials can be obtained in amorphous state by a number of other methods such as condensation of vapours on cold substrates, bombardment of crystalline solids by neutrons or by other heavy particles, gelation of solutions followed by removal of solvents, mechanical shear, solvent evaporation or in some cases application of high pressures. The products obtained in all these processes give rise to X-ray diffraction patterns, which lack crystalline features such as sharp diffraction peaks. Their electron diffraction patterns generally consist of one or two diffuse hallows as shown in Figure 2.01. But many such amorphous materials do not exhibit glass transition.

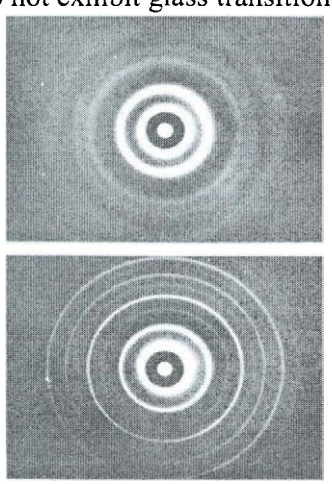

Figure 2.01: Electron diffraction pattern of amorphous (upper) and crystalline (lower) iron. (After Ichikawa, 1973)

Therefore it is assumed, unless stated otherwise, that glasses are only those amorphous solids which are obtained by the supercooling of melts. When a liquid is cooled from a high temperature to its melting temperature, (T_m), it generally solidifies to a crystalline product. It is only rarely that melts do not crystallize when they are cooled slowly. Therefore in order to obtain a glass the rate of supercooling has to be such that crystallization is bypassed. This requires rapid quenching in order to bypass crystallization. Thus the cooling or quenching rate, Q, which is a kinetic parameter is of great significance for glass formation. Crystallization is governed by two factors, one, the nucleation and two, the growth. We discuss the nucleation and growth more quantitatively later. It is sufficient to note here that both nucleation and growth rates exhibit rapid increase followed by a slowing down as the temperature is lowered below T_m. As a consequence, the rate of crystallization itself appears as in Figure 2.02. The kinetics of both nucleation and growth are dependent on the viscosity of the melt as will be seen later. Bypassing crystallization means that the liquid has to be cooled rapidly from T_m through the region marked by the dotted line in Figure 2.02, which shows the behaviour of crystallization rate as a function of temperature. For materials whose viscosities are very low just above T_m the rate of cooling has to be really very high. The required cooling rates therefore are determined by the velocity of crystallization, v, of the material. v is given by,

$$\mathrm{v} = \frac{L(T_m - T)}{3\pi a^2 \eta T_m} \tag{2.01}$$

where L is the heat of fusion, a is the typical distance through which the particles have to move during crystallization and is of the order of lattice spacing and η is the melt viscosity. Since viscosity increases exponentially during cooling, v decreases rapidly and the crystallization is suppressed by a rapid cooling through the difficult zone indicated in Figure 2.02.

Preparation of glasses

In the case of good glass forming materials like SiO_2, GeO_2 or B_2O_3, the required rate of cooling of the melts is remarkably low because the maximum crystallization velocities in these materials are themselves very low. For example, for SiO_2, GeO_2 and P_2O_5, the rates are 22 Å, 420 Å and 15 Å per second (Urbain et al., 1982, Fontana et al., 1966 and Cormia et al., 1963) respectively. In the case of B_2O_3 crystallization does not

occur unless the melt is subjected to pressure. Melts of atactic polymers do not crystallize when cooled under whatever condition. But melts of mixed salts like $x Ca(NO_3)_2 \cdot (1-x)KNO_3$ or $xK_2SO_4 \cdot (1-x)ZnSO_4$ form glasses only when they are quenched sufficiently fast, at rates varying 10-1000 degrees/second. It is still worse in the case of several metallic alloys where the quenching rates have to be extremely high. These are of the order of 10^6-10^7 degrees/second and require the use of special quenching techniques. In these techniques molten alloys to be made into a glass are jetted onto cooled rollers spinning at very high speeds. Quenched glassy metallic ribbons are formed which are lifted off from the roller.

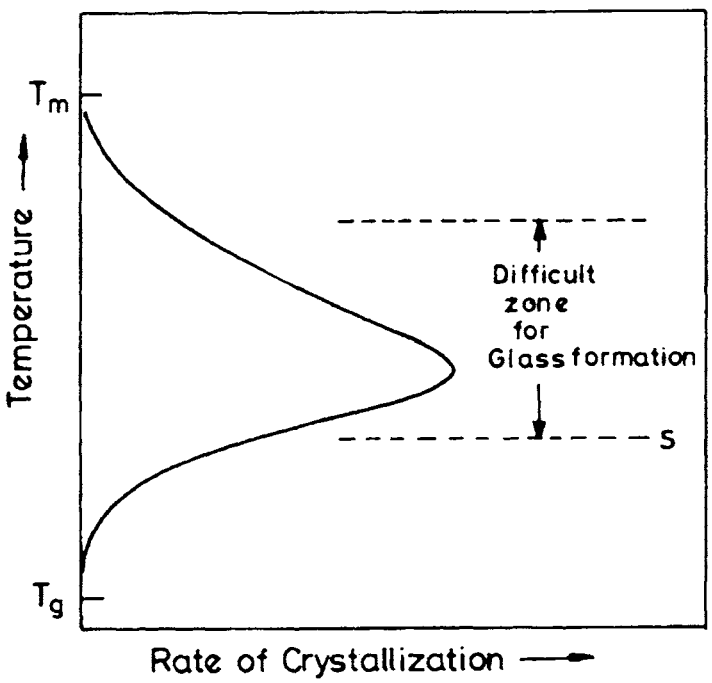

Figure 2.02: Dependence of rate of crystallization of an undercooled liquid on temperature.

Continuous ribbons can be obtained at speeds of the order of 1 Km/minute. Molten alloys can be injected into the space between spring loaded and cooled rollers spinning in opposite directions. Removal of heat in such a set-up is even better than when a single roller is employed because of the effective use of both the surfaces of the ribbon. Methods have also been developed where drops (instead of jets) of the liquid are

rapidly pressed between cooled plates mechanically driven and timed so as to trap the falling liquid drop.

Still higher rates of quenching are achieved in vapour deposition techniques, where molecules in the vapour state are suddenly brought to rest at the surface of a substrate. It is estimated that quenching rates can be as high as 10^{11}-10^{12} degrees/second. But it is only in few cases such as the Group V chalcogenides that vapour deposited amorphous materials are found to exhibit glass transition and may be described as glasses. Amorphous chalcogenides like As_2S_3 obtained from chemical reactions such as by bubbling of H_2S through As_2O_3 solution, also exhibit glass transition. Probably chalcogenides are unique in this respect. Similar (or slightly higher) rates of quenching are achieved in laser glazing, where a laser pulse incident on the material melts a few layers at the surface leading to an essentially ephemeral liquid state, from which heat is rapidly dissipated into the bulk by the lattice phonons. The top layers become glassy. The rate of quenching corresponds to the rate of heat flow by lattice phonons and is estimated to be 10^{13} degrees/second. Therefore, it appears that any liquid can be quenched into a glass provided the required high degree of quenching rate is achieved and this aspect will be discussed later.

Microwave heating in glass preparation

The conventional heating used for the preparation of glass forming melts can be replaced by microwave heating. Many materials, particularly salt mixtures, couple to microwaves. The advantage of microwave heating is that it is extremely rapid. Since it does not involve flow of heat from another source as in a furnace and the heat is generated throughout the solids by the very nature of coupling to electromagnetic waves, it is not only rapid but the process is also one of volumetric or bulk heating. Since the coupling to microwaves generally increases with increase in temperature in solids, the heating profile indicates a rapid escalation of temperature. However, once the melt is formed, the temperature of melt appears to remain nearly constant. This may be a consequence of reduced coupling and increased conduction of the heat at the container-melt interfaces. The point of interest is that there is no fear of dangerous escalation of melt temperature. Since the container can be made of a material of very poor microwave coupling, there is no wastage of energy. This may be important when microwave method is adopted for large scale preparation of glasses. It is enough if any one of the components of the

charge (starting materials for making glass) couples to microwaves. The rest of the procedure for glass preparation remains the same. The method is also advantageous where evaporation losses or thermal decomposition of a component poses a problem, because of the short duration of time needed for melting and homogenizing. Several glasses have been prepared by this method using a domestic microwave oven. In fact in the case of AgI based glasses such as in $AgI\text{-}Ag_2MoO_4$ system, microwave method gives glasses with no decomposition of the silver salts.

Sol-gel process

Sol-gel process (Ganguli, 1989; Brinker and Scherer, 1990) is another important method of preparation of glasses. Sol-gel method is essentially a *chimie-douce* process. A *sol* by definition is a suspension of colloidal particles, which are of submicron or nanometric size. If these particles have surface active groups such as hydroxyls, interparticle connections are established by a condensation reaction. If the condensation occurs in such as way that the condensation product namely H_2O, or the solvent is locked up in the matrix of sol particles, a mildly rigid product is formed, which is known as a *gel*. A colloidal particle formation can be an intermediate stage and it is not necessary to start with a colloidal suspension only. For example, when sodium silicate is dissolved in H_2O, it is hydrolyzed to give silicic acid which forms a gel. $Si(OH)_4$ molecules condense to form Si-O-Si linkages as follows:

$$Na_2SiO_3 + 3H_2O \rightarrow Si(OH)_4 + 2NaOH$$
$$Si(OH)_4 \rightarrow SiO_{2/2}(OH)_2 + H_2O$$

The silicon atom in $SiO_{2/2}(OH)_2$ is connected to two other silicon atoms by Si-O-Si bridges. Therefore in the process of gelation, the most important step is the formation of Si-O-Si linkages or M-O-M bonds. This leads to gradual and extensive polymerisation and locking up of small groups of liquid particles, whose dimensions are again nanometric. When these particles have submicron sizes and are suspended, they are colloids and the suspension is the *sol*. As the sol particles begin to grow, they impinge on each other, get bonded by condensation and result in the formation of a giant molecule of SiO_2 with incorporated tiny packets of water. Water itself constitutes a continuous medium, and the product is known as a *gel*. SiO_2 gel may thus be considered as microporous SiO_2 structure with all the pores filled with water. The process of formation of gel from sol is

associated with rapid increase of viscosity and the transformation is known as the *sol-gel transition*. A gel is thus not a real solid because it has an entrapped liquid in the pores of a 3-dimensional macromolecule. It has a weak resistance to shear stresses and also deforms elastically. It may be noted that although it is described as a macromolecule of SiO_2, a significant percentage of O-H groups are retained in the gel. Since H_2O molecules are held in the voids of the structure, it is also known as *hydrogel*.

Since the key to gelation is the formation of extensive M-O-M linkages, it can be brought about by the controlled hydrolysis of metalorganics. For example, tetra-ethoxy silane (TEOS) is a metal organic, soluble in ethanol. This solution can be kept stirred with continuous and slow addition of H_2O, which brings about the following reactions,

$$Si(OC_2H_5)_4 + 4H_2O \rightarrow 4C_2H_5OH + Si(OH)_4 \rightarrow .....\text{silica gel}$$

It involves first the formation of a sol containing silicic acid, which condenses to form silica gel where its structural pores are filled with alcohol and water. Such a gel is known as *alcogel*. The process of gel formation is very slow and it is catalyzed by the presence of both acids and bases. While the acid catalyzed gel leads to the formation of chain like product, base catalyzed product is more branched. Several studies have been performed on the kinetics of gelation. Lower values of ethanol to TEOS ratio combined with optimal H_2O to TEOS ratio favors fast gelation. The liquid phase present in the gel (water and ethanol) is removed by drying. The resulting dry gel is known as *xerogel*. It must be noted that some H_2O is still present in the xerogel in the form of uncondensed OH groups. The formation of the xerogel can be accomplished at temperatures of no more than 100 to 120 ^{0}C. During the removal of H_2O and (or) ethanol, the gel body gradually collapses. Because of the huge capillary stresses during evaporation, gels crack up. But monolithic bodies of small thickness can be obtained by slow drying at lower temperatures assisted by mild vacuum. Since monoliths are often needed for industrial applications, methods have been developed to obtain them. One of them is to use appropriate chemical additives such as formamide during gelation. It leads to a uniform distribution of stresses. The monolith of SiO_2 thus obtained is a glass. A schematic of sol-gel preparation of glasses is shown in Figure 2.03.

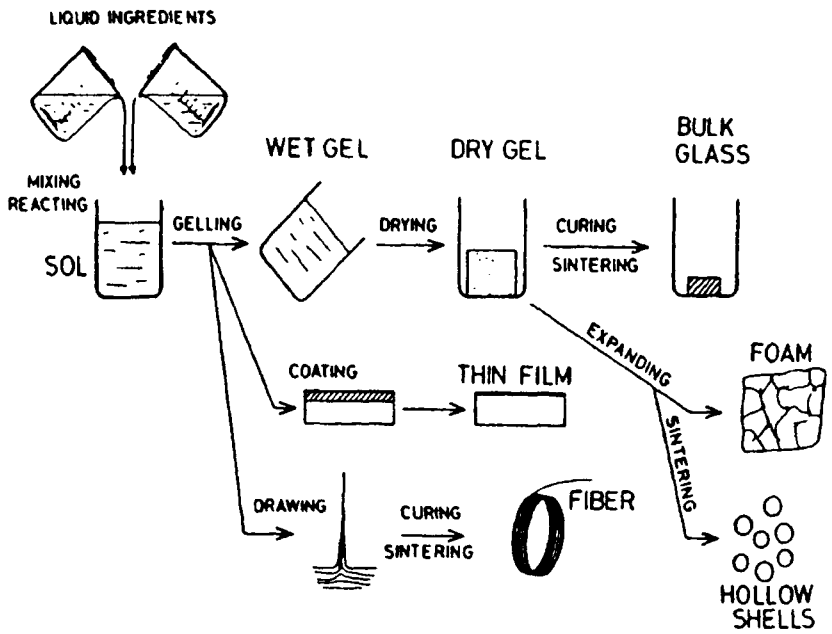

Figure 2.03: Schematic diagram of the sol-gel route to glass making. (After Zarzycki, 1993).

Instead of obtaining the high density monolithic glass from the gel, one can obtain an *aerogel* by drying it under supercritical condition. This method generally leads to the formation of extremely porous bodies with very fine pore sizes. A schematic for the formation of aerogel is shown in Figure 2.04. The gel is taken in an autoclave, whose remaining volume is filled with ethanol. From a starting pressure and temperature (P_1, T_1), the pressure is increased to P_2, where $P_2 > P_C$ (critical pressure). The temperature is then raised to T_2, when $T_2 > T_C$ (critical temperature). At (P_2, T_2), the gel is now held under supercritical ethanol – there is no interface between liquid and gaseous ethanol. The system is now repeatedly flushed with an inert gas such as argon. Since the whole medium is gaseous, the inter capillary ethanol is completely exchanged with the inert gas, resulting in the formation of a dry gel at (P_2 , T_2), held under argon. The pressure is then gradually brought down to P_1 and the temperature is returned to T_1. The resulting dry gel has a high porosity of ~ 99 %, distributed in extremely fine sizes and is known as the silica aerogel, which is an excellent thermal insulator and also a catalyst support.

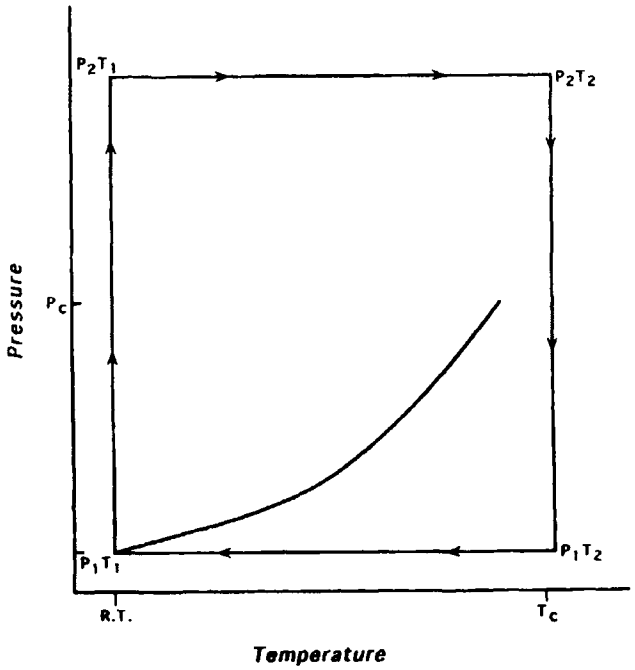

Figure 2.04: Pressure-temperature diagram for hypercritical drying.

Sol-gel procedure provides a convenient route to make silicophosphate glasses which are otherwise difficult to make. P_2O_5 can be introduced as phosphoric acid during gelation. Modifiers such as Na_2O can also be introduced as hydroxides. Transition elements can be introduced into the gel as nitrates and B_2O_3 as boric acid. The sol-gel process has the disadvantage of being very slow and in the absence of catalyst, formation of silica gel can take up to 1000 hours. Formation of monolith bodies is also very difficult. But it is a low temperature process providing a method of building continuous 3-dimensional structure of otherwise difficult systems.

The amorphous state, therefore, can be arrived at by methods other than melting and quenching and all such methods result in the loss of crystalline order. All these processes introduce additional enthalpy into the disordered material. Therefore amorphous materials crystallize irreversibly when heated to a temperature, T_{cr} below T_m of the parent crystalline material and the process is exothermic. The free energy of the amorphous state of a material is higher than that of its crystalline state. Thus the enthalpy addition (ΔH) during amorphization has to be generally

higher than the decrease in free energy caused by the entropy term introduced by the disorder. If G_A, H_A and S_A are the free energy, enthalpy and entropy respectively of the amorphous state and G_C, H_C and S_C are the corresponding quantities for the crystalline state, then the requirement that G_A be greater than G_C can be expressed as follows: $G_A > G_C$ or $(H_A - TS_A) > (H_C - TS_C)$. Therefore, $(H_A - H_C) > T(S_A - S_C)$.

When cooled through the difficult zone of Figure 2.02, and the melt crosses the lower border S (broken line), it becomes a glass at T_g. In fact, the entire supercooled region between T_m and T_g is thermodynamically metastable. The procedure of quenching generally does not allow the material to equilibrate even in the metastable region between S and T_g. Of course we should recognize that the region between S and T_g can be very small in many materials. Many glassy alloys indeed crystallize before they arrive at T_g which means that the boundary S is located even below a hypothetical T_g. However in the case of glasses where S and T_g are well separated, reheating the material to temperatures between S and T_g enable equilibration of metastable liquid structure.

Chemical nature of glass forming materials

Glass formation occurs in materials of all chemical types; covalent, ionic, molecular, metallic and hydrogen bonded materials. Glasses have been made from elements, simple chemical compounds, complex organic molecules, salt mixtures and alloys. There is no particularly advantageous way of grouping glass forming materials. Examples of variety of glass forming materials are listed in Table 2.1.

The considerations discussed above regarding glass formation give an impression that the key factor in the preparation of glasses is just how fast the melt can be quenched. Implied in such an approach is that once the material is quenched into solid state the disorder is frozen and reorganization required for crystallization is impossible in the solid state. We will see later that metallic glasses, which can be modelled as amorphous assemblies of spheres of equal size, are found to be stable in glassy state only when metalloids are present in them or when there are at least two different elements. Thus their stabilities require either a directional character of bonding or size asymmetries of constituent atoms. Therefore the role of quenching rate cannot be overstated and made to appear as the sole determining factor in glass formation. There are other factors which influence glass formation, notably the structural aspects of glass forming materials.

Table 2.1: Examples of glass forming systems (Doremus, 1973)

Types	Examples
Elements	S, Se, Te (?), P
Oxides	B_2O_3, SiO_2, GeO_2, P_2O_5, As_2O_3, Sb_2O_3, In_2O_3, Tl_2O_3, SnO_2, PbO_2, SeO_2. (glass formers) TeO_2, ScO_2, MoO_3, WO_3, Bi_2O_3, Al_2O_3, V_2O_5, SO_3 etc. (conditional glass formers)
Sulfides	As_2S_3, Sb_2S_3 and various sulfides of B, Ga, In, Te, Ge, Sn, N, P, Bi. CS_2, Li_2S-B_2S_3, P_2S_5-Li_2S etc.
Selenides	Various selenides of Tl, Sn, Pb, As, Sb, Bi, Si, P
Tellurides	Various tellurides of Tl, Sn, Pb, As, Sb, Bi, Ge
Halides	BeF_2, AlF_3, $ZnCl_2$, Ag(Cl, Br, I), Pb(Cl_2, Br_2, I_2), and multi-component mixtures.
Nitrates	KNO_3-$Ca(NO_3)_2$ and many other binary mixtures containing alkali and alkaline earth nitrates.
Sulfates	$KHSO_4$, K_2SO_4-$ZnSO_4$-Na_2SO_4 and other binary and ternary mixtures.
Carbonates	K_2CO_3-$MgCO_3$
Simple organic compounds	o-terphenyl, toluene, 3-methyl hexane, 2,3-dimethyl ketone, diethyl ether, isobutyl bromide, ethylene glycol, methyl alcohol, ethyl alcohol, glycerol, glucose. As droplets only: m-xylene, cyclopentane, n-heptane, methylene chloride.
Polymeric organic compounds	Polyethylene (- CH_2 -) and many others.
Aqueous solutions	Acids, bases, chlorides, nitrates and others.
Metallic alloys	Au_4Si, Pd_4Si, $Te_xCu_{25}Au_5$

Structural approach to glass formation

The earliest effort to relate glass formation to the structure was made by Goldschmidt (1926) who recognized the importance of radius ratios in simple glass forming oxides. He pointed out that in all glass forming oxides then known, r_c/r_o is 0.2 - 0.4, where r_c and r_o are the ionic radii of the cation and the anion respectively. This value of r_c/r_o is also the ratio found in oxides where the cation is coordinated to four oxygens because the tetrahedral hole has a radius equal to 0.225 times the radius of the surrounding atoms. The observed glass formation in SiO_2 and GeO_2 support Goldschmidt's approach. Although lacking in appreciation of the bonding type and treating all oxides as purely ionic, Goldschmidt's views spurred on further work by Zachariasen (1932) who formulated the famous rules for glass formation now bearing his name. The small radius ratio implies low coordination number. The requirement that the structures should be disordered in glasses suggests that open structures are more likely to give rise to such disorder, because the coordination polyhedra need not share edges and faces. Edge and face sharing induces crystalline order. Further, Zachariasen argued that the energies of the glassy and crystalline states of the glass forming oxides should not be very different since the mechanical properties are similar in the two states. Also if the energy of the glass is very much higher, it may induce crystallization. Thus Zachariasen formulated his thoughts as rules for glass formation, which are as follows. In a glass forming oxide of the formula A_mO_n,

(1) Oxygen atom may be linked to no more than two A atoms.
(2) The number of oxygen atoms surrounding A atoms must be small.
(3) The oxygen polyhedra share only corners with each other, neither edges nor faces.
(4) At least three corners in each polyhedron must be shared.

These rules emphasize the presence of the same type of oxygen polyhedra of low coordination number to be present in both crystalline and glassy states (similar energies). The loss of crystalline order is visualized as due to variation of A-O-A bond angles. Thus it leads to the formation of a random network of oxygen polyhedra. By contrast, in highly ionic materials the cohesive energy is largely due to the Madelung term and the long range coulombic interactions force edge and face sharing of the oxygen polyhedra. Therefore, highly ionic compounds are not good glass formers. MgO, Al_2O_3 or TiO_2 are examples of this type. In the case of B_2O_3 and SiO_2, Zachariasen's rules are well obeyed. While BO_3 is triangular, SiO_4 is tetrahedral; the bonding is significantly covalent and the

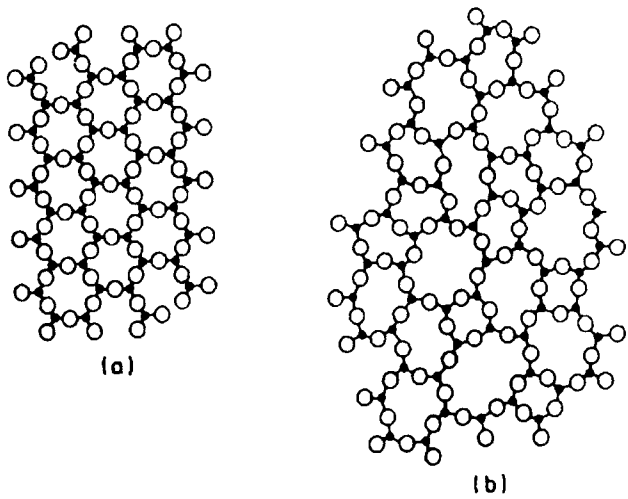

Figure 2.05: Structural representation of (a) A_2O_3 crystal and (b) A_2O_3 glass.

building of corner shared structure becomes easy. The crystalline and the glassy structures are schematically represented for an oxide A_2O_3 in Figure 2.05. Therefore, Zachariasen's model defines a glass as an extended network of corner sharing oxygen polyhedra which lacks periodicity and whose energy is comparable to that of the corresponding ordered crystalline network.

Glass forming range of oxides like B_2O_3, SiO_2 and P_2O_5 can be extended by the addition of alkali oxides. In a chemical sense this leads to a network "modification" which will be discussed later. When the glass is modified, polyhedra cannot share all corners. Therefore, it reveals that not all the corners of oxygen polyhedra are required to be shared. The third Zachariasen rule is strictly redundant in view of rule (1). In order to accommodate these observations, a modified version of Zachariasen rules have been formulated which can be stated as follows.

(1) A high proportion of (network forming) cations are surrounded by oxygen tetrahedra or triangles.
(2) The oxygen polyhedra only share corners with each other.
(3) Some oxygen atoms are linked to only two cations, and do not form additional bonds with any other cations.

Modification can be understood as follows. SiO_2 can be considered as forming three dimensional network of tetrahedral $[SiO_{4/2}]^0$ units. All the four oxygens in SiO_4 tetrahedra are shared and therefore the unit as such is

neutral (SiO_2 unit) and superscript '0' indicates the charge. This unit is represented as

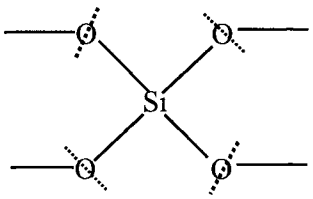

The dotted line across O is to indicate that it is shared between tetrahedra. The dotted line is often not indicated but understood. The glass therefore contains Si-O-Si linkages. When a highly ionic oxide like Na_2O ($2Na^+ + O^{2-}$) is added to SiO_2, the following reaction occurs.

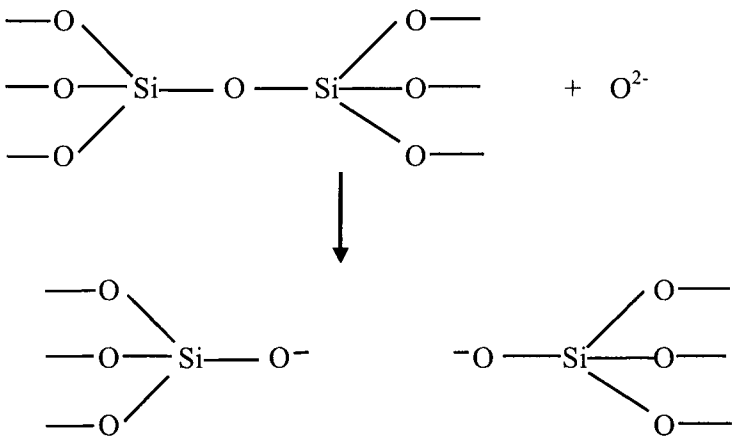

This is succinctly written as

$$2[SiO_{4/2}]^0 + Na_2O \rightarrow 2[SiO_{3/2}O]^- + 2Na^+$$

The effect of Na_2O is to 'break' the Si-O-Si linkage and form $Si\text{-}O^-$ terminations; the oxygen bridge in the structure is broken. Thus the structure is 'depolymerised' or 'modified'. The oxygen in the Si-O-Si linkage is known as a 'bridging oxygen' or 'BO' and oxygen in $Si\text{-}O^-$ is known as 'non-bridging oxygen' or 'NBO'. The ionic oxide, Na_2O, which brought about the NBO→BO conversion, is known as a network 'modifier'. SiO_2 itself is referred to as a 'network glass former' or simply as a 'network former'.

Continuous random network model

The 3-dimensional network formed by SiO_2 glass itself is extensive and therefore 'continuous'. It is lacking in periodicity and therefore 'random'. Hence it is known as a 'continuous random network' or 'crn'. crn can be two dimensional as in A_2O_3. Due to the A-O-A angle flexibility the network can fold, surround itself and expand in all the three directions. Typical of them is B_2O_3. The crn model for glasses is based on Zachariasen's well founded observations on covalent oxides. Evidently crn cannot be expected to explain glass formation observed in highly ionic materials or metal alloys. No such corner sharing oxygen polyhedra can be visualized in a $x Ca(NO_3)_2 \cdot (1-x)KNO_3$ glass.

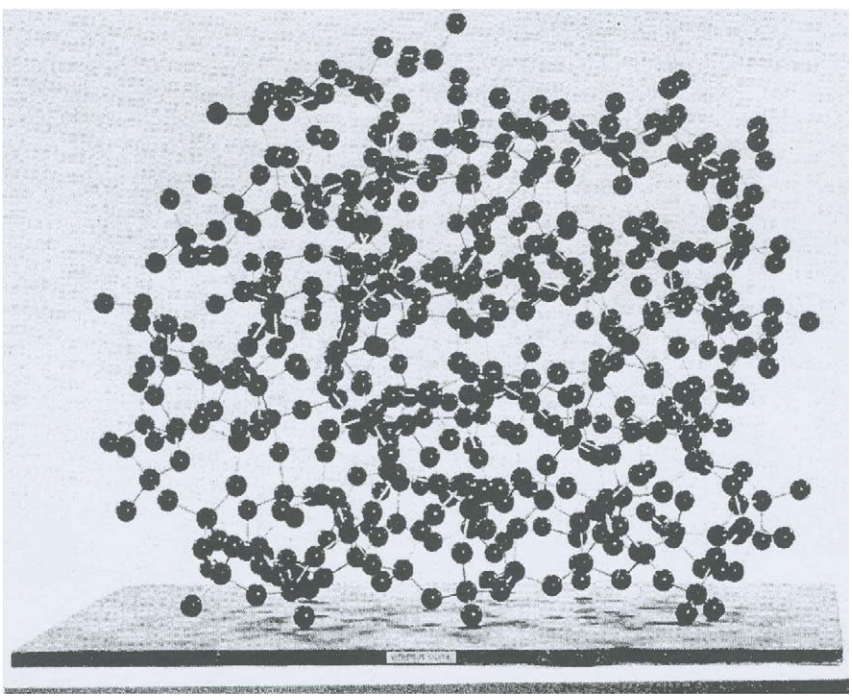

Figure 2.06: Continuous random network model simulating the structure of amorphous SiO_2 (After Bell and Dean, 1966).

Further the Zachariasen requirement that energy difference between crystalline and amorphous phases of a glass forming oxide should not be very high, has also been proved to be incorrect. In the case of the archetypal SiO_2 glass, crn model (Figure 2.06) has been found to be

consistent with the results of careful X-ray diffraction studies (Figure 2.07), (Jeanloz and Williams, 1991, Gaskell et al., 1983, Colmenero and Alegna, 1990, Soules, 1985, Verrall et al., 1988).

An alternate structural model is based on considering glasses as an assembly of ultra micro crystals, no more than a few angstroms in size and separated by amorphous layers. In fact, it was argued that the radial distribution functions (RDF) (discussed later) obtained from XRD of silicate and borosilicate glasses correspond to the weighted sums of the RDF of the fine particles of component oxides. This model is now known to be incorrect. But the view that the glass structure may correspond to an assembly of ultra-microcrystalline (or highly ordered) regions has continued to receive active consideration in glass science.

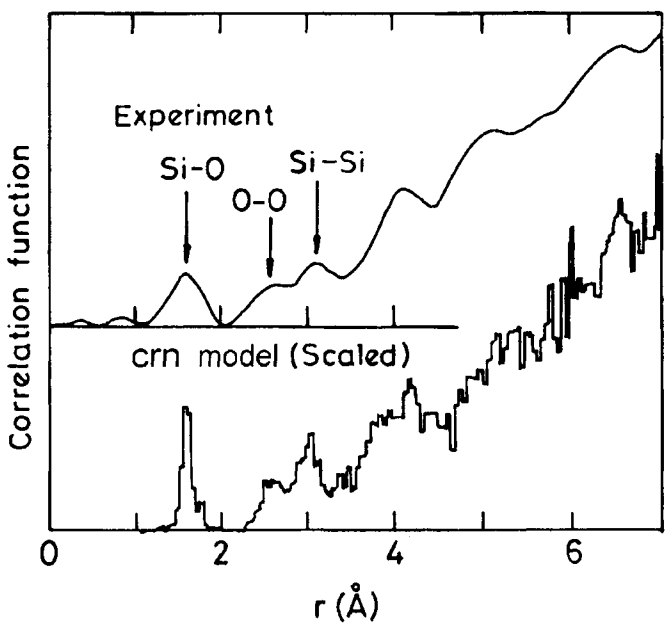

Figure 2.07: Comparison of experimental x-ray RDF for fused silica and that measured for the Bell and Dean model. (After Bell and Dean, 1966)

The primary polyhedral unit remains the same in glass as in its crystalline phase in the crn model. This defines a local or short range configuration with a length scale defined by the first neighbour distance. This is referred to as 'short range order' or 'SRO'. Building of model structures reveals that the second neighbours, or sometimes even more distant neighbours, may also have to be located at fixed distances and in

fixed geometries unless the bond angles and bond lengths are not severely distorted. Such distortions lead to very high disturbances of local energies and are unlikely to be present. Extension of bond lengths and bond angles within reasonable limits in combination with rotation around single bonds lead to complete loss of periodicity over long distances. The length scale over which a reasonable semblance to some positional ordering is still retained defines, what is known as 'intermediate range order (IRO)' or 'medium range order or MRO'. Positional ordering over long distances is known as 'long range order or LRO' and is a characteristic of a crystalline state. Its absence defines the glassy state.

A quantitative description of crn is not accomplished when only the primary polyhedral unit is described. The connectivities of these polyhedra in the glass define closed paths along the bonds which are called rings. In an oxide like SiO_2, starting from Si, the smallest ring can be constituted with 4 Si-O bonds. Evidently such rings will not be favoured because Si-O-Si angle of 90° is a severe distortion from tetrahedral 109°28′ present in $[SiO_{4/2}]$ units. Similarly, very large rings containing 12 or more Si-O links may also not be favoured because it reduces cohesive energy. Therefore there is a predominance of rings consisting of 6, 8 or 10 Si-O bonds. There cannot be rings with odd number of bonds because it would imply Si-Si or O-O bonds, which are again energetically highly unfavourable. The statistics of the distribution of ring sizes present in a crn is required for a more quantitative description of the glass structure. We may note that the Si-O-Si bond angle distribution (Mozzi and Warren, 1969) and the distribution of Si-O-Si-O dihedral angles are also determined by the ring statistics.

Another successful demonstration of the applicability of crn to amorphous structures is provided by *a*-Si (also of *a*-Ge). *a*-Si is not a glass in the sense we have defined. Important properties of *a*-Si are discussed later. It is obtained in its hydrogenated form (*a*-Si:H) using chemical vapour deposition (CVD) techniques. A crn model of this was built by Polk (1971) starting with 4-coordinated Si atoms. The RDFs of *a*-Si obtained experimentally using XRD and calculated from crn model are shown in Figure 2.08. Remarkable agreement of the main features in the RDF shows that a truly amorphous structure can be built with modest deviations from bond angles. There are defects in *a*-Si lattice in the form of open unconnected bonds, also known as the dangling bonds or broken bonds and they are saturated with hydrogen. The experimental RDF of *a*-Si:H and that of a mosaic of very small crystallites of silicon were also found to be clearly in disagreement.

It may be appropriate to note here that model building is an integral part of research in glasses. Models can be built by hand or using a

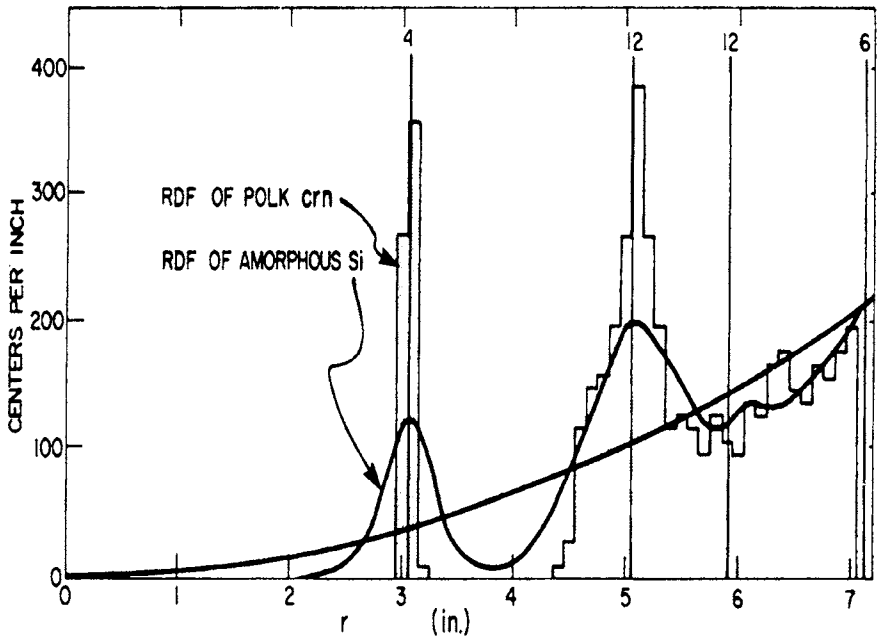

Figure 2.08: Early test of Polk model (1971) via a comparison of its distribution function with that of amorphous silicon.

computer. Hand built models such as those of Bell and Dean (1966) for SiO_2, Polk (1971) for *a*-Si, Greaves and Davis (1974) for amorphous As, etc. are quite revealing. In the hand built models a predetermined distribution of bond angles is used and any bias during the course of building the model is carefully avoided. The coordinates of all the atoms from a chosen origin are then collected and the atomic connectivities catalogued. When suitable potentials of inter-atomic interactions are available, it is possible to minimize the energies of the model structure by relaxing the coordinates and the bond angles. Since the bond distances do not vary much, the bond angle distribution can be iteratively optimised to obtain a good fit with the experimental RDF. crn model represents an ideal amorphous structure since defects such as dangling bonds and voids are completely avoided. The models generally yield high density structures. Approximate crn suitable for representing the structure of one glass can often be generated from that of the other. The method is known as "decoration technique". An example of this is shown in Figure 2.09. In

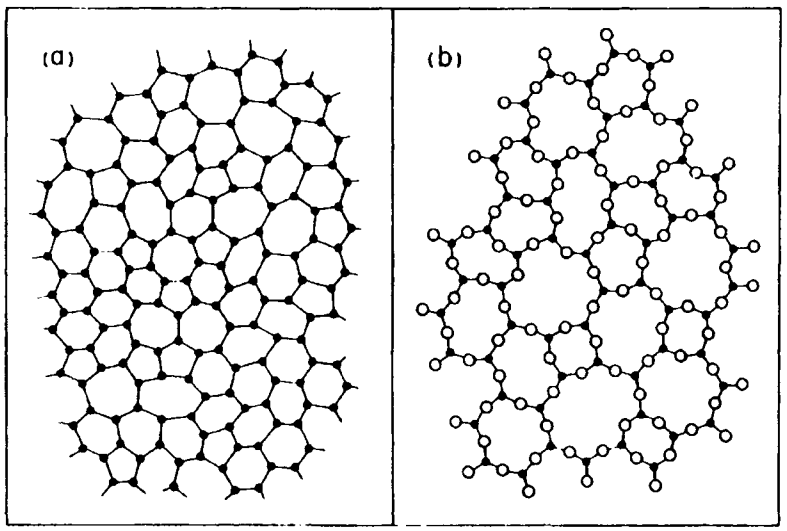

Figure 2.09: (left) random network of amorphous Si; (right) random structure of SiO_2, generated using decoration technique.

3-dimensions, for example one can construct the crn for SiO_2 from the crn of Si by introducing oxygen on every Si-Si bond.

Exceptions to Zachariasen's model should not be overlooked. Although in oxides, oxygen appears to be strictly two coordinated and therefore the polyhedra are corner connected, it is not quite essential for glass formation. In $GeSe_2$ which is similar to SiO_2 (or GeO_2) and in B_2S_3 which is similar to B_2O_3, there is extensive edge sharing of the polyhedra. This not only reduces the dimensionality of the network, but facilitates loss of LRO. Therefore Zachariasen's rules for glass formation are largely inapplicable for non-oxide glasses. Nevertheless, crn, which is based on Zachariasen's rules still provides a clear visualization of the topological disorder in network forming glasses. The distribution in bond angles leads to a distribution in the ring sizes. In turn, the distributions, alter completely the local connectivities and hence the *topological disorder*. We may note that there is another type of disorder known as *chemical disorder* in which SRO itself is altered because of the presence of like atoms in the first coordination. For example in the stoichiometric SiO_2, there are only $[SiO_{4/2}]^0$ tetrahedral units. Each silicon is coordinated to 4 oxygen atoms and each oxygen to two silicon atoms. This is the chemical ordering. But in SiO_x where $1 \leq x \leq 2$, there is evidence for the formation of Si-Si bonds because there are not enough oxygens in the structure. Therefore the SRO

in SiO_x consists of $[SiO_{3/2}Si_{1/4}]^0$, $[SiO_{2/2}Si_{2/4}]^0$ etc. units which are randomly distributed in the structure. The like atom bonding is even more prevalent in chalcogenide glasses and will be discussed later. The presence of both, like atom bonds and unlike atom bonds together constitutes chemical disorder. Therefore a topologically disordered material may not have a chemical disorder but a chemical disorder generally implies a topological disorder.

Random close packing model

One of the requirements to apply crn model is that the glass forming compound must have strong and highly covalent directional bonds. But a number of glasses do not satisfy this requirement. Their cohesive energies are mainly due to non-directional bonding such as ionic, metallic or van der Waals and crn model would be unsuitable for them. Metallic glasses which are obtained by rapid quenching from their melts require a different structural model known as 'random close packing', rcp, (of spheres) model. This was developed in the historic work of Bernal and co-workers (1959, 1964). Briefly rcp model is as follows.

It is well known in crystallography that spheres of equal size can be packed in two close packing arrays namely cubic close packing (ccp) and hexagonal close packing (hcp). Both types of close packing give rise to the most efficient manner of filling space, with packing efficiency of 0.74. In both ccp and hcp, close packed layers of spheres are laid one above the other. In face centred ccp (also known as face centred cubic close packing, fcc), the layers are stacked one above the other in the sequence ABCABC... In hcp, the stacking is as ABAB... In the layer itself each sphere is coordinated to 6 atoms but in the 3-D structure each sphere is coordinated to 12 others. The voids in the structure have regular geometries; they are either tetrahedral or octahedral. They are so designated because when the centres of the voids are connected to the centres of surrounding spheres, they form a tetrahedron or an octahedron. The number of tetrahedral and octahedral voids present in an assembly of N spheres is equal to 2N and N respectively (N being sufficiently large). Crystal structures of a large number of metals in the Periodic Table correspond to one of these two packing geometries.

If instead of carefully laying the layers one above the other, the spheres are simply packed into an odd shaped container, the process is known as 'random close packing' or 'rcp'. The requirement of odd shape of the container is to prevent any deliberate introduction (nucleation) of

ordered arrangements at the container surface. The rcp is distinct from ccp (and hcp) in several ways. The efficiency of packing reduces to 0.60- 0.63 compared to 0.74 in ccp and hcp. There is a distribution of coordination numbers and the average is 14.25 compared to 12 in ccp and hcp. The voids all become irregular in geometry. More importantly in the rcp assembly, most of the voids have (irregular) tetrahedral geometries. There are four other geometries of the voids but the total number of such voids put together (~0.1N) is much lower than the number of tetrahedral voids (~2.9 N) in the rcp structure. Together the five different types of voids are known as Bernal's canonical holes and are shown in Figure 2.10.

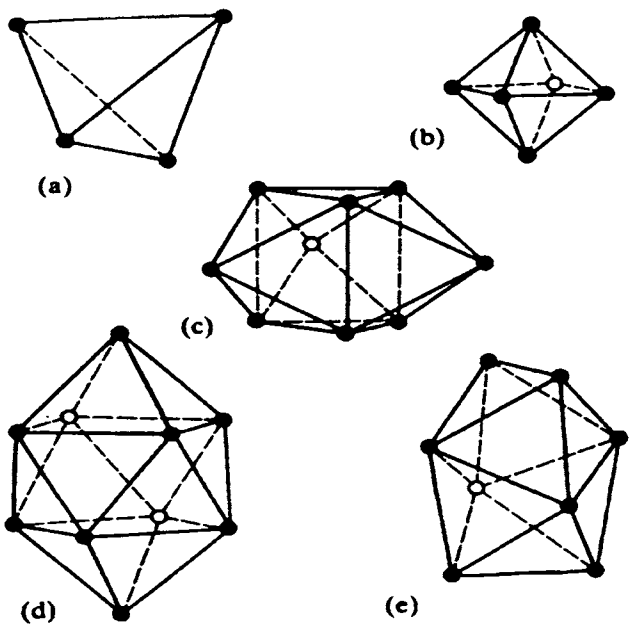

Figure 2.10: The 'canonical holes' of Bernal (1964). They are; (a) tetrahedron; (b) octahedron (often present as half-octahedra); (c) trigonal prism (shown capped with three half-octahedra); (d) Archimedian anti-prism (shown capped with two half-octahedra); (e) tetragonal dodecahedron.

Like in the ball and stick models of crn, in the rcp model also the positional coordinates of spheres in the assembly are carefully determined. Space filling polyhedra can be built around each sphere in the assembly, in the manner of building Wigner-Seitz cell in a reciprocal lattice; that is, by erecting perpendicular planes at the mid points of the lines connecting the

centre of a given atom to the centres of its nearest neighbours. Such polyhedra are evidently not identical and they are known as *Voronoi polyhedra*. The average number of faces of these polyhedra is equal to the average coordination number (14.25). The interesting feature is that a very large number of faces of Voronoi polyhedra are pentagonal. The appearance of five fold symmetry of the pentagon is the hallmark of noncrystalline geometries. It is not rare to find pentagonal dodecahedra in such random assemblies. It is of historical importance to note that two centuries ago, formation of such pentagonal faces was noticed when wet peas were allowed to swell in confinement in tightly closed bottles – analogous to filling space with Voronoi polyhedra. Larger and larger rcp assemblies have been built or computer generated (Finney, 1977). The computer-generated models generally tend to give lower packing efficiencies of 0.61.

rcp model is particularly well suited to describe the structures of metallic glasses because the atoms in simple metallic glasses have approximately the same size and metallic bonding is non-directional. Metallic glasses give rise to RDFs with the specific signature of a split second peak. Shown in Figure 2.11 are the reduced RDFs (see chapter 4) of amorphous $Ni_{76}P_{24}$ which is compared with the predicted RDF from the rcp model. There is a remarkable agreement of RDF features up to 12 Å and there is clear evidence of the split second peak (the sizes of Ni and P atoms being very similar, the rcp model was assumed to be applicable). The split second peak is more clearly shown in Figure 2.12a and it arises because of the presence of two second neighbour distances as shown in Figure 2.12b. The larger of the second neighbour distances gives rise to the lower magnitude peak.

rcp model gives a packing fraction 0.637 when incompressible spheres are packed and it corresponds to the highest density achieved with rcp. This packing is often referred to as 'dense random packing' (drcp or simply drp). In real atomic assemblies, the radii are defined with reference to particular coordination number and crystal structures. The effective radii of atoms and ions are higher for higher coordination numbers. In the literature, rcp corresponding to a packing fraction of 0.60 is referred to as "loose random packing". In metallic glasses also there is almost always the presence of a second metal or metalloid and the metal-metalloid bonding is generally more covalent and introduces directionality. In matching the RDFs of rcp model with the experimental RDFs, the model rcp is subjected to energy minimization, which involves relaxation of the structures using suitable potentials to represent the interactions.

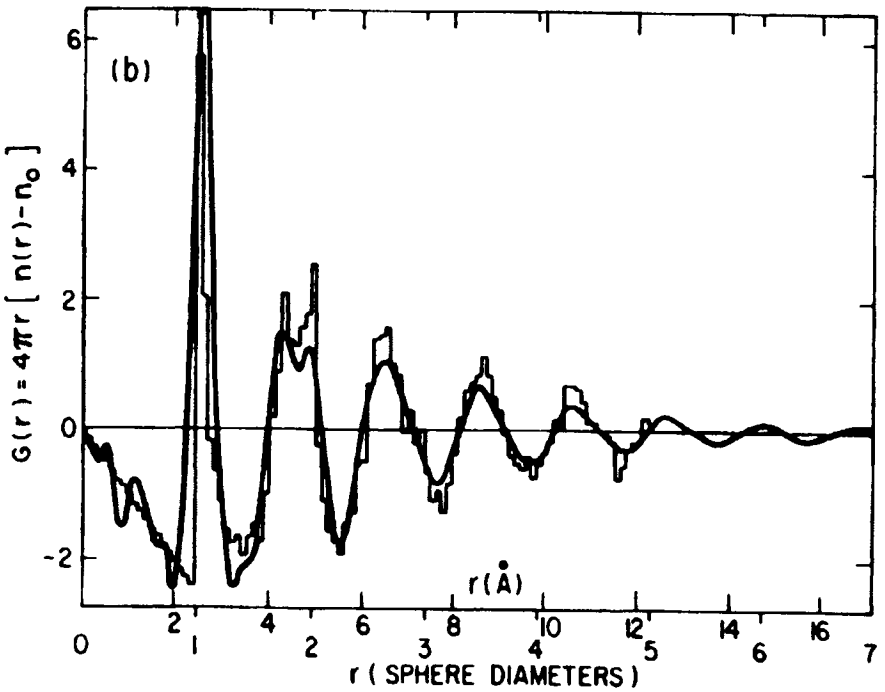

Figure 2.11: Early test of applicability of the RCP structure to amorphous metals. (After Cargill, 1975)

The most popular of the potentials has been the Lennard-Jones (6-12) potential which is of the form,

$$E = -\frac{A}{r_{ij}^{6}} + \frac{B}{r_{ij}^{12}} \qquad (2.02)$$

where E is the energy of interaction, A and B are constants and r_{ij} is the distance between atoms i and j. Since these potentials are soft and enable overlap of the spheres, rcp based on L-J potentials are also referred to as "dense random close packing of soft spheres".

It is possible to extend the rcp model to describe the structure of ionic glasses also provided the anions are large and they constitute most of the volumes. Some oxyanions such as SO_4^{2-} are essentially spherical in shape due to the nature of filled molecular (bonding) orbitals. In K_2SO_4-$ZnSO_4$ glasses the molar volumes can be derived starting with rcp of SO_4^{2-} spheres and with the voids occupied by cations with slight modifications

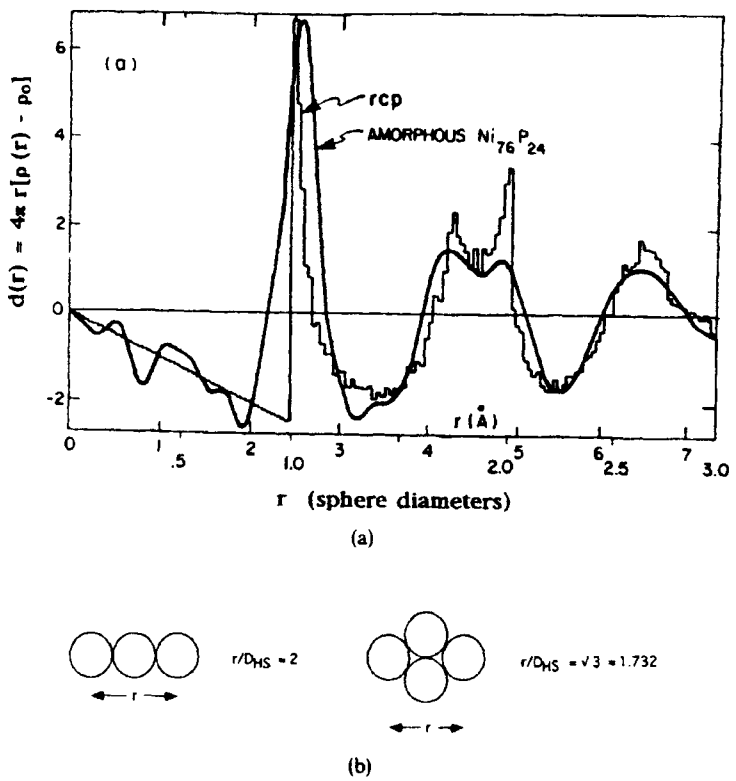

Figure 2.12: (a) Comparison of the differential correlation function for Finney's drp of monosized spheres and the experimental curve for a-$Ni_{76}P_{24}$. (b) the origin of second split peak. D_{HS} is the diameter of the hard sphere. (After Cargill, 1975)

of local structures around Zn^{2+} ions. In many oxide glasses also, oxide ion accounts for almost all the volume and can be considered as being present in an rcp assembly.

The crn and rcp models describe two rather distinct classes of glass structures, but there appears to be a hidden topological relation between them. The holes in rcp, which are entirely tetrahedral can be retained suppressing all the spheres. Tetrahedra may now be connected among themselves. This may require little reorientation of the tetrahedra. Otherwise they may be connected by recognizing the junctions also as atomic positions. In the first approach, one can produce (after scaling the bond lengths), a crn of a-Si or a-Ge. In the second, treating the junctions as oxygen positions, crn of SiO_2 glass can be generated.

Bonding theories

The major weakness of structural approaches is that the nature of bonding (which in principle should determine the structure) is not clearly taken into consideration. In Zachariasen's rules which form the basis of crn, it appears irrelevant whether SiO_2 is ionic or covalent as evident from the listed rules. It was only an interpretational convenience to use ionic model to start with (radius ratio) in Zachariasen's approach, but the resulting crn model is more suited to covalent glass formers. Approaches have been made to relate the nature of bonding in inorganic materials to their glass forming tendencies. Smekel (1951) recognized that mixed ionic and covalent bonding was an essential requirement for glass formation. This is because LRO can be eliminated only when bond lengths and bond angles can vary over a small range unlike in completely covalent compounds. Purely covalent bonding would induce crystalline order. Similarly a completely ionic bonding is also unhelpful because long range potentials induce crystalline order in such materials. Smekel not only attributed glass formation in SiO_2 and B_2O_3 to mixed bonding (polar-covalent), but also in S and Se in which there is mixed covalent and van der Waals bonding. Stanworth (1946, 1948a, b, 1952) introduced an electronegativity criterion, according to which glass formation occurs in oxides, AO_n, if the electronegativity differences between oxygen and A is not very high (equivalently the ionicity of A-O bond is very low). If AO_n is highly ionic, it behaves as a modifier. This leads to the recognition of a few oxides in which covalency is moderately high as intermediate glass formers. The discovery of TeO_2 glasses is based on such consideration. But the electronegativity criterion does not hold rigidly because in Sb_2O_3 electronegativity difference is the same as in SiO_2, but the glass formation is not easy. On the contrary, BeF_2, in which the bond ionicity is 80 %, forms glass easily. Another empirical relation involving bonding was proposed by Winter (1955) who considered that *p* electrons are essential for glass formation. The criterion established by her was that the ratio of the total number of *p* electrons in the constituent atoms to the total number of atoms should be greater than 2. This rule seems to be related to the strength of the metal-oxygen bonds which peaks in each period for the element whose oxide has a known tendency towards glass formation and is very limited in its applicability. The importance of covalent bonding in glass formation was recognized by Myuller who noted that organic polymers which have a completely covalent backbone are good glass formers. Similarly inorganic oxides which are no more than 50 % ionic in

character and non oxide glasses such as sulphides and selenides in which ionic character is no more than 10 % are all good glass formers. The ionicity introduces a tendency towards ordering because of the non-directional character. We may note that ionicity of a bond A-B is calculated using the famous Pauling (1960) formula,

$$I = 1 - \exp\left(-\frac{\Delta\chi^2}{4}\right) \tag{2.03}$$

where $\Delta\chi = \chi_A - \chi_B$ is the difference in the electronegativities of A and B atoms. That there should be a direct connection between bond strength and glass formation was recognized by a number of investigators. A bond energy criterion for glass formation was suggested by Sun (1947). Sun and Huggins (1947) calculated these bond energies as equal to the dissociation energy, E_d, of the oxide. E_d is the energy required to dissociate the oxide into its constituent gaseous atoms. These energies were calculated on a per bond basis which enabled them to group oxides as glass formers, intermediates ("conditional glass formers") and modifiers as shown in Table 2.2. In these calculations a double bond was treated as equivalent to the single bond. The Table contains the coordination numbers, which were used by Sun and Huggins. The criterion is simple: high values of bond strength increases glass forming tendency. Although of some value, this approach cannot be used directly to predict glass formation in a system without a consideration of a various other factors. For example, the difficulty of forming a glass of V_2O_5 which has similar single bond strengths as P_2O_5 or non formation of glass by Al_2O_3 are glaring examples of its failure. Rawson (1956) considered Sun's criterion as only partial. Although when strong bonds are present in a glass forming melt, reorganization of the structure (crystallization) through bond breaking becomes difficult, the temperature of the melt is also important because higher the temperatures, higher is the bond breaking probability. As a reference temperature the crystallization (melting) temperature, T_m, itself is more appropriate to examine the ratio of the specific bond energy to the melting temperature. In Table 2.3, the values of these ratios are given for a number of oxides. An interesting point to note from the Table 2.3 is that this ratio is highest in B_2O_3 which may be one of the reasons why B_2O_3 does not crystallize easily. But Rawson's criterion also does not account for the marked differences between P_2O_5 and V_2O_5 in their glass forming tendencies.

Table 2.2: Calculated bond strengths of oxides. (Sun, 1947).

M in MO_x	Valence	Dissociation energy per MO_x E_d (kcal)]	Co-ordination No.	Single bond strength B_{M-O} (kcal)
Glass formers				
B	3	356	3	119
Si	4	424	4	106
Ge	4	431	4	108
Al	3	402-317	4	101-79
B	3	356	4	89
P	5	442	4	88-111
V	5	449	4	90-112
As	5	349	4	70-87
Sb	5	339	4	68-85
Zr	4	485	6	81
Intermediates				
Ti	4	435	6	73
Zn	2	144	2	72
Pb	2	145	2	73
Al	3	317-402	6	53-67
Th	4	516	8	64
Be	2	250	4	63
Zr	4	485	8	61
Cd	2	119	2	60
Modifiers				
Sc	3	362	6	60
La	3	406	7	58
Y	3	399	8	50
Sn	4	278	6	46
Ga	3	267	6	45
In	3	259	6	43
Th	4	516	12	43
Pb	4	232	6	39
Mg	2	222	6	37
Li	1	144	4	36
Pb	2	145	4	36
Zn	2	144	4	36
Ba	2	260	8	33
Ca	2	257	8	32
Sr	2	256	8	32
Cd	2	119	4	30
Na	1	120	6	20
Cd	2	119	6	20
K	1	115	9	13
Rb	1	115	10	12
Hg	2	68	6	11
Cs	1	114	12	10

Table 2.3: Ratio of single bond strength to melting point (K) for oxides. (Rawson, 1956)

Oxide	Single bond strength B_{M-O} (kcal)	Melting Point, T_m, (K)	B_{M-O}/T_m
B_2O_3	119 or 89	723	0.164 or 0.122
SiO_2	106	1993	0.053
GeO_2	108	1388	0.078
P_2O_5	88-111	843	0.104 - 0.131
V_2O_5	90-112	943	0.095 – 0.119
TiO_2	73	2123	0.034
ZrO_2	81	2923	0.023
MoO_3	92	1068	0.086
WO_3	103	1748	0.059
TeO_2	68	1006	0.067
MgO	37	2913	0.013
CaO	32	2773	0.011
BaO	33	2193	0.015

However an important outcome of Rawson's approach is that it rationalizes glass formation in mixed oxides. Rawson ratio shoots up in the region of eutectic composition because the weighted average bond energies vary roughly linearly but the liquidus temperature dips in the intermediate regions. Glass formation is observed in composition regions surrounding eutectic as shown in Figure 2.13 for the case of $PbO-V_2O_5$. In fact this also explains why V_2O_5 behaves like a conditional glass former.

Thus in general high bond energy and covalency seem to help glass formation. Similarly tendency towards formation of polymeric species also introduces glass formation tendency. This tendency is pronounced when the coordination number of atoms is no less than 2 and no more than 4. With larger coordination as in octahedral species, polymerization is not favored as it requires corner sharing which results in overcrowding and consequent crystallization. In order to rid LRO, which is the primary requirement for glass formation, flexibility of the bond angles is essential. This is possible only when the coordination numbers are low. The appearance of LRO is assisted by long range forces such as coulombic interactions and therefore the ionicity value has to be low. The overall cohesive energy of a compound is always significantly higher

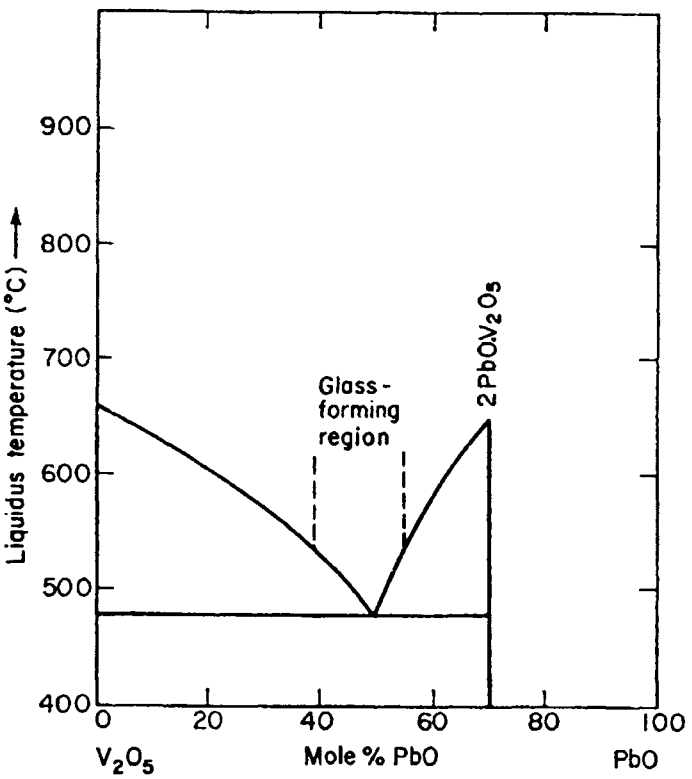

Figure 2.13: The glass-forming region in relation to the phase diagram for the system PbO-V_2O_5 (After Rawson, 1956).

when the bonding is ionic than when it is covalent (Sanderson, 1983). But the advantage in forming the covalent bonds is that the energy is localized between the bonded atoms and therefore does not affect the flexing of bonds away from the site. In cases where the bonding is ionic, its long range positive influence on crystallization can be mitigated by going off the stoichiometric compositions or by increasing the number of ionic species in the compositions. This is because, the melting temperatures are shifted downwards towards the eutectic in the non-stoichiometric compositions and advantage is taken of Rawson's criterion. Also, the fact that at lower temperatures there is an exponential increase in viscosity adversely affects the growth and nucleation kinetics. In a deeper sense it is taking full advantage of the entropy factor to counter the crystallization tendencies. Entropy factor is also directly involved in the formation of organic glasses where asymmetric molecules exhibit a greater tendency

towards vitrification (compare CCl_4 and salol). Therefore a consideration of various aspects of bonding is very vital for understanding glass formation tendencies. After all the nature of bonding determines not only the structure but also the melting temperatures and the rheological properties of the melts, all of which are determinants of glass formation.

A very large number of useful and practical glasses are based on oxides and that too of the oxides of just three or four elements namely Si, P, B and to some extent Al. Al_2O_3 is not a primary glass former but it helps to extend the glass forming regime of SiO_2 by taking up tetrahedral positions. The glasses are all constituted of oxygen bridges. The bridge bonds are formed by the overlap of either p or sp^n ($n<3$) hybridized orbitals of oxygen and are of σ type. The O-M-O bond angle (where M is Si, B or P) is fairly rigid and well defined. It is only the M-O-M bond angle which has a broad distribution and is essential for elimination of LRO. This distribution of bond angles implies a continuous variation of the nature of hybridisation of the oxygen orbitals. When the M-O-M angle is 90° it involves pure p-orbitals on oxygen. The sp^n hybridisation can vary this angle through 109°28′, 120° and 180° (sp^3, sp^2 and sp hybridisations). The energy cost involved in such hybridisation is to some extent recovered by increased overlap of the orbitals. This evidently affects the bond distances also. The more important point is that hybridization is present in all oxide glasses. The nature of M-O-M angle distribution in SiO_2 case is shown in Figure 2.14. The maximum in bond angle distribution occurs at 144° which suggest that there is a preferential hybridisation on oxygen atom between sp and sp^2. The bond angle distribution in B_2O_3 glass is dominated by the presence of boroxol rings (to be discussed later) and the 120° angle makes major contribution. It is interesting to note that in phosphate glasses also the P-O-P angle peaks around 130°. A high value of M-O-M angle means that one or two of the p-orbitals on oxygen are not involved in hybridisation and they carry the lone pair electrons. Boron has a deficiency of electrons (B is from 3rd group of periodic table) and a vacant p-orbital perpendicular to the plane of $BO_{3/2}$. The presence of the lone pair containing p-orbital on oxygen and vacant p-orbital on boron readily gives rise to π-bonding. In fact this causes the B-O bond to shrink from its theoretical length of 1.43 Å to 1.38 Å as measured in BO_3 triangles. It has been estimated that this shrinkage corresponds to about 20 % π-bonding in addition to the σ bond between B and O. In fact Coulson and Dingel (1968) estimated that in metaborate containing B-O-B bridges, the π contribution can be as high as 40 % and in a B-O bond where oxygen is non-bridging it can be as high as 60 %.

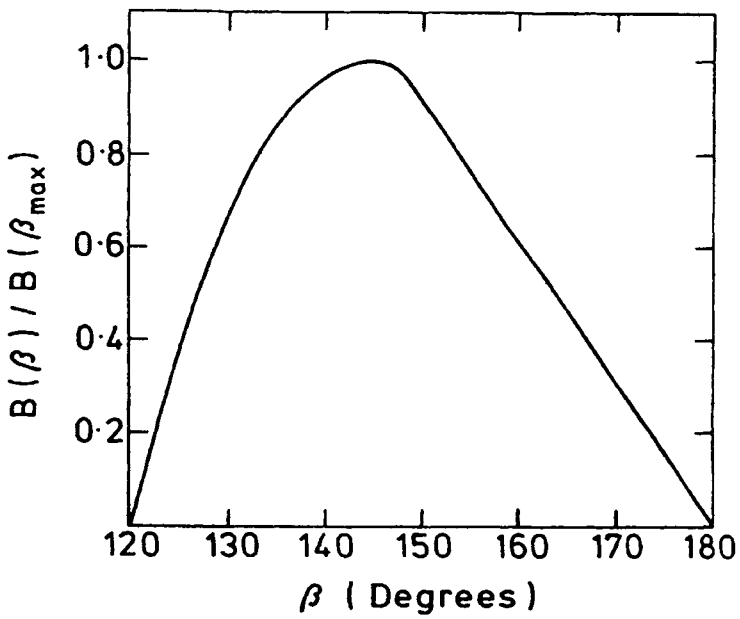

Figure 2.14: The Si-O-Si bond angle distribution (β) for vitreous silica; B is the number count of the angles (After Mozzi and Warren ,1969).

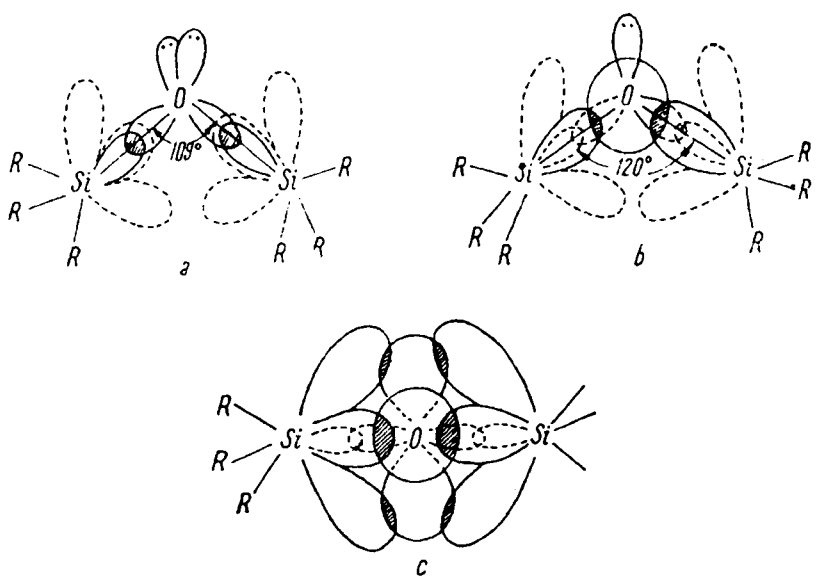

Figure 2.15: Electron configuration of the Si-O-Si oxygen bridge: (a) sp^3 hybridisation; (b) sp^2 hybridisation; (c) sp hybridisation (After Balta and Balta, 1976).

Formation of the boroxol rings, which are planar hexagons containing boron and oxygen, and almost benzene-like, leads to a reported stabilization energy of 11.8 kcal/mole of boroxol units. π-bonding or back bonding occurs in Si-O linkages also. But in silicon, the electrons are accepted into the vacant *d*-orbitals as shown for various geometries in Figure 2.15. The extent of back bonding increases as hybridisation changes from sp^3 to *sp* on oxygen. This type of $d\pi$-$p\pi$ interaction is responsible for the differences in Si-O^- (shorter) and Si-O (longer) bond lengths (Cruikshink,1961).

In modified silicate glasses, the extent to which the $d\pi$-$p\pi$ bonding occurs depends upon the polarizability of the oxygen or the electropositivity of the cation in the modifier oxide. In the case of P_2O_5 and phosphate glasses the easy excitability of one of the three *p* electrons to 3*d* state establishes a full π-bond with one of the coordinating oxygen atoms and this bond is formally represented as P=O and is already shorter than the other P-O bonds in the P-O-P linkages. However $d\pi$-$p\pi$ bonding of the three bridging oxygens with the central phosphorous in phosphate glass is not ruled out. In the orthophosphate ion the nature of bonding and hybridisation is complex, since the bond lengths are equal and the hybridisation is expected to be spd^2. More importantly when the extent of modification is gradually increased and NBOs are created, the P=O and P-O^- gradually become indistinguishable (Brow, 1994). It is often considered that it is due to the delocalisation of π-bond. Therefore we recognize the importance of the nature of bonding which determines both bond lengths and bond angles in a coupled manner and in structural modelling this aspect should not be ignored. Several related bonding aspects are discussed in the chapter on oxide glasses (chapter 12).

Thermal behaviour of glasses

Glass transition, we noted, is the second important characteristic of the glassy state, the presence of which distinguishes glasses from other amorphous materials. Glass transition is recognized as a thermal event, which marks the smooth passage of a glass to the supercooled molten state while heating, or passage of a highly viscous supercooled melt into a solid (glass) while cooling. Glass transition region is marked by changes in several properties of the supercooled melts. In Figure 2.16 variation of volume of a simple glass-forming melt is shown schematically. Also shown is the corresponding behavior of the crystalline phase of the same material through its melting transition.

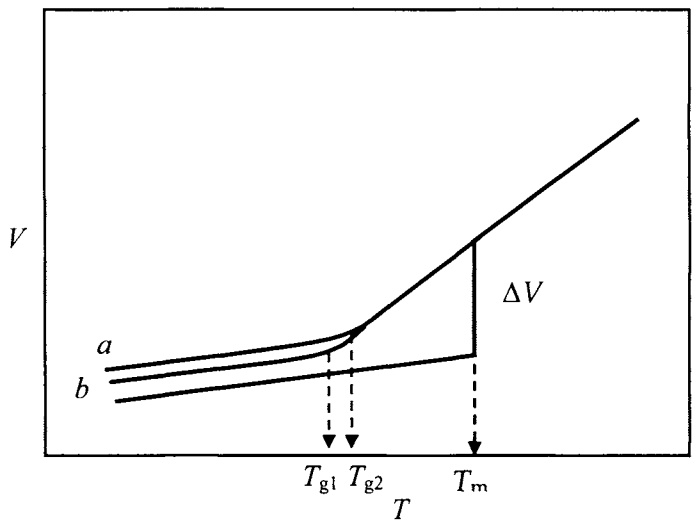

Figure 2.16: Variation of volume of a simple glass forming melt along with that of the crystal. The cooling rate for curve *a* is higher than that for curve *b* (schematic).

Temperatures T_m, T_{g1} and T_{g2}, in Figure 2.16 designate the melting point of the crystalline phase and the glass transition temperatures observed at two different cooling rates. The volume changes discontinuously on melting a crystalline material. The slopes of the variation of volume with temperature above and below T_m are different and is greater for the melt. The slope ($dV/dT = V\alpha$) represents the thermal expansivities. On cooling the melt from above T_m, generally a reverse transformation occurs to the crystalline phase at (in practice slightly below) T_m. In order to form a glass, it is necessary that the melts are supercooled below T_m in a manner that circumvents crystallization in the difficult zone (see Figure 2.02). This is achieved by cooling sufficiently rapidly in the region below T_m and down to low enough temperatures. Volumes of such supercooled melts decrease along the path indicated. Around temperatures marked T_{g1} or T_{g2}, the *rate of shrinkage* of volume with decreasing temperature drops to a lower value more or less suddenly. Hence a bend is observed in the V-T plot. T_{g1} and T_{g2} are referred to as glass transition temperatures. These are temperatures below which the supercooled melt exhibits solid-like properties. We may note here that the rate of cooling Q (= - dT/dt) in the experiment can be varied and in a typical thermal measurement the characteristic time scales could vary from few seconds to a few minutes. The value of T_g (T_{g1} or T_{g2}) depends on Q; generally higher the value of Q, higher the T_g. Well below T_g the

change in volume of the glass is very little. Q for curve a is higher than Q for curve b in Figure 2.16.

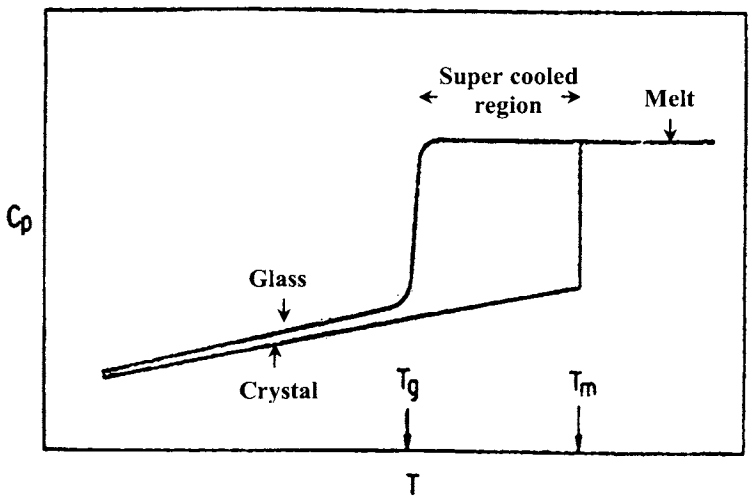

Figure 2.17: Variation of C_P of a glass forming melt and a crystal.

The behavior of entropy and enthalpy of glass-forming melts is very similar. Discrete changes are observed at T_m in both enthalpy (ΔH) and entropy (ΔS) for the crystalline phase, but for the glass, a continuous change occurs at T_g with only a change of slope.

However heat capacity changes abruptly at the glass transition as shown in Figure 2.17. Two features of importance commonly observed in heat capacity plots are a hump on the liquid side of the transition, sometimes referred to as overshoot, and diffuse pre-transition endotherms or exotherms, they are not shown in Figure 2.17 but will be discussed later (chapter 3). $C_P = (\partial H/\partial T)_P$ exhibits a step like change at T_g because there is a change of slope in ΔH vs T at T_g. In fact, the thermal expansivity, α, and volume compressibility, β, also exhibit step-like changes at the glass transition, in a manner similar to heat capacity. The step-like changes in C_P, α and β are due to change of slopes in ΔH, V and S respectively (Figure 2.17) at T_g. Corresponding thermodynamic relations can be derived using Gibbs free energy function. Gibbs free energy change can be expressed in terms of its natural variables P and T as,

$$dG = -SdT + VdP \tag{2.04}$$

The supercooled melt and the glass are in the metastable states, which are well separated from the corresponding crystalline states by large barriers. We may therefore assume that equilibrium thermodynamics can be applied to such metastable states*. Hence the free energy variation of a glass is also represented by equation (2.04) and we may therefore write,

$$\left(\frac{\partial G}{\partial P}\right)_T = V \quad \text{and} \quad \left(\frac{\partial G}{\partial T}\right)_P = -S \tag{2.05}$$

Corresponding second differentials of G are

$$\left(\frac{\partial^2 G}{\partial T^2}\right)_P = -\left(\frac{\partial S}{\partial T}\right)_P = \frac{C_P}{T} \tag{2.06}$$

$$\left(\frac{\partial^2 G}{\partial P^2}\right)_T = \left(\frac{\partial V}{\partial P}\right)_T = -V\beta \tag{2.07}$$

$$\left(\frac{\partial^2 G}{\partial P \partial T}\right) = -\left(\frac{\partial S}{\partial P}\right) = \left(\frac{\partial V}{\partial T}\right) = V\alpha \tag{2.08}$$

Referring to Figure 2.16 and 2.17, we note that at the glass transition the first derivative quantities of the Gibbs free energy (V and S) remain continuous while the second derivative quantities (C_P, α and β) exhibit (apparent) discontinuities. Glass transition, therefore, behave as a second order transition in the Ehrenfest sense (Rao and Rao, 1978). It is often described as a *pseudo second order* transition, since the discontinuities are not sharp and generally spread out over a reasonably broad range of temperature. In fact T_g is often thoughtfully referred to as the 'glass transition range'.

It is even more interesting to examine the variation of a dynamical property like viscosity, η (or fluidity, $\phi = 1/\eta$) as a function of temperature for a glass forming liquid. The behaviour of logarithmic viscosity ($\ln \eta$) as a function of inverse temperature ($1/T$) is shown in Figure 2.18, for a typical glass-forming material like SiO_2 and GeO_2.

* See chapter 9 for additional thermodynamic aspects.

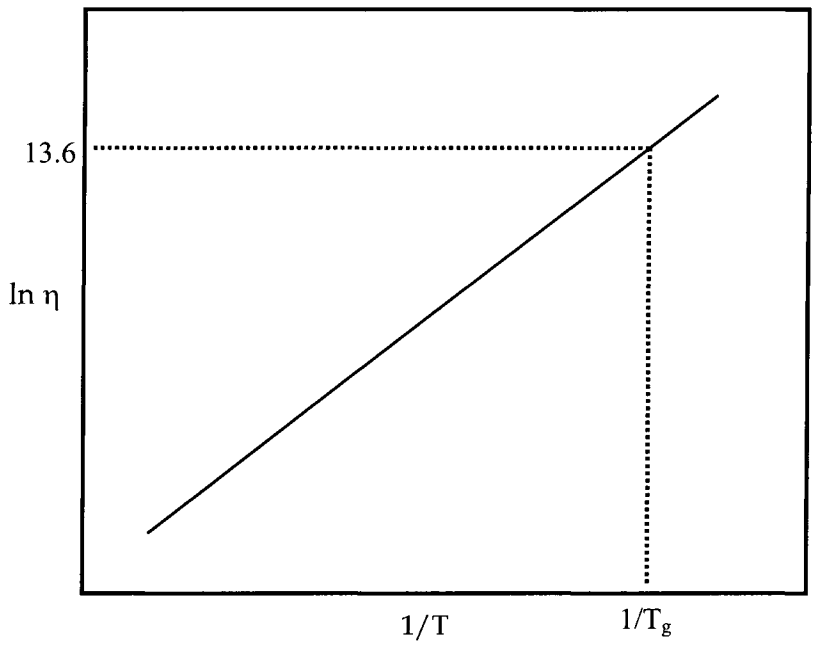

Figure 2.18: Variation of logarithmic viscosity as a function of inverse temperature for a simple glass forming liquid (schematic). η is in Poises.

Figure 2.18 represents an Arrhenius plot and the slope of ln η gives E_η/R, where E_η is the activation energy for viscosity. Since η is the property of only a liquid, there is no comparison made with the crystal. The dotted line drawn horizontally corresponds to the limiting high viscosity of $10^{13.6}$ poises and the vertical dotted line marks $1/T_g$. Glass forming liquids typically undergo several orders of magnitude change in viscosity as they are cooled from above their melting temperatures down to T_g. One can visualize that at such high viscosities, the supercooled liquid is essentially a solid because further structural rearrangements - *relaxation* - cannot occur as the *relaxation times* become very long. The characteristic relaxation time, τ, is related to η, and can be estimated as

$$\tau = \frac{\eta}{G_\infty} \approx \frac{10^{12.6}\ \text{Pa s}}{10^{10}\ \text{Pa}} = 400\ \text{secs.} \qquad (2.09)$$

(1Pa s = 10Poises) G_∞ is the infinite frequency shear modulus, which varies little with temperature compared to η and has a typical value of

10^{10} Pa for a glass at T_g. T_g marked in Figure 2.16 and 2.17 corresponds roughly to these viscosities. The above consideration implies that glass is indeed a supercooled liquid of very high viscosity, in which the relaxation time become much longer compared to the time scales used for the measurement of various physical properties. It is therefore relevant to recognize here an isoviscosity definition of glass transition – glass is a supercooled liquid whose viscosity reaches $10^{13.6}$ poises. However since glass transition is observed using Differential Scanning Calorimetry (DSC) plots, enthalpy relaxation times are more appropriate and it is of the order of 100s at T_g when the heating and cooling rates of 10 K/min is generally employed.

It would be interesting to consider the quantitative change that occurs in the value of entropy as the glass transition is approached from the liquid state. This is accomplished through the use of heat capacity plots shown in Figure 2.19. An illustration of the entropy calculation is also shown as hatched areas for the case of a simple glass-forming liquid. The heat capacities have been plotted as a function of $\ln T$ for the crystal, the glass and the liquid. At T_m, the process of melting adds an entropy $\Delta S_m = (\Delta H_m/T_m)$ to the melt whose heat capacity is C_P^m. During cooling, the melt loses entropy at a higher rate than the crystal because C_P^m (melt) is greater than C_P^c (crystalline). The sudden increase in heat capacity at T_m is because there is a sudden increase in its entropy (ΔS_m=$\Delta H_m/T_m$). This excess entropy of the melt can be assumed to be largely configurational in at least simple glass forming melts. Structure of the melt can be visualized as capable of having several distinguishable configurations for the same value of energy which reflects this entropy. If $\Delta C_p = C_P^m - C_P^c$, then, $\Delta S = \int_{T_g}^{T_m} \Delta C_p d\ln T$, represents the excess entropy lost by the melt as it is cooled from T_m to T_g, (as compared to the crystal). The entropy loss corresponds to the hatched area in the Figure. This entropy loss is still less than ΔS_m. Below T_g, therefore, excess entropy of the glass is equal to $\Delta S_m - \int_{T_g}^{T_m} \Delta C_p d\ln T$. This is the entropy 'frozen' into the glass. At T_g, this entropy retained by the glass can be a substantial fraction of the melting entropy, ΔS_m, particularly in glasses like B_2O_3. But in $60Ca(NO_3)_2 \cdot 40KNO_3$ glass (here after referred to as CKN) the value of frozen entropy is rather small.

If the glass transition were not to occur during cooling, the liquid would continue to lose entropy at the same high rate and a situation would arise when the entropy lost by the supercooled liquid would exceed the melting entropy. Therefore the actual entropy of the supercooled liquid would become lower than that of its crystalline phase. The cross-hatched region to the left of T_g in Figure 2.19 indicates the temperature T_K below which this situation would occur, if the glass transition had not intervened. There is no glass transition known where $T_g \leq T_K$. The fact that such an imminent thermodynamic entropy crisis (particularly in glasses like CKN) is averted by the intervention of a purely kinetic phenomenon, namely exponential increase in viscosity or the relaxation times, is generally referred to as **Kauzmann paradox**. The resolution of this paradox, even to date, is unsatisfactory.

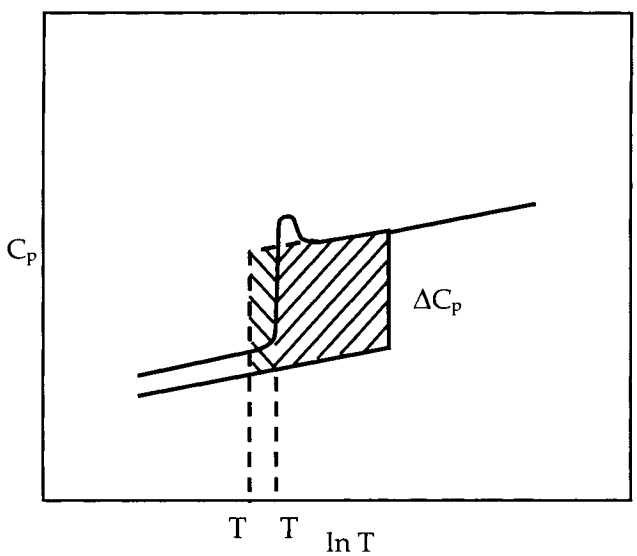

Figure 2.19 : An illustration of entropy calculation. Heat capacity is plotted as a function of logrithmic temperature.

In many examples, particularly in 'fragile glass-forming liquids' discussed in detail in chapter 3, the entropy lost by the time the system arrives at T_g is such a large fraction of ΔS_m that the entropy crisis is imminent in just under 20 K below T_g. Therefore, any suggestion that the remaining entropy may be lost so slowly that T_K becomes equal to 0 K appears impossible. Kauzmann's own resolution of this paradox has been

that at the point of entropy crisis, crystallization would intervene because the nucleation barrier is essentially zero at these temperatures. A more thought-provoking resolution comes from Adam-Gibbs theory of glass transition, discussed later. According to this approach, at T_K where the configurational entropy (S_c) becomes zero, a second order transition occurs and as a result an ideal glass with a unique ground state energy and configuration would form. But the inaccessibility of this transition due to extremely long relaxation times makes it difficult to verify the true nature of either the transition or any other associated changes. Thus a supercooled liquid exhibits continuously increasing viscosity and when it reaches very high values, rearrangement of constituent particles in the liquid cannot occur in experimental time scales. Therefore, it transforms to a glass at a temperature T_g which marks the terminus of the liquid regime.

T_g and experimental time scales

The notion of time scale of the experiment is implied in marking T_{g1} and T_{g2} in Figure 2.16, corresponding respectively to faster (shorter time scale) and slower (longer time scale) rates of quenching. In fact, T_g depends on how slowly one can make a measurement. This is illustrated by the measurement of shear relaxation of a liquid close to T_g. If the ultrasound frequency employed for the measurements is very high, the liquid would exhibit solid-like shear modulus at temperatures significantly higher than the T_g measured in a DSC experiment. This is because in a typical ultrasound experiment at 10 MHz frequency, the experimental time scale is 10^{-7}s, while in a DSC experiment it is 10-100s. It is worthwhile to note here that for many fragile liquids (see later), at the thermally determined glass transition temperatures, the viscosities are still only about 10^{11} poises. Definition of glass transition itself can therefore be imprecise. Polymer literature often recognizes T_g as the temperature at which the heat capacity measured during heating attains half its ultimate value in the transition region. But generally glass transitions are reported as the temperature of intersection of the extended line of glassy heat capacity with the extended linear region of the falling portion of the transitional heat capacity in a DSC thermogram. Glass transition temperatures are perhaps better defined using the plots of property changes obtained during cooling. In Figure 2.20, variation of C_P in the well documented CKN glass is presented. On the cooling cycle, the precipitous drop of heat capacity begins to occur when supercooled melt falls out of equilibrium. The temperature at which it happens is described

as *ergodicity breaking* (EB) temperature because the system cannot access all the available configurational states due to slow kinetics. The EB process becomes complete when the heat capacity drops to values characteristic of a solid i.e., glass. On the heating cycle, the sudden rise is marked by the beginning of the evolution of kinetic freedom which enables the system to access gradually the available configurational states and is defined as the point of *ergodicity making* (EM).

Experimentally a simple differential thermogram (DTA) itself can be used to identify the glass transition. In a DTA thermogram, generally a weak endotherm is observed which, often, may manifest simply as a smeared broad feature. But in a DSC scan, a step-like change in heat capacity is observed. Here again, the step-like change may be sharp or broad with varying magnitudes depending on the nature of the glass itself.

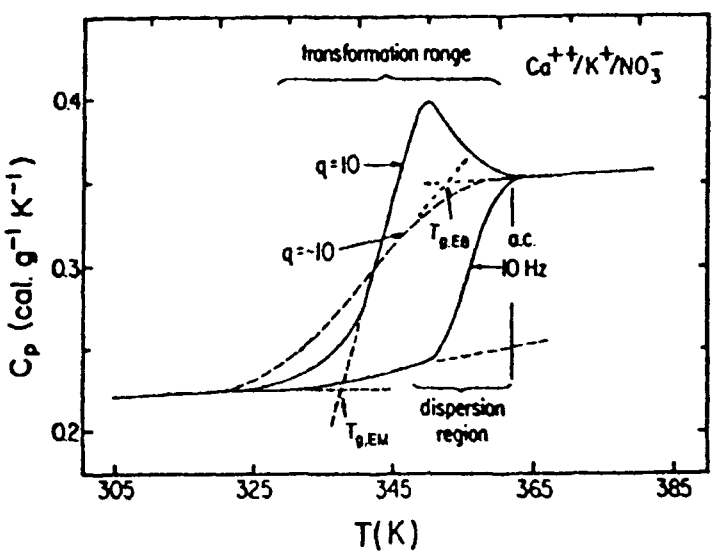

Figure 2.20 C_p as a function of Temperature for CKN glass. q = ln(Q) is the logarithmic cooling rate (After Angell and Torell, 1983).

Since the transition is dependent on the quenching rate, it is dominantly a kinetic event. Therefore T_g can be thought of as a consequence of *Deborah number* becoming unity. *Deborah number* is defined as the ratio of the time scales of the observed and the observer and the glass transition occurs when these time scales become equal. The glass transition temperature, T_g, observed in an experiment depends on the time

scale itself. As noted earlier, in ultrasound experiments, the time scale of the measurement is of the order of micro-seconds. Therefore, T_g manifests as shear modulus dispersion even while the material is in the molten state. But in a heat capacity experiment, where the time scale is of the order of a few seconds and at T_g the material is in the glassy state. Thus T_g can be expressed in terms of rate of change of some characteristic time scale τ determined during cooling. If τ has a simple Arrhenius dependence on temperature, $\tau = \tau_0 \exp[\Delta H/RT]$, then the Deborah number, DN, criterion can be expressed as

$$DN = \frac{d\tau}{dt} = \left(\frac{d\tau}{dt}\right)\left(\frac{dT}{dt}\right) = \left(\frac{\Delta H_{eff}}{RT_g^2}\right) Q_c . \tau \approx 1.0 \qquad (2.10)$$

ΔH_{eff} is the effective activation energy at T_g for the variation of the characteristic time τ. It is governed by the relation, $\Delta H_{eff}/R = [\Delta \ln \tau / \Delta(1/T)]_{Tg}$. Q_c is the cooling rate dT/dt. In many glasses, it has been observed that $\Delta H_{eff}/RT_g^2$ is of the order of unity (0.1 - 1.0 K^{-1}), so that $DN \approx Q_c . \tau$. For a typical cooling rate of 10 K/sec, τ at $T_g \approx$ 10-100 s. Deborah number has been alternately described as Lillie number by Cooper (1982). Although the observed T_g is dependent on the time scale of the experiment, there does not seem to be any size effect on T_g in the sense that nano glass particles (~2nm) obtained by quenching emulsions exhibit T_g values which are the same as those observed in bulk glasses. (Dubochet et al., 1984)

As noted earlier, glass transition can be defined from a rheological point of view as temperature corresponding to $\eta = 10^{13.6}$ Poises. Below this temperature, during the course of formation of bulk glasses, stresses develop in the glass. These stresses can be removed by annealing which is done by heating the glass to a temperature at which its viscosity is about 10^{13}-10^{14} Poises. From the annealing temperature the glass objects are cooled slowly. It may be noted that in order to make the glass stress-free for the Mount Palomar telescope it took eight months of slow programmed cooling. Since working with practical glasses has a long history, several standard temperatures have conventional designations. Thus the 'annealing point' is the temperature at which the viscosity is $10^{13.4}$ Poises and the 'strain point' is defined as the temperature at which viscosity is $10^{7.6}$ Poises. The latter corresponds to a temperature at which the deformation of the glass body due to its own weight becomes noticeable. The 'working point' is the temperature at which viscosity is 10^4 Poises

which is the temperature convenient for manipulating the shapes of glass objects.

Kinetic criteria for glass formation

Melting, is a thermodynamic first order transition and as represented in Figure 2.21a, occurs at the intersection of the free energy curves of the liquid and crystal phases. When a liquid is cooled below T_m and if the cooling rate is not high, crystallization takes place rapidly at some temperature below T_m. Some degree of undercooling is essential (Rao and Rao, 1978). During crystallization, there is a certain rate at which the liquid transforms into the crystal and this is considered to occur through the processes of nucleation and growth (discussed later). The variation of this rate can be represented by a characteristic time τ_{out} (inverse of rate) as shown schematically in Figure 2.21b. Even as τ_{out} is

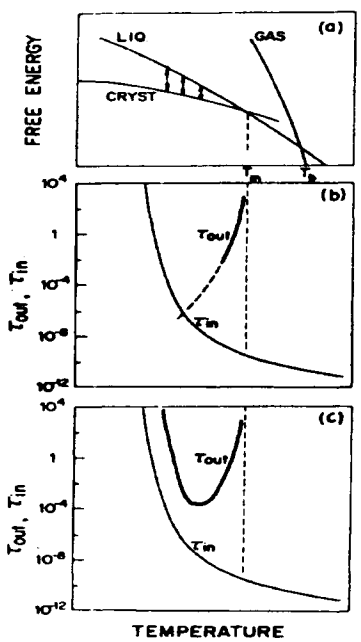

Figure 2.21: (a) Free energy versus temperature curves for gas, liquid and crystalline states of a substance, illustrating build up of thermodynamic driving force for crystallization with increasing supercooling. (b) Variation with temperature of τ_{in} and τ_{out}, for crystallization of a fixed volume fraction. (c) Actual variation of τ_{out} with respect to τ_{in} for a very weakly glass forming liquid. (After Angell, 1988).

becoming shorter, τ_{in} which is the structural relaxation time of the supercooled liquid that keeps the melt from crystallizing, increases due to the increasing viscosity (Angell 1988). This is due to contraction of the liquid volume. At some temperature below T_m, τ_{in} and τ_{out} might both intersect. Below this temperature, if τ_{out} decreases further, there is no stopping of the crystallization. However, τ_{out} arises from a combination of both, nucleation and growth rates, the latter being affected by viscosity in the same manner as τ_{in}. This can lead to a behaviour represented in Figure 2.21c, which shows that τ_{out} turns around with a typical U-shape. For glass formation to occur, it is essential that τ_{in} and τ_{out} do not intersect. However, Figure 2.21 is relevant to distinguish between natural glass formers like B_2O_3 or atactic polymers (2.21b) and other materials (2.21c) which crystallize unless quenched fast. τ_{out} in natural glass formers is rather high and before any crystallization can be observed, τ_{in} increases well above τ_{out}. τ_{out} has to turn around as in Figure 2.21c for a weakly glass forming liquid. It is intuitively clear that this can be achieved by mixing another component, which lowers the melting point and thus squeeze the regime of τ_{out} to a smaller size. Alternately, additives which will increase the viscosity of the system may be used if the melting points cannot be brought down for whatever reasons. In any multi-component glass-forming system, we should expect that both these mechanisms are operative.

T-T-T diagrams

In practice, it is useful to consider the so-called T-T-T diagrams as a guide to glass formation. The three T's in T-T-T are the temperature, time and the transformation respectively. In T-T-T diagrams, points corresponding to fixed extent of transformation are plotted on a temperature-time graph. Shown in Figure 2.22 is the T-T-T diagram of GeO_2 melt studied by Uhlmann and co-workers (1990). The loci of transformation (crystallization) has the shape of a cone with its nose corresponding to minimum time required for crystallization to be observed at temperatures below T_m. (The volume fraction of crystallized material is fixed at 10^{-6} for plotting the C curve). The lines drawn in the Figure represent the cooling rates. The cooling rate, - dT/dt, should be such as to bypass the cone of crystallization in order to enable the supercooled melt to transform into a glass. The tangent drawn to the cone from the melt temperature (from where quenching is done) determines the critical cooling rate, R_c, required for glass formation.

The C-shaped curve is a direct consequence of the factors mentioned in connection with Figure 2.21a. In slow cooling, the undercooling required for the incidence of crystallization is readily satisfied. Consider the case where the cooling line intersects the C-curve as A in Figure 2.22. If during cooling experiment the same constant cooling rate is maintained, the line intersects at the top and the C-curve and again at some lower temperature. Below this second intersection the crystallization stops. Within the region of the C-curve there is partial crystallization.

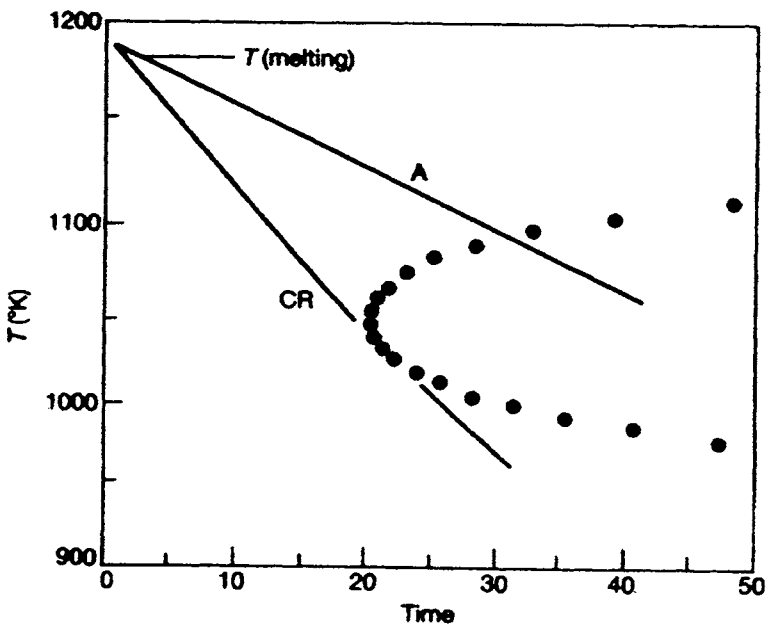

Figure 2.22: T-T-T diagram for GeO_2. The line with the steeper slope gives critical cooling rate for glass formation. A is a slow cooling rate line (After Weinberg et al., 1990).

Crystallization rate studies are used to generate the T-T-T diagrams. This is done by first determining the time required at a given temperature for a given volume fraction of crystallization to occur. Since the lower limit for crystallization, to be observable experimentally, is roughly $\sim 10^{-6}$,(volume/volume), the time required is determined for this limiting value of crystallization. The crystallized fraction, X, is very low and is given by the Avrami-Johnson-Mehl equation (1939, 1940, 1941),

$$X = 1 - \exp\left(\frac{-\pi I U^3 t^4}{3}\right) \approx \frac{\pi I U^3 t^4}{3} \tag{2.11}$$

where I and U are the nucleation and growth rates respectively (these are discussed in the following section) and t is the time. The T-T-T cone corresponds to fixed value of X=10^{-6}. At various temperatures and with reasonable values of parameters entering into I and U, one can evaluate the value of t as $[3X / \pi IU^3]^{1/4}$ and plot the values on a T vs t diagram. The locus of these points represents the transformation (crystallization) to the same extent, namely 10^{-6}. This is the T-T-T diagram, the shape of which is due to the behaviour of I and U in the above expression and most generally it is C-shaped. It is important to note that t is proportional to $(X)^{1/4}$. Therefore, a slight variation in X does not alter the shape of the curve.

In actual experiments, one adopts a continuous cooling rather than the quench-and-hold schedule implied in the above discussion. The so-called continuous cooling curves can be obtained by methods described by Onorato and Uhlmann(1976). Experimentally determined U are used in combination with theoretical nucleation rates in obtaining T-T-T diagrams. Critical cooling rates obtained from such diagrams are quite useful in fixing the quench procedures for making glasses.

Another useful quantity of interest to experimentalists is the evaluation of the maximum thickness of a glass slab obtainable from a melt from the knowledge of T-T-T diagrams. Assuming the critical cooling rate which corresponds to the nose of the C-curve, the maximum thickness, Y, of a slab, which can be made can be calculated as,

$$Y = (D_{TH} . t_N)^{1/2} \tag{2.12}$$

where D_{TH} is the thermal diffusivity and t_N is the time corresponding to the nose of the T-T-T diagram. The basis of this equation is that the thermal diffusivity sets the limit to cooling rates.

A convenient and fast method of determining T-T-T diagrams was described by Angell (1988) and Lucas and Bouaggad (1987) The method is suitable when high temperatures are not required and when only homogeneous nucleation is present. For example, salt solutions like LiCl-H_2O can be dispersed as an emulsion consisting of extremely small particles (micron-sized), in which only homogenous nucleation occurs. In

these experiments, a "quench-nucleate-heat" scheme is followed as shown in Figure 2.23.

The nucleation stage (t_1 in Figure 2.23a) ensures the presence of nuclei, which are then allowed to grow at the temperature of up-quench and give rise to an exotherm of crystallization (as shown in Figure 2.23b). In fact, the stage of temperature down-quench can be dispensed with no substantial loss of information. The peak temperatures in the exotherms of Figure 2.23b for various temperatures of up-quench exhibit a C curve as shown in Figure 2.24 which is a reflection of the behaviour of τ_{out} (τ_{out} of Figure 2.21c rotated by 90° in the clockwise direction).

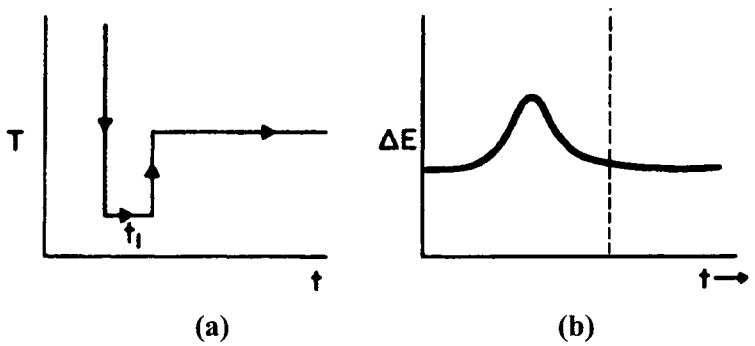

Figure 2.23: A simple scheme to study T-T-T behaviour using DSC experiments (After Angell, 1988).

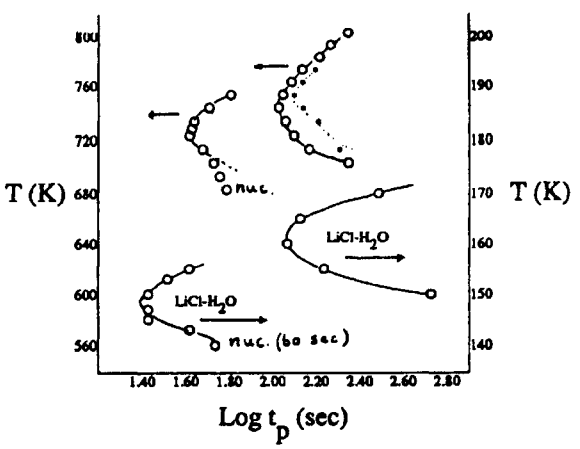

Figure 2.24: The C-curve obtained form the method shown in Figure 2.22 (After Angell, 1988).

The reason for using emulsified samples is to ensure that only homogeneous nucleation takes place, because, when the specimen size is reduced to ~10μ diameter (as is the case with droplets in the emulsion), more than 99% of such droplets do not contain any nucleating heterogeneities. This ensues from the fact that the density of heterogeneities is ~ 20 million/cc and no more. Such DSC studies* for the experimental generation of T-T-T diagrams is, however, not feasible for the more useful high temperature glass systems, particularly those where crystallization may not be associated with large enthalpies.

Critical cooling rate, R_c, can also be obtained on the basis of an empirical correlation between the crystallization onset temperature (T_{cr}) obtained from the exothermic peaks in the DTA curves and the cooling rate, R, employed in the DTA experiment using the relation,

$$\ln R = \ln R_c - \frac{1}{(T_L - T_{cr})^2} \tag{2.13}$$

where T_L is the liquidus temperature. Thus a plot of ln$R$ vs $1/(T_L\text{-}T_{cr})^2$ gives ln(R_c) as the intercept. (Yamane and Asahara, 2000).

Effect of heating and cooling rates on T_g

T_g is affected by heating and cooling rates (Q) employed for their preparation. The variation of T_g as a function of Q (heating rate) has been examined in the case of the, $Pd_{40}Ni_{40}P_{19}Si$ and the B_2O_3 glass by Brüning and Samwer (1992). Variation of ΔC_P (at T_g) for various heating rates and of T_g as a function of log(Q) for the metallic glass are shown in Figures 2.25(a) and (b) respectively. (φ in Figure 2.25 is identical to Q in the text). It is interesting to note that T_g varies as

$$T_g = T_g^0 + A \ln\left(\frac{Q}{Q_0}\right) \tag{2.14}$$

where T_g^0 and Q_0 are obtained from curve fitting to Figure 2.25(b). Although T_g^0 in this curve-fitting is rather arbitrary, it makes a curious suggestion that there exists a T_g^0 corresponding to an infinitely slow

* It has been shown by Angell (1988) that the peak temperature in such DSC experiments corresponds to 45% crystallization.

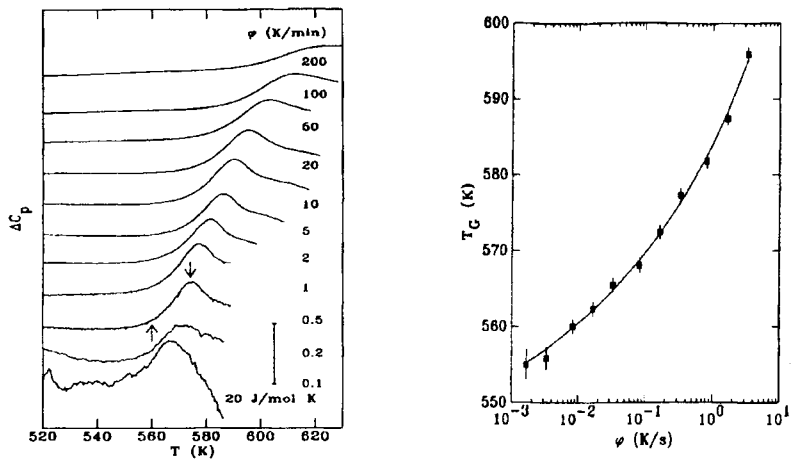

Figure 2.25: (left side) Change of the specific heat at the glass transition of $Pd_{40}Ni_{40}P_{19}Si$ upon heating with rates φ (≡Q) varying between 0.1 and 200 K/min. Before heating the sample was cooled through the glass transition with the rate -φ (≡-Q) (right side). Dependence of the onset of the glass transition in $Pd_{40}Ni_{40}P_{19}Si$ on the logarithm of the heating rate. (After Brüning and Samwer, 1992).

heating rate - rather than a cooling rate from the molten state. For the metallic glass $Pd_{40}Ni_{40}P_{19}Si$, $T_g^0(518 \pm 6K)$ is extremely close to its T_K, the Kauzmann temperature (517 ± 5K). Further, the width of the glass transition ΔT was found to vary linearly with the logarithm of heating rate. This suggests that for ΔT to be zero, the heating rate has to be rather low and at T_g, a sharp transition (rise in ΔC_P) like in an ideal second order transitions should be expected. Below this heating rate, glassy state measurements, including T_g should become independent of Q. In these experiments heating rates adopted were the same as the rates at which the melts were cooled. The experimental observations are very thought provoking particularly in the context of "fragilities" of glass forming liquids which will be discussed in chapter 3 where use is made of ΔT.

The viscosity expression of Richert and Bassler (1990) (see Chapter 3) suggests the presence of a logarithmic relaxation time which varies as $1/T^2$. A relation between experimental glass transition temperatures and quenching rates has been obtained on this basis which is given by,

$$kT_g = 1.07\sigma[-\ln(Qt_0r_0^{-1})]^{-\frac{1}{2}} \qquad (2.15)$$

where t_0 is a reference time (10^{-12} s) representing an elementary jump rate, r_0 is a constant of the order of unity, Q is the quenching rate, and σ is a parameter which characterizes the width of the density of states for the elementary motional process. It is approximately 5 times kT_g. Variation of T_g with log q ($q \equiv Q$) for three different systems is shown in Figure 2.26, which validates the above relation.

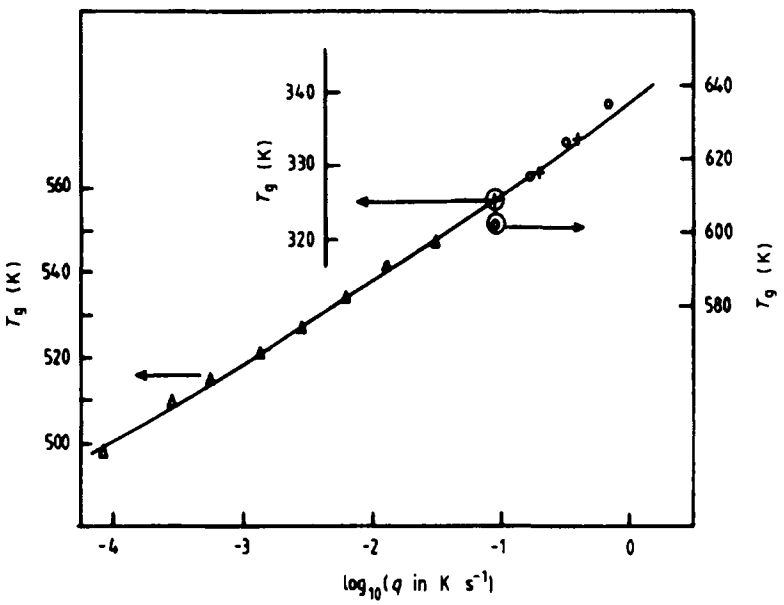

Figure 2.26: Glass transition temperature as a function of cooling rate q. (After Richert and Bassler, 1990).

In the earlier discussion on Deborah number, it was clear that T_g depends on the time scale of the experiment. By the same argument T_g is also dependent on the rate of quenching, because the latter acts as a time scale of the experiment. T_g marks the temperature at which the time scales of Q and of the internal structural relaxation (τ_{in}) are equalized. Therefore T_g is a function of Q.

Constraints model

We now return to a discussion of the relation between structure and glass formation on the basis of more recent developments. We noted earlier in this chapter that two length scales are relevant for a description of the glass structure. They are the short-range order (SRO), which

involves the first (and in some instances second) neighbours and the medium range order (MRO), which extends up to several Angstroms (typically 10-20 Å) in many inorganic glass systems. Phillips (1979) recognized that the SRO in the glass structure should be such that there cannot be too many allowed configurations, which may generate much entropy in view of the Kauzmann condition that the ideal glass cannot have configurational entropy. The simplest approach to account for good glass-forming tendency is to examine if the degrees of freedom available to the constituent atoms are balanced by the constraints present in the short-range structure. This is done very simply. The number of degrees of freedom N_d of an atom in a structure is equal to the dimensionality of the structure itself. N_d=2 for 2-D and 3 for 3-D structures. Constraints arise in a covalently bonded structure as restrictions to their moving out of their positions. In a typical three atom unit, A-B-C, movement of A,B and C are restricted by (a) the stretching modes of A-B and B-C and (b) the bending mode centred on the atom B ($\angle$ABC). In general, a chemical unit consisting of n atoms, where $n = \sum n_i$ and n_i is the number of atoms of ith type and having coordination number m_i (the valency of the covalently bonded atom), can be represented as a pseudo atom with a coordination number m, where

$$m = \frac{\sum (n_i m_i)}{\sum n_i} \tag{2.16}$$

The total number of constraints of a chemical unit can be evaluated as follows. First, we note that there are only two types of constraints in the unit, the stretching and the bending types. The number of stretching constraints of the pseudo atom is equal to $m/2$ since it takes two atoms to stretch and since its coordination number is m (connected to m other pseudo atoms). The bond bending requires the choice of two bonds emanating from the pseudo atom. Therefore, the number of bond bending constraints is equal to $m(m\text{-}1)/2$. Thus the total number of constraints, N_c on the pseudo atom is

$$N_c = \frac{m}{2} + \frac{m(m-1)}{2} = \frac{m^2}{2} \tag{2.17}$$

The degrees of freedom of the pseudo atom are equal to 3 in 3-dimensional structure. The requirement for good glass formation is that

the total number of constraints be equal to degrees of freedom ($N_c = N_d$). Therefore $m^2/2 = 3$ or $m=m_0= 2.45$, where m_0 is the optimal value of m (m_0 has been shown by Thorpe (Thorpe, 1983; He and Thorpe, 1985) to be 2.40 and not 2.44 by more rigorous arguments). For SiO_2, As_2Se_3 and $Ge_{0.16}Se_{0.84}$, the values of m are 2.67, 2.40 and 2.32 respectively. SiO_2 is thus slightly 'over-constrained' while the other two are slightly 'under-constrained' compared to the ideal value. Nevertheless, they are close to m_0 and indeed they are excellent glass-formers. The relation between the difficulty of glass formation and m has been studied in GeSe glasses (Figure 2.27). The least difficult glass forming composition indeed corresponds to m_0. The concept of pseudo atom and the average coordination is somewhat similar to the use of virtual crystal approximation in crystalline solids. The extension of Phillips's ideas in determining average coordination where an atom is connected by a single covalent bond to another in the structure - the terminal atoms in the structure - has also been discussed in the literature.

The constraints model sketched above has a natural extension to it. In network forming multi-component glasses such as 432 (Ge-As-Se) chalcogenide glasses, locally there will be the regions of the structure where the average coordination, $\langle m_l \rangle$ is lower than m_0. Such regions are easily deformable and are described as floppy, under constrained or

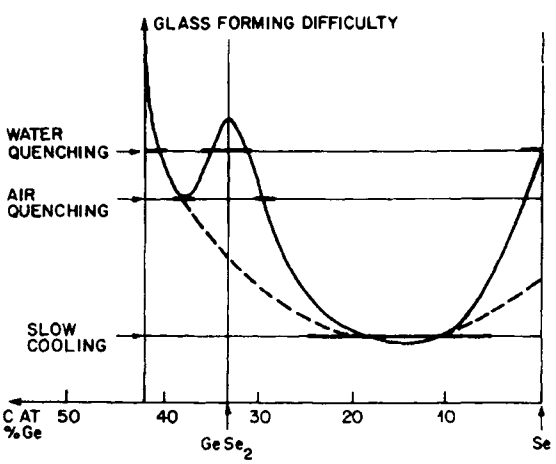

Figure 2.27: The quenching rate (or difficulty of glass formation) is plotted qualitatively as a function of x in Ge_xSe_{1-x} alloys. Experimental data are indicated by solid horizontal bars for various rates of cooling (water, air and slow quenching). The solid line is drawn through the data to guide the eye; the prediction of Phillips's mechanical constraint theory is shown by the dashed line (After Phillips, 1979).

spongy (Thorpe, 1983). Regions where $\langle m_l \rangle > m_0$, are rigid or over-constrained. The presence of floppy and rigid regions in the structure naturally present a percolation problem. A rigid to floppy or floppy to rigid transition is expected at some critical concentration of the floppy regions.

There are further notable consequences of the presence of floppy and rigid regions. To appreciate this, let us consider the vibrational potential energy, V, of a network of N atoms. V can be written as

$$V = \frac{1}{2}\sum_{\langle i,j \rangle} \alpha_{ij} \left(\Delta r_{ij}\right)^2 + \frac{1}{2}\sum_{\langle i,j,k \rangle} \beta_{ijk} \left(\Delta \theta_{ijk}\right)^2 \tag{2.18}$$

The enclosures on ij and ijk indicate that the bonds and bond angles involve only nearest and next nearest neighbours. α_{ij} and β_{ijk} are the stretching and bending force constants and Δr_{ij} and $\Delta\theta_{ijk}$ are small perturbations in bond distance and bond angle respectively. With the above potential function, one can determine the number of vibrational modes. These modes constitute the linearly independent constraints, n_c, and represent the number of eigen vectors of the dynamical matrix corresponding to the above equation. The interesting thing to note is that in under-constrained systems $n_c<3N$ ($3N$ represents the degrees of freedom). The extra degrees of freedom are considered as having zero energy. Therefore there exists $M_0 = 3N\text{-}n_c$ modes, known as zero frequency modes in under-constrained systems. These M_0 modes represent displacements that can be carried out with no cost of energy. These zero frequency modes play an important role in floppy region dynamics. When M_0 tends to zero, rigidity pervades the entire structure. Since M_0 is likely to tend to zero smoothly (for chemical reasons), this transition is referred to as rigidity percolation. The floppy to rigid transition described here is a composition dependent transition, because when the concentration of atoms of higher coordination (like Ge) is increased, $\langle m_l \rangle$ increases. The dynamics may involve use of M_0 modes to re-organize the floppy regions, which may induce crystallization. In the over-constrained regime also, order can get induced which can eventually lead to crystallization.

There have been several reports (Boolchand et al., 1999) on glass-forming liquids to show that a transition from floppy to rigid states as a function of composition is associated with discontinuities in one or the other properties of the system. These experiments include inelastic neutron scattering to characterize the floppy modes, Lamb-Mössbauer factors,

viscosity activation energies, specific heat jumps, Raman vibrational mode frequencies, thermal expansivities, etc. Minima have been observed in ΔC_P values corresponding to floppy-rigid transition. This observation has been thoughtfully analyzed by Senapathi and Varshneya (1995). Since the configurational entropy just above T_g can be considered as

$$S_c = \int_{T_K}^{T_g} \left(\Delta C_p\right)_{\min} d\ln T \tag{2.19}$$

where T_K is the Kauzmann temperature. $(\Delta C_P)_{\text{minimum}}$ implies minimum configurational entropy. In turn it implies a high viscosity prior to glass transition because, according to Adam-Gibbs theory (see chapter 3),

$$\eta = \eta_0 \exp\left[\frac{B}{TS_c}\right] \tag{2.20}$$

Therefore association of m_0 with easy glass-forming ability seems to be justifiably related to configurational entropy minima providing a good justification to Phillips' approach.

Constraint model has been extended to include glasses containing singly coordinated atoms (Boolchand and Thorpe, 1994, Boolchand et al., 1996). In a 3-dimensional network consisting of N atoms, with n_m atoms possessing coordination number m, $m \geq 2$ and the remaining n_1 atoms with coordination number of 1, the total number of constraints is given by

$$N_c = \frac{1}{N}\left[n_1\left(\frac{1}{2}\right) + \sum_{m\geq 2} n_m\left(\frac{m}{2} + (2m-3)\right)\right] \tag{2.21}$$

We may note that in equation (2.21), the required modification of equation (2.16), for the bond bending constraints has been introduced ($2m$-3 instead of $m(m$-1)/2). The above equation can be simplified by the use of average coordination number $\langle m\rangle$ so that

$$N_c = \frac{5}{2}\langle m\rangle + \frac{n_1}{N} - 3 \tag{2.22}$$

Imposing the condition that constraints are equal to the dimensionality,

N_d - N_c = 0, leads to $\langle m \rangle$ = 2.4 - 0.4n_1/N. It is easy to verify that this equation* indeed works well in rationalizing the high glass-forming tendency in the chalcogenide, $Ge_xS_{1-x-y}I_y$. The m values for Ge, S and I in $Ge_xS_{1-x-y}I_y$ are 4,2 and 1 respectively. In this particularly simple formulation $\langle m \rangle$ can be calculated as

$$\langle m \rangle = 4x + 2(1 - x - y) + y = 2x - y + 2 \tag{2.23}$$

This can be equated with the above formula for $\langle m \rangle$, so that 2.4 – 0.4y = 2x - y +2. Therefore, y = (10x-2)/3. The loci of y as a function of x seems to agree very well with the glass-forming compositions.

Döhler et al (1980) suggested a modification of the constraints formula as follows

$$N_c = \left(\frac{m}{2}\right) + \frac{1}{2m(m-1)} \qquad \text{for all } m < N_d - 1 \tag{2.24}$$

and

$$N_c = \left(\frac{m}{2}\right) + \frac{1}{2(N_d - 1)(2m - N_d)} \qquad \text{for all } m > N_d - 1 \tag{2.25}$$

This modified formula also leads to satisfactory rationalization of glass-forming compositions in systems like xNa$_2$O · (1-x)TeO$_2$. Assuming that Na^+ is attached to O^- (a non-bridging oxygen in the structure) and treating the m value of Na^+ as 1 and that of O and Te as 2 and 4 respectively, one can obtain N_c simply as $N_c = \sum N_{ci} f_i$, where f_i is the corresponding mole fraction. The values of N_{ci} are equal to 0.5, 2 and 7 respectively for Na, O and Te. Thus N_c becomes equal to 1/3[2x(1/2) + (1-x)7 + (2-x)2] for the

---

* An algebraic manipulation has been done in arriving at equation (2.22) by first expanding the summation from $m \geq 1$ and then subtracting m=1 term in equation 2.21. It is then easy to see

$$N_c = \left[\left(\frac{1}{2}\right)\left(\frac{n_1}{N}\right) + \sum_{m>1}\left(\frac{5}{2}\right)\left(\frac{mn_m}{N}\right) - \left(\frac{5}{2}\right)\left(\frac{n_1}{N}\right) - \sum_{m>1} 3\left(\frac{n_m}{N}\right) + 3\left(\frac{n_1}{N}\right)\right]$$

$$= \frac{1}{N}\left[n_i\left(\frac{1}{2}\right) + \sum_{m\geq 2} n_m\left(\frac{m}{2} + (2m-3)\right)\right] = \frac{5}{2}\langle m \rangle + \frac{n_1}{N} - 3$$

above glass composition. Equating N_c to N_d, one obtains $x = 0.25$, which is close to 0.20 for the best glass forming composition. Zang and Boolchand (1994) have further considered the possibility of relaxing the bond angle constraint and have shown that x indeed is 0.20 for the above case. Mitkova and Boolchand (1998) have reviewed several applications of the constraint model and revised constraint counting methods to rationalize glass-formation in a number of the ternary chalcogenide systems.

The relation between glass-forming tendencies and the connectivity among various polytopes in glass structures were also analyzed and formulated elegantly by Cooper and his school (1978, 1982) in the late seventies and eighties around the same time as Phillips formulated the constraints model. Gupta (1992) has reviewed expertly the relation between rigidity, connectivity and glass-forming ability in a number of glass-forming systems like SiO_2, P_2O_5, B_2O_3, silicon oxynitrides, amorphous metals, etc. Gupta has used a similar approach wherein the degrees of freedom f (equivalent of M_o) is given by

$$f = D - \left(\frac{c}{V}\right)\left[\delta V - \frac{\delta(\delta+1)}{2}\right] \tag{2.26}$$

where D is the dimensionality of the network, c is the connectivity of polygons and V is the number of vertices of each polygon, and δ is the dimensionality of the polytope. Critical requirement for glass-formation in this analysis is the possibility of the formation of infinitely connected network of polytopes. In Cooper-Gupta analysis, $f \geq 0$ indicates the possibility of large topologically distorted network of polytopes. Too much freedom (high value of f) can lead to crystallization. $f = 0$ implies slowest critical cooling rates.

Nucleation and Growth

We have already used at several places in this chapter, the notion of nucleation and growth. We discuss this extremely important concept in some more detail here. When a melt - which for simplicity is of a single component glass-forming material - is cooled below its melting point slowly, it crystallizes at an undercooling equal to $(T_m\text{-}T_{cr}) = \Delta T$. The crystallization involves two processes - one, the nucleation and the other, the growth of the crystals. Nucleation is the step in which, by virtue of thermal fluctuations alone the constituent particles order spontaneously into a tiny units called 'embryo'. These embryos redissolve spontaneously

unless they achieve a critical size and the embryos of this critical size are known as a 'nuclei'. Nuclei, with sizes greater than or equal to critical size, r_c, grow spontaneously because free energy decreases for $r > r_c$. This may be understood as follows. Let us suppose that the embryos and the nuclei have spherical shapes. The melt - nucleus interface has a specific interfacial energy γ, which is positive in sign. If the nucleus has a volume v, then its bulk free energy is $-v.\Delta G_v$, which is negative in sign (ΔG_v is the bulk free energy/cc). If the radius of the nucleus is r, then its surface area is $4\pi r^2$ and volume $(4/3)\pi r^3$. The net free energy of formation of the nucleus, w, can be written as

$$w = 4\pi r^2 \gamma - \left(\frac{4}{3}\right)\pi r^3 \Delta G_v \tag{2.27}$$

Evidently, w must exhibit a maximum (w_{max}) for some value of $r = r_c$, which can be determined by setting $\partial w/\partial r = 0$, i.e., $8\pi r\gamma - 4\pi r^2 \Delta G_v = 0$. Therefore, $r_c = 2\gamma/\Delta G_v$ and $w_{max} = 16\pi\gamma^3/3\Delta G^2{}_v$ (nuclei with $r < r_c$ re-dissolve spontaneously). For $r > r_c$, the free energy decreases continuously. Therefore, w_{max} constitutes the barrier for nucleation. The nucleation step involves yet another barrier, which is a kinetic barrier. This is the barrier, E_D (energy per mole), experienced by an atom at the melt-nucleus interface for crossing over from melt onto the surface of the nucleus. We may assume that every atom in the neighbourhood of the nucleus makes an attempt to jump over to the surface of the nucleus and the number of such attempts per second is approximately equal to the vibrational frequency, v. Thus, there are n atoms/cc which are making attempts to cross over to the surface of the nucleus by overcoming, first the kinetic barrier, ΔE_D, and then the thermodynamic barrier, w_{max}, for the formation of the nucleus. The rate of nucleation is therefore a product function, given by,

$$I = n\nu \exp\left(-\frac{N_A w_{max}}{RT}\right)\exp\left(-\frac{\Delta E_D}{RT}\right) \tag{2.28}$$

(N_A is the Avagadro number). The nucleation process just described is known as homogenous nucleation and the nuclei formed are due to thermal fluctuation. The thermodynamic barrier, w_{max} for the homogeneous nucleation can decrease significantly if the nucleation takes place on surfaces of other materials (particles) already present in the melt,

such as for example, the container surfaces or impurities which can be present in melts. The effect of the heterogeneity depends on the wetting behaviour at the interface. The situation is shown diagrammatically in Figure 2.28. θ in the Figure is the wetting angle. There are two additional interfacial energies to consider, the first, between the liquid and the substrate (γ_{LS}) and the second between the crystal and the substrate (γ_{CS}). γ_{LC} which is the interfacial energy between liquid and crystal is the same as γ in homogeneous nucleation) A_{LC} is the area of the crystal in contact with the liquid. The surface energy, therefore becomes

$$\text{Surface energy} = A_{LC}\gamma_{LC} + (\pi r^2 \sin^2\theta)(\gamma_{CS} - \gamma_{LS}) \tag{2.29}$$

Once again the net change in the total energy w during the formation of the nuclei would be

$$w = \mathrm{v}\Delta G_{\mathrm{v}} + A_{LC}.\gamma_{LC} + (\pi r^2 \sin^2\theta)(\gamma_{CS} - \gamma_{LS}) \tag{2.30}$$

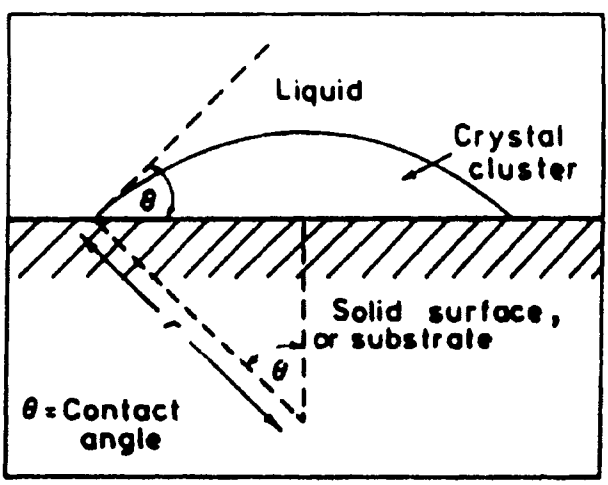

Figure 2.28: Formation of a crystalline cluster on a solid substrate.

With reference to Figure 2.28, we may write

$$A_{LC} = 2\pi r^2(1 - \cos\theta) \tag{2.31}$$

and

$$v = \left(\frac{\pi r^3}{3}\right)(1-\cos\theta)^2(2+\cos\theta) \tag{2.32}$$

We also note that at the edge of the nuclei the equalization of forces requires that

$$\gamma_{LS} = \gamma_{CS} + \gamma_{LC}\cos\theta \tag{2.33}$$

Upon substitution of this condition into the expression for w, one can calculate the value of $w_{\max}$ by differentiating the expression with respect to r as before. In fact r_c can be found to be equal to $2\gamma_{LC}/\Delta G_v$, which is the same as that for homogeneous nucleation. However, w_{max} for heterogeneous nucleation $w_{max}(hetero)$ works out to be,

$$\begin{aligned} w_{\max}(hetero) &= \left[\frac{16\pi\gamma_{LC}^3}{3\Delta G_v^2}\right]\left[(1-\cos\theta)^2\frac{(2+\cos\theta)}{4}\right] \\ &= w_{\max}(homo)\left[(1-\cos\theta)^2\frac{(2+\cos\theta)}{4}\right] \end{aligned} \tag{2.34}$$

Thus, in heterogeneous nucleation, there is a θ dependence and the wetting characteristics contain the essential physics of heterogeneous nucleation. When $\theta = 0$, $w_{\max}(hetero) = 0$. When $\theta = 90°$, $w_{max}(hetero) = w_{max}(homo)/2$ and for non-wetting condition of $\theta = 180°$, $w_{max}(hetero) = w_{max}(homo)$. Thus, there is no barrier for nucleation when the substrate is fully wetting. On such a surface, which satisfies the complete wetting condition, the interatomic distances in the surface and in the nucleated material match well - good registry - and we have an excellent situation for epitaxial growth. However, epitaxial growth is known to take place even when disregistry is as high as 7 %. Thus wetting angle affects the nucleation rates rather profoundly, which in turn affect the critical cooling rates required for glass formation. In Table 2.4, some calculated critical cooling rates for glass formation are presented for various values of wetting angles.

ΔG_v is given by, $\Delta G_v = \Delta H - T\Delta S$. Under conditions of constant pressure, and only slightly below the melting point, we can assume that ΔH and ΔS to be temperature independent so that $d(\Delta G)/dT = -\Delta S$. This can be integrated from T_m to T_{cr} (temperature of crystallization) so that

$$\Delta G(T_c) - \Delta G(T_m) = -\Delta S(T_c - T_m) = \Delta S.\Delta T \tag{2.35}$$

where $\Delta T = (T_m - T_{cr})$. Since $\Delta G(T_m)$ (the change in free energy at the equilibrium melting temperature) is zero, the change in free energy is just $\Delta G_v(T_{cr})$, which is identical to ΔG_v. Therefore, $\Delta G_v = \Delta T \Delta S \approx \Delta T \Delta S_m = \Delta T(\Delta H_m/T_m)$. where ΔS_m is the melting entropy. Substituting this equation into the expression for nucleation rate, we obtain

$$I = n\nu \exp\left\{-\left(\frac{N_A}{RT}\right)\left(\frac{16\pi\gamma^3}{3\Delta H_m^2}\right)\left(\frac{T_m}{\Delta T^2}\right)\right\}\exp\left\{-\frac{\Delta E_D}{RT}\right\} \tag{2.36}$$

It is readily recognized that at and just below the melting point, ΔT being nearly zero, I=0. At lower temperatures, $\exp\{-\Delta E_D/RT\}$ tends to zero so that $I \rightarrow 0$ again. I is controlled by thermodynamics at higher temperature and by kinetics at lower temperature (Turnbull, 1956, Turnbull and Cohen, 1960). The general shape of nucleation rate as a function of temperature is, therefore, as shown in Figure 2.29.

Table 2.4: Effect of contact angle of heterogeneities (2×10^7 cm^{-3}) on calculated critical cooling rates (Ks^{-1}) for glass formation. (After Onarato and Uhlmann ,1976)

Material	Homogeneous nucleation	Heterogeneous nucleation			
		$\theta = 100°$	$\theta = 80°$	$\theta = 60°$	$\theta = 40°$
SiO_2	9×10^{-6}	1×10^{-5}	2×10^{-4}	8×10^{-3}	2×10^{-1}
GeO_2	3×10^{-3}	3×10^{-3}	3×10^{-2}	1	20
$Na_2O.2SiO_2$	6×10^{-3}	8×10^{-3}	3×10^{-1}	10	3×10^2
$CaO.Al_2O_3.2SiO_2$	3×10^2	3×10^2	5×10^3	2×10^5	2×10^6

Nucleation as quantified in equation (2.36), describes one part of the process of crystallization. The other part is the growth of the nuclei. Growth involves movement of atoms or ions, again from across the interface on to the surfaces of the growing nuclei. The free energy of a particle in the melt side, which is in its own potential well, is slightly higher as compared to its free energy in the growing crystal. The difference is ΔG_v. The kinetic barrier, which frustrates successful transport

across the interface (as earlier) is equal to ΔE_D. It must be remembered that a particle from the surface of the nuclei can jump over into the melt

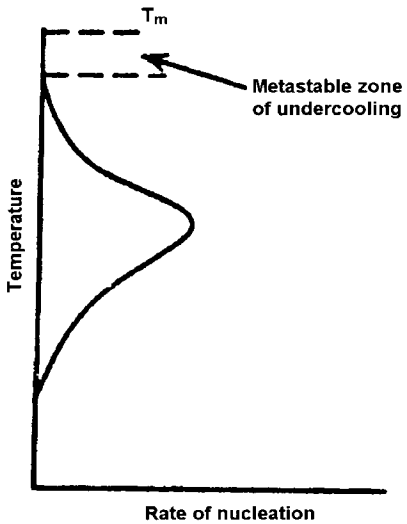

Figure 2.29:Variation of nucleation rate, *I*, with temperature, T.

(dissolution) by overcoming a barrier equal to (ΔG_v + ΔE_D). We may formulate the rate at which net accumulation of atoms - growth - occurs by summing the rates at which atoms arrive at and jump out of the surface of the nuclei and that gives, the rate of crystal growth, *U*,

$$U = a\nu\left[\exp\left(-\frac{\Delta E_D}{RT}\right) - \exp\left\{-\left(\Delta G_v + \frac{\Delta E_D}{RT}\right)\right\}\right]$$
$$= a\nu\exp\left(-\frac{\Delta E_D}{RT}\right)\left[1 - \exp\left(-\frac{\Delta G_v}{RT}\right)\right] \qquad (2.37)$$

a represents the jump distance corresponding to the distance between two sites (typically interatomic distance) and ν, as mentioned earlier, is the vibrational (attempt) frequency. It should be noted that use of ΔE_D in place of a general activation barrier is clearly an approximation. Two useful substitutions are made at this stage. One is $D = a^2\gamma\exp(-\Delta E_D/RT)$, where *D* is the diffusion coefficient and $\Delta G_v = \Delta T_m \Delta H_m / T_m$. The crystal growth rate expression becomes,

$$U = \left(\frac{D}{a}\right)\left[1 - \exp\left\{-\frac{\Delta H_m \Delta T_m}{RTT_m}\right\}\right] \tag{2.38}$$

D may again be substituted by the viscosity η using Stokes-Einstein relation $D = RT / (3\pi N_A \sigma \eta)$, where σ is assumed to be the diameter of the diffusing species and is roughly same as a in the earlier expression. Thus

$$U = \left(\frac{fRT}{3\pi N_A \sigma^2 \eta}\right)\left[1 - \exp\left\{-\frac{\Delta H_m \Delta T_m}{RTT_m}\right\}\right] \tag{2.39}$$

where f is the fraction of the surface area, where growth occurs. The above expression indicates that growth rate is low when η is high. The maximum growth rates in highly viscous glass forming liquids are extremely low as in GeO_2, SiO_2, P_2O_5 or B_2O_3 melts, and are of the order of 10^{-6} to 10^{-7} cm/s. In poor glass-formers such as toluene and methyl alcohol, it can be a fraction of a cm per second. Addition of small impurities reduces the nucleation barrier significantly and is exemplified by the rates of crystal (cristobalite) growth in pure fused silica and fused silica containing 0.32 % of Na_2O. The rates are shown in Figure 2.30.

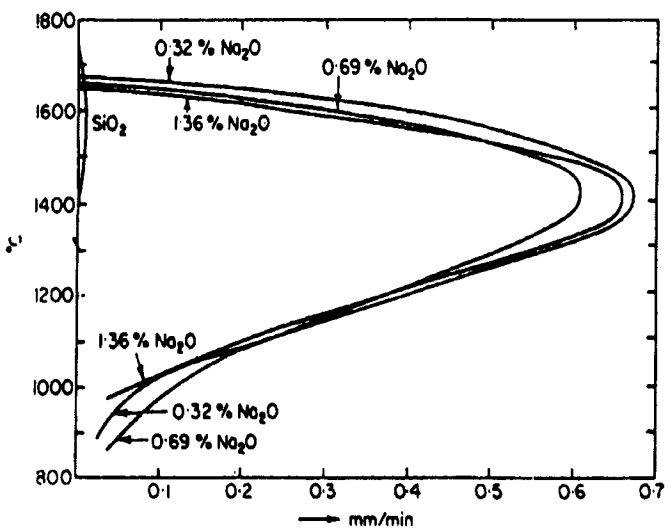

Figure 2.30: Crystal growth rate of cristobalite in SiO_2 and three soda silica melts containing low Na_2O. (After Dietzel and Wickert, 1956).

Thus the crystallization of a melt (which should be avoided for glass formation) is governed by two functions expressed in equations (2.36) and (2.39) corresponding to nucleation and growth. Their behaviour is shown schematically in Figure 2.31.

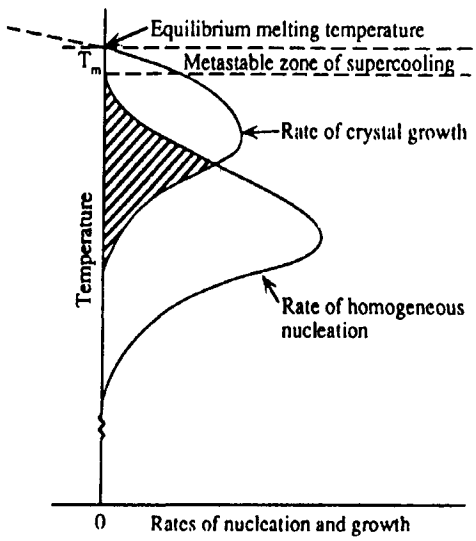

Figure 2.31: Variation of the crystal growth rate, U and nucleation rate, I, as a function of temperature, T (schematic).

The region of overlap of the nucleation and growth rates is the temperature region, which has to be quickly passed over by fast quenching in order to obtain a glass.

References:

Angell, C. A., 1988, J. Non-Cryst. Sol., **102,** 205.

Angell, C. A., 1984 J. Phys. Chem., **88**, 6727.

Angell, C. A., and L. M. Torell, 1983, J. Chem. Phys., **78**, 937.

Avrami, M., 1939, J. Chem. Phys., **7**, 1103.

Avrami, M., 1940, J. Chem. Phys., **8**, 212.

Avrami, M., 1941, J. Chem. Phys., **9**, 177.

Balta, P. and E. Balta, 1976, Introduction to the physical chemistry of the vitreous state, (Abacus, Kent).

Bell, R. H. and P. Dean, 1966, Nature, **225**, 1354.

Bernal, J. D., 1959, Nature, **183**, 141.

Bernal, J. D., 1964, Proc. Roy. Soc,. **A 280**, 299.

Boolchand, P., and M. F. Thorpe, 1994, Phys. Rev. B., **50**, 366.

Boolchand, P., M. Zhang and B. Goodman, 1996, Phys. Rev. B., **53**, 488.

Boolchand, P., X. Feng, D. Selvanathan and W.J. Bresser, 1999, in Rigidity Theory and Applications, eds. M.F. Thorpe and P.M. Duxbury (Plenum Publishers, New York) p. 279.

Brinker, C. J., and Scherer, 1990, Sol-gel Science (Academic Press, New York).

Brow, R. K., D. R. Tallant, J. J. Hudgens, S. W. Martin and A. D. Irwin, 1994, J. Non-cryst. Sol., **177**, 221.

Brüning, R., and K. Samwer, 1992, Phys. Rev. B., **46(18),** 11318.

Cargill, G. S., 1975, Solid State Phys., **30**, 227.

Colmenero, J., and A. Alegna, eds., Basic Features of the Glassy State, 1990, (World Scientific, Singapore).

Cooper, A. R., 1982, J. Non-Cryst. Sol., **49**, 1.

Cooper, A.R., 1978, Phys. Chem. Glasses, **19**, 60.

Cormia, R. L., J. D. Mackenzie and D. Turnbull, 1963, J. App. Phys., **34**, 2239.

Coulson, C. A., and T. W. Dingel, 1968, Acta. Crystallogr., **B24,** 153.

Cruikshink, 1961, J. Chem. Soc., 5486.

Dietzel, A. and H. Wickert, 1956, Glastech. Ber. **29,** 1.

Döhler, G. H., R. Dandoloff and H. Blitz, 1980, J. Non-Cryst. Sol., **42**, 87.

Doremus, R. H., 1973, Glass Science, (J. Wiley & Sons, New York).

Dubochet, J., Adrian, J. Teixera, C. Alba, R. A. Kadiyala, D. R. MacFarlane and

Finney, J.L., 1977, Nature, **266**, 309.

Fontana, E. J., and W. A. Plummer, 1966, Phys. Chem. Glasses, **7**, 139.

Ganguli, D., 1989, in Current Trends in the Science and technology of Glass, eds. H. Jain, A.R. Cooper, K.J.Rao and D. Chakravorty (World Scientific, Singapore) p. 359.

Gaskell, P. H., Parker J. M., and E. A. Davis, eds., 1983, The Structure of Non-Crystalline Materials, (Taylor & Francis, London).

Goldschmidt, V. M., 1926, Skrifter Norske Videnskaps (Oslo). I. Math-Naturwiss. Kl. No. 8, 7.

Greaves, G. N., and E. A. Davis, 1974, Philos. Mag., **29**, 1201.

Gupta, P. K., 1992, J. Am. Ceram. Soc., **76**, 1088.

He, H., and M. F. Thorpe, 1985, Phys. Rev. Lett., **54**, 2107.

Ichikawa, T., 1973, Phys. Status Solidi A **19,** 707.

Jeanloz, R., and Q. Williams, 1991, Nature, **350**, 659.

Johnson, W. A., and R. F. Mehl, 1939, Trans. AIMME, **135**, 416.

Lucas, J., and A. Bouaggad, 1987, Mat. Res. Bull., **22**, 685.

Mitkova, M., and P. Boolchand, 1998, J. Non-Cryst. Sol., **240**, 1.

Mozzi, R. L., and B. E. Warren, 1969, J. Appl. Crystallogr., **2**, 164.

Onorato, P. I. K., and D. R. Uhlmann, 1976, J. Non-Cryst. Sol., **22**, 367.

Pauling, L., 1960, Nature of Chemical Bond, (Academic Press, New York).

Phillips, J. C., 1979, J. Non-Cryst. Sol., **34**, 153.

Polk, D. E., 1971, J. Non-Cryst. Sol., **5**, 365.

Rao, C.N.R., and K.J. Rao, 1978, Phase Transitions in Solids (McGraw-Hill, New York).

Rawson, H., 1956, in: Pro. IV Int. Cong. On Glass, Paris. (Imprimerie Chaix, Paris).

Richert, R., and H. Bassler, 1990, J. Phys: Cond. Mattt., **2**, 2273.

Sanderson, R. T., 1983, Polar Covalence, (Academic Press, New York).

Senapathi, H. L., and A. K. Varshneya, 1995, J. Non-Cryst. Sol., **185**, 289.

Smekal, A., 1951, J. Soc. Glass Technol., **35**, 411.

Soules, T. F., 1985 J. Non-Cryst. Sol., **73**, 315.

Stanworth, J. E., 1946, J. Soc. Glass Technol., **30**, 54.

Stanworth, J. E., 1948a, J. Soc. Glass Technol., **32**, 154.

Stanworth, J. E., 1948b, J. Soc. Glass Technol., **32**, 366.

Stanworth, J. E., 1952, J. Soc. Glass Technol., **36**, 217.

Sun K. H., and M. L. Huggins, 1947, J. Phys. Colloid Chem., **51**, 438.

Sun, K. H., 1947, J. Am. Ceram. Soc., **30**, 277.

Thorpe, M. F., 1983, J. Non-Cryst. Sol., **57**, 355.

Turnbull, D., 1956, in: Solid State Physics, Vol 3, eds. F. Seitz and D. Turnbull (Academic Press, New York) p. 226.

Turnbull, D., and M. H. Cohen, 1960, in: Modern Aspects of Vitreous State. Vol 1, ed. J. D. Mackenzie (Butterworths, London) p. 38.

Urbain, G., Y. Bottinga and R. Richet, 1982, Geochem. Cosmochim. Acta, **46**, 1061.

Verrall D. J., Gladden L. F., and S. R. Elliott, 1988, J. Non-Cryst. Sol., **106**, 47.

Weinberg, M. C., B. J. Zelinski, D. R. Uhlmann and E. D. Zanotto, 1990, J. Non-Cryst. Sol., **123,** 90.

Winter A., 1955, Verres Réfract., **9**, 147.

Yamane, M., and Y. Asahara, 2000, Glasses for Photonics, (Cambridge University Press).

Zachariasen W. H., 1932, J. Am. Chem. Soc. **54,** 3841.

Zang, M., and P. Boolchand, 1994, Science, **266,** 1355.

Zarzycki, J., 1993, Proc. III Int. Conf. Adv. In Fusion & Processing of Glass, Ceram. Trans. **29** (Varshneya A. K., Bickford D. F., and P. P. Bihuniak, eds.). pp 519.

In nature's infinite book of secrecy, a little I can read.
- W. Shakespeare.

CHAPTER 3

THE GLASS TRANSITION PHENOMENON

Understanding glass transition phenomenon is of primal importance in the study of glasses. In chapter 2, the general features of glass transition were introduced. In this chapter, various approaches made towards explaining this phenomenon are discussed. To begin with, we note that in the supercooled region the viscosity increases exponentially to values as high as $10^{13.6}$ poises. At this stage the supercooled liquid rapidly transforms into a glass, although viscosity itself suffers no discontinuity at T_g. Nevertheless one should expect a proper theory of viscosity of liquids to be able to account for the glass transition and associated features. The first major development in this direction has been the formulation of free volume theory of liquid viscosities.

Free volume and glass transition

At the time of development of free volume theory, two important empirical equations of viscosity were known. They are the Doolittle (1951) equation (3.01) and the Vogel, Tamman and Fulcher (VTF) equation (3.02) (Vogel, 1921, Fulcher, 1923, Tammann and Hesse, 1926), which are given below.

$$\eta = A \exp\left[\frac{B \mathrm{v}_{occ}}{\mathrm{v}_f}\right] \tag{3.01}$$

$$\eta = \eta_0 \exp\left[\frac{C}{T - T_0}\right] \tag{3.02}$$

In equation (3.01), A and B are empirical constants, v_{occ} is the volume occupied by the constituent particles and v_f is the free volume. In equation (3.02), η_0, C and T_0 are constants. VTF equation implies that viscosities of glass forming supercooled liquids are non-Arrhenius and T_0 is the temperature which linearizes the data of the non-Arrhenius plot. Cohen and Turnbull (Cohen and Turnbull, 1959; Turnbull and Cohen, 1961,

1970) addressed the problem of finding the basis of the relation between free volumes and viscosity. The approach is briefly as follows. The particles in a liquid can be assumed to be present in their cages, which are the *Voronoi polyhedra* (see Chapter 2). The motion of particles within the polyhedra is governed by a potential energy function. Potential energy profile of the particle inside a Voronoi polyhedron is shown in Figure 3.01.

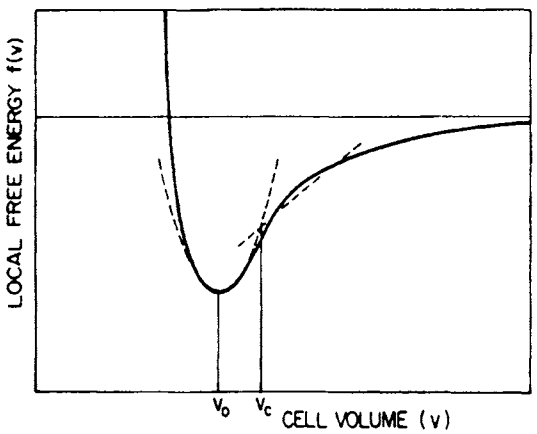

Figure 3.01: General form for the local free energy as a function of cell volume and the approximate form (dashed line) used by Cohen and Grest (1979, 1981) to distinguish between solid-like and liquid-like cells.

The variation of the potential energy of the particle slightly above the bottom of the potential well is nearly linear, while at the bottom itself the potential is harmonic. At high temperatures, characteristic of the liquid region, cage volumes are high and the region of potential variation applicable to the situation is the linear portion. It is easy to visualize that the two adjoining Voronoi Polyhedra can shrink and expand respectively to a certain extent in such a way that their total volume is conserved. There is also no change in the total energy of the system during such an exchange of volume between the polyhedra. This volume, which can be exchanged between Voronoi Polyhedra without costing any energy has been defined as the *free volume*. When the size of the Voronoi polyhedron increases the free volume available for the particle also increases. Physically this corresponds to opening up of the surroundings of a given particle, which enables the particle to move out of its own cage, thereby effecting a diffusive motion. This type of motion is considered as responsible for the transport in glass forming liquids. A minimum of free

volume is, however, necessary for transport to occur. If we designate v_f as the available free volume and v^* as the minimum free volume required for transport to occur, all that is needed is to find out the number of cells associated with volumes greater than v^*. This can be obtained from the size distribution function $P(v)$ (a probability function) of the free volume, which is given by

$$P(v) = \frac{\gamma}{v_f} \exp\left(-\frac{\gamma v}{v_f}\right) \tag{3.03}$$

where γ is a free volume overlap correction constant, and has a numerical value between 1/2 and 1. The relevant quantity for the free volume theory is D, the diffusion coefficient, which is given by,

$$D = gu \int_{v^*}^{\infty} a(v)P(v)dv \tag{3.04}$$

where g is the geometric factor, u is the gas kinetic velocity in the direction of the jump, $a(v)$ is the characteristic jump distance and v^* is the minimum size of the void (distributed free volume, which permits the diffusive motion). Since D is related to η by the Stokes-Einstein relation,

$$D = \frac{kT}{3\pi a_0 \eta} \tag{3.05}$$

where a_0 is the molecular diameter, one can combine equations (3.03), (3.04) and (3.05) so that,

$$\eta = \left(\frac{kT}{3\pi a_0 a^* gu}\right) \exp\left(\frac{\gamma v^*}{v_f}\right) \tag{3.06}$$

Equation (3.06) suggests that as v_f decreases, η increases exponentially and the transport is severely curtailed. Correspondingly, the motion of the particle gets confined to the Voronoi polyhedron and as expected the motion becomes more and more oscillatory. The empirical VTF equation (3.02) may be recovered from equation (3.06) by a proper substitution of v_f. One plausible assumption is that $v_f \cong v_i - v_g \cong \Delta\alpha(T-T_g)$ where v_i is the

volume of the Voronoi polyhedron in the melt at temperature T and v_g is its volume in the glassy state at T_g. However theoretical evaluations have been carried out with v_f taken as the difference between the total volume, V, and the dense random close packing volume, V_{rcp} (see chapter 2) and evaluated for a single Voronoi polyhedron. The essential simplicity of the approach has lent free volume theory an undiminishing attraction. Important features of glass transition are easily interpreted in terms of the free volume theory if there is no insistence on a complete and quantitative agreement. The use of V_{rcp} has been found to fit shear viscosities of liquids only at higher temperatures and leads to considerable discrepancies at lower temperatures.

Although a distribution of free volume has been considered in Cohen-Turnbull approach and a certain critical lower limit has been set for v_f available with individual cells which enables diffusion, such availability of v_f with individual cells alone may not enable motion. It requires a certain minimum number of them to come together, and engage in redistribution of their free volumes so as to enable motion. Cohen and Grest (1979) extended the free volume theory and introduced the element of coming together of such cells to enable diffusive motion. They developed the free volume theory into a thermodynamic theory, which addresses the glass transition problem directly so as to investigate the enigmatic nature of the hypothetical transition at T_K.

Briefly stated, a minimum volume of the cell above which sharing of free volume is possible is used to distinguish solid-like ($v < v_c$) and liquid-like ($v \geq v_c$) cells in the liquid. v_c is indicated in Figure 3.01. When liquid-like cells come together they form islands of liquid-like region (Figure 3.02) or in a supercooled liquid solid-like cells begin to form as

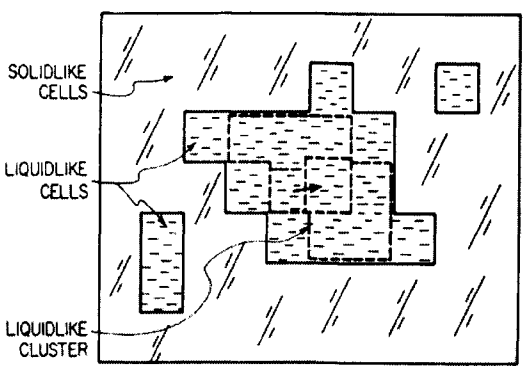

Figure 3.02: Percolation of solid-like and liquid-like clusters.

islands. The growth of these islands becomes extensive and interconnected as T_g is approached. This corresponds to percolation of the solid-like regions with $v < v_c$. The liquid-like clusters in which the free volume is shared, possess excess entropies as a consequence of the diffusional contributions to density fluctuations. It is the difference between the entropy of the given system of particles and that of the reference system, in which the particles are confined to their respective cells. This entropy arising from shared physical space available to the cells is known as *communal entropy*, S(comm). It is central to the glass-liquid transition in the Cohen-Grest theory. When communal entropy of the supercooled liquid goes to zero, it results in glass transition. Since the liquid-like and solid-like cells exhibit percolation characteristics as a function of temperature, the typical sigmoidal behaviour is expected to be exhibited by S(comm) and is shown schematically in Figure 3.03. When the fraction

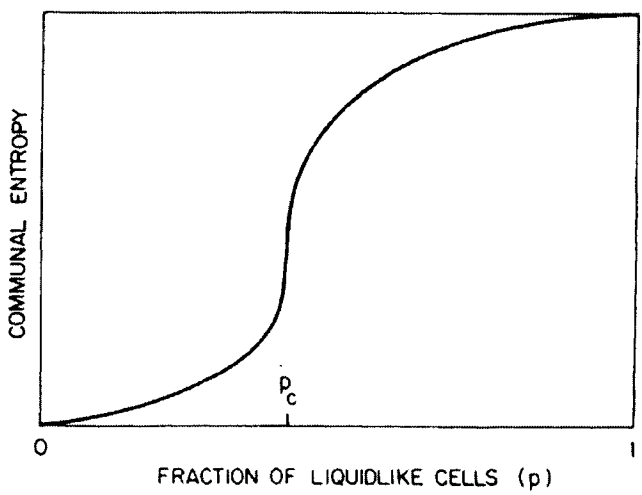

Figure 3.03: Sketch of the communal entropy as a function of the fraction of liquidlike cells in the Cohen-Grest percolation formulation of the glass transition.

of liquid-like cells decreases towards the percolation limit, p_c, during cooling, there is a precipitous drop in the communal entropy, which suggests that it corresponds to a thermodynamic transition to glassy state and that it has a first order characteristic. However this does not find support from any experiments. Cohen-Grest theory, therefore, requires further assumptions to be able to describe the experimental observations on glass transition.

Entropy theory

One important feature of the molten state is its large entropy compared to the parent crystalline state. As stated earlier a large part of this entropy is acquired discontinuously at its melting point. This acquired entropy is likely to be mostly configurational. In the entropy theory, transport is conceived to be consequence of a local rearrangement of particles into different configurations, which is also the origin of configurational entropy (Gibbs and DiMarzio 1958; Gibbs 1960; Adam and Gibbs 1965). During the cooling of the melt, the configurational entropy decreases and configurational changes require participation of more and more particles in order to rearrange (reorganize) the local structure - it becomes more and more cooperative - so that a transport event can occur. At a sufficiently low temperature, the configurational entropy may go to zero in which case a second order transition should be expected to occur. The resulting solid is an *ideal glass*. However, in real situations, there is the intervention of kinetic solidification as a result of prohibitively long relaxation times. The consequence is that the transition to the glassy state occurs even before the configurational entropy becomes zero and the glass retains frozen entropy. Let us consider the cooperative rearrangement of a small group of z particles, which is at the heart of entropy theory. Configurational rearrangement or transition probability, $W(T)$, of the group is given by (Adam and Gibbs 1965)

$$W(T) = A\exp\left[-\frac{z\Delta\mu}{kT}\right] \tag{3.07}$$

where $\Delta\mu$ is the potential energy hindering the rearrangement and k is the Boltzmann constant. In order that at least one rearrangement can occur, there must be some minimum size of the rearranging unit, which may be designated as z^*. Considering all such clusters, which yield non-zero transition probabilities, the average transition probability may be obtained as,

$$\overline{W}(T) = \overline{A}\exp\left(-\frac{z^*\Delta\mu}{kT}\right) \tag{3.08}$$

In the theory, z^* is later related to the total configurational entropy S_c because $s_c^*/S_c = z^*/N$, where s_c^* is the entropy of the unit of minimum or critical size, z^* (s_c^* cannot be less than $k\ln 2$). Further, the relaxation time,

τ is related to $\overline{W}(T)$ as $\tau = 1/\overline{W}(T)$ and η, itself scales as τ. Thus Adam and Gibbs (AG) obtained an equation for η which is

$$\eta = A' \exp\left(\frac{B}{TS_c}\right) \tag{3.09}$$

where $B = (N s_c^* \Delta\mu/k)$. Thus η diverges as $S_c \rightarrow 0$ and at high values of η ($\geq 10^{13}$ P) the supercooled liquid is kinetically frozen into a glass. Equation (3.09) has an important implication in that it leads to a definition of a glass with zero configurational entropy; or an ideal glass, which is a unique ground state structure. At $T = T_0$ where $S_c = 0$, a second order transition[#], in the Ehrenfest sense, would occur had the kinetics not intervened and led to an experimentally observed transition at T_g. That is why the resulting glass at T_g retains a part of the configurational entropy as frozen entropy. The VTF equation may be derived from the AG equation (3.09) as follows. Since

$$S_c = \int_{T_0}^{T} \Delta C_P \, d\ln T \tag{3.10}$$

where $\Delta C_P = C_P$(liquid) - C_P(ideal glass) $\approx C_P$(liquid) - C_P(crystalline state). Since ΔC_P exhibits a hyperbolic dependence on T in several glass forming liquids, $\Delta C_P \sim 1/T$.

$$S_c = \int_{T_0}^{T} \frac{a}{T} d\ln T = \int_{T_0}^{T} \frac{a}{T^2} dT = a\frac{(T - T_0)}{TT_0} \tag{3.11}$$

Upon substitution of equation (3.11) to AG equation (3.09),

$$\eta = A' \exp\left[\frac{DT_0}{T - T_0}\right] \tag{3.12}$$

[#] T_0 is a temperature indicative of divergences of η and τ, while T_K is an (extrapolated) limiting temperature, which avoids an entropy absurdity implied in the Kauzmann Paradox. T_g/T_0 values have been evaluated from the VTF equation fits to viscosity, where as T_g/T_K has been determined by calorimetric measurements for four glasses, which illustrate that indeed T_K and T_0 represent the same temperature. (T_g/T_K : T_g/T_0) sets of values are; As_2Se_3 (1.93:1.86); glycerol (1.37:1.34); ethanol(1.34:1.34) and; $Li_2O{\cdot}B_2O_3$(1.11:1.08). (Angell, 1991).

which is the well-known VTF equation. In equation (3.12), $D = (B/a) = (Ns_c^* \Delta\mu/ka)$ is a constant.

Both the free volume and entropy theories have been subjected to experimental verification and continue to enjoy the *first choice* status while discussing any experimental studies in glass science. But in both the theories, experimental glass transition is understood as due to the intervention of forbidding kinetic factors – high viscosities. Therefore it is implied that either a minimum free volume or a minimum configuration entropy remains frozen in the glass at T_g. Neither v_f nor S_c has yet become zero at T_g. There have been attempts to find out if either or both of these frozen minimum values, v_f^m or S_c^m, could be considered as universal features of the experimental glass transition or whether they are equivalent. A thermodynamic test of this is based on the following arguments. Since v_f^m = constant and S_c^m = constant, $dv_f^m = dS_c^m = 0$ at T_g. In general, volume V and entropy S of the supercooled liquid can be treated as functions of P and T. We may therefore write,

$$dV = \left(\frac{\partial V}{\partial P}\right)_T dP + \left(\frac{\partial V}{\partial T}\right)_P dT \tag{3.13}$$

and

$$dS = \left(\frac{\partial S}{\partial P}\right)_T dP + \left(\frac{\partial S}{\partial T}\right)_P dT \tag{3.14}$$

Also,

$$\left(\frac{\partial V}{\partial P}\right)_T = -V\beta;\ \left(\frac{\partial V}{\partial T}\right)_P = V\alpha;$$
$$\left(\frac{\partial S}{\partial T}\right)_P = \frac{C_P}{T};\ \left(\frac{\partial V}{\partial P}\right)_T = -\left(\frac{\partial V}{\partial T}\right)_P = -V\alpha \tag{3.15}$$

V and S in the above equations are molar volumes and entropies. At T_g, the molar (minimum) free volume is given by $N v_f^m$, where N is the Avagadro number. Therefore, $N v_f^m = (V_l - V_g)$ and $S_c^m = (S_l - S_g)$. In view of the fact $dv_f^m = dS_c^m = 0$ at T_g, it is easily seen that, the two equations yield two different equations for dT_g/dP;

$$\frac{dT_g}{dP} = \frac{\Delta\beta}{\Delta\alpha} \qquad \text{(minimum free volume)} \qquad (3.16)$$

$$\frac{dT_g}{dP} = \frac{T_g V_g \Delta\alpha}{\Delta C_P} \qquad \text{(minimum entropy)} \qquad (3.17)$$

In equations (3.16) and (3.17), ΔX, where X is α, β or C_P, is given by X(liquid) - X(glass). Indeed the two expressions (3.16 and 3.17) provide a means of experimental verification of the two theories because variation of glass transition with pressure can be experimentally determined along with other quantities, namely, $\Delta\alpha$, $\Delta\beta$ and ΔC_P. Some of these quantities have been measured on several polymeric and non-polymeric glass-forming compounds and the data are presented in Table 3.1. It is evident that

Table 3.1: Calculated and observed values of (dT_g/dP) (After O'Reilly, 1962).

Substance	T_g, °C	V cc	$\Delta\alpha$ x 10^4, $°C^{-1}$	ΔC_P, cal/g. °C	$TV\Delta\alpha/\Delta C_P$ deg/atm	(dT_g/dP), deg/atm	Method
Polyvinyl acetate	298	0.855	4.0	0.10	0.025	0.022	D, V
Polyisobutene	198	1.048	4.5	0.09	0.024	0.024	C
Polyvinyl chloride	353	0.75	3.1	0.068	0.030	0.016	D
Glycerol	183	0.762	2.4	0.212	0.004	0.004	D
n-Propanol	95	0.915	4	0.16	0.005	0.007	D
Selenium	303	-	-	0.045	0.011	0.013	V
Salicilin	316	-	-	0.37	0.005	0.005	V
B_2O_3	520	0.54	5.5	0.14	0.027	0.020	V

D = dielectric; V = volume; C = dynamic compressibility.

experimental observations are in good agreement with the predictions of the entropy theory. However in a thoughtful discussion, Zallen (1983) has suggested that the two approaches are nearly equivalent because lack of minimum free volume renders the system unable to explore other configurational states leading to minimum frozen entropy. If S_c^m is proportional to v_f^m, the two approaches lead to identical results and there

is effectively only one frozen variable (v_f^m or S_c^m) controlling the glass transition. The Prigogine-Defay ratio (Prigogine and Defay, 1954), Π, where

$$\Pi = \frac{\Delta C_P \Delta\beta}{T_g V_g (\Delta\alpha)^2} \tag{3.18}$$

becomes unity if S_c^m is proportional to v_f^m, because the right hand side of equations (3.16) and (3.17) become equal to each other. However, generally it is found that $\Pi > 1$.

There has been considerable discussion on the validity of AG equation in the literature. Laughlin and Uhlmann (1972) plotted log η of salol as a function of $1/TS_c$ (Figure 3.04) and found it to be quite nonlinear

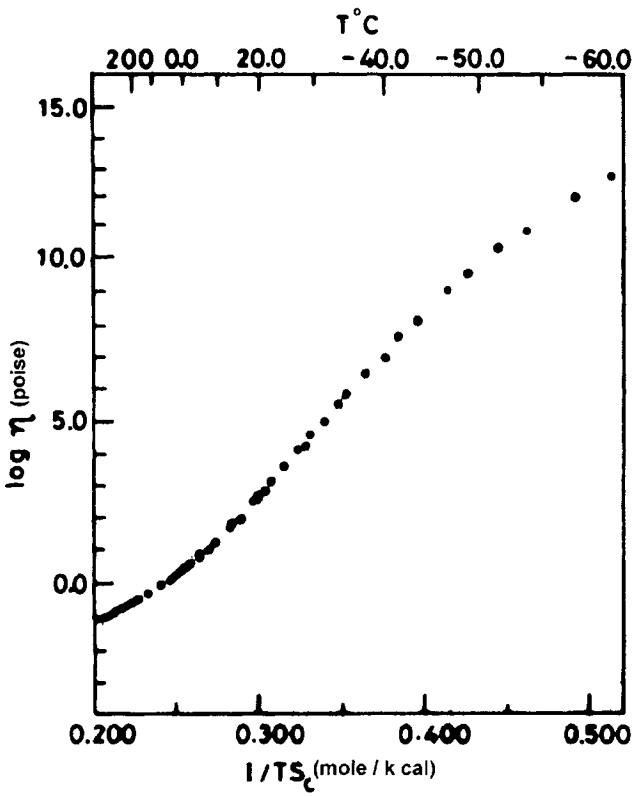

Figure 3.04: Variation of viscosity with configurational entropy for salol. (After Laughlin and Uhlmann, 1972).

suggesting the inadequacy of AG theory. Laughlin and Uhlmann also found, in their analysis, unphysically high values of $\Delta\mu$ and low values of z^*. In AG equation for viscosity, it appears that if η has a fixed value ($\approx 10^{13.6}$ poises) at T_g, then $T_g S_c^m$ must be expected to be a constant and not just S_c^m (see section on Fragility). Takahara et. al. (1994) have examined this aspect. Shown in Figure 3.05 is the measurement of C_P on 3-Methyl pentane and 1-Propanol. There is clearly a shift in the glass transition temperatures (also a moderate increase in the C_P values) as a function of pressure. Analysis of these results indicated constancy of $T_g S_c^m$ values independent of pressure. Thus this analysis provides a significant support for AG theory.

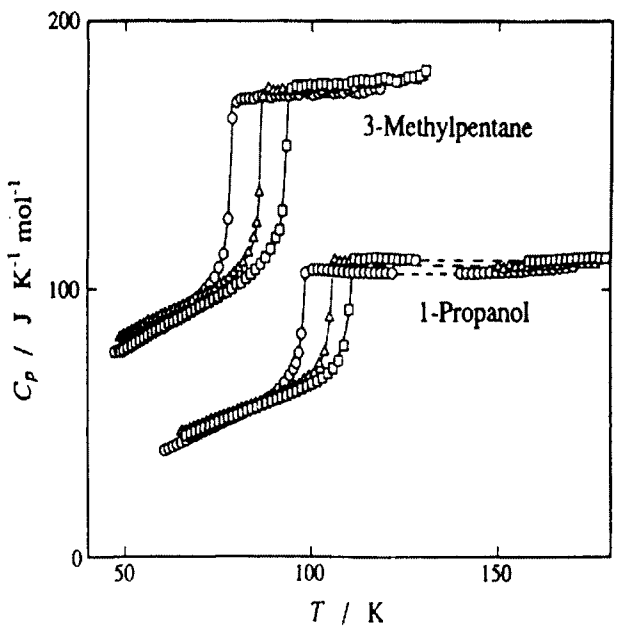

Figure 3.05: Heat capacities of glassy and liquid states of 1-propanol and those of 3-methylpentane. The heat capacity curve for 3-methylpentane is shifted by 30 J K^{-1} mol^{-1} for clarity (After Takahara et al., 1994).

It may be noted that the entropy of the melt is considered as entirely configurational in AG theory. At T_m, it is equal to $\Delta S_m = \Delta H_m / T_m$. The manner of decrease of this quantity is considered as determined by the difference between the heat capacities of melt and the crystalline phases in the supercooled region. At T_g, the frozen entropy, S_c^m is calculated as

$$S_c^m = \Delta S_m - \int_{T_g}^{T_m} \Delta C_P d \ln T \qquad (3.19)$$

At T_g, ΔC_P = C_P(melt) - C_P(crystal). S_c^m is expected to remain constant down to 0 K . Experiments reveal that $S_c^m(0)$ (=S_c^m at 0 K) is indeed, significantly lower than S_c^m as seen from Table 3.2($S_0^0 = S_c^m$ in the table).

Table 3.2: Measured and calculated values of entropies for several glass forming liquids (After Johari, 2000).

Material	T_g, K	S_c^m $Jmol^{-1}K^{-1}$	$S_c^m(0)$ $Jmol^{-1}K^{-1}$	$S_c^m - S_c^m(0)$ $Jmol^{-1}K^{-1}$	T_0 K	$z^*(T_g)$
1-Butene	60	19.8	12.8	7	54	10
2-Methylpentane	78	-	16.7	-	65	6
Toluene	117	12.2	7.9	4.3	<108	<13
Ethylbenzene	115	23.5	12	13.5	-	-
o-Terphenyl	240	21.5	15	6.5	202.4	6.4
Tri-α-napthylbenzene	342	50.2	33	17.2	200	2.4
Ethanol	97	13.6	8.9	4.7	70-75	2.6
Ethyene glycol	153	17	9	8	109	3.4
Glycerol	185	26.9	23.4	3.3	127	3.2
Butanethiol	92	18.8	16.2	2.6	-	-
Salol	220	27.1	14.3	12.8	175.2	4.9
$H_2SO_4.3H_2O$	157	34.8	24.7	10.1	10.1	-
B_2O_3	521	24.5	9.9	14.6	14.6	-
Selenium	300	6.3	3.7	2.6	251	6.1

T_g is the glass softening temperature, $\Delta S(T_g)$the difference between the entropy of a glass and its crystal at T_g, T_0 is the Vogel-Fulcher-Tamman temperature and $z^*(T_g)$ is the minimum size of the cooperatively rearranging region.

This decrease in S_c^m clearly indicates that there is a vanishing part of S_c^m which is attributable to vibrational contribution present in the measured entropies. In fact Johari and Goldstein (1970, 1971) have pointed out that S_c^m and also the measured S_c consist of contributions from the vibrational spectrum arising from the structural differences between the crystalline and disordered states. The vibrations in the disordered state are more anharmonic than in the crystal. Therefore in calculating the configurational entropy, care is needed to subtract out the vibrational contributions. The vibrational part of the measured excess heat capacities, ΔC_P, has been reported to range from 15 to 80 %. This accounts for a large fraction of configurational entropies. A few known values are listed in Table 3.3. In the glassy state we have to recognize the presence of two other contributions to entropy, namely those arising from β relaxations and those arising from the high frequency tail portions of the α relaxations (α relaxation is associated with the observed glass transition, see Chapter 9).

Table 3.3: Various parameters extracted from C_P measurements (After Goldstein, 1976).

Substance	T_g (K)	ΔC_p (J/K-M)	S_c^m (near T_g)	$S_c^m(0)$ (0 K)	Configurational fraction
Diethyl phthalate	178	115	3.64	2.80	0.77
cis -1,4-polyisoprene	200	30.5	0.97	0.77	0.79
o-Terphenyl	240	113	0.78	0.22	0.28
Selenium	300	14.4	0.51	0.35	0.68
Polyethyl methacrylate	335	13.2	0.48	0.07	0.15
Polyvinyl chloride	350	18.4	0.19	0.11	0.58 average=0.54

Thus, the main problem with the various inferences drawn from Adam-Gibbs theory seems to emanate from the fact that the evaluation of the configurational entropy on the basis of ΔC_P values is erroneous. This

limitation can be inferred in other ways also (Johari, 2000). For example, in the AG expression (equation 3.09), s_c^* can be taken as a temperature invariant critical entropy, equal to $k$ln2. On a molar basis, this is equal to $N_A s_c^* = N_A \times 0.956 \times 10^{-23}$ JK^{-1} = 5.764 $Jmol^{-1}K^{-1}$ for all liquids. The quantity z^*, which is the minimum size of the cooperatively rearranging region generating different configurations can be directly determined as,

$$\frac{Ns_c^*}{S_c} = \frac{5.764}{S_c} \tag{3.20}$$

It may be noted that if $s_c^* \Delta\mu / k$ ($=B$) in AG equation were to be a constant, it requires that liquids exhibiting Arrhenius behaviour at high temperature possess constant value of S_c – temperature independent configurational entropy, which is not correct.

However, the value of frozen configuration entropy at T_g is strictly equal to only $S_c^m(0)$. In view of this, z^* at T_g should be equal to $5.764/S_c^m(0)$ (and not $5.764/S_c^m$). Also, since there should be at least one molecular entity for a configurationally rearranging unit to be meaningful, this implies a limiting value of the frozen configurational entropy, which is 5.764 entropy units. The heat capacity measurements on o- terphenyl are shown in Figure 3.06 (left) and the various contributions to the

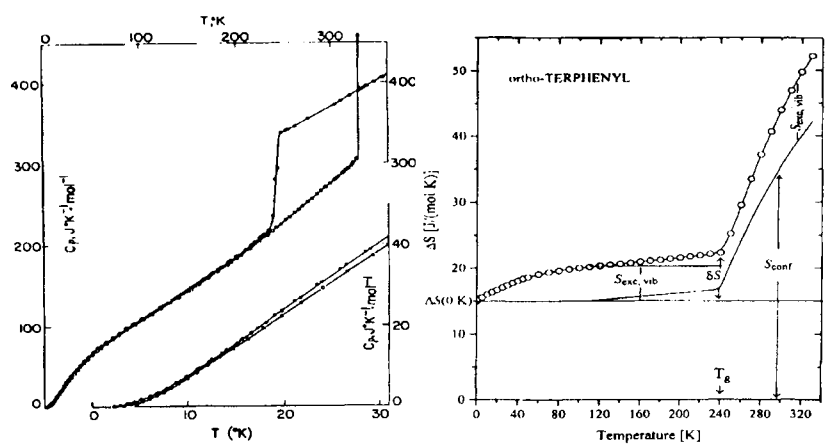

Figure 3.06 (left): Heat capacity of o-terphenyl: □, crystal; ●, annealed glass; O, quenched glass and liquid. (After Chang and Bestul, 1972). (right): The entropy of glassy and liquid states of o-terphenyl minus the entropy of its crystal state plotted against the temperature. The calculated configurational entropy, T_g, the excess vibrational entropy and other quantities are indicated. (After Johari, 2000).

measured entropies are shown in Figure 3.06(right). The fact that substantial vibrational contribution is present in ΔS_m, which goes to zero only at 0 K, has implications for the definition of the Kauzmann temperature T_K also. This is because even when the supercooled liquid loses all the configurational entropy in a hypothetical infinitely slowly cooled glass, the entropy of the glass will still be higher than that of the crystal because of the vibrational contribution. But the sudden change in the slope of S should still give the characteristic feature of an Ehrenfest second order transition in an ideal situation.

Possibility of a divergence of z^* at the ideal glass transition temperature, T_0, is expected because of the following reason. Since $z^* = Ns_c^*/S_c$, and also since S_c can be written as $C(1-T_0/T)$ assuming a hyperbolic variation of ΔC_P, z^* varies as $(1-T_0/T)^{-1}$. Therefore, z^* diverges as the ideal glass transition temperature is approached. In fact, efforts have been made to associate z^* with some correlation length. A thoughtful suggestion has been to consider this as representing a dynamical characteristic length and associate the same with the ratio of the speed of sound to the Boson peak frequency in Raman spectra (see later).

Significant structures approach

Another attempt to understand glass transition phenomenon from the theory of viscosity was made by Eyring and co-workers (1962, 1970). In their significant structures approach, the total partition function of the liquid was expressed as a product of solid-like and gas-like contributions. Then the viscosity is obtained from the activated complex theory after ignoring the contribution from gas-like part to viscosity. The final working expression for the viscosity of a system of rigid spheres was obtained as,

$$\eta = \frac{A\sqrt{T}}{V - V_s} \exp\left[\frac{\varepsilon^{\neq}}{kT}\right] \tag{3.21}$$

where A is a constant involving the free distance between nearest neighbours, mass of the particles and a constant transmission coefficient. V and V_s are the total volume and solid-like part of the liquid volume respectively. $\varepsilon^{\neq}$ is the activation energy for jump of a molecule. Isoviscosity (rheological) criterion for glass transition was used so that at T_g the value of $\eta = 10^{13.6}$ poises. In the homologous series of substituted benzenes, the T_g variations were properly reflected from the theory.

Considering that T_g is initially used to evaluate V_s and the volume of the gas-like part, and the fact that this theory involves several other assumptions*, significant structures approach is inherently weak. Further, the approach inherits all the limitations of free-volume theory in so far as it relates the viscosity to an essentially free volume term, $(V - V_s)$.

Bond-lattice model

Since glasses are disordered solids, it should be of interest to view glass transition as a feature of the amorphous solid state. This is the approach made in the bond-lattice model (Rao and Angell, 1971; Angell and Rao 1972). Most glasses have a short-range order akin to that in the parent crystalline phases. The constituent particles may, therefore, be looked upon as connected to the nearest neighbours but not ordered over long range. Therefore, it should be possible to abstract a lattice of bonds from such arrangements. These bonds may be of any type including secondary bonds (the long-range interactions do not enter into the model specifically). This abstracted lattice of bonds is in some sense similar to Polk-Turnbull (Polk 1971, Polk and Turnbull, 1972) lattice of amorphous germanium. When such a glass is heated, the thermal energy excites these bonds and the bonds are said to be "broken". The excitation is considered as associated with a slight local rearrangement of the structure so that there is a small change in volume, ΔV associated with it. Structural (bond) excitation is also associated with an entropy change ΔS, which arises as a result of vibrational frequency shifts. The excitation is assumed to be random. For the simple case where the presence of only one excited state is assumed (a two-state model) the fraction of bonds broken (f) and the corresponding change in the heat capacity, ΔC_P are given by

$$f = \left[1 + \exp\left(\frac{\Delta G}{RT}\right)\right]^{-1} \tag{3.22}$$

and

$$\Delta C_P = \frac{\Delta H^2}{RT^2} f(1-f) \tag{3.23}$$

* Description of glass transition as an isoviscous phenomenon appears to be incorrect because in a variety of fragile liquids, the calorimetric T_g ($\tau \approx 100$ s) occurs when the liquid viscosities are as low as 10^{10} poises (see Chapter 9).

where ΔG and ΔH are the molar free energy and enthalpy changes during the excitation process. Variation of ΔC_P with temperature does not exhibit any singularity but shows an asymmetrical peak like behaviour. The magnitude of maximum value of ΔC_P is dependent on ΔS while the peak temperature, identified as T_g in this approach, is determined by ΔH. ΔC_P itself is considered as configurational heat capacity. The two-state model does not, however, give rise to sufficiently steep rise of ΔC_P as observed in experimental glass transitions. Possibility of improving the sharpness of rise in ΔC_P has been examined by considering a large number of excited states and also by allowing a part of the excitation enthalpy ΔH to vanish (as in Bragg-William cooperative transition (Rao and Rao, 1978) as a function of temperature. Introduction of n excited states leads to a configurational heat capacity $\Delta C_P(n)$, which is given by,

$$\Delta C_P(n) = \sum_{i=1}^{n} \frac{\Delta H_i^2}{RT^2} f_i(1 - f_i) - \frac{1}{RT^2} \sum_{i,j=1, i \neq j}^{n} \Delta H_i \Delta H_j f_i f_j \tag{3.24}$$

where

$$f_i = \exp\left(-\frac{\Delta G_i}{RT}\right)\left[1 + \sum_{i=1}^{n} \exp\left(-\frac{\Delta G_i}{RT}\right)\right]^{-1} \tag{3.25}$$

The n state model does improve the steepness of the rise in ΔC_P but is still insufficient to simulate the real transition behaviour. Considering $\Delta H = \Delta H_1 + \Delta H_2$, where ΔH_2 is treated as cooperatively vanishing term with the following heuristically chosen functional form:

$$\Delta H_2 = \frac{\Delta H_2^0}{1 + \exp\left(\frac{T - T_r}{D}\right)} \tag{3.26}$$

ΔC_P could be made arbitrarily steep so as to very closely simulate the experimental glass transition. In the above expression, $\Delta H_2{}^0$ refers to the maximum value of this enthalpy (at 0 K); T_r and D are adjustable temperatures. The idea of cooperativity used here is unconventional. It is understandable, however, that as temperature increases, a few secondary bonds get broken (such as hydrogen bonds in glassy water), the strains in

primary bonds (responsible for cohesion and not necessarily rigidity) relax and strengthen while the energies of remaining secondary bonds decrease to a new constant value. But there has been no direct evidence to this effect. The concept of this type of cooperativity in glass transition has been considered doubtful (Goldstein 1969) and alternate methods of attaining arbitrarily sharp rise in ΔC_P has been suggested (Goldstein 1969). This model has however been employed with a reasonable success to discuss the behaviour of $ZnCl_2$ (Angell 1971; Angell and Rao 1972) and As-Se glasses (Rao and Mohan 1979). But it may be recognized that solid state approach to glass transition phenomenon is beset with many conceptual difficulties regarding both the nature of bonds of relevance and their mutual interactions. The bond-lattice model, however, emphasizes the fact that the glass transition may not be a second order transition at all in the Ehrenfest sense. The model has recently been used to fit the heat capacities of a variety of glass forming molecular liquids by treating the number of excitable bonds per molecule as an adjustable parameter (Moynihan and Angell, 2000).

The excited states in the configurational excitation model can be associated with various structural entities in a glass. Mazurin (1991) treated sodium borate glass in this spirit and considered $[BO_{4/2}]Na \leftrightharpoons [BO_{2./2}O]Na$ as equilibrium of two species. The two states differ by a free energy ΔG_0. Further, the dynamics between the two states, which are different in their coordinating environments, is characterized by another high free energy barrier ΔG^*. If x and $(1\text{-}x)$ are the equilibrium concentrations of the two states at a given temperature, then $-dx/dt = (1/\tau)[x(t) - x(\infty)]$ is the rate of conversion of one state to another at a given temperature. The relaxation time τ is given by

$$\tau = \frac{\exp\left(\frac{\Delta G^*}{RT}\right)}{k_0\left[1+\exp\left(\frac{\Delta G^0}{RT}\right)\right]} \tag{3.27}$$

where k_0 is a small constant. Since $\Delta G^* >> \Delta G^0$, τ (and hence η) increases very rapidly as the glass transition is approached. When x is calculated including its time dependence as $x = x(t, T)$, Mazurin found that most of the experimental characteristics of the glass transition can be quantitatively reproduced. But the expression contains two activation barriers, unlike in two state bond lattice model and includes the influence

of the structural relaxation. Thus, this approach is, in essence, the same as the empirical Tool-Narayanaswamy (TN) equation (see chapter 9). There is merit in Mazurin's approach, because it identifies chemical/structural species and treats glass formation as a temperature-time evolution of these species as the liquid is supercooled towards the glass transition. Since it leads to TN type of expression, it has the advantage of describing the properties of glass in the transition region more completely than other approaches.

In the Phillips-Thorpe constraints model, discussed in chapter 2, the glass-forming ability or the stability of the resulting glasses is highest when constraints are equal to the degrees of freedom. This leads to an average coordination number $<n>$ being equal to 2.4 for the most stable glass compositions. Above T_g, these constraints are gradually and increasingly broken as the temperature increases. Conversely at the experimental glass transition arrived at by cooling the melts, not all the constraints are re-established and a residual concentration of the broken constraints is present in the glass. Angell (1999) has attempted to relate these broken constraints to the broken bond concentration (x) of the simple two-state configurational excitation model. Since the event of 'flow' is associated with a critical concentration of broken bonds (presence of a critical concentration of broken bonds enable the atoms to diffuse and lead to a cooperative rearrangement in the region), Angell has suggested that the relaxation probability is related to the broken bond concentration as $W(T) = \exp(f^*/x)$; both W and x are temperature dependent, f^* is the critical value of the fraction of (locally) broken constraints and can be taken as unity. x is from the two-state model and its value is determined by ΔH and ΔS. Variation of $W(T)$ is directly related to the relaxation time and it exhibits a variation similar to VTF behaviour.

Bond lattice model is found relevant in several other contexts also. In the two state model, the highest value of ΔC_P is controlled by the value of ΔS and the strongest liquids (see section on fragility) correspond to ΔS being close to zero, much in the same manner as D having very low values for very strong liquids. The two-state model has strong connections to the new developments based on the concept of energy landscapes, which we will discuss in a later section.

Theory of potential energy surfaces

Goldstein proposed a model of potential energy surfaces to account

for the glass transition in viscous liquids (Goldstein 1969). In this model the energy of an N-particle system can be described by a (3N+1) dimensional energy hypersurface. At high temperatures, the liquid is represented by a hyperspherical surface. As the liquid is cooled, a number of dents (wells) develop on the hyper surface, each characterized by a minimum. The system can be visualized as moving on the surface and exploring these minima in time. As the temperature is further lowered towards T_g, the system explores relatively fewer of these minima, which grow deeper and deeper. Therefore, the configurational entropy of the supercooled liquid becomes very low. When the system is trapped in one of these relatively deep minima it results in glass transition. In this theory, the most important feature is that, the activation energy, which is the depth of an average potential well, is temperature dependent. The theory also predicts that below the glass transition temperature, there must be frozen islands of mobility, which are responsible for secondary relaxations (sub-glassy relaxations). It is now known experimentally that secondary relaxations are quasi-universal features of glassy state (Johari and Goldstein 1971; Goldstein 1976, 1977).

The energy surface model has recently gained much importance. The multiply dented energy surface is described as energy landscape. A small cross-section (in 2 dimensions) of the energy profile is visualized in Figure 3.07. Energy landscapes have now been characterized through computer simulation experiments (see chapter 5) and found to be very informative. In computer simulations, melts have been quenched from

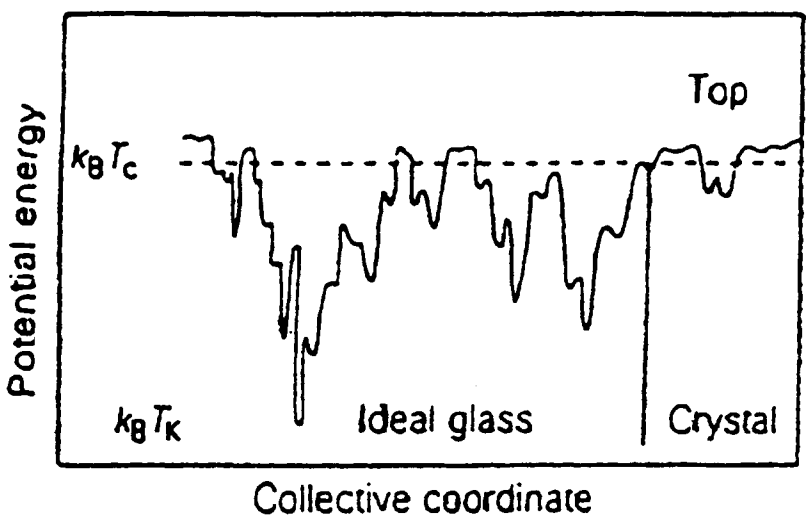

Figure 3.07. 2-dimensional representation of energy landscape (After Angell et al., 1999).

high temperatures and the quenched ensemble energies are computed. The simulations reveal that some configurations are visited by the system more frequently than others and have been termed as *inherent structures*. These inherent structures are local minima and all the states which flow into the same inherent structure (IS) under local energy minimization defines a basin or the valley of the inherent structure (Stillinger and Weber, 1982) Crisanti and Ritort (2000) developed a partition function in terms of these basins of different inherent structures. If all the IS of the same energy E, are grouped, then the partition function can be written as

$$Z_N(T) \approx \int \exp\left[N\left\{-\beta E + S_c(E) - \beta f(\beta, E)\right\}\right] dE \tag{3.28}$$

where $f(\beta,E)$ is the free energy density of the system ($\beta = 1/kT$) which is confined to one of the basins associated with an inherent structure of energy E. $S_c(E)$ represents the configurational entropy density and is also defined as the complexity. The average energies of a system quenched and equilibrated at various temperatures exhibit an energy profile shown in Figure 3.08. It is interesting to note the influence of the quenching rates on the low energy side of resulting energies. The system stabilizes at higher

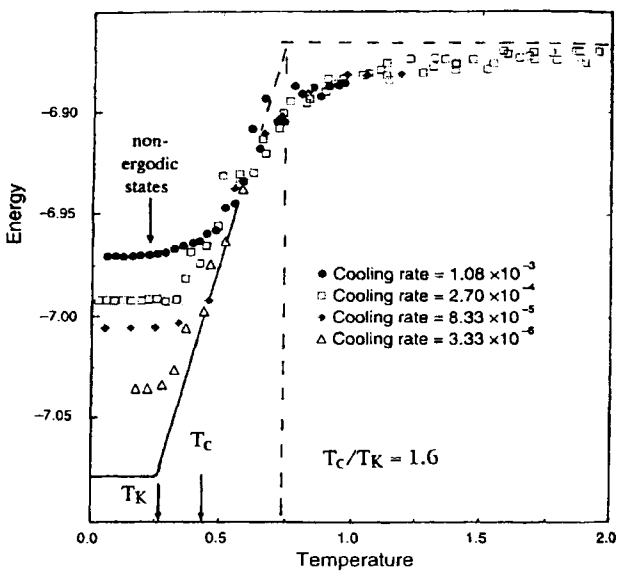

Figure 3.08: Energies of computer quenched IS of a system of mixed LJ particles. (From Angell, 1999, see references in Angell (1999) for other details and definition of temperature).

and higher energies for higher and higher cooling rates indicating clearly that they have fallen out of equilibrium - ergodicity is broken at higher temperatures for high cooling rates. The decreasing portion of the energies can be extrapolated to still lower cooling rates, which may, however, be computationally very expensive. The average energy of the inherent structures, in fact, varies in a manner rather similar to the variation of f of the two-state model. Since $f\Delta E$ (bond excitation energy) represents the same quantity, a simple two-state model appears to generate the essential features of the energy landscape. A point of interest is that the extrapolation of f in two-state model to zero gives the configurational ground state (Kauzmann) temperature of the glass, T_K. This T_K can be used as a reference temperature and the average energy can be obtained by extrapolation from the landscape energy plot. This temperature has also been found to be in accordance with a T_K derived from the energy landscape model itself assuming the relation, $T_C/T_K = 1.6$, where T_C is the 'cross-over' temperature from mode-coupling theories (to be discussed later in this chapter). This relation has been found to be valid in a variety of molecular liquids. Between the temperatures T_C and the ground state temperature T_K, large changes in viscosity and relaxation time (several orders of magnitude) occur whereas the system energy itself decreases comparatively very little.

Stillinger and Weber (1984) analyzed the results of the molecular dynamics of a 150-particle Ni-P system and obtained valuable insights regarding the structures of glass-forming liquids. The potential energy of the whole system, as stated earlier, is represented as a point in the (3N+1)-dimensional space and it was found that a very large number of minima existed for any given value of energy. These minima were connected by saddle points in the configurational space and when the structural rearrangement takes place, the system excurses through the saddle points. Due to particle dynamics in a liquid, the *average potential energy* of the particles, ϕ, in the system seen as a function of time (step numbers) exhibits the oscillatory pattern as shown in Figure 3.09(a). It was observed that when the system is in a potential energy minimum, it jumps to other minima several times. The transitions, however, very rarely take the system to identical arrangement of atoms. The distinguishable number of minima calculated on a per atom basis (σ) and plotted as a function of average potential energy per atom, ϕ, has been the most revealing and shown in Figure 3.09 (b). σ increases exponentially as a function of average potential energy. The lowest energy configurations are attributed to crystalline packings. The density of minima itself exhibits a maximum

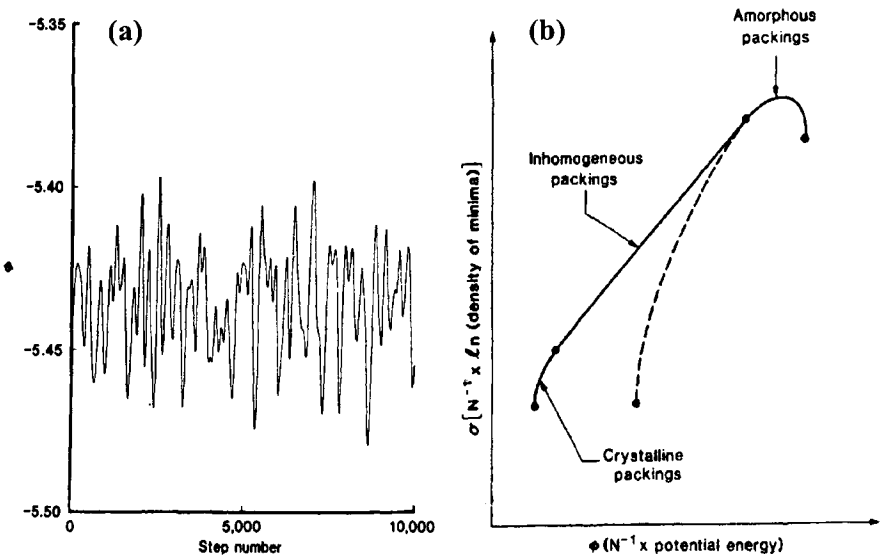

Figure 3.09: (a) Time variation of ϕ, the potential energy per atom in a 150-atom nickel-phosphorous amorphous deposit, as simulated by computer. (b) Logarithm of the distribution of potential energy minima, plotted against potential energy per atom. (After Stillinger and Weber, 1984).

and the maximum corresponds to amorphous structure. Evidently, closer to maxima, which has a flatness, the states corresponding to amorphous packings can be explored for small energy changes implying that these states can have arbitrarily small barriers between them. If the sampling temperature is at or above the melting temperature corresponding to a liquid in thermodynamic equilibrium, then Figure 3.09(b) suggests that all quenched samples have nearly indistinguishable structures in terms of radial distribution functions. They correspond to states of minimum energy in the liquid structure which lie within energy equal to kT. In a supercooled liquid, if the system can find an exit path to take it to inhomogeneous packings consisting of both crystal and amorphous regions, the system would crystallize. But if this does not happen, then it would follow the dotted line path where its energy density increases and finally even as the melt viscosity increases rapidly, the system gets quenched into a glass. Since the Y-axis represents the logarithmic density of minima, the dotted line also indicates the rate at which the configurational entropy of the system changes towards the glass transition. The path corresponding to inhomogeneous packing and leading ultimately to crystallization is never realized, because, nucleation and growth occur

at a temperature in the supercooled regime corresponding to some definite values of the liquid configurational entropy and energy densities. In reality, it is discontinuous. In Figure 3.09 (b), the dashed line corresponds to amorphous packings explored by supercooled liquid which did not have a chance to explore the other identical path whereby it would have crystallized. The deep (global) minima in the configurational hypersurface represents stable crystal structures. The structure surrounding the relatively shallower (glassy states) are the basins, mentioned earlier and for a system trapped in any of these basins, transitions to other basins occur through a passage over barriers. The process appears to involve a local rearrangement of only a small number of molecules.

Inherent structure formalism suggests that glass structure consists of a discrete number of frozen-in energy minima. Therefore, in principle, it defines a heterogeneous structure since the minimum depends on the coordinates of only a small number of particles within some localized region. Interestingly, this model recognizes existence of local particle groupings, which are packed in a near-optimal fashion. The packing requirements of such groups cannot be met with simultaneously because of similar requirements of the neighbouring regions. This structural frustration can lead to a weakly bonded interface between the regions. Another important feature of the energy landscape model is that the dynamics is cooperative since transitions between minima involve coordinates of all particles in some localized region. Also any transition that occurs in the energy landscape is, in essence, an ergodicity restoring process.

Glass transition models based on heterogeneity

A well-recognized feature of supercooled liquids is the presence of density fluctuations. Fluctuations dissipate with characteristic relaxation times. The relaxation times become very long as T_g is approached. This is suggestive of the freezing in of heterogeneities due to variations in densities. Density differentiated regions are expected to be present with a distribution of sizes. The length scales of such heterogeneities at temperatures close to T_g can be of the order of a few nanometres. Thus formation of heterogeneities describes in a natural way a crossover from liquid-like to solid-like behaviour of a supercooled liquid at T_g. The z^* value calculated from Adam-Gibbs theory (referred to earlier) corresponds to cooperatively rearranging regions of only a few molecules, of the order of ten, and are too small in comparison to these solid-like cluster entities.

The average size of such regions can be calculated. Near T_g the volume fluctuation gives rise to a fluctuation in T_g's of these regions. If the glass volume is considered as constituted of a large number of small domains of volume δV, one can relate δV to the fluctuations occurring in the glass transition temperatures in each region. T_g is the temperature at which structural relaxation time in that region becomes of the order of 100 s. The size of the domain, ξ, can be related to fluctuations as,

$$\delta V = \xi^2 = \frac{k\langle T_g \rangle^2}{C_v \rho \langle \delta T_g \rangle^2} \tag{3.29}$$

Here $\langle T_g \rangle$ is the average of the glass transition temperature of all the small domain volumes, ρ is the density, C_V is the constant volume heat capacity and δT_g is the difference in glass transition temperatures between different domains. Using plausible values such as $\langle T_g \rangle$ = 400K, δT_g = 10K, ρ = 1g/cc and $C_V = 1JK^{-1}g^{-1}$, the value of ξ is found to be of the order of 3nm. The value of δT_g of 10K corresponds to a spread in the relaxation times of about an order of magnitude in the glass transition region.

In the AG theory, z^* defines the size of a cooperatively rearranging region (CRR) at T_g, which is necessarily its maximum value. Donth (1982) has evaluated the size of a CRR by assuming that the region is sufficiently big for the application of thermodynamic relations. From fluctuation theory,

$$\delta T_g^2 = \frac{kT_g^2}{nC} \tag{3.30}$$

where $\delta T_g{}^2$ is fluctuation in T_g, n is the number of particles in CRR and C is the heat capacity per particle in CRR. δT_g can be approximated as half the width of the glass transition interval measured in temperature units. CRR may be assumed to be spherical. If the density of the glass is ρ and $1/C \approx 1/C(\text{glass}) - 1/C(\text{melt}) \approx 1/\Delta C_P$, the volume of CRR at T_g can be approximated as

$$\delta V = \frac{4\pi\xi^3}{3} = \frac{k\langle T_g \rangle^2}{\rho \langle \delta T \rangle^2 \Delta C_P} \tag{3.31}$$

This analysis also yields ξ values of 1-2 nm. A significant feature to note

is that up to a distance of ξ = 1-2 nm, the RDF of such glasses should exhibit non-randomness, since the particles in CRR are reasonably structured. Fluctuation leading to heterophase formation has the attraction that creating small, dense clusters in which particles are better packed, helps reduce the entropy of the system. In the supercooled regime, formation of solid-like droplets of such size (sub nano meter clusters) consisting of 10-15 molecules were assumed by Bakai (1996). As the supercooling progresses towards the glass transition, the fraction of molecules present in such clusters necessarily increase. When it exceeds about 15 % - the percolation threshold- solid-like regions become spacially continuous. When about 85 % of the molecules are thus relegated to solid-like clusters, spacial continuity of the interpenetrating liquid regime is broken up and entrapment of liquid-like clusters occurs. This has been found to happen at temperatures of about $1.2T_g$.

Formation of heterogeneity*, therefore, appears to be a precursor stage to the actual incidence of glass transition. This is indicated by various experiments, including glass transition studies in colloids, which in essence, is a scaled-up system for the study of the glass transition phenomenon (one nanosecond in a glass forming liquid corresponds to one second in a colloidal suspension, which is considered a quasi-atomic liquid).

Strong evidence for the presence of heterogeneities, arising from density fluctuation, has been provided by the anomalous scattering (of light) studies as T_g is approached, first reported by Bokov and Andreev (1989) and is shown in Figure 3.10. T_g is also marked on the figure. The cooling curve in the figure exhibits an anomalous sigmoidal shape reminiscent of mean square deviation, $\langle \Delta V^2 \rangle$, in the transition region of the glass volumes. Several such observations have been made subsequently even in small angle X-ray scattering. Intrinsic light scattering from liquids and glasses is caused by density fluctuations in the glass transition region because concentration fluctuations generally freeze out well above T_g. The density (ρ) fluctuation or correspondingly the volume fluctuation can be written as (Moynihan and Schroeder, 1993)

$$\frac{\langle \Delta^2 \rho \rangle}{\rho^2} = \frac{\langle \Delta^2 V \rangle}{V^2} = \frac{kT\Delta\kappa}{V} \tag{3.32}$$

*Following Sillescu (1999), "A system may be called as dynamically heterogeneous if it is possible to select a dynamically distinguishable sub-ensemble by experiments or computer simulations."

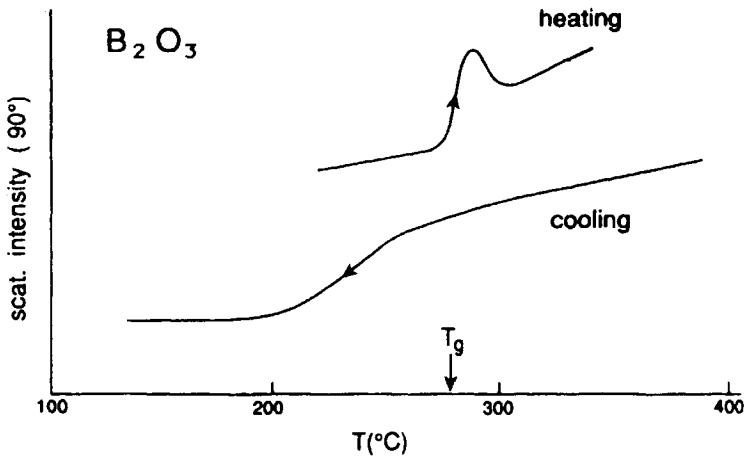

Figure 3.10: Intensity (arbitrary units) of light scattered at 90° from vitreous B_2O_3 during cooling and subsequent reheating through the glass transition region. Cooling and heating curves are displaced for clarity. (After Moynihan and Schroeder, 1993).

where $\Delta\kappa$ is the difference between isothermal compressibilities of liquid and glass and V is a reference volume. The anomalous behaviour in scattering appears to be due to the fact that small regions of low density relax faster than regions of high density. Assuming that such regions exist, and following a procedure similar to that of Donth (referred earlier) and also assuming that the relaxation time is described well by AG theory, Moynihan and Schroeder (1993) have derived an expression relating $\langle\Delta^2 \ln\tau\rangle$ to V_{AG}, which is the correlation volume obtained using AG theory. They found that $(V_{AG})^{1/3}$ to be of the order of 2-3 nm, which is in agreement with the estimates of the correlation lengths of the CRRs obtained by Donth (1982). Thus, the anomalous scattering studies also establish a length scale of the frozen fluctuations which correspond to nano-scale heterogeneities in real glasses.

In the following, glass transition models which recognize the presence of heterogeneity in glass structure, are discussed.

Structural frustration model

Kivelson and Tarjus (1998) have considered the attractive possibility of invoking the concept of "structural frustration" in supercooled liquids, to account for the observed liquid viscosity behaviour. Around the melting temperature, T (T>1.3T_g), most melts behave 'normally' in the sense of exhibiting an Arrhenius temperature

dependence of relaxation times. The molecular entities tend to arrange themselves into locally preferred structures upon cooling in order to minimize their free energies. The sizes of such preferred structural groupings cannot grow bigger than a certain size because it is thwarted by a structural frustration since these structures cannot lead to periodic tiling of space, except by introducing severe strains. Thus, the liquid, below some temperature T^* breaks up into domains which tend to minimize the strain and hence the free energy. T^* is the temperature which marks a crossover from normal molecular liquid behaviour to that of a domain-influenced behaviour; or from Arrhenius to VTF kind of behaviour. Theoretical consequence of the structural frustration and hence of the domain formation in liquids is that above T^* (Arrhenius region), there is a single temperature-independent activation barrier, E_∞ but below T^* the activation energy becomes $E_\infty + B(1-T/T^*)^{8/3}$. The experimental data on glass-forming liquids is consistent with the above expectation. The unusual exponent, 8/3, also seems to be borne out in experiments. This basically heterogeneous model provides a theory for the variation of the effective activation barrier, within the framework of an Arrhenius model.

Kivelson and Tarjus (1998) have examined further the dynamics in the supercooled region and the Kauzmann paradox and catastrophies* in the above light. The domain sizes increase modestly as the temperature is lowered further. Since there is an increasing order associated with the formation of domains, the configurational entropy of the melt decreases as the temperature of the melt decreases. Correspondingly the structural relaxation time slows down because of the domain growth. The growing time scale of this relaxation leads to the breakdown of thermodynamic equilibrium and to the glass transition. These domains are essentially clusters whose free energy is composed of three terms.

$$F_{\text{cluster}} = \sigma L^2 - \phi L^3 + sL^5 \tag{3.33}$$

Where L is the length scale of the cluster. The first term constitutes a surface free energy term while the second is the bulk free energy term. The third term represents a strain term arising from the structural frustration which prevents the growth of the size of domains. It is this term which distinguishes the cluster free energy from an otherwise similar description of the free energy of the nuclei in nucleation and growth

* Kauzmann catastrophe can be understood with reference to Figure 2.16. If S decreases in the same manner as V, in a (hypothetically) supercooled liquid, it would become zero at some value of $T>0$. This is a catastrophe in the light of the laws of thermodynamics.

phenomena (see Chapter 2). Below the glass transition, it is argued that the trend of variation in S_c is different from the same above T_g and hence Kauzmann paradox or catastrophe may not occur at all since $S_c \rightarrow 0$ only as $T \rightarrow 0$.

Similar heterogeneous model has been used to develop a relaxation function by Chamberlin and Kingsbury (1994), who consider the localized normal modes to be involved in the relaxation process. Localized (domains) regions are assumed to be present between T_g and T^*. They are described as dynamically correlated domains (DCD). A Gaussian distribution of the domain sizes has been assumed, with each domain characterized by a Debye relaxation time. Expressions for the dielectric susceptibility have been derived and used to fit the experimental susceptibilities of salol, glycerol and many other substances with remarkable agreement over 13 decades of frequency (even when only one adjustable parameter is employed).

Cluster model of glasses and glass transition

The cluster model of glass transition gives primacy to the presence of heterogeneity in glass structure. Occurrence of glass transition is visualized as follows. Density (and to a small degree, composition) fluctuations "nucleate" the clusters at low enough temperatures in the super-cooled region. The clusters grow in size rapidly but their growths are self-limiting. They attain a size of few nm. Glass transition occurs when a major part of the melt is thus transformed to clusters the remaining material simply freezes (Rao and Rao, 1982, Rao, 1984) into a tissue of lower density compared to clusters. The degree of positional correlation in the tissue does not extend beyond SRO. Such a description of glass structure is particularly relevant to ionic, metallic and molecular (small molecules) glasses. Even in highly covalently bonded glasses like SiO_2, GeO_2, B_2O_3, As_2Se_3, etc also, clusters can form during cooling by re-bonding of molecular fragments in their melts.

The reason for the self-limiting growth is that in some cases, clusters grow into amorphons, whose size becomes energetically unfavourable above few nm (Burton 1970, 1973). In the case of the covalently-bonded clusters, the occurrence of topological disorder (wrong bonds and wrong dihedral angles) may act to terminate growth (Phillips, 1982). In metallic and multi-component ionic glasses self-limiting growth may be a consequence of compositional disorder at the interface between

the cluster and tissue over nanometric scales. A simple model, particularly relevant for ionic glasses has been formulated on this basis.

Particles in a glass made up of cluster and tissue (CT glass; Figure 3.11(a)) fall into three categories. (a) Particles inside the cluster, whose motion is governed by an essentially harmonic potential. (b) Particles in the tissue region, whose motion is governed by highly anharmonic potential. (c) Particles on the cluster surface, whose motion is also governed by high degree of anharmonicity but more so towards the tissue region. The effect of temperature on particle motion in such a glass is more marked in tissue region because their potential profiles coalesce at higher (thermally accessible) energies (Figure 3.11(b)). At higher and higher energies, more and more potential wells are coalesced in the tissue region. By increasing the temperature, particles are vibrationally excited to coalesced potential regions and lead to systematic increase in particle amplitudes. Particles on the surface of clusters also behave similarly. Important consequence of large amplitude vibrations of particles is to enable a permanent escape of such particles from their original potential wells. This happens to particles on the surfaces of the clusters also. As more and more particles leave the surface of a cluster, it shrinks in size and the volume of the tissue region increases at the expense of clusters. The process continues till the clusters disappear (and thus transform) into the tissue region. The temperature at which clusters vanish is recognized as the glass transition temperature, T_g^0, of the model. Thus the model visualizes a gradual evolution of translatory motion from a vibratory motion by involving the presence of highly anharmonic coalescing potential profiles in tissue region.

The cluster surfaces act as a source of particles for the tissue during heating and these particles are distributed into the spectrum of energy levels. There is thus a quasi-equilibrium between particles on the surface and particles in the spectrum of energy levels.

Particles on cluster surface $\leftrightharpoons$ Particles in the vibrational energy manifold

The problem of glass transition, therefore, reduces to finding out the temperature dependence of cluster size, which in turn is related to the rate at which the surface particles 'melt' into the tissue. Using plausibility arguments, an assumption has been made that the population of the vibrational ground state in the tissue remains constant till T_g^0. If f_0 represents the fraction of particles in the ground vibrational state of tissue region at a temperature T and if N_t is the total number of particles in the

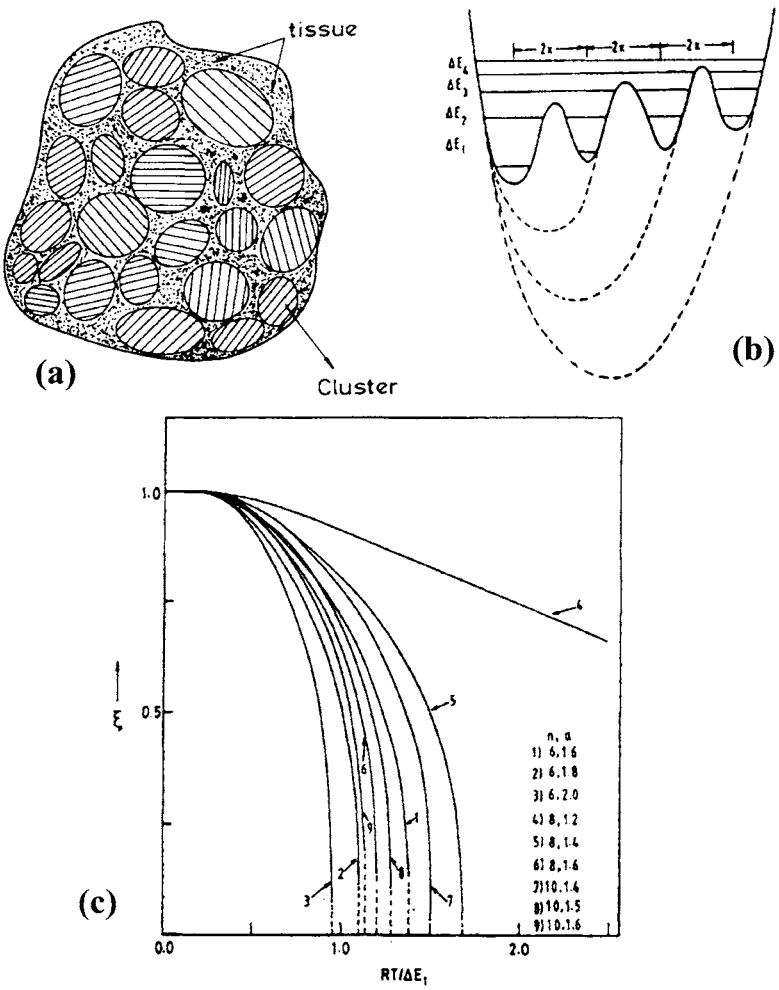

Figure 3.11: (a) Cluster (hatched) -tissue (dotted) texture of glass, (b) coalesced potential wells and energy separations and (c) variation of ξ in model calculations as a function of $RT/\Delta E_1$ for various sets of n and a values. Doted portions show steep fall of ξ to zero. (After Rao, 1984).

tissue region, then $N_t f_0$ = constant according to this assumption. Therefore, $d(N_t f_0)/dT = 0$, or

$$\frac{d \ln N_t}{dT} = -\frac{d \ln f_0}{dT} \tag{3.34}$$

Further if V_c and V_t are the volumes of clusters and tissue, the total volume

$V = V_c + V_t$ is also approximately constant. If ρ is the number density of particles (assumed equal for both tissue and cluster regions), then $V_c + (N_t/\rho_0)$ = constant. Therefore

$$\frac{dV_c}{dT} = -V_t\left(\frac{d\ln N_t}{dT}\right) = -(V - V_c)\left(\frac{d\ln N_t}{dT}\right) \tag{3.35}$$

Combining equations (3.34) and (3.35),

$$\frac{1}{V - V_c}\left(\frac{dV_c}{dT}\right) = \frac{d\ln f_0}{dT} \tag{3.36}$$

Integrating both sides with respect to temperature and re-organizing the terms,

$$\ln\left[\frac{V - V_c^0}{V - V_c^T}\right] = \ln f_0(T) \tag{3.37}$$

since $f_0(0) = 0$, V_c^0 and V_c^T are cluster volumes at temperatures 0 and T respectively. If the total volume and the volume of clusters at 0 K are related as $V = aV_c^0$, where a is a constant (ignoring the effect of thermal history), the above equation may be simplified as

$$\frac{V_c^T}{V_c^0} = a\left[1 - \left(\frac{a-1}{a}\right)\left(\frac{1}{f_0(T)}\right)\right] \tag{3.38}$$

Using a simple form of partition function,

$$Z = \sum_{i=0}^{n} \exp\left[-\frac{\Delta E}{RT}\right] \tag{3.39}$$

and with $\Delta E_0 = 0$, we have $f_0(T) = 1/Z$, so that

$$\frac{V_c^T}{V_c^0} = a\left[1 - \left(\frac{a-1}{a}\right)Z\right] \tag{3.40}$$

The above equation implies (V_c^T/V_c^0) decreases from unity to zero as T increases from 0 to T_g^0, the glass transition temperature. Since V_c is total cluster volume, $V_c = \sum v_{ci}$ where v_{ci}, is volume of the ith cluster. If cluster volumes have a narrow distribution, then $V_c = n \langle v_{ci} \rangle$, where $\langle v_{ci} \rangle$ is the average cluster volume and n is the total number of clusters. One can then define a linear dimension of the cluster, ξ, as

$$\xi = \left(\frac{\langle V_c \rangle}{\langle V_c^0 \rangle} \right)^{1/3} = \left[a \left(1 - \frac{a-1}{a} Z \right) \right]^{1/3} \tag{3.41}$$

As $T \rightarrow T_g^0$, $\xi \rightarrow 0$. In order to investigate the behaviour of ξ as a function of temperature the energy spectrum needed to evaluate Z has to be specified and a reasonable value of "a" must be assigned. For a collection of spherical clusters of equal radii touching each other, $V/V_c^0 = a \approx 1.6$, a value suggested by the random close packing model. No unique representation of connected potential wells can however be prescribed. Coalescence of the energy wells, however, bring about a decrease in the separation of energy levels, $\Delta E_n < \Delta E_{n-1} < \ldots\ldots < \Delta E_1$. Assuming that the separation of energies follow a simple function, $\Delta E_n = (1/n)\, \Delta E_1$, Rao and Rao (1982) evaluated Z. ξ has been evaluated with a few representative values of a and n. The behaviour of ξ is shown in Figure 3.11(c) as a function of the inverse of scaled energy $\Delta E_0/RT$. The nature of variation of ξ in Figure 3.11(c) is remarkable for it is highly reminiscent of the variation of order parameter in cooperative transitions. ξ decreases very rapidly towards higher values of $(RT/\Delta E_1)$ and $\xi \rightarrow 0$ as $T \rightarrow T_g^0$. Therefore ξ can be used as an order parameter for glass transition. The free energy density of the glass (Rao and Rao, 1978) may then be expanded in terms of ξ in the neighbourhood of T_g^0.

$$\phi(\rho, T, \xi) = \phi_0(\rho, T) + b\xi^2 + c\xi^4 + \ldots\ldots \tag{3.42}$$

This mean field model leads to standard results:

$$b = B\left(T - T_g^0\right) \tag{3.43}$$

$$\xi = B^{1/2}\left(T - T_g^0\right)^{1/2} \tag{3.44}$$

and

$$\Delta C_P = \frac{B^2 T_g^0}{2d} \tag{3.45}$$

Glass transition can thus be attributed with the characteristics of a standard second order transition to it as envisaged in the AG model. Further T_g^0 can be estimated in this model from a knowledge of ΔE. Thus for example in Li^+ containing glasses Li^+ cage vibrations occur ~ 400 cm^{-1}. If a ~ 1.6 and n = 4 –10, T_g^0 given by the model is around 600 K.

Boson peak and FSDP

Micro-heterogeneity, therefore, seems to be almost a universal feature of glasses, the origin of which is considered to be density fluctuations. Heterogeneity can be due to the formation of domains caused by frustration or any other reason. The important point to note is that the intermediate range order sets in in small regions and this order cannot propagate any further. Presence of such intermediate range order gives rise to two significant and apparently correlated experimental phenomena. First is the appearance of *Boson peaks* in low energy Raman spectra. Second is the appearance of the *First Sharp Diffraction Peak*, *FSDP*, in the structure factor spectra. FSDP can only be associated with the presence of correlations over long distances, ranging up to 25Å. FSDP spectra are shown in Figure 3.12 for several glasses studied by Sokolov et al. (1992). The correlation length, R_c can be obtained from the half width of the FSDP, ΔQ, by using the relation $R_c \approx 2\pi/\Delta Q$. ΔQ itself has been calculated by making a Lorentzian fit to the FSDP at Q_1.

$$I(Q) = \frac{\Delta Q}{(Q - Q_1)^2 + \Delta Q^2} \tag{3.46}$$

(Note: Fitting has been done to the small Q side of the FSDP obtained from X-ray scattering). Values of ΔQ and Q_1 are listed in Table 3.4. It may be seen that these values indeed range from 12-26 Å. Glasses like As_2Se_3 (R_c =10Å) and Se (R_c =11Å) have also been found to exhibit similar FSDP phenomena. Several models have been proposed to understand FSDP. Thoughtful among them is the model by Elliot (1990). In this model the

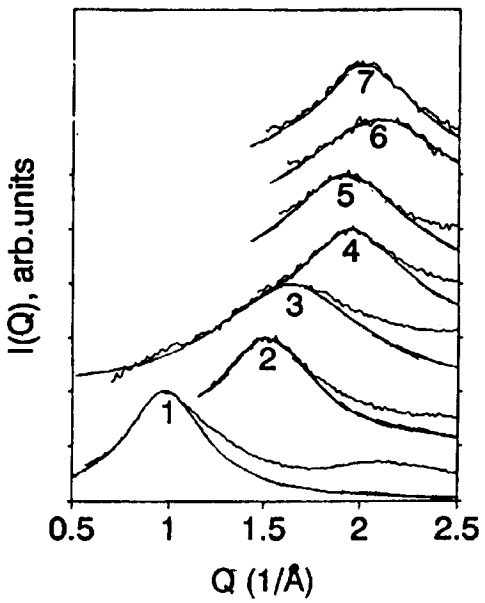

Figure 3.12: X-ray diffraction pattern in the glasses (the numbers correspond to the numbers in Table 3.4). Thin lines are Lorentzian fits. (After Sokolov et al., 1992).

Table 3.4: Frequencies of the Boson peak maximum, sound velocities and parameters of FSDP in oxide glasses along with R_c values. (After Sokolov et al., 1992).

No.	Samples	ω_{max} (cm^{-1})	V_t (km/s)	V_l (km/s)	Q_l ($Å^{-1}$)	ΔQ ($Å^{-1}$)	R_c (Å)
1	PMMA	16.5	1.42	2.78	0.98	0.26	24.15
2	SiO_2	51.5	3.79	5.92	1.51	0.31	20.26
3	GeO_2 –5.4%Na_2O	48.5	2.46	4.1	1.63	0.47	13.36
4	SF1	38.5	2.22	3.77	1.95	0.36	17.44
5	F1	43.5	2.47	4.15	1.92	0.40	15.70
6	BaSF64	83.5	3.51	6.23	2.09	0.49	12.82
7	LaSF9	64.0	2.98	5.43	2.01	0.35	17.94

presence of interstitial volume is considered as giving rise to such medium range order through atom-void correlations.

Presence of medium range order gives rise to another phenomenon observed in spectroscopy, known as Boson peaks. These arise from the quasi-local excitations sustained by regions in which such intermediate order (IRO) is present. Several studies have indicated the presence of anomalies of vibrational properties such as excess vibrational density of states at low energies observed at low temperatures. This manifests as Boson peaks in Raman spectra. The normalized Raman spectra in the low frequency region are shown in Figure 3.13 for the same glasses for which

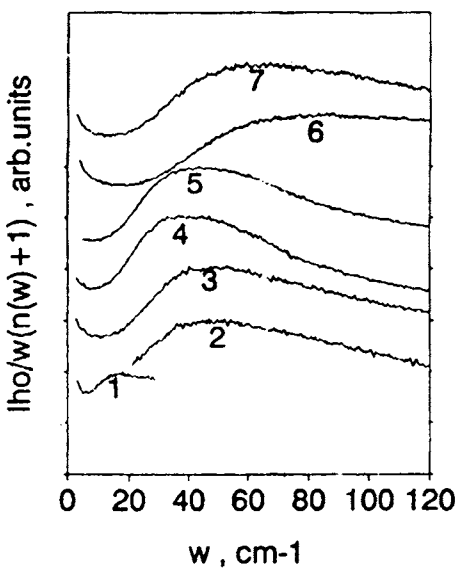

Figure 3.13: Low frequency normalized Raman spectra (the numbers correspond to the numbers in Table 3.4). (After Sokolov et al., 1992).

the FSDP are shown in Figure 3.12. The normalized Raman intensity is given by

$$I(n) = \frac{I}{\omega[n(\omega)+1]} \tag{3.47}$$

where $[n(\omega)+1]$ is the Boson factor for the Stokes component. The designation, Boson peak, is because its intensity varies with temperature as the Bose population factor. The origin of this Raman scattering peak is

due to the fluctuation of elastic (and also elasto-optic) constants over the range, R_c, the correlation length. ω_{max} is given by the expression

$$\omega_{max} \approx \frac{V_t}{cR_c} \tag{3.48}$$

where V_t is the velocity of the transverse sound waves and c the velocity of light. These have been calculated using the values of V_t and ω_{max} listed in Table 3.4. Elliot (1990) has derived a similar expression for R_c using Ioffe-Regel condition, which states that $ql = 2\pi$, where $q = 2\pi/\lambda$ and λ is the phonon wavelength. The condition gives the limiting value of the mean free path, l, (which is equal to R_c) in the strong scattering limit, which localizes the phonon. The R_c calculated from FSDP and Boson peaks seem to correlate very well as shown in Figure 3.14. Boerjesson et al. (1993), however, failed to observe any correlation between FSDP and Boson peak in borate glasses. Nevertheless, the occurrence of Boson peaks and FSDP seems to be near universal features and strengthen the view that glasses may, in general, possess heterogeneous structures. It appears that glass literature of the eighties and nineties is densely dotted with

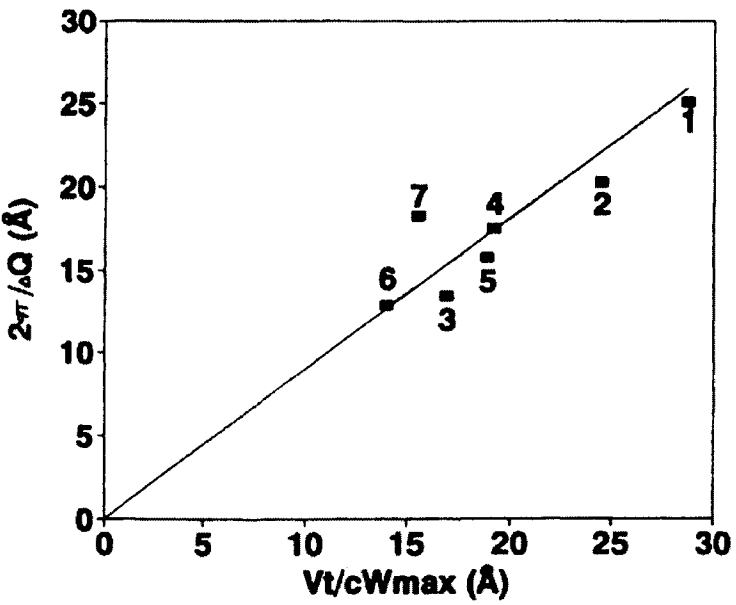

Figure 3.14: Correlation length obtained from the FSDP vs that from the Boson peak maximum; the numbers correspond to Table 3.4. (After Sokolov et al., 1992).

descriptions like domains, clusters, blobs, medium range order, frozen density fluctuations, etc., all of which refer essentially to the same micro-heterogeneities. It is also interesting to note that from both, theoretical analysis and scattering experiments, the dimensions of such micro-heterogeneities is in nanorange, 1 nm $\leq R_c \leq$ 5 nm, which suggests a new length scale appropriate for glass structures.

Mode Coupling Theory (MCT)

MCT is a popular liquid viscosity theory (Gee, 1970; Götze et al., 1981; Leutheuser, 1984, Jäckle, 1989). It is based on the description of the dynamical properties of density fluctuations in terms of a dynamical structure factor. There are inherent density fluctuations in liquids, which decay with characteristic relaxation times. The decay becomes slower as the temperature is lowered due to increase of viscosity. It is controlled by dynamically correlated collisions. The equations governing the decay are non-linear. Analysis of the non-linear equation of motion of the density fluctuations gives a density correlation function of the type

$$\phi(z) = -\frac{1}{z - \dfrac{\Omega_0^2}{z + D(z)}} \tag{3.49}$$

where $D(z) = i\gamma + 4\lambda\Omega_0{}^2\mathcal{L}\,[\phi^2(t)]$ and $(z = i\omega)$. $D(z)$ is the longitudinal viscosity and $\Omega_0{}^2$ is the second frequency moment and γ is the damping constant. The important parameter is the dimensionless coupling constant λ. $D(z)$ can be set equal to $i\gamma$ when the correlation function, $\phi(z)$, will be described by two poles.

Leutheuser (1984) has shown that when the coupling constant λ is set equal to $\lambda_c = 1$, a critical value, the density fluctuations do not decay to zero for long times. This in essence, characterizes transition to the glassy phase. The glass transition in MCT is thus expressed through the cessation of the decay of the density fluctuation. The MCT formulations are mathematically rich and enable deduction and interpretation of several properties of liquids. Of particular interest is the divergence of the longitudinal and shear viscosities which increase as $[1-\{\lambda/\lambda_c\}]^{-\mu}$, where the exponent μ has a value 1.765. It may be recognized that while for small values of λ, $D(z)$ is a constant and equal to $i\gamma$, for larger γ, it becomes frequency dependent. Viscosity increases, relaxations slow down and the

system becomes more rigid. Thus the product of two density modes which are coupled by λ lead to enhancement of the longitudinal viscosity which in turn slows down the relaxation of the density fluctuations. This is a sort of self-induced slowing down of relaxation. Viscosity increase - structural relaxation slowing down - increasing of the contribution of the density mode to the viscosity, is the sort of feedback mechanism, which leads to divergence of viscosity.

It is, therefore, expected from MCT that η exhibits a divergence with decrease in temperature from above a temperature T_C (corresponding to λ_c) as $\eta = \eta_0 [(T/T_C) - 1]^{-\mu}$. A test of MCT prediction, has been made by Angell (1998) by plotting $1/\eta^{(1/1.8)}$ vs T/T_g (temperature scaled by T_g) for a variety of glass-forming liquids, some of which are shown in Figure 3.15. T_g was obtained by thermal analysis. Firstly, it is found that the behaviour is non-linear for liquids like ethanol requiring higher values of μ.

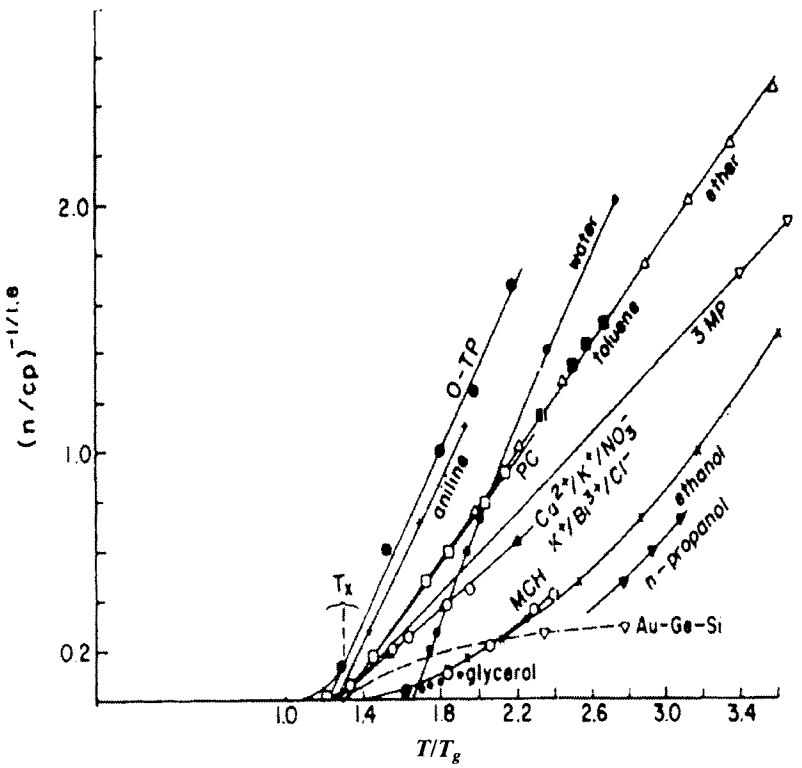

Figure 3.15: Test of the mode coupling theory power law predictions for viscosity temperature dependence for a variety of molecular and ionic liquids. T_g is the glass transition temperature determined by thermal analysis at 10 K/min scanning (After Angell, 1998).

Secondly, and more importantly, viscosity divergence does not occur at T_g. It occurs at a temperature T_C, which is on an average 1.3 times T_g. Thus the purely kinetic approach of MCT, which attempts to track the glass transition temperature via the divergence of η leads to a transition temperature T_C, much higher than T_g. T_C lies well within the supercooled region. In fact VTF analysis becomes more relevant only below T_C. Therefore, T_C is a "crossover" temperature, the crossover being from a power law regime to a VTF regime in viscosity behaviour as the glass-forming liquid is cooled. Also, T_C occurs in the η range of about 10 poises, where activated processes begin to dominate the liquid relaxation. Thus it marks a crossover from collective to cooperative regimes of liquid relaxations*. T_C appears to be the temperature where the supercooled liquid begins to explore the (3N+1) dimensional potential energy surface.

It may be instructive to note that at T_C most of the entropy of fusion is still present in the liquid and perhaps correspondingly a large part of the viscosity increase is yet to occur. Parameters obtained from MCT analysis of viscosity of a few glass-forming liquids are given in Table 3.5. It is seen that T_C/T_g ratio is of the order of 1.3 for strong network formers and is 1.16-1.20 for fragile liquids. This indicates that the configurational constraints imposed by the network topology obstruct collective motions. Onset of collective motions, therefore, require higher temperature ($T \geq T_C$).

Table 3.5: Values for critical exponent γ, critical temperature T_c and the glass transition temperature T_g for the few systems (After Richert and Bassler, 1990).

System	γ	T_c(K)	T_g(K)	T_c/T_g
B_2O_3	3.0	707	534	1.32
Glycerol	3.2	250	186	1.33
o-Terphenyl	3.0	285	238	1.20
o-Crysol	3.6	243	208	1.17
Polystyrene	3.45	445	384	1.16

* Angell (1998) remarks that MCT brings us "to the edge of the real problem (which is glass transition)."

Other viscosity theories

The question arises as to whether there are viscosity expressions other than the VTF and MCT equations, which contain divergence temperatures (T_0 or T_C). An empirical formula of some merit which fits the viscosity data over as many as 8 decades, particularly in the high viscosity regime ($\eta > 10^6$ poises), was proposed by Richert and Bassler (1990) $\eta = \eta^0 \exp(T_0'/T)^2$. T_0' is constant with units of temperature. This formulation is attractive because it avoids having to invoke any other temperature of divergence as in VTF equation. The fit is exemplified for the case of polystyrene in Figure 3.16. Such a T^2 law has been derived from energy landscape model applying an effective medium approximation by Bassler (1987). Viscosities of B_2O_3 and o-terphenyl are also found to comply with the above equation. A good correlation is observed between T_g and the T_0' as shown in Figure 3.17 in the case of several organic and inorganic glasses.

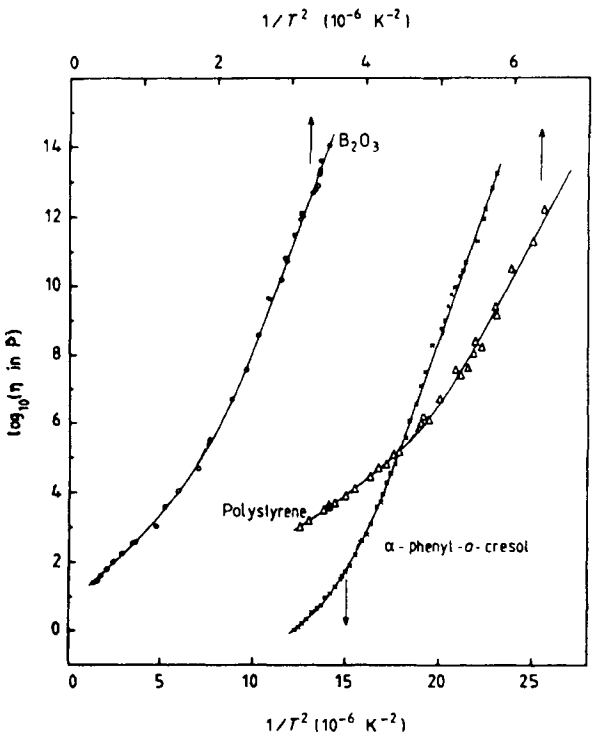

Figure 3.16: Viscosity data for polystyrene, B_2O_3 and α-phenyl-o-cresol plotted as $\log\eta$ vs $1/T^2$. (After Richert and Bassler, 1990).

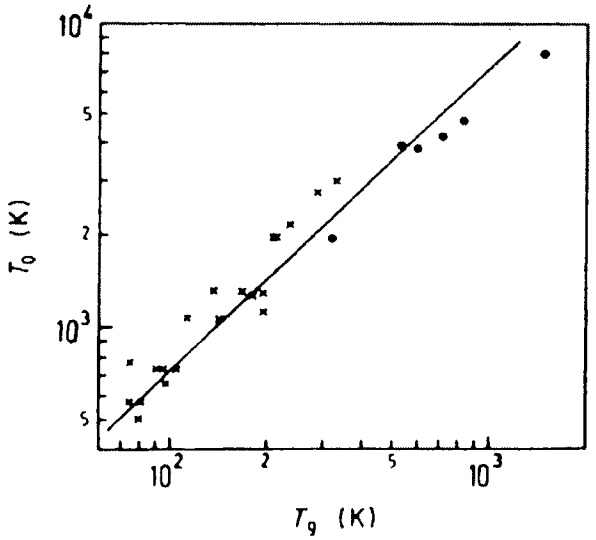

Figure 3.17: Correlation between the characteristic temperature T_0 ($\equiv T_0'$, in the text) and the glass transition temperature T_g for a series of organic glass formers. (After Richert and Bässler, 1990)

A different approach was made by Dyre et al. (1996) to account for the experimental viscosity variations with temperature as an alternative to VTF and AG models. They considered the flow in viscous liquids to arise from sudden events involving motion and reorganization of several molecules. From the viewpoint of mechanism, the energy required for such flow is minimized if the surrounding liquid is shoved aside to create the necessary volume for rearrangement. This volume is fundamentally different from the volume of the free volume theory and is, in principle, an activation volume. The free energy involved may be written as

$$\Delta F(T) = G_\infty(T).V_C \tag{3.50}$$

where G_∞ is the shear modulus, V_C is some characteristic volume, which is related to the activation volume, ΔV, and the volume of the liquid before shoving. It is given by,

$$V_C = \frac{2(\Delta V)^2}{3V} \tag{3.51}$$

The expression for η, the viscosity, in terms of $\Delta F(T)$ is given by

$$\eta = \eta_0 \exp\left[\frac{\Delta F(T)}{kT}\right] \tag{3.52}$$

The non-linearity of the log viscosity as a function of inverse temperature arises due to the fact that $G_\infty(T)$ itself is temperature-dependent. Variation of $\ln(\eta)$ as a function of T_g/T is shown in Figure 3.18, along with the

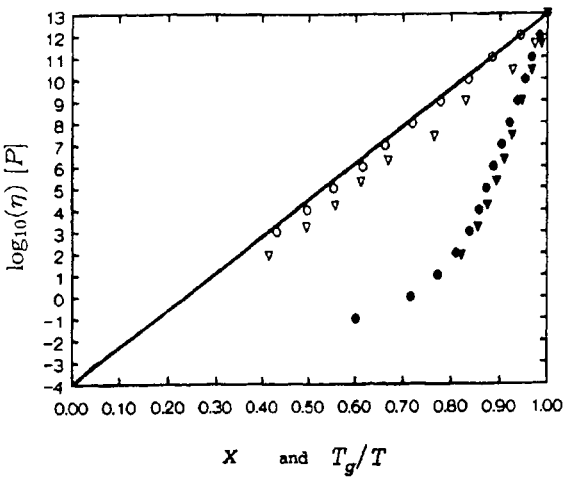

Figure 3.18: Logarithm of the viscosity in Poise as a function of T_g/T (filled symbols) and as function of the variable x (open symbols) normalized to one at $T = T_g$. G_∞ was obtained from depolarized Brillouin scattering. (After Dyre, 1996)

variation of $\ln(\eta)$ as a function of x, where x is $\{G_\infty(T)/\ G_\infty(T_g)\}.\{T_g/T\}$. It is therefore interesting to note that $\{G_\infty(T)/\ G_\infty(T_g)\}$ or more simply $G_\infty(T)$ is itself playing the role of D of the VTF equation or of $(1/S_c)$ in the AG equation. Since VTF relation itself has been derived from AG equation, assuming a hyperbolic ($\propto 1/T$) relation between ΔC_P and T, it implies that if $1/G_\infty$ also varies as $(1\text{-}T_0/T)$ in the region of glass transition, viscosity variation expected from AG relation and from the relation suggested by Dyre et al. (1996) would lead to qualitatively similar results. Nevertheless, it is interesting to know that in the viscosity regime of about 10^4-10^{13} poises, $\ln(\eta)$ vs $1/(T\text{-}T_0)$ and $\ln(\eta)$ vs $G_\infty(T)/T$, both linearise the data leaving unclear the exact nature of the molecular mechanism of viscosity.

Polyamorphism

A thought-provoking question in glassy state is concerned with the

possibility of polymorphism or more simply the possibility of the presence of a plurality of amorphous structures, which are not necessarily connected by transitions among themselves. The arrival at the glassy state is conditioned by kinetics. In the supercooled liquid, kinetics governing the quasi-continuous change into thermodynamic states of lower and lower energy slows down. Further, there are evidences of liquid-liquid transitions which suggests that at least two reasonably well-defined thermodynamic states are likely to be present in supercooled liquids. In order to explore their thermodynamics and their structures, it is necessary to quench the melts into glassy states and reach above and below the critical point characterizing the transition between two liquid states. But nucleation and growth of crystalline phases in the supercooled region can obscure the liquid-liquid transition.

Polyamorphism studies have been reported on several liquids (Schober et al., 1998, Poole et al., 1997) whose structures are built from tetrahedra such as Si, Ge, SiO_2, GeO_2 and H_2O. In an ingenious flash irradiation experiment, a first order glass-liquid transition has been reported in Si (cited in Poole et al., 1997). Abrupt changes in density at low temperatures have been observed in the case of amorphous H_2O, SiO_2 and GeO_2 indicating transitions between frozen phases. A multi-component Y_2O_3-Al_2O_3 melt has also been found to give rise to two co-existing glass structures (cited in Poole et al., 1997). An organic liquid, triphenyl phosphite, has been reported to exhibit polymorphism in liquid state and the number of liquids in which polymorphism is observed continues to increase. Pressure induced crystallization has also been observed in many glasses (materials with tetrahedral structures are somewhat unique and crystal to glass reversible transition has been reported in many such materials (Sikka, 1992)).

Polyamorphism of water deserves a special mention. In a clever experiment, Schober et al. (1998) pressurized hexagonal ice (I_h) at 77K to obtain high density amorphous ice (I_{hda}); density = 1.17 ± 0.02 g/cc. It was gradually warmed to about 127 K where it transforms to low density ice, I_{lda}. Vibrational density of states of the phases were determined using inelastic neutron scattering technique (time-of-flight spectrum using incoherent approximation). Shown in Figure 3.19 is the density of states as a function of energy. It is evident that the vibrational spectra of I_{hda} and I_{lda} are markedly different. The 8meV peak is both shifted to 6meV in I_{lda} and also becomes sharp confirming the occurrence of the transition. There was no clear evidence of the involvement of nucleation and growth mechanism in this transition.

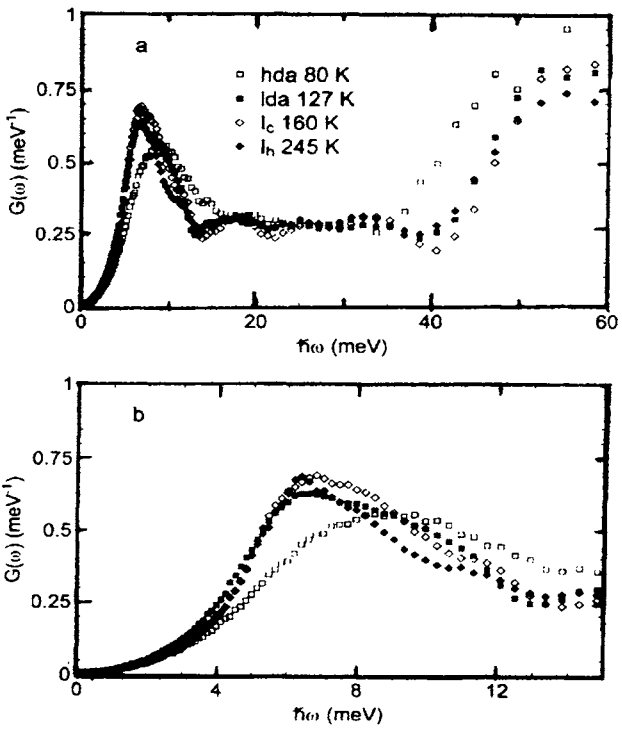

Figure 3.19: (a) Comparison of the generalized density-of-states for I_{hda}, I_{lda}, I_c and I_h ice; (b) The region of 1-16 meV has been expanded. (After Schober et al., 1998).

Fragility and glass forming liquids

We now discuss the concept of fragility for which references were made repeatedly. Glass transition marks the terminus of the liquid state and is arrived at via a continuously increasing viscosity. All of the dynamical changes which determine the structure of the resulting glasses occur in the supercooled region, in fact, in several of them, close to T_g. Thus, there is much to learn about the glass transition by examining the behaviour of viscosities in the supercooled region. Such an approach has led to the formulation of new ideas. A careful analysis of log viscosity vs inverse temperature plots has led to the concept of fragility. $\ln(\eta)$ vs T_g/T plots were historically first constructed by Oldekop (1957) and later by Laughlin and Uhlmann (1972). A departure from Arrhenius behaviour was noted by both. Angell (1986, 1995) analyzed the behaviour keenly and found that they are indeed the same (as VTF) plots with different D values

when the x-axis was chosen as T_g/T instead of $1/(T\text{-}T_0)$. Angell proposed a classification of liquids based on the extent of departure from linearity.

The fragility plot of Angell is reproduced in Fig 3.20(a) (ln η vs T_g/T). However, plots of similar kind using T^* as an iso-viscosity

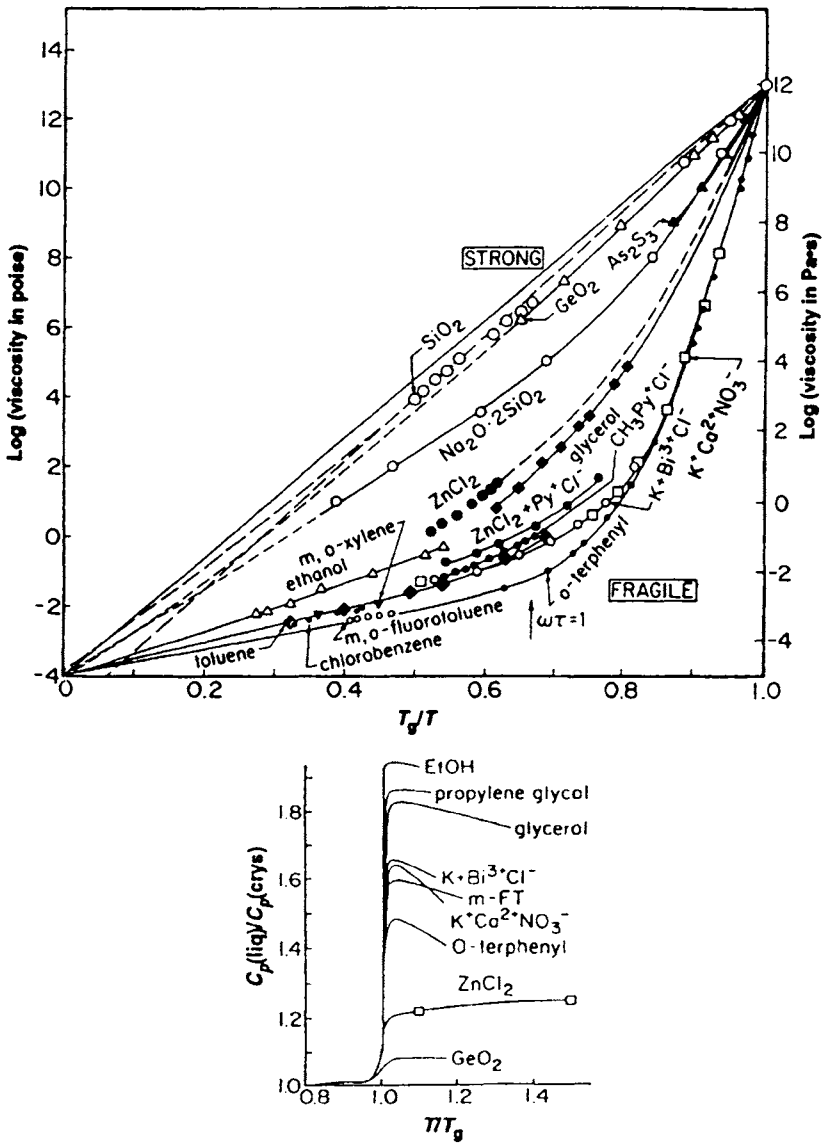

Figure 3.20: (top) Arrhenius plots of the viscosity data with temperature scaled by T_g. and (bottom) ratio of melt heat capacity to that of crystal plotted against reduced temperature. (After Angell, 1995).

temperature instead of T_g (with a viscosity value of $10^{13.6}$ poises) can also be used. Figure 3.20(a) reveals that molten silica and germania are remarkably Arrhenius in character, while liquids like propanol or CKN exhibit pronounced departure from Arrhenius behaviour; they follow VTF equation. These viscosity plots can be simulated by plotting VTF viscosities as a function of T_g/T and varying the parameter D in VTF equation (equation 3.12). The curvature in the fragility plots is thus quantitatively related to D. The implication of large curvature is that just above the glass transition, in a very narrow temperature range, the viscosity decreases rapidly as if the glass structure - its rigidity - has broken down precipitously. Shown in Figure 3.20(b) is the plot of C_P(liquid)/C_P(crystal) as a function of T_g/T. From the Figure 3.20(b), it is evident that VTF liquids also exhibit very large changes in heat capacity at the glass transition temperature. Therefore, large configurational changes should occur in such liquids just above T_g, a feature absent in the case of tetrahedral glasses like GeO_2 and SiO_2. These aspects are thoughtfully captured by Angell in his evocative phrases 'fragile' for the VTF liquids and 'strong' for the Arrhenius liquids. Increased fragility represents increased curvature and hence low values of D.

It is interesting to note that Donth (1982) found large values of ξ associated with the fragile glasses while the strong glasses have a lower value of ξ. Ito et al. (1999) have discussed the various approaches made to quantify fragility. All of them are consistent with the notion that fragility is a metric of the rate of structural change. One of the quantification is on the basis of T_g/T_K values, where T_K is the Kauzmann temperature, much the same as the use of T_g/T_0 where T_0 is the VTF temperature. However, both, T_K and T_0 have to be obtained only by extrapolations. The inherent ambiguities in such approaches can be removed by redefining fragilities through other quantities like $F_{1/2}$. $F_{1/2}$ is defined as,

$$F_{1/2} = 2\left(\frac{T_g}{T_{1/2}}\right) - 1 \tag{3.53}$$

where $T_{1/2}$ is the temperature at which the relaxation time on the log scale is half way between its value at T_g(~10^2s) and the value at infinite temperature (~10^{-14}s). $F^c_{1/2}$ from calorimetric measurements is defined as,

$$F^c_{1/2} = \frac{T_{1/2}}{T_m} \tag{3.54}$$

where $T_{1/2}$ is the temperature at which half of the fusion entropy, ΔS_m, has been lost by the supercooled liquid. Another approach is based on the observation that the glass transition region has different widths, $\Delta T_g = T_g' - T_g$, for different liquids as shown in Figure 3.21 (inset), being larger for strong liquids and smaller for fragile liquids. This region generally corresponds to a change in relaxation time of about 1.5-2.5 orders of magnitude. Thus ΔT_g represents a temperature measure for recapturing the ergodic state. Variation of $\Delta T_g/T_g$ as a function of $F_{1/2}$ is shown in Figure 3.21, which can be fitted to a function (IMA equation),

$$\frac{\Delta T_g}{T_g} = 0.151\left(\frac{1-F_{1/2}}{1+F_{1/2}}\right) \tag{3.55}$$

so that $F_{1/2}$ fragilities are readily determined from ΔT_g values.

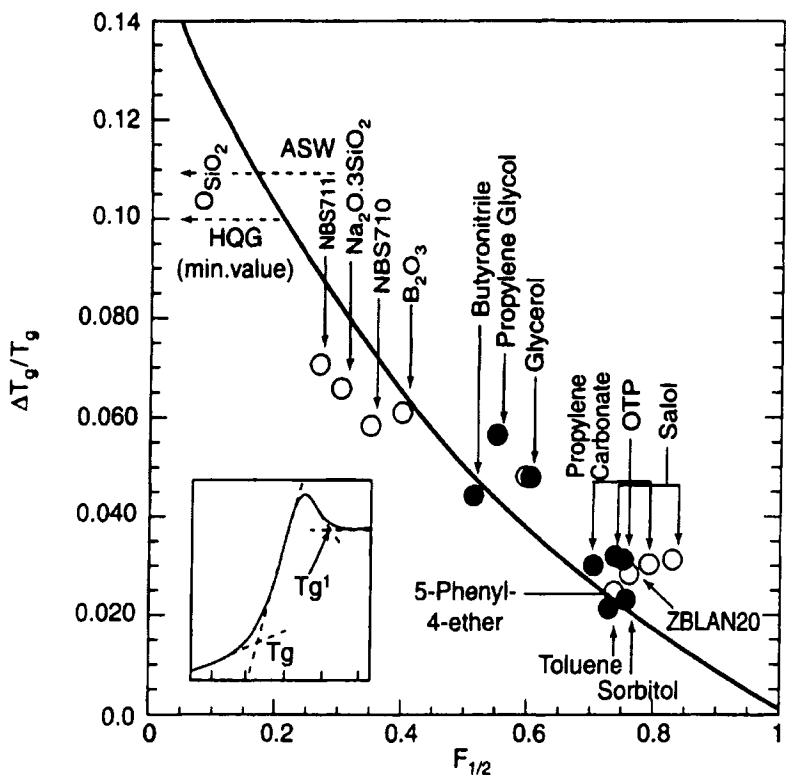

Figure 3.21: Correlation between metrics $\Delta T_g/T_g$ and $F_{1/2}$. (After Ito et al., 1999)

Strong liquids are generally associated with very little or even undetectable changes in C_P at the experimental glass transition, where as fragile liquids are associated with large and clearly measurable changes in ΔC_P. This can be related to the behaviour of the C_P jump in the two-state model, which simply corresponds to a Schottky anomaly. ΔC_P - the configurational heat capacity – increases only smoothly being equal to $R\ln\omega$, where ω is the degeneracy arising due to excitation from the ground state. It was shown in the configurational excitation model (discussed earlier) that this ΔC_P can have larger magnitude and also rise sharply if the excited state is associated with a change in ΔS. Fragile liquids, such as modified alkali silicate melts reveal a large increase in the number of configurational states immediately above the glass transition (Angell, 1998).

Angell suggested that fragile glass-formers would have a high density of minima in the energy landscape just above the glass transition* which with reference to Figure 3.09b can be looked upon as related to the steep increase in σ as a function of ϕ close to the glass point in the figure. This implies that, in the glass, a large number of locally rearrangable configurations would get frozen in fragile liquids giving rise to high density of two-level-states (see Chapter 9).

Da Ming Zhu (1996) found that fragility is indeed directly related to the density of two-level states (TLS) in glasses. These unidentified but reorganizable groupings are responsible for unique TLS properties. The density of TLS is determined from ultrasonic attenuation measurements carried out at cryogenic temperatures and they show a linear relation with fragility as shown in Figure 3.22.

The variation of viscosity close to glass transition temperature itself provides a quantitative measure of fragility. This fragility, F, is given by the reduced activation energy, E_η/RT_g.

$$F = \left[\frac{\partial \ln \eta}{\partial (T_g/T)}\right] = \frac{E_\eta}{RT_g} \tag{3.56}$$

This representation actually gives the steepness index – a measure of the rapid rise in η close to T_g. Some typical values of F, determined this way are given in Table 3.6.

* Multiplicity of the energy minima close to T_g in the supercooled state suggested by Angell has not been borne out by experiment and has been discussed by Johari (2000).

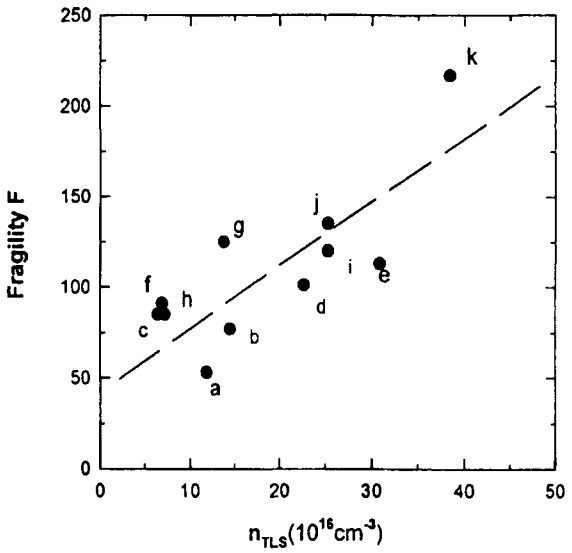

Figure 3.22: Fragility of different glasses versus n_{TLS}. The dashed line is a guide to the eye. (After Da Ming Zhu, 1996).

Table 3.6: F values of several glass forming liquids (After Da Ming Zhu, 1996).

Substance	T_g (K)	F
SiO_2	1446	53
GeO_2	820	77
B_2O_3	526	85
$3SiO_2$-Na_2O	735	101
$3B_2O_3$-K_2O	690	113
As_2S_3	454	91
Se	300	125
As_2Se_3	455	85
Glycol	172	120
PS	370	135
$CaK(NO_3)_2$	330	217

Rault (2000) related fragility to T_0 of VTF equation and T^* ($\approx T_c$) as

$$F = \frac{T_0}{T^*} \approx 1 - \frac{BR}{E_\beta} \tag{3.57}$$

B is from VTF equation and (assumed to be) independent of T. T^* and T have to be very close in magnitude to give very high fragilities (Table 3.5). Low fragilities are expected when E_β is high.

Heat capacity jump, ΔC_P, at the glass transition temperature, can be related to F in the following way. The configurational entropy of the glass ΔS, at the melting temperature T_m is

$$\Delta S_m = \frac{\Delta H_m}{T_m} = \int_{T_0}^{T_m} \Delta C_P d\ln T \tag{3.58}$$

If ΔC_P is a constant and $T_m \approx T^*$, $T_g \approx T_0$, then

$$\Delta S_m = \Delta C_P \ln\left(\frac{T_m}{T_g}\right) = \Delta C_P \ln\left(\frac{T^*}{T_0}\right) = -\Delta C_P \ln F \tag{3.59}$$

Thus, ΔC_P = - $\Delta S_m/\ln F$. ΔS_m is roughly a constant in a given class of materials (although in general it varies rather widely between classes). Thus, ΔC_P tends to zero for very strong liquids.

ΔC_P and T_g seem to be definitely correlated to fragility. Xia and Wolynes (1999) have examined this relation in the context of their investigation of first order transition in glasses using density functional approach. They found that D in the VTF equation, which is inversely proportional to fragility is equal to $32R/\Delta C_P$. Thus $F = \Delta C_P/32R$. (This expression is interesting because when $F = 1$, $\Delta C_P \approx 64$ cal/mole, which sets an upper limit for ΔC_P). In their analysis, Xia and Wolynes also found that near the glass transition the cooperatively rearranging region (CRR) may consist of approximately 90 - 100 molecules with a size of ~ 4.5 times the radius of the molecule.

The term fragility always draws attention towards rapid fall of viscosity above T_g. But the converse namely rapid rise of viscosity close to T_g and its analysis can be quite revealing. Coupling model of Ngai (discussed later) tries to address the origin of this increase in viscosity. Coupling model is parametrised by the exponent n. It is generally found that n is a constant in strong liquids and has a smaller value ($1-n \approx 1$). Non-zero n value is indicative of stretched exponential relaxations as will be discussed in chapters 7 and 9. The stretching exponent, β, is related to n as $\beta = 1-n$. Therefore, when n is very low, $\beta \approx 1$. As a result, the relaxation behaviour tends to be Arrhenius. In fragile liquids, the behaviour is

opposite. The activation energies E_a and E_a^* (of global and local relaxations respectively) are related as $E_a^* = E_a/(1\text{-}n)$. Since n is temperature dependent and increases with cooling in fragile liquids, the effective activation barrier for relaxation increases as a function of cooling towards T_g. Increase in the value of n is concomitant with the increase in number of molecular entities present in the co-operatively rearranging region (CRR) in the AG theory. Thus, the variation of n is a factor, which helps the rapid rise in τ or η as the glass transition is approached.

In order to understand fragility it is vital to examine its relation to the nature of bonding in the material. Fragilities represent a measure of the susceptance of molecular architecture to thermally induced breakdown. This breakdown causes the evolution of liquid-like configurational rearrangements of the constituent entities. Such rearrangements become facile when the cohesive interaction among constituent entities is non-directional. The cohesive energy of a fragile liquid therefore, is required to have a significant non-directional component in it. An implication of this nature, albeit indirect, can be recognized as built into equation (3.53), because high fragilities result from low ΔT_g values and the latter are associated with high ionicity (non-directional bonding) of glasses as in the case of CKN. Structural rearrangements and related molecular motions occur as a consequence of thermal excitation of bonds. Presence of a high density of low energy excited states (high entropies associated with such excited states) accessible to thermal excitation is another factor, which contributes to facile configurational rearrangements. These states can be identified as the shallow wells in the energy landscape with similar depths as the potential well in which the glass is found. Low energy configurational states may be expected to result from large bond distances, d, between constituent atoms/ions and high densities of such states can result when the atoms/ions have high coordination numbers (many more ways of realizing equi-energetic states). The latter is again high for large d as evident from crystallographic data.

Two factors, therefore, act as determinants of fragility. The first is the non-directional component of cohesive energy. This is readily seen as the ionic part of the energy in polar covalent liquids but in van der Waals bonded molecular liquids it is the entire cohesive energy. The second, the distance d, the bond length of the weakest bond in the material. Rao et al. (2001) have defined fragility on the above basis as,

$$F = \frac{0.22 - x}{0.22 + x} \tag{3.60}$$

where $x = 0.04[(10-\Delta\chi^2)/d]$, $\Delta\chi$ being the difference in electronegativities of the bonded atoms. (Compare with equation (3.53) which gives $F_{1/2} = [(0.151-x')/(0.151+x')]$, with $x' = \Delta T_g/T_g$). Since the cohesive energy is due to van der Waals interactions and the intermolecular bonding is non-directional in glass forming molecular liquids such as salol, use of $\Delta\chi$ is not relevant in them. Also retention of the constant 10 in x severely overestimates the total energy, besides leading to very low values of fragility. x is therefore defined as $0.08\chi/d$ for molecular liquids, where d is an average diameter, $(V_m/N)^{1/3}$. The calculated values of fragilities are listed in Table 3.7 along with reported $F_{1/2}$ values.

Although the most dramatic manifestation of fragilities occurs in the metastable supercooled region close to T_g in ln (η) vs T_g/T plots, they are already expressed in the equilibrium liquid at T_m ($T_g/T \approx 0.6$). At temperatures not much higher than T_m ($T_g/T \sim 0.5$), most liquids are Arrhenius and the reduced activation barriers ($E/2.303RT_g$) for viscosity are in the reverse order of steepness indices or fragilities. Since the ln (η) trajectories do not generally intersect, the ordering remains unaffected in any viscosity related measurements of fragility in the region close to T_g. In view of its (experimental) inverse relation with reduced activation barriers above T_m, fragility can be considered as an equilibrium property. The reduced viscosity plots of $\ln(\eta/\eta_0)$ ($\equiv \ln\eta_r$) vs (T_g/T) ($\equiv T_r$), can be generated using a heuristic function,

$$\log(\eta_r) = \frac{E_r}{T_r^{1/(1-F)}} \tag{3.61}$$

as shown in Figure 3.23 for different F values. The plots are astonishingly similar to the experimental viscosity-reduced temperature plots. As an example the behaviour of the experimental viscosities of o-terphenyl, for which F and $F_{1/2}$ values are respectively 0.77 and 0.75 (Table 3.7), are reproduced well by F=0.80 line in Figure 3.23. The reason for this can be understood when we re-cast the right hand side of equation (3.61) as,

$$\frac{E_r}{T_r^{F/(1-F)}}\frac{1}{T_r} = \frac{E_r(eff)}{T_r} \tag{3.62}$$

which is the Arrhenius form with a T_r dependent activation barrier. In fact, $[E_r/T_r^{F/(1-F)}]$ is to be compared with $(B/2.303S_cT_g)$ of the Adam-Gibbs equation. The T_r dependent, effective reduced activation barriers

Table 3.7: Glass forming materials with their $\Delta\chi$, d, F and $F_{1/2}$ values. (After Rao et al., 2001).

Composition	$\Delta\chi$ (or χ)	d (Å)	F	$F_{1/2}$
GeO_2	1.43	1.74	0.09	-
SiO_2	1.54	1.62	0.08	0.10
As_2S_3	0.40	2.24	0.11	-
As_2Se_3	0.37	2.41	0.15	0.18
Se	0	3.8	0.35	-
$PbO\text{-}Li_2O\text{-}B_2O_3$ (20:40:40)	1.84	1.96	0.24	0.31
$Pb_2P_2O_7 - Li_4P_2O_7$ (50:50)	1.68	1.96	0.20	0.25
$Ag_2P_2O_7 - Li_4P_2O_7$ (50:50)	1.65	1.96	0.19	0.25
$ZnCl_2$	1.51	2.32	0.25	-
$Li_2O\text{-}GeO_2\text{-}P_2O_5$ (40:20:40)	1.96	1.96	0.27	0.33
B_2O_3	1.40	1.48	0.01	
		2.76	0.31	0.39
P_2O_5	1.25	1.63	0.03	
		2.78	0.29	-
$Na_2O\text{-}3SiO_2$	1.75	2.21	0.27	0.30
$PbO\text{-}PbCl_2$ (50:50)	1.43	3.07	0.36	0.43
BeF_2	2.41	1.54	0.34	-
$K_2O\text{-}MoO_3\text{-}P_2O_5$ (20:40:40)	1.59	2.61	0.32	0.40
$K_2O\text{-}WO_3\text{-}P_2O_5$ (20:40:40)	1.58	2.61	0.31	0.34
$Li_2SO_4\text{-}Li_2O\text{-}B_2O_3$ (20:40:40)	1.98	3.12	0.48	0.52
$PbO\text{-}PbF_2$ (50:50)	1.84	2.59	0.37	0.43
$SnO\text{-}NaPO_3$ (05:95)	2.11	2.26	0.38	0.34
$NaPO_3$	2.14	2.26	0.39	0.36
$Li_2SO_4\text{-}Li_2O\text{-}P_2O_5$ (20:40:40)	2.13	3.12	0.52	0.48
K_2SO_4- Na_2SO_4- $ZnSO_4$ (22.5:07.5:70)	1.84	3.77	0.52	0.50
$KCl\text{-}2BiCl_3$	2.04	3.14	0.49	-
CKN	2.44	3.79	0.67	-
		5.67	0.77	
HDW	0.29	2.38	0.14	0.05
H_2O	2.55	3.1	0.54	-
Propylene Glycol	2.44	4.96	0.70	0.56
Glycerol	2.5	4.94	0.69	0.62
Toluene	2.36	5.62	0.74	0.74
Salol	2.46	6.56	0.76	0.74
Butyronitrile	2.37	5.26	0.72	0.54
Sorbitol	2.52	5.88	0.73	0.75
OTP	2.39	6.84	0.77	0.75

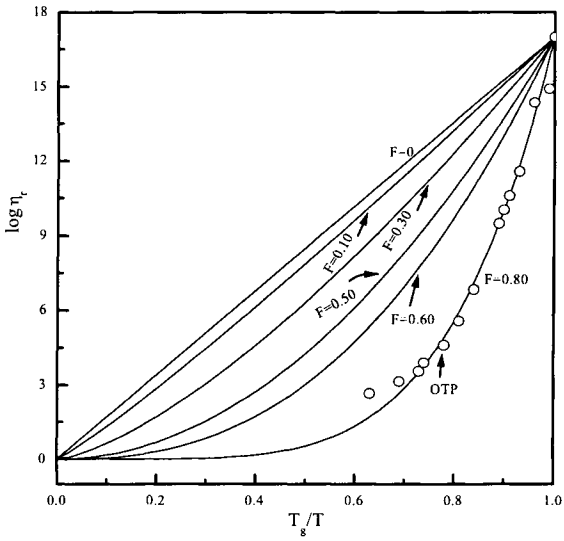

Figure 3.23: Variation of log (η_r) as a function of T_g/T, for different F values. The range of log (η_r) is 17 decades. O are experimental points of o-terphenyl (After Rao et al., 2001).

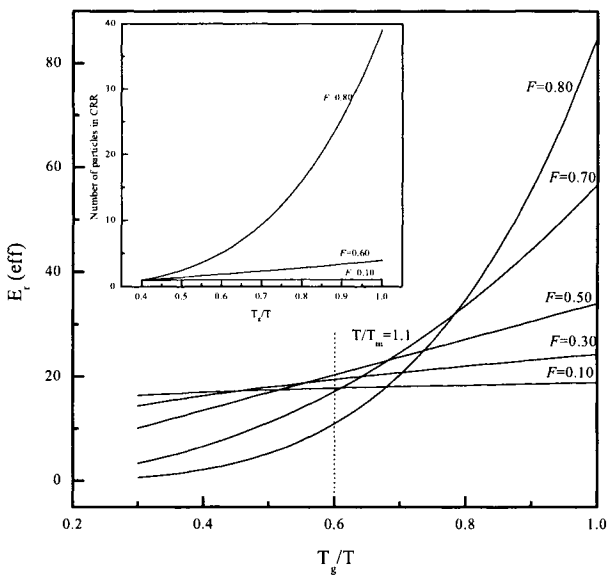

Figure 3.24: E_r(eff) vs T_g/T for different values of F. Dotted vertical line indicates the equilibrium melt temperature for most liquids. (After Rao et al. 2001).

are obtained by differentiation as $[E_r/(1\text{-}F)]/T_r^{F/(1-F)}$. The variation of these barriers for various F values are shown in Figure 3.24. It is clear that in high F liquids, E_r(eff) is low to start with and increases as T_g is approached. This variation is the essence of fragile behaviour. Since E_r(eff) is largely independent of T_r in strong liquids, (B/T_gS_c) is expected to be a constant. In highly fragile liquids it increases, since B/TS_c $(=(B/T_gS_c))$. $(1/T_r))$ varies as $(E_r/T_r^{F/1-F})(1/T_r)$, constancy of B would require that $S_c \sim T_r^{F/1-F}$. However, for liquids of intermediate F values, $S_c \sim \int (\Delta C_P/T)\ dT \sim T^1$ (for constant ΔC_P), and this enables a direct derivation of VTF relation from AG equation as noted earlier. Such hyperbolic temperature dependence of S concomitantly requires B to vary as $T_r^{-1/1-F}$.

The temperature dependent activation energy barriers in Figure 3.24 can be interpreted as $n.\Delta\mu$ of AG equation, where $\Delta\mu$ is the activation barrier per rearranging particle. Assuming that at temperatures sufficiently above T_g ($T_g/T \leq 0.4$), most of the configurational entropy arises from single particle (n=1) movement, the variation of the number of particles present in cooperatively rearranging region (CRR) have been evaluated and shown in inset to Figure 3.24. It is seen that in very fragile liquids, the number of particles involved in cooperative rearrangements can be quite high (F = 0.80: there are 40 particles in CRR at T_g)[#].

References:

Adam, G., and J.H. Gibbs, 1965, J. Chem. Phys., **43**, 139.

Angell, C.A., 1986, Ann. NY Acad. Sci., **484**, 241

Angell, C.A., 1991. J. Non-Cryst. Sol., **131-133**, 13.

Angell, C.A., 1995, Science, **267**, 1924.

Angell, C.A., 1998, J. Phys. Chem. Solids, **49**, 863.

Angell, C.A., 1990, Chem. Rev., **90**, 523.

Angell, C.A., B.E. Richards and V. Velikov, 1999, J. Phys. Cond. Mat.,**11**, A75.

Angell, C.A., 1971, J. Phys. Chem., **75**, 3698.

[#] The concept of fragility discussed above has nothing to do with the mechanical properties of the glass. Several polymers which are very fragile in terms of fragility indices such as polymer glasses have very good impact and stretching properties compared to very low values of the same for low fragility glasses such as silica and silicates.

Angell, C.A., and K.J. Rao, 1972. J. Chem. Phys., **57**, 470.

Angell, C.A., 1999, in Rigidity Theory and Applications, eds. M.F. Thorpe and P.M. Duxbury (Plenum Publishers, New York) p. 297.

Bakai, A.S., 1996, Low Temp. Phys., **22,** 733.

Bassler, H., 1987, Phys. Rev. Lett., **58**, 767.

Boerjesson, L., A.K. Hassan, J.Swenson, L.M. Torrell and A. Fontana, 1993, Phys. Rev. Lett., **70**, 127.

Bokov, N.A., and N.S. Andreev, 1989, Sov. J. Glass Phys. Chem., **15**, 243.

Burton, J.J., 1970, J. Chem. Phys., **52**, 345.

Burton, J.J., 1973, J. Chem. Phys., **56**, 3133.

Burton, J.J., 1973, J. Chem. Soc. Faraday II, **69**, 540.

Chamberlin, R.V., and D.W. Kingsbury, 1994, J. Non-Cryst. Sol., **172-174**, 318.

Chang, S.S., and A.B. Bestul, 1972, J. Chem. Phys., **56**, 503.

Cohen, M.H., and D.Turnbull, 1959, J. Chem. Phys., **31**, 1164.

Cohen, M.H., and G.S. Grest, 1979, Phys. Rev. B, **20**, 1077

Cohen, M.H., and G.S. Grest, 1981, Adv. Chem. Phys., **48**, 455.

Cohen, M.H., and G.S. Grest, 1984, J. Non-Cryst. Sol., **61&62**, 749.

Crisanti, A., and F. Ritort, 2000, J. Phys. Condens. Mat., **12**, 6413.

Da Ming Zhu, 1996, Phys. Rev. B, **54**, 6287.

Donth, E., 1982, J. Non-Cryst. Sol., **53**, 325

Doolittle, A.K., 1951, J. App. Phys., **22**, 1471.

Dyre, J.C., N.B. Olsen and T. Christensen, 1996, Phys. Rev. B, **53**, 2171.

Elliott, S.R., 1990, Europhys. Lett., **19**, 201.

Fauber, L., S.W. Kim and H. Eyring, 1970, J. Chem.Phys., **74**, 3510.

Fulcher, G.S., 1923, J. Am. Ceram. Soc., **8**, 339.

Gee, G., 1970, Contemp. Phys., **11**, 313.

Gibbs, J.H and E.A. Dimarzio,1958, J. Chem. Phys, **28**, 373,807.

Gibbs, J.H., 1960, in Modern Aspects of the Vitreous state, ed. MacKenzie (Butterworth).

Goldstein, M., 1969, J. Chem. Phys., **51**, 3728.

Goldstein, M., 1976, J. Chem. Phys., **64**, 4767.

Goldstein, M., 1976, Ann. (N.Y.) Acad. Sci., **279**, 68.

Goldstein, M., 1977, J. Chem. Phys., **67**, 2246.

Götze, W., E. Leutheusser and S. Yip, 1981, Phys. Rev. A, **23**, 2634.

Ito, K., C.T. Moynihan and C.A. Angell, 1999, Nature, **398**, 492

Jäckle, J., 1989, J. Phys. C: Solid State Phys., 1, 267.

Johari, G.P., 2000, J. Chem. Phys. **112**, 8958.

Johari, G.P., and Goldstein, M., 1970, J. Chem. Phys., **53**, 2372.

Johari, G.P., and Goldstein, M., 1971, J. Chem. Phys., **55**, 4245.

Kivelson, D., and J. Tarjus, 1998, J. Non-Cryst. Sol., **235-237**, 86.

Laughlin, W.T., and D.R. Uhlmann, 1972, J. Phys. Chem., **76**, 2317.

Leutheuser, E., 1984, Phys. Rev. A, **29**, 2765.

Mazurin, O.V., 1991, J. Non-Cryst. Sol., **129**, 259.

Moynihan, C.T., and C.A. Angell, 2000, J. Non-Cryst. Sol., **274**, 131.

Moynihan, C.T., and J. Schroeder, 1993, J. Non-Cryst. Sol., **160**, 52

O'Reilly, J.M., 1962, J. Polymer Sci., **57**, 429.

Oldekop, W., 1957, Glasstech Ber., **30**, 8.

Phillips, J.C., 1982, Solid State Phys., **37**, 93.

Polk, D.E., 1971, J. Non-Cryst. Sol., **5**, 365.

Polk, D.E. and D. Turnbull, 1972, Acta. Met., **20**, 493.

Poole, P. H., T. Grande, C.A. Angell and P.F. McMillan, 1997, Science, **275**, 322.

Prigogine, I., and R. Defay, 1954, Chemical Thermodynamics, (Longman Greens).

Rao, K.J., and C.A. Angell, 1971, in Amorphous Materials, eds. R.W. Douglass and B.E. Ellis (John Wiley, New York).

Rao, K.J., and R. Mohan, 1980, J. Phys. Chem., **84**, 1917 (1980).

Rao, K.J. and C.N.R. Rao, 1978, Phase Transitions in Solids (McGraw-Hill International Book Company, New York)

Rao, K.J., and C.N.R. Rao, 1982, Mat. Res. Bull., **17**, 1337.

Rao, K.J., 1984, Proc. Indian Acad. Sci., **93**, 389.

Rao, K.J., S. Kumar and M.H. Bhat, 2001, J. Phys. Chem. B, **105**, 9024.

Rault, J., 2000, J. Non-Cryst. Sol., **271**, 177.

Ree, T.S., T. Ree and H. Eyring, 1962, Proc. Natl. Acad. Sci. U.S., **48**,501.

Richert, R., and H. Bassler, 1990, J. Phys. Cond Mat., **2**, 2273.

Schober, H., M. Koza, A. Tölle, F. Fujara, C.A. Angell and R. Böhmer, 1998, Physica B, **241-243**, 897.

Sikka, S. K., 1992, in Proc. Of XIII AIRAPT Int. Conf. On High Pressure Tech., eds., A. Singh, K., (Oxford & IBH Publ. Co. Pvt. Lt., New Delhi) p. 254.

Sillescu, H. 1999, J. Non-Cryst. Sol., **243**, 81.

Sokolov, A.P., A. Kisliuk, M. Soltwisch and D. Quitmann, 1992, Phys.Rev. Lett., **69**, 1540.

Stillinger, F.H., and M.J. Weber, 1984, Science, **225**, 983.

Stillinger, F.H., and M.J. Weber, 1982, Phys. Rev. A., **25**, 978.

Takahara, S., O. Yamamuro and H. Suga, 1994, J. Non-Cryst. Sol., **171**, 259.

Tammann, G. and W. Hesse, 1926, Z. Anorg. Allg. Chem., **156**, 245.

Turnbull, D. and Cohen, M. H., 1961, J. Chem. Phys., **34**, 120.

Turnbull, D. and Cohen, M. H., 1970, J. Chem. Phys., **52**, 3038.

Vogel, H., 1921, Phys. Z, **22**, 645.

Xia, X., and P.G. Wolynes., Cond. Matt., /9912442

Zallen, R., 1983, The Physics of Amorphous Solids (John-Wiley and sons, New York).

It is only when they go wrong that machines
remind you how powerful they are.
- Clive James.

CHAPTER 4

STRUCTURAL TECHNIQUES

In chapter 2 we noted in advance that the structures of glasses and other amorphous materials are quite complex. The absence of 3-dimensional periodicity takes away the convenience of describing the structure in terms of a few parameters like inter atomic distances, bond angles and symmetry which describe the unit cell. Therefore the description of the glass structure with the same precision as that of a crystal is impossible. We may easily visualize that every chosen arbitrarily small part of a glass is in principle structurally different from the other. It is as if glass is an assembly of an infinitely large number of polyamorphic phases with no discernable differences in their thermodynamic properties. This also introduces a new dimension to the problem because the history of preparation itself can introduce different structures. Therefore we are restricted to discuss the structure in terms of an averaged 1-dimensional description of amorphous solids through their radial distribution functions (RDF). It is one dimensional because glasses are isotropic in their structure and properties. The RDF to be discussed further below describes how the number densities of atoms vary as a function of distances from an arbitrarily chosen atom at the centre. Although various notations have been used for RDF in the literature, we use here the more familiar notation of $G(r)$ and define RDF. $G(r)$ is defined in terms of the function $\rho(r)$ as

$$G(r) = 4\pi r^2 \rho(r) \tag{4.01}$$

where $\rho(r)$ gives the number of atoms lying between r and $(r + dr)$ from a given atom as shown in Figure 4.01 (a). $\rho(r)$ is the radial density function. $\rho(r)$ and $G(r)$ are shown in Figure 4.01b and 4.01c respectively. Pair correlation function is evidently zero at values of r less than the average nearest neighbour distance since there are no atoms in that range. $\rho(r)$ itself should acquire a constant average value which is ρ^0 for large values of r as shown by the dotted line in Figure 4.01b. Similarly in the RDF shown in Figure 4.01 (c), the dotted line represents $4\pi r^2\rho^0$ line. The undulations around the dotted line mark the distances at which the number

density increases. This is because from the chosen arbitrarily center these are the distances at which other atoms are located. Before we proceed further, we take note of two other correlation functions generally used to represent data. They are the differential correlation function $D(r)$, given by

$$D(r)=4\pi r[\rho(r)-\rho^0] \tag{4.02}$$

and the total correlation function $T(r)$, given by

$$T(r) = 4\pi r\rho(r) \tag{4.03}$$

and they are shown in Figure 4.01(d) and 4.01(e) respectively. We will discuss how the RDFs are obtained from experiments little later. The structural investigations of a glass consists in understanding the origin of the few peaks seen in RDF.

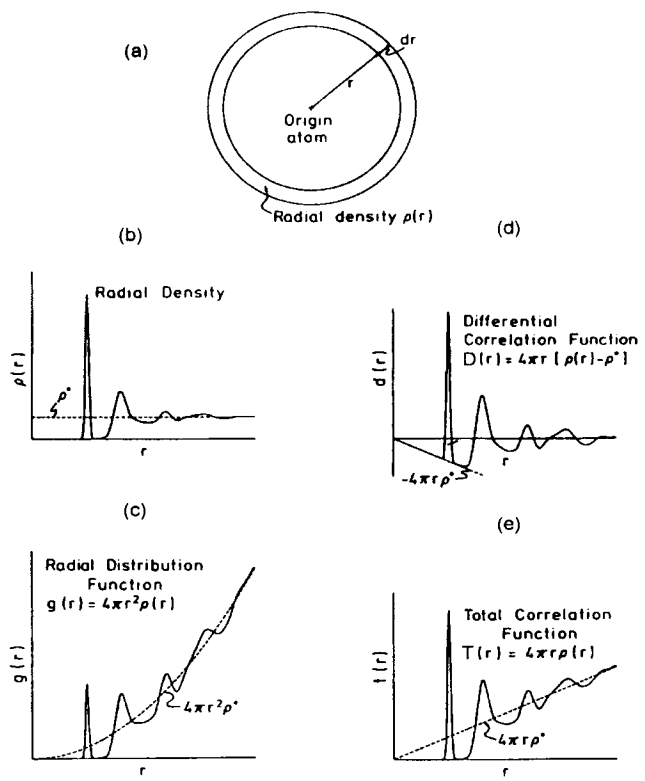

Figure 4.01: Real space correlation functions for a monatomic amorphous solid.

Consider the example of SiO_2 glass. We know for certain from chemical considerations that silicon should be present in $[SiO_{4/2}]^0$ tetrahedra in the glass structure. Figure 4.02 shows how the silicate tetrahedra are connected. It is the variation of the torsional and bond angles α and β which gives rise to a non-crystalline arrangement of the tetrahedra. We expect to be able to analyse RDF of SiO_2 and to provide the information of bond distances and the bond angles.

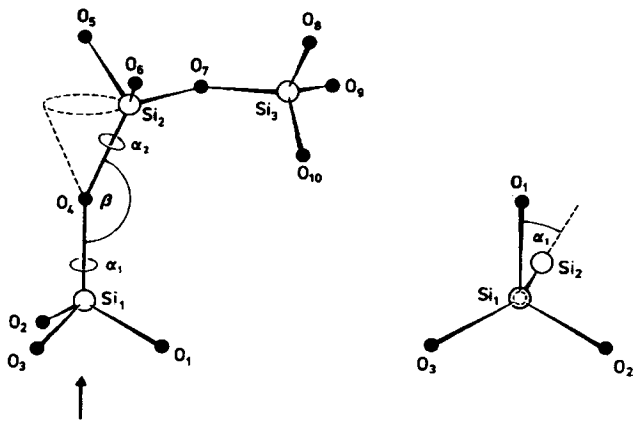

Figure 4.02: Definition of the bond angle, β and the torsion angle α_1 and α_2 for vitreous silica.

X-ray diffraction from glass

The diffraction experiment conducted with a glassy sample is no different from that with a crystalline material (Warren, 1969; Wright, 1974; Wright and Leadbetter, 1976; Wagner, 1978;). In a diffractometer, X-rays are incident on a sample surface at an angle θ to its normal and are diffracted at an angle 2θ with respect to the incident beam direction. Intensities of the diffracted beams are recorded as a function of 2θ. The scattering geometry and the relation between the scattering vectors are shown in Figure 4.03. If the scatterers are point charges, then the scattering intensity, I_{eu}, is given by,

$$I_{eu} = f_e f_e^* \tag{4.04}$$

Where f_e is the scattering factor, which is complex and is given by,

$$f_e = \int \exp[(2\pi i / \lambda)(\mathbf{s} - \mathbf{s}_0).\mathbf{r}]\rho(r)dV \tag{4.05}$$

where the electron charge is assumed to be distributed in a small volume dV and $\rho(r)$ is the corresponding density variation as a function of r.

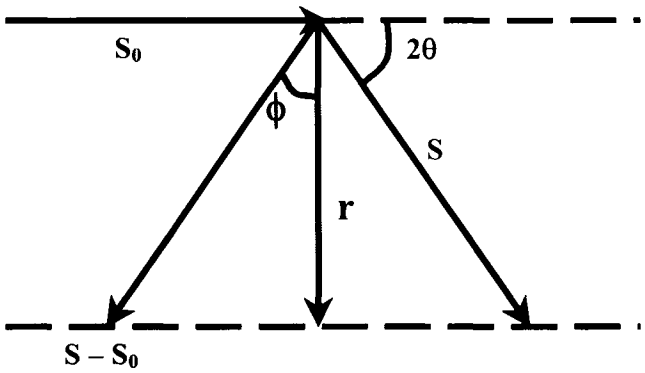

Figure 4.03: Relation between scattering vectors.

On the basis of Figure 4.03, the dot product $(\mathbf{s} - \mathbf{s}_0).\mathbf{r}$ is easily seen to be equal to $2r\sin\theta\cos\phi$. Substituting for λ from the relation $k = (4\pi\sin\theta)/\lambda$ in the exponential, the scattering factor can be written in terms of ϕ and r as,

$$f_e = \int_{r=0}^{\infty}\int_{\phi=0}^{\pi} \exp[ikr\cos\phi]\rho(r).2\pi r^2 dr.\sin(\phi)d\phi \tag{4.06}$$

in which electron distribution is assumed to have a spherical symmetry so that r is simply treated as a scalar. Integration over ϕ gives,

$$f_e = \int_0^{\infty} 4\pi r^2 \rho(r)\left(\frac{\sin kr}{kr}\right)dr \tag{4.07}$$

This can be generalized to an atom where there are several electrons so that it represents the atomic scattering factor, also called the "form factor" and is given by,

$$f = \sum_n f_{e,n} = \sum_n \int_0^{\infty} 4\pi r^2 \rho_n(r)\left(\frac{\sin kr}{kr}\right)dr \tag{4.08}$$

where again $\rho_n(r)$ is the density distribution of electrons. It is evident that the quantity, $\sum_n \int_0^\infty 4\pi r^2 \rho_n(r) dr$, should give the total number of electrons in the atom or atomic number, Z and (sin kr)/(kr) tends to unity for small value of r, therefore f itself tends to Z as k tends to zero. The atomic scattering factor, f, therefore is a function of k and the variation of $f(k)$ as a function of k is shown in Figure 4.04.

Figure 4.04: Schematic illustration of the dependence of the X-ray atomic form factor on scattering vector.

f_e in the scattering intensity function, I_{eu}, (= $f_e f_e^*$), is now the sum of the scattered amplitudes resulting from each atom. The amorphous solid is isotropic and the probability of finding two atomic scatterers at a distance r_{mn} from a given atom is identical in all directions. This property can be utilized to show that the scattering intensity I_{eu} for an assembly of atomic scatterers is given by the Debye equation,

$$I_{eu} = \sum_m \sum_n f_m f_n \frac{\sin kr_{mn}}{kr_{mn}} \tag{4.09}$$

Let us suppose that the assembly we are considering consists of only one type of atoms. Then I_{eu} can be written as,

$$I_{eu} = \sum_m f^2 + \sum_m \sum_{n \neq m} f^2 \frac{\sin kr_{mn}}{kr_{mn}} \tag{4.10}$$

This equation allows us to introduce a density function $\rho_m(r_{mn})$ considering m as the atom at the origin so that the summation can be substituted by an integration and I_{eu} is written as,

$$I_{eu} = \sum_m f^2 + \sum_m f^2 \int \rho_m(r_{mn}) \frac{\sin kr_{mn}}{kr_{mn}} .dV_m \tag{4.11}$$

Now the scattering intensity is over the sample volume with an assumed spherical symmetry. Expressing the density as an appropriate isotropic function of r and taking into consideration that at sufficiently large distances ρ tends to ρ^0, which is the constant average density, it can be shown that the above equation becomes

$$I_{eu} = Nf^2 + Nf^2 \int_0^\infty 4\pi r^2 \left[\rho(r) - \rho^0\right] \frac{\sin kr}{kr} .dr \tag{4.12}$$

where all the quantities are now referenced to macroscopic dimensions consisting of N atomic scatterers. We recognize that $4\pi r^2\rho(r)$, which is the radial distribution function should be related to the scattering intensity through a Fourier transformation. In order to achieve this, a reduced scattering intensity function, $F(k)$, has to be defined as,

$$F(k) = k\left[\frac{(I_{eu}/N) - f^2}{f^2}\right] \tag{4.13}$$

Using equation (4.12),

$$F(k) = k \int_0^\infty 4\pi r^2 \left[\rho(r) - \rho^0\right] \frac{\sin kr}{kr} .dr \tag{4.14}$$

The differential or reduced radial distribution function, $D(r)$, is given by,

$$D(r) = 4\pi r\left[\rho(r) - \rho^0\right] = \frac{G(r)}{r} - 4\pi r\rho^0 \tag{4.15}$$

These functions oscillate about zero and do not increase or decrease as functions of k or r. Therefore $F(k)$ itself is now equal to

$$F(k) = \int_0^\infty D(r) \sin kr.dr \tag{4.16}$$

Thus we have a function $F(k)$ which is obtained from the experimental scattering intensity in the k-space, which is related to pair distribution in the real space for an amorphous solid. They are therefore related through a Fourier transform which can be written as

$$D(r) = \frac{2}{\pi} \int_0^{\infty} F(k).\sin kr.dk \tag{4.17}$$

Although $\sin(kr)$ appears in both expressions, $\sin(kr)$ in k-space arises from the Debye equation, while in $D(r)$ it is a consequence of Fourier transform. How good is $D(r)$ depends on range of k, which is formally assumed to have a range of 0 to ∞, but in practice, it is limited by the energy of the X-ray photon.

The more useful RDF is therefore obtained starting from experimentally determined $F(k)$ but sometimes $F(k)$ itself can be used to examine subtle structural aspects. It may also be noted here that $F(k)$ is related to the structure factor $S(k)$, where $S(k)$ is defined as,

$$S(k) = \frac{I_{eu}(k)}{Nf^2} \tag{4.18}$$

so that $F(k) = k[S(k) - 1]$. The k-weighting of $S(k)$ in the expression for $F(k)$ makes it particularly useful in the high k range. It may also be noted that when $F(k)$ exhibits oscillatory behaviour up to very large values of k, it is indicative of the presence of well defined first coordination polyhedra in the structure and well defined first neighbour distances because the sinusoidals in the k-space are built by the Fourier transform (FT) of each and every peak in $D(r)$. The peaks in $D(r)$ correspond to successive coordination shells and quite generally exhibit increasing widths. Such wide peaks give rise to highly damped sinusoidal waves in Fourier transform. The only oscillations, which survive at large k values are those arising from the FT of the first peak in $D(r)$.

The use of X-ray diffraction technique to obtain structural information in glasses consist of collecting the total scattered intensity as a function of k. The collected intensity should be first corrected for incoherent contributions such as Compton scattering and any other background contributions. These intensities as expected oscillate around f^2 curve (see equation 4.12) from which $F(k)$ is computed as a function of k. Since f^2 decreases sharply as a function of θ, one would expect a sharp fall

off in intensity as a function of θ in XRD. The experimental set up is generally the same as that used for the study of the crystals. The diffraction of a collimated beam of X-rays is studied either in transmission or in reflection modes. In the laboratory, one uses either Mo Kα with λ = 0.71 Å or Cu Kα with λ = 1.54 Å. This limitation is overcome in synchrotron sources, where higher energies are available. X-ray energies are monochromatized by reflecting them off from a select plane of a single crystal (such as Si(1 1 1)) before collimation. The usual detector systems these days are solid state counters which give accurate measurements of X-ray intensities. The intensities are first corrected for contributions from the substrate, from the instrumental noise and from the polarization factor followed by a correction for Compton scattering. The corrected $I(k)$ is then converted into $F(k)$. The k-range is dependent on λ and the maximum values are 17.7 Å^{-1} for Mo Kα and just 8.2 Å^{-1} for Cu Kα. The Fourier transform of the data to obtain $D(r)$ assumes that we have infinite range of k values. Therefore this gives rise to what is known as termination error, because of the finite range of k. Termination error is reduced significantly in synchrotron work. λ can be taken down to ~ 0.1 Å. But in practice termination errors are reduced to a significantly low level by artificially smoothing the data around $k = k_{max}$ so that there is no discontinuity at k_{max}. One of these mathematical tricks is to Fourier transform $F(k).M(k)\sin(kr).dk$ instead of $F(k)\sin(kr).dk$, where $M(k)$ is $(k_{max}/\pi k).\sin(\pi k/k_{max})$ and is known as Lorch function (1969). Use of such functions generally reduces the real space resolution. It is worthwhile to note here that there are three important limitations of the XRD technique itself. The first is that the scattering intensity is superposed upon the f^2 function which is itself a function of k. This reduces the accuracy of intensity computed at high k values. Second is that the value of k_{max} attainable which is not sufficient with normal laboratory X-ray sources. The third point is that XRD in principle measures the electron density correlations, which for light atoms may not be the same as correlation of the atomic positions because significant fraction of electrons are in bonding (interatomic) regions.

Neutron scattering

Using neutron scattering (Wright, 1980) for structural work has several advantages. Most importantly, neutron sources from nuclear reactors have a wavelength range of 0.1-1 Å (corresponding to an energy range of 8 eV-80 meV). Secondly, the role of the atomic scattering factor,

f of XRD is replaced by the neutron scattering length, $\overline{b}$, which is isotropic and is independent of the value of k. The scattering is only by the nuclei. $\overline{b}$ values of isotopes of a given element can vary both in sign and magnitude. This is used to advantage in structural work because isotopic substitution can identify the source of observed scattering intensities. $\overline{b}$ is the average scattering length and its variation across the periodic table is shown in Figure 4.05. In neutron scattering therefore the atomic number of the scatterer is not a problem because light elements scatter as efficiently as heavier ones.

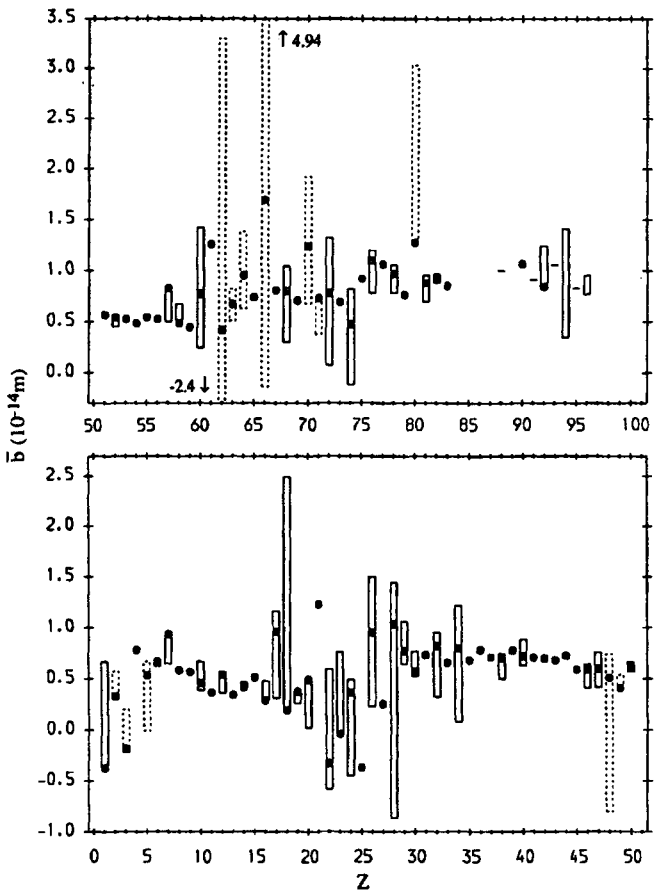

Figure 4.05: The neuron scattering length, $\overline{b}$, as a function of atomic number, Z, showing the value for the natural element (⊕) and the range of isotopic variation (bar). A dashed bar denotes elements with complex $\overline{b}$ and only the variation in the real part of $\overline{b}$ at a wavelength of 1 Å (From Wright, 1993).

When a neutron beam is incident on a material, due to the large mass of neutron there is a great chance of energy and momentum transfer. This renders the inelastically (Compton) scattered component of neutrons quite significant. The inelastically scattered component contains dynamical information, which can be separated and analysed. Further, neutrons carry spins and therefore when the amorphous solid contain spin bearing species, there is a new contribution to the scattered intensity due to magnetic scattering which is also useful. However our focus in this section is confined to the elastic scattering of the neutrons from an amorphous solid from which structural information can be gathered. The scattering formalism is the same for both X-rays and neutrons. In the practice of neutron work, the scattering vector, k, is generally represented as Q. The scattering intensity is represented by the equation,

$$I_N^T(Q) = N\bar{b}^2 + N\bar{b}^2 \int_0^\infty 4\pi r^2 \rho(r) \frac{\sin Qr}{Qr}.dr \tag{4.19}$$

where the superscript, T and subscript, N on I indicate total (scattering) and neutron respectively. The expression for reduced intensity $F(k)$ is represented by,

$$F(k) = Q\,I(Q) \tag{4.20}$$

where $I(Q)$ is the equivalent of the reduced intensity in XRD. Therefore the working expression for structure work is,

$$QI_N(Q) = N\bar{b}^2 \int_0^\infty D(r) \sin Qr.dr \tag{4.21}$$

Use of the above expression is described as static approximation because all neutrons are detected irrespective of elastic or inelastic scattering. This is avoided by using an additional monochromator in a triple axes spectrometer in which only the elastically scattered neutrons are detected.

Inelastic neutron scattering

Inelastic neutron scattering (Sinclair, 1985; Leadbetter, 1973) can be used to investigate vibrational spectra of glasses. Thermalized neutrons have energies under 50 meV (roughly 400 cm^{-1}). Therefore, during the

process of neutron scattering, they interact with the particles in the glass to either loose part of their energy and create phonons or gain energy from phonons in the system. The process constitutes the inelastic neutron scattering. Therefore, in inelastic scattering, the scattering parameter becomes energy dependent. The structure factor is represented as $S(Q, \omega)$ rather than $S(Q)$. Therefore, the pair correlation function, which is the Fourier transform of $S(Q)$ would be a function of time, which is $G(r, t)$ instead of $G(r)$. $G(r, t)$ consists of self and distinct parts of the correlations, $G(r, t) = G_S(r, t) + G_D(r, t)$. At large values of Q, $G_D(r, t)$ can be neglected and this corresponds to the neglect of the contribution to the interference of neutrons scattered by other atoms. This is known as incoherent approximation and is valid for $Qr_0 >> 1$. Therefore retaining only the self-part amounts to scattering being proportional to the phonon density of states. It has been shown (Wright, 1980) that the density of states $\rho(\omega)$ can be obtained from scattering cross section as,

$$\rho(\omega) = cg(Q, \omega)$$

where

$$g(Q,\omega) = \left(\frac{d^2\sigma}{d\Omega dE'}\right).\frac{\mathbf{k}}{\mathbf{k}'}.\frac{2\omega}{N[n(\omega)+1]Q^2} \tag{4.22}$$

where the first term in the bracket is the neutron scattering cross section, $\mathbf{k}$ and $\mathbf{k}'$ are the incident and scattered wave vectors and $(n(\omega)+1)$ is the Boson factor, Q is the momentum transfer vector ($\hbar\boldsymbol{Q} = \hbar(\mathbf{k} - \mathbf{k}')$) and c is a frequency dependent term, given by,

$$c = \left[\frac{\langle \bar{b}^2 \rangle}{M}\left(\langle u^2(\omega)\rangle e^{-2W}\right)\right] \tag{4.23}$$

$\langle \bar{b}^2 \rangle$ is the average scattering length, M is the atomic mass, $\langle u(\omega)\rangle$ is the average displacement and e^{-2W} is the Debye-Waller factor.

Many glasses have been studied using inelastic neutron scattering. Vitreous SiO_2 has been investigated using inelastic neutron scattering and vibrational density of states has been obtained by Price and Carpenter (1987). The spectra are shown in Figure 4.06, which clearly reveals the existence of the splitting of the high frequency modes of SiO_2. One other interesting observation from inelastic neutron scattering studies has been

to show the absence of 808 cm^{-1} peak in B_2O_3 glass. The presence of this vibrational frequency has been ascertained in Raman studies. This observation led Elliott (1978) to consider that the contribution of boroxol rings may not be important to the structure of B_2O_3 (see chapter 12).

Electron scattering

Electrons are also used in scattering studies. An electron microscope is employed for the purpose in which the wavelength of the electrons is readily available down to 0.05 Å. The scattering of the electrons occurs both due to nuclei and electrons in the atoms. The scattering experiment consists of using constant λ and variable scattering angles by tilting the sample geometry. The term in electron diffraction corresponding to the atomic scattering factors in XRD is given by,

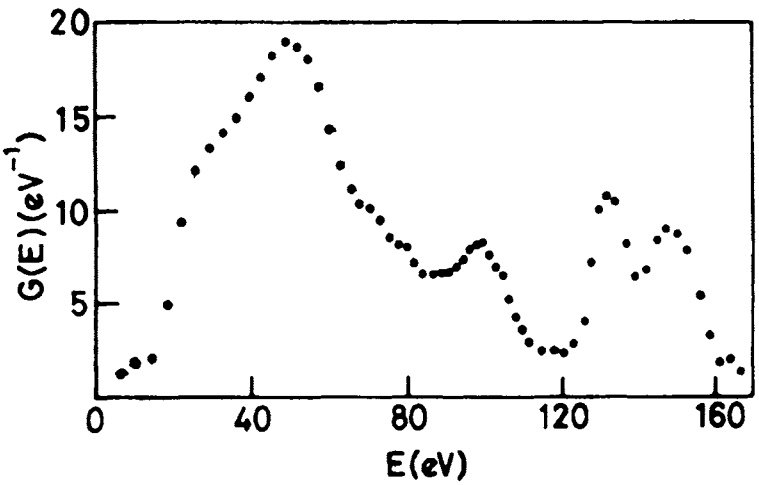

Figure 4.06: Effective density of states obtained from inelastic neutron scattering for vitreous silica (After Price and Carpenter, 1987).

$$f^e(k) = \frac{2m_e e^2}{\hbar^2}\left[\frac{\{Z - f^x(k)\}}{k^2}\right] \tag{4.24}$$

where $f^e(k)$ is the electron scattering factor, m_e is the electron mass, Z is the atomic number, $f^x(k)$ is the X-ray atomic scattering factor. Scattering formalism again remains the same as for as the other two (X-rays and neutrons). The form factor is high compared to X-rays because of the

strong columbic interaction of electrons with both the electrons and nuclei of the atoms. The samples used for electron scattering work, however, have to be very thin because of both pronounced inelastic processes and multiple scattering. A good example of the use of electron diffraction in determining RDF is that of $96B_2O_3 \cdot 4TeO_2$ glasses, which is shown in Figure 4.07. RDF obtained with powdered samples in electron diffraction

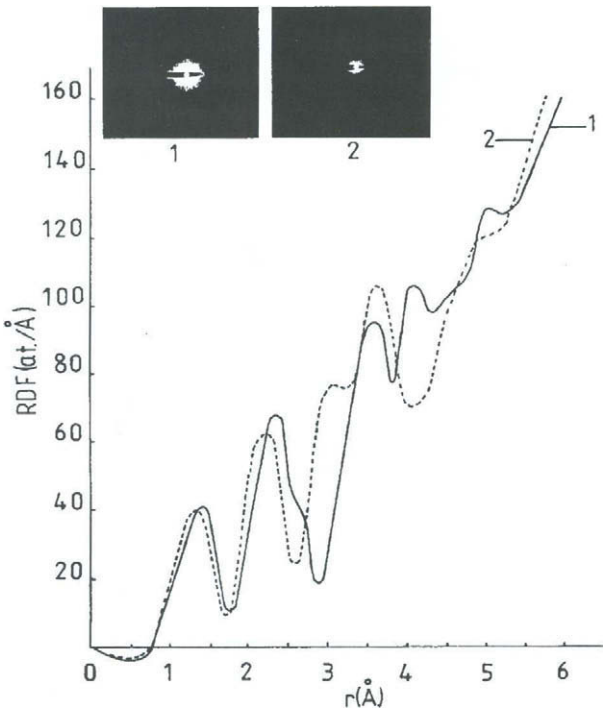

Figure 4.07: RDF curves for powdered samples of (1) B_2O_3 glass and (2) B_2O_3. 4 TeO_2 glass (After Bursukova et al, 1995). 96

studies is also shown in Figure 4.07 for comparison. The differences between the two RDFs is attributed to greater disorder in the case of thin films. The merits of three diffraction techniques are compared in Table 4.1.

All the scattering expressions discussed above are relevant for single component materials. But most glasses are multicomponent materials and consist of several atoms with different scattering factors. In a material consisting of n different atoms, there are $n(n\text{-}1)/2$ pair correlation functions and each of them contribute to the observed scattering intensities.

Table 4.1: Advantages and disadvantages of various scattering techniques (After Elliott, 1984).

Techniques	Advantages	Disadvantages
X-rays (fixed λ, variable θ)	Convenient laboratory sources and equipment. Powdered or thick samples can be used. Atomic form factor can be calculated.	Small k_{max} for many X-ray sources. Significant Compton contribution to scattering at large k. Partial correlation functions difficult to extract for multicomponent systems. Atomic form factor strongly decreasing function of k.
Neutrons (fixed λ, variable θ, double or triple axis)	Scattering length independent of k. Partial correlation functions easier to extract for multicomponent systems. Isotopic substitution possible to determine partial correlation functions.	Reactor source required. Placzek corrections required for double-axis experiments (static approximation). Large volume of material required. b must be determined.
Neutrons (fixed λ, variable θ, time of flight)	(In addition to the above) Large values of k_{max} attainable. Fixed geometry simplifies experiment set-up, e. g. for pressure studies. Simultaneous collection of data for all k-values facilitates time-resolved experiments. Higher count rates (if LINAC used).	Pulsed source required (chopper + steady-state reactor or LINAC source).
Electrons (fixed λ, variable θ)	Uses scanning electron microscope. In situ grown thin films can be examined. High count rates.	Scattering very strong and multiple scattering important for thickness greater than 100 Å. Thin films may not be representative of the bulk structure. Large inelastic scattering background (due to plasmons, etc.)

Generalized XRD intensity function for an n component polymeric system is given by,

$$\frac{I_{eu}}{N} = \sum_{i=1}^{n} x_i f_i^2 + \sum_{i=1}^{n}\sum_{j=1}^{n} x_i x_j f_i f_j \int_0^{\infty} \frac{4\pi r^2 \rho_{ij}(r)}{x_j} \frac{\sin kr}{kr} dr - \left[\sum_{i=1}^{n} x_i f_i\right]^2 \int_0^{\infty} 4\pi r^2 \rho^0 \frac{\sin kr}{kr} dr \quad (4.25)$$

where x_i is the atomic fraction of element i and f_i is the form factor of element i and $\rho_{ij}(r)$ is the average number of j atoms per unit volume at distance r from ith atom. Reduced scattering intensities can be obtained from the above expression.

A single X-ray scattering experiment will not enable determination of all the pair correlation functions or the partial structure functions because a single Fourier transform of the experimentally obtained $F(k)$ functions will not enable individual $\rho_{ij}(r)$ to be determined from such experiment. As a matter of fact using weighted f over the entire range of k is itself strictly incorrect. However in the case of neutron diffraction the k (or Q) independence of $\bar{b}$ is an advantage in deriving the RDFs. Even then assumption has to be made regarding the distribution of the atomic species or the function $\rho_{ij}(r)$. Partial structure factors are given in neutron scattering experiment by suitable isotope substitution because the scattering lengths can be varied without affecting the chemistry and also it is reasonable to assume that isotope substitution does not alter the structure. Since some of the elements allow the change of even the sign of $\bar{b}$ during isotope substitution (see Figure 4.04), it enables determination of individual pair correlation function in neutron scattering. In general $n(n\text{-}1)/2$ pair correlations to be determined increases the complexity and number of experiments to be performed.

In just a binary metallic glass such as $Ni_{81}B_{19}$, it needs 3 isotopic substitutions to evaluate all the three correlation functions. $Ni_{81}B_{19}$ is also a good example of the successful application of neutron diffraction technique and the determination of all the three partial structure factors using isotopic substitution are shown in Figure 4.08.

Particular pair correlation function among a number of pair correlation functions can possibly be determined by isomorphous substitution, that is, by substituting one element by another chemically similar element. The implied assumption is that the structure around the atoms of the given element is not altered. There are also other methods

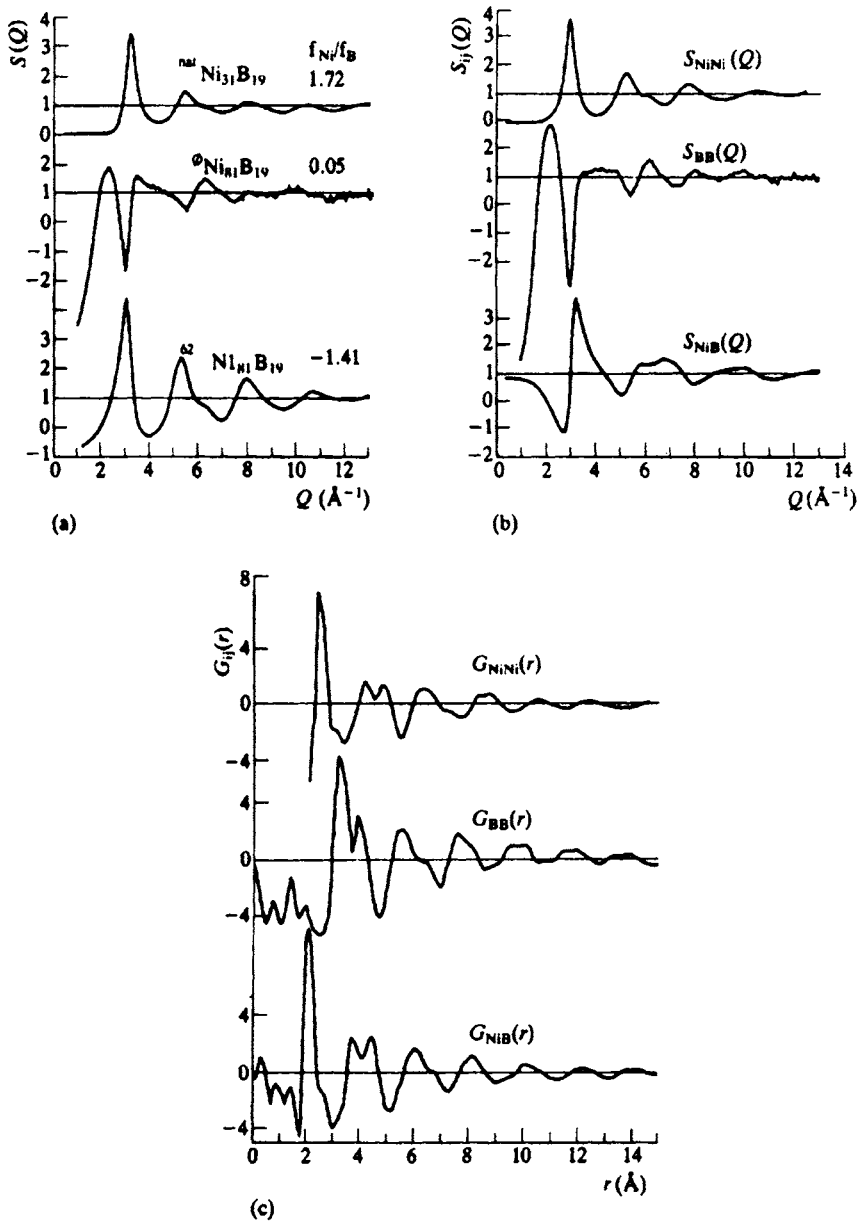

Figure 4.08: Structural studies of $Ni_{81}B_{19}$ using isotopic neutron diffraction; (a) Structure factor for different isotopically substituted alloys. (b) Partial structure factors obtained form those shown in (a). (c) Partial reduced RDFs obtained by Fourier transformation of the $S_{ij}(Q)$ shown in (b) (After Lamparter et al., 1982).

like use of anomalous scattering in X-ray diffraction method, where the scattering factor of a given atom is not only dependent on k but is also dependent on the energy of the X-ray photon. This is because X-ray scattering varies anomalously near the absorption edge. $f(k)$ becomes $f(k,\omega)$ and can be represented as,

$$f(k,\omega) = f^0(k) + f'(k,\omega) + if''(k,\omega) \tag{4.26}$$

The first term f^0(k) is the X-ray atomic scattering factor and the other two terms are the dispersion corrections. Similar anomalous scattering occurs for neutrons also and the neutron scattering factor is formulated in a similar way.

Extended X-ray Absorption Fine Structure

From preceding section, we note that the structural information obtainable from X-ray, neutron and electron scattering techniques is largely limited to obtaining RDF. The RDFs so determined are convolutes of a number of pair correlation functions except in the simplest case of A_mB_n which consists of three pair correlation functions, A-A, B-B and A-B and where three different diffraction experiments can be designed. The task of obtaining individual pair correlations is very difficult. A technique which enables acquiring structural information more directly around a given chemical element is the analysis of "Extended X-ray Absorption Fine Structure" or "EXAFS". It will soon become evident that EXAFS is element specific. It involves ionisation of a core electron of a given atom which propagates outwards from the atom and in the process undergoes diffraction by being scattered from the neighbouring atoms in the structure. The return of the scattered waves affect the absorption coefficient of the given atom, as a result of which the absorption coefficient exhibits undulations. These undulations constitute the EXAFS. Therefore EXAFS technique is the one, which involves diffraction of *in situ* generated low energy electrons. The observed intensity function has built into it a Fourier transform relation to the structure, and therefore, the structure is obtainable through Fourier transform of the observed EXAFS.

Consider X-rays incident on an atom A in a glass such as A_mB_n. The absorption coefficient, μ, for X-rays can be plotted for as a function of photon energy ($\hbar\omega$), an example of which is shown in Figure 4.09. When the energy of the photon corresponds to the binding energy of a core electron like $2p$, $2s$ or $1s$ of the element A, the absorption coefficient

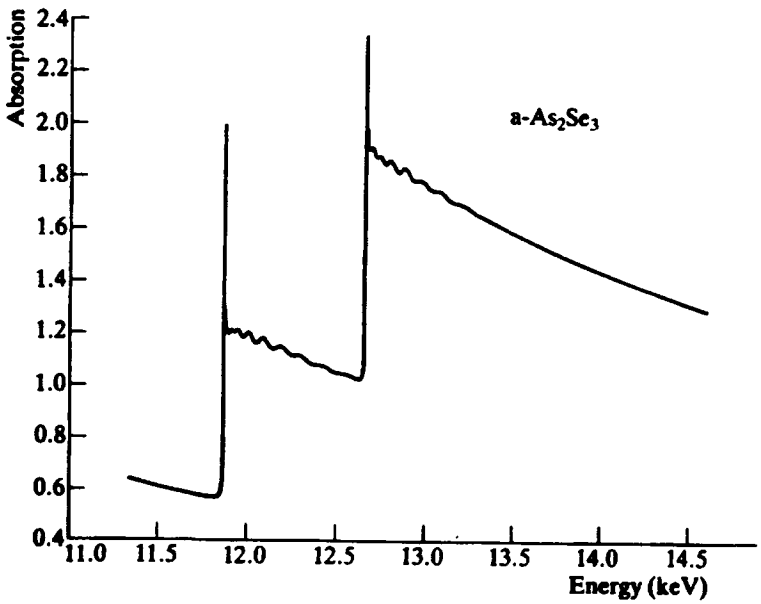

Figure 4.09: Extended X-ray absorption fine structure for a-As_2Se_3 showing the fine structure beyond the As and Se K edges (From Elliott, 1984)

suddenly peaks up. Following every peak absorption there are EXAFS undulations in absorption coefficients. The amplitude of the undulations falls off with increasing energy. The magnitudes of the EXAFS undulations are calculated using the formula,

$$\chi(E) = \frac{\mu(E) - \mu_o}{\mu_0} \quad \text{or} \quad \chi(k) = \frac{\mu(k) - \mu_0}{\mu_0} \tag{4.27}$$

where μ_0 is the background absorption (often one uses $\mu_0 M(k)$ in the denominator where $M(k)$ is known as McMaster correction term).

The origin of the undulations can be understood with reference to Figure 4.10. The X-ray photon liberates a photoelectron from one of the core states (say). This liberated electron propagates as a spherical wave outwards from A, as indicated in Figure 4.10. The propagating wave is now diffracted by the surrounding atoms, which also consists of electrons and nuclei. The phase of the diffracted wave depends on the state of its incidence on the neighbouring atoms. Thus the diffracted wave now returns to the origin in general with a difference in phase and amplitude. It would be instructive to imagine an experiment in which the photoelectron

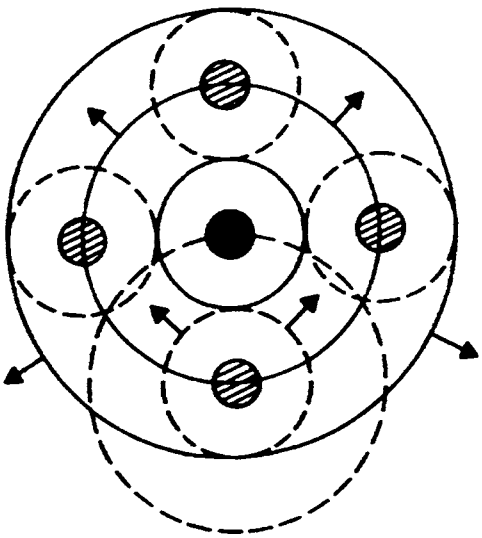

Figure 4.10: Schematic illustration of the EXAFS process.

is ejected with constant energy and the distance of the scatterer is gradually increased. If the wavelength of the photoelectron is λ, then varying the position of the scatterer by a distance λ, the reflected wave will return to the origin with phase differences covering all the values from 0 to 2π. In an actual experiment the distance is not varied, instead, the photoelectron energy or its wavelength itself is varied and the phases of the reflected waves are affected in the same manner.

The superposition of the outgoing and incoming waves alters the wave function of the photoelectron at the site of the given emitter. The final state wave function, $|f\rangle$, becomes $|\varphi_e\rangle + |\varphi_{sc}\rangle$ where φ_e and φ_{sc} are the emitted and scattered wave functions. The photoelectron absorption process involves the final state wave function and the quantum mechanical expression for the X-ray absorption coefficient is given by,

$$\mu = 4N_0\pi^2e^2\frac{\omega}{c}\left|\langle f|z|i\rangle\right|^2\rho(E^f) \tag{4.28}$$

where e is the electronic charge, ω is the X-ray frequency, c is the velocity of light, N_0 is the number density of the absorbing atoms and $\rho(E^f)$ is the density of the final states $|f\rangle$. $\rho(E^f)$ generally varies monotonically because these are free electrons of low energy propagating through the

medium. $|i\rangle$ is the initial core state which is also a smoothly varying function. Therefore the undulations or the oscillatory behaviour of μ in EXAFS can only arise from $|f\rangle$. This, as noted, is a consequence of superposition of propagating and back scattered waves.

Theoretical expression for $\chi(k)$ was derived by Sayers et al. (1971) using single scattering formalism and back scattering of planar waves from shells of atoms surrounding a given emitter and it is given by,

$$\chi(k) = -\sum_j \left(\frac{N_j}{R_j^2}\right)\frac{|f_j(\pi)|}{k}\exp\left(-\frac{2R_j}{\lambda_e}\right)\exp\left(-2\sigma_j k^2\right) .\sin\left(2kR_j + 2\delta(k) + \eta_j(k)\right) \tag{4.29}$$

The sum taken over all back scattering atoms in a shell indexed by j and containing N_j atoms at a distance R_j. It should be noted carefully that the magnitude of the EXAFS is proportional to N_j, which is the number of back scattering atoms and it is inversely proportional to R_j^2, because, the amplitude of the outgoing wave has decreased by $1/R_j$ while going out and once more by the same factor as it returns to the emitter. The back scattering amplitudes $f_j(\pi)$ is in general complex and therefore its magnitude is used. The amplitude of the outgoing wave is also generally attenuated because of the finite mean free path, λ_e, of the electrons (~2000 Å) and the effect is taken care of by the term, $\exp(-2R_j/\lambda_e)$, which has only a very weak influence on the amplitude. σ_j is the root mean square displacement which expresses the static or thermal disorder about the equilibrium bond length and is the Debye Waller factor. The sinusoidal function expresses the influence of the phase shift of the electron on μ and consists of three terms for a given value of k or the energy of the photon. First term is $2kR_j$ indicating the influence of emitter scatterrer distance, R_j. The second and third terms ($\delta(k)$ and $\eta_j(k)$) arise because the photoelectron is emitted and back scattered respectively under the influence of emitter-scatterer potentials. The wave number of the photoelectron is given by,

$$k = \frac{2\pi}{\lambda} = \left[\frac{2m_e(E - E_0)}{\hbar^2}\right]^{1/2} \tag{4.30}$$

where E_0 is the threshold energy. Thus the above expression consists of N_j, R_j and σ_j which are structural parameters to be determined from EXAFS

and f_i, ϕ_j (the phase term $2kR_j+2\delta(k)+\eta_j(k)$) and λ_e which are the scattering parameters. In actual EXAFS experiments $\chi(k)$ is determined using equation (4.27) up to as high a value of energy as possible, but starting with at least 30-40 eV above the edge (k values of ~ 4 and above). This is because for energies lower than 30-40 eV multiple scattering becomes dominant and also the assumption of a planar wave in the derivation of equation (4.29) is not strictly valid. In fact it is safe to consider EXAFS undulations as only those, which occur above 80 eV from the edge. The amplitude parameters have been theoretically calculated and listed as functions of k for various atoms. η and δ are not generally available as they are material dependent. The most widely used procedure involves use of Fourier transformation technique, where the Fourier transform yields $\phi(r)$ which is a radial function. It is in principle a pair distribution function and is given by

$$\phi(r)=\left(\frac{1}{2\pi}\right)^{1/2}\int_{k_{\min}}^{k_{\max}}\chi(k)M(k)k^n\exp(2ikr)dk \tag{4.31}$$

$M(k)$ is a window function and k^n is k weighing used with $\chi(k)$ which enhances the weightage of amplitude in $\chi(k)$. This helps in obtaining better Fourier transform. Since $\exp(2ikr)$ ignores η and δ, the peaks obtained in $\phi(r)$ do not represent true distances and are shifted. In order to overcome this problem $\chi(k)$ is obtained for a known crystalline solid for the same emitter-scatterer atom pairs so that the phase shifts (and if necessary even amplitudes) are fixed on the basis of the analysis of the crystal data. These phase shifts are then assumed to be transferable so that $\chi(k)$ of the given glass is fitted with such phase parameters. The phase and amplitude parameters, however, have been determined from first principles for several glasses (Gurmann and Pettifier, 1979).

In general, EXAFS can be carefully analysed to obtain distances of first and second neighbours to within ± 0.01Å. But N_j (j = 1) can be accurate up to only ± 20 %. In the analysis of glass structure, EXAFS has a very important role because with the availability of synchroton radiation, core electrons of most of the elements can be excited from $1s$, $2s$ or $2p$ (two) states. In fact these edges are known as K, L_1, L_2 and L_3 edges respectively. It is possible to study even M edge spectra for suitably chosen elements. The K, L_1 and L_2 edge spectra of Nd in fluoroberyllate glasses studied by EXAFS is shown in Figure 4.11. The general procedure

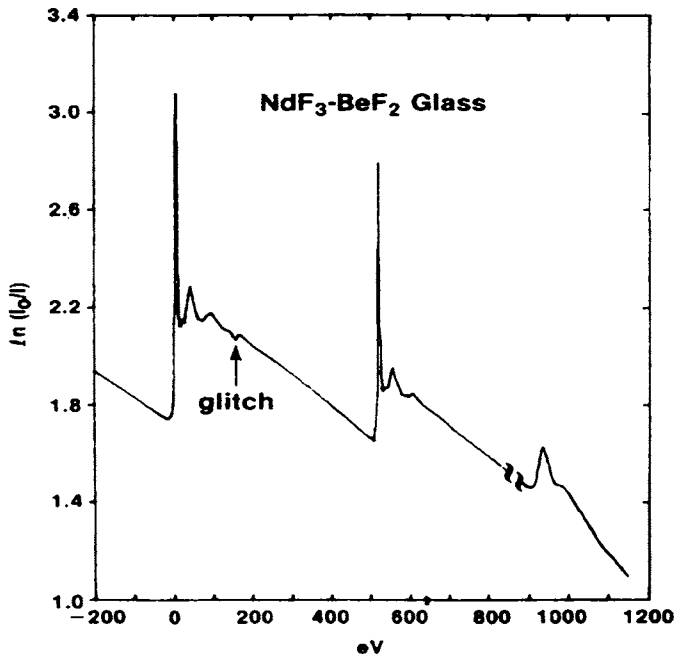

Figure 4.11: Room-temperature experimental XANES and EXAFS scans of BeF_2 glass containing 4 mol % Nd at the Nd L_3, L_2 and L_1 edges (After Rao et al., 1983).

adopted in the analysis of EXAFS is represented in Figure 4.12. The "raw" $\chi(k)$ obtained from the spectra like in Figure 4.11 is converted into a k-weighted EXAFS, $k^n \cdot \chi(k)$. In Figure 4.12(a), $n = 1$ and $k \cdot \chi(k)$ has been plotted as a function of k. The Fourier Transform of this is shown in Figure 4.12(b), which is the RDF. It consists of various peaks and each peak in principle represents a shell and the distances to various neighbours can be thus determined. But the distances are generally smaller because of the k weighting of the $\chi(k)$ before Fourier transformation. One of the widely used procedures is to recover $k^n \cdot \chi(k)$ for the individual peaks – generally the first peak - by inverse FT of the "windowed" peak (between the lowest values of RDF on either side of the peak). Having recovered $k^n \cdot \chi(k)$ it is now fitted for theoretical EXAFS using scattering parameters as inputs and adjusting the structural parameters (a least squares fitting procedure is adopted). Phase parameters in fitting the data for Figure 4.12(c) were determined from the data on crystalline NdF_3. The quality of the fit determines the accuracy of the structural parameters. In the present case, N_j of Nd was found to be ~ 7 and distances vary from 2.33-3.04 Å.

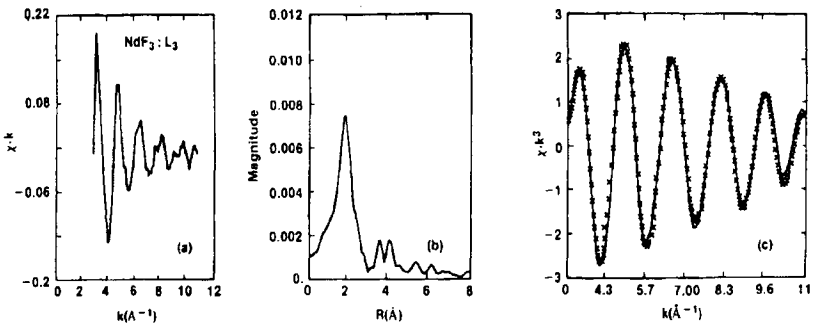

Figure 4.12: (a) Normalized Nd L_3 EXAFS for crystalline NdF_3; (b) Fourier transform of (a) and (c) inverse transform (line) and simulated EXAFS (points) in the region 0.2 to 3.2 Å (After Rao et al, 1983).

One of the serious limitations of EXAFS technique is with regard to phase parameters. These are quite generally obtained from analysis of EXAFS of crystalline compounds of known structure. In order that such phase information be transferable, the structure around the given atom should be very similar. This admittedly is a weakness because the structure of the glass is clearly unknown. Further use of these phase parameters in fitting the experimental EXAFS of a glass imposes a genetic influence on the structure in the sense that it tries to fit the EXAFS of unknown with as many subshells of atoms (as many sets of phase parameters) as there are in the model crystalline compound.

X-ray Absorption Near Edge Structure

XANES is the acronym for X-ray absorption near edge structure. In principle it should include absorption features, which are described as both pre-edge and post-edge. Glasses consisting of transition metal ions often exhibit sharp pre-edge absorption just before the major X-ray absorption peak. On the high energy side of the major peak is the EXAFS. The peaks are attributed to excitations to bound states. These bound states can be low lying bonding and antibonding states in many atoms or the crystal field split vacant levels of the transition metals or they can be unoccupied Rydberg states of the ion below the ionisation potential. The allowed core electron excitation ($s \rightarrow p$ or $p \rightarrow d$ etc.) gives rise to sharp features. A well studied example of excitation to crystal field split levels is that of Ti and is given in Figure 4.13. There is a pre-edge peak attributed to $1s \rightarrow 3d$ transition in the K edge spectra. This peak is sensitive to local

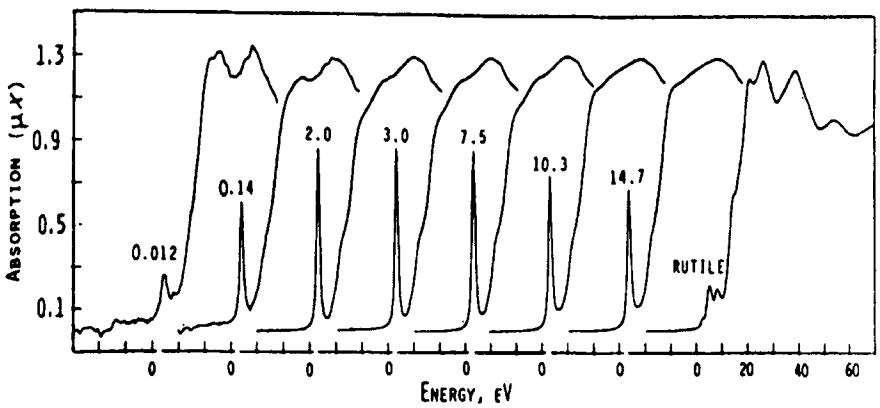

Figure 4.13: The near-edge K absorption spectra of a series of TiO_2-SiO_2 glasses plus a standard material, rutile, TiO_2. The concentration of TiO_2 is labelled in wt % (After Lewis, 1989).

symmetry being absent in rutile but present in anatase. In several cases these so-called pre-edge phenomena merge with the main threshold absorption and become indistinguishable, primarily because of poor resolution, inadequate to observe such bound state to bound state excitations. If the absorption is an allowed transition to vacant *p* or *d* state, the absorption can be sufficiently intense. Immediately next to absorption edge also a few absorption coefficient undulations are observed. The peaks close to the absorption edge are likely to arise from excitation to allowed bound states and an analysis of the structure of near edge can yield valuable information on the symmetry of the ligand ions. This is fairly clearly observed when the excitation occurs from 2*p* core level to vacant *nd* levels; the splitting of *nd* levels determines the number of peaks in the XANES, while the splitting itself is a consequence of the crystal field symmetry around the atom. While T_d or O_h symmetries lead to two split levels, lower symmetries can give rise to more. Let us suppose that the analysis of EXAFS associated with the same edge reveals the presence of 4 or 6 nearest neighbours. It is suggestive of a crystal field geometry of T_d or O_h respectively around the given ion if the XANES has just two sub peaks (can be often seen in derivative XANES spectra). Thus a combination of EXAFS and XANES in such cases can be a very powerful tool for the study of SRO. However, XANES is viewed as low energy portion of EXAFS itself for which the single scattering formalism is inadequate and is therefore left out of the analysis. Care is hence necessary in the analysis of near edge data.

Nuclear Magnetic Resonance

Structural investigations in glassy state, particularly in the regime of SRO, has been helped tremendously by the technique of nuclear magnetic resonance (NMR). Several important elements frequently found in glasses fortunately possess nuclear magnetic moment, such as for example B, Al, Si, O, Li, F, Pb, Te, Sn etc. Proton and carbon which are constituents of all organic glasses also possess nonzero spin. The nuclear spin values and natural abundances of these elements are listed along with their Larmour frequencies in Table 4.2.

The basis of application of NMR technique (Fyfe, 1983) is that the degenerate nuclear spin levels of atoms are split when an external magnetic field is applied – due to Zeeman interaction. If I is the nuclear spin which may be integral or half integral, it splits into equally spaced $(2I+1)$ states in a magnetic field. If the strength of the magnetic field is H, then the separation of the energy levels is given by ΔE, and

$$\Delta E = \gamma.\hbar H \tag{4.32}$$

where γ is the gyromagnetic ratio of the nuclei and $\hbar\,(= h/2\pi)$ is the Planck constant. The spins are distributed into various Zeeman split states following a Boltzmann distribution law. If the system is now irradiated with electromagnetic radiation of frequency ν_0 such that $h\nu_0=\Delta E$, then the spins in the lower energy states absorb the energy and get excited to higher energy. Under the ideal condition, i.e. in the absence of any other interaction, a sharp absorption peak is expected to be present in its NMR absorption spectrum. It is illustrated in Figure 4.14 schematically for the case of $I = 3/2$. In the actual spectrum, the absorption peaks are not sharp delta functions (Figure 4.14 (b)) but are broadened peaks as illustrated in Figure 4.14 (c). This is due to several interactions of the magnetic moments of the nuclei, which affect the splitting. The most important of them is the dipolar interactions. The magnetic moment, $\vec{\mu}$ is a vector given by,

$$\vec{\mu} = \gamma.\hbar\vec{I} \tag{4.33}$$

Two dipoles $\vec{\mu}_1$ and $\vec{\mu}_2$ are situated at a distance r_{12} interact with an energy proportional to $(\vec{\mu}_1.\vec{\mu}_2)/r_{12}^6$. The dipolar interactions have the effect of broadening the resonance frequencies. The magnitude of this

Table 4.2: Characteristic nuclear properties of various elements. (After Zarzycki, 1982)

Nuclei	Natural abundance %	Larmour frequency MHz (at 10^4 Gauss)	Magnetic moment (in nuclear magnetons)	Spin (in ħ units)	Electric quadrupole moment (10^{-24} cm^2)
^{1}H	99.9844	42.577	2.7927	½	-
^{7}Li	92.57	16.547	3.2560	3/2	-4.2×10^{-2}
^{9}Be	100	5.983	-1.7740	3/2	2.0×10^{-2}
^{11}B	81.17	13.660	2.6880	3/2	3.55×10^{-2}
^{19}F	100	40.055	2.6273	1/2	-
^{23}Na	100	11.262	2.2161	3/2	0.1
^{27}Al	100	11.094	3.6385	5/2	0.149
^{29}Si	4.70	8.460	-0.55477	1/2	-
^{31}P	100	17.235	1.1305	1/2	-
^{45}Sc	100	10.343	4.7491	1/2	-
^{51}V	~ 100	11.193	5.1392	7/2	0.3
^{73}Ge	7.61	1.485	-0.8768	9/2	-0.2
^{75}As	100	7.292	1.4349	3/2	0.3
^{111}Cd	12.86	9.028	-0.5922	1/2	-
^{113}Cd	12.34	9.444	-0.6195	1/2	-
^{125}Te	7.03	13.45	-0.8824	1/2	-
^{133}Cs	100	5.585	2.5642	7/2	< 0.3
^{205}Tl	70.48	24.57	1.614	1/2	-
^{207}Pb	21.11	8.899	0.5837	1/2	-

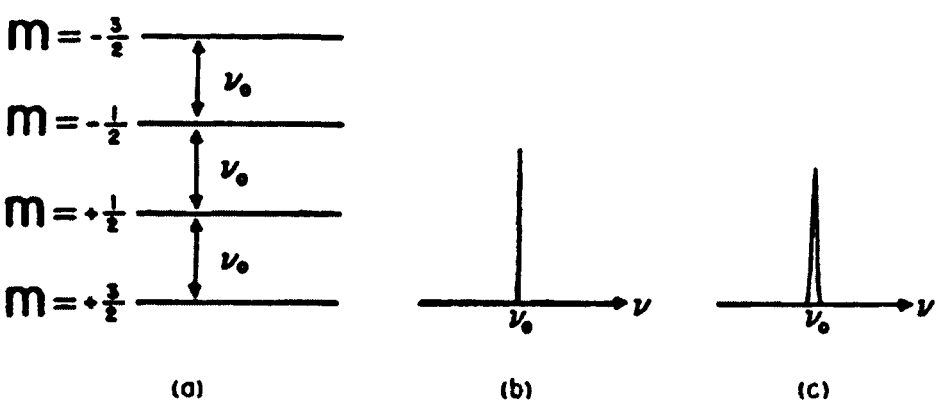

Figure 4.14: (a) Energy levels for a spin 3/2 nucleus in the presence of a magnetic field. (b) The resultant NMR absorption spectrum in a single peak at the frequency ν_0. (c) Dipolar interactions broaden the resonance symmetrically so that it is not the delta-function response depicted in (b).

broadening contribution to the full width at half maximum (FWHM) of a resonance peak can be calculated using van Vleck's (1948) method. This dipole-dipole contribution, δ, is given by,

$$\delta = 2.36\sqrt{M_2^I} \tag{4.34}$$

where M_2^I is the second moment of the nuclear spin. If there are spins with two different values, say I and I', then M_2^I is a sum of two terms:

$$M_2^I = \Delta_{I,I} + \Delta_{I,I'} \tag{4.35}$$

where

$$\Delta_{I,I} = \frac{3}{5}\gamma_I^4 \hbar^2 I(I+1)\sum\left(\frac{1}{r^6}\right) \tag{4.36}$$

and

$$\Delta_{I,I'} = \frac{4}{5}\gamma_I^2 \gamma_{I'}^2 \hbar^2 I'(I'+1)\sum\left(\frac{1}{r^6}\right) \tag{4.37}$$

Of greater interest to the chemistry of glasses is the chemical shift interaction term. This arises from the fact that the extra nuclear electrons in the atom also respond to the applied magnetic field by virtue of which they shield the nucleus from the external magnetic field. As a consequence, a small shift occurs in the resonance frequency and this is known as the chemical shift. It is measured in parts per million (ppm). The chemical shift interaction energy, E_{CS} can be written as,

$$E_{CS} = \gamma \hbar \vec{I} \tilde{\sigma} \vec{H} \tag{4.38}$$

Where $\tilde{\sigma}$ is the chemical shift tensor. The observed resonance frequency ν is given by,

$$\nu = \nu_0(1-\sigma_{zz}) \tag{4.39}$$

where σ_{zz} is the component of the chemical shift tensor in the direction of

the applied field. If the diagonal elements of the chemical shift tensor along the principal axes are represented for convenience as σ_1, σ_2 and σ_3, ν for arbitrary orientation is given by,

$$\nu = \nu_0[1 - \sigma_{iso} - \sigma_{axial}(3\cos^2\theta - 1) - \sigma_{aniso}(\sin^2\theta \cos 2\phi)] \tag{4.40}$$

where σ_{iso} and σ_{aniso} are the isotropic and anisotropic chemical shift values. In terms of σ_1, σ_2 and σ_3,

$$\begin{aligned} \sigma_{iso} &= \frac{1}{3}(\sigma_1 + \sigma_2 + \sigma_3) \\ \sigma_{axial} &= \frac{1}{6}(2\sigma_3 - \sigma_1 - \sigma_2) \\ \sigma_{aniso} &= \frac{1}{2}(\sigma_2 - \sigma_1) \end{aligned} \tag{4.41}$$

θ and ϕ are the polar angles of the field H with respect to the principal axis of the chemical shift tensor. In a glass or a powdered sample, all orientations are possible and therefore the spectrum is an envelope of the responses for all values of θ and ϕ. The theoretical powder patterns appear as shown in Figure 4.15. The sharp shoulders and the divergences are smoothened out in the real spectrum due to dipolar interaction.

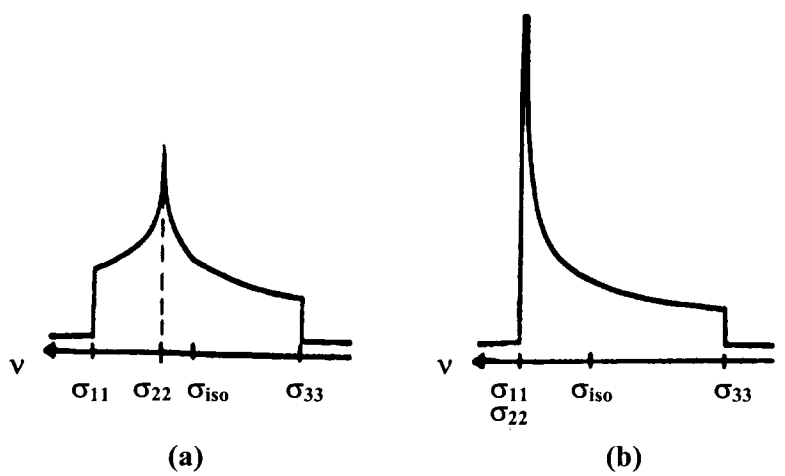

Figure 4.15: Chemical shift powder patterns for (a) asymmetric and (b) axially symmetric anisotropies (After Emerson and Bray, 1993).

Another important interaction which contributes to broadening of resonance peaks is the quadurpolar interaction. When the nuclear spin, $I \geq 1$, the nuclei possess electric quadurpole moment, eQ. The quadurpole moment Q is a measure of the distortion of spherical symmetry of the nuclear charge distribution. Quadurpole moment interacts with the electric field gradient, EFG, present at the nucleus. These are the fields caused by the electrons in the atom. Spherical distribution of electrons in closed shells do not produce any EFG at the nucleus but the bonding electrons do. Therefore the quadurpolar interaction can be used to obtain information on chemical bonding. Quadurpolar interaction shifts the Zeeman levels. The first order correction due to quadurpolar interaction to the Zeeman splitting between levels m and (m-1) is given by,

$$\nu_{m\to m-1} = \nu_0 - \nu_Q\left(\frac{m-(1/2)}{2}\right)\left[(3\cos^2\theta - 1) - \eta\sin^2\theta\cos 2\phi\right] \tag{4.42}$$

where

$$\nu_Q = \frac{3Q_{CC}}{2I(2I-1)} \tag{4.43}$$

and Q_{cc} is the quadurpolar coupling constant, given by

$$Q_{CC} = \frac{eQV_{zz}}{H} \tag{4.44}$$

Where V_{zz} is the principal axes component of the EFG tensor. The asymmetry parameter, η, is a measure of the departure of EFG from cylindrical symmetry.

$$\eta = \frac{(V_{xx} - V_{YY})}{V_{zz}} \tag{4.45}$$

such that $0 \leq \eta \leq 1$. θ and ϕ are, as noted earlier, polar angles of the magnetic field with respect to the principal axes of the EFG tensor. Therefore the spin bearing nuclei have both field dependent and field independent (zero field) terms, which determine the energy states and their splitting.

The nuclear Hamiltonian relevant for NMR studies is therefore given by

$$H_{NMR} = -\gamma \hbar \vec{I} \vec{H} + \gamma \hbar \vec{I} \tilde{\sigma} \vec{H} + \vec{I} \tilde{D} \vec{I} + \vec{I} \tilde{Q} \vec{I} \qquad (4.46)$$

In equation 4.46 the first term represents the Zeeman splitting, second the chemical shift, third the dipolar and fourth the quadurpolar terms. NMR spectrum of nuclei in the liquid state are very sharp while they are very broad in the solid state. This is largely due to the third term which is due to dipole-dipole interaction. In liquids there is a natural freedom for atoms and molecules to take any orientation so that dipolar interactions average out, but this is not the case in solids. Thus all the anisotropic interactions in liquids essentially become zero and the observed line widths in NMR are of the order of 1 Hz which arises from the magnetic field inhomogeneity. The large widths of the order of several kHz observed in solids arise from these anisotropic interactions. The first attempt to overcome this problem was made by Andrew et al. and independently by Lowe in 1959 by using a specimen rotation technique, known as magic angle spinning (MAS) NMR. When carefully examined, the interaction terms in equation (4.44) which are sources of anisotropy and broadening reveal that they consist of a term, which is $(3\cos^2\theta_{ij} - 1)$, where θ_{ij} is the angle between the magnetic field direction and the internuclear vector. Therefore, when this angle, $\theta = 54°44'$, all the anisotropic terms become zero and NMR signal should become narrow. What is required therefore is to spin the sample at that angle of 54°44′ with respect to field direction. In particular the broadening caused by dipolar interaction is completely removed by such spinning. It has been shown that broadening due to chemical shift anisotropy is also removed so that the resulting narrow lines in the NMR spectrum can be used to identify different chemical environments of the nuclei. In order to achieve very narrow lines the rate of rotation must exceed the line widths, otherwise the transfer magnetization decays faster than the time it takes to complete one revolution and this results in the retention of broadening.

There are other methods of analysis of NMR of glassy solids such as the broad line or continuous wave NMR particularly valuable for quadurpolar nuclei like ^{11}B. In Figure 4.16, broad line NMR spectrum of ^{11}B in B_2O_3 glass is presented along with the MAS NMR to illustrate the effect of spinning on the widths of resonance peaks. Comparison is also provided with the MAS NMR of crystalline B_2O_3. Several examples of the

use of MAS NMR in structural investigations are cited in this book in subsequent chapters.

Pulsed NMR spectroscopy (Fukishima and Roeder, 1981; Farrar and Becker, 1971) is another technique very useful in glass science. A short and intense pulse consisting of the entire range of frequencies of interest is used to irradiate the sample. The total magnetisation of the sample gets rotated from its equilibrium position along the z-axis by an angle θ_p, which is given by,

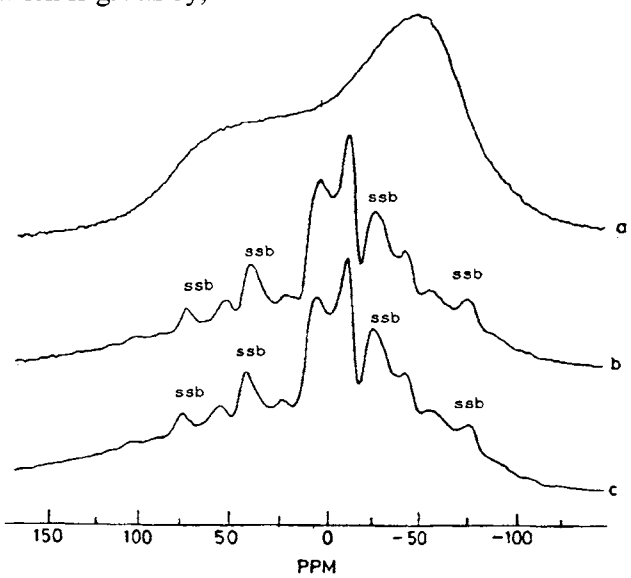

Figure 4.16: ^{11}B NMR spectra of B_2O_3. (a) Powder pattern of glassy B_2O_3; (b) MAS spectra (~ 3 kHz) of glassy B_2O_3; (c) MAS spectra (~ 3 kHz) of crystalline B_2O_3. (ssb, spinning side bands). (After Prabakar et al, 1990)

$$\theta_P = \gamma H_1 t_P \tag{4.47}$$

where the angular frequency is expressed as γH_1 and duration of the pulse by t_p as shown in Figure 4.17. With reference to the figure, the components of the magnetisation vector ($\boldsymbol{M}$) lying in the x-y plane give rise to an induction in a receiver coil. This is designated as the free induction. The pulse induces the alignment of the individual spins, but the interaction between individual spins, spin-spin interaction, causes dephasing, which therefore decreases the magnitude of $\boldsymbol{M}$. The spin-spin interaction is characterized by a time constant T_2 while corresponding spin-lattice time constant is designated as T_1. Spin-lattice relaxation occurs

through a coupling to the phonon spectrum of the material. The effect of the spin-lattice relaxation is to bring down the magnetisation to its equilibrium value and therefore to diminish the free induction. The free induction picked up by the receiver coil decays with time and is appropriately called a free induction decay (FID). With repeated pulses, the corresponding FID signals are accumulated and averaged. It is Fourier transformed and the real part of the FID (which is a complex quantity) gives the NMR absorption spectrum. The decay of the FID is generally

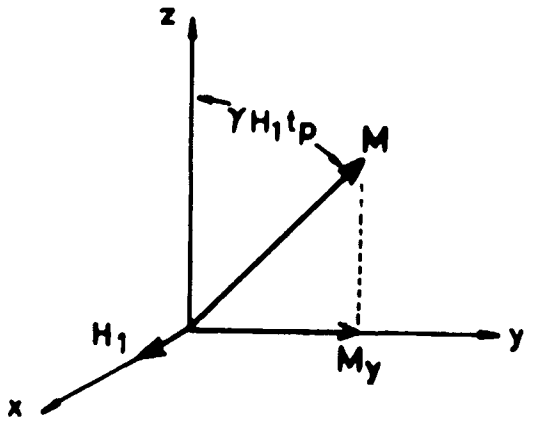

Figure 4.17: A pulse of length, t_p rotates the magnetization vector from its equilibrium position by an angle, $\theta_p = \gamma H_1 t_p$.

exponential and is characterized by the time constant, T_2^* or the apparent T_2, and T_2^* is related to the FWHM as

$$FWHM = \frac{2}{T_2^*} \tag{4.48}$$

T_2^* actually is the total effect of both spin-spin and spin-lattice time constants and is given by,

$$\frac{1}{T_2^*} \approx \frac{1}{2T_1} + \frac{1}{T_2} + \text{a small term} \tag{4.49}$$

The small term is due to the broadening caused by the magnetic field inhomogeneity. In solids, spin-lattice relaxation time, T_1 is much longer

and therefore the free induction decay (FID) gives directly, T_2 as $T_2 \approx T_2^*$. Thus this powerful technique of pulsed NMR gives the important dynamical quantity T_2, which is of particular significance in studying ion transport. It is necessary in such experiments that the pulse rate is adjusted so as to avoid insufficient decay. The inverse of pulse frequency must be significantly higher than T_1. The problem of long T_1 can be circumvented particularly when structural information is required, by putting small paramagnetic species in the sample so that enough FIDs are collected from which the FT yields the necessary spectrum.

A further advance in the use of pulse technique is the spin echo method (Hahn, 1950; Waugh et al., 1968; Mehring, 1978; Emerson and Bray, 1993). Briefly in this technique, a 90^0 pulse is applied at $t = t_0$. 90^0 pulse is that for which $\theta_p = \pi/2$. This causes an induction, which then dephases and begins to decay. After a time τ, a 180^0 pulse is imposed, which now rotates the spins by 180^0. As a consequence, the same mechanism which was responsible for dephasing of spins in the xy plane, now acts to rephase the spins. After a time interval of 2τ, a spin echo is formed. The spin echo therefore represents cumulative action of two FIDs taking place from opposite directions. The FT of the second half of the spin echo gives the absorption spectrum.

MAS NMR often consists of a number of resonances of similar structure on either side of the main signal. While the main resonance peaks remain unaffected by the spinning speed in terms of their chemical shifts, these similar looking features on either side of the main resonance shift for different spinning speeds. These are known as 'spinning side bands' or SSBs. Large SSB intensities are an indication of particularly high degree of chemical shift anisotropy.

Another important observation in the NMR spectra of glasses (also of several crystalline solids) is the so-called motional narrowing effect. The resonance peaks become narrow (FWHM decreases) in the wide line NMR (NMR spectrum obtained without spinning) when the temperature is increased. A typical example is ^{7}Li NMR in Li^+ ion conducting glasses. ^{7}Li NMR is particularly helpful in determining activation energies for lithium ion motion in glasses. Several theories have been adopted (from the study of similar effects in liquids) or developed to explain the observed motional narrowing effect. A phenomenological equation derived by Hendrickson and Bray (1973) using a two-state model for the diffusing ion has been the most popular. When inhomogeneous broadening is negligible, the narrowing effect can be expressed through the following equation:

$$\ln\left(\frac{1}{\Delta\omega}-\frac{1}{\Delta\omega_0}\right)=-\frac{E_a}{kT}-\ln\left(\frac{1}{B}-\frac{1}{\Delta\omega_0}\right) \tag{4.50}$$

where $\Delta\omega$ is the NMR linewidth at temperature T and $\Delta\omega_0$ is the rigid lattice linewidth, E_a is the activation energy for motion of the ion under consideration and B is a constant. Dominant use of NMR in glasses is in the study of speciation in many complex glass systems. We will discuss in later chapters a number of applications of NMR - particularly MAS NMR - in deducing SRO in glasses.

Vibrational spectroscopy

Infrared (IR) and Raman spectroscopic techniques are widely used in the structural investigation of glasses (Bendow, 1993). These techniques very often provide complementary information. Since there are excellent books (Wong and Angell, 1976; Long, 1977; Fadini and Schneppel, 1989; Mitra, 1969; Balkanski, 1971; Rao, 1963; Sathyanarayana, 1996) and reviews (Lerner and Adar, 1989; Loudon, 1964) on the subject, only a brief introduction to this subject is presented in this section. Both IR and Raman use electromagnetic radiation to probe fundamental excitations such as phonos, plasmons etc. In IR spectroscopy, a direct coupling of the electromagnetic radiation to the dipole moment associated with the vibrational excitation is involved. In the case of Raman scattering use is made of a single frequency of usually visible light, whose inelastically scattered components consist of the information on the phonons of the system. In the technique of IR spectroscopy, continuously increasing wavelengths are made either to pass through the material (transmission mode) or reflected from the surface of the material (reflection mode). Peaks are seen both in absorption and reflection corresponding to the frequencies of vibration in the material. In the Raman scattering, the incident frequencies are shifted both in positive and negative direction by magnitudes corresponding to vibrational frequencies. The negatively shifted frequencies are the Stokes lines and the positively shifted frequencies are the anti-Stokes lines. It is schematically represented in Figure 4.18. Stokes lines correspond to the creation and anti-Stokes to the annihilation of phonons. Theoretical considerations reveal that anti-Stokes lines generally have much lower intensity and the study of Raman (vibrational) spectra is thus the study of the Stokes lines. The origin of Raman spectra can be understood on the basis of first order scattering theory. It precludes non-linear effects, which manifest at higher

intensity of incident radiation. The process involves scattering from phonons of wide energy range originating from various vibrational modes in a given system. They can be very low frequency acoustic modes also. In the experiments the main irradiating light beam itself emerges slightly broadened due to elastic scattering (no energy change), which is the

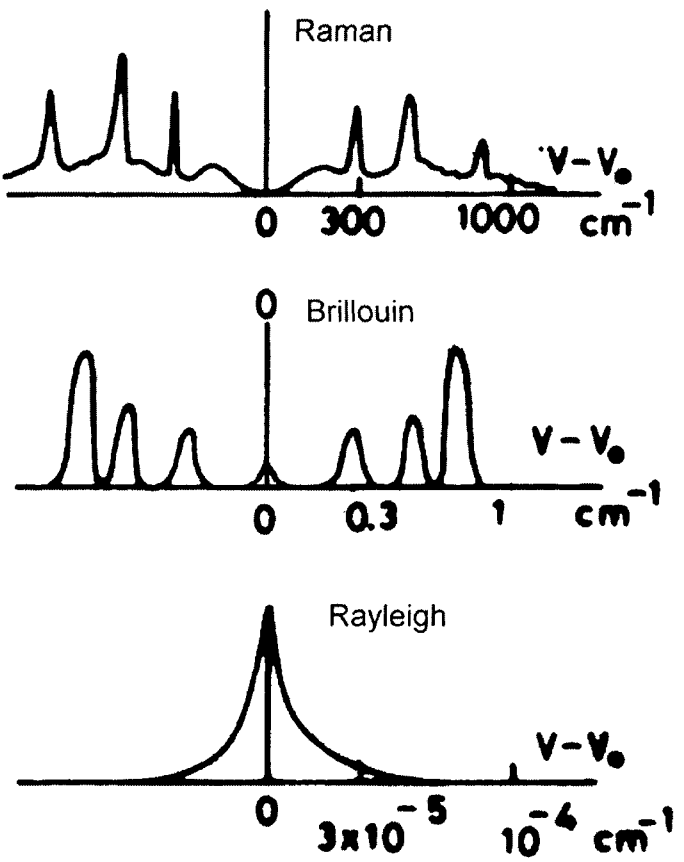

Figure 4.18: Schematic of Raman, Brillouin and Rayleigh scattering spectra in solids, indicating the characteristic frequency ranges for each type of scattering. (After Cummins, 1971)

Rayleigh scattering. The inelastic scattering due to low energy acoustic phonons appear close to the Rayleigh peak and constitute Brillouin spectra. The vibrational modes whose energies are higher are generally

due to either optical phonons or high frequency acoustic phonons and constitute what is generally known as Raman scattering. The widely used configuration for recording Raman spectra is the 90° geometry where the elastically scattered component is absent. Raman and IR spectra provide complementary information about the structure. This is because although they probe the same vibrational frequencies of a material, the selection rules for the Raman and IR spectroscopies are different and therefore the structural details are more completely probed by the use of both the techniques.

It would be instructive to consider the origin of phonons in amorphous solids because the observed characteristic vibrational peaks are sometimes quite sharp in both IR and Raman spectra of many glasses. They are associated with particular chemical or structural species. The question is how is the sharpness of peaks justified. In the simplest case, an isolated molecule can be considered as atoms connected to each other with characteristic force constants. If it is a diatomic molecule with a single spring of force constant, f, with the two atoms vibrating against each other, it is easy to show by setting up the equation of motion that this is governed by the relation

$$\omega_0^2 = \frac{f}{\mu} \tag{4.51}$$

$1/\mu = (1/m_1) + (1/m_2)$, where m_1 and m_2 are the masses of the atoms in the molecule. For larger molecules consisting of several springs and therefore several spring constants, there will be several ways in which the atoms are displaced and therefore several vibrations. Each such set of displacements is designated a vibrational mode and for a molecule containing N atoms, there are $(3N\text{-}6)$ such modes which are independent of each other (meaning, no one mode is described by any combination of other modes). In linear molecules this number is reduced by 1 because of the existence of an axis of rotation, which acts as a constraint. These are also known as normal modes of vibration. The vibrational spectrum of a molecule, in principle, should consist of a set of distinct narrow peaks. Of course, not all the peaks appear both in IR and Raman. Some peaks appear exclusively in either of the spectra. This is because of the selection rules. For a vibrational mode to be IR active it requires that electromagnetic radiation couples directly to the vibrational mode through the coupling of electrical vector of the IR radiation to the dipole moment associated with the vibrational mode. In the simplest diatomic molecule we considered

above, if it is a homopolar diatomic molecule, the only mode of vibration has no dipole moment change and therefore the mode is not IR active. The matrix element for IR absorption will be non-zero only when there is a net dipole moment change. *

IR spectroscopy

The understanding of IR spectra of glasses is helped by first considering the IR spectra of crystalline solids. A crystal corresponds to a 3-*d* periodic array of atoms, ions or molecules connected by springs except that all the spring connectivities repeat themselves from unit cell to unit cell. If it is a molecular crystal such as orthoterphenyl or salol, the intramolecular spring constants (and hence the corresponding interactions) are much higher than the intermolecular spring constants. Therefore the vibrational frequencies within the molecules are much stronger than those between the molecules as they are characterised by van der Waals interactions. In the case of an ionic or covalently bonded crystal, if there are N atoms in the unit cell, there are ($3N$-3) vibrational modes, and in the crystal it can be shown that they become ($3N$-3) branches in which each branch spans a number of frequencies as a function of wave vector k. The wave vector which characterizes the Brillouin zones restrict the number of vibrational modes in the crystal. A unit cell consisting of two atoms

---

* The general approach to understanding the IR absorption is the same as described under dielectric absorption. The complex dielectric constant $\varepsilon^*(\omega)$ is $\varepsilon^*(\omega) = \varepsilon' + i\varepsilon'' = n^2 - \kappa^2 + 2in\kappa$, where n is the refractive index and κ is the extinction coefficient. The infrared response is characterised through reflectivity R and absorption coefficient, α, given by the relations

$$R = \frac{(n-1)^2 + \kappa^2}{(n+1)^2 + \kappa^2} \quad \text{and} \quad \alpha = \frac{4\pi\kappa}{\lambda}$$

The frequency dependent dielectric constant for a damped anharmonic oscillator of characteristic frequency ω_0 and damping constant γ is given by

$$\varepsilon(\omega) = \varepsilon(\infty) + \frac{\varepsilon(0) - \varepsilon(\infty)}{\left(1 - \frac{\omega}{\omega_0}\right)^2 + i\left(\frac{\gamma}{\omega_0}\right)\left(\frac{\omega}{\omega_0}\right)}$$

In the dielectric spectra therefore the IR active mode gives rise to an absorption peak near $\omega = \omega_0$ whose width is proportional to γ. This is the transverse optical (TO) mode. The longitudinal optical (LO) mode appears as a peak in a plot of $1/\varepsilon(\omega)$ vs ω.

therefore leads to the formation of 3 branches; 2 acoustic and one optical. The acoustic branch is that whose frequency becomes zero at $k = 0$ while the optical branch is that whose frequency has a finite value at $k = 0$. In the IR spectroscopy, the wave number of light used being very small the radiation couples to the optical phonons only near $k = 0$, which results from the requirement of momentum conservation. Also, the electromagnetic waves couple only to the transverse optical modes (because of the need for a dipole). Thus, although there is a continuous range of phonon energies in a crystal (for various k values), the IR spectrum consists of only a few discrete absorption peaks representing the number of optical vibrational modes at $k \approx 0$. It is to be noted that the presence of fewer absorption peaks in IR of a crystal is not due to the paucity of phonons of different energies but due to the condition of coupling with electromagnetic radiation which restricts it to optical phonons with $k \approx 0$. There is a Raman-IR complementarity in the spectra; totally symmetrical vibrational modes are Raman active and IR inactive (this complementarity is a result of mutual exclusion rule according to which a normal mode is not active in both Raman and IR spectra if the vibrational species has an inversion centre).

As we mentioned earlier, two distinct groups of vibrations can be identified in molecular crystals. The first category is the group of internal modes of the molecule which remain largely unaffected in the crystal. The second is the group of the external modes which like in the crystal discussed above exhibit the behaviour of lattice phonons. We may now consider the vibrational spectrum to be expected from a glass or an amorphous solid. Since there is no long range order, the small units of the structure which possess short range order, are connected to each other with no repetition. These small units may all be compositionally similar but may be considered as weakly coupled among themselves. Therefore the spectra will consist of features attributable to those units except that the inherent spread in bond angles, bond lengths and occasionally compositions would broaden the spectral features either due to a spread in the values of force constants or due to damping terms. If this were not the case, there would have been a continuous density of vibrational states with no momentum conservation rules to impose, and we would have observed a totally featureless IR spectrum contrary to experimental observations. The same conclusion can be arrived at by treating glass as a disordered crystal and relaxing the $k = 0$ absorption condition. However, the observed spectra can be consistent only when the IR coupling strength to a given mode is a strongly decreasing function of k.

Raman spectroscopy

The theory of Raman spectroscopy suggests that the scattering depends on electronic polarizabilities of the atoms and the dipole moments accompanying the changes in polarizabilities. Raman scattering is in principle a three step process (1) the change in polarizability causing a transition from the ground state to a virtual excited state (2) creation (or annihilation) of phonons by an electron-phonon interaction and (3) return to the electronic ground state. Thus the polarizability plays a key role in Raman spectroscopy. Both the polarizability, α, (which is a tensor) and the associated electric moment M (a vector) can be expanded in terms of normal mode displacements (which are vectors). Thus

$$\alpha = \alpha^{(0)} + \alpha^{(1)}x + \alpha^{(2)}x^2 + ... \tag{4.52}$$

where x is the normal mode displacement. The electric dipole moment M can now be written as

$$M = \alpha E = \alpha^{(0)}E_0 e^{i\omega t} + \alpha^{(1)}xE_0 e^{i(\omega \pm w_j)t} + \alpha^{(2)}x^2 E_0 e^{i(\omega \pm 2w_j)t} + ... \tag{4.53}$$

The above equation contains the origin of all the spectra we observe. The first term is a simple excitation-deexcitation process leading to the Rayleigh scattering. The second term involves the first derivative of polarizability and is responsible for creation and annihilation of phonons of frequency ω_j. When the phonons are due to low frequency acoustic modes, it corresponds to Brillouin scattering with an energy range of 0.1-1 cm^{-1}. When these phonons have energies in the infrared region, as high as 10^2-10^3 cm^{-1}, it corresponds to Raman scattering. It may involve both high energy acoustic and optical phonons. The term consisting of $\alpha^{(2)}$ in the above equation describes the multiphonon processes.

Thus the condition for observation of Raman spectrum is a non-zero $\alpha^{(1)}$, which is the selection rule. The intensity of Raman scattering, however depends on a number of factors, which includes the frequency of the scattered light (energy separation and hence populations), the density of vibrational states, the damping constant etc. In the case of glasses, an expression due to Shuker and Gammon (1971) for the Raman intensity of the Stokes lines is given by,

$$I(\omega) \approx \frac{1+n(\omega)}{\omega}\sum_b c_b g_b(\omega) \tag{4.54}$$

where b is the vibrational band index and $g_b(\omega)$ is the density of states, for the band b and c_b is the factor which depends on the correlation length associated with the modes in band b. Thus, the spectrum consists of the weighted sum of the densities of states of various bands. The explicit temperature dependence can be removed by dividing the measured intensities by $[1 + n(\omega)]$, which is the Bose-Einestein factor. The resulting spectrum is known as the reduced Raman spectrum. In the Raman spectra of glasses, a quantity known as Raman depolarization ratio is often reported and it is very useful in the interpretation of the spectra. The depolarization ratio ρ is given by,

$$\rho = \frac{I_{\parallel}}{I_{\perp}} \tag{4.55}$$

where $I_{\parallel}$ and $I_{\perp}$ are the Raman intensities measured with their plane of polarization parallel to and perpendicular to that of the incident beam respectively. Instead of stating parallel or perpendicular they are often subscripted as *HH*, *VV*, *VH* and *HV*, where *H* and *V* stand for horizontal and vertical polarization and their order being first for the incident and then for the scattered frequencies. The variation of the depolarization ratio for amorphous solids is somewhat similar to those of molecules. For a completely isotropic disordered solid, ρ lies between 0 and 3/4 and only the non-symmetric modes give a ρ value equal to 3/4. Thus, the depolarization ratio can be used as a factor in inferring the presence of symmetric modes of vibrations. The preceding discussion provides the necessary background for understanding the IR and Raman spectra to be discussed in subsequent chapters. Generally the glass spectra reveal the presence of frequencies attributable to chemical entities and together with other data related to the chemistry of the glass, fair amount of structural information can be obtained even using a 'fingerprint' identification process, which is why vibrational spectroscopy has been the most popular tool in the structural investigation of glasses.

X-ray Photoelectron Spectroscopy

X-ray photoelectron spectroscopy (XPS) and ultraviolet photoelectron spectroscopy (UVPES) are two techniques of great value in the study of the structure of glasses. In recent times, quantitative study of non-bridging oxygens in glasses, surface phenomena such as nitridation etc. have been studied (Stephenson and Binkowski, 1976; Nagel et al.,

1976; Fischer et al., 1977; Ching et al., 1985) using photoelectron spectroscopy (PES). The technique is based on the use of the well-known photoelectric effect. When X-ray or UV photons are incident on the surface of a glass (or any material), electrons are ejected from the material. This photoionization is governed by the relation,

$$h\nu = \phi + \frac{1}{2}m\mathrm{v}^2 \tag{4.56}$$

where ϕ is the binding energy and $(1/2)m\mathrm{v}^2$ is the kinetic energy of the photoelectron. The binding energies are the characteristic energies of the electrons in an atom and are therefore atom specific. When UV photons are used, the energies are sufficient to liberate electrons only from valence levels. But X-ray photons such as Al-Kα or Mg-Kα, which have energies of 1487 eV and 1254 eV respectively, used in XPS are capable of ionizing electrons from the core levels of atoms. The study of PES, therefore, consists of determining the kinetic energy of the ejected electrons, which through equation (4.56) determine the binding energy of the electrons for a fixed energy of irradiating photon. Thus in an atom, where electrons are present in various levels with different binding energies, PES consists of a series of peaks corresponding to the binding energies of various electrons. The electron binding energies decrease in the order 1*s*, 2*s*, 2*p*, 3*s*, 3*p*, 4*s*, 3*d*, 4*p* etc. levels. Further, due to Russell-Saunders coupling 2*p*, 3*p*, 3*d* etc. levels are split as $2p^{1/2}$, $2p^{3/2}$, $3p^{1/2}$, $3p^{3/2}$, $3d^{3/2}$, $3d^{5/2}$ etc. A few factors complicate the situation and render the equation (4.56) above, approximate. First is the assumption that the energy levels in the atom are frozen and therefore the ionisation process does not affect other energy states. But in practice, there is always a relaxation associated with photoionization, which therefore reduces the kinetic energy of the ionised electron. The second factor is that the released photoelectron has to cross a surface barrier, ϕ_a, before reaching the detector, which again reduces the kinetic energy of the photoelectron. During irradiation of an insulator, the surface of the sample gets charged due to both PES and Auger processes (see later) and emission of low energy secondary electrons. This build up of the positive charge also decreases the kinetic energy of the photoelectrons. A simple method of removing this last effect is to flood the surface of the sample with low energy electrons using an electron flood gun. The relaxation energy is however a characteristic of the atom and is independent of the composition and chemical structure. The binding energy value is therefore readily corrected. In the standard practice, the

binding energy is determined using a calibrant along with the material under investigation and the photoelectron binding energies of the calibrant are known. C 1*s* binding energy (= 285 eV) (Swift, 1982; Hohiki and Oki, 1984) is used almost universally. Since most specimen exposed to atmosphere, contain carbonaceous surface contamination, there is generally a C 1s peak of the adventitious carbon, which always provides a fortuitous calibration. In glasses, sometimes it is advantageous to have an internal standard of an element, which is a component of glass itself. It is further considered advantageous to refer the binding energy to the Fermi level rather to the vacuum level.

A secondary effect occurs in most photo-emission experiments and is known as Auger emission. Auger electron spectra is also a valuable experimental technique. When a core electron, say, from 1s level of an element is ionized, the hole created in the K shell leaves the atom in an excited state. The deexcitation of the atom occurs by the jumping of an outer shell electron into the K-shell vacancy, which now emits a X-ray photon corresponding to the energy difference of the two levels involved. This newly emitted X-ray photon (necessarily of lower energy) ionizes yet another electron, usually in the outer levels. This is the *Auger electron.* The process may involve, for example, an L electron jumping into the K shell and the energy released ionising another L electron. It is schematically shown in Figure 4.19. Thus the Auger process involves 3 levels – core level corresponding to the first photoionization (K), the level

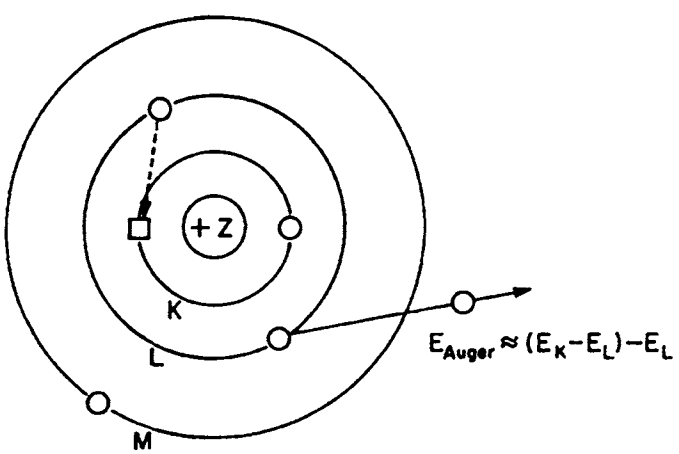

Figure 4.19: Orbital model of the electron transitions associated with de-excitation of a core-level vacancy by the Auger (KLL) emission process. The two L levels are the L_1 and L_2 in the text.

from which the electron jumped to fill the core level (L_1) and the level from which Auger electron was liberated (L_2). Since the levels involved are at fixed energies, the emitted electron has a characteristic kinetic energy. Therefore, the kinetic energy of Auger electron, designated as E_{KLL} is given by

$$E_{KLL} = E_K - E_{L1} - E_{L2} - \phi_a \tag{4.57}$$

where ϕ_a is the energy difference between vacuum and Fermi levels. These energies have been listed for various atoms. Auger emissions are particularly dominant for low Z atoms in the photo electron spectrum. In the literature, a quantity known as Auger parameter, is often measured. This is the difference in the kinetic energies of any chosen photoelectron and that of an Auger electron. These are generally constant for a given element and useful in the identification of that element in compositional analysis.

The most valuable application of XPS is in the determination of the chemical state of a given element through the measurement of the chemical shift. Chemical shift is the alteration of binding energy caused by the nature of the chemical environment and bonding characteristics of an element to its neighbours, Thus, for example, Si 2*p* binding energy varies by as much as 7 eV in its compounds as shown in Table 4.3. This variation in binding energy can also be very low (a fraction of an eV) as in the case of O 1*s* levels for the bridging and non-bridging varieties. Measurements of such differences require a very high resolution photoelectron spectrometer.

Table 4.3: Variation of Si 2*p* binding energy in different compounds (After Castle and West, 1980).

Sample	Formula	Si 2p BE (eV)
Silicon	Si	99.6
Silicon carbide	SiC	103.9
Silicon nitride	Si_3N_4	102.0
Silicon dioxide	SiO_2	102.6
Zinc silicate	$ZnSiO_3$	108.1
Silica gel	$SiO_2.xH_2O$	107.0

Both PES and Auger spectroscopies are considered as surface techniques. It is because the ejected photo electron has to escape from the surface with its true kinetic energy in order that the measurement is accurate. Electron should not suffer any inelastic scattering before its escape. Therefore, there is a characteristic depth parameter or the permissible escape depth, λ, which is also known as inelastic mean free path. It is the depth from below which the liberated electron has less than 63 % chance of escape without experiencing an inelastic scattering event. About 95 % of the detected signal in XPS originates from sampling depths of about 3λ. λ is of course a function of electron kinetic energy and in the range of 100 – 1000 eV. λ is of the order of 5 – 50 Å in oxides but it is much less for metals.

XPS has been used very successfully for the investigation of modification in oxide glasses. A typical example is shown in Figure 4.20.

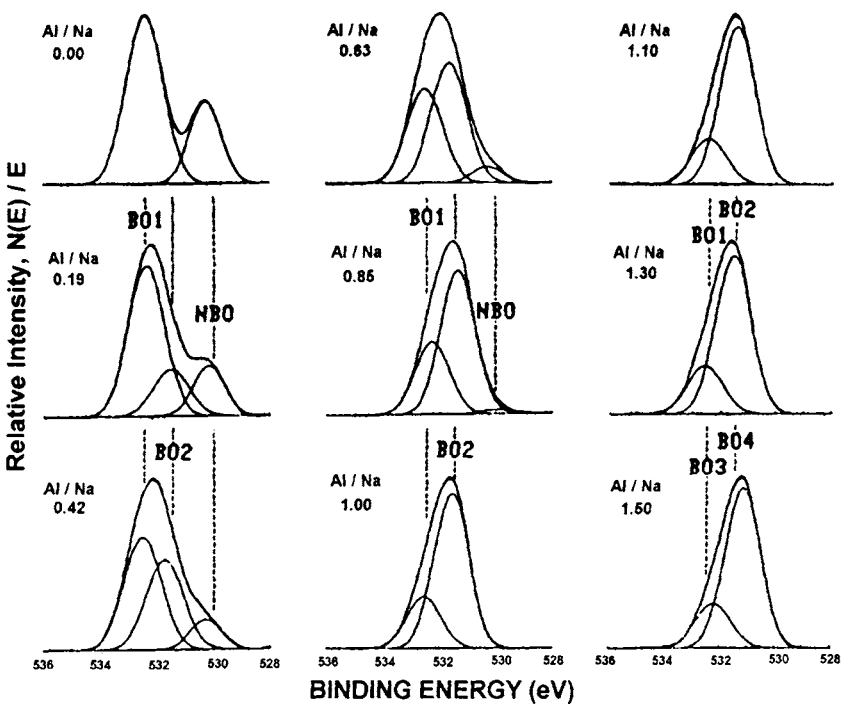

Figure 4.20: High-resolution O 1s spectra of sodium-aluminosilicate glasses with various Al/Na concentration ratios; each spectra was deconvoluted assuming three Gaussian components of constant width but varying binding energy (After Tusker et al., 1985).

The most important observation in the spectra of Figure 4.20 is the reduction of NBO when Al/Na ratio increases systematically.

In principle all of the techniques used for the investigation of crystalline solids are equally useful in the investigation of glasses. Several such characterization techniques are described briefly in other chapters where they are of immediate relevance. The effort in this chapter has been to put together the most important structural techniques used in glass science.

References:

Andrew, E.R., A. Bradbury and R.G. Eades, 1959, Nature, **183**, 1802.

Balkanski, M., 1971, Light scattering in Solids (Flammarion Sciences, Paris).

Bendow, B., 1993, in Experimental Techniques in Glass Science, eds. C.J. Simmons and O.H. El-Bayoumi (The American Ceramic Society, Ohio) p. 33.

Bursukova, M.A., E.A. Kashchieva and Y.B. Dimitriev, 1995, J. Non-Cryst. Sol., **192&193**, 40.

Castle, J.E., and R.H. West, 1980, J. Elect. Spec., **18**, 355.

Ching, W.Y., Y.P. Li, B.W. Veal and D.J. Lam, 1985, Phys. Rev. B., **32**, 1203.

Cummins, H. in Light scattering in Solids ed. M. Balkanski, 1971, (Flammarion Sciences, Paris) p. 3.

Elliott, S.R., 1978, Philos. Mag. B., **37**, 435.

Elliott, S.R., 1984, Physics of Amorphous Materials (Longman, London).

Emerson, J.F., and P.J. Bray, 1993, in Experimental Techniques in Glass Science, eds. C.J. Simmons and O.H. El-Bayoumi (The American Ceramic Society, Ohio) p. 77.

Fadini, A., and F.M. Schneppel, 1989, Vibrational Spectroscopy Methods and

Applications (Ellis Horwood Ltd., Chichester).

Farrar, T.C., and E.D. Becker, 1971, Pulse and Fourier Transform NMR: Introduction to Theory and Methods (Academic Press, New York).

Fischer, B., R.A. Pollak, T.H. DiStefano and W.D. Grobman, 1977, Phys. Rev. B., **15**, 3193.

Fukishima, E., and S.B.W. Roeder, 1981, Experimental Pulsed NMR, A Nuts and Bolts Approach (Addison-Wesley, Reading, Massachusettes).

Fyfe, C.A., 1983, Solid State NMR for Chemists (C.N.S. Press, Guelph).

Gurmann, S. and R.F. Pettifier, 1979, Philos. Mag. B., **40** 345.

Hahn, E.L., 1950, Phys. Rev. Lett., **80**, 580.

Hendrickson, J.R., and P.J. Bray, 1973, J. Mag. Reson., **9**, 341.

Hohiki, S., and K. Oki, 1984, J. Electron Spectrosc. Relat. Phenom., **33**, 375.

Lamparter, P., W. Sperl, E. Nold, G. Rainer-Harbach and S. Steeb, 1982, Proc. 4th Int. Conf. On Rapidly Quenched Metals, eds. Masumoto and J. Suzuki, (Jpn. Inst. Of Metals), p. 343.

Leadbetter, A.J., 1973, in Chemical Applications of Thermal Neutron Scattering, ed. B.T.M. Wills (OUP) p. 146.

Lerner, J.M., and F. Adar, 1989, Laser Focus World, **25**, 73.

Lewis, M.H., 1989, Glasses and Glass Ceramics (Chapman and Hall, New York).

Long, D.A., 1977, Raman Spectroscopy (McGraw-Hill, New York).

Lorch, E., 1969, J. Phys. C., **2**, 229.

Loudon, R., 1964, Adv. Phys., **13**, 423.

Lowe, I.J., 1959, Phys. Rev. Lett., **2**, 285.

Mehring, M., 1978, High Resolution NMR Spectroscopy in Solids (Springer-Verlag, Heisenberg).

Mitra, S.S., 1969, Opical Properties of Solids (Plenum Press, New York) p. 333.

Nagel, S.R., J. Tauc and B.G. Bagley, 1976, Solid State Comm., **20**, 245.

Prabakar, S., K.J. Rao and C.N.R. Rao, 1990, Proc. Royal Soc. (London), **A429**, 1.

Price, D.L., and J.M. Carpenter, 1987, J. Non-Cryst. Sol., **92**, 153.

Rao, C.N.R., 1963, Chemical Applications of Infrared Spectroscopy (Academic Press, New York).

Rao, K.J., J. Wong and M.J. Weber, 1983, J. Chem. Phys., **78**, 6228.

Sathyanarayana, D.N., 1996, Vibrational Spectroscopy: Theory and Applications (New Age Int. Publishers, New Delhi).

Sayers, D.E., E.A. Stern and F.W Lytle, 1971, Phys. Rev. Lett., **27**, 1204.

Shuker, R., and R. Gammon, 1971, Light scattering in Solids (Flammarion Sciences, Paris) p. 334.

Sinclair, R.N., 1985, J. Non-Cryst. Sol., **76**, 61.

Stephenson, D.A., and N.J. Binkowski, 1976, J. Non-Cryst. Sol., **22**, 399.

Swift, P., 1982, Surf. Interface Anal., **4**, 47.

Tusker, G.W., D.R. Uhlmann, P.I.K. Onorato, M.N. Alexander and C.W. Struck, 1985, J. de Physique, **C8**, C8-273.

Van Vleck, J.H., 1948, Phys. Rev., **74**, 1168.

Wagner, C.N.J., 1978, J. Non-Cryst. Sol., **31**, 1.

Warren, B.E., 1969, X-ray Diffraction (Addison-Wesley).

Waugh, J.S., L.M. Huber and U. Haeberlen, 1968, Phys. Rev. Lett., **20**, 180.

Wong, J., and C.A. Angell, 1976, Glass Structure and Spectroscopy (Marcel Dekker, Inc., New York).

Wright, A.C., 1993, in Experimental Techniques in Glass Science, eds. C.J. Simmons and O.H. El-Bayoumi (The American Ceramic Society, Ohio) p. 205.

Wright, A.C., 1974, Adv. Struct. Res. Diffr. Meth., **5**, 1.

Wright, A.C., and A.J. Leadbetter, 1976, Phys. Chem. Glasses, **17**, 122.

Wright, A.C., 1980, J. Non-Cryst. Sol., **40**, 325.

Zarzycki, J., 1982, Les Verres et L'état Vitreaux (Masson, Paris).

We used to have lots of questions to which there were no answers. Now with the computer, there are lots of answers to which we haven't thought up the questions.
- Peter Ustinov.

CHAPTER 5

THEORETICAL STUDIES

We discussed in Chapter 2 models like rcp suitable for description of amorphous solids. Such models are known as stochastic models. The well-known rcp model was built by random close packing of spheres and the continuous random network (crn) model was built by using balls and sticks (subject to justified variation of bond lengths and bond angles). These prototypes, rcp and crn models, gave enormous insight into the structure of glasses. It was mentioned briefly that the random assemblies are subjected to relaxation using appropriate interaction potentials. This has been done after painstaking collection of particle coordinates, which are later handled on a computer. There are two other powerful approaches to modelling the structure of glasses known as Monte Carlo (MC) (Catlow et al., 1985; Gillan, 1985; Abraham, 1980; Soules, 1990) and Molecular Dynamics (MD) (Allen and Tildesley, 1987; Vashishta, 1986) simulations.

Monte Carlo and Reverse Monte Carlo methods

In the MC simulation of a glass, one starts with a random assembly of a fairly large number of constituent particles of a glass – determined by the chemical composition. The positions can be chosen randomly to be filled into a volume fixed on the basis of known experimental density the glass. The number of particles is generally chosen on the basis of the available computational time. Several good simulations have been performed with just about 150 particles. These particles are made to interact according to an assumed potential. Lennard-Jones potentials have been particularly popular in glass simulation studies because of their short-range nature. Such an ensemble therefore has an initial energy, say, E_0. One could even evaluate the radial distribution function (RDF) of the ensemble. MC method consists of now moving randomly an atom in the ensemble in a random direction. The move may or may not be the one, which changes the energy of the system towards greater stability (lowering of energy). If the move decreases the energy, it is accepted and the new coordinates are registered in the place of the old. If the move increases the

energy, it is either rejected or it is accepted with a certain weightage. This is because such energy increasing moves are required to allow for thermal fluctuations. The weightage is the Boltzmann factor $\exp(-\Delta E/kT)$ where ΔE is the increase in energy caused by the move. The move is accepted only if $\exp(-\Delta E/kT)$ is greater than a random number between 0 and 1. By this method the system moves towards lower energy in successive steps. It may not get stuck in a local energy minimum because the allowed higher energy explorations will enable the system to eventually access lower minima. The technique therefore allows the system to evolve towards a free energy minimum. One has a choice of increasing the temperature so that in the $\exp(-\Delta E/kT)$, the probability of allowing the move increases which may increase the rate at which the energy minimum is reached by the MC system. By its very nature, MC method has an attraction because rules can be so built into the program that a given property of the system can be optimised. Once the positions of the particles are thus determined, statistical methods can be used to determine all the thermodynamic properties. Reduction of temperature and volume can be used effectively to simulate quenching and to obtain a glass from its melt. Isopentane glass was studied by Yashonath et al. (1985) using Monte Carlo method. It was shown that annealing of glasses lead to lower energies of the system. Brawer and Weber (1980) simulated $BeF_2:Eu^{3+}$ glass structures successfully to obtain important quantities like fluorine coordination of Eu (Figure 5.01).

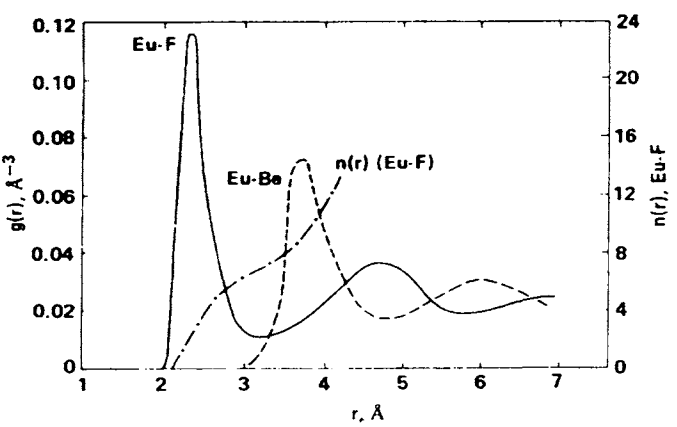

Figure 5.01: Calculated Eu-F and Eu-Be radial distribution functions (After Brawer and Weber, 1980).

In the Reverse Monte Carlo (RMC) method, the allowdness of MC

simulation is determined differently. The move is allowed if the move brings about a closer agreement of the calculated RDF with the experimental RDF. RMC, therefore, does not require the use of any interatomic potentials. The procedure to execute RMC simulation consists of 4 steps: (1) Fixing the box size such that when filled with the required number of atoms it represent the number density of the bulk material. (2) Giving random displacements for the atoms and at each stage calculating either the RDF or the structure factor, $S(Q)$. The move may be allowed or disallowed at this stage itself depending on whether the atoms overlap with the neighbouring atoms, what constitutes overlap is being initially defined through an excluded volume around each atom. (3) The resulting pair correlation function $G(r)$ or structure factor $S(Q)$ is compared with the same quantity in the previous step. The improvement is determined by the smallness of χ^2, where

$$\chi^2 = \frac{\sum_i \left[S_{\exp t}(Q_i) - S_{\mathrm{mod}}(Q_i)\right]^2}{\sigma_i^2} \qquad (5.01)$$

The subscript "expt" denotes experimental and "mod" denotes model. $\sigma = (n - 1)$ is the number of points used for computing χ^2. The move is allowed only if χ^2 decreases, otherwise it is accepted with a probability, $P = \exp(-\Delta\chi^2/2)$. (4) The process is repeated till an acceptable value of minimum $\Delta\chi^2$ is obtained. Another criterion used to stop configuration is based on the rejection rates of steps employed. For example, if only one step is allowed in every 1000 steps, it is indicative of the best structure having been arrived at. In RMC the choice of the box length is also important. It should be at least twice the value of r, for which the undulations in the pair correlation function essentially becomes zero. In their RMC work on amorphous Ge, Walters and Newport (1996) imposed the condition that no three Ge atoms touch each other because this would produce the high energy small sized rings. This approach is typical of RMC simulations, where restrictions based on the knowledge already available on such structures is imposed. The RMC simulation of amorphous Ge is shown in Figure 5.02 where excellent agreement of the experimental data has been achieved. RMC is thus very similar to Reitveld procedure used in crystallography for refining structures using X-ray diffraction.

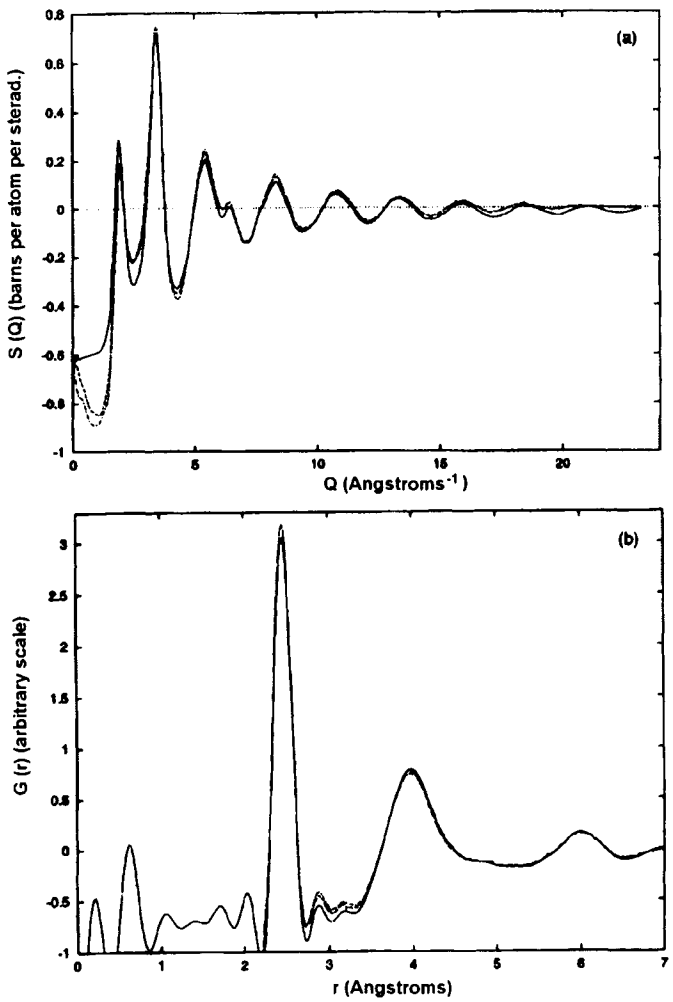

Figure 5.02: (a) RMC-generated fits to the experimental structure factor of amorphous Ge; (b) RMC-generated fits to the experimental pair correlation functions: experimental data (_____). (.....) and (_._._) are from the model (After, Walters and Newport, 1996)

MD simulation

MC simulation is good for calculating energies of the metastable equilibrium configuration in glass. But in order to obtain dynamical information it is better to employ Molecular Dynamics (MD) simulation. In MD simulations the emphasis is on the motion of the particles.

Classical equations of motion of particles are solved and evolution of the system with time is examined. The procedure therefore provides the complete history of each particle and enables extracting the dynamical information. A chosen number of particles are assembled in a box which is generally of cubical shape (in phase transition studies use is made of parallelopipeds). The number of particles should be preferably a few hundreds because of the problem of termination errors particularly when coulombic potentials are used. Initially the positions and momenta (velocities) of the particles in the box are assigned randomly. The velocities are generally chosen to represent a Maxwellian distribution. The total kinetic energy of the particles is fixed by the temperature through the relation

$$\frac{3}{2}NkT = \sum_{i=1}^{N} \frac{1}{2} m_i v_i^2 \qquad (5.02)$$

where N is the number of particles, m_i and v_i are their masses and the velocities. The MD simulation consists in solving Newtonian equations of motion. The procedure adopted is to move randomly the atoms for a short period, generally of the order of one femto second (10^{-15} s). The particle experiences a net force due to the potential acting on it which is given by $F = -\nabla\phi$, where ϕ is the net potential. Therefore in the given time and under the influence of the field, the given particle moves a certain distance, which is computed and registered. The operation is repeated in turn for all the particles chosen at random. Evidently the particles which are present in high energy states tend to move in very few time steps (in less than a 1000 time steps, or in about a pico second) towards equilibrium positions so that the total energy of the system rapidly moves towards some equilibrium value for that temperature. This energy consists of both potential and kinetic contributions. It can be easily seen that the procedure is highly time intensive in computation. There are several algorithms developed for the purpose of making MD simulations effective and computationally economical. Two of the most widely used are the Verlet algorithm (Haile, 1991; Verlet, 1967; Beeman, 1976; Swope et al., 1982 and Berendsen and van Gunsteren, 1986) and the Gear predictor-correlator (PC) algorithm (Haile, 1991; Rahman, 1964 and Gear, 1971). Verlet algorithm is faster although PC method is more accurate. The basis of Verlet algorithm is that the displacement of the particles in the small time step, Δt, can be expressed through a Taylor's expansion.

$$x(t+\Delta t) = 2x(t) - x(t-\Delta t) + (d^2x(t)/dt^2)(\Delta t)^2 + O[(\Delta t)^4] \tag{5.03}$$

Therefore if the positions are calculated up to the third term in the above expression, the error due to truncation of the series is only of the order of $(\Delta t)^4$. The velocity is calculated as

$$\mathrm{v}(t) = [x(t+\Delta t) - x(t-\Delta t)]/(2\Delta t) \tag{5.04}$$

This algorithm therefore requires storage of three vectors (more simply, quantities) per particle. In the PC method higher order derivatives are used to calculate the Taylor's series approximation and the particle positions and velocities are corrected using a corrector expression for the particular predictor.

$$\mathrm{v}_i'(t+\Delta t) = \mathrm{v}_i(t) + \frac{1}{2}[a_i(t) + a_i(t+\Delta t)]\Delta t \tag{5.05}$$

and corrected positions are given by,

$$\mathrm{r}_i(t+\Delta t) = \mathrm{r}_i(t) + \frac{1}{2}[\mathrm{v}_i(t) + \mathrm{v}_i'(t+\Delta t)]\Delta t \tag{5.06}$$

The method is more accurate but due to the use of higher order derivatives the method needs at least six vectors to be stored per particle.

In the simulations of glass forming systems, two potentials very widely used are the Lennard-Jones (LJ) (1924) and the Born-Mayer-Huggins (BMH) (Busing, 1972). LJ potentials are of short range and generally smaller ensembles are sufficient for simulations. In such cases, PC is chosen because of computational feasibility. Systems which are simulated using BMH potentials which are of long range generally have to be of larger size and a preference for the use of Verlet algorithm is evident in published literature.

For both algorithms it requires to evaluate the second derivative of the particle position, which is the acceleration term. This, as pointed out earlier, requires the evaluation of the net force acting on the particle. In principle all particles exert forces on all other particles in a glass, this is an infinite sum. But the magnitude of the interaction falls off fairly rapidly with BMH potential. Even then it becomes negligible only beyond a certain distance, which may extend in some cases up to about 10 Å. It only

means that the computation of the interactions of particles present up to 10 Å radius may have to be performed explicitly and the terms in the summation of the interaction can be truncated at that distance. Even these distances are very large and therefore several force truncation procedures have been developed which render the force function zero at some reasonable separation. For the Coulombic interaction use of the Ewald's procedure (Ewald, 1921) has been well known. It is based on a use of a cubic crystalline lattice and its success is because it can be shown that the sum of forces arising from an array of alternating charges in a cubic ionic lattice is effectively only of short range. Woodcock and Singer (1971) suggested a truncation term which is of the form,

$$T_E = erfc\left(\frac{r}{\beta}\right) \tag{5.07}$$

where β is an empirically adjusted parameter. Thus the truncation function limits the number of interacting pairs for the given atom and reduces the computational time. The particle has to execute several time steps before the nature of its surrounding changes significantly. Therefore it is possible to maintain a list of neighbours of a given particle and such a list needs updating only after every 10 or 20 time steps. However MD simulations have been performed where the forces are calculated without the use of truncation terms in the force function. Typical BMH potential function modified with Ewald truncation is given by,

$$U_{ij}(r) = \frac{z_i z_j e^2}{r_{ij}} erfc\left(\frac{r_{ij}}{\beta_{ij}}\right) + A_{ij} \exp\left(-\frac{r_{ij}}{\rho}\right) \tag{5.08}$$

where ρ is the hardness parameter whose value varies between 0.29 Å for oxides and 0.345 Å for halides.

In simulating partially covalently bonded structures purely ionic potential is found to be inadequate to account for the experimentally observed bond angle distribution. A method of overcoming this in MD simulations is by introducing what are known as three-body interaction or three body potential terms. There are several such potentials described in the literature such as those suggested by Keating (1966) or Stillinger and Weber (1985) or by Vashishta et al. (1990) which have been used successfully to simulate partially covalent structures. Usually they involve an angle θ_{ij}, which can have a restricted range of values or constants.

Another aspect of potential functions used in MD simulations which needs careful attention is the magnitude of electrical charges on the ions. It has been found that the use of formal charges is incorrect since the charge on a given atom in many crystalline material is known to be less than their formal charge. This was noted long ago by Pauling (1960). Therefore, charges lower than their formal values, and adjusted so as to maintain electrical neutrality are employed. Their magnitudes are fixed on the basis of their consistency with the dielectric and optical property calculations. Thus Tsuneyuki et al., (1988, 1989 and 1990) developed a potential suitable for MD simulation of silicates. One of the important problems in simulating silica structure is to be able to obtain correct Si-O-Si bond angle distribution. Experimentally it is found that the distribution of Si-O-Si angles peak at 144°. Earlier simulation efforts (even with the use of three-body interactions) had not been successful in reproducing this feature. But with the use of adjusted charges obtained from dielectric and optical properties of the material, it was found possible to reproduce the experimental Si-O-Si angle distribution.

The advantage of MD simulation is that the motion of individual particles can be tracked and so also their immediate environment. From the mean square displacements, MSD, the diffusion coefficient, D, can be calculated directly (using Einstein relation) knowing the time involved in the displacement. From the diffusion coefficients, conductivities can be calculated using Nerst-Einstein relation. Therefore,

$$MSD = \frac{1}{n}\sum_{i=1}^{n}\left[x_i(t) - x_i(0)\right]^2 + \left[y_i(t) - y_i(0)\right]^2 + \left[z_i(t) - z_i(0)\right]^2 \qquad (5.09)$$

where n is the number of particles.

Then the diffusion coefficient, D, is given by

$$D = \frac{MSD}{6t} \qquad (5.10)$$

and conductivity is given by,

$$\sigma = \frac{ne^2 D}{kT} \qquad (5.11)$$

The *MSD*s are obtained by considering both ensemble and time averages. Particle coordinates having been known, the pair correlation functions are readily obtained. These pair correlation functions can be combined with the atomic scattering factors for the respective atoms and then convoluted to obtain a combined pair distribution function, which can be compared with experimental RDF. This is a vital step in the glass structure simulations.

The function described by,

$$\gamma(t) = \frac{\langle \sum_i \mathrm{v}_i(t_0).\mathrm{v}_i(t_0 + \Delta t) \rangle}{\langle \sum_i \mathrm{v}_i(t_0).\mathrm{v}_i(t_0) \rangle} \tag{5.12}$$

(where v represents the velocity of the particle) calculated over the ensemble gives the velocity autocorrelation function ($\gamma(t)$). The Fourier transform of the velocity autocorrelation function gives the density of the phonon states, which describes the vibrational spectrum of the material. In fact the infrared spectrum can be obtained using a similar autocorrelation function of the dipole moment.

Simulations can be used to evaluate several other rather informative correlation functions such as van Hove correlation function given below,

$$G(\vec{r}, t) = \frac{1}{N} \langle \sum_i^N \sum_j^N \delta[\vec{r} + \vec{r}_i(0) - \vec{r}_i(t)] \rangle \tag{5.13}$$

These space-time functions are useful in following relative movements of different particles in the system.

In the actual simulation of a glass, one generally starts the simulation and computation of properties at a very high temperatures around 3000 or 4000 K. At this temperature the energies rapidly attain equilibrium values in under about 10,000 time steps. The actual data required for the computation of various structural and dynamical properties are collected after equilibration, usually in another thirty to fifty thousands steps. The system is then quenched to a lower temperature initially in large steps and the same procedures are followed to collect data at lower temperatures. From ~1000 K and below, the temperature steps are reduced depending on the nature of quantities to be computed. The glass transition itself in indicated by the variation of the several properties such

as variation of the slope of energies or by the change of slope of what is known as Wendt-Abraham ratio (Wendt and Abraham, 1978), which is the ratio of the heights of the first peak minimum to the first peak maximum in the structure factor (structure factor, $S(Q)$ is calculated from $G(r)$ (see chapter 4) and $G(r)$ is directly computed in MD simulation).

It should be noted that the glasses obtained in MD simulation are products of quenching at very high rates because even using a time step of a pico second, and a temperature step of 10°, it amounts to a quenching rate of 10^{11} K per second. Thus it appears that MD glasses are thoroughly out of range for comparison with the laboratory glasses which are quenched at a far lower rates of about 100 K per second. It was pointed out by Simmons et al. (1993) that "the structure simulated (by MD) can only resemble that of real glasses if the viscoelastic process scales in time about 13 orders of magnitude (relaxation time of 10 ps for the MD glass and 100 second for the real glass). The interesting aspect of glass science that one uncovers when considering this question is that the viscoelastic behaviour of some glasses (SiO_2, GeO_2) does scale over 10 to 14 orders of magnitude." MD simulations have been used successfully in simulating the structure and dynamics of a variety of glass forming systems. It is of course impressive to note from the examples cited below that MD simulations indeed give rise to excellent agreement with the experimental results despite the extraordinarily different cooling rates. Evidently the simulated glasses have a high fictive temperature and unlikely to yield reasonable values of T_g. Woodcock et al. (1976) studied silicate glasses to determine equilibrium structures and various properties. Balasubramanian and Rao (1993) examined the origin of mixed alkali effect using MD simulation employing Tsuneyuki potentials. They analysed the self and distinct part of the van Hove correlation functions computed for a system consisting of 960 particles of which the total alkali oxide particles were 10 %. They were able to show as pointed out elsewhere in the book that alkali ions jump preferentially to the sites vacated by the same type of alkali ions and not of the other kind which in essence defines individual pathways for the migration of alkali ions. Karthikeyan and Rao (1997) used MD simulation of $AgI\text{-}Ag_2MoO_4$ glasses using only two body potentials and adjusted charges and ascertained that Ag^+ ion motion in FIC is not confined to moving in I^- environment only. Recently, Karthikeyan et al. (1999) simulated phosphate glasses which reproduced the experimental NBO and BO populations and have observed extremely fast bond switching involving NBO-BO conversions which is governed by very low activation barriers. These aspects are discussed later in the book.

MD has been used very effectively to elucidate vibrational spectra. Garofalini (1982) reported vibrational modes at 400, 800 and 1100 cm^{-1} in vitreous SiO_2 compared to 450, 800 and 1050 cm^{-1} observed in Raman and 465, 800 and 1100 cm^{-1} observed in IR and 350, 800 and 1080 cm^{-1} observed in inelastic neutron scattering. Experimental observation such as non-Newtonian behaviour of glass forming melts (Simmons et al., 1982), brittle fracture of SiO_2 (Ochoa et al., 1991) are only some of the other successful simulations using this powerful technique.

Unphysical quenching rate is not the only limitation of MD. Since the potential used enable computations of only central forces, it is suitable for simulations of glasses, which are significantly ionic. It is also successful for the simulations of metallic glasses where use is made of optimised pseudo potentials obtained from first-principle calculations. But in largely covalent materials, MD cannot be of much use unless suitable effective potential functions are developed which take care of non-central nature of the forces as well. In the next section we discuss further advances in MD simulations based on the use of quantum mechanical calculations, which optimise the local geometries and therefore provide more accurate simulations of structure.

Generally, MD is performed to simulate a continuous phase trajectory in the microcanonical (N,E,V) ensemble, while in MC method, individual phase points of an (N,V,T) ensemble are simulated. As far as the equilibrium properties are concerned, the "trajectory average" of MD and the configurational average of MC are equivalent (Allen and Tildesley, 1987). Recently, MD simulation of other types of ensembles also have been achieved. In the (N,E,V) simulations, volume and total energy are held constant and the temperature and pressure are allowed to fluctuate. Andersen (1980) suggested methods for simulation of isobaric-isoenthalpic (N,P,H) and isobaric-isothermal (N,P,T) ensembles. A constant pressure bath can be simulated by considering volume as a dynamic variable and setting up equations of motions for volume coordinates. The "mass" associated with this additional degree of freedom affects the dynamical properties, but not the equilibrium properties. By subjecting the particles to stochastic collisions and by controlling the collision frequency, a constant temperature bath can be simulated. But this scheme has the drawback that when the collision probability exceeds a certain value, the diffusion coefficient decreases rapidly. An alternate scheme has been proposed by introducing an additional degree of freedom (just like in the case of pressure) and allowing the total energy to fluctuate. By this purely dynamical method, (N,V,T) ensemble calculations have

been extended to complex molecular systems (Nose, 1984; Nose and Klein, 1983).

Quantum chemical calculations

Calculations of approximate energy band structure are possible on the basis of the assumption that the energy bands are mostly determined by the short-range order. This aspect will be discussed in Chapter 8. The absence of periodicity on the one hand and presence of extensive polymeric structure in most important glasses on the other, are factors which severely restrict the use of quantum mechanical calculations. Most quantum mechanical calculations are restricted to investigations of small clusters because of the prohibitive increase of the computational cost with size.

The basis of the use of quantum mechanics is that we can construct a total molecular wave function using which a time independent non-relativistic Schrödinger equation of the form,

$$H\,\Psi = E\,\Psi \tag{5.14}$$

can be solved. In equation (5.14), E represents the total energy of the cluster and ψ is the molecular wave function. The Hamiltonian of the system consists of the kinetic energies of all the nuclei and the electrons and the potential energies due to interelectronic, internuclei and electron-nuclei interactions. The Born-Openheimer adiabatic approximation is used in order to separate the nuclear and electronic coordinates and related variables because the masses of nuclei being about 10^5 times higher than the electron rest mass, the relative motion of nuclei are negligible. Therefore the solution to the Schrodinger equation is obtained with electron wave functions only and the nuclear kinetic energy term is added to the resulting solution. The nuclear coordinates are fixed using an iterative technique in which the nuclear coordinates are chosen eventually as those, which minimize the total energy of the cluster.

Electron coordinates themselves cannot be separated and therefore the solution to the Hamiltonian is through the application of several approximate methods. The important methods of such approximate calculations are the Hartree Fock (HF) calculation, the modified HF calculation and the HF along with configurational interaction (CI) calculations. These are generally referred to as *ab initio* calculations. Briefly, the HF calculation (Zhidomirov and Kazannsky, 1986) is based on

a self-consistent field approximation. In the stable electronic configuration of a cluster under consideration, every electron moves in the potential field of all other electrons. Neglecting the correlation effect and considering each electron as a quasi independent particle, enables writing the total electronic wave function as antisymmetrized product wave functions of one electron molecular orbitals, described by Slater determinants,

$$\Psi = (-1)^n \, [\Phi_1(1)\Phi_2(2)\Phi_3(3).....\Phi_n(n)] \qquad (5.15)$$

In equation (5.15), $\Phi_i(j)$ is the i^{th} spin orbital of the j^{th} electron. These individual orbitals are then expanded using a basis set $\{X_k\}$ which is centred on the k^{th} nucleus. The total energy is then minimized using variational principle. $\Phi_i(j)$, which are one electron molecular orbitals, are themselves obtained by minimizing the total electronic energy using variational principle. The molecular orbitals are spread over the entire molecule and are delocalised. This results in an energy spectrum consistent with observed spectroscopic properties.

In the HF method with configuration interaction (HF + CI), instead of the one electron molecular orbitals, a linear combination of antisymmetrized product molecular orbitals are made use of. Evidently this procedure is highly restrictive because of the magnitude of the computational problems. Generally, clusters consisting of more than 10 electrons are not handled with (HF + CI) methods (Zhidomirov and Kazansky, 1989). The common practice is to use linear combination of atomic orbitals (LCAO) for obtaining MOs and Slater type orbitals (STO) as basis sets. Standard soft wave packages are available for making calculations. Descriptions like STO–3G or STO–3G* indicate that MOs have been generated using STOs which are approximated using 3 Gaussian functions (in STO-3G) or have also added 3*d* orbitals in the STO–3G basis (in STO–3G*).

In the context of glasses such as silicates, neutral clusters are generated by saturating the dangling bonds by addition of hydrogen or sometimes fluorine. Thus HF calculations have been performed on $H_6Si_2O_7$ molecule (Lasaga and Gibbs, 1987) using STO–3G* basis set (3*d* orbitals of Si included). The calculation revealed that the energy minimum does correspond to an Si-O-Si angle of 144°. Also it was found that variation of the Si-O-Si angle from 130 to 155 ° costs only 1 kcal/mol of energy. These are important results supporting experimental observations and inferences from other stochastic models. HF calculations have recently been reported by Uchino and Yoko (1998) on a large cluster

of $H_6B_9O_{18}Na_3$. These authors have not only optimised the geometry of the borate structure but have also rationalized the infra red spectra of the Na^+ vibrations by suggesting that Na^+ ions execute vibrations in perpendicular directions and give rise to a composite peak in the spectra.

Quantum mechanical calculations in glasses have been done using a number of semi-emperical methods. One of the successes of these methods has been to reduce the matrix size involved in the calculations. Therefore the methods focus on approximations, which could be made regarding the size of the wave function matrix. The differential overlap between the electronic wave functions of the basis set, which is represented by all the off diagonal terms in the overlap matrix, is neglected to various degrees in these methods. In CNDO, MNDO etc. methods, either there is complete neglect (CN) or modified neglect (MN) of the differential orbitals. In the INDO (Pople and Beveridge, 1970; Bacon and Zerner, 1979) and the MINDO methods, I stands for 'intermediate' neglect of the differential orbitals. All these methods are generally parametrised to give the best results with respect to certain physical properties like charge distribution, dipole moment, polarizability, electronic energy states etc.

A widely used modification of the HF calculation is the local density approximation (LDA) also known as density functional (DF) method. The approach made in LDA is that the electronic energy should depend on the electronic density, because the bonding electrons move in a potential, which is dictated by the local electron density. From this point of view electron exchange term in the calculation is substituted by an approximate function of electron density (Kohn and Sham, 1965). Further the role of core electrons is subsumed in an effective pseudo potential (a core potential). This step reduces the magnitude of calculation enormously so that calculation, involving elements even beyond the second row of the periodic table can also be handled. This enables quantum chemical calculations to be extended to address problems of practical glasses. Quantum chemical calculations have been used in the investigations of several amorphous materials such as silicon and germanium (Joannopoulos, 1985; Bar-Yam et al., 1988).

In the context of MD simulation, an important advance has been made by combining classical MD with density functional approach by Carr and Parrinello (1985). While the MD as a whole would be looking for the minimization of the ensemble energy, DF part ensures minimization of the energies of configurations or the structural units. This enables obtaining a better description of the structure. Excellent overview articles

are available on this subject (see Simmons et al., 1993 and references therein).

References:

Abraham, F.F., 1980, J. Chem. Phys., **72**, 359.

Allen, M.P., and D.J. Tildesley, 1987, Computer Simulation of Liquids (Clarendon, Oxford).

Andersen, H.C., 1980, J. Chem. Phys., **72**, 2384.

Bacon, A.D., and M.C. Zerner, 1979, Theoret. Chimica Acta, **53**, 21.

Balasubramanian, S., and K.J. Rao, 1993, J. Phys. Chem., **97**, 8835.

Bar-Yam, Y., S.T. Pantelides, J.D. Jonnopoulos, D.C. Allan and M.P. Teter, 1988, Mat. Res. Soc. Symp., **105**, 223.

Beeman, D., 1976, J. Comput. Phys., **20**, 130.

Berendsen, H.J.C., and W.F. van Gunsteren, 1986, in Practical Algorithms for Dynamic Simulations, eds. G. Civvotti and W.G. Hoover (North-Holland, Amsterdam).

Brawer, S.A., and M.J. Weber, 1980, Phys. Rev. Lett., **45**, 460.

Busing, W.R., 1972, J. Chem. Phys., **57**, 3008.

Carr, R., and M. Parrinello, 1985, Phys. Rev. Lett., **55**, 2471.

Catlow, C.R.A., C.M. Freeman and R.L. Royle, 1985, Physica B., **131**, 1.

Ewald, P.P., 1921, Ann. Phys. (Paris), **21**, 1087.

Garofalini, S.H., 1982, J. Chem. Phys., **76**, 3189.

Gear, C.W., 1971, Numerical Initial Value Problems in Ordinary Differential Equations (Prentice-Hall, Englewood Cliffs).

Gillan, M.J., 1985, Physica B., **131**, 157.

Haile, J. M., 1991, Molecular Dynamics Simulation (John Wiley, New york).

Joannopoulos, J.D., 1985, Physics of Disordered Solids (Plenum Press, New York).

Karthikeyan, A., and K.J.Rao, 1997, J. Phys. Chem. **101**, 3105.

Karthikeyan, A., P. Vinatier, A. Levassuer and K.J. Rao, 1999, J. Phys. Chem. B., **103**,6185.

Keating, P.N., 1966, Phys. Rev., **145**, 637.

Kohn, W., and L.J. Sham, 1965,Phys. Rev., **140**, A1133.

Lasaga, A.C., and G.V. Gibbs, 1987, Phys. Chem. Minerals, **14**, 107.

Lennard-Jones, J.E., 1924, Proc. Roy. Soc. (London), **106A**, 441; ibid, 463.

Nose, S., 1984, Mol. Phys., **52**, 255.

Nose, S., and M.L. Klein, 1983, Mol. Phys., **50**, 1055.

Ochoa, R., T.P. Swiler and J.H. Simmons, 1991, J. Non-Cryst. Sol., **128**, 57.

Pauling, L., 1960, Nature of the Chemical Bond (Cornell University Press, New York).

Pople, J., and D.L. Beveridge, 1970, Approximate Molecular Orbital Theory (McGraw-Hill, New York).

Rahman, A., 1964, Phys. Rev. A., **136**, 405.

Rao, C.N.R., and S. Yashonath, 1987, J. Solid State Chem., **68**, 193.

Robertson, J., 1983, Adv. Phys., **32,** 361.

Simmons, C.J., R. Ochoa and T.M. Neidt, 1993, in Experimental Techniques in Glass Science, eds. C.J. Simmons and O.H. El-Bayoumi (The American Ceramic Society, Ohio) p. 315.

Simmons, J.H., R.K. Mohr and C.J. Montrose, 1982, J. Appl. Phys., **53**, 4075.

Soules, T.F., 1990, J. Non-Cryst. Sol., **123**, 48.

Stillinger, F.H., and T.A. Weber, 1985, Phys. Rev. B., **31**, 5262.

Swope, W.C., H.C. Andersen, P.H. Berens and K.R. Wilson, 1982, J. Chem. Phys., **76**, 637.

Tsuneyuki, S., M. Tsukada, H. Aoki and Y. Matsui, 1988, Phys. Rev. Lett., **61**, 869.

Tsuneyuki, S., Y. Matsui, H. Aoki and M. Tsukada, 1989, Nature, **339**, 209.

Tsuneyuki, S., H. Aoki, M. Tsukada and Y. Matsui, 1990, Phys. Rev. Lett., **64**, 776.

Uchino, T, and T. Yoko, 1998, Solid State Ionics, **105**, 91.

Vashishta, P., 1986, Solid State Ionics, **18&19**, 3.

Vashishta, P., R.K. Kalia, J.P. Rino and I. Ebbsjo, 1990, Phys. Rev. B., **41**, 12197.

Verlet, L., 1967, Phys. Rev., **159**, 98.

Walters, J.K., and R.J. Newport, 1996, Phys. Rev. B, **53**, 2405.

Wendt, H.R., and F.F. Abraham, 1978, Phys. Rev. Lett., **41**, 1244.

Woodcock, L.V., C.A. Angell and P. Cheesman, 1976, J. Chem. Phys., **65**, 1565.

Woodcock, L.V., and K. Singer, 1971, Trans. Faraday Soc., **67**, 12.

Yashonath, S., K.J. Rao and C.N.R. Rao, 1985, Phys. Rev. B., **31**, 3196.

Zhidomirov, G.M., and V.B. Kazansky, 1986, in Advances in Catalysis, Vol. 34, eds. D.D. Eley, H. Pines and P.B. Weisz (Academic Press, New York).

That is the essence of science: ask an impertinent question
and you are on the way to a pertinent answer.
- Jacob Bronowski

CHAPTER 6

D.C. CONDUCTIVITY

Study of ionic conductivity in glasses is a very fascinating area of research (Angell, 1983, 1990, 1992; Ingram, 1987). While crystalline materials like stabilised zirconia, β–alumina and AgI were known to exhibit high ionic conductivities, it was long unknown that glasses can also exhibit similarly high conductivities. Glasses provide several advantages over crystalline materials, such as easy formability over wide ranges of composition, isotropicity, absence of grain boundaries, ease of fabrication into complex shapes etc., which make them particularly attractive in practical applications.

Ionic conductivity in solids has always been viewed as associated with jumping of an ion from one minimum energy position to another energetically similar position in the structure. In crystalline materials, such positions are easily identified and transport occurs through the participation of vacancies and Frenkel defects (Lidiard, 1957). In view of the absence of three-dimensional periodicity, there has been a great hesitation to extend the concept of point defects to interpret ionic conduction in glasses. Therefore understanding ion transport in glasses has been based on several new concepts and their discussion constitutes the subject of this chapter. Transport which occurs under the application of a unidirectional unit field is known as 'direct current' (d.c.) conductivity. D.c. conductivity and associated phenomena in glasses are discussed below.

The total conductivity, σ, of a glass sample is equal to the sum of the conductivities of all the charge carriers in the glass,

$$\sigma = \sum t_i \sigma_i \tag{6.01}$$

where t_i is the transport number and σ_i is the conductivity of the i^{th} charge carrying species. In the case of a glass where the conduction occurs predominantly due to a single ionic species ($t_i \approx 1$), the conductivity becomes

$$\sigma = \sigma_i = n \mid Ze \mid \mu \tag{6.02}$$

(hereafter simply written as $n(Ze)\mu$), where n is the concentration of the carrier, (Ze) is the charge and μ is the mobility. When an external field, E, is applied, there is a force which causes the ion to diffuse - move - in the glass and this force is given by ZeE. The induced motion causes a concentration gradient of the relevant ion which works as a force in the opposite direction. The force due to concentration gradient is given by $(kT/n)\cdot\nabla n$, where n and ∇n are respectively the concentration and the concentration gradient, T is the temperature and k is the Boltzmann constant. Application of the field therefore establishes a dynamic equilibrium where fluxes caused by the opposing forces are balanced. The flux balance condition can be written as

$$D\nabla n = n\mathrm{v}_d \tag{6.03}$$

where D is the diffusion coefficient and v_d is the drift velocity. Since $(kT/n)\cdot\nabla n = ZeE$, one can substitute $(n/\nabla n)$ by (kT/ZeE) in (6.03) and obtain an expression for D as

$$D = kT\left(\frac{\mathrm{v}_d}{ZeE}\right) = \left[\frac{kT}{(Ze)}\right]\mu \tag{6.04}$$

where we have used the relation $\mu = (\mathrm{v}_d/E)$. Further, using equation (6.02), σ can be related to D as,

$$D = \frac{\sigma\, kT}{n(Ze)^2} \tag{6.05}$$

which is the well-known Nernst-Einstein (NE) relation. For the case of an ionic conductor the relation between the diffusion coefficient, D, jump frequency, Γ, and the distance between the two sites λ, is obtained by resorting to random walk calculation (Tuller et al., 1980; Hughes and Isard, 1972) as

$$D = \frac{1}{6}\lambda^2\Gamma \tag{6.06}$$

Replacing D in equation (6.05) with the above expression and rearranging the terms, we get

$$\sigma = \left[\frac{n(Ze)^2 \lambda^2}{6kT}\right]\Gamma \tag{6.07}$$

The jump frequency, Γ, in a thermally activated process and is related to the cation vibrational frequency ν_0. If the free energy barrier for migration is $\Delta G_m = \Delta H_m - T\Delta S_m$, then Γ can be written as

$$\Gamma = \nu_0 \exp\left(\frac{\Delta S_m}{k}\right)\exp\left(-\frac{\Delta H_m}{kT}\right) \tag{6.08}$$

ΔS_m and ΔH_m are the entropy and enthalpy of migration respectively. Substituting equation (6.08) in equation (6.07) we can write

$$\sigma = \left[\frac{n(Ze)^2 \lambda^2 \nu_0}{6kT}\right]\exp\left(\frac{\Delta S_m}{k}\right)\exp\left(-\frac{\Delta H_m}{kT}\right) \tag{6.09}$$

Equation (6.09) can now be written as

$$\sigma = \sigma_0 \exp\left(-\frac{\Delta H_m}{kT}\right) \tag{6.10}$$

where

$$\sigma_0 = \frac{n(Ze)^2 \lambda^2 \nu_0}{6kT}\exp\left(\frac{\Delta S_m}{k}\right) \tag{6.11}$$

In equation (6.10), σ_0 is strictly not temperature independent. Therefore the temperature term is sometimes shown explicitly. Also, ΔH_m is replaced by $\Delta E_m (\equiv E_a)$ as the $P\Delta V_m$ term in ΔH_m (= ΔE_m + $P\Delta V_m$) is not significant. The resulting expression is

$$\sigma = \frac{\sigma_0'}{T}\exp\left(-\frac{E_a}{kT}\right) \tag{6.12}$$

where E_a is the activation energy. E_a is derived from plots of logarithmic

conductivity versus reciprocal temperature. Again, the influence of T in the pre-exponential part of equation (6.12) is much smaller than in the exponential part. Thus equation (6.12) is often written in the more familiar Arrhenius form as

$$\sigma = \sigma_0 \exp\left[-\frac{E_a}{kT}\right] \tag{6.13}$$

In order to understand the nature of the activation barrier, E_a, in the context of structure and chemistry of glasses, several conceptually important models have been developed and they are discussed below.

Anderson-Stuart model

The mechanism of ion transport was thoughtfully analysed in the widely cited model due to Anderson and Stuart (AS) (1954). Conduction is assumed to arise from the hopping of ions between equivalent sites separated by an activation barrier. During the course of its motion, the ion has to first work against the coulombic interactions, which hold it in its site. Next it has to work its way through a narrow passage known as doorway. Doorway is the opening among the anions which are generally in contact. When three ions are in mutual contact, this doorway is a triangular opening. In oxide glasses like alkali silicates, the doorway oxygens can be a combination of both bridging (BO) and nonbridging (NBO) oxygen atoms. In the AS model this doorway is assumed to be in the middle of two equivalent ion sites which are well separated. Since the passage of ions require the doorway to be opened, it involves work for pushing the oxygen atoms outwards leading to the compression of atoms in the doorway. This work also contributes to the activation energy. The model, therefore, estimates the activation barrier E_a as the sum of two terms:

$$E_a = E_b + E_s \tag{6.14}$$

where E_b and E_s are electrostatic binding energy and (doorway opening) strain energy respectively. E_b is taken as the difference between the coulombic energy of the carrier ion at the saddle point position - the point of the highest barrier corresponding to the center of the doorway - and the energy in its own (stable) site. In a typical oxide glass, the energy

difference according to AS model is given by:

$$E_b = \frac{ZZ_O e^2}{r + r_O} - \frac{ZZ_O e^2}{\lambda / 2} \tag{6.15}$$

The first term corresponds to its energy in the stable lattice position, and the second term, to the energy in the saddle point position. Ze and $Z_O e$ are the charges on the cation and the oxygen ion respectively, r and r_O are the corresponding radii of the ions and λ is the distance between the two equivalent sites. E_s is obtained using an equation from continuum mechanics,

$$E_s = 4\pi G r_D (r - r_D)^2 \tag{6.16}$$

G is the shear elastic modulus, r_D is the doorway radius in the normal state. AS assumed that the covalency of bonding between the carrier atom and oxygen reduces the magnitude of the coulomb energy and introduced a correction term, γ. The final AS expression for activation barrier is given by,

$$E_a = \frac{\beta Z Z_O e^2}{\gamma (r + r_O)} + 4\pi G r_D (r - r_D)^2 \tag{6.17}$$

where β is another structure related (Madelung type) constant. The AS model is depicted pictorially in Figure 6.01. Assuming a reasonable value of β and setting γ as equal to relative dielectric permittivity, ε, Anderson and Stuart first succeeded in accounting for variation of E_a with composition in alkali silicate glasses. Although use of ε was expedient, it implied reduction of the coulombic interaction to a small fraction of its normal value, which would make alkali ion - oxygen ion bonding in silicate glass far more covalent than it should be. Another serious problem in this model is that for λ values less than $2(r + r_O)$, E_b would become negative (typically for $\lambda < 4.8$ Å in oxide glasses for Na^+ ions). In the AS model, which has been used to examine the variation of E_a as a function of modifier oxide concentration, the charge carrier concentration is expected to be twice the concentration of the modifier oxide itself. Therefore, the

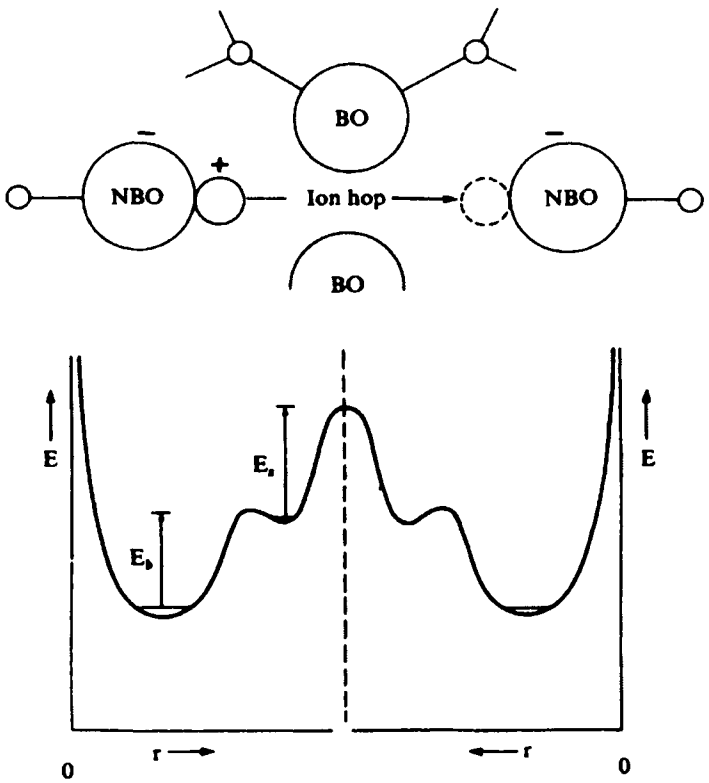

Figure 6.01. A pictorial view of the Anderson-Stuart model. (After Martin and Angell, 1986).

activation energy should be determined by inter-carrier distances as the only variable (the elastic energy term is roughly a constant and of a smaller magnitude because shear modulus changes very little even up to 40% Na_2O). The AS model, under this assumption, would lead to an activation energy,

$$E_a = B_1 + B_2\left[\frac{1}{r_O + r_{Na}} - \frac{1}{R}\right] \tag{6.18}$$

where B_1 and B_2 are constants, R is the inter-sodium ion distance $\approx B_3/C^{1/3}$, where again B_3 is a constant and C is the concentration of Na_2O). But the activation energy data was found to fit very badly (Simmons and Simmons, 1979).

Vacancy model

Rao et al. (1993) recognized the limitations arising from several avoidable assumptions in the AS model. They analysed the Li^+ migration in a lithium thioborate glass. The activation barrier is considered as the difference of the two energies, the energy of the saddle point state and the energy of the ground state of the glass, containing a cation and a neighboring vacancy. The migrating ion is visualized as located at the center of the two polyhedra sharing a face where the face constitutes the doorway configuration. The connected polyhedra around the cation or the vacancy are considered as region *I*. Their interaction energy arising from within this region, $E_{I\text{-}I}$ is presumably the largest in magnitude. Atoms and ions outside of this region are considered as belonging to region *II*. Therefore, the relevant energies can be calculated as:

$$E_{\text{ground state}} = E_{I-I} + E_{I-II} + E_{II-II} \tag{6.19}$$

Similarly the saddle point energy is given by,

$$E_{\text{saddle point}} = E'_{I-I} + E'_{I-II} + E'_{II-II} \tag{6.20}$$

$$E_a = \Delta E = E_{\text{saddle point}} - E_{\text{ground state}} \tag{6.21}$$

Terms in $E_{I\text{-}I}$ etc. comprise coulombic, repulsive (overlap), polarisation and van der Waals interactions of the ions in the respective regions. Coulombic interactions (E_C) are of the type $Z_iZ_je^2/r_{ij}$, repulsive interactions (E_R) are short range and of the type $B_{ij}\exp(-r_{ij}/\rho_{ij})$; where B_{ij} and ρ_{ij} are the repulsive parameters and have been assumed to be equal for all pairs, so that the same B and ρ have been employed for all pairs. Polarisation energy, which varies as $1/r^4$ gives rise to more complex terms. The vacancy and the ion induce dipoles in opposite directions and they are vectorially summed in the calculations. $E_{II\text{-}II}$ is ignored because the terms in $E_{II\text{-}II}$ remain unaffected to a first approximation when the ion moves to the saddle point position and therefore get cancelled in the final expression for ΔE. Among the I-II interactions also, only significant terms need to be retained. Rao et al. (1993) evaluated the saddle point strain energy using the expression of McElfresh and Howitt (1986),

$$E_{strain} = \left(\frac{\pi}{\sqrt{3}}\right) G\xi^2 r^3 \tag{6.22}$$

where ξr is the outward radial displacement of the doorway ions. For an assumed octahedral occupation of Li^+ ions in x Li_2S·(1-x) B_2S_3 glasses the above approach gave an activation barrier of $\approx$ 0.3eV in good agreement with the experimental values. Realistic values of the repulsive parameters B and ρ and experimentally known values of r (2.25 and 2.20 Å) were employed in the calculations. The variation of E_a ($\equiv\Delta E$) as a function of the doorway displacement indicates a minimum as shown in Figure 6.02. The individual contributions of various energies of interactions to the ground (subscript G) and saddle-point (subscript S) are given in Table 6.1. The superscript C, R, P, S and T represent coulombic, repulsive, polarisation, strain and total energies respectively.

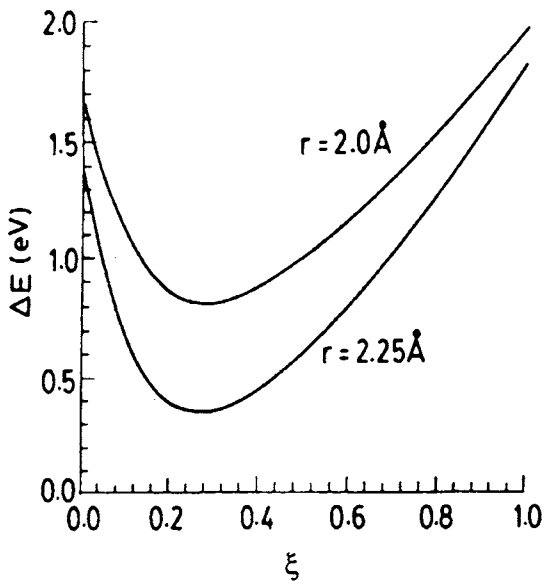

Figure 6.02. Variation of ΔE as a function of ξ with E_G^R / E_G^C = 0.34 and ρ = 0.34×10^{-8}cm (After Rao et al., 1993).

Most importantly this model considers the equivalent site to which the Li^+ ion jumps as a vacancy. It has also brought out clearly the importance of polarization terms in determining the energetics of ion migration in glasses. Similar conclusions were arrived at by Elliott (1994)

Table 6.1(a): Energy contributions for the ground-state and excited-state configurations for different values of B and ρ with $E_G^R / E_G^C = 0.34$ and $r = 2.20$ Å (After Rao et al., 1993)

		Energy contributions to the ground state				Energy contributions to the excited state					Total energy ΔE(eV)
B (10^{-9} erg)	ρ (10^{-3} erg)	E_G^C (eV)	E_G^R (eV)	E_G^P (eV)	E_G^T (eV)	E_S^C (eV)	E_S^R (eV)	E_S^S (eV)	E_S^P (eV)	E_S^T (eV)	
0.12	0.34	-4.80	1.64	-3.32	-6.48	-4.38	0.696	0.07	-2.06	-5.67	0.81
0.18	0.32	-4.80	1.63	-3.29	-6.47	-4.37	0.636	0.07	-2.04	-5.70	0.77
0.28	0.30	-4.80	1.63	-3.27	-6.44	-4.36	0.580	0.08	-2.02	-5.73	0.71

Table 6.1(b): Energy contributions for the ground-state and excited-state configurations for different values of B and ρ with $E_G^R / E_G^C = 0.34$ and $r = 2.25$ Å.

		Energy contributions to the ground state				Energy contributions to the excited state					Total energy ΔE(eV)
B (10^{-9} erg)	ρ (10^{-3} erg)	E_G^C (eV)	E_G^R (eV)	E_G^P (eV)	E_G^T (eV)	E_S^C (eV)	E_S^R (eV)	E_S^S (eV)	E_S^P (eV)	E_S^T (eV)	
0.24	0.34	-4.27	1.45	-2.07	-4.89	-3.92	0.57	0.09	-1.28	-4.54	0.35
0.37	0.32	-4.27	1.45	-2.07	-4.89	-3.91	0.52	0.10	-1.27	-4.56	0.31
0.60	0.30	-4.27	1.45	-2.07	-4.89	-3.90	0.47	0.10	-1.26	-4.59	0.27

with regard to the role of polarization terms. In both AS and vacancy models all cations are treated as potential carriers. They are both 'strong electrolyte' approaches. Such assumption is considered as incorrect in weak electrolyte models.

Weak electrolyte models

Ravaine and Souquet (1977) (RS) made extensive electrical conductivity measurements on sodium silicate glasses. They also measured the alkali oxide activities in these glasses by measuring the potentials across concentration cells of the type

$$\text{Pt, } O_2(1\text{ atm}) \mid x\,SiO_2,\ (1\text{-}x)\,Na_2O \mid 0.6\,SiO_2,\ 0.4Na_2O \mid \text{Pt, } O_2(1\text{ atm})$$

The variations of the conductivity ratios as a function of the activity ratios found in such measurements, are shown in Figure 6.03 for a variety of alkali silicate glasses. It is evident from the figure that

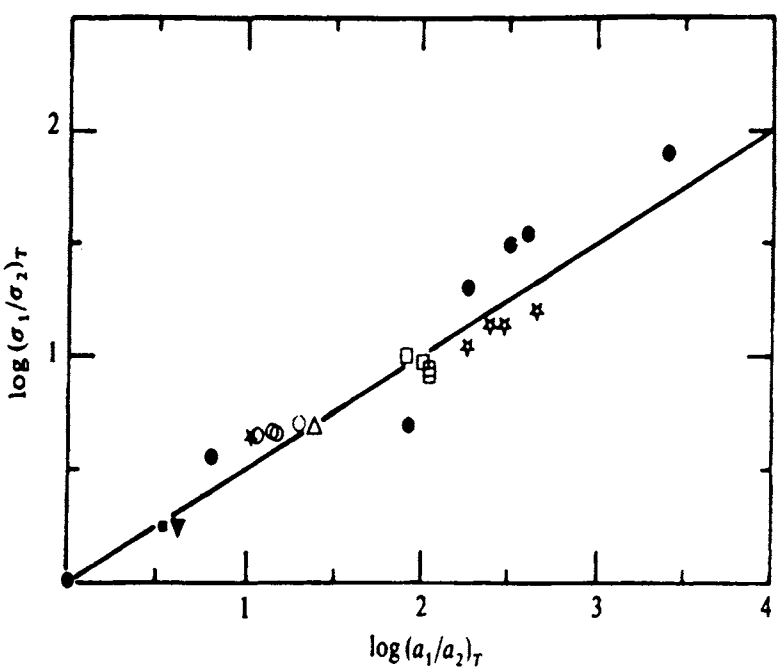

Figure 6.03. Variation of the logarithmic ratio of conductivities as a function of the logarithmic ratio of thermodynamic activities of alkali oxide (symbols differentiate the various silicate glasses) (After Ravine and Souquet, 1977).

$$\left[\frac{\sigma_1}{\sigma_2}\right]_T = \left[\frac{a_1(M_2O)}{a_2(M_2O)}\right]_T^{1/2} \tag{6.23}$$

This clearly establishes a 'root of activity' of the modifier oxide dependence of the conductivity. The finding was attributed to the dissociation equilibrium of alkali oxide in the silicate glass. The alkali oxide M_2O is assumed to dissociate as a weak electrolyte.

$$M_2O \leftrightharpoons M^+ + OM^- \tag{6.24}$$

so that the equilibrium constant, $K = ([M^+][OM^-])/[M_2O] \approx a^2$, where $a = [M^+] = [OM^-] << 1$. This is the mobile ion concentration which is much lower than the concentration of M_2O in the glass. Thus not all M^+ ions in M_2O are considered as carriers in this model. Since the activity of M_2O is essentially constant (there is little dissociation) the chemical potential, μ, of M_2O is given by

$$\mu(M_2O) = \mu^0(M_2O) + RT \ln a(M_2O) \tag{6.25}$$

But in view of equation (6.24) for dissociation of M_2O

$$\mu(M_2O) = \mu(M^+) + \mu(OM^-) \tag{6.26}$$

Hence

$$\mu(M_2O) = \mu^0(M_2O) + RT \ln\{[M^+][OM^-]\} \tag{6.27}$$

$$= \mu^0(M_2O) + RT \ln[M^+]^2 \tag{6.28}$$

Therefore by comparison,

$$a(M_2O) = [M^+]^2 \tag{6.29}$$

Consider two different glasses where the activities of M_2O are a_1 and a_2 respectively. It follows that

$$\frac{a_1(M_2O)}{a_2(M_2O)} = \left[\frac{c_1(M^+)}{c_2(M^+)}\right]^2 \tag{6.30}$$

where $c_1(M^+)$ and $c_2(M^+)$ are the concentrations of M^+ ions in the two glasses. Therefore (c_1/c_2) (dropping M^+ and M_2O in the brackets for convenience) is given by

$$\left(\frac{c_1}{c_2}\right) = \left(\frac{a_1}{a_2}\right)^{1/2} \tag{6.31}$$

The mobilities of the ions are assumed to be unaffected by the composition in RS model which therefore makes $\sigma \propto c$ in the conductivity expression $\sigma = ce\mu$. Therefore,

$$\frac{\sigma_1}{\sigma_2} \approx \frac{c_1}{c_2} = \left(\frac{a_1}{a_2}\right)^{1/2} \tag{6.32}$$

Equation (6.32) explains the experimental behaviour shown in Figure 6.03. This relation is interpreted as suggesting that the conductivity arises due to variations of the *concentration of the mobile species only* and assumes that the mobility of the charge carriers is independent of the glass compositions.

Weak electrolyte model of RS has been employed to calculate activity coefficients and to use activity coefficients to determine the activation barriers for conductivity. The agreement between the experimental and theoretical activation energies has been found to be satisfactory (Ravine and Souquet, 1977).

A conceptually different approach, which is also referred to as weak electrolyte model, has been proposed by Ingram, Moynihan and Lesiker (IML)(1980). In the IML model, ion transport is assumed to involve interstitialcy mechanism. The mobile ions move among interstitial sites, which defines a conduction path. But the hop from one interstitial position to another occurs when the motion of the ion is triggered by the arrival of a second ion to a nearby interstitial site. For example, consider the case of Na^+ ion conduction in a silicate glass. We shall designate three Na^+ ions as Na_1, Na_2 and Na_3. When Na_1 has arrived near to Na_2 as neighbouring interstitial ion, Na_2 migrates. It may migrate to an interstitial

site close to Na_3, so that the process continues. The ionic motion therefore involves $(Na_1Na_2)^*$ type of complexes - starred because it is a sort of excited state configuration of two interstitial neighbors. The mechanism is visualised as

$$(Na_1Na_2)^* + Na_3 \rightarrow (Na_2Na_3)^* + Na_1$$

$(Na_1Na_2)^*$ and $(Na_2Na_3)^*$ are thus local complexes, or crowdions of slightly higher energy. The migration of the charge carriers is brought about by the exchange of partners. Therefore, the conductivity depends upon the concentration of carrier ions in defect interstitial sites. There is thus a correspondence between the concentration in interstitial defect ions of IML model and the mobile ion concentration in RS weak electrolyte model. Formation of interstitial cations M^* can also be represented using a quasi-chemical equilibrium relation,

$$M + h^* \rightarrow M^* + h$$

M and M^* are occupied normal and interstitial sites respectively where as h and h^* are unoccupied normal and interstitial sites respectively. The equilibrium constant K is written as

$$K = \frac{[M^*][h]}{[M][h^*]} \tag{6.33}$$

If $[M^*] = [h] = c$, then $c^2 = K[M][h^*]$. Since both $[M]$ and $[h^*]$ are very large compared to $[M^*]$, and have nearly unit activity, the concentration of the interstitial ions $c = K^{1/2}$. Since ΔG for the above reaction can be written as $-RT\ln K$, c is given by

$$c = K^{1/2} = \exp\left(-\frac{\Delta G}{2RT}\right) \approx c_0 \exp\left(\frac{\Delta E'}{RT}\right) \tag{6.34}$$

where c_0 is a pre-exponential term of the Arrhenius type expression, which also includes the entropy term from ΔG, $\Delta E' = \Delta E/2$, is the energy for moving a cation from a normal site to an interstitial site next to a similarly occupied interstitial. If the ion mobilities in such "exchange of partners" type motion is assumed to be a constant, then σ will be equal to $ce\mu$. For

two different concentrations, c_1 and c_2 of charge carrier ions, $\sigma_1/\sigma_2 = c_1/c_2 = [K_1/K_2]^{1/2}$. But $c^2 = k[M][h^*]$ and h^* is large, constant and essentially independent of the concentration of the modifier oxide. Therefore, $c^2 \propto [M]$. But $[M] = x$, the concentration of M_2O. Therefore $c_1/c_2 \approx [x_1/x_2]^{1/2}$ which represents the ratio of the concentrations of the modifier oxides. Obviously, one can recognise the similarity between the two weak electrolyte models. Both weak electrolyte models seek to establish two cation populations; one, a low concentration of mobile ions and the other, a high concentration of essentially immobile ions. RS model does it by non-dissociation and IML theory, through non-occupation of interstitial sites.

Cluster bypass model

Ingram et al. (1988) proposed a "*cluster bypass*" model to explain ionic conduction in glasses. The model recognizes the "cluster-tissue" texture of glasses which was discussed in chapter 3. Vitrification was regarded as the congealation of ordered microdomains or "clusters" (≈50 Å in linear dimension) embedded in a truly amorphous, low density "tissue" material. However regarding the detailed structure of these clusters, Ingram et al. (1988) have used the model of Goodman (1985) according to which the inter-cluster space is filled by a residual liquid which on cooling below T_g solidifies and forms a residual phase or "connective tissue". The central idea of cluster bypass model is that the preferred pathways for ion migration lie within the connective tissue region. The model explains the curvature seen in the Arrhenius plots of certain AgI-rich glasses as due to the continuous exchange of material between the cluster and tissue regions. The authors are able to account for the mixed alkali effect (see later) using this model. Anomalously high dielectric losses in alkali silicate glasses reported by Hyde et al. (1987) have been attributed in this model to the motion of ions along "partially blocked" pathways. Conductivity enhancements in mixed anion glasses as well as the effects of "dopant" salts such as LiCl have also been explained. NMR studies of sodium silicate glasses have been found to provide supportive evidence to this model.

Optical basicity and ionic conductivity

Perhaps the first attempt to involve the influence of chemistry on

the ionic conductivity in glasses was done by Hunter and Ingram (1984). The variation of the d.c. conductivities due to Na^+ ions in a variety of glasses were considered. The variation of the activation energies as a function of optical basicity was found to be as in Figure 6.04. The activation barriers decrease drastically with increasing basicity. Optical

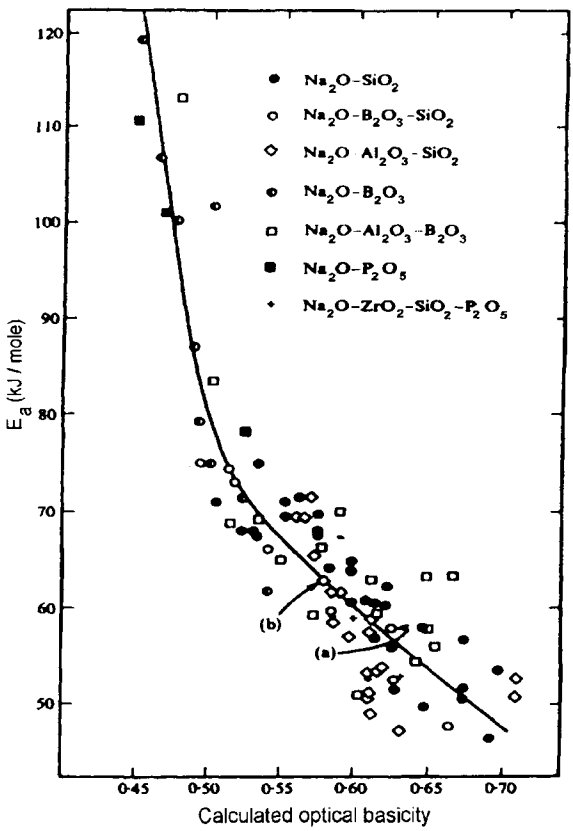

Figure 6.04. Activation energies for Na^+ ion conducting glasses showing dependence on the optical basicity parameter Λ (After Hunter and Ingram, 1984).

basicity denotes the electron donating capacity of the material. It has been defined on the basis of singlet ^1S to triplet ^3P ($S \rightarrow P$) transition energies of Pb^{2+}, Bi^{3+} ions dissolved in a given compound compared to the same energies in CaO, which are taken as standards. Thus Λ, the optical basicity is defined as the ratio of the electron donating capacity of the compound to the electron donating capacity of CaO,

$$\Lambda = \frac{(\nu_f - \nu)}{(\nu_f - \nu_{CaO})} \tag{6.35}$$

where ν_f is the absorption frequency of the free ion, ν is the absorption frequency in the given medium and ν_{CaO} is the absorption frequency in CaO. Λ of mixed oxides as in glass compositions are often expressed as weighted sums of the optical basicities of the constituent oxides, weighted by their equivalent fractions.

$$\Lambda = x_1\Lambda_1 + x_2\Lambda_2 + ... \tag{6.36}$$

Therefore the observed dependence of activation barriers on Λ suggests that during its actual motion in the glass, the cation may carry a positive charge less than its formal charge. Shastry et al. (1993) have shown that the optical basicity in principle should vary as a function of $1/\chi$, where χ is molecular electronegativity of the given compound, $\chi(A_xB_y) = [\chi_{(A)}^{x} \cdot \chi_{(B)}^{y}]^{1/(x+y)}$. They have also shown that when the same cation is involved, use of $1/\chi_{(A)}$ is equivalent to the use of structural unpinning number (S), (discussed later in this chapter). The equivalence of these parameters is shown in Figure 6.05, where $\log\sigma$ (at 300°C) of the

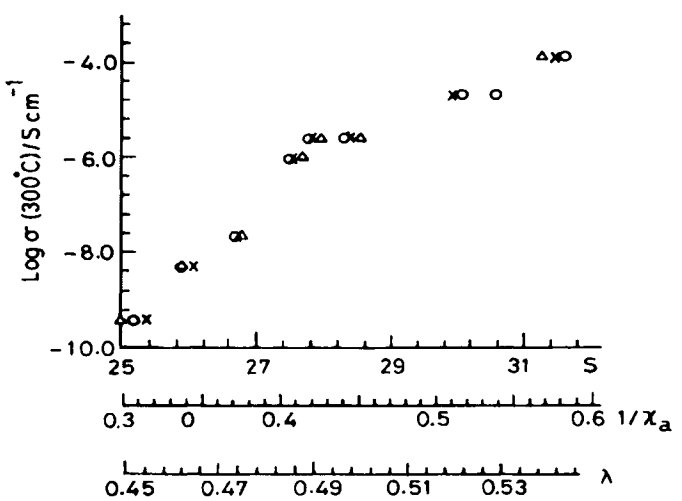

Figure 6.05. Dependence of Na^+ ion conductivity (at 300°C) on λ, S, $1/\chi_a$ for the glasses in the $Na_2O{\cdot}B_2O_3$ system. (o)λ; (×) S; (Δ)$1/\chi_a$ (After Shastry et al., 1993).

glasses in Na_2O-B_2O_3 system are plotted together. In their approach, Shastry et al. (1993) have also shown that when E_a is treated as a function of S, using the empirical relation between $\ln\sigma$ and structural unpinning number (S), E_a decreases as a function of increasing S, an observation consistent with that of Hunter and Ingram (1984). Therefore it appears that ion transport is conditioned significantly by the chemical nature of the material; in glasses it is the chemical nature of the component oxides.

Mixed Alkali Effect

It has been found in many glass systems containing alkali oxides that a gradual substitution of one alkali by another leads to highly non-linear variation of several properties. This is most notable in electrical conductivity, dielectric loss, internal friction and viscosity, all of which involve ionic motion. Most widely investigated are conductivity and dielectric loss in mixed alkali containing glasses. The phenomenon is known as mixed alkali effect (MAE). MAE in properties other than conductivity has been found to be of lower magnitude. Some of the known data are summarised in Table 6.2. An example of MAE in resistivity is presented in Figure 6.06. MAE has been observed both in network type

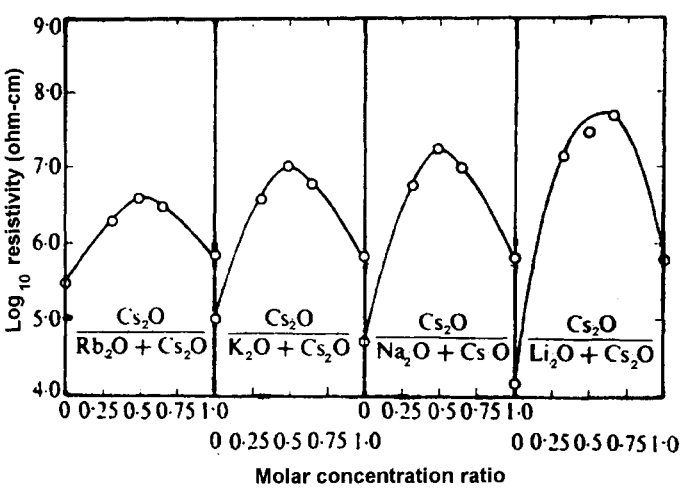

Figure 6.06. Resistivity isotherms at 350°C for (15-x)Cs_2O·xR_2O·85SiO_2 glasses (mol%), where R = Li, Na, K and Rb (After Hakim and Uhlmann, 1967).

glasses and in highly ionic glasses containing only small discrete anions such as in alkali sulphate–zinc sulphate glasses (Rao and Sundar, 1980). In

Table 6.2: Summary of properties for mixed alkali glasses (After Day, 1976).

Property	Derivation of linearity (additivity) with addition of second alkali
Physical	
Density	Small, ≈ ± 10%
Refractive index	Small, ≈ ± 10%
Molar volume	Slight, < ± 5%
Hardness	Small, ≈ ± 10%
Thermal expansion	Small, ≈ ± 10%, usually positive deviation
Chemical durability	Moderately higher, alkali extraction lowered 4-6 times
Mechanical	
Strength	No reported data
Static fatigue	No reported data
Elastic modulus	Small, ≈ ± 20%, deviation temperature dependent
Compressibility	No reported data
Internal friction	Major, large new peaks
Electrical	
Conductivity	Major, negative deviation, lower by a factor 10^{2-6}
Dielectric loss	Major, negative deviation, lower by a factor 10^{1-3}
Dielectric constant	Small (≈25%) to moderate (≈50%) usually negative deviation, but temp. and freq. Dependent
Mass transport	
Alkali diffusion coefficient	Major, lower by a factor 10^{2-4}
Viscosity	Major, negative temperature dependent deviation, lower by a factor 10^{1-2}
Gas permeability	Small, <10% negative deviation

general, a resistivity maximum is observed as a consequence of MAE. The corresponding conductivity decrease in mixed alkali systems (compared to single alkali case) can be 3-4 orders of magnitude. The resistivity maxima (conductivity minima) occur around the middle region of inter alkali variation. Magnitude of MAE is also dependent on both the total concentration of the alkali and on the temperature of observation. It generally decreases at higher temperatures and with lower values of total alkali concentration. In MAE studies, the observed property, like σ (or ρ) is generally plotted as a function of the fraction of one of the alkali ions. It

is also conventional to use the fractional variation of the lighter alkali in such plots. In conductivity measurements, activation energies and pre-exponential factors also exhibit MAE.

Since conductivity is related to diffusion coefficient, diffusion plays a major role in MAE. The diffusion coefficients have been measured in several systems, an example of which is shown in Figure 6.07. The

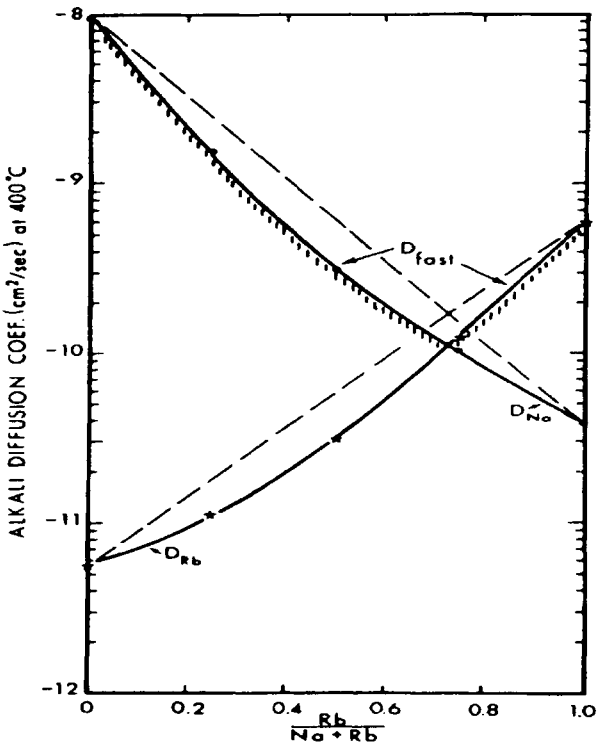

Figure 6.07. Sodium and rubidium diffusion coefficients at 400°C in $(1\text{-}x)Na_2O{\cdot}xRb_2O{\cdot}3SiO_2$ glasses. Cross-hatched curve denotes ion having larger diffusion coefficient (After McVay and Day, 1970)

diffusion coefficient of the smaller ion decreases while that of the larger ion increases in the mixed alkali glasses. Above the cross-over point the diffusion coefficient of the larger ion becomes dominant. The hatched line corresponds to variation of the diffusion coefficient of the faster ion in the MAE compositions. From the Nernst-Einstein relation, it is expected that the conductivity of such a glass exhibits a minimum. Figure 6.07 also reveals that diffusion coefficient of the minority ion - the one whose concentration is lower (imprecisely referred as the impurity ion) - is

always lower than that of the majority carrier ion. It may be noted that the diffusion crossover concentration is also dependent on the nature of the alkali couple. Further, MAE is observed only when the total alkali content is ~10 mole% or more.

In dielectric property measurements, MAE manifests as a loss minimum and the magnitude of the loss minimum can be as high as ~ 1 order of magnitude. Rather dramatic changes occur in the mixed alkali regions in the internal friction behaviour. Shown in Figure 6.08 is the

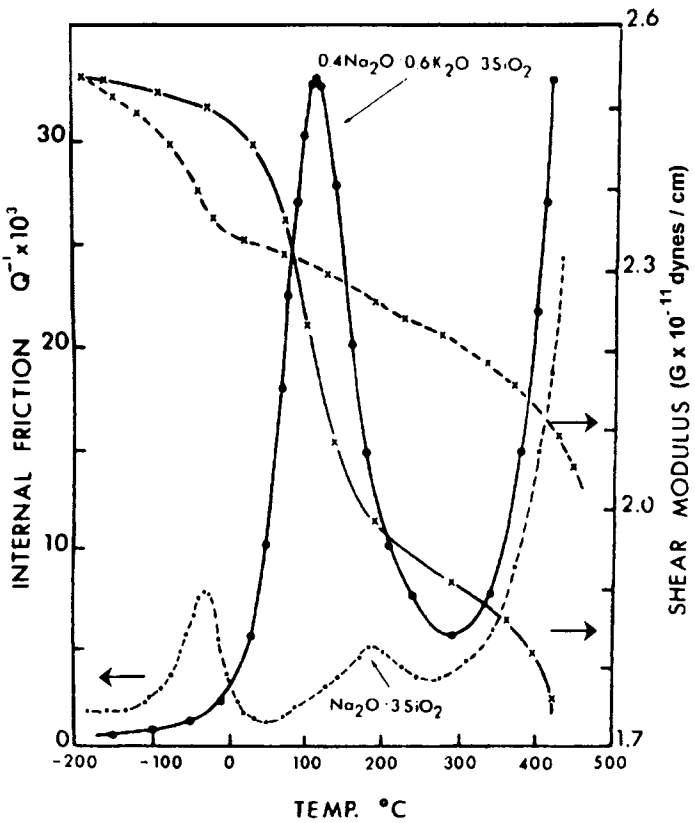

Figure 6.08. Internal friction and shear modulus relaxation in $Na_2O{\cdot}3SiO_2$ and $0.4Na_2O{\cdot}0.6K_2O{\cdot}3SiO_2$ glasses. The frequency used in the measurements = 0.4 Hz. (After Day, 1972).

behaviour of the internal friction measured in sodium potassium trisilicate glasses. $Na_2O \cdot 3SiO_2$ glass containing only Na^+ ions exhibits two small internal friction peaks, around 200^0C and -40^0C. Correspondingly variations in shear modulus are also observed as shown in Figure 6.08.

The internal friction peaks in the single alkali (Na^+ ion) silicate glass are attributed to sodium ion motions, which are induced by the stress field impressed upon the sample in the experiments. But in a mixed alkali glass, a new and large internal friction peak appears and gives rise to a shear modulus relaxation of a much larger magnitude. This single, dominant internal friction peak is a characteristic feature and in this case occurs around 100°C for the mixed alkali composition $(0.4Na_2O \cdot 0.6K_2O) \cdot 3SiO_2$ While the small peak in $Na_2O \cdot 3SiO_2$, which appears around -40°C correlates with the mobility of the smaller ion, the mixed alkali internal friction peak itself correlates with the mobility of the *less mobile ion*. The mixed alkali peak seen in internal friction studies as a function of temperature is characteristic of the alkali pair and when three alkalis are present, the three different alkali pairs give rise to three characteristic MAE peaks. Further insights are provided by relaxation studies (see chapter 9). The relaxation times for mechanical losses of the MAE peaks do not exhibit any correlation with the relaxation times for the dielectric losses and is, therefore suggestive of the fact that the elastic dipoles may be electrically neutral. Further, the dominant loss peak occurs at a higher temperature in a fixed frequency scan, which implies that it is due to a slower process. Therefore, it indicates that MAE involves some cooperative action between two mobile species.

Theories of MAE

A number of approaches have been made to understand the origin of the MAE. Broadly, these approaches emphasize on either structural or bonding aspects as the origin of MAE. Among early approaches, Stevels (1951) argued that the nature of filling interstices in the glass structure is responsible for MAE. Since the interstices have a distribution of sizes, alkali ions in mixed alkali glasses fill the interstices better because of the differences in their sizes. The interstices are therefore filled in a structurally more stable manner in a mixed alkali glass. This is responsible for increased activation barrier for ion migration. Theories based on bonding considerations are typified by Mazurin's approach (1965). According to this the differences in field strengths of the alkali ions give rise to differences in the polarizations of the non-bridging oxygens or the alkali ion oxygen bond strength. Unfortunately, such an approach predicts increased mobility for the larger ion, when a smaller ion is added to the system, which is just the opposite of what happens - the mobility actually decreases.

Hendrickson and Bray (1972) were the first to make a quantitative theory for MAE. They attributed MAE to the mass differences of the alkali ions. Briefly their analysis is as follows. In a mixed alkali glass, the two types of alkali ions are bound to their own sites. Each ion, in general, finds some of the sites in the neighbourhood occupied by the ions of the other kind. Because of the absence of periodicity, the phase correspondences in the vibrations of these dissimilar ions break down in a glass (the conditions for normal modes are relaxed). Therefore the ionic vibrations in their respective sites become independent cage vibrations. The vibration of the alkali ion and that of the center of gravity of surrounding negative charge (on the surrounding negative ions of the cage) create an oscillating electric dipole. This is associated with a corresponding oscillating field of the dipole. The strength of this field decreases rapidly with distance. Nearby ions are affected by the field. Consider two sites 1 and 2, occupied by alkali ions. If $E_1 \sin \omega_1 t$ is the field of the ion at the site 1 experienced by the ion at site 2 which has a dipole moment $p_2(t)$ parallel to $E_1(t)$ then the interaction energy of the dipole with the field is given by

$$W = -p_2(t) E_1 \sin \omega_1 t \tag{6.37}$$

This is described as electrodynamic coupling, central to this approach. The induced dipole moment is given by, $p_2(t) = e.x_2(t)$, where e is the charge on ion 2, and $x_2(t)$ is the time-dependent displacement of ion 2. The equation of motion governing the displacement of ion 2 corresponds to that of a forced damped oscillator and is given by

$$\frac{d^2x_2}{dt^2} + \frac{R_2}{\lambda_2} \cdot \frac{dx_2}{dt} + \omega_2^2 x_2 = \left(\frac{E_1 e}{\lambda_2} \right) \sin(\omega_1 t) \tag{6.38}$$

where λ_2 is the effective mass of the oscillator 2 and ω_2 is its rotational resonance frequency. R_2 is the damping coefficient. λ_2 is given by

$$\lambda_2 = \frac{m_2 M}{(m_2 + M)} \tag{6.39}$$

where m_2 is actual ionic mass and M is the effective mass of the network

configuration to which ion is bound in its site. If (R_2/λ_2) is denoted by Γ_2, which is evaluated approximately from the FWHM of the resonance absorption, solution to equation (6.38) is given by

$$x_2(t) = E_1 e\left[\frac{\sin(\omega_1 t - \varphi)}{\lambda_2\left\{(\omega_2^2 - \omega_1^2)^2 + \omega_1^2\Gamma_2^2\right\}^{\frac{1}{2}}}\right] \tag{6.40}$$

where φ is the phase lag of the second oscillator while the corresponding field is given by E_1. W itself can therefore be calculated, because

$$W = \left[-\frac{E_1^2 e^2 \sin(\omega_1 t)\sin(\omega_1 t - \phi)}{\lambda_2\left\{(\omega_2^2 - \omega_1^2)^2 + \omega_1^2\Gamma_2^2\right\}^{\frac{1}{2}}}\right] \tag{6.41}$$

The time average of W denoted as $\langle W\rangle$ is found by integrating the sinusoidal factors over one period of the field E_1 and then using standard results from the theory of forced damped oscillations. $\langle W\rangle$ can be calculated as

$$\langle W\rangle = -\frac{[E_1^2\, e^2(\omega_2^2 - \omega_1^2)]}{2\lambda_2[(\omega_2^2 - \omega_1^2)^2 + \omega_1^2\Gamma_2^2]} \tag{6.42}$$

The sign of $\langle W\rangle$ depends on whether ω_2 is > or < ω_1. Thus as a result of the interaction, two energy levels are created which are separated by $2\langle W\rangle$. By virtue of the fact that a lowering of the energy is possible by $\langle W\rangle$ term, the negative energy level will be populated by a larger number of oscillators. In a typical mixed alkali glass, value of $\langle W\rangle$ is ~ 0.5eV and at a typical temperature of about 300^0C, the ratio of oscillators in the two levels, n_+ in the $+\langle W\rangle$ state and n_- in $-\langle W\rangle$ state is given by

$$\frac{n_+}{n_-} = \exp\left\{-\frac{2(W)}{kT}\right\} \approx \exp(-19) = 5.6\times10^{-9} \tag{6.43}$$

which means that most oscillators are in a state of interaction that stabilises the pair. This stabilization energy is equivalent to digging the

potential well deeper for the ion. If E_a is the activation energy for ionic mobility, μ, in the absence of interaction (single alkali), μ in the mixed alkali compositions becomes

$$\mu = \mu_0 \exp\left(-\frac{E_a + \langle W \rangle}{kT}\right) \tag{6.44}$$

The Hendrickson-Bray analysis discussed above is rather elegant and is consistent with the absence of such effect in single alkali case. A mixed alkali type of effect should manifest when a different isotope of the same alkali is present according to this approach, because the reduced masses and the corresponding vibrational frequencies are different. Hendrickson and Bray (1974) made measurements on lithium borate glasses containing ^{6}Li and ^{7}Li isotopes to further confirm that the ion masses play a dominant role in MAE. They measured ^{7}Li NMR line-widths and evaluated the jump frequencies (using Bloembergen, Purcell and Pound, BPP, equation, $\nu_J \approx \Delta\nu / \tan[\pi / 2(\Delta\nu / A)^2]$ where $\Delta\nu$ is the FWHM and A is the value of $\Delta\nu$ corresponding to the rigid lattice - low temperature) and found that the ^{7}Li jump frequency does decrease much the same way as in mixed alkali glasses.

It should be possible to express the observed ionic conductivities in MAE as

$$\sigma = N_1 \mu_1 e + N_2 \mu_2 e + (\alpha - N_1 - N_2)\mu_A e \tag{6.45}$$

The first two terms arise from alkalis 1 and 2 unassociated by electrodynamic coupling in the structure and the last term is due to those associated by such effect. α is the total number of alkali ions. N_1 and N_2 can be evaluated statistically assuming *a priori* probabilities of their distribution. When μ_1 and μ_2 are known, conductivity behaviour may be examined with three adjustable parameters, namely N_1, N_2 and μ_A. An example of sodium-potassium silicate conductivities where excellent fits were obtained is shown in Figure 6.09. In the figure, conductivities normalised with respect to the maximum conductivity in the single alkali silicate glasses (at 150 °C), have been plotted.

However there are problems with the Hendrickson-Bray approach. The pre-exponential factor σ_0 in the conductivity expression is assumed

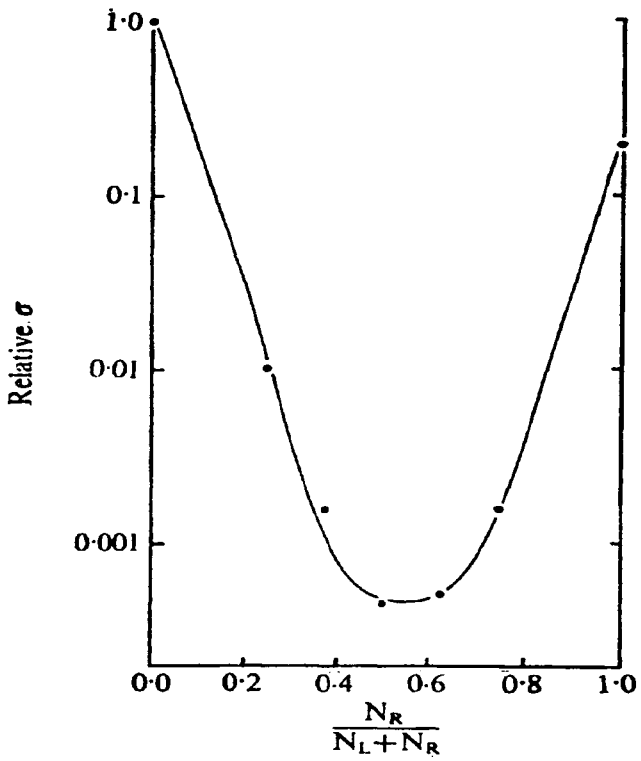

Figure 6.09. Ionic conductivity data for sodium potassium silicate glasses fitted to Hendrickson-Bray function (After Hendrickson and Bray, 1972).

to be unaffected in this theory. But experimentally it is known that σ_0 also exhibits a maximum during alkali replacement. Downing et al. (1982) failed to notice mixed alkali effect in lithium isotope substituted $Li_2O \cdot 3B_2O_3$ glasses. Conductivity measurements on $x(Na,Ag)_2O \cdot (1-x)B_2O_3$ glasses also did not exhibit MAE (Han et al., 1979). It may also be noted that Hendrickson-Bray model requires MAE to be related to the ratio of the masses. In (Cs-Rb) and (K-Na) couple containing glasses, m_{Cs}/m_{Rb}=1.55 ~ m_K/m_{Na}=1.7, but the ratios of the diffusion coefficients at comparable alkali ratios in MAE systems (at 673K) are D_K/D_{Na}=5, while D_{Cs}/D_{Rb}=1.3, clearly in disagreement. Thus mass difference alone is unlikely to be the single determining parameter for MAE.

IML model was extended by Kone et al. (1983) to understand MAE in the case of $(Li_2O\text{-}Na_2O) \cdot 3B_2O_3$ glasses by using available

thermochemical data. The basic feature in this approach is that the conductivities arise from an equilibrium concentration of interstitial alkali ions. The MAE is due to the formation of mixed pairs like $(Li^{+}\text{-}Na^{+})^{*}$ or $[(Li\text{-}Na)^{2+}]^{*}$, whose mobilities are assumed to be low, because of additional interaction. Since the concentration of such low mobility pairs pass through a maximum, the resulting conductivities exhibit a minimum. But this approach has been found to be wrong because like alkali ion pairs which are expected to be more mobile than the unlike ion pairs are not so. But Jain and Peterson (1983) found that when traces of ^{86}Rb was introduced into $(Na_2O\text{-}Cs_2O)\cdot 3SiO_2$ glass, the diffusion coefficient D_{Rb} was similar to that of Cs and Rb was more mobile than Cs. Therefore, the evidence for formation of immobile alkali ion pair, with either Na or Cs, is absent.

Zhong and Bray (1989) examined the boron coordination in mixed alkali borate glasses $(M_1, M_2)O\cdot 0.2B_2O_3$ and found indirect evidence for formation and preponderance of mixed alkali pairs, which are immobile and therefore cause conductivity minima. These immobile mixed pairs prefer to stay in the environment of NBO's, whose formation they encourage and therefore suppress formation of B_4. The histogram of N_4 shown in Figure 6.10 for the four different alkali pairs and compared with N_4 of end members is quite convincing in this regard. Such pair formation is central to the MAE models proposed by Ingram et al. (1983).

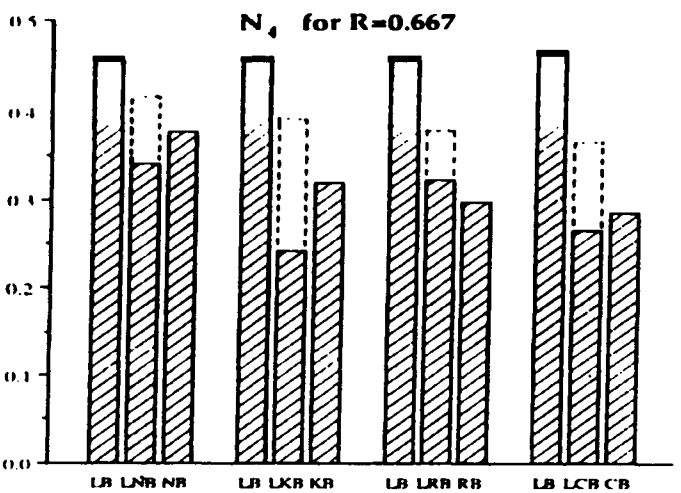

Figure 6.10. N_4 as a function of R for alkali borate glasses. L = lithium, N = sodium, K= potassium, R = rubidium, C = cesium and B = borate. Unhatched block in mixed alkali compositions represent excess N_4. (After Zhong and Bray, 1989).

Mixed ionic effect

MAE is mimicked by several other mixed ionic systems. A rather unusual case has been reported in the conductivity behaviour of Na_2O-SiO_2 glass containing water (Na_2O-H_2O-SiO_2 glass) by Molinelli et al. (1985). These glasses were prepared by hydrothermal procedure at 900°C at 100 MPa pressure. The conductivity behaviour is shown in a typical mixed alkali plot in Figure 6.11, but with the X-axis representing $[H_2O]/([Na_2O] + [H_2O])$. There is a clear manifestation of the MAE-like

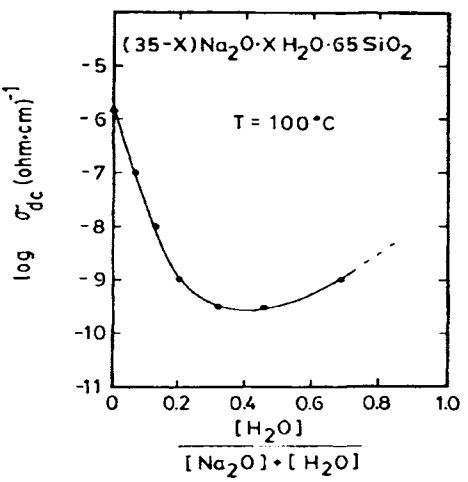

Figure 6.11. Plot of log σ_{dc} vs $[H_2O]/\{[Na_2O]+[H_2O]\}$ for 35 mol% alkali at 100°C (After Monlinelli et al., 1985)

effect. It is argued that water can exist in the combined state as in SiOH along with molecular H_2O. The observed activation energies vary in a manner suggestive of the participation of SiOH, rather than neutral H_2O. The Haven ratio[#] also increases towards unity with increasing water content, suggesting depletion of charge carriers supporting the above conclusion. However, variation of other quantities like the pre-exponential σ_0 and the activation barriers do not bear such strong resemblance to mixed alkali glasses.

Ngai and Jain (1986) investigated the a.c. electrical conductivity (discussed in chapter 7) of mixed isotope and mixed alkali glasses and

[#] Haven ratio, H_R, first defined by Le Claire (1970)is the ratio, D_t/D_σ where D_t and D_σ are the tracer and conductivity diffusion coefficients respectively. The implication of H_R for ion transport has been discussed by Mundy and Jin (1986).

examined the relaxation behaviour on the basis of coupling model. They employed a stretched exponential function in their analysis and found that the stretching exponent β was greater in the case of the mixed isotope glass than in mixed alkali glass. The β of the mixed alkali glass was also greater than that of the single alkali glass. But the a.c. conductivity studies and their analysis using power law fitting also reveal that s (= n = 1-β) remains unaffected in the mixed alkali region (Pradel and Ribes, 1994).

Even dissolution of two salts of the same conducting cation appear to influence the conductivity and give rise to mixed anion effect. Carrete et al. (1983) reported mixed anion effect (of rather small magnitude) in the two systems (i) $(1\text{-}z)[x\mathrm{Ag_2S}\cdot y\mathrm{GeS_2}]\cdot z[t\mathrm{AgBr}\cdot(1\text{-}t)\mathrm{AgI}]$, where $x = y = 0.5$, $z = 0.4$ and $0 \le t \le 0.3$ and $x = 0.4$, $y = 0.6$ and $z = 0.15$, with $0 \le t \le 1.0$ and (ii) $0.24\mathrm{Li_2S}\cdot 0.36\mathrm{GeS_2}\cdot 0.4[t\mathrm{LiBr}\cdot(1\text{-}t)\mathrm{LiI}]$, where $0 \le t \le 0.6$.

Mixed anion effect in borophosphate glasses has been investigated by Tsuchiya and Moriya (1980). By altering the ratio of P_2O_5 to B_2O_3, conductivity was found to increase and the activation energies decrease. The minimum was also found to correspond to the formation of BPO_4 units in the structure. Combining their studies with Raman spectroscopy (BPO_4 gives Raman peaks at ~ 495 cm^{-1} and 1120cm^{-1}) it was concluded that mixed anion effect was a consequence of the formation of tight BPO_4 units. This gives rise to a microheterogenous structure in which BPO_4 units are less tightly bound to the remaining part of the glass. As a consequence additional pathways of lower activation energy are created which enhances the conductivity.

The electrical conductivity studies in $\mathrm{LiF\text{-}PbF_2\text{-}Al(PO_4)_3}$ has revealed yet another interesting mixed ion effect. In this system, Li^+ and F^- are the charge carriers, and are of opposite signs. The conductivity and activation barrier variations are shown in Figure 6.12. The total conductivities are indeed quite low and the activation barriers are high, but the occurrence of maxima in activation barrier and minima in conductivity around f_{Li} of 0.25 appears very much like a *mixed mobile ion effect*. This could nevertheless be due to a depression in the glass transition temperature itself, because when σ is examined using a reduced temperature (T/T_g) scale, the maxima get suppressed significantly. Pradel and Ribes (1994) observed classical MAE in chalcogenide glasses of composition $0.5[x\mathrm{Na_2S}\cdot(1\text{-}x)\ \mathrm{Li_2S}]\cdot 0.5\ \mathrm{SiS_2}$. The observation is shown in Figure 6.13. Since the T_g also exhibits a minimum corresponding to the minimum in σ in the mixed alkali glasses the magnitude of MAE on a corresponding temperature scale can be larger.

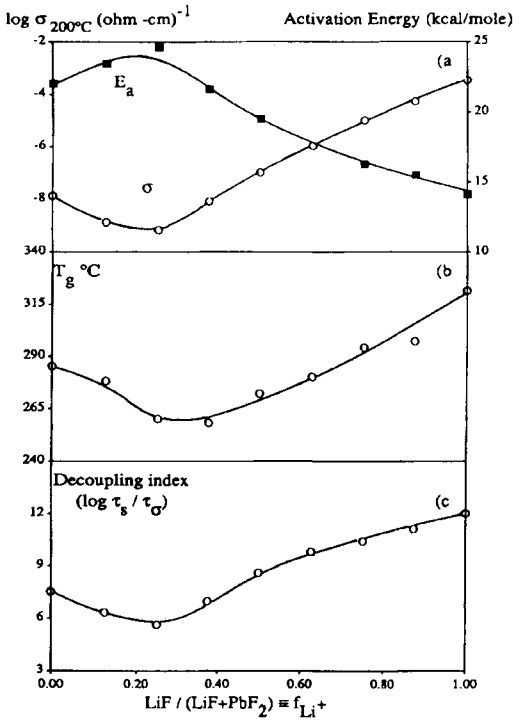

Figure 6.12. Dependence on lithium mole fraction of (a) conductivity and activation energy, (b) glass transition temperature and (c) decoupling index in LiF-PbF_2-$Al(PO_4)_3$ glasses. (After Kulkarni and Angell, 1988)

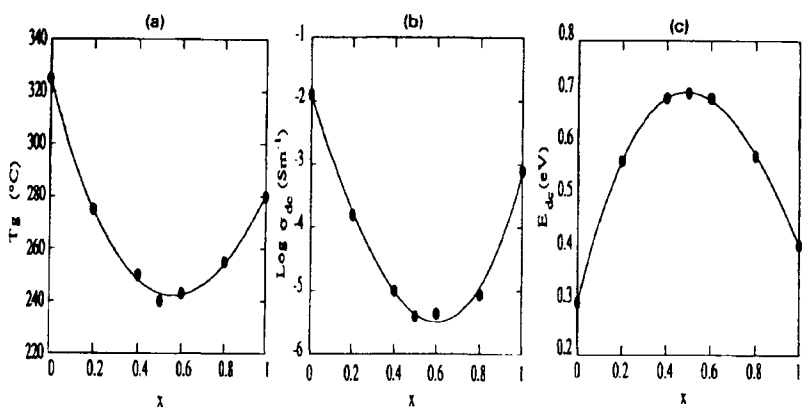

Figure 6.13. Variation of glass transition temperature T_g, conductivity, σ_{dc}, at room temperature and activation energy of conductivity, E_{dc}, for $0.5[x Na_2S - (1\text{-}x)\ Li_2S] - 0.5\ SiS_2$ (After Pradel and Ribes, 1994).

Simulation studies of MAE problem

Maas et al. (1992) have studied the conductivity anomalies in mixed alkali glasses using Monte Carlo simulations on a square lattice. These authors have observed a power law relation between conductivity (σ) and the concentration (c) of alkali ions, $\sigma \sim c^{A/T}$, A being a parameter in their model. The model predicts remarkably well the MAE in glasses, both its temperature and frequency variations. The model has the following features in relation to a mixed alkali glass: There are two types of cations A and B with their respective *distinct* sites A and B. This assumption is supported by EXAFS (Greaves et al., 1991) and other experimental data. If A moves out of its site, a vacancy created designated as $\overline{A}$. $\overline{A}$ remains vacant for a characteristic period of time when it is more probable for another A cation to occupy it rather than a B cation. This is an important assumption in the model, which presently does not have any direct experimental evidence. This difference in the probability of occupation arises due to the fact that 'lattice' (the glass network) has to distort to accommodate an alkali ion of the other type. (In a recent paper Tomozawa (1993) calculated the enthalpy of mixing between 2 alkali components based on migration to 'wrong sites' and found it to be negative. He argues that if two 'wrong migrations' of opposite type occur in the neighbourhood of each other, the stress fields cancel each other.) After a period of time during which the vacancy is said to be 'alive', the $\overline{A}$ vacancy converts itself into a $\overline{C}$ vacancy and the latter is of a general type and thus is considered to be equally receptive to both A and B cations. Using a set of parameters (transition rates), these simple assumptions have been found to provide a fluctuating percolation path at any concentration for the richer cation in the glassy matrix. Thus the mobility of the poorer cation is restricted and it leads to the observed MAE.

A crucial factor in the model of Maas et al. is the topological dimensionality of the conduction path of the alkali ions. As we have seen at any composition, the model predicts a percolation path only for the richer cation, because the conduction path of the poorer cation is blocked by unlike ion sites and hence it cannot percolate. Blocking will be effective in decreasing the overall conductivity only if there does not exist alternate ways of circumventing the original path. Such a situation will come about only if the conduction path has a low dimensionality. Whether it is really so is not clear at present, though various workers have claimed that the conduction path of alkali ions in glasses is topologically one-dimensional.

In view of the importance of this problem, MAE has been investigated using molecular dynamics. It is appropriate to use MD simulations because MD addresses both the static structure and dynamics of ions. Very effective potentials of interaction, mainly of the Born-Mayer-Huggins (BMH) type and their variations can be employed to simulate glass systems. It is fairly straightforward to obtain reliable values of diffusion coefficients of the ions from their mean square displacements and evaluate the conductivities. One can also study in detail the energetics and pathways of the migrations of the alkali ions in glasses. A detailed MD study of the MAE has been performed by Balasubramanian and Rao (1993). MD simulations have been performed on alkali disilicate glasses, $(xLi_2O\cdot(1\text{-}x)\ K_2O)\cdot 2SiO_2$. The system consisted of 960 atoms (224 alkalis, 208 silicon and 528 O atoms) in the micro-canonical ensemble (N, E, V). The initial configuration was chosen randomly with a minimum inter-atomic separation of 1.8 Å. Use was made of Born-Mayer-Huggins potential and dynamical equations of motion were integrated using Verlet algorithm with a time step of 1 femto second. The properties of the system, including pair-correlation functions, mean square displacements (MSD) and velocity auto-correlation functions (VAF) and time dependent pair correlation functions were evaluated using data collected over 90 pico seconds exclusive of equilibration time of 40 pico seconds. Diffusion coefficients were determined for individual alkali ions from their MSD values and converted into conductivity values using Nernst-Einstein relation. The variation of D and σ are shown in Figure 6.14. The figure

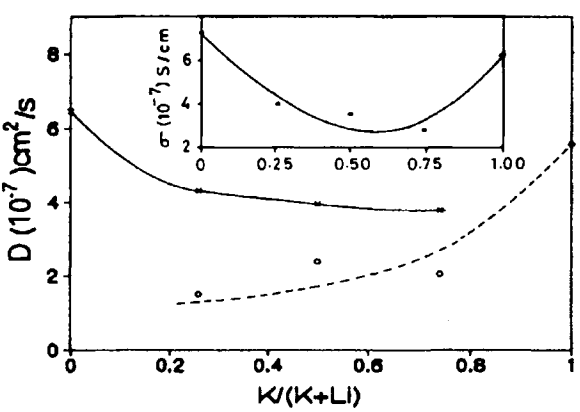

Figure 6.14. Variation of self-diffusion coefficient of Li^+ (×) and K^+ (o) ions with mole fraction of potassium. Inset: variation of electrical conductivity with mole fraction of potassium. Lines are only indicative of trends. Note the occurrence of the mixed alkali effect in σ. (After Balasubramanian and Rao, 1993).

clearly reveals incidence of MAE in disilicate glasses. In order to gain further insight into ionic motion, the time-dependent pair correlation functions known as van Hove correlation function (VHC) designated by $G^{ij}(r,t)$ were computed. $G^{ij}(r,t)$ describes the relative motions of alkalis, both with respect to the same (self part) and the different (distinct part) alkalis. These powerful functions can give information regarding the destination of the diffusing ions in the medium. For example, sitting on a given site at zero time, $G_d^{ij}(r,t)$, which is the distinct part of the correlation function can give information as to what type of ion visits the same site after a lapse of time t. This computational result is summarised for the disilicate glass in Figure 6.15. The most important information

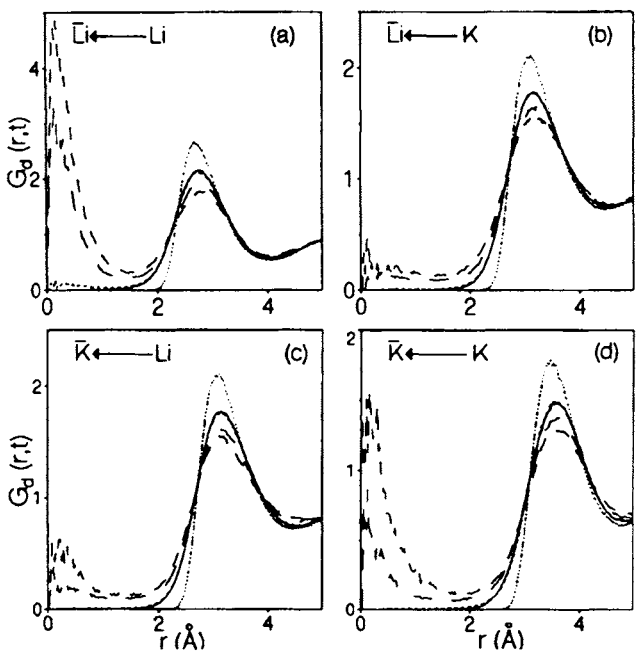

Figure 6.15. Time dependent pair correlation function $G_d(r,t)$ in composition $35[0.5Li_2O \cdot 0.5K_2O] \cdot 65SiO_2$ for (a) Li^+ ion migration to Li^+ vacancy, (b) K^+ ion migration to Li^+ vacancy, (c) Li^+ ion migration to K^+ vacancy, and (d) K^+ ion migration to K^+ vacancy. Time in picoseconds: (...) 0, (———) 0.2, (- - - -) 1, (—) 20, (— —) 50 (After Balasubramanian and Rao, 1993).

regarding MAE is contained in this figure, i.e. when a vacancy is created on a Li^+ or K^+ ion site by diffusion of the ions out of their respective sites, it is more likely visited and occupied by ions of the same type, rather than

by ions of the other type (Li^+ visits a Li^+ vacancy and not of a K^+, and vice versa). This has an energetic basis, which is summarized below:

ion	site energy
Li^+ ion in Li^+ site	- 8.80 ± 0.56 eV/mol
Li^+ ion in K^+ site	- 5.18 ± 0.52 eV/mol
K^+ ion in K^+ site	- 4.41 ± 0.36 eV/mol
K^+ ion in Li^+ site	- 3.08 ± 0.52 eV/mol

Therefore an alkali ion of one type is energetically less stable in the site of the alkali ion of another type. This establishes that the individual alkali ion migration involves preferred sites and hence preferred paths. Therefore, reduction in diffusion coefficient and hence of the conductivity, is due to interruption of these paths as evidenced in MD simulations.

MAE is of considerable practical interest. For example in glass thermometers, ageing of the glass during thermal cycling leads to the so-called secular rise of zero. Due to relaxation of the glass, the volume of the thermometer bulb (and also of the stem) shrinks so that the mercury level at the ice point rises above the calibrated point over long times. Although all glasses exhibit some degree of volume relaxation in such thermal cycling, it has been found to be very significant in mixed alkali glasses. The mechanism seems to be that during the fabrication of the thermometer, the interior cools slowly compared to the surface whereupon the outside is stressed and the interior is subjected to a strain. Alkali ions, therefore, begin to migrate in a manner that the stresses and strains are relieved and more markedly during thermal cycling in mixed alkali glasses. Nevertheless, alkali ion migration ceases when the electrical potential gradient, which develops in the opposite direction, eventually prevents it. Commercial thermometer glasses are therefore formulated with single alkali oxides, for example, Corning glass, CGW0041 used in thermometers has a composition SiO_2 (61%), B_2O_3 (<1%), Al_2O_3 (2%), PbO (24%), Na_2O (11%) and K_2O (~1%). Since mixed alkali compositions lead to loss minima, low loss glasses have also been designed by using a combination of alkalis. For example, glass with a composition $53.3SiO_2 \cdot 10.2PbO \cdot 4.5CaF_2 \cdot 14.2Na_2O \cdot 17.8K_2O$ has been found to have a loss tangent of less than 10^{-3} at 1.5 MHz. MAE is exploited in chemical strengthening (toughening) of glasses. The fact that diffusion coefficients of the major ion is higher than the minor ion, can be used to exchange alkali ions on the surface by dipping objects in appropriate molten salts. Thus when K^+ or Rb^+ is exchanged for Na^+ in a sodium silicate glass, it is the diffusion coefficients of K or Rb that

controls the exchange rate. If exchange is allowed to occur for a long duration, K^+ or Rb^+ diffuse into the glass from the surface. Since Na^+ is the majority ion in the glass, the diffusion coefficients of Rb^+ and K^+ in the glass are very low compared to that of Na^+ ions. Thus K^+ or Rb^+ ions stay in the layers closer to the surface and create a tangential stress in the surface as they are larger ions. Hence the glass becomes tough because crack propagation becomes difficult. However, the inter-diffusion of ions increases and it becomes a mixed alkali glass and the diffusion coefficient eventually exhibits a minimum during such ion-exchange process.

Fast Ion Conduction

We have noted in the previous sections that most inorganic glasses exhibit significant ionic conduction. Glasses containing monovalent cations like Li^+ and Ag^+ exhibit particularly high values of ionic conductivity. Lithium borosulphate glasses are already in use as conductors in thin film solid state batteries. Glasses which exhibit high values of ionic conductivity are described as fast ion conducting or super ion conducting glasses. The first name does not really refer to mobilitites being high, nor does the second to any qualitative relation to super (electronic) conduction. But the names have been retained. We prefer in this book use of the description "fast ion conduction", FIC, to indicate this class of glasses which exhibit high ionic conductivities. The central question addressed in this chapter is, why do some glasses exhibit very high ionic conductivities?

Several approaches have been made to understand the origin of fast ion conduction in glasses. Typical Arrhenius plots of some of the FIC glasses based on Ag^+ and Li^+ are shown in Figure 6.16. A large number of FIC glasses are those derived from mixed salts. Does the high value of σ indicate that all the Ag^+ or Li^+ ions in the glass participate in conduction? The ***random site model*** assumes that all ions (Ag^+ or Li^+) are potential charge carriers and that their motion is characterized by a distribution (usually Gaussian) of activation barriers. Their mobilities also vary accordingly. The change in conductivity is therefore controlled by the *mobilities* and not by the concentration of charge carriers. In the light of weak electrolyte theory (see earlier section) applied to FIC's, only a fraction of the ions can be considered as involved in the charge transport and rest as immobilized by some chemical interaction. The increased conductivity can, therefore, be only due to temperature dependent increase of the number of charge carriers and their mobilities remain unaffected.

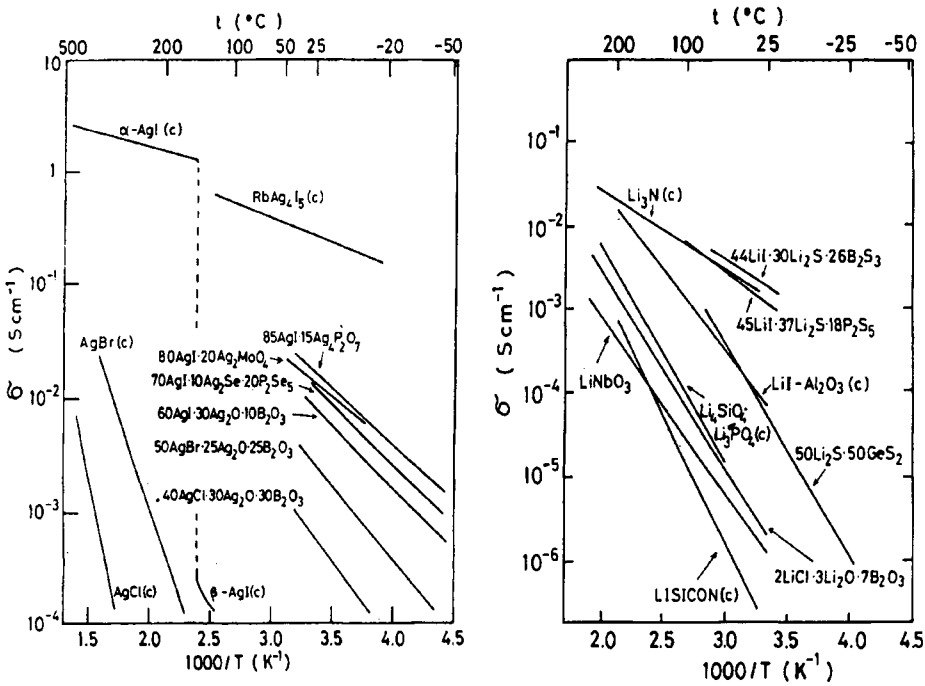

Figure 6.16. Temperature dependence of conductivity of fast ion conducting glasses. Left: Ag^+ ion conducting glasses, right: Li^+ ion conducting glasses. Results of some crystalline conductors (c), are shown for comparison (After Minami, 1985)

Minami (1985) has argued that both approaches are inadequate. The random site model is inadequate because the conductivities at laboratory temperature are found to correlate well with concentration of Ag^+ ions in several AgI-Ag_2MoO_4 glasses, when Ag^+ ion concentration from AgI alone is considered but not when total Ag^+ ion concentration (from both Ag_2MoO_4 and AgI) is considered. The weak electrolyte theory is also inadequate because the mobilities estimated as (σ/ne) and plotted as a function of mole % of AgI, increase by an order of magnitude. Brillouin scattering studies also do not support weak electrolyte model in AgI rich Ag_2O-B_2O_3 glass of the composition $0.6AgI{\cdot}0.4Ag_2B_4O_7$. The relaxation behaviour at hypersonic frequencies revealed that only the mobilities of the Ag^+ ions change with temperature and not their number.

Minami proposed a ***diffusion path model***, in which a path is defined by connectivities of sites with different potential depths. At least three distinct pairs of interactions are present in AgI-Ag_2MoO_4 glasses, which characterize such potential wells. The Ag^+ ion migrates in a minimum energy path defined by the connectivities of the wells.

Structurally these are the wells defined by completely I^-, completely O^{2-} or mixed I^-/O^{2-} neighborhoods. They give rise to potential wells which are shallow (I^-), shallow-deep (I^-/O^{2-}) and deep (O^{2-}). Their connectivities lead to shallow-shallow, shallow-deep and deep-deep combinations. The Ag^+ ions present in wells generated by shallow-shallow interactions contribute most to the conductivity, because their mobilities depend upon connectivity of wells in the glass structure. Thus the well depths and connectivities define both the diffusion path and the mobility.

Free volume concept also held much attraction in modeling fast ion conduction in glasses. Ionic conduction is formulated by assuming that the mobile cation, i has its own transition rate ν_i which depends on its characteristic activation volume v_i^* and its attempt frequency ν_i^0 (Figure 6.17) is given by,

$$\nu_i = \nu_i^0 \exp(-\gamma_i v_i^* / v_f) \tag{6.46}$$

where v_f is the average free volume and γ_i is the free volume overlap factor which is of the order of unity. Average free volume v_f frozen-in

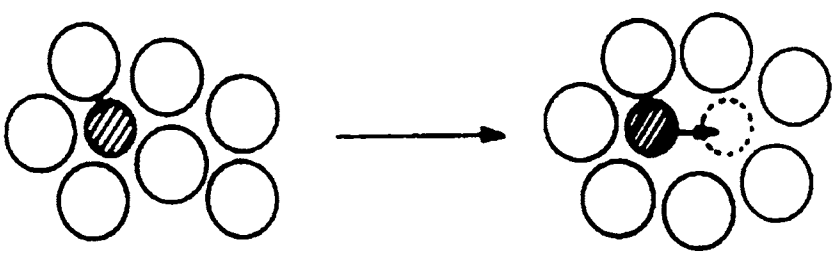

Figure 6.17. Free-volume model extended to the multi-component system. The transition rate ν_i of species i is dependent on its activation volume v_i^* and attempt frequency ν_i^0.

at T_g is given by the relation,

$$v_f = v_{eq} + v_{ex} \tag{6.47}$$

where v_{ex} is the excess free volume and v_{eq} is the free volume of the corresponding equilibrium liquid. Further,

$$v_{eq} \approx \alpha_l v_0 (T - T_0) \tag{6.48}$$

where α_l is the thermal expansion coefficient of the free volume of the liquid, v_0 is the volume of the equilibrium liquid at T_0 and T_0 is the temperature at which equilibrium free volume vanishes. With the substitutions, one can write for v_i as

$$v_i = v_i^0 \exp\left[-\frac{B_i}{\alpha_l (T - T_0) + \delta}\right] \tag{6.49}$$

where $B_i = \gamma_i (v_i^* / v_0)$ and $\delta = v_{ex} / v_0$.

δ can be approximated as

$$\delta = \delta_0 + \alpha_g (T - T_0) \tag{6.50}$$

where δ_0 is the fractional free volume remaining at T_0 and α_g is the thermal expansivity of the glass. Therefore, on the assumption that ionic conductivity σ arises only from the relevant cation, for example, Ag^+ in $AgI\text{-}Ag_2MoO_4$ glasses, one can write

$$\sigma = A v(Ag^+) = A v_0 (Ag^+) \exp\left[-\frac{B(Ag^+)}{\alpha_l (T - T_0) + \delta}\right] \tag{6.51}$$

$$= A v_0 (Ag^+) \exp\left[-\frac{B(Ag^+)}{\alpha_g (T - T_0')}\right] \tag{6.52}$$

(because in the glassy region, $(T\text{-}T_0)$ vanishes a few degrees below experimental T_g, $\alpha_l (T\text{-}T_0)$ is ignored). $T_0' = T_0 - \delta / \alpha_g$; if T_0' is close to 0 K, the above equation becomes the well-known Arrhenius equation. However, σ can be numerically evaluated with the above equation only when several parameters are known. Kawamura and Shimoji (1986) were successful in doing the calculations albeit using eight parameters. Their studies have revealed that the high mobility of Ag^+ ions is largely due to very small size of the Ag^+ ion compared to those of other constituent anions.

Decoupling index

High mobilities of cations are characteristic of FIC glasses. The high values of mobilities seem to have been inherited by the FIC glasses from the supercooled state. Moynihan et al. (1971) were the first to note in their investigation of LiCl solutions that as the glass transition is approached, the ratio of shear relaxation time $\langle \tau_s \rangle$ (= η/G_∞) (see also chapters 7 and 9 for more information on τ) to the conductivity relaxation time $\langle \tau_\sigma \rangle$ (= $\varepsilon_0 \varepsilon_s / \sigma(0)$) becomes very large (a factor of 5 to 10 orders of magnitude). They also noted that this may be a common feature of all ionic liquids and suggested that it may be a consequence of the more mobile ion persisting with its mobility through the glass transition. More interestingly Moynihan et al. (1971) also noted that this ratio can be as high as 10^{10} for alkali silicate glass when reasonable values of dielectric constant and G_∞ were used. This ratio was later described by Angell as decoupling index.

Variation of $\langle \tau_s \rangle / \langle \tau_\sigma \rangle$ as a function of temperature is shown in Figure 6.18 for the CKN glass which is a typical behaviour (Howell et al., 1974). Close to the glass transition temperature, $\langle \tau_s \rangle / \langle \tau_\sigma \rangle$ rises very

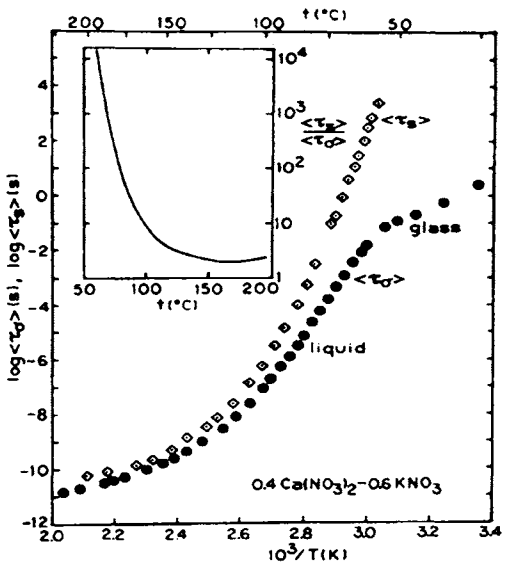

Figure 6.18. Arrhenius plots of mean conductivity relaxation times $\langle \tau_\sigma \rangle$ and mean shear relaxation times $\langle \tau_s \rangle$ for vitreous $0.4Ca(NO_3)_2 \cdot 0.6KNO_3$. Inset shows $\langle \tau_s \rangle / \langle \tau_\sigma \rangle$ ratio vs. temperature (Howell et al., 1974).

steeply by almost 4 orders of magnitude. $\langle \tau_\sigma \rangle$ variation also exhibits a change of shape in the region of glass transition, suggesting that there is a change in the mechanism of the ion transport. The nature of this change involves the onset of typical ion diffusion in glassy state in contrast to ionic motion coupled to structural rearrangement in supercooled region. FIC glasses are generally characterized by very high values of decoupling indices. In Table 6.3, the decoupling indices of several FICs at their glass transition temperatures have been listed.

Table 6.3: Decoupling indices $R_\tau = \tau_S/\tau_\sigma$ for various fast ion conducting glasses at their T_g (After Angell, 1986).

No	System	σ_{25} $\Omega^{-1}cm^{-1}$	T_g K	σ_{Tg} $\Omega^{-1}cm^{-1}$	$\tau_{\sigma(Tg)}$ sec	$R_{\tau(Tg)}$
1	75AgI.25Ag_2MoO_4	13.6×10^{-3}	325	2.8×10^{-3}	3.8×10^{-11}	5.3×10^{12}
2	73AgI.20 Ag_2MoO_4.7 $Ag_2Mo_2O_7$	22.4×10^{-4}	344	9.08×10^{-2}	11.7×10^{-12}	1.7×10^{13}
3	20AgI.80($Ag_2O.B_2O_3$)	1.5×10^{-5}	603	2.2×10^{-2}	4.73×10^{-11}	4.23×10^{12}
4	80AgI.20($Ag_2O.B_2O_3$)	3.1×10^{-2}	483	38.0×10^{-2}	2.8×10^{-12}	7.15×10^{13}
5	66.7AgI.25Ag_2O.8.3P_2O_5(AgI-Ag orthophosphate)	1.5×10^{-2}	323	2.47×10^{-2}	4.3×10^{-11}	4.0×10^{12}
6	65 AgI.23.3 Ag_2O.11.7P_2O_5:(AgI-Ag pyrophosphate)	2.0×10^{-2}	321	2.96×10^{-2}	3.59×10^{-11}	5.57×10^{12}
7	50 AgI.25 Ag_2O.25P_2O_5:(AgI-Ag metaphosphate)	5.0×10^{-3}	337	1.25×10^{-2}	8.0×10^{-11}	2.35×10^{12}
8	35AgCl.45AgI.20CsCl	4.7×10^{-2}	259	1.26×10^{-2}	8.44×10^{-11}	2.37×10^{12}
9	36GeS_2.24Li_2S.40LiI	1.0×10^{-4}	499	18.51×10^{-2}	5.74×10^{-12}	3.48×10^{13}
10	NaSi glass ($Na_{3.75}Zr_{1.1}Si_{2.75}P_{0.25}O_{10.2}$)	1.9×10^{-3}	1035	5.2×10^{-2}	1.53×10^{-12}	1.3×10^{14}

It is interesting to ask the question, how high a conductivity can be achieved in FIC glasses. From the Nernst-Einstein relation, σ is given by ne^2D/kT, where n is the carrier concentration. The maximum value of D, which can be realized in glasses is about 2-5 $\times$ 10^{-5} cm^2sec^{-1}, (this value is deliberately assumed to be smaller than the D of alkali ions in silicate melts). The maximum value of n can be similarly estimated as 2-5 $\times$ 10^{22} cc^{-1}. The maximum value of σ thus works out to be 2.4-15 Scm^{-1} (at

25°C) and this is the upper limit. Experimentally, Ag^+ ion containing glasses have recorded the maximum value of σ, which is 2 orders of magnitude lower than this estimated limit.

A feature associated with high value of decoupling index is a high value of vibrational anharmonicity of the mobile ions. Thus the essential feature of a FIC glass is the presence of structural entities with very different vibrational anharmonicities, i.e., the presence of anharmonicity heterogeneity. On the basis of this observation, Angell (1998) has suggested classification of glassy conductors as "tight" and "loose". These suggestive descriptions imply that the cations responsible for FIC are held either "tightly" or "loosely" in the glass structure and therefore their conductivity relaxation times are correspondingly either long (in tight) or short (in loose) (the involvement of relaxation times establishes a natural connection to fragilities). Figure 6.19 summarizes tight-loose classification in a reduced plot. In the region where T_g/T is just below

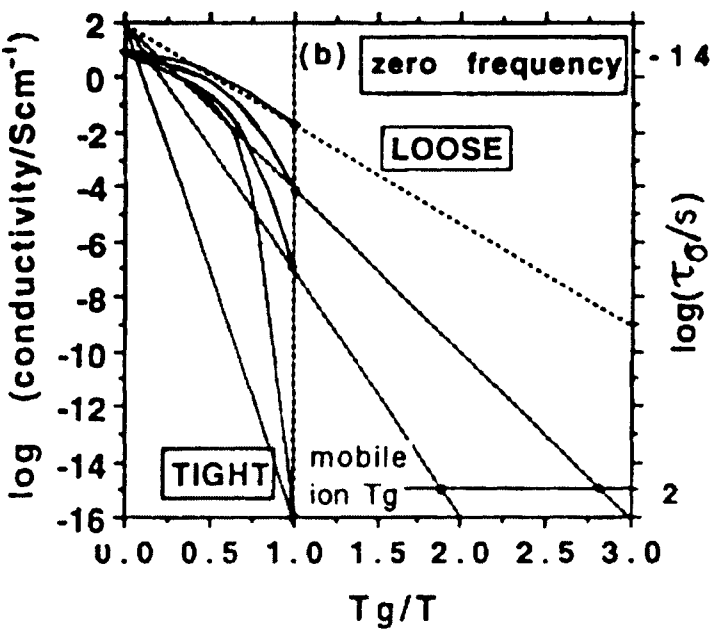

Figure 6.19. Classification of FIC glassy conductors as "tight" and "loose", based on plots of σ(d.c.) vs. (T_g/T). Corresponding variation of $\log\langle\tau_\sigma\rangle$ is also indicated on the right hand side (Schematic after Angell, 1998)

unity, τ_s and τ_σ are approaching the bifurcation point (relaxation time splits off into two branches). Above this point the branches, shear

relaxational responsible for $\langle \tau_s \rangle$ and conductivity relaxational responsible for $\langle \tau_\sigma \rangle$, exhibit different slopes. $\langle \tau_s \rangle$ reaches $\approx 10^2$ seconds around $T_g/T = 1.0$ (see chapter 9 for more information). The $T_g/T = 1$ line itself can be used to represent R_τ values. Since $\log\langle \tau_\sigma \rangle$ for the ideally "tight" glass is –14.3 at T_g, and $\log R_\tau = 0$, the scale for R_τ can be given as

$$\log R_\tau = 14.3 + \log \sigma(T_g) \tag{6.53}$$

Decoupling index is thus a dimensionless measure of the looseness of the glassy ionic conductor.

Chemical approach

R_τ values suggest that the conductivity relaxation times in FIC glasses are far lower than their structural relaxation times. Therefore in a typical FIC glass like AgI-Ag_2MoO_4, the anion framework consisting of I^- ions along with other oxyanions remain firm, while that of the complementary Ag^+ ions does not. In fact in crystalline FIC's this has lead to descriptions like molten sublattices. This infirmity suggests a weakening of the coulombic interactions of Ag^+ ions which are loosened out of their coulombic cages. Ag^+ ions are small in size (compared to anions in the matrix), are spherical, are fairly well separated and are "loosened" from their sites in the sub-lattice. Ag^+ ions are thus "unpinned" from their sites. The weakening of coulombic interactions can be a consequence of lowering of effective electrical charge of the Ag^+ ions which is compensated by a similar lowering of charge of the surrounding anions. The decreased value of the charge on Ag^+ is a consequence of Ag^+ ion reclaiming electrons from the anions, because it has an unscreened nuclear charge, z^* which is significantly high. The on-site electronegativity of the anions are also very low. Together; it is a situation where reverse charge flow can occur from the anion matrix to the Ag^+ ion so that the charge on Ag^+ ion is reduced from +1 and that of I^- and MoO_4^{2-} from –1 and –2 respectively. The important point to note is that during the reverse flow of charge from I^-, the 5s orbital of Ag^+ ion receives the electron. As a result, it creates a spherical charge density. The electron density on donor anions (I^- or MoO_4^{2-}) is also present in diffuse s-like clouds because the frontier molecular orbitals of tetrahedral anions are essentially spherically symmetric. In such a situation the "ploughing back" of the electron density does not lead to the formation of the highly directional covalent bonds but

only result in the formation of anion-cation pairs of reduced charges with minimal overlap. The coulombic interaction is thereby reduced. This causes a reduction of the depth of the potential well in which Ag^+ ion is present. Ag^+ ion is thus structurally "unpinned" from its otherwise deep well and hence "loosened".

Using electronegativity of the anion, the unscreened nuclear charge of Ag^+ ions and the available open space in the glass structure for the motion of the ion, Shastry and Rao (1989) defined a structural unpinning number, S, where

$$S = C\left(\frac{z^*}{\chi_{av}}\right)\left(\frac{V_m}{N}\right) \tag{6.54}$$

where C is simply a constant equal to 1.0 $cm^{-3.5}$ included to render S a nondimensional quantity. The unscreened nuclear charge, z^*, was determined using the well known Slater rules. χ_{av} was determined as the sum of the mole fraction weighted electronegativities of iodide and oxyanions, $\chi_{av} = f.\chi_{I^-} + (1\text{-}f).\chi_{oxyanion}$. The conductivity variation of number of glasses is shown as a function of S in Figure 6.20, which clearly

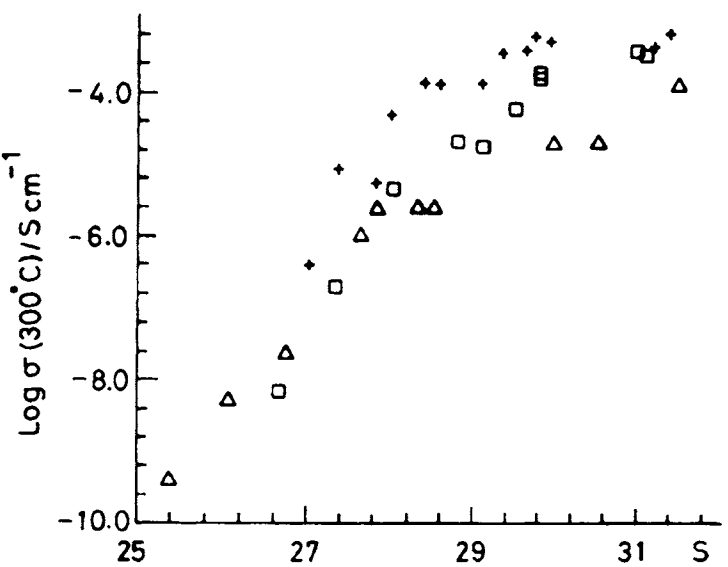

Figure 6.20. Variation of the conductivity (at 300°C) with the structural unpinning number, S for various glasses (After Shastry et al., 1993).

demonstrates that increasing S increases conductivity. It also suggests that glass composition can be engineered through a choice of χ. Reference was already made to the conceptual and functional parallelism between basicity model and structural unpinning approach because of the involvement of the effect of anion matrix on conduction in both approaches.

Origin of fast ion conduction, particularly in α-AgI and related double salts in the crystalline state have been addressed in a variety of ways. Although it does not form the subject matter in this book, a thoughtful analysis of FIC crystalline materials by Phillips (1976) can be of interest to glassy FIC's also. Phillips noted that the silver sub-lattice is essentially molten in α-AgI and the volume change at the $\beta \rightarrow \alpha$ phase transition of AgI correspond to $(\Delta V/V) = -0.05$. Compare this with the tetrahedrally coordinated and partially covalent semiconductors at their melting temperatures. The relative change in their volumes is of the order of -0.15. There is a suggestion in this comparison. Qualitatively a part of FIC crystalline structure – by association, that of Ag^+ sub-lattice in AgI - could have melted at the β–α transition. In the case of $RbAg_4I_5$, there is already a contraction in the formation volume, which as a ratio $\Delta V/V$ is $[V(RbAg_4I_5)-V(RbI)-4V(AgI)]$ / $V(RbAg_4I_5)$ = - 0.04. This volume contraction is consistent with the suggestion that a large part of AgI in $RbAg_4I_5$ is molten. The predominance of tetrahedral coordinations in glasses is known. But the reduction in volume upon glass formation (compared to the sum of volumes of component oxides, sulphides, etc.) has not been examined in glasses from the above perspective. In crystalline materials, the diffusing cation such as Ag^+ in $RbAg_4I_5$ can access a very large number of inequivalent sites having nearly equal energy. This has the effect of a very substantial anharmonic softening or lowering of barrier heights compared to the barriers in uncorrelated hopping situations. In a distantly related way, Minami's diffusion path model (1985) implies a very similar situation in glasses, because the path is created by the connectivities of favourable shallow-shallow type of potential wells.

There are a great variety of FIC glasses which have been reported in the literature because of their potential for industrial applications in batteries and supercapacitors. Although Ag^+, Li^+, Cu^+, Na^+, F^- and O^{2-} ions have all been reported to give rise to high ionic conductivity in crystalline state, Ag^+, and to a significant extent Li^+, are the only two cations which are found useful as high conductivity glasses. A brief overview of the systems is given in the following sections.

Ag^+ ion conducting glasses

AgI-$AgBO_2$ pseudobinary glasses exhibit very high Ag^+ ion conductivities. Some of the glass compositions and their room temperature d.c. conductivities are given in Table 6.4. The highest conductivity is exhibited by the composition with about 65 mol% of AgI. The conductivity prefactor, σ_0, appears to be quite insensitive to the composition. Chiodelli et al. (1982) studied the NMR relaxation (^{11}B NMR) of these glasses and found a wide distribution of barrier heights, which also changes with composition. They found no evidence for the presence of two distinct Ag^+ ion populations. The distinct populations are supposed to arise from silver halide (AgX) and the modifier Ag_2O according to several conductivity models (see earlier section).

Table 6.4: Typical examples of fast ion conducting glasses containing Ag^+ or Li^+ ions (After Minami, 1985)

Composition (mol%)	$\sigma_{d.c.}$(25°C) $\Omega^{-1}cm^{-1}$
$75AgI.25Ag_2MoO_4$	1.4×10^{-2}
$85AgI.15Ag_4P_2O_7$	1.8×10^{-2}
$60AgI.30Ag_2O.10B_2O_3$	8.5×10^{-2}
$60AgI.40Ag_2ScO_4$	3.1×10^{-2}
$33AgI.33.Ag_2O.33GeO_2$	1.3×10^{-2}
$50AgBr.25Ag_2O.25B_2O_3$	2.6×10^{-2}
$40AgCl.30Ag_2O.30B_2O_3$	6.4×10^{-2}
$44LiI.30Li_2S.26B_2S_3$	1.6×10^{-2}
$45LiI.37Li_2S.18P_2S_5$	1.0×10^{-2}
$50Li_2S.50GeS_2$	4.3×10^{-2}
$17LiCl.25Li_2O.58B_2O_3$	1.9×10^{-2}

AgI-Ag_2O-B_2O_3 glasses exhibit high ionic conductivities and the conductivity activation energy for the glass with the highest Ag^+ ion content (80 %) is as low as 4.65 kcal/mol (σ_{dc} =$3.50\times10^{-2}Scm^{-1}$). The variation of activation energies as a function of AgI concentration also smoothly extrapolates to that of α–AgI, but glasses with >80% AgI tend to phase separate. When the compositions of AgI - Ag_2O - B_2O_3 glasses are expressed as xAgI·(1-x)[$Ag_2O \cdot nB_2O_3$], the d.c. conductivity activation

energies, E_a and the composition are found to be linearly related (Chiodelli et al., 1982) as $E_a(x, n) = 5.0\ [n\ (0.66 - x) + 1.1]$ kcal mol^{-1}.

Silver borophosphate glasses doped with AgI also exhibit very high Ag^+ ion conductivities of the order of 10^{-2} S cm^{-1}. It is thought that presence of α-AgI structures in the glass is responsible for the high conductivity. Also, Ag^+ ions are considered as rotating around I^- ions so that a continuous transfer of Ag^+ ions from I^- to I^- takes place (Magistris et al., 1983). In AgI-Ag_2MoO_4 system, it is found that the glass with the composition 75AgI· 25 Ag_2MoO_4 has the highest conductivity of 1.4x 10^{-2} $(\Omega\ cm)^{-1}$.

Structural studies of Ag^+ ion FIC's have been performed using simulation and modeling. Swenson et al. (1998), for example, performed reverse Monte-Carlo (RMC) modelling of 0.5AgI·0.5$AgPO_3$ and 0.6AgI·0.4$AgBO_2$ glasses. They also observed the presence of FSDP in neutron diffraction which shifted as a function of composition in such a way that it indicated moving apart of the phosphate and borate chains by the insertion of the dopant salt, AgI. The diffusion rates of Ag^+ ion increased rapidly with increase in AgI content. The conductivity was found to be a function of free volume, Δv, as $\sigma/\sigma_0 = [\Delta v / v]^3$, where Δv is defined as $(v-v_0)$, v and v_0 being the volumes per network atom in the doped and the undoped glasses respectively. It seems that salt doping not only increases the charge carriers but also increases the number of conduction pathways. A very highly conducting glass has been made by melt-quenching of $Ag_7I_4AsO_4$, with a conductivity value of 1.3×10^{-2} Scm^{-1} at 298K. The heat capacity of this glass also exhibits unusual features as a function of temperature (Finleyson et al., 1980) and has been attributed to the possibility of the onset of AsO_4 rotation in this system above 180°C. Ternary AgI - AgCl - CsCl systems exhibit very high Ag^+ ion conductivities. Glasses of composition 40AgI·35AgCl·25CsCl exhibit a record conductivity of 4.7×10^{-2} S cm^{-1} at room temperature, but the T_g of this glass is also very close to room temperature (Liu and Angell, 1986). Devitrification studies reveal that the glass structure is similar to $RbAg_4I_5$ and not to α-AgI. High conductivity is thus attributed to the presence of a plethora of conduction paths as in crystalline $RbAg_4I_5$.

Relaxation behaviour (discussed in chapter 9), of both electrical and mechanical properties, has been studied in phosphate and borate systems. Increased concentration of AgI shifts the mechanical relaxation peaks to lower temperatures at constant frequencies and no new peak was observed which could be associated with a separate population of mobile Ag^+ ions. The relaxed modulus, however, extrapolates to that of the

crystalline α-AgI when plotted as a function of mole fraction of AgI, suggesting that Ag^+ ions from only AgI are mobile and responsible for the observed mechanical relaxation. But in glasses the matter of apportioning Ag^+ ions into two different populations is still a moot point. Logarithmic plots of τ_m (mechanical) and τ_σ (electrical) relaxation times are shown together in Arrhenius plots for various AgI-$AgPO_3$ glass compositions in Figure 6.21. The variation of the τ values suggests that the mobile (Ag^+)

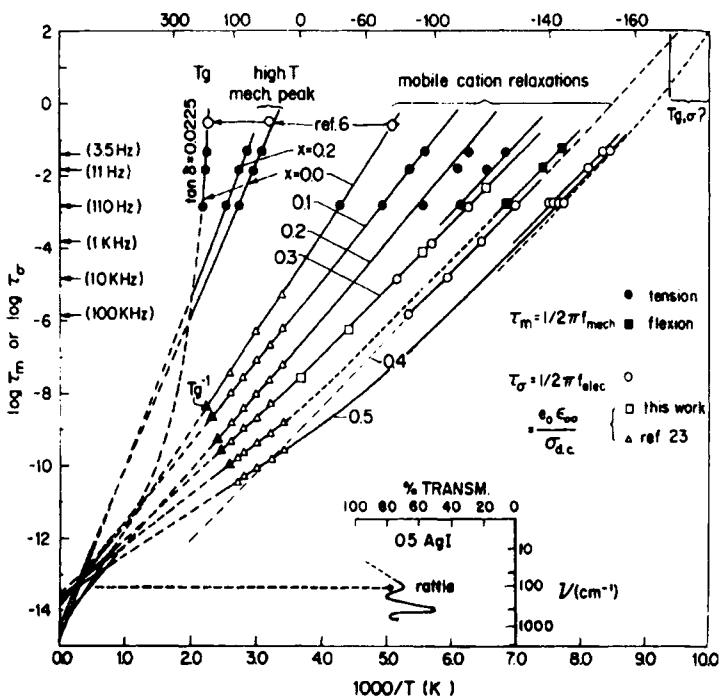

Figure 6.21. Relaxation 'map' for observations on mechanical and electrical relaxation in xAgI·(1-x)$AgPO_3$ glasses. Inset; Low frequency portion of thin film transmission IR spectra for 0.5AgI·0.5$AgPO_3$ glass (After, Liu , Angell, 1986).

cation relaxations may eventually exhibit a freezing out at some low temperature which corresponds to a second glass transition due to immobilization of cations. This may occur in the vicinity of ~100K for AgI rich glasses where relaxation times become ~10^2s (see top of the figure). The figure also shows the IR spectra in the inset, in which the Ag^+ ion rattling peak frequency is seen around ~10^{-13}s. This value corresponds to the region of convergence of the individual Arrhenius plots once again confirming that all observations indeed refer to Ag^+ ion motion only. This

interesting second glass transition due to motional arrest of cations has been calorimetrically detected by Hanaya et al. (1995).

Li^+ ion conducting glasses

Otto (1966) recognized long ago that high Li^+ ion conductivities could be attained by manipulating the glass compositions, particularly by addition of salts to the glasses. By adding Li_2SO_4 and Li-halides to Li-borosilicate glasses, Otto was able to achieve conductivities of the order of $10^{-4}Scm^{-1}$ at 100°C. Presence of highly polarisable anions (such as I^-) seems to increase conductivity and simultaneously increase the decoupling indices. Mercier et al. (1981) prepared lithium thiophosphate glasses containing maximum quantity of LiI and observed conductivities of the order of $10^{-3}Scm^{-1}$ at 25°C. The decoupling index of this glass at T_g (125°C) is $10^{12.5}$.

Very high Li^+ ion conductivities are exhibited by chalcogenide glasses (Malugani et al. 1983). The glass compositions in the Li_2S-P_2S_5-LiI and their conductivities at 25°C are shown in Figure 6.22. The glass formation range is rather narrow and confined to the neighbourhood of tie-line compositions of $Li_4P_2S_7$ as shown in the Figure (6.22a). Electronic conductivities in these glasses are low and typically 10^{-9} S cm^{-1} at laboratory temperature.

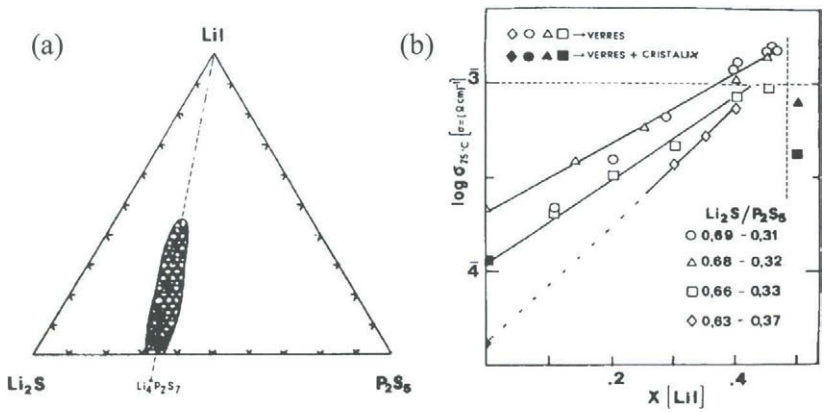

Figure 6.22. (a) Glass forming region in the system Li_2S-P_2S_5-LiI. (b) Influence of composition (mole% LiI) on the conductivity (After Malugani et al., 1983).

Levasseur et al. (1978, 1979) recognized two important factors which influence σ. The first was that the replacement of O by S in alkali borate glasses (Li_2O-B_2O_3 to Li_2S-B_2S_3), which increased the room

temperature conductivity by a 1000 times and the second is that dissolution of alkali salts further enhanced the conductivities, the increase ranging in the same manner as polarisabilities of the anions ($I^- > Br^- > Cl^- > F^-$). Based on this experience, they synthesised LiI - Li_2S - B_2S_3 glasses of various compositions and achieved very high conductivities. Thus for example $0.44LiI{\cdot}0.30Li_2S{\cdot}0.26B_2S_3$ glass was found to have a conductivity of 1.7×10^{-3} Scm^{-1} at 25°C with an activation energy of 0.30 eV. It has been a well thought out strategy, because substitution of O by S increases the anion polarisability, which enhances the cation conductivities by reducing the barriers due to polarization energy contributions. Burckhardt et al. (1984) made even more versatile glasses by dissolving LiI in thioborates. The ternary glass forming domain in $(LiI)_2$-Li_2S-B_2S_3 system is shown in Figure 6.23. The region marked I corresponds to transparent glasses in

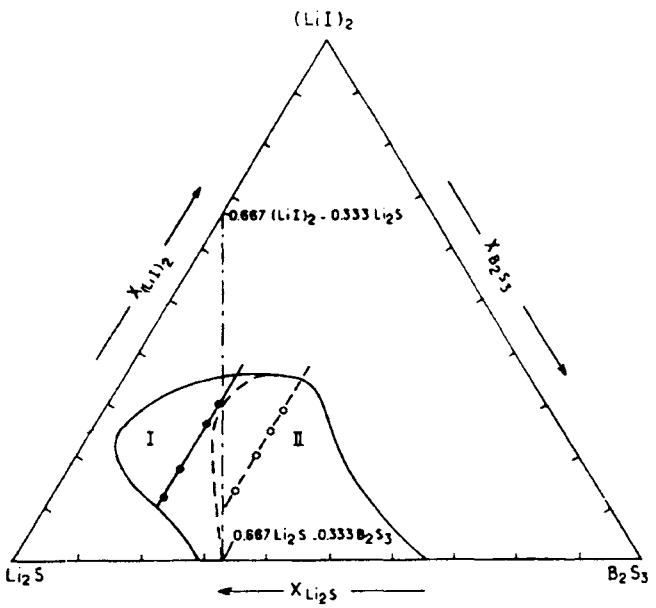

Figure 6.23. Glass forming region in the ternary system $Li_2S \cdot (LiI)_2 \cdot B_2S_3$. (•) transparent glasses, (o) opaque glasses. (After, Burckhardt et al., 1984)

which up to 30% $(LiI)_2$ can be present. Increased LiI appears to decrease the activation barriers as evident in Table 6.5. Room temperature conductivities of up to $2.5x10^{-3}$ Scm^{-1} has been achieved in these ternary glasses. Melts of simple lithium salts are generally very difficult to quench into glassy state. Nassau et al. (1980) reported the first use of twin-roller quenching technique to make lithium molybdate and lithium tungstate

Table 6.5: D.c. conductivity activation barriers in the fast ion conducting lithium iodide-lithium thioborate glasses (After Burckhardt et al., 1984).

Composition			Δ(eV)
$(LiI)_2$	Li_2S	B_2S_3	
0.143	0.571	0.286	0.36
0.154	0.692	0.154	0.374
0.250	0.500	0.250	0.341
0.304	0.392	0.304	0.325

glasses. Quenching rates of the order of 10^7K/s were achieved. These glasses are rather metastable and they crystallize immediately above T_g as shown in Figure 6.24. However, these glasses exhibit Li^+ ion

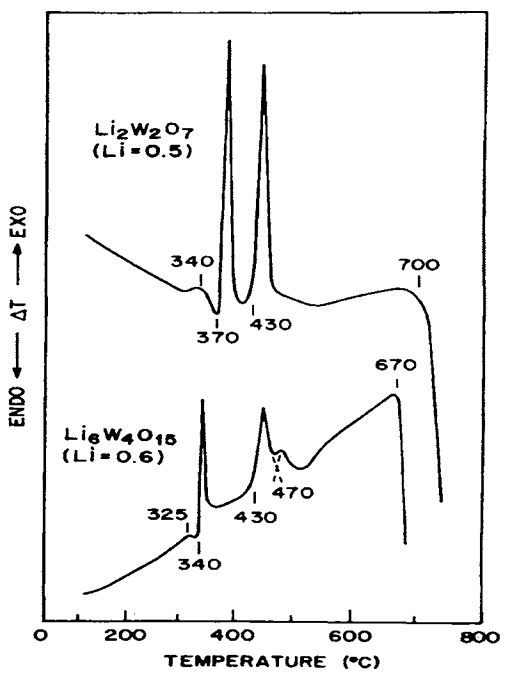

Figure 6.24. DTA of quenched $Li_2W_2O_7$ (Li=0.50) and $Li_6W_4O_{15}$ (Li=0.60) in flowing N_2 at 20°C/minute (After Nassau et al. 1980).

conductivities in the range of 10^{-5}-10^{-6} Scm^{-1} (as shown in Figure 6.25). Since both Mo and W in the glasses can be reduced to lower valence states

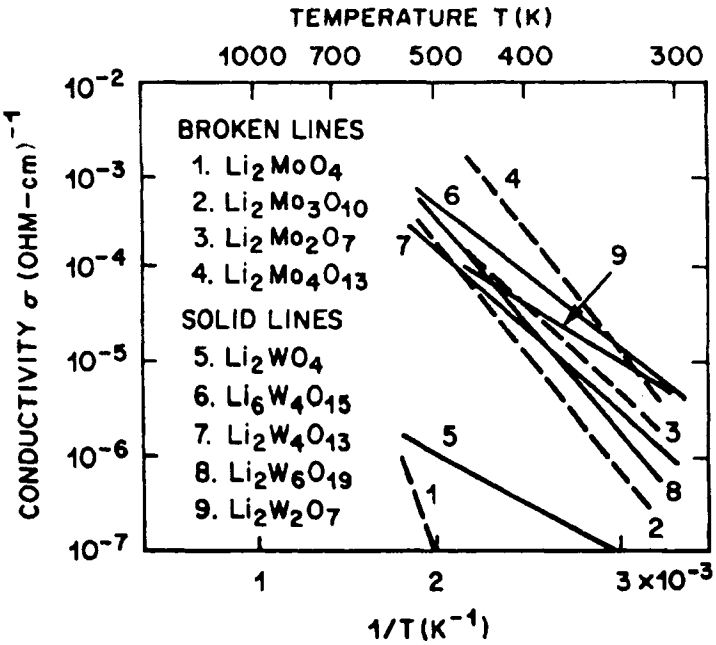

Figure 6.25. Ionic conductivity of quenched lithium molybdate and lithium tungstate glasses. Samples were completely glassy except for 1 and 5, which were largely crystalline. (After Nassau et al., 1980)

they are likely to find applications as cathode materials.

Roller quenching technique has been used to prepare a variety of aluminate, gallate and bismuthate glasses containing Li^+ ions. They all exhibit increased conductivity with increasing Li^+ ion concentration. In Figure 6.26, the variation of log σ (at 500 K) has been plotted as a function of Li^+ ion mole fraction for all the glasses. The linear variation suggests that the activation energies decrease with Li^+ ion concentration (x), as $E_\sigma = E_0 - ax$, where $E_0 \sim (1.4 \pm 0.2)$ eV and $a = (1.1 \pm 0.2)$ eV per mole fraction. This observation (Glass and Nassau, 1980) is consistent with random site model because of the following reason. If the activation energies have a Gaussian distribution, then n_i, the number of ions with activation barrier E_i is given by

$$n_i = \frac{N}{\rho\pi^{1/2}} \exp\left[-\frac{(E_i - E_0)^2}{\rho^2}\right] \tag{6.55}$$

where ρ is the width of the distribution, N is the total density of the alkali

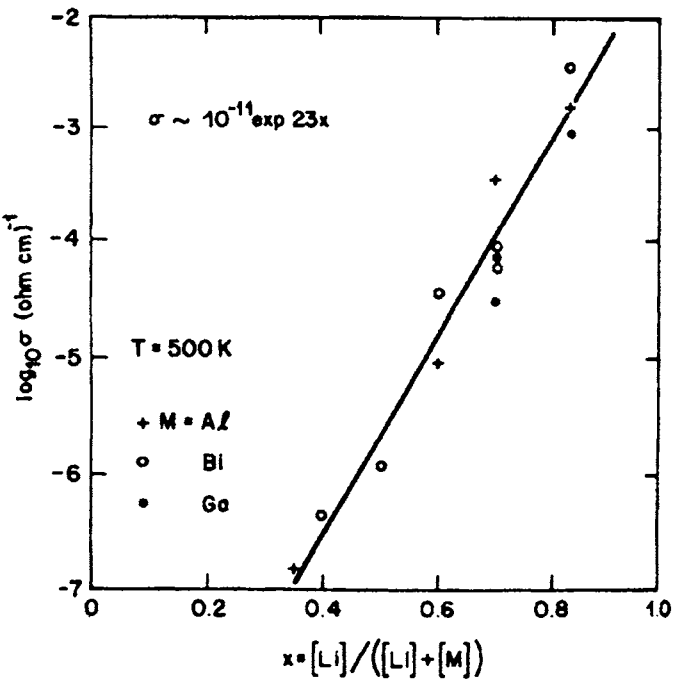

Figure 6.26. Temperature dependence of the conductivity of various lithium ion conducting glasses (After, Glass and Nassau, 1980).

ions and E_0 is the activation barrier corresponding to the maximum in the distribution. The conductivity, σ, is given by

$$\sigma = e\mu_0 \int_i n_i \exp\left[-\frac{E_i}{kT}\right] dE_i = Ne\mu_0 \exp\left[\left(-\frac{1}{kT}\right)\left(E_0 - \frac{\rho^2}{4kT}\right)\right] \qquad (6.56)$$

Therefore the apparent activation energy, $E_a = E_0 - \rho^2 / 4kT$. Making plausible assumptions ρ can be shown to vary as $x^{1/2}$ and at constant temperature the observed linear decrease of activation energies is consistent with the random site model.

Systematic transport studies of Li^+ ions in oxide and chalcogenide glasses of the general formula, $xLi_2X \cdot (1\text{-}x)SiX_2$ (X = O, S or Se) by Pradel and Ribes (1994), revealed that conductivities in oxide glasses are significantly low. The d.c. conductivities were found to vary as Ax^{α} and this behaviour found support in Monte Carlo computer simulation. Since

σ_{dc} also follows Arrhenius law, it is implied that $\sigma = \sigma_0 \exp(-E_{dc}/kT) = Ax^{\alpha}$. Therefore, $E_{dc} = B + C\ln x$, where $B = kT(\ln\sigma_0 - \ln A) =$ constant and $C = -\alpha kT$ so that $\alpha = -C/kT$. The behaviour of E_{dc} was found consistent with this expectation.

Still higher conductivities have been realised in $x\text{Li}_2\text{S}\cdot(1\text{-}x)\text{SiS}_2$ glasses, doped with Li_2SO_4 and Li_3PO_4. A 3% Li_3PO_4 doped 59 $Li_2S \cdot 38\ SiS_2$ glass has been found to have a conductivity value of 6.9×10^{-4} S cm^{-1} at room temperature. Ribes et al. (1980) have investigated conductivities of glasses formed in the three generic glass forming chalcogenide systems modified by both lithium and sodium sulphides. These are GeS_2, SiS_2 and P_2S_5 glasses. The transport number for the alkali conduction has been found to be very high (close to unity) and glasses could also be obtained over much wider ranges of composition than in corresponding oxide systems. The range of glass formation is particularly enhanced in alkali modified GeS_2 systems, for example Na_2S-GeS_2 has a range of 0-60% Na_2S compared to Na_2O-GeO_2 in which modifier content can be increased only up to 38%. In the case of Li_2S-GeS_2, up to 50% Li_2S has been introduced which is almost double the range of Li_2O in GeO_2 glasses. The laboratory temperature conductivities of select glass compositions and the corresponding activation energies are given in Table 6.6. Lithium ion conduction behaviour in the Li_2S-GeS_2 glass is also compared with other Li^+ ion conducting systems in Figure 6.27.

Table 6.6: D.c. conductivities and activation barriers in some modified chalcogenides (After Ribes et al., 1980).

Composition (mol%)	E_0 (eV)	σ_{25} (Scm^{-1})
$33Na_2S.66GeS_2$	0.54	1.0×10^{-8}
$42Na_2S.58GeS_2$	0.53	2.2×10^{-7}
$50Na_2S.50GeS_2$	0.51	1.0×10^{-6}
$60Na_2S.40GeS_2$	0.44	7.3×10^{-6}
$30Li_2S.\ 70GeS_2$	0.63	4.4×10^{-7}
$40Li_2S.\ 60GeS_2$	0.52	3.2×10^{-6}
$50Li_2S.\ 50GeS_2$	0.51	4.0×10^{-5}
$50Na_2S.50P_2S_5$	0.54	3.9×10^{-6}
$66Na_2S.33P_2S_5$	0.70	2.6×10^{-6}
$50Na_2S.50SiS_2$	0.43	1.2×10^{-5}

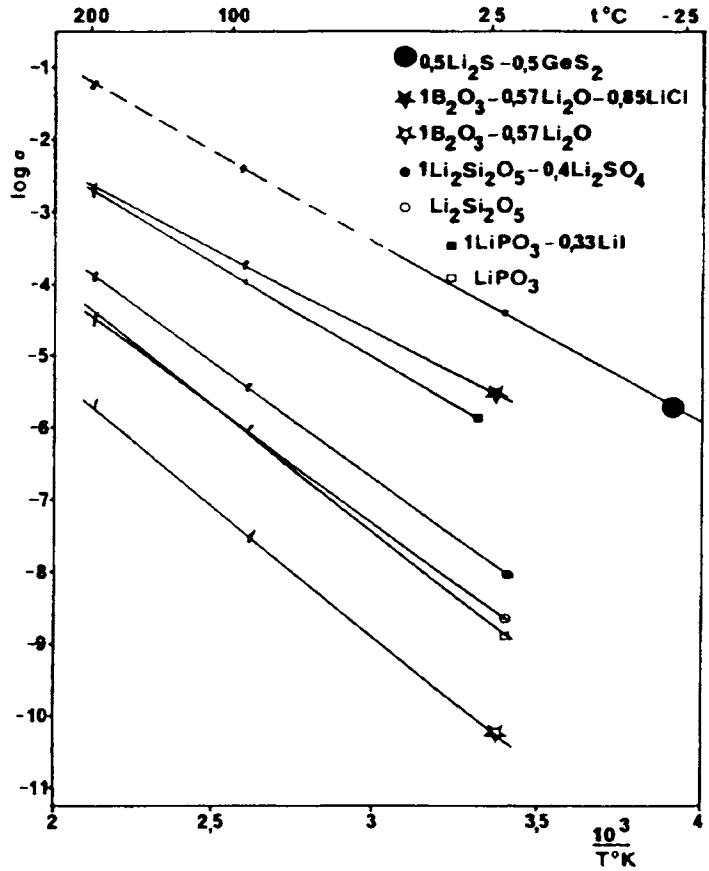

Figure 6.27: Temperature dependence of the conductivity of various lithium conductive glasses (After Ribes, 1980).

In oxide glasses large concentrations of the conducting cations like Li^+ can be introduced but it requires complete depolymerization or modification of the glass network. For example in silicates, phosphates and borates, modifier oxides have to be added to an extent that orthosilicates, orthophosphates and orthoborates are formed which contain small discrete anions. But the melts of such ortho salts are extremely difficult to quench into glassy state and have been only recently (Hirai et al., 1995) vitrified by using quenching rates of the order of 10^9 K/s. These salt-like compositions exhibit significantly lower T_g (190°C for lithium orthosilicate). Salts can also be vapor-deposited as in films of borates, thioborates, etc. to achieve high conductivities. Tatsumisago et al. (1985) made several glasses in Li-Al-niobate system shown in Figure 6.28 by

using fast quenching techniques. The curves drawn through the points in the Figure indicate compositions of the same T_g values. However the highest conductivities obtained were only of the order of 10^{-5} Scm^{-1} at 500 K.

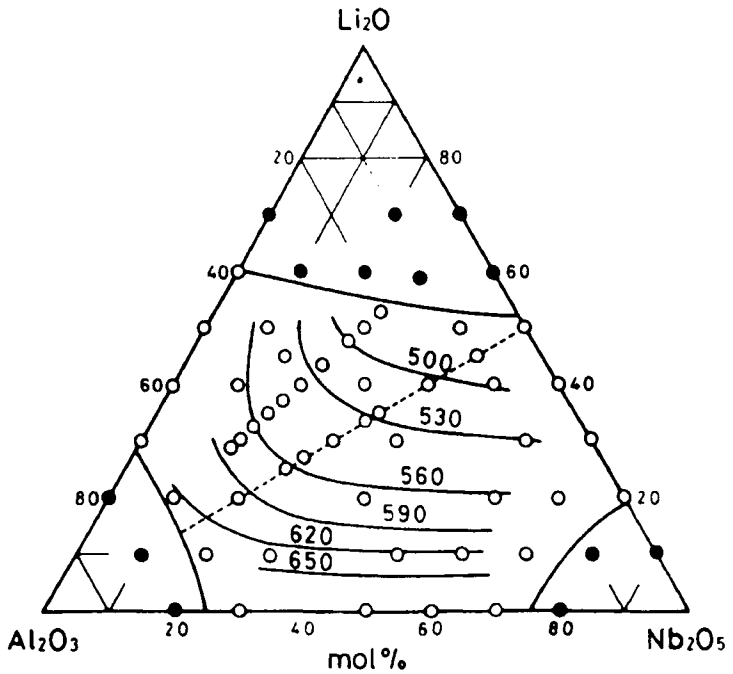

Figure 6.28. Glass forming region and iso-T_g (°C) curves for the system $Li_2O{\cdot}Al_2O_3{\cdot}Nb_2O_5$; (o) glassy, (•) crystalline (After Tatsumisago, 1985)

Other FIC glasses

The so-called NASICONs or sodium super ion conductors are crystalline solids of the general formula $A_1B_2(PO_4)_3$ where A is a monovalent cation and B is either a single or combination of tri, tetra and penta valent ions. They generally crystallize in $R\bar{3}C$ or related (open) structures. The monovalent A ions migrate in the lattice with low activation energies. Spurred on by this observation Susman et al. (1983) synthesised glasses of NASICON compositions, which they described as NASIGLAS. These glasses have been prepared by melt route and with compositions close to $Na_{1+x}Zr_{2-x/3}Si_xP_{3-x}O_{12-2x/3}$. Phosphorous was introduced as Na_3PO_4 along with other oxides. The conductivities at

300°C and the activation barriers are given in Table 6.7. It is evident that activation barriers in these glasses are generally higher although the conductivities are similar.

Doping chalcogenide FIC glasses with oxide glasses increases conductivity. For example by optimally doping $0.6Li_2S \cdot 0.4SiS_2$ glass

Table 6.7: Ionic conductivities of NASIGLAS $Na_{1+x}Zr_{2-x/3}Si_xP_{3-x}O_{12-2x/3}$ at 300°C (After Susman et al., 1983).

x	$\sigma_{300^\circ C}$ $(\Omega^{-1}cm^{-1})$	E_σ (eV)
3.00	1.23 – 2.1	0.55
2.75	1.93	0.55
2.50	1.10	0.61
2.25	1.55	0.61
crystalline 3.0	1.6 - 4	0.44

with about 5% Li_4GeO_4 glass, it is found that the conductivity increases. The dopant generates non-bridging sulphur in the structure and at the same time bridging oxygens are formed by exchange of the modification roles of oxide and sulphide ions. The observed increase in Li^+ ion mobilities (Tatsumisago et al., 1997) is attributed to this effect.

Na^+ ion containing glasses have also been known to exhibit high conductivities. For example, $50(0.7TeO_2 \cdot 0.3V_2O_5) \cdot 50Na_2O$ glass exhibits Na^+ ion conductivity of the order of 10^{-3} Scm^{-1}at room temperature.

Protonic FIC glasses

We very briefly refer to H^+ ion (protonic) conductors here just for purposes of comparison. Hodge and Angell (1977) have examined the conductivities of and relaxation behaviour in protonic conductors. Some of the relevant data are presented in Table 6.8.

The first thought that conductivities should be very high because proton is the lightest and the smallest ion conceivable, appears quite wrong. Proton conducting glasses generally exhibit poor d.c. conductivity and very low diffusion coefficients. The $\langle \tau_\sigma \rangle$ values are also relatively high.

Table 6.8: D.c. conductivities and derived quantities for acid and salt solutions at their glass transition temperature T_g (After Hodge and Angell, 1977)

System	T_g K	σ_{dc} $\Omega^{-1}cm^{-1}$	E_{act} (T_g) Observed Kcal $mole^{-1}$	$\langle\tau_\sigma\rangle$ sec	D cm^2sec^{-1}
$H_2Cr_2O_7.6\ H_2O$	161.9	4.0×10^{-9}	31	1.3×10^{-4}	5.6×10^{-14}
$HZn_2Cl_5.4\ H_2O$	185.6	8.9×10^{-9}	34	9.9×10^{-5}	2.9×10^{-13}
$HZnCl_3.4\ H_2O$	169.5	7.7×10^{-9}	34	1.1×10^{-4}	1.7×10^{-13}
$H_3Zn_2Cl_7.12H_2O$	164.3	4.4×10^{-9}	28	1.8×10^{-4}	9.1×10^{-14}
$H_2ZnCl_4.10\ H_2O$	152.0	3.5×10^{-10}	24	1.9×10^{-3}	6.4×10^{-15}
$H_2ZnCl_4.12\ H_2O$	147.1	2.7×10^{-10}	36	2.4×10^{-3}	5.3×10^{-15}
$HCl.6\ H_2O$	128.2	2.0×10^{-12}	-	2.6×10^{-1}	3.0×10^{-17}
$Li_3Zn_2Cl_7.12H_2O$	163.9	5.5×10^{-12}	42	9.6×10^{-2}	1.1×10^{-16}

References:

Anderson, O.L. and D.A. Stuart, 1954, J Am. Ceram. Soc., **37**, 573.

Angell, C.A., 1983, Solid State Ionics, **9-10**, 3.

Angell, C.A., 1990, Chem. Rev., **90**, 523.

Angell, C.A., 1992, Ann. Rev. Phys. Chem., **43**, 693.

Angell, C. A., 1986, Solid State Ionics, **18-19**, 72.

Angell, C.A., 1998, Solid State Ionics, **105**, 15.

Balasubramanian, S. and K.J. Rao, 1993, J. Phys. Chem., **97**, 8835.

Burckhardt, W., M. Makyta, A. Levasseur and P. Hagenmuller, 1984, Mater. Res. Bull. **19**,1083.

Carrete, B., M. Ribes and J.L. Souquet, 1983, Solid State Ionics, **9-10**, 735.

Chiodelli, G. and A. Magistris, M. Villa and J.L. Bjorkstam, 1982, J. Non-Cryst. Sol., **51**, 143.

Day, D.E., 1976, J.Non-Cryst. Sol., **21**, 343.

Day, D.E., 1972, Amorphous Materials, ed. R.W. Douglas and B. Ellis, (Wiley Interscience) pp39.

Downing, H.L., N.L. Peterson and H. Jain, 1982, J. Non-Cryst. Sol., **50**, 203.

Elliott, S.R., 1994, J. Non-cryst. sol., **172-174**,1343.

Finleyson, D.M., G.A. Leiper and C.A. Vincent, 1980, Solid St. Commun., **36**, 261.

Glass, A.M. and K. Nassau, 1980, J. App. Phys., **51**, 3756.

Goodman, C.H.L., 1985, Phys. Chem. Glasses, **26**, 1.

Greaves, G.N., S.J. Gurman, C.R.A. Catlow, A.V. Chadwick, S. Houde-Walter, C.M.B. Henderson and D.B. Dobson, 1991, Philos. Mag. A., **69**, 1059.

Hakim, R.M. and D.R.Uhlmann, 1967, Phys. Chem. Glasses, **8**, 174.

Han, Y.H., N.J. Kreidl and D.E. Day, 1979, J. Non-Cryst. Sol., **30**, 241.

Hanaya, M., M. Nakayama, A. Hatate and M. Oguni, 1995, Phys. Rev. B, **52**,3234.

Hendrickson, J.R. and P.J. Bray, 1972, Phys. Chem. Glasses, **13**, 43.

Hendrickson, J.R. and P.J. Bray, 1974, J. Chem. Phys., **61**, 2754.

Hirai, K., M. Tatsumisago and T. Minami, 1995, Solid State Ionics, **78**, 269.

Hodge, I. M., and C. A. Angell, 1977, J. Chem. Phys., **67**,1647.

Howell F.S., R.A. Bose, P.B. Macedo and C.T. Moynihan, 1974, J.Phys.Chem., **78**, 639.

Hughes, K. and J.O.Isard, 1972, Physics of Electrolytes, vol.I, Ed. J.H. Hladik, Academic Press, New York, pp351.

Hunter, C.C. and M.D. Ingram, 1984, Sol. State Ion., **14**, 31.

Hyde, J.M., M. Tomozawa and M. Yoshiyagawa, 1987, Phys. Chem. Glasses, **28**, 174.

Ingram, M.D., 1987, Phys. Chem. Glasses, **28**, 215.

Ingram, M.D., C.T. Moynihan and A.V. Lesikar, 1980, J. Non-cryst. Sol., **38-39**, 371.

Ingram, M.D., M.A. Mackenzie, W. Muller and M. Torge, 1988, Solid State Ionics, **28-30**, 677.

Ingram,M.D, C.T. Moynihan and H. Dietzel, 1983, Phys. Chem.Glasses, **24**,172.

Jain, H. and N.L. Peterson, 1983, J.Am.Ceram. Soc., **66**, 174.

Kawamura, J. and M.Shimoji, 1986, J. Non-Cryst. Sol., **88**, 295.

Kone, A., J.C. Reggiani and J.L. Souquet , 1983, Solid State Ionics, **9 & 10**, 709.

Kulkarni, A.R. and C.A. Angell, 1988, J. Non-Cryst. Sol, **99**, 195.

LeClaire, A.D., 1970, in Physical Chemistry, eds. H. Eyring, D. Handerson and W. Jost, vol 10 (Academic Press, New York).

Levasseur, A., B. Cales, J.M. Reau and P. Hegenmuller, 1978, Mat. Res. Bull., **13**, 205.

Levasseur, A., J.C. Brethaus, J.M. Reau and P. Hegenmuller, 1979, Mat. Res. Bull., **14**, 921.

Lidiard, A.B., 1957, Handbuch de Physik, **20**, 246.

Liu, C. and C.A. Angell, 1986, J. Non-Cryst. Sol., **83**,162.

Maas, P., A. Bunde and M.D. Ingram, 1992, Phys. Rev. Lett., **68**, 3064.

Magistris, A., G. Chiodelli, M. Duclot, 1983, Solid State Ionics, **9 & 10**, 611.

Malugani, J.P., B.Fahys, R.Mercier, G.Robert, J.P. Duchange, S. Baudry, M.

Broussely, J.P. Gabano, 1983, Solid State Ionics, **9&10**, 659.

Martin, S.W. and C.A. Angell, 1986, J. Non-cryst. Sol., **83**, 185.

Mazurin, O.V., 1965, Structure of glass, vol. **4**, Consultants Bureau, New York, pp5.

McElfresh, D.K. and D.G. Howitt, 1986, J. Am. Cer. Soc. **69**, c-237.

McVay, G.L. and D.E. Day, 1970, J. Am. Ceram. Soc., **53**, 508.

Mercier, R., J.P. Malugani, B. Fahys and G. Robert, 1981, Solid State Ionics, **5**,663.

Minami, T., 1985, J. Non-cryst. Sol., **73**, 273.

Molinelli, J., M.Tomozawa and M. Takata, 1985, J. Am. Ceram. Soc. **68**, 165.

Moynihan, C.T., N. Balitactac, L. Boone and T.A. Litovitz, 1971, J.Chem. Phys. **55**, 3013.

Mundy, J.N., and G.L Jin, 1986, Solid State Ionics, **21**, 305.

Nassau, K., A.M. Glass, M. Grasso and D.H. Olson, 1980, J. Electrochem. Soc., **127**, 2743.

Ngai, K. L. and H. Jain, 1986, Solid State Ionics, **18 & 19**, 362.

Otto, K.,1966, Phys. Chem. Glasses, **7**, 29.

Phillips, J.C., 1976, J. Elecrochem. Soc., **123**, 934.

Pradel, A. and M. Ribes, 1994, J.Non-Cryst.Solids, **172-174**, 1315.

Rao, K. J, C. Estournes, A. Levasseur, M.C.R. Shastry and M. Menetier, 1993, Philos. Mag. B, **67**, 389.

Ravaine, D. and J.L.Souquet, 1977, Phys. Chem. Glasses, **18**, 27.

Ribes, M, B. Barrau and J. L . Souquet, 1980, J. Non-Cryst. Sol., 38-39, 271.

Shastry, M.C.R., K.J. Rao, A. Levasseur and M. Menetrier, 1993, Solid State Ionics, **62**, 5.

Shastry, M.C.R. and K.J. Rao, 1989, Solid State Ionics, **37**, 17.

Simmons. C.J and J.H. Simmons, 1979, J. Am. Ceram. Soc., **62** (9-10), 479.

Stevels, J.M., 1951, Verres. et. Refract., **5**, 4.

Rao, K.J., and H.G.K. Sundar, 1980, Phys. Chem. Glasses, **21**, 216.

Susman, S., C.J. Delbecq, J.A. McMillan and M.F. Roche, 1983, Solid State Ionics, **9&10**, 667.

Swenson, J., R.L. McGreevy, L.Börjesson, J.D. Wicks, 1998, Solid State Ionics, **105**, 55.

Tatsumisago, M., K. Hirai, T. Minami and M. Takahashi, 1997, Phys. Chem. Glasses, **38**, 63.

Tatsumisago, M., A. Hamada, T. Minami and M. Tanaka, 1985, J.Am. Cer. Soc., **66**, 890.

Tomozawa, M., 1993, J. Non-Cryst. Sol., **152**, 59.

Tsuchiya, T. and T. Moriya, 1980, J. Non-Cryst. Sol., **38-39**, 323.

Tuller, H.L., D.P.Button and D.R. Uhlmann, 1980, J. Non-cryst. Sol., **40**, 93.

Zhong, J. and P.J. Bray, 1989, J. Non-cryst. Sol., **111**, 67.

Clear writers like fountains do not seem so deep
as they are; the turbid looks the most profound.
- W.S. Landor.

CHAPTER 7

A. C. CONDUCTIVITY

When an alternating electric field (a.c.) is applied across an insulator, a time dependent polarization current flow is induced. This is because the electrical charges present in the atoms and molecules in the material respond to the changing directions of the field. This is also referred to as dielectric response of the material. When the frequency of the applied field is well below the phonon frequencies, the dielectric polarization of the bound charges is instantaneous. Therefore, the dielectric constant, $\varepsilon(\infty)$, characterizing the bound charge response, is frequency independent. The frequency dependent part of dielectric constant is by definition related to the frequency dependent conductivity, $\sigma^*(\omega)$ as

$$\sigma^*(\omega) - \sigma(0) = i\omega[\varepsilon(\omega) - \varepsilon(\infty)]\varepsilon_0 \tag{7.01}$$

$\sigma^*(\omega)$ itself can be written as

$$\sigma^*(\omega) = \sigma'(\omega) + i\sigma''(\omega) \tag{7.02}$$

$\sigma^*(\omega)$ is the frequency (ω) dependent conductivity, $\sigma(0)$ is the zero frequency conductivity, $\varepsilon^*(\omega)$ is the frequency dependent dielectric constant and $\varepsilon(\infty)$ is the high frequency limiting value of ε. σ' and σ'' are the real and imaginary parts of the conductivity. Implied in equation (7.02) is that $\sigma''(\omega)$ is not equal to zero and indicates the presence of a phase difference between the applied field and free charge current. The most fascinating aspect of a.c. conductivity is that $\sigma(\omega)$ of solids at high frequencies in general are quite similar, whether they are glasses, polycrystalline semi-conductors, polymers, transition metal oxide or even organic-inorganic composites (Overhof, 1998). This represents an as yet unclearly understood *universality*; which transcends the differences in conduction mechanisms, because, while ionic conductivity arises by a barrier crossing process, electronic conduction occurs via a quantum mechanical tunneling between localized states. Taylor (1956, 1957, 1959)

was the first to recognize the universality in a.c. conductivity behaviour which is represented in the Taylor-Isard scaling function (Isard, 1961)

$$\tilde{\sigma} = \frac{\sigma(\omega)}{\sigma(0)} = f\left(\frac{C\omega}{\sigma(0)}\right) \tag{7.03}$$

where $\tilde{\sigma}$ is the scaled conductivity and C is proportional to $1/T$. This relation has been widely used in the literature and we will see later that a scaling function used by Roling et al. (1997) is of the Taylor-Isard class.

Important and common characteristics of a.c. conductivity behaviour have been excellently summarized by Dyre and Schrøder (2000) recently. They are as follows: (1) Real part of a.c. conductivity increases with frequency. (2) At high frequencies $\sigma'(\omega)$ varies as ω^s where s is a constant. (3) s itself exhibits a weakly increasing dependence on frequency and generally lies between 0.6 and 1.0. (4) It is generally observed that in a fixed frequency range s increases to unity as temperature tends to zero – s is close to unity when d.c. conductivity itself tends to zero. (5) The power law regime of conductivity has much lower temperature dependence than the d.c. conductivities, and when s is close to unity σ' is almost temperature independent. (6) a.c. conductivity obeys time-temperature superposition principle, in the sense that the shape of $\sigma'(\omega)$ in a log-log plot is temperature independent and therefore, the plots can be collapsed onto a master curve through suitable scaling. (7) The master curve itself is approximately same for all disordered solids, which is the essence of universality. (8) A dielectric loss peak is observed only when $\sigma(0)$ or σ_{dc} is measurable. (9) The dielectric loss peak occurs around the frequency, ω_m, which corresponds to the onset of a.c. conduction. (10) ω_m itself satisfies Barton-Nakajima-Namikawa (BNN) relation (Barton, 1966; Nakajima, 1972; Namikawa, 1975), $\sigma(0) = p\Delta\varepsilon\,\varepsilon_0\omega_m$ where p is a numerical constant of the order of unity. $\Delta\varepsilon = (\varepsilon(0)-\varepsilon(\infty))$ is the dielectric strength and ω_m is the frequency of the dielectric loss peak. (11) $\Delta\varepsilon$ itself is virtually independent of temperature and therefore, the temperature dependence of $\sigma(0)$ and ω_m are expected to be the same and hence the corresponding activation energies.

The validity of BNN relation has been verified experimentally as shown in Figure 7.01. BNN relation also provides a method of scaling the frequencies, which has been used recently by Sidebottom (1999) and we will refer to it later. Much of the experimental and theoretical work in the area of a.c. conduction in glasses is devoted to understanding the above

general observations. The dielectric behaviour and a.c. conductivity are completely interrelated. We first collect some of the relevant definitions and formulae, which helps us follow the rather enormous work presently carried out in this field.

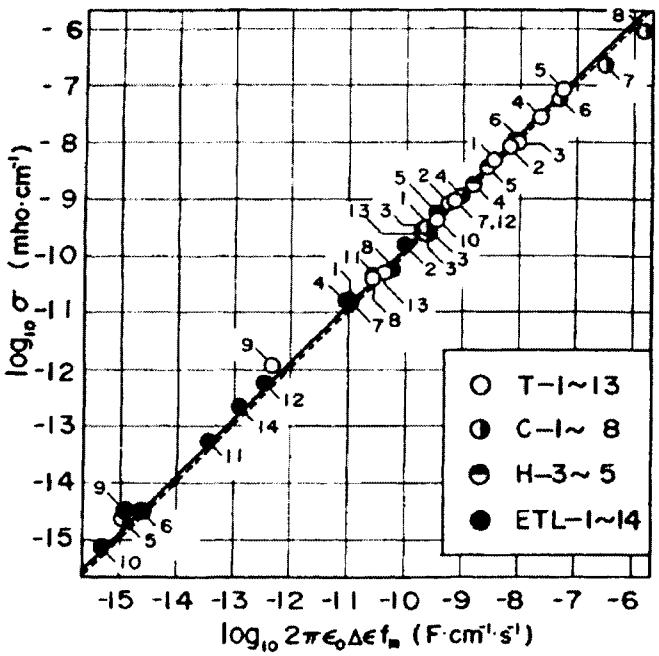

Figure 7.01. Test of Barton-Nakajima relation for 40 different alkali ion conducting oxide glasses. (after Dyre and Schrøder, 2000)

A.c. conductivity and dielectric quantities

When a field $\boldsymbol{E}$ is applied across a dielectric (a simple parallel plate condenser, for example), the resulting displacement current, $\boldsymbol{D}$ is related to $\boldsymbol{E}$ as $\boldsymbol{D} = \tilde{\varepsilon}\boldsymbol{E}$. In glasses, which are dielectrically isotropic, the permittivity, $\tilde{\varepsilon}$ behaves as a scalar quantity and is equal to $|\boldsymbol{D}|/|\boldsymbol{E}|$. While $\boldsymbol{E}$ is an experimentally controlled alternating field of arbitrary frequency, $\boldsymbol{D}$ and ε are the material dependent responses and $\boldsymbol{D}$, which represents the polarization current is not always in phase with $\boldsymbol{E}$. ε is, therefore, a complex frequency dependent quantity. The complex permittivity, ε^*, is defined as

$$\varepsilon^* = \varepsilon' - i\varepsilon'' \tag{7.04}$$

Using the relation $\varepsilon'' = \sigma/(\omega\varepsilon_0)$,

$$\varepsilon^* = \varepsilon' - i\left(\frac{\sigma}{\omega\varepsilon_0}\right) \tag{7.05}$$

where ε' and ε'' are the relative permittivity (dielectric constant) and the dielectric loss respectively and $\sigma = \sigma(\omega)$ is the a.c. conductivity, ω is the angular frequency and ε_0 is the permittivity of free space. Since ionic glasses exhibit significant d.c. conductivities $\sigma(0)$, the above expression is to be modified to include $\sigma(0)$

$$\varepsilon^* = \varepsilon' - i\left(\varepsilon'' - \frac{\sigma(0)}{\omega\varepsilon_0}\right) \tag{7.06}$$

The frequency dependent behaviour of ε^*, therefore, depends on the response of the polarization to the applied field. The above relation can be recast into the form cited at the beginning. The change of polarization direction in response to the external field is characterized by a time constant of the material, known as relaxation time τ. When the material has a single relaxation time, this relation can be reduced to,

$$\varepsilon^* = \varepsilon_2 + (\varepsilon_1 - \varepsilon_2)\left(\frac{1}{(1 + i\omega\tau)}\right) \tag{7.07}$$

ε_1 is the limiting value of ε' for $\omega\tau << 1$ and ε_2 is the limiting value for $\omega\tau >> 1$. The dielectric dispersion however occurs over a broad frequency range and requires the use of a distribution of relaxation times to fit the dielectric data. Polarization itself involves movement of ions which in glasses occurs by the barrier hopping. Since there is a distribution of such barriers in glasses, it results in a distribution of relaxation times.

Modulus representation

In the analysis of the relaxation data we often need to represent the dielectric as a combination of pure resistances and capacitances. The manner of their connection in the dielectric is also assumed. It is through the use of such circuit representation that the dielectric data are analysed.

Relaxations in such assumed circuits can proceed through two independent processes known as *serial* and *parallel* processes. Macedo et al. (1972) proposed on the basis that impedances (and not admittances) are additive in a series process, use of a dimensionless parameter, $M^* = 1/\varepsilon^*$, as appropriate for the analysis of conductivity relaxation. M^*, therefore, is also resolved into real and imaginary parts as:

$$M^* = \frac{1}{\varepsilon^*} = \frac{\varepsilon'}{(\varepsilon'^2 + \varepsilon''^2)} + \frac{i\varepsilon''}{(\varepsilon'^2 + \varepsilon''^2)} \tag{7.08}$$

Re-expressing the earlier definition (equation 7.06) of ε^* for an ionically conducting glass, using ε_s to represent the frequency independent dielectric constant and $\sigma(0)$ the conductivity,

$$\varepsilon^* = \varepsilon_s - \left(\frac{i\sigma(0)}{\omega\varepsilon_0}\right) \tag{7.09}$$

We may introduce two new parameters τ_σ ($= \varepsilon_0\varepsilon_s/\sigma(0)$) and M_s ($= 1/\varepsilon_s$) and combine the three equations to obtain

$$M^* = M_s\left(\frac{i\omega\tau_\sigma}{(1 + i\omega\tau_\sigma)}\right) = M_s\left[\frac{(\omega\tau_\sigma)^2 + i\omega\tau_\sigma}{1 + (\omega\tau_\sigma)^2}\right]$$

$$= M' + iM'' \tag{7.10}$$

τ_σ is known as the conductivity relaxation time and represents the electric field ($\boldsymbol{E}$) decay in an ionic glass (assuming the displacement vector to be a constant) and is defined by the relation:

$$\boldsymbol{E} = \boldsymbol{E}_o \exp\left(-\frac{t}{\tau_\sigma}\right) \tag{7.11}$$

The above expression suggests that in the limits $\omega\tau_\sigma << 1$ and $\omega\tau_\sigma >> 1$, M' becomes zero and $1/\varepsilon_s$ respectively. Similarly M'' for the same limits would be identically zero and gives rise to a peak in M'' at $\omega\tau_\sigma = 1$. The fact that M' becomes zero at low frequencies indicates that in a static electric field, there is no restoring force for the flow of charge and

therefore, it is very similar to the behaviour of real part of the shear modulus G′ in a viscous liquid at the low frequencies. When the conductivity is governed by a distribution of relaxation times instead of a single τ_σ, the corresponding relation is

$$M^* = M_s \int_0^\infty g(\tau_\sigma) d\tau_\sigma \left[\frac{(\omega\tau_\sigma)^2 + i\omega\tau_\sigma}{1+(\omega\tau_\sigma)^2} \right] \tag{7.12}$$

$$\equiv M_s \left\langle \frac{(\omega\tau_\sigma)^2 + i\omega\tau_\sigma}{1+(\omega\tau_\sigma)^2} \right\rangle \tag{7.13}$$

since the integral represent the expectation value for the quantity in the square bracket. By the introduction of a distribution of relaxation times $g(\tau_\sigma)$,ε' and ε'' relations also get modified.

$$\varepsilon' = \frac{M'}{(M'^2 + M''^2)} \tag{7.14}$$

$$= \frac{1}{M_s} \left[\frac{\left\langle \frac{(\omega\tau_\sigma)^2}{(1+(\omega\tau_\sigma)^2} \right\rangle}{\left\langle \frac{(\omega\tau_\sigma)^2}{(1+(\omega\tau_\sigma)^2} \right\rangle + \left\langle \frac{\omega\tau_\sigma}{(1+(\omega\tau_\sigma)^2} \right\rangle} \right] \tag{7.15}$$

It is immediately recognized that in the limit of $\omega\tau_\sigma << 1$

$$\varepsilon'(0) = \left(\frac{1}{M_s} \right) \frac{\langle \tau_\sigma^2 \rangle}{\langle \tau_\sigma \rangle^2} = \varepsilon_s \frac{\langle \tau_\sigma^2 \rangle}{\langle \tau_\sigma \rangle^2} \tag{7.16}$$

and for $\omega\tau_\sigma >> 1$,

$$\varepsilon'(\infty) = \frac{1}{M_s} = \varepsilon_s \tag{7.17}$$

Thus the dispersion in ε' as a consequence of introducing a distribution of

conductivity relaxation times, has a magnitude of

$$\varepsilon'(\infty)-\varepsilon'(0)=\frac{\langle\tau_\sigma^2\rangle-\langle\tau_\sigma\rangle^2}{\langle\tau_\sigma\rangle^2} \tag{7.18}$$

Obviously, there is no dispersion when there is a single relaxation time. The dispersion in conductivity itself can be determined from the relation

$$\sigma=\omega\varepsilon_0\varepsilon''=\omega\varepsilon_0\left[\frac{M''}{M'^2+M''^2}\right] \tag{7.19}$$

$$=\omega\varepsilon_0\varepsilon_s\left[\frac{\left\langle\frac{\omega\tau_\sigma}{1+(\omega\tau_\sigma)^2}\right\rangle}{\left\langle\frac{(\omega\tau_\sigma)^2}{(1+(\omega\tau_\sigma)^2}\right\rangle^2+\left\langle\frac{\omega\tau_\sigma}{1+(\omega\tau_\sigma)^2}\right\rangle^2}\right] \tag{7.20}$$

Limiting value of σ for $\omega\tau_\sigma << 1$ is equal to σ (0) which is the d.c. conductivity and is given by,

$$\sigma(0)=\frac{\varepsilon_0\varepsilon_s}{\langle\tau_\sigma\rangle}=\frac{\varepsilon_0}{M_s\langle\tau_\sigma\rangle} \tag{7.21}$$

The other limit of σ, for $\omega\tau_\sigma >> 1$ is given by,

$$\sigma(\infty)=\varepsilon_0\varepsilon_s\left\langle\frac{1}{\tau_\sigma}\right\rangle \tag{7.22}$$

The above expression is consistent with the fact that there is no dispersion in the conductivity for the case of a single relaxation time. When there is a distribution of relaxation times, $1/\langle\tau_\sigma\rangle < \langle 1/\tau_\sigma\rangle$ and therefore, $\sigma(0) < \sigma(\infty)$. Similarly, it can be shown that the low and high frequency limit of ε'' are respectively $\varepsilon_s/(\omega\langle\tau_\sigma\rangle)$ and $\varepsilon_s/(\omega\langle 1/\tau_\sigma\rangle)$. Since $\langle 1/\tau_\sigma\rangle$ is greater than $1/\langle\tau_\sigma\rangle$, ε'' in the high frequency limit represents an excess loss. Most ionic conductors on which measurements have been made can be represented by equivalent circuits of the type shown in Figure 7.02. The complex moduli

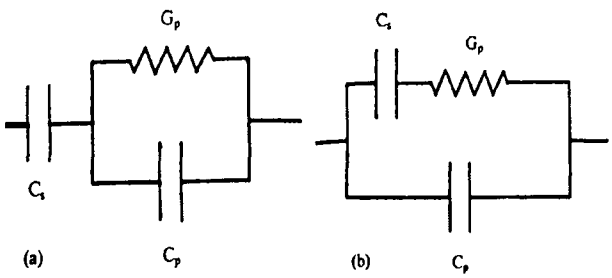

Figure 7.02. Experimental circuits for ionic conductors.

corresponding to the equivalent circuits are both equal to

$$M^* = \frac{1}{\varepsilon^*} = \frac{1}{\varepsilon_1} + \left(\frac{1}{\varepsilon_2}\right)\left(\frac{i\omega\tau_\sigma}{(1+i\omega\tau_\sigma)}\right) \tag{7.23}$$

where ε_1 and ε_2 are the dielectric constants due to series and parallel capacitances respectively. Since $\varepsilon_1 >> \varepsilon_2$, it is seen that M^* values are unaffected by ε_1, which generally represents the capacitance which is present at the electrode interface. This is an advantage in the analysis of dielectric data using modulus formalism and accounts for its wide application.

An alternate way of formulating the electric moduli is to represent it as:

$$M^*(\omega) = M' + iM''$$

$$= M_s\left[1 - \int_0^\infty dt \exp(-i\omega t)\left(-\frac{d\phi(t)}{dt}\right)\right] \tag{7.24}^{\#}$$

$$= M_s \int_0^\infty d\tau_\sigma\, g(\tau_\sigma)\left(\frac{i\omega\tau_\sigma}{(1+i\omega\tau_\sigma)}\right) \tag{7.25}$$

where

The second term is evaluated by obtaining Laplace transform of $(-d\phi/dt)$. This has been achieved by Moynihan et al. (1973) for β values other than 0.5 and 1.0 by elegantly expanding $\phi(t)$ in 14 terms. β can therefore be obtained by interpolating in graphs of these β values vs R where R is the ratio of FWHM (M″ peaks) to Debye width (1.144).

$$M_{\infty} = \lim_{\omega \to \infty} M' = \frac{1}{(\lim_{\omega \to \infty} \varepsilon')} = \frac{1}{\varepsilon(\infty)} \tag{7.26}$$

The limiting low frequency dielectric constant ε(0) and the limiting high frequency dielectric constant ε (∞) are related as

$$\varepsilon(0) = \lim_{\omega\tau_{\sigma} << 1} \varepsilon' = \varepsilon(\infty) \frac{\langle \tau_{\sigma}^{2} \rangle}{\langle \tau_{\sigma} \rangle^{2}} \tag{7.27}$$

Dielectric constant and conductivity are simply related to moduli as

$$\varepsilon^{*} = \varepsilon' - i\varepsilon'' = \frac{1}{M^{*}} \tag{7.28}$$

$$\sigma = \sigma' + i\sigma'' = \frac{i\omega\varepsilon(0)}{M^{*}} \tag{7.29}$$

The time scale of the electric field relaxation is given by $\langle \tau_{\sigma} \rangle = \int_{0}^{\infty} \phi(t) dt$.

This in its turn is related to the d.c. conductivity, σ(0) as

$$\sigma(0) = \frac{\varepsilon_{0}\varepsilon(\infty)}{\langle \tau_{\sigma} \rangle} \tag{7.30}$$

A good example of the analysis of the dielectric data using modulus representation is that of the CKN glass (0.4 $Ca(NO_3)_2 \cdot 0.6\ KNO_3$ glass), which is widely cited in the literature. It is shown in Figure 7.03.

$\phi(t) = \exp[-\left(\frac{t}{\tau}\right)^{\beta}]$ has been used to fit the observed M^{*} data. $\langle \tau_{\sigma} \rangle$ and $\langle \tau_{\sigma}^{2} \rangle$ were then calculated using the expressions involving Gamma functions (Γ)

$$\langle \tau_{\sigma} \rangle = \left(\frac{\tau_{0}}{\beta}\right) \Gamma\left(\frac{1}{\beta}\right) \tag{7.31}$$

and

$$\langle \tau_{\sigma}^{2} \rangle = \left(\frac{\tau_{0}^{2}}{\beta}\right) \Gamma\left(\frac{2}{\beta}\right) \tag{7.32}$$

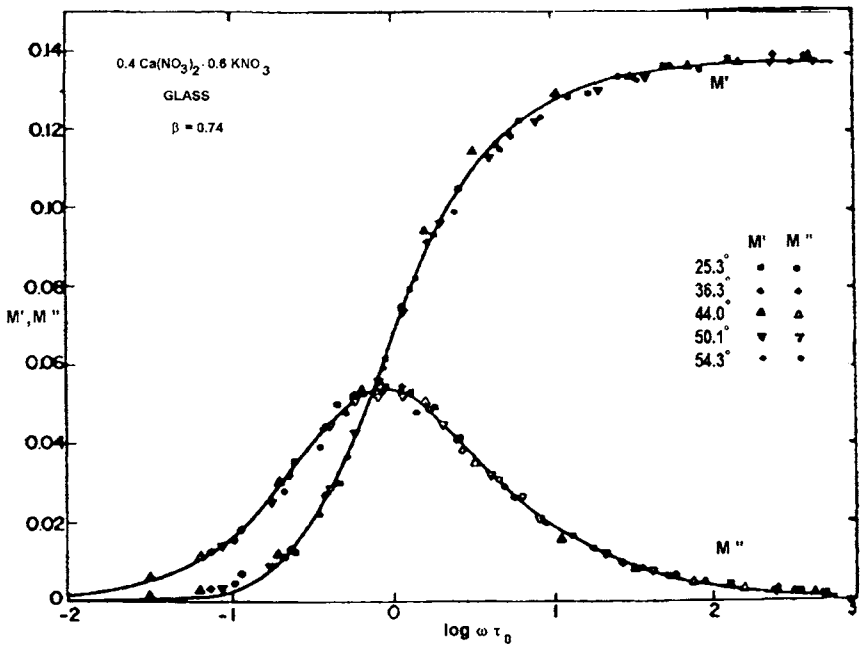

Figure 7.03. Real and imaginary parts of the electric modulus vs. reduced frequency $\omega\tau_0$ for 0.4 $Ca(NO_3)_2 \cdot 0.6KNO_3$ glass (After Howell et. al., 1974)

It may be noted that the modulus (M″) spectrum is expected to be Lorenztian if the relaxation process is simply exponential.

The dielectric modulus approach has been widely used in recent times in the analysis of dielectric data. But the standard method of using electrical modulus formalism has also been criticized (Elliott, 1994) in the literature for some of its limitations. First is that modulus is not a directly measurable quantity and is a function of other measured quantities like ε', ε'' and $\sigma(0)$. Secondly, the modulus is not directly related to any microscopic physical process even though it is obtained from the Laplace transformation of the time derivative of an electrical relaxation function $\phi(t)$, making it difficult for interpretation. Elliot has pointed out another important practical problem and that is the range of frequencies over which M'' (ω) is significantly non-zero. Since the conductivity increases according to power law in the region where M'' peak decreases towards zero on the high frequency side, larger range and more accurate σ measurements becomes essential in order to analyze M'' (ω) data. Often, $M''(\omega)$ peak occurs in a region where conductivity itself has no dispersion at all. However, the advantage of modulus formalism cannot be ignored.

Jain and Huang (1994) have argued that since M'' is calculated as $(\omega GC_0)/(G^2 + \omega^2C^2)$, ($C_0$ is the vacuum equivalent capacitance and C is the actual capacitance), the undesirable effects arising from the use of blocking electrode is suppressed. Further, measurements over only a limited range of frequency is needed (a few decades on either side of $\tau_{d.c} = CG$) in order to study the electrical relaxation, when modulus formalism is used.

Alternate formulation of dielectric data

Dielectric data itself is often presented as complex permittivities and susceptibilities. They are related as follows:

$$\chi^*(\omega) \equiv \frac{\varepsilon^*(\omega) - \varepsilon(\infty)}{\varepsilon_0} \tag{7.33}$$

$$= \chi'(\omega) - i\chi''(\omega) \tag{7.34}$$

where ε_0 is permittivity of free space and $\varepsilon(\infty)$ is a limiting high frequency permittivity. The emphasis in this formulation is on *parallel processes*, which contributes to the real and imaginary components of the polarization. We may recall that the dielectric modulus emphasizes a *series process*. The complex capacitance $C^*(\omega)$ is given by $(A/d)\varepsilon^*$, where A and d are the area and thickness of the dielectric respectively. The admittance of a sample represented by an equivalent circuit providing a parallel conductance $G(\omega)$ and capacitance $C(\omega)$ is given by

$$Y^*(\omega) = \frac{1}{Z^*(\omega)} = i\omega C^*(\omega) = G(\omega) + i\omega C(\omega) \tag{7.35}$$

The complex impedance $Z^*(\omega)$ of the sample is defined as the reciprocal of admittance and is equal to $1/Y^*(\omega)$, which again reverts the emphasis on to a series process.

We may note here for future discussion in this chapter that dielectric data is generally presented in a log-log form and a power function of ω is used to represent $\chi^*(\omega)$ and related quantities:

$$\chi^*(\omega) \propto (i\omega)^{n-1} \qquad \text{where } o<n<1 \tag{7.36}$$

The above function is known as *universal law* and can be seen to be equivalent to

$$\chi^*(\omega) \propto \{\omega \exp(i\pi/2)\}^{n-1} \tag{7.37}$$

$$\propto \omega^{n-1}[\cos\{(n-1)\frac{\pi}{2}\} + i\sin\{(n-1)\frac{\pi}{2}\}] \tag{7.38}$$

That the electric polarization (other than the instantaneous electronic part) of materials is due to the presence of electrical dipoles and that they respond to applied alternating electric field is a concept first introduced by Debye (1929). The Debye function is given by

$$\chi^*(\omega) = \frac{B}{1 + i(\omega/\omega_p)} \tag{7.39}$$

$$= B\left(\frac{1 - i\omega/\omega_p}{1 + \omega^2/\omega_p^2}\right) \tag{7.40}$$

where B is a constant and ω_p is the frequency of the dielectric loss peak. It may be noted that Debye relaxation corresponds in time domain to the existence of a single relaxation time ($\tau_p = 1/\omega_p$). When χ'' is plotted as a function of ω, a Debye loss peak is observed whose characteristic width is 1.144 decades. However, when the polarization arises mainly due to the response of hopping charge carriers of low mobility such as in ionic conductors, the materials may not exhibit loss peaks. Instead, at high frequencies, they exhibit relatively shallow fractional power law with exponents $0.1 < (1\text{-}n) < 0.3$. Since the power law behaviour is common to both dipole and charge carriers at high frequencies, it is referred to as *universal dielectric response*. It is universal in the sense the ratio $\chi''(\omega)/\chi'(\omega)$ is independent of frequency and equal to cot $(n\pi/2)$. The physical significance of this simple property is that when a dielectric is subjected to an external field, the ratio of the macroscopic energy lost per radian (χ'') to the energy stored at the peak (χ') is independent of frequency (Jonscher, 1977, 1983, 1996). Therefore, in the analysis of the dielectric data, observation of frequency independent energy relation enables fitting the dielectric spectrum with a power law with the exponent $(1\text{-}n)$.

Departure from the Debye behaviour of the relaxation phenomena

is immediately recognized in the $\chi''(\omega)$ vs ω plots because the FWHM exceeds 1.144 decades. Generally the departure is understood as either due to the presence of a distribution of relaxation times or due to the stretching of relaxation times. The latter requires the use of the Kohlrausch-Williams-Watts stretched exponential (KWW) function[#] for the analysis of the dielectric spectrum. Use of KWW function is perhaps more appropriate because an approximate derivation of the KWW function is provided by the coupling model (see later). Also, Weron (1991, 1992) who treated relaxation as a stochastic process has, on a strictly mathematical basis, shown that the relaxation function has the form of KWW expression. Thus, KWW function seems to be dictated by the stochastic nature of the relaxation process.

A word on the choice of the formalism for presenting the dielectric data is in order. The characteristic time of a process obtained from a given set of data depends on the formalism employed. Thus

$$\frac{\tau(\text{susceptibility formalism})}{\tau(\text{modulus formalism})} = \frac{\varepsilon_0}{\varepsilon_\infty} = \frac{M_\infty}{M_0} \tag{7.41}$$

It may however, be noted that among many ways of presenting the data of ionically conducting dielectric materials, Dyre (1988) suggests that presentation of $\sigma(\omega)$ is preferable because conductivity is the more fundamental quantity as it is related to equilibrium current-current fluctuations through Kubo (1957) formula:

$$\sigma(\omega) = \frac{1}{3kTV}\int_0^\infty \langle \boldsymbol{J}(0).\boldsymbol{J}(t)\rangle \exp(-i\omega t)\, dt \tag{7.42}$$

where $\boldsymbol{J}$ is the total current in volume V, k is the Boltzmann constant and T is the temperature.

Theoretical models of a.c. conductivity

The early conductivity model of Stevels (1957) and Taylor (1956, 1959) is in a sense a *random potential energy model.* It is assumed in this model that the ions experience randomly varying potential energy which is due to the presence of a random structure. For the d.c. conduction, the

---

[#] It is interesting to note that the stretched exponential function was first used by Kohlrausch in his studies on electrical relaxation of leyden jar (a glassy ionic material) in 1847 (cited by Ngai, 1996).

charge carrier has to overcome the largest barrier for hopping to another site while for the a.c. conduction, the charge carrier hops over relatively lower barriers and hence the charge carrier travels a very limited distance. The hopping models, in general, assume that the charge carrier jump probabilities are time-independent and hence are Markovian. Hopping conductivity is thus well described by rate theory. The d.c. conductivity is recognized as $\sigma(0)$ in a.c. conductivity measurements. While $\sigma(0)$ often varies by several orders of magnitudes between different solids, $\sigma(\omega)$ for reasonably high values of ω varies relatively much less. This can be understood from Dyre's (1993) expression for a.c. conductivity,

$$\sigma(\omega) = \sigma(0)\left(\frac{i\omega\tau}{\ln(1+i\omega\tau)}\right) \tag{7.43}$$

From this expression, if $\sigma_1(\omega)$ and $\sigma_2(\omega)$ are the conductivities of two solids, then at high frequency ($\omega \rightarrow \infty$),

$$\frac{\sigma_1(\omega)}{\sigma_2(\omega)} = \frac{\sigma_1(0)\tau_1}{\sigma_2(0)\tau_2} = \frac{\Delta\varepsilon_1}{\Delta\varepsilon_2} \tag{7.44}$$

because, the dielectric strength, $\Delta\varepsilon$, is given by the relation:

$$\Delta\varepsilon = \left(\frac{1}{2}\right)\frac{\sigma(0)\tau}{\varepsilon_0} \tag{7.45}$$

Since $\Delta\varepsilon$ differs only little for various solids, the a.c. conductivities of most solids differ very little at high frequency.

Jump relaxation model

Funke (1993) proposed a jump relaxation model, based on the following plausible stages of ion transport. The charge carrier (ion) hops on atomic scales in both space and time. When an ion at time $t = 0$ hops from site A to a vacant neighboring site B, there are competing relaxation processes to consider. First, the ion may hop back to site A, which constitute the forward-backward hop. It is possible that before the ion decides to hop back, the surroundings of the new site relax in such a way that the ion finds the site as its new quasi-permanent address (like it was at site A before hopping). The probability, therefore, of finding the ion back

at site A is reduced. In general, the probability $W_A(t)$ of finding the ion back at site A is given by,

$$W_A(t) = 1 - \Gamma_0 \int_0^t W_A(t')W_A(t-t')dt' \tag{7.46}$$

Where Γ_0 is the temperature dependent hoping rate of the ion and $W_A(t)$ is the probability that the correlated backward hop has not yet been performed at time t. Solution of this rate equation provides the analytical relaxation function of Funke's jump relaxation model. In the model, it is also expected that the rising portion of ac conductivity (ω^s portion) should level off above ~200 GHz. But in this region there are the high frequency vibrational (IR) modes. IR absorption varies as ω^2 on the low frequency side of the IR band in this region as experimentally verified in 0.44 LiBr · 0.56 ($Li_2O \cdot B_2O_3$) glass. If this ω^2 dependent contribution to the conductivity is subtracted from the measured values, a leveling off of the conductivity is indeed found to occur.

Diffusion Controlled Relaxation model

Elliott (1987, 1988 and 1989) approached the relaxation problem differently. In his diffusion controlled relaxation (DCR) model, Elliott, like Charles (1961) considers ionic motion to occur by an interstitialcy mechanism. There is a local motion of cations (for example Li^+ ion in a silicate glass) among equivalent positions located around a NBO ion. Motions of cations among these positions causes the primary relaxational event and it occurs with a characteristic microscopic relaxation time τ. The process gives rise to a polarization current. However, when another Li^+ ion hops into one of the nearby equivalent positions with a probability $P(t)$, a double occupancy results around the anion and this makes the relaxation instantaneous. Since the latter process involves the diffusion of a Li^+ ion, the process as a whole involves both polarization and diffusion currents. Thus the relaxation function can be written as $[1\text{-}P(t)]\exp(-t/\tau)$. $[1\text{-}P(t)]$ is a function of the jump distance and the diffusion constant. Making use of the Glarum-Bordewijk relation (Glarum, 1960; Bordewijk, 1975) for $[1\text{-}P(t)]$ Elliott (1987) has shown that

$$\phi(t) = \exp\left[-\left(\frac{t}{\tau_1}\right)^{\frac{1}{2}}\right]\exp\left(-\frac{t}{\tau}\right) \tag{7.47}$$

where τ_1 is the effective relaxation time equal to $\pi l_0^2/4D$ where l_0 is a

characteristic jump distance and D is the diffusion coefficient. Equation (7.47) has the attraction that its Laplace transform can be determined numerically. Then a plot of $\chi''(\omega)$ against $\chi'(\omega)$ can be obtained. When the same plot is fitted to a Davidson-Cole function (see chapter 9), a β_{CD} can be determined. Elliott and co-workers have shown that this method indeed predicts a value of β_{CD} very close to β from the KWW expression ($\mathcal{L}(-\partial\phi/\partial t)$ - $\mathcal{L}$ indicates Laplace transform - and Davidson-Cole function were expanded and the coefficients were compared). Since β in $\phi(t) = \exp[-(t/\tau)^{\beta}]$, is related to s as $s = (1 - \beta)$, it has been shown that,

$$s = \left(\frac{\pi\tau}{4\tau_1}\right)^{\frac{1}{2}} = \left(\frac{D\tau}{l_0^2}\right)^{\frac{1}{2}} \tag{7.48}$$

Since τ is the relaxation time characterizing the motion of an ion between equivalent positions around a NBO, it is an activated process and has a temperature dependence

$$\tau = \tau_0 \exp\left(\frac{W}{RT}\right) \tag{7.49}$$

where W is the barrier for the above diffusion-independent motion. W can be calculated from the temperature dependence of dielectric loss peaks. D is given by $D = aT\sigma_{dc} = aT\sigma_0 \exp(-E_{dc}/RT)$ (D is temperature dependent) where E_{dc} is the activation barrier obtained from d.c. conductivity measurements. Equation (7.48) can therefore be written as

$$s = T^{\frac{1}{2}} b \exp\left[\frac{(W - E_{dc})}{2kT}\right] \tag{7.50}$$

where $b = (a\sigma_0\tau_0/l_0^2)^{1/2}$ and $a = k/ce^2$. k, e and c are the Boltzmann constant, electronic charge and concentration of (ionic) charge carries respectively. Equation (7.50) is interesting because it shows that s is not only temperature dependent but it also exhibits a minimum when $W\text{-}E_{dc} = kT$.

One of the advantages of the DCR model is that it provides an expression for s which rationalizes its temperature variation. However, the DCR model is based on the same assumptions as those made in Anderson-Stuart (1954) and Charles (1961) models to describe non-local and local

ionic motions. Rao et al. (1993, 1994) have addressed the problem of a.c. conductivity on the basis of ***vacancy model*** discussed in chapter 6. A potential energy profile along the migration path of the ion which is same as that of the vacancy is shown in Figure 7.04 (a) and for simplicity, is shown as a one dimensional conduction path. Sites 1, 2, 6 and 7 are

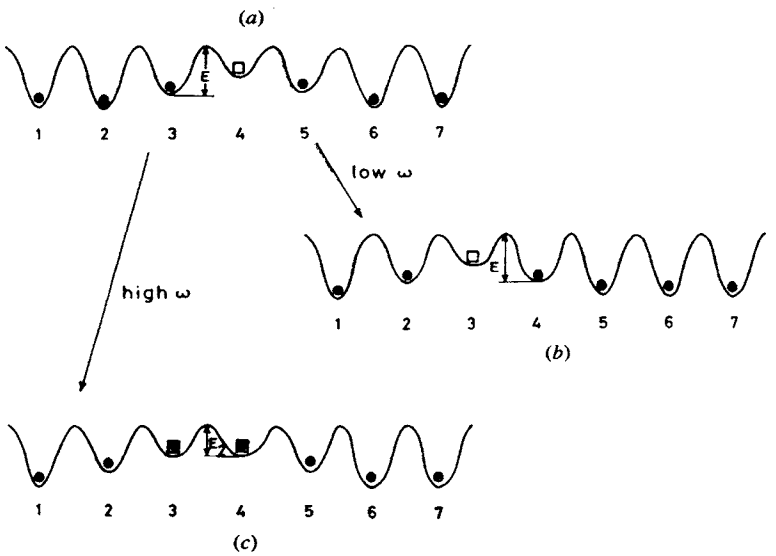

Figure 7.04. (One-dimensional) illustration of potential energy profiles relevant for vacancy-based ionic conduction. (a) before an ion hops into vacancy at site 4; (b) after the hopping of ion 3 into the vacancy; (c) the situation envisaged at high frequencies. (After Rao et al, 1994)

'normal' cation sites sufficiently removed from the vacancy and correspond to the deepest potential wells. The vacancy site 4 itself is characterized by a potential depth shallower than at sites 1 or 2. Sites 3 and 5 which are immediate neighbours of the vacancy have an intermediate depth. Because of the shallowness of the potential around the defect the barrier to migration of ions 3 or 5 into the vacancy is reduced and hence this migration is more favoured. When the migration of ion 3 (or 5) occurs, position 3 (or 5) becomes a vacancy and position 4 becomes a site like 3 was prior to becoming a vacancy, as shown in Figure 7.04(b). A reverse hopping (correlated hopping) occurs from 4 into 3 which is expected to be more facile than hopping to distant vacancies. This hopping process around a vacancy is governed by the relaxation time τ through the relation,

$$\phi(t) = \exp\left(-\frac{t}{\tau}\right) \tag{7.51}$$

The time τ characterizes the jump time within which all the induced dipoles switch over to new orientations. These jumps give rise to a polarization current (a.c.). Up to this point, the above description is rather similar to that visualized by Jonscher (1977) for relaxation in ionic solids. But now we may consider the possibility of a distant 'vagrant' ion such as the one at site 1 or 7 in Figure 7.04(a) hopping into a vacancy at 4. Suddenly the configuration relaxes into what appears like site 1, 2, 6 or 7. But a vacancy is created afresh far away from 4, where all the steps are recreated. The relaxation process associated with the vacancy 4 occurs according to equation (1) subject to the condition that a vagrant ion did not jump into the vacancy. If it did, we assume that the relaxation becomes instantaneous. Using the probability $P(t)$ for the arrival of the vagrant ion, the relaxation function is modified as,

$$\phi(t) = [1 - P(t)]\exp\left(-\frac{t}{\tau}\right) \tag{7.52}$$

$[1-P(t)]$ expresses the probability that normal relaxation occurs uninterruptedly. Equation (7.52) is identical in form with that used by Elliott in DCR model. The quantity $[1- P(t)]$ which characterizes the abrupt appearance of an ion from far away can be approximated by Glarum and Bordewijk expression,

$$[1 - P(t)] = \exp\left[-\frac{2}{l_0}\left(\frac{Dt}{\pi}\right)^{\frac{1}{2}}\right] \tag{7.53}$$

The behaviour of s as a function of temperature can be derived from equation (7.53) by the same approach as in DCR model. Although functionally DCR and vacancy models are identical, there are important differences. Firstly, the assumptions such as multiple occupancy around NBO site, etc. made in the DCR model are absent in the vacancy model. Secondly, vacancy model avoids being specific to a moderately modified network glass. The vacancy model itself is rather relevant for discussion of ion migration, because, when an alkali ion in its stable position jumps out of it, the vacated site in principle causes both electrical and elastic

discontinuity in the structure. In Figure 7.04, situations (a) and (b) are visualized as low frequency events. But at high frequencies the correlated jumps can not follow the field since relaxation times are still low. The situation is represented in 7.04(c) in which the effective activation barrier is lower than in 7.04(b).

Debye-Falkenhagen-Tomozawa effect

The origin of the non-Debye behaviour of relaxations has also been discussed in terms of interionic Coulombic interactions. Coulombic interactions of mobile ions can manifest in a broad relaxation spectrum, which is characteristic of glassy state relaxations. The influence of the structure of glass itself is then considered as secondary. Also, several conductivity data on alkali containing glasses indicate that they behave like weak electrolytes. Thus the mobile ion concentration in such glasses is in the Debye-Huckel regime. The broadening of the electrical relaxation spectrum may, therefore, be due to the relaxation of Debye-Huckel ion atmosphere, for which reason Tomozawa (1977) derived the dielectric functions using Debye-Falkenhagen theory (1934). The *Debye-Falkenhagen-Tomozawa* approach was extended by Lesikar et al. (1980). Since these concepts are important and can serve as the basis for further extension, a brief account is given below:

A typical network oxide glass, like alkali silicate, is assumed to consist of only immobile oxygen anions, whose negative charges are neutralized by the charges on mobile univalent cations. Thus each anion is surrounded by Debye-Huckel ion atmosphere of cations, which is characterized by a Debye screening parameter, K, the inverse of which is defined as the Debye screening length.

$$K^2 = \frac{2Ce^2}{\varepsilon(\infty)\varepsilon_0 kT} \tag{7.54}$$

where C is the average cation or anion concentration. When an electrical field is applied, cation drift occurs in response to the field, which gives rise to a polarization of the anion-cation complex. The polarization is opposed by a retarding coulombic force, arising from the center of gravity of positive and negative charges and this reduces the cation mobility. The relaxation of the ionic atmosphere in response to an alternating applied electrical field is characterized by the conductivity relaxation time, τ_σ. Since the change in the field direction cannot be followed at high

frequencies, the polarization disappears and, therefore, a dispersion takes place in the electrical conductivity, which shows up in the real part of the dielectric constant. The dispersion in the real part of the dielectric constant is also associated with the appearance of dielectric loss peak.

A.c. conductivity and NMR relaxation

Conductivity arises from ionic motions in response to the applied electrical field. The associated field fluctuations affect the nuclear spin relaxations of constituent spin bearing nuclei. Therefore, a direct correlation between the two - nuclear spin relaxation (NSR) and the conductivity relaxations - is to be expected.

In NSR studies, the spin-lattice relaxation time, T_1, is measured and $\log T_1$ is plotted as a function of $1/T$. $\log T_1$ vs $1/T$ plots generally deviate from the expectations of the well known Bloembergen-Purcell-Pound (BPP) theory (1948), which assumes an exponential decay of the fluctuations. The activation energy from the $\log T_1$ vs $1/T$ plot is not equal to the d.c. conductivity activation barrier. The pre-factor from NSR fluctuation correlation time is also unphysically low. In alkali silicate and borate glasses, the $\log T_1$ vs $1/T$ plot were found to be well fitted using Davidson-Cole function (Göbel et al., 1979), which is diagnostic of complex relaxation behaviour. Using fluctuation dissipation theorem, Ngai established a relation*

$$\frac{1}{T_{1\rho}} \approx \left(\frac{kT}{\omega^2}\right)\sigma(\omega) \tag{7.55}$$

The variation of $1/T_{1\rho}$ as a function of temperature for germanate glasses is shown in Figure 7.05. The vertical line separates approximately the high

---

* Experimentally one generally distinguishes several spin- lattice (longitudinal) relaxation times, T_{1DD}, T_{1Q}, $T_{1\rho}$ etc.. In glasses due to the presence of random potential energy barriers, the relaxation times exhibit a distribution. In general, they can be expressed as:

$$\left(\frac{1}{T_1}\right) = C\left[\int_0^\infty \frac{G(\tau)}{(1+\omega_0^2\tau^2)}\,d\tau + 4\int_0^\infty \frac{G(\tau)}{(1+4\omega_0^2\tau^2)}\,d\tau\right] \tag{7.56}$$

where $\int_0^\infty G(\tau)\,d\tau = 1$, is a distribution function for the correlation time. For $1/T_{1DD}$, $C = C_D = (3/2)\gamma^2 M_2$, where M_2 is the second moment of the relaxation spectra and γ is the gyromagnetic ratio. For $1/T_{1Q}$, $C = C_Q = (1/25)\,(e^2qQ/h^2)\,(1+\eta^{2/3})$, where eQ is the quadrupole moment, eq is the dipole moment and η is the asymmetry parameter. For the case of $(1/T_{1\rho})$, which refers to the relaxation of nuclear magnetization in rotating frame, $C \approx (3/2)\,\gamma^2 M_2$.

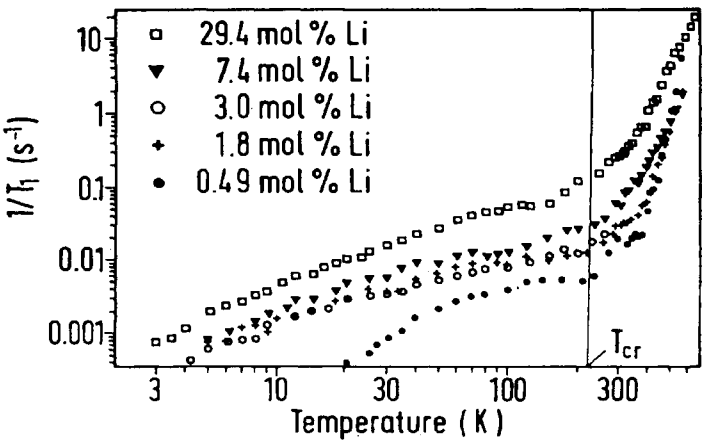

Figure 7.05. Temperature dependence of ^{7}Li NSR rates $1/T_1$ ($\equiv 1/T_{1\rho}$) in different GeO_2:Li glasses observed at 70 MHz. The figure shows clearly the low-temperature and the high-temperature region below and above T_{cr} (~250K). (After Kanert et. al., 1991).

temperature and low temperature region of NSR in these germanate glasses. $T_{1\rho}$ measurements were made for the high temperature region and was corrected for contribution from the low temperature asymmetric double well potential, ADWP, induced background rate. Since the NSR has been studied at 200 kHz, it is appropriate to compare the ac conductivities at this frequency. The Ngai relation (eqn. 7.55) can be recast as:

$$\sigma_{ac} T \approx a\left(\frac{1}{T_{1\rho}}\right) \tag{7.57}$$

where $\sigma_{ac} \equiv \sigma(\omega)$ and $a = (\omega^2/k)$. It is assumed that $T_{1\rho}$ refers to the relaxation time corresponding to the ion diffusion in the high temperature regime. a is a constant with units of Ks/ (Ωm). The validity of this equation has been verified by plotting $\sigma_{ac}T$ and $a(1/\ T_{1\rho}\ )$ together as a function of $1/T$ as shown in Figure 7.06. At low temperatures correlation of conductivity and NSR is more complicated primarily because it is unclear as to how charge transport occurs at low temperatures. But in general, it is found that at low temperatures $1/T_1$ itself varies as:

$$\frac{1}{T_1} = T^{1+\alpha}\omega_0^{-\beta} \tag{7.58}$$

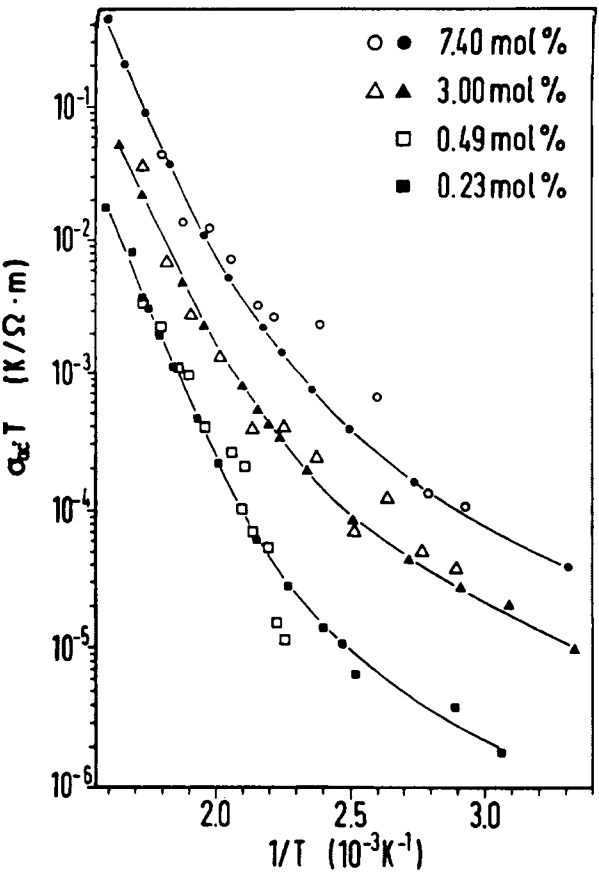

Figure 7.06. Comparison of the temperature dependence of electrical conductivity σ_{dc}·T (full symbols) and the diffusion-induced part of the NSR rate, $1/T_{1Q|diff}$ (open symbols) vs inverse temperature for different GeO_2:Li glasses. Actual Li content is listed in the Figure. (After Kanert et al., 1991).

α is such that, $0 \leq \alpha \leq 1$, (generally between 0.1–0.5) and β is also a constant which varies generally between 0.6–1.5. It is visualized that the process of spin flipping is coupled to transitions in ADWP, a schematic of which is shown in Figure 7.07. On the left side of Figure 7.07 is a conceptualized ADWP which is supposed to be present as a universal feature in glasses. The quantities Δ, Δ_0 and V in the Figure represent the asymmetry parameter, the ground state tunneling splitting and the barrier height respectively. The transitions among these states is considered to occur only by tunneling at temperatures < 10 K. Above this temperature, barrier hopping becomes important. Correlation time corresponding to

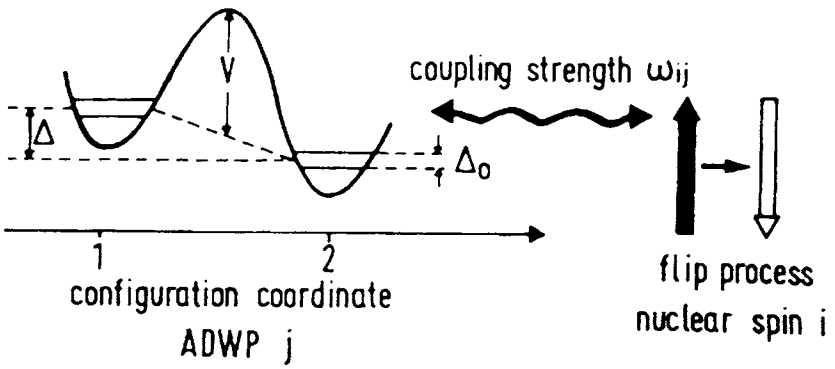

Figure 7.07. Schematic illustration of an NSR process due to a transition 1→2 in an asymmetric double-well potential (ADWP) characterizing the local low-energy configurations in glassy solids (after Kanert et al., 1994).

barrier hopping (thermally activated transition from state 1 to state 2) is given by

$$\frac{1}{\tau_1} = \left(\frac{1}{\tau_0}\right)\cosh\left(\frac{\Delta}{2kT}\right)\exp\left(-\frac{V}{kT}\right) \tag{7.59}$$

The phonon assisted tunneling on the other hand has a correlation time τ_2 given by:

$$\frac{1}{\tau_2} = A\Delta_0^2 \coth\left(\frac{E}{2kT}\right) \tag{7.60}$$

where A is the strength of the phonon tunneling coupling and $E = (\Delta_0^2 + \Delta^2)^{1/2}$. The total correlation time, therefore, is given by τ_c, where

$$\frac{1}{\tau_c} = \frac{1}{\tau_1} + \frac{1}{\tau_2} \tag{7.61}$$

It is the presence of a large density of ADWP with a broad distribution of both Δ and V, which eventually determines the average value of τ_c and hence $1/T_1$ (the NSR rate). The expected variation of $1/T_1$ as well as $\sigma_{ac}T$ (shown as σT) as a function of T and ω was noted earlier. Shown in Figure 7.08 is the variation of $1/T_1$ as a function of temperature at various frequencies of NSR measurements in a log-log plot for a LiF containing

lithium borate glass. A similar behaviour has been observed in other heavy metal fluoride glasses. It is possible to write $1/T_1$ expression as:

$$\frac{1}{T_1} = (\text{constant})\omega_0^{-\beta} \exp\left(-\frac{E_{NMR}}{kT}\right) \tag{7.62}$$

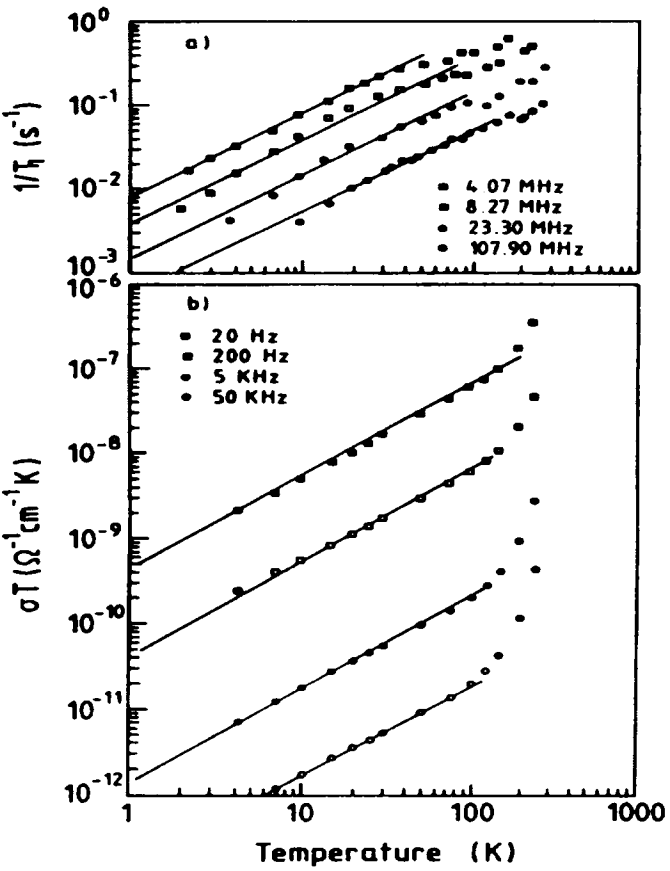

Figure 7.08. Temperature dependence (a) of the ^{7}Li NSR rate, $1/T_1$, and (b) of the electrical conductivity, σT, for $0.1Li_2F_2{\cdot}0.9Li_2O{\cdot}B_2O_3$ glass at different frequencies. Solid lines are fits of the data (After Kanert et al., 1994).

on the basis of experimentally observed variation of ln $(1/T_1)$ as a function of $1/T$. The activation energies calculated on the basis of this approach are much lower than E_{dc}, the activation energy from d.c. conductivity measurements as observed in the case of lithium germanate glasses. However, when Li^+ ion concentration is very low as a result of which the

coulombic interactions between the mobile ions become negligible, E_{NMR} almost approaches E_{dc}. NSR studies have been made on several salt solutions using spin probes in the low temperature glassy region. The relation of $1/T_1$ to T and ω have been found to be valid and found to originate from the dynamics involving ADWP states.

It was also found that the variations of $1/T_1$ required a Davidson-Cole distribution function for best fit. In the mixed alkali glasses the $1/T_1$ plots at high temperatures become symmetrical and broader. The activation energies determined from NMR, E_{NMR} , and the E_σ from conductivity measurements have also been compared. Since ^{7}Li NMR senses only the lithium ion and not the other alkali, the E_{NMR} in mixed alkali regions are observed to be lower than E_σ.

The activation energy determined from the low temperature branch of $1/T_1$ plots in NSR studies are found to be lower than the d.c. activation barrier, E_σ, but comparable with the activation energies for the frequency independent a.c. activation energies. Pradel and Ribes (1991) have deduced β values as $E_{ac}/ E_{dc} \approx E_{NMR}/ E_{dc}$. They found additionally that β values did not have a clear correlation to 1-s values, where s is the exponent in ω^s fits to a.c. conductivity.

Another NMR application in the characterization of ion dynamics in glasses is the study of ***motional narrowing***. For example, in glasses with Li^+ ions as carriers, the high temperature regime corresponds to significantly enhanced mobilities. The high mobilities result in the averaging out of the dipolar and the quadrupolar interactions, which cause the broadening of the NMR resonance. As a result, the NMR resonance becomes narrow. Motional narrowing is experimentally investigated by evaluating the second moments, M_2. Göbel et. al (1979) have studied the NMR of a number of alkali modified silicate, borate and phosphate glasses and determined the rigid lattice second moments and the onset temperature of the motional narrowing. These data are summarized in Table 7.1. The rapid decrease of second moments in the region of transition is also shown in Figure 7.09 where the second moments are plotted as a function of (1/T). The jump frequency, τ_c^{-1}, is related to the second moment M_2 by

$$\frac{1}{\tau_c} = \gamma (M_2)^{\frac{1}{2}} \tag{7.63}$$

where γ is the gyromagnetic ratio. From the Figure 7.09, it is seen that at the onset temperature, τ_c is $\approx (6 - 10) \times 10^{-5}$ seconds.

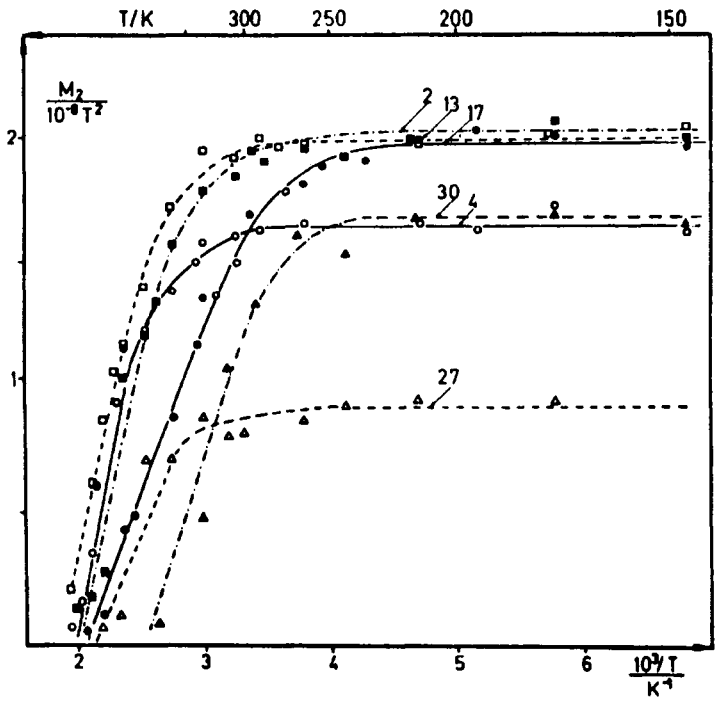

Figure 7.09. The truncated second moment of the ^{7}Li NMR in six glasses (2, 4, 13, 17, 27 and 30 as indicated in Table 7.1), at temperatures ranging from 140 to 500K (After Göbel et al., 1979).

Power law behaviour of a.c. conductivities

A.c. conductivities in glasses have long been found to obey a power law,

$$\sigma(\omega) = \sigma(0) + A\omega^s \tag{7.64}$$

where $\sigma(0)$ is the d.c. limiting (low frequency) conductivity corresponding to the frequency independent flat part in ln σ vs ln ω plots. The exponent, s, lies in the range 0 to 1. A is a constant. If A is written as $\sigma(0)\tau_0^s$, the equation can be transformed into

$$\sigma(\omega) = \sigma(0)[1 + (\omega\tau_0)^s] = \sigma(0)\left[1 + \left(\frac{\omega}{\omega_0}\right)^s\right] \tag{7.65}$$

Table 7.1: Composition of glasses in the various systems investigated and experimentally determined values of the rigid lattice second moment and of the temperatures where motional narrowing occurs (After Göbel et al., 1979).

Sl No.	Composition (mole%)	$\frac{M_2^{rl}}{10^{-8}T^2}$	$\frac{T^*}{K}$
1	82 SiO_2 18Li_2O	1.94	282
2	67 SiO_2 33Li_2O	1.98	278
3	60 SiO_2 40Li_2O	2.22	277
4	67 SiO_2 16.5Li_2O 16.5Na_2O	1.64	378
5	62.5 SiO_2 15Li_2O 22.5Na_2O	1.57	388
6	54 SiO_2 40Li_2O 6Na_2O	2.71	307
7	67 SiO_2 16.5Li_2O 16.5K_2O	1.45	346
8	55 SiO_2 41Li_2O 4K_2O	2.06	298
9	76 SiO_2 18Li_2O 6Cs_2O	1.68	308
10	67 SiO_2 25Li_2O 8Cs_2O	2.05	305
11	65 SiO_2 32Li_2O 3Cs_2O	2.21	283
12	79.5B_2O_3 20.5Li_2O	2.04	330
13	67B_2O_3 33Li_2O	2.03	341
14	56B_2O_3 44Li_2O	2.35	327
15	46.5B_2O_3 53.5Li_2O	3.17	329
16	67B_2O_3 10Li_2O 23Na_2O	1.96	344
17	67B_2O_3 16.5Li_2O 16.5Na_2O	1.98	355
18	67B_2O_3 25Li_2O 8Na_2O	1.98	360
19	64B_2O_3 18Li_2O 18K_2O	2.21	326
20	57B_2O_3 33Li_2O 10K_2O	2.31	337
21	51B_2O_3 44.5Li_2O 4.5K_2O	2.67	351
22	73B_2O_3 20Li_2O 7Cs_2O	2.26	322
23	61B_2O_3 35Li_2O 4Cs_2O	2.37	321
24	56.5B_2O_3 42Li_2O 1.5Cs_2O	2.50	299
25	90P_2O_5 10Li_2O	0.66	407
26	80P_2O_5 20Li_2O	0.71	398
27	70P_2O_5 30Li_2O	0.86	337
28	60P_2O_5 40Li_2O	1.39	324
29	50P_2O_5 50Li_2O	1.52	281
30	40P_2O_5 60Li_2O	1.66	276

where $\omega_0 = 1/\tau_0$ is the frequency corresponding to $\omega\tau = 1$. Thus it is verified that $\sigma(\omega) = 2\ \sigma(0)$, when $\omega = \omega_0$ which defines the characteristic frequency. In an extensive investigation of sodium trisilicate glass, Nowick et al. (1994) recognized that s is temperature dependent but it defines two regions of $s \sim 1.0$ and $s \sim 0.6$ and the transition occurs over a relatively narrow range of temperature. This is a widely prevalent behaviour in a large number of dielectric materials and the temperatures where $s \approx$ constant and equal to 0.6 is referred to as Jonscher regime. Generally in the Jonscher regime and for $\omega\tau >> 1$ (atleast >10), the frequency dependence is well described by a stretched exponential relaxation function. In fitting experimental data, the stretched exponential function (the exponent, β, is also occasionally referred to as the stretching fraction), which is in time domain has to be transformed into frequency domain (where the exponent is s). In many studies it has been found that the value of s is equal to $(1-\beta)$.

When $s = 1.0$, $\sigma(\omega)$ is proportional to ω or $\varepsilon'' = \sigma/(\omega\varepsilon_0)$ becomes frequency independent. This region is therefore referred to as constant loss regime, the presence of which seems to be fairly universal at low temperatures. In the constant loss regime ε'' is also only very weakly dependent on temperature and is therefore not likely to be activated. Evidently, presence of constant loss means absence of mixed alkali effect in this regime (see chapter 6). Novick et al. (1994) have shown that in the region of temperature between constant loss regime and Jonscher regimes where s drops from a value of 1.0 to ~ 0.6, it is possible to treat the data as a superposition of both the regimes. In other words,

$$\sigma(\omega) = \sigma(0) + A\omega^{s} + B\omega^{1} \tag{7.66}$$

where s is the higher temperature value of the exponent. Such double power law is now widely employed in the analysis of conductivity behaviour. Two examples of the fit to double power law are shown in Figure 7.10. In Figure 7.10 (b) plot of reduced conductivity has been fitted to a double power law.

The exponent value of 0.6 in Jonscher regime is considered to arise by the ion-ion interactions, usually of the coulombic type. During the process of the hopping of the ions, even separate hopping events may have a broad distribution of relaxation times, and this effect can manifest as stretching of the relaxation times. Ngai's coupling model accounts for stretched exponential relaxation and considers it as a consequence of

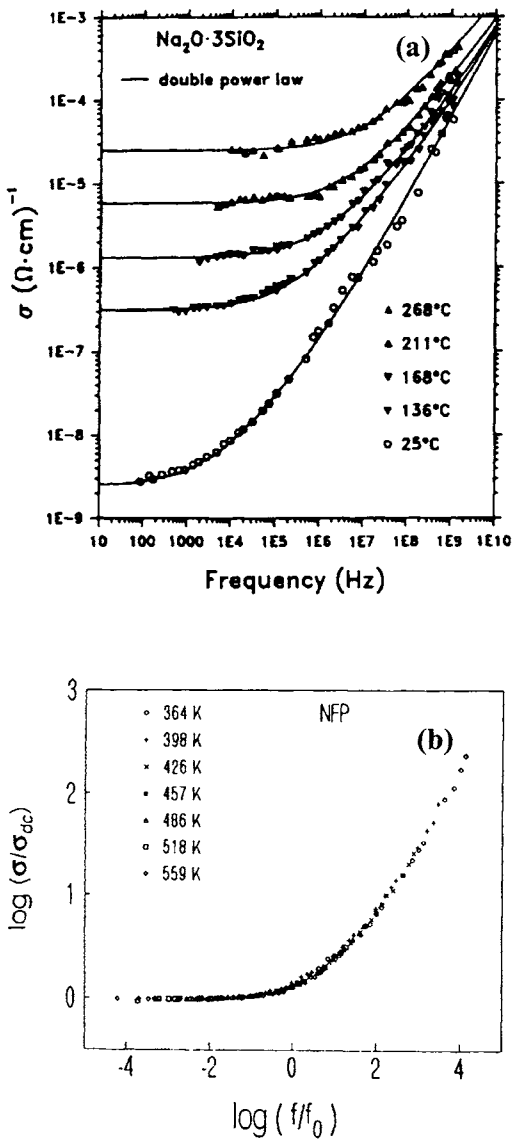

Figure 7.10. (a) Conductivity data for $Na_2O \cdot SiO_2$ glass fitted to the double-power law. (After Nowick et al., 1994) (b) Plot of the reduced conductivity vs the reduced frequency for the NFP glass (composition, $Na_3Fe_2(PO_4)_3$) at various temperatures which could be fitted to double-power law (After Sobha and Rao, 1995).

switching on the coulombic interactions. The average relaxation time, $\langle \tau \rangle$, is the Maxwell's relaxation time and it varies inversely as the d.c. conductivity. This naturally leads to an equivalence of E_{dc} and E_{τ}. The

activation energy* for the primitive process in Ngai's description is therefore given by $E_A = (1\text{-}s)\ E_{dc}$. E_A is the activation energy for the parameter A in equation $\sigma(\omega) = \sigma(0) + A\omega^s$. This is the familiar Ngai relation.

The constant loss regime is usually accounted for by assuming the presence of ADWP or two level systems (Figure 7.07). The inter-well distances are assumed to be constant and V and Δ are assumed to be uniformly distributed between 0 and maximum values of V_m and Δ_m. Assuming that only hopping over such barriers is operative, the conductivity is given by

$$\sigma(\omega) = \sigma_{hop} + \sigma_{tunnel} = B\omega\left[\frac{\tanh\left(\frac{\Delta_m}{2kT}\right)}{\left(\frac{\Delta_m}{2kT}\right)}\right] + C\omega\tanh\left(\frac{\Delta_0}{2kT}\right) \tag{7.67}$$

where B and C are constants and Δ_0 is the tunneling splitting. The value of $(\sigma_{hop} + \sigma_{tunnel}) / \omega\varepsilon_0$ has been shown to be essentially constant over a wide range of temperature using the data of crystalline alumina substituted calcium titanate, and is expected to be valid for glasses as well. The constant loss regime, also referred to as near constant loss regime, has been a subject of much discussion and has recently been attributed to polarization currents arising from motion of the counter ions such as NBO's in oxide glasses by Elliott (1994). It is interesting to note here that Dyre (1993) has suggested on the basis of a percolation model (percolation path approximation), that an expression for universal a.c. conductivity given by

$$\tilde{\sigma} = \frac{i\tilde{\omega}}{\ln(1 + i\tilde{\omega})} \tag{7.68}$$

where the scaled conductivity $\tilde{\sigma} = \sigma(\omega)/\sigma(0)$ and $\tilde{\omega} = \omega/\omega_m$, ($\omega_m$ is the frequency of the dielectric loss peak)(compare with equation 7.43). The above relation can be easily seen to be consistent with the observation that $\sigma(\omega) = \sigma(0)$, when $\tilde{\omega}$ tends to zero and $\sigma(\omega)$ varies as ω^1 when $\tilde{\omega}$ tends

* The d.c. conductivity activation energy is often designated as E_σ, E_0, E_a, E_{dc} and $E(0)$ in the literature and all are equivalent. We have used E_{dc} as preferred description in this book although in chapter 6, E_a has been used to make it known that it is an activation barrier. But otherwise E_a represents the primitive activation barrier observed in a.c. measurements.

to ∞. Additionally it suggests a smooth variation of the exponent without being a three term expression.

Pradel et al. (1998) reported a.c. conductivity studies on 0.5 $Ag_2S \cdot 0.5\ GeS_2$ glasses at very high frequencies (up to 60 GHz). The conductivity function takes the form $\sigma(\omega) = \sigma_{dc} + A\ \omega^{s1} + B\omega^{s2}$, where $s2$ values range from 1.0-1.25, but $s1$ remains ≈ 0.5. It was also found that while A is activated, B is not and it exhibits a scatter around 10^{-12}. These measurements were carried out between –77 ^{0}C and 20 ^{0}C. The high frequency and low temperature behaviour with $s2 > 1.0$, according to these authors, could arise from participation of excitations in the ADWP configurations.

β and its relation to other transport parameters

Coupling model (see chapter 9 for the model) suggests that the stretching exponent $\beta = 1\text{-}n$, arises from interaction among carrier cations, which has the effect of stretching the relaxation time. Therefore, n (= 1-β) should be directly related to the carrier concentration. Since increasing the carrier concentration makes the potential energy profiles of nearest neighbor cations intersect, the effective barrier height, decreases as visualized by Martin and Angell (1986). Therefore, a general relation between conductivity activation barrier, E_{dc} and the KWW stretching parameter, β, should be expected to be present. Ngai and Martin (1989) examined conductivity data on a very large number of glasses, based on phosphate, silicate, borate, aluminosilicate, germanate and aluminogermanate glasses containing different alkalies and evaluated $E_A = (1\text{-}n)\ E_{dc} = \beta\ E_{dc}$, where E_A represents the primitive activation barrier of the coupling model and E_{dc} is the d.c. conductivity activation energy. A good correlation was found in the trends of E_A and β. The plot of n (=1-β) vs E_A from their work is shown in Figure 7.11. E_{dc} seems to correlate well with β, but varying the glass former concentration is found to affect the primitive activation barrier, E_A, not n (or β) even when total cation concentration is held constant.

There have been several attempts made to correlate β to other conductivity parameters like E_{dc} and inter-carrier-ion distance d^*. Martin has been successful in correlating β with distance d, which varies as $C^{-1/3}$, where C is the concentration of carrier ions. In general, β is found to decrease monotonically with increasing concentration. This is in

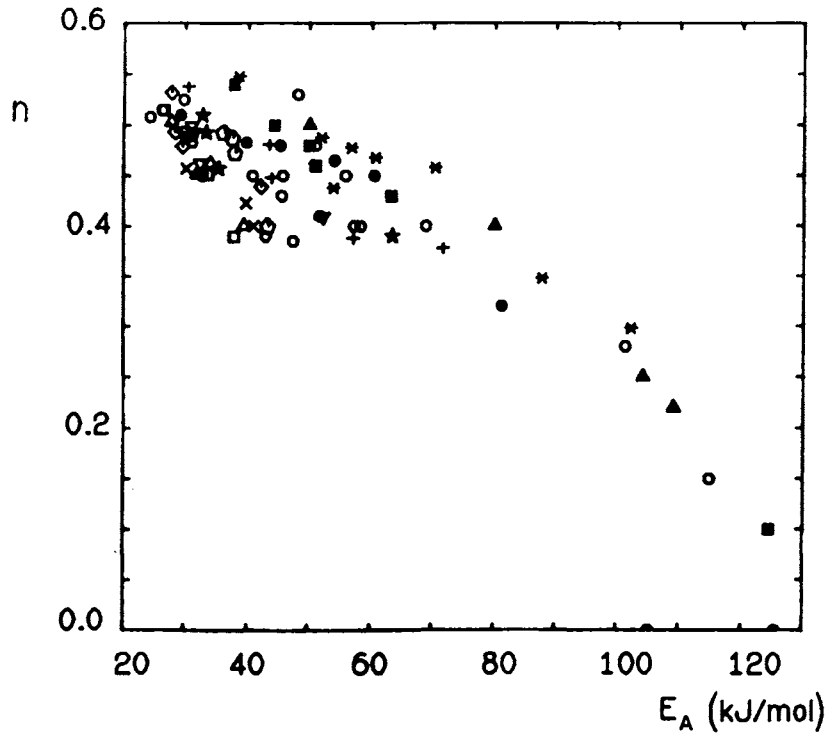

Figure 7.11. A plot of the coupling parameter n vs E_A for alkali oxide glasses having various total alkali oxide contents (After Ngai and Martin, 1989).

consonance with the coupling model because as the distance decreases, inter-cationic interaction increases, which slows down τ and decreases β. A significant part of dielectric and a.c. conductivity studies in glasses has been devoted to understanding the non-Debye relaxation behaviour. KWW function has found much favour particularly in the analyses of data based on modulus representation. Efforts have also been made to relate the stretching exponent, β, to several other experimental parameters and will be discussed later in this chapter.

The conductivity relaxation measurements (Martin and Angell, 1986) have revealed that β (the stretching exponent from conductivity measurements) are well correlated to the activation barrier, E_A. The correlation between β and βE_A is even better (Ngai and Martin, 1989). Electrical relaxation studies have been reported (Hasz et al., 1994) in so-called CLAP glasses, which are fluoride glasses constituted of CdF_2, LiF, AlF_3 and PbF_2 (however, these glasses contained substantial amount of

CdO and smaller amounts of $CdCl_2$, YF_3 and LaF_3). The modulus relaxation spectrum has been fitted to stretched exponential function and it has been found that β has a roughly constant value in the glassy state and above T_g, it decreases rapidly. Since decoupling index also decreases rapidly above the glass transition temperature, it is suggestive of an implicit relation between R_τ and β. It is also noted that R_τ at T_g itself is inversely correlated to the corresponding β values and β decreases linearly with log R_τ at T_g (also see Hunt, 1994)

Further, as noted in chapter 6, (FIC glasses) R_τ is very high and of the order of 10^{13}-10^{14} since σ_{dc} is very high. The decoupling index therefore is directly related to the differences in the behaviour of shear and conductivity relaxation times. Since both shear viscosity and conductivity obey the VTF equation, of the form,

$$\phi = \phi_0 \exp\left[-\frac{B'}{(T - T_0)}\right] \tag{7.69}$$

where ϕ is either the fluidity (= $1/\eta$) or $\sigma(0)$, R_τ should be related to the ratio of corresponding B' parameters. B' is generally considered as temperature invariant. It is also intuitively evident that R_τ is related to the free volume and the requirement of free volume is different for conductivity and viscous relaxation mechanisms. In a log $\sigma(0)$ vs T_g/T plot, spanning T_g/T from 0 - 1, higher values of R_τ are found associated with greater departure from the Arrhenius behaviour (higher fragility). Deviation from Arrhenius behaviour is associated with lower values of β in the relevant stretched exponential function used to fit conductivity relaxation data in this region. Therefore, β should decrease with increasing R_τ (Angell, 1990). Figure 7.12 also reveals that since the limiting far infrared conductivity is ~10 S cm^{-1}, the limiting R_τ value at T_g should be around $10^{15.4}$. An extrapolation of β vs log R_τ data suggests (Angell, 1990) that the lower limit to β is 0.44. It is suggested that $\beta < 0.44$ may involve more than one relaxation process operating simultaneously.

Scaling behaviour of a.c. conductivity

Reference was made in the context of universality of the a.c. conductivity behaviour to the Taylor-Isard scaling function. By virtue of scaling behaviour, $\sigma(\omega)$ can be made to collapse on to master curves. Presence of scaling behaviour is indicative of the presence of common

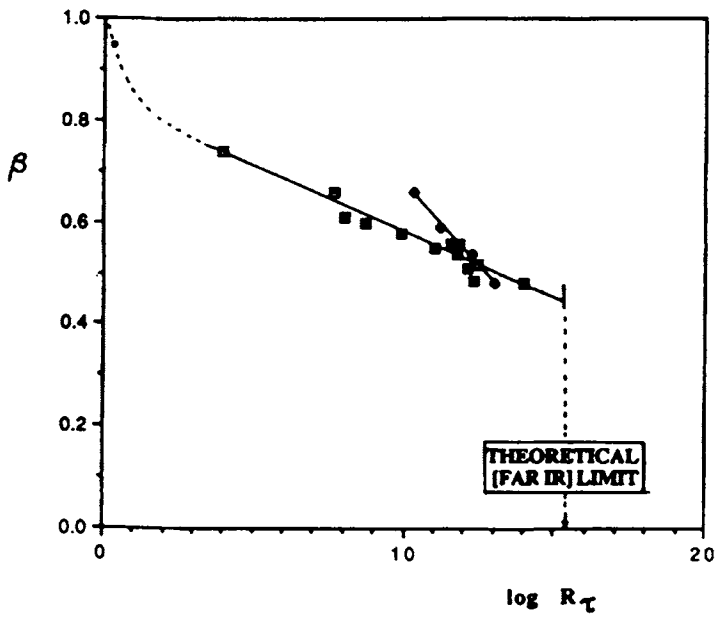

Figure 7.12. Correlation of nonexponentiality parameter β of Kohlrausch function with decoupling index R, for a variety of ionic glasses (After Angell, 1990).

conductivity mechanism and hence of universality. We briefly summarize below some of the well-known scaling laws (see also chapter 9 for related discussion).

(i) A.c. conductivity in the frequency range of MHz to GHz can be expressed as

$$\sigma(\omega) = \sigma(0) + A\omega^s = \sigma(0)\left[1 + \left(\frac{\omega}{\omega_0}\right)^s\right] \tag{7.70}$$

or

$$\frac{\sigma(\omega)}{\sigma(0)} = F\left(\frac{\omega}{\omega_0}\right) \tag{7.71}$$

where F(x)=1+y^s. Therefore, on a log-log plot, $\sigma(\omega)/\sigma(0)$ can be plotted against (ω/ω_0) so that single line of slope s is observed. An example of measurements on CKN glass over a range of temperature on either side of T_g is shown in Figure 7.13 (bottom). The same type of data collapse has

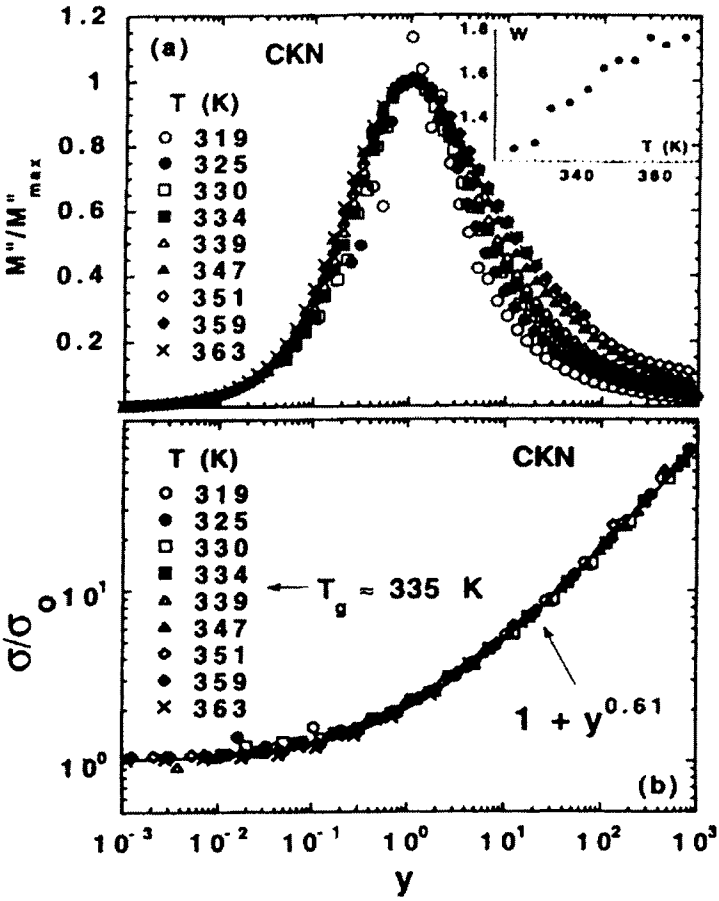

Figure 7.13. (a) $M''(\omega)$ of CKN reduced so that peaks coincide showing the failure of scaling. The inset shows the width of $M''(\omega)$ (normalized to that of a Debye relaxation) narrows with decreasing temperature, (b) $\sigma(\omega)$ of CKN reduced according to equation 7.70. Both above and below T_g, the data collapse upon a common power law with $s = 0.61 \pm 0.03$ ($\sigma_0 = \sigma(0)$) (After Sidebottom et. al., 1997).

not been found to occur by plotting M''/M''_{max} vs ω/ω_0 (Figure 7.13 top). The value of s for the collapsed curve in the reduced conductivity plot is 0.61. It also indicates that in CKN, the mechanism of ion transport, both above and below T_g, is likely to remain the same. It is also found that $s = 1-\beta$ relation is satisfactorily obeyed. The validity of the above scaling law is because the near constant loss term, $B\omega^1$ could be ignored in the high temperature but not so in the high frequency region.

(ii) Roling and coworkers (1997) recognized that $\sigma(0)$ is affected by the concentration of charge carriers and therefore ω_0 is also affected. Hence they proposed, that in the scaling law, ω_0 be expressed in terms of d.c. conductivity, the concentration of the mobile charge carriers and temperature. They examined the conductivity behaviour of $x\mathrm{Na_2O}\cdot(1\text{-}x)\cdot\mathrm{B_2O_3}$ glasses and showed that for any composition, $\sigma(\omega)$ measured at different temperatures could be scaled (according to the above law) when ω_0 is expressed as $\sigma(0)T/x_c$, which incorporates the effects arising from the change in carrier concentration and the temperature. The plots exhibited a remarkable collapse as shown in Figure 7.14 for $0.1 \leq x \leq 0.3$, over several decades of frequencies.

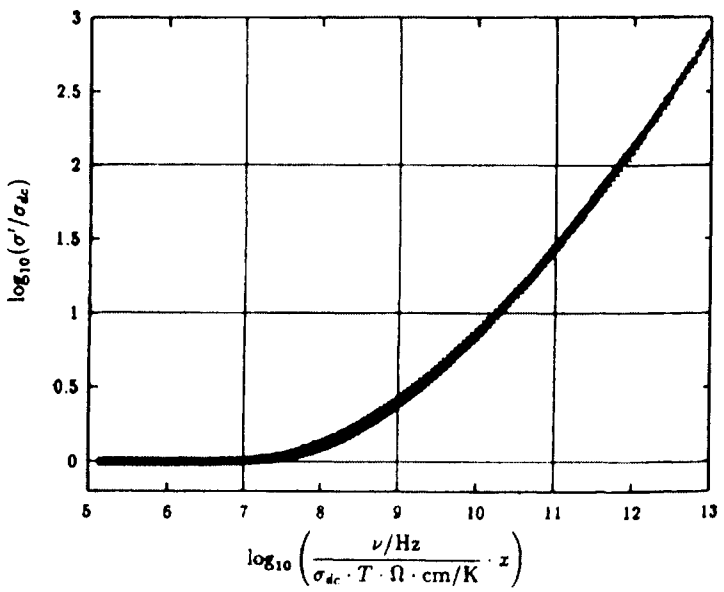

Figure 7.14. Conductivity master curves for $x\mathrm{Na_2O}\cdot(1\text{-}x)\mathrm{B_2O_3}$ glasses where x is included as an additional scaling factor (After Roling et al., 1997).

(iii) However, Sidebottom (1999) has examined the applicability of the scaling function proposed by Roling et al. (1997) for the case of $x\mathrm{Na_2O}\cdot(1\text{-}x)\mathrm{GeO_2}$ glasses for the low range of x values, $0.003 \leq x \leq 0.1$, and found the collapse of data on to the master curve unsatisfactory, particularly at higher values of $(\omega\cdot x)/[\sigma(0)T]$. This discrepancy was traced to the fact that there are terms neglected by Roling et al. in their

formulation of ω_0. This may be understood with reference to Nernst-Einstein relation, $\sigma(0) = [(\gamma Nq^2d^2)/(6kT)].H_R\ \upsilon_H$, where γ is the fraction of mobile cations, q is the charge of the cation, d is the distance traversed in a single hop and υ_H is the rate at which these hops occur ($\upsilon_H \approx \omega/\pi$), H_R is the Haven ratio and N is the cation density proportional to x. Thus this relation can be recast as $\omega_0 = (C.\sigma(0)T/x)(1/d^2)$, C being equal to 12 $\pi k/(\gamma a q^2 H_R)$, where a is a constant ($N = ax$). Thus the scaling function of Roling et al. (1997) is equivalent to treating $1/d^2$ as a constant, which is evidently incorrect when x is very low. Sidebottom recognized that d^2 dependence can be introduced through dielectric properties because the same d^2 dependence is present in the Debye expression for dielectric strength as:

$$\Delta\varepsilon = \frac{\left(\gamma N q^2 d^2\right)}{\left(3kT\varepsilon_0\right)} \tag{7.72}$$

Since N and T in the above expression are already present in the scaling function of Roling et al. (1997), the scaling expression could be modified as:

$$\frac{\sigma(\omega)}{\sigma(0)} = F\left(\frac{\omega\varepsilon_0\Delta\varepsilon}{\sigma(0)}\right) = 1 + \left(\frac{\omega\varepsilon_0\Delta\varepsilon}{\sigma(0)}\right)^s \tag{7.73}$$

It is seen in Figure 7.15 that this function brings about a very satisfactory collapse of the data in the composition region, where the scaling function of Roling et al. was found inadequate. In Figure 7.16 this scaling function is shown to work equally efficiently in collapsing the a.c. conductivity data of both CKN and $x\mathrm{K_2S} \cdot (1\text{-}x)\ \mathrm{B_2S_3}$ glasses also.

(iv) Ghosh and Pan (2000) have recently identified a scaling function very similar to that of Sidebottom (1999), except for using hopping frequency (ω_H) itself instead of ω_0 and have observed that the conductivity data in $0.3\mathrm{Li_2O} \cdot 0.7\mathrm{TeO_2}$ glasses can be made to collapse over a wide range of frequencies.

A.c. conductivity at very high frequencies

A.c. conductivities have been measured at infrared frequencies using spectroscopic absorption methods. It is obtained by determining the

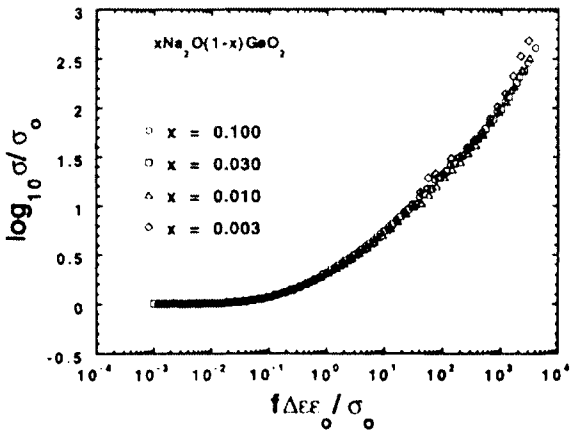

Figure 7.15. The ac conductivity in $(Na_2O)_x \cdot (GeO_2)_{1-x}$ glasses scaled using $f_0 = \sigma_0 / \varepsilon_0 \Delta\varepsilon$ (After Sidebottom, 1999).

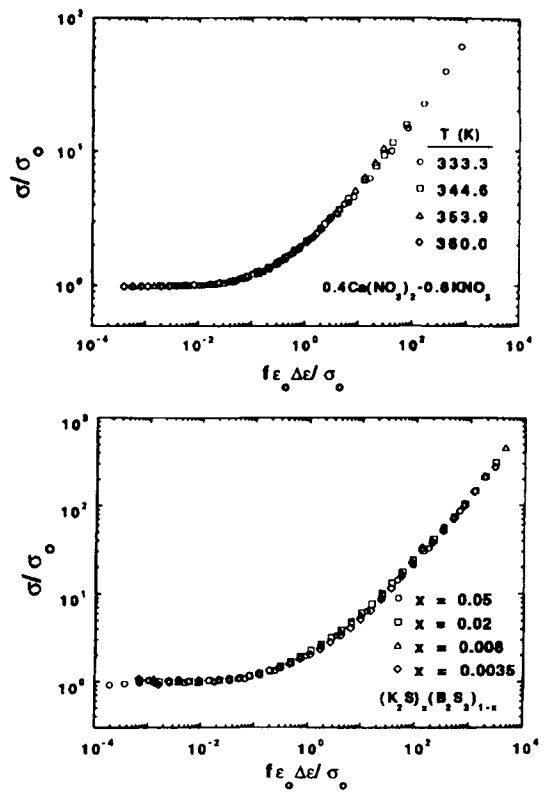

Figure 7.16. The ac conductivity in (a) $0.4Ca(NO_3)_2 \cdot 0.6KNO_3$ at four temperatures, (b) $x K_2S \cdot (1\text{-}x)\ B_2S_3$ scaled using $f_0 = \sigma_0 / \varepsilon_0 \Delta\varepsilon$ (After Sidebottom, 1999).

loss of energy of far infrared beam, which acts as a source of oscillating electric field. The absorption coefficient, α, and conductivity, σ, are related as,

$$\alpha(\omega) = \frac{\sigma(\omega)}{\varepsilon_0 cn(\omega)} \tag{7.74}$$

where ε_0 is the permittivity of free space, c is the velocity of light and $n(\omega)$ is the frequency dependent refractive index. $\alpha(\omega)$ is expressed as Neper cm^{-1}. As noted earlier (see Funke's model), these conductivities are of importance to several theoretical studies.

The high and low frequency a.c. conductivities of $0.7Na_2O \cdot 0.3B_2O_3$ and $0.35Na_2O \cdot 0.65B_2O_3$ glasses are shown in Figure 7.17(a). The top portion of high conductivities are from the respective

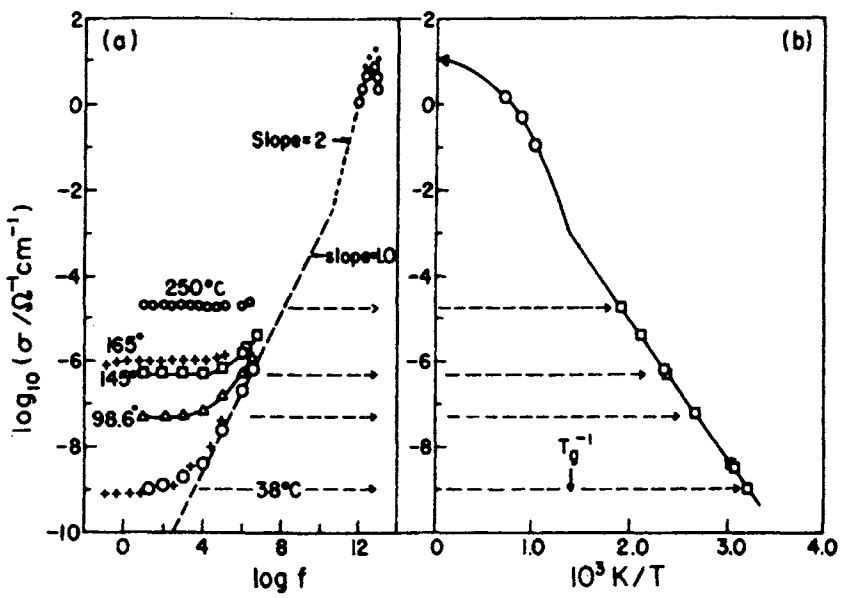

Figure 7.17. (a) Connection between the infrared conductivities and the conventional lower frequency (admittance bridge) conductivities for $0.35Na_2O{\cdot}0.65B_2O_3$ (open symbols). Low temperature plateau data are supported by lower frequency data on the 35% Na_2O aluminoborate glass, shown as crosses. Solid points in IR range are for $0.7Na_2O{\cdot}0.3B_2O_3$ glass. (b) Arrhenius plot of the dc conductivity, including liquid state data, showing agreement of the extrapolated limiting high temperature conductivity with the ambient temperature infrared conductivity (After Liu and Angell, 1990).

IR absorption data. The conductivities at low frequencies are connected to those at high (IR) frequencies through a broken line with two slopes; the longer of slope 1.0 and a short one of slope 2.0. The higher slope in the IR region has been confirmed from similar studies by Strom et al. (1974). α therefore varies as ω^2 in this region and is attributed to disorder induced coupling of the relaxation to the vibrational density of states (DOS).The higher level of absorption in this region is connected with the higher ionicity, which make them more IR-active. Limiting values of conductivities from temperature dependent d.c. conductivities are also seen as being similar from Figure 7.17(b).

Comparison of electrical and mechanical relaxations

Mechanical relaxation experiments reveal that relaxation of shear moduli are similar to those of electrical moduli. Relaxation studies are generally conducted using either a torsion pendulum arrangement or a rheovibron instrument. The former measures G^* directly and the latter gives Young's (tensile) modulus (E^*). In the ultrasonic and hypersonic frequency regime, absorption and dispersion studies are made by measuring either G^* or longitudinal modulus M_l^*. M_l^* can be converted to shear modulus (G^*). The relevant relations are

$$E^* = G^*\left[\frac{(3K^* - 4G^*)}{(K^* - G^*)}\right] \tag{7.75}$$

and

$$M_l^* = \left[K^* + \frac{4G^*}{3}\right] \tag{7.76}$$

Since G^* vanishes for the liquid, the real part of M_l^* remains finite, but E^* vanishes (Angell, 1990) in view of the above equation. In general mechanical relaxation spectra (tan $\phi = G''/G'$ or tan $\phi = E''/E'$) exhibit a higher value of FWHM compared to M'' (electrical relaxation spectra). However, the mechanical relaxation data can also be collapsed on to master plots, suggesting temperature independence of the spectral shape like in dielectric relaxation A comparison is made in Figure 7.18 of the master plots for the mechanical and electrical relaxations observed in F^- ion containing ZBLAN glass (ZrF_4–BaF_2 based heavy metal fluoride

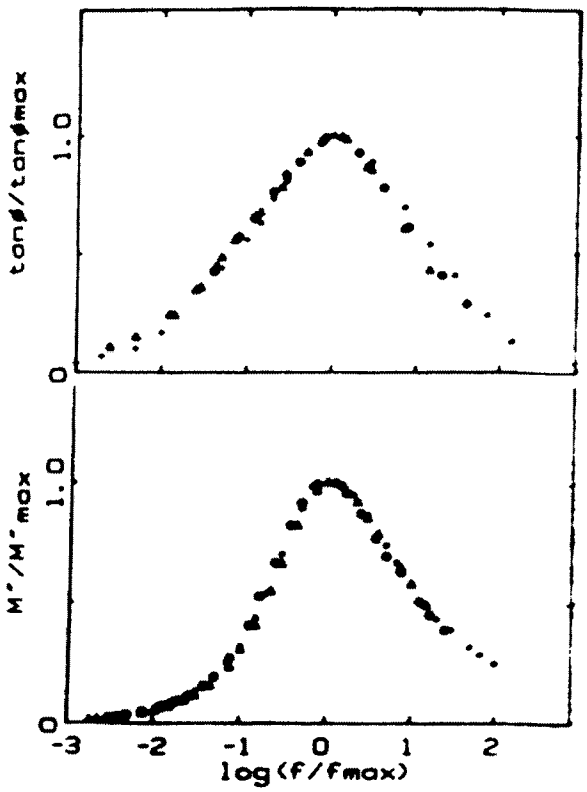

Figure 7.18. Master plots for electrical and mechanical relaxation in an anion-conducting (F^-) heavy-metal fluoride glass (After Angell, 1990).

glass; see chapter 14) which supports the above conclusion.

Ultrasonic and Brillouin scattering experiments are also used to evaluate elastic properties of glass using the following relation:

$$C_{11} = \lambda = \rho V_L^2 \tag{7.77}$$

$$C_{44} = \mu = \rho V_T^2 \tag{7.78}$$

$$Y = C_{44}\frac{3C_{11} - 4C_{44}}{C_{11} - C_{44}} \tag{7.79}$$

$$K = C_{11} - \frac{4}{3}C_{44} \tag{7.80}$$

where μ, Y and K are the shear, Young's and bulk modulii respectively (see chapter 10 for definition). V_L and V_T are the longitudinal and transverse velocities respectively. From Brillouin spectra, one determines the average velocity, V, of the acoustic waves using the relation:

$$V = \frac{\lambda f}{2n\sin(\theta/2)} \tag{7.81}$$

where λ is the wavelength of incident light, n is the refractive index of the glass and θ is the scattering angle.

References:

Anderson, O.L. and D.A. Stuart, 1954, J Am. Ceram. Soc., **37**, 573.

Angell, C.A., 1990, Chem. Rev., **90**, 523.

Barton, J.L., 1966, Verres et Refr., **20**, 328.

Bloembergen, N., E.M. Purcell and R.V. Pound, 1948, Phys. Rev., **73**, 679.

Bordewijk, P., 1975, Chem. Phys. Lett., **32**, 1115.

Charles, R.J., 1961, J. App. Phys., **32**, 1115.

Debye, P., 1929, Polar Molecules (Dover Publications, Inc., New York).

Dyre, J.P., and T.B. SchrØder, 2000, Rev. Mod. Phys., **72**, 873.

Dyre, J.C., 1988, J. App. Phys., **64**, 2456.

Dyre, J.C., 1993, Phys. Rev. B., **48**, 12511.

Elliott, S.R., 1987, Adv. Phys., **36**, 135.

Elliott, S.R., 1988, Solid State Ionics, **27**, 131.

Elliott, S.R., 1989, Mat. Sci. Eng., **B3**, 69.

Elliott, S. R., 1994, Solid State Ionics, **70/71**, 27.

Elliott, S.R., 1994, J. Non-Cryst. Sol., **170**, 97.

Falkenhagen, H., 1934, Electrolytes (Oxford University Press, Clarendon).

Funke, K., 1993, Prog. Solid State Chem., **22**, 111.

Ghosh, A., and A. Pan, 2000, Phys. Rev. Lett., **84**, 2188.

Glarum, S.H., 1960, J. Chem. Phys., **33**, 639.

Göbel, E., W. Müller-Warmuth and H. Olyschläger, 1979, J. Mag. Reson., **36**, 371.

Hasz, W.C., C.T. Moynihan and P.A. Tick, 1994, J. Non-Cryst. Sol., **172-174**, 1363.

Howell, F.S., R.A. Bose, P.B. Macedo and C.T. Moynihan, 1974, J. Phys. Chem., **78**, 639.

Hunt, A., 1994, J. Non-Cryst. Sol., **168**, 258.

Isard, J.O., 1961, Proc. Inst. Electr. Eng., **109B**, suppl. No. 22, 440.

Jain, H., and W.C. Huang, 1994, J. Non-Cryst. Sol., **172-174**, 1334.

Jonscher, A.K., 1977, Nature, **267**, 673.

Jonscher, A.K., 1996, Universal Relaxation Law (Chelsea Dielectrics, London).

Jonscher, A.K., 1983, Dielectric Relaxation in Solids, (Chelsea Dielectrics, London).

Kanert, O., M. Kloke, R. Küchler, S. Rückstein and H. Jain, 1991, Ber. Bunsenges. Phys. Chem., **95**, 1061.

Kanert, O., R. Küchler, J. Dieckhöfer, X. Lu, H. Jain, and K.L. Ngai, 1994, J. Non-Cryst. Sol., **172-174**, 1277.

Kubo, R., 1957, J. Phys. Soc. Jpn., **12**, 570.

Lesikar, A.V., C.J. Simmons and C.T. Moynihan, 1980, J. Non-Cryst. Sol., **40**, 171.

Liu, C, and C.A. Angell, 1990, J. Chem. Phys., **93**, 7378.

Macedo, P.B., C.T. Moynihan and R. Bose, 1972, Phys. Chem. Glasses, **13**, 171.

Martin, S.W., and Angell, C. A., 1986, Solid State Ionics, **23**, 185.

Moynihan, C.T., L.P. Boesch and N.L. Laberge, 1973, Phys. Chem. Glasses, **14**, 122.

Nakajima, T., 1972, Conf. on Electrical Insulation and Dielectric Phenomena, (National Academy of Sciences, Washington), p. 168.

Namikawa, H., 1975, J. Non-Cryst. Sol., **18**, 173.

Ngai, K.L., 1996, J. Non-Cryst. Sol., **203**, 232.

Ngai, K.L., and Martin, S.W., 1989, Phys. Rev. B., **40**, 10550.

Nowick, A.S., B.S. Lim and A.V. Vaysleyb, 1994, J. Non-Cryst. Sol., **172-174**, 1243.

Overhof, H., 1998, J. Non-Cryst. Sol., **227-230**, 15.

Pradel, A., and M. Ribes, 1991, J. Non-Cryst. Sol., **131-133**, 1063.

Pradel, A., G. Taillades, C. Cramer and M. Ribes, 1998, Solid State Ionics, **105**, 139.

Rao, K.J., Estournès, M. Mènètrier and A. Levasseur, 1994, Philos. Mag. B., **70**, 809.

Rao, K.J., C. Estournès, A. Levasseur, M.C.R. Shastry and M. Mènètrier, 1993, Philos. Mag. B., **67**, 389.

Roling, B., A. Happe, K. Funke and M.D. Ingram, 1997, Phys. Rev. Lett., **78**, 2160.

Sidebottom, D.L., P.F. Green and R.K. Brow, 1997, Phys. Rev. B., **56**, 170.

Sidebottom, D.L., 1999, Phys. Rev. Lett., **82**, 3653.

Sobha, K.C., and K.J. Rao, 1995, Solid State Ionics, **81**, 145.

Stevels, J.M., 1957, Handbook der Physik, ed., S. Flügge (Springer, Berlin), p. 350.

Strom, U., J.R. Hendrickson, R.J. Wagner and P.C. Taylor, 1974, Solid State Comm., **15**, 1871.

Taylor, H.E., 1956, Trans. Faraday Soc., **52**, 873.

Taylor, H.E., 1957, J. Soc. Glass Technol., **41**, 350T.

Taylor, H.E., 1959, J. Soc. Glass Technol., **43**, 124T.

Tomozawa, M., 1977, Treatise on Materials Science, Vol. XII, eds. M.Tomozawa and R.H. Doremus (Academic Press, New York) p. 335.

Weron K., 1991, J. Phys.: Condens. Mat., **3**, 9151.

Weron K., 1992, J. Phys.: Condens. Mat., **4**, 10507.

It is characteristic of science that the full explanations are often seized in their essence by the percipient scientist long in advance of any possible proof.
- J. D. Bernal

CHAPTER 8

SEMICONDUCTING GLASSES

There are several materials which exhibit semiconducting behaviour in glassy state and are technologically important for their proven and potential device applications. The most notable of them are the amorphous silicon and a number of chalcogenide and pnictide glasses. In this chapter, we put together briefly the understanding we have of electron transport in such amorphous semiconductors.

In crystalline semiconductors, it is relatively easy to understand the formation of gaps in energy states of electrons and hence of the valence and conduction bands using band theory (see Ziman, 1972). Band structure arises as a consequence of the translational periodicity in the crystalline materials. For a typical crystalline material which is a periodic array of atoms in three dimensions, the crystal hamiltonian is represented by a periodic array of potential wells, v($\boldsymbol{r}$), and therefore is of the form, $H_{\text{crystal}} = (\boldsymbol{p}^2/2m) + \text{v}(\boldsymbol{r})$, where the first term $(\boldsymbol{p}^2/2m)$ represents the kinetic energy. It imposes the condition that the electron wave functions, which are solutions to the hamiltonian equation, $H\Psi_i = E_i\Psi_i$ are of the form

$$\Psi_{n,k}(\boldsymbol{r}) = u_{n,k}(\boldsymbol{r})\exp(i\boldsymbol{k}.\boldsymbol{r}) \tag{8.01}$$

These are known as Bloch functions. $u_{n,k}(\boldsymbol{r})$ has the periodicity of the crystal lattice so that, $u_{n,k}(\boldsymbol{r}+\boldsymbol{R}) = u_{n,k}(\mathbf{r})$, where $\boldsymbol{R}$ is the translational vector connecting the lattice points. $\exp(i\boldsymbol{k}.\boldsymbol{r})$ modulates the wave function which represents a plane wave. $\boldsymbol{k}$ is the wave vector whose value is determined by reciprocal lattice vectors and all allowed $\boldsymbol{k}$ values ($\boldsymbol{k}$ is thus a quantum number) are determined by the symmetry of the crystal lattice. $\boldsymbol{r}$ is simply the distance vector in the direct lattice. The above Bloch functions are solutions – eigen functions - of the hamiltonian and the corresponding energies are functions of $\boldsymbol{k}$. The allowed solutions of the hamiltonian give rise to energy bands. Crystal hamiltonian has no solutions for certain range of energy values. These are the forbidden regions and they represent the energy gaps. The allowed energies of the electrons can, therefore be represented in the wave vector space as energy

bands. A schematic E vs $\boldsymbol{k}$ is shown in Figure 8.01. If the restriction imposed by Bloch wave, $u_{n,k}(\boldsymbol{r})$ was not there, the problem corresponds to that of free electron propagation and the energies would be equal to $\hbar^2k^2/2m$, with E having a parabolic dependence on $\boldsymbol{k}$. Thus the lattice potential which imposes the restriction of periodicity is responsible for the opening up of the gap, shown in Figure 8.01(a). Since the gaps open up at $\boldsymbol{k}$ values of $\pm\pi/a$, it corresponds to Bragg reflection of electron waves from the lattice planes; in the reciprocal lattice these are points at $\boldsymbol{k}$ values of $\pm\ \pi/a$. The region in $\boldsymbol{k}$-space between - π/a and + π/a defines the first Brillouin zone. A more detailed treatment of band theory is not relevant for our purpose, but it is sufficient to note that wave functions are constituted from the orbitals in the valence shell of the atoms and therefore the bands refer to the energy states resulting from the valence shell electrons. The energy levels in the band structure are filled by the valence electrons of the constituent atoms (the chemical interactions which are responsible for cohesion arise only from the valence electrons). The result is the formation of a metal or an insulator and the distinction arises from the availability of electron to fill the states. A detailed analysis shows that in metals there are insufficient electrons to fill all the available states in the topmost band, as in 8.01(c), while in insulators, they just fill all the available states in such a band; the higher energy band is empty. There

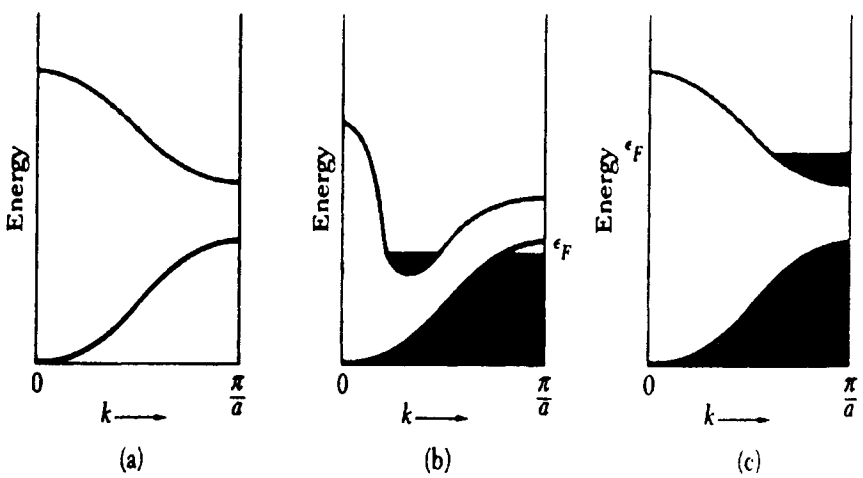

Figure 8.01. Occupied states and band structures giving (a) an insulator, (b) a metal or semimetal because of band overlap, and (c) a metal because of partially filled band. In (b) the overlap need not occur along the same directions in the Brillouin zone. If the overlap is small, with relatively few states involved, it is called a semimetal.

may arise situations like in Figure 8.01(b), where the energy states of the upper band overlap in energy values with that of the lower band for some values of $\boldsymbol{k}$ in the Brillouin zone. If the number of electrons is not high in the upper band, it behaves like a semi-metal.

The problem before us is how to describe the electron energy band in an amorphous material, because there is no possibility of using a reciprocal lattice description and therefore of using $\boldsymbol{k}$ as a quantum number. Nevertheless since electrons do exist in various energy states, "density of states" (DOS), which gives the number of electrons present per unit energy (eV) in a unit volume of the material, is a very useful quantity in describing the electron structure of amorphous materials. The DOS is represented by $g(E)$ and is given by

$$g(E) = \left(\frac{1}{V}\right)\sum_{n} \delta(E - E_n) \tag{8.02}$$

where V is the volume and n designates the states (δ is the Kronecker delta). The integrated DOS, $N(E)$ can be written as:

$$N(E) = \int_{-\infty}^{E} g(E).dE \tag{8.03}$$

DOS and energy gaps

Glasses also exhibit semiconducting behaviour, their resistivities decrease with increasing temperature. Therefore the next problem is, are there energy gaps in the DOS of a glass? This can be answered after developing an independent method for generating DOS. The answer lies in recognizing (Weaire and Thorpe, 1971) that the essential features of the DOS, $N(E)$, are determined almost entirely by the short-range order (SRO) of the arrangement of atoms in any material. This short range order is present both in crystals and in glasses. The hamiltonian relevant for SRO problem is the Weaire-Thorpe hamiltonian which is developed as follows. Let there be two types of atoms α and β, whose valence orbitals overlap and form a covalent bond (a common feature in semiconductors, both crystalline and amorphous), as shown in Figure 8.02. There are principally two interactions to consider, one the interaction between the electrons in orbitals of the same atom α or β, intra-atomic, and the other interaction arising from the electrons in the orbitals of the two different atoms α and β (inter-atomic).

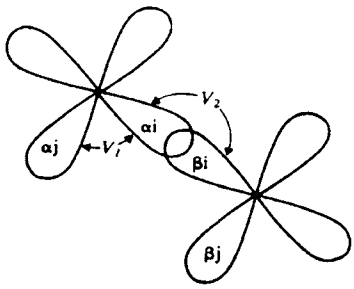

Figure 8.02. Interactions and basis functions in the Weaire-Thorpe Hamiltonian.

If the intra-atomic interaction is V_1 and the inter atomic interaction is V_2, then the Hamiltonian can be written as:

$$H = \sum_{\alpha i j} \langle \alpha_i \mid V_1 \mid \alpha_j \rangle + \sum_{\alpha\beta i} \langle \alpha_i \mid V_2 \mid \beta_i \rangle \tag{8.04}$$

which assumes that there are only single bonds between α and β. $|\alpha_i\rangle$ and $|\beta_i\rangle$ etc. are the corresponding wave functions. In a covalent network built of atoms α and β, it is assumed that the site orbitals are all orthogonal and V_1 and V_2 are identical for all atoms. In fact V_1 which represents intra-site interaction, is found to be responsible for the width of the band, while V_2, which is due to intersite interaction, is responsible for the separation of bonding and anti-bonding bands. It has been shown that the energy E, corresponding to the solutions of the above hamiltonian, leads to the formation of valence and conduction bands. The valence band energy levels lie between $(V_2 - V_1)$ and $(V_2 + 3V_1)$ and the conduction band energy levels between $(-V_2 + 3V_1)$ and $(-V_2 + V_1)$. For values of $|V_2| > 2|V_1|$, there is no overlap between the bands and therefore a gap is formed and hence semiconduction. The magnitude of the band gap is given by,

$$E_g = 2 \mid V_2 - 2V_1 \mid \tag{8.05}$$

The DOS resulting from Weaire-Thorpe Hamiltonian for germanium is compared with the same obtained from more rigorous band structure calculation for crystalline germanium in Figure 8.03. The formation of an energy gap in amorphous germanium is quite evident and the low energy features of the $N(E)$ of valence band are also satisfactory. The DOS at the top of the valence band and in the entire conduction band compare poorly. The origin of this lies in the composition of the Hamiltonian.

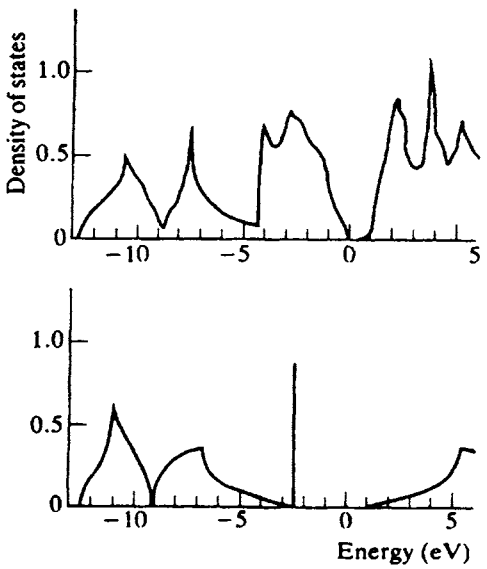

Figure 8.03. (top) The density of states from rigorous band structure calculations (the zero of energy marks the Fermi level), (bottom) the density of states calculated using Weaire-Thorpe Hamiltonian (After Weaire et al., 1972).

In a more realistic hamiltonian one would take into consideration the topological disorder, the variations in the nature of hybridization of the atomic orbitals and the interactions among further neighbours. Rigorous calculations using structural details available from various models, such as continuos random network (crn) model, have been found to give DOS which is qualitatively very similar to DOS in crystalline materials. This justifies Weire-Thorpe assumption that short-range order is the determining factor for the density of states. Calculation of the DOS of amorphous solids such as *a*-As, has also been done using the more rigorous Cluster-Bethe-Lattice method (Joannopoulos and Cohen, 1976, Joannopoulos, 1979). In this method symmetrical clusters containing several atoms are considered, whose surface dangling bonds are made to have the same connectivity as the host network avoiding the formation of closed rings of atoms. As shown in Figure 8.04 for the cases of amorphous and crystalline arsenic, the calculated density of states exhibit very similar features and are also in agreement with the XPS results. Thus we understand that for glasses to be semiconductors it is enough if there are energy gaps in the DOS and the presence of short range order is enough to give rise to such DOS.

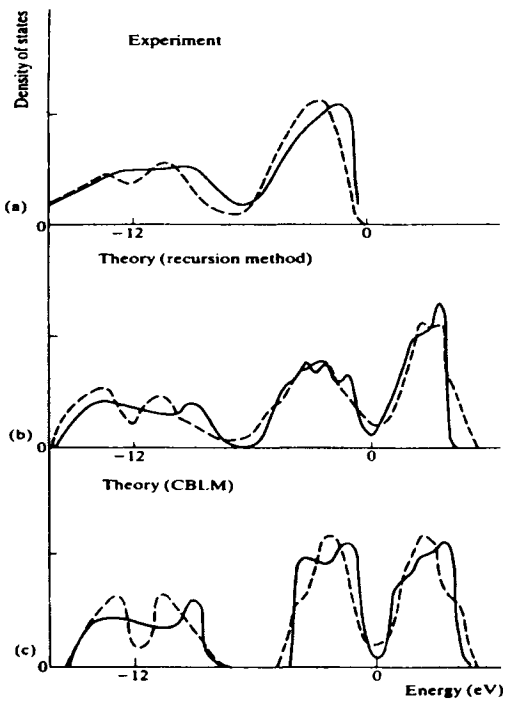

Figure 8.04. Comparison of densities of states for amorphous (solid line) and crystalline rhombohedral (dashed line) As. Experimental data are from XPS of Ley et al. (1973), and theoretical curves are from Kelly (1980) (recursion method) and from Pollard and Joannopoulos (1978) (cluster-Bethe-lattice method, CBLM) (Combined Figure from Elliott, 1984).

Characterization of DOS

Photoelectron Spectroscopy is the most useful tool to study DOS. We may recall briefly (see chapter 4) that ultraviolet photoelectron spectroscopy (UVPES) uses the ultraviolet light within the energy range of 10 - 50 eV, while X-ray photoelectron spectroscopy (XPS) employs Al-K_α or Mg-K_α excitations with energies of 1486.6 eV and 1256.6 eV respectively. The escape depth of the photoelectron is generally 5 Å for UPS and 50 Å for XPS. The photo-emission in PES is a three step process, (i) optical excitation of the electron, (ii) its transport through the solid and (iii) its escape from the surface, after which its kinetic energy is analysed. Therefore in a PES experiment, the intensities of the energy distribution curves of the photoelectrons is given by a convolution of all the three processes.

$$I(E,h\nu) = P(E,h\nu).T(E).D(E) \tag{8.06}$$

P (E, $h\nu$) is the distribution of photoelectron energy, E, excited by photon of energy, $h\nu$, $T(E)$ is the transmission function and $D(E)$ is the escape function. Both $T(E)$ and $D(E)$ are smoothly varying functions. Therefore the structures in the observed intensities are almost entirely determined by $P(E, h\nu)$. The photoelectron energy distribution function is given by,

$$P(E,h\nu) = (constant)N_c(E).N_v(E-h\nu).M^2(E,E-h\nu) \tag{8.07}$$

where N_c and N_v are the conduction and valence band DOS respectively, M is the excitation matrix element, which is generally a constant for limited photoelectron ranges. The above equation shows that the energy distribution curves (EDC's) involve joint density of states (of valence and conduction bands), which is a convolution of both occupied and unoccupied energy levels. Therefore in actual experiments UV photoelectron spectra can look very different from XPS, because, in the case of UV photoelectron spectra N_v (E - $h\nu$) can partially or fully overlap with $N_c(E)$ and hence has a convolution of both valence and conduction band DOS. But in XPS, $N_v(E$ - $h\nu)$ is pushed up way above the conduction band DOS because of the value of $h\nu$ and the resulting EDC represents very closely the actual DOS.

Weaire-Thorpe hamiltonian consists of intra- and inter-atomic interactions relevant to short-range order and give rise to gaps in DOS. When the intra atomic interaction potential V_1 increases, the DOS progress into the gap region and the gap gets closed when $V_2 = 2V_1$. The situation is very much like this in tetrahedral semi-conductors like Si and Ge. But in semiconductors containing chalcogenide (6th group elements, S, Se and Te) or pnictogen atoms (5th group elements, As, Sb and Bi) atoms, there is a difference, because, these atoms carry lone pairs. The lone pair energies lie in the gap region or on the top of the valence band (see later). The two different DOS scenarios, which develop as a consequence of this are shown in Figure 8.05. Figure 8.05(b) represents the model proposed by Cohen-Fritzsche and Ovshinsky (CFO) (1969). The band tails are hatched in both (a) and (b) and marked as E_c and E_v respectively. These hatched states correspond to the so-called localized states (see below), and E_c and E_v are designated as mobility edges in conduction and valence bands respectively. The Fermi energy (E_F) in both the cases lie near the center of the E_c and E_v. But in Figure 8.05(b) there is no gap in the DOS.

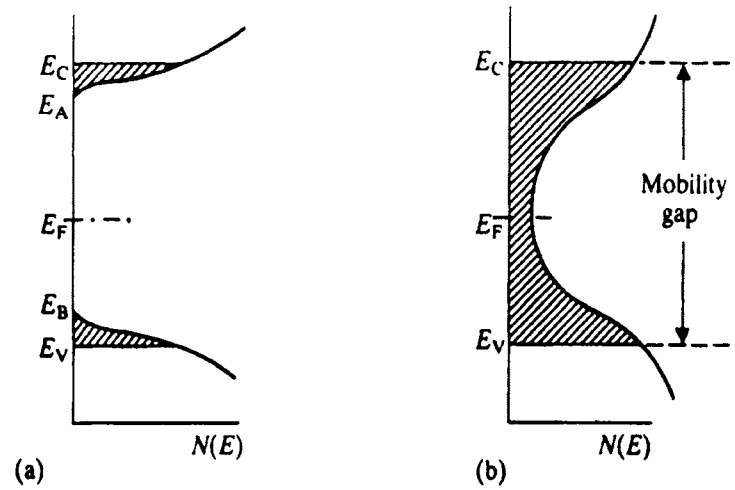

Figure 8.05: Models for the density of states of an amorphous semiconductor. (a) A true gap in density of states with some band tailing. (b) The Cohen-Fritzsche-Ovshinsky (1969) model of overlapping valence and conduction band tails (After Mott and Davis 1979)

Localization of electron states

The existence of a gap in DOS can, in principle, account for semiconduction, as excitation across the gap between the valence and conduction band is the same as in crystalline semiconductor. But it is when there is no gap as in a CFO semiconductor of Figure 8.05(b) that it becomes necessary to investigate the origin of semiconduction. One of the effects of disorder on the DOS is to smoothen out (removal of van Hove singularities) the sharp structures in density distribution of states and the other is to cause tailing of states into the gap. An even more important consequence of disorder is that the electron states become 'localized', which means that the electron present in such state would be spatially confined to the vicinity of predominately a single atomic site. It is intuitively clear that such localized states must correspond to those tail states, whose presence itself is a consequence of the disorder. Anderson (1958) examined the criterion for localization or the absence of diffusion in random lattices. If an electron is located on an atomic site (corresponding to an energy state) at time $t = 0$, the state of the electron is localized, if the electron has not diffused out of the site at $t = \infty$. Electron is deemed to be confined to a small volume around an atomic site with a finite probability proportional to exp $(-2\alpha r)$ where α^{-1} is known as the

localization length and r is distance from the reference atomic site. The variation of electron wave function is shown schematically in Figure 8.06. The envelope varies as exp(-αr) in Figure 8.06(b) and the square of it given by exp(-2αr) represents the probability of finding the electron within a volume r^3. In an elementary sense, therefore, localized states are like isolated impurity states, the latter are associated with the presence of spatially distributed defects in amorphous materials. Dangling bonds, homo-atomic bonds in a binary covalent compound etc. are also similar defect states. Creation of localized states implies breaking the extended nature of electron wave functions.

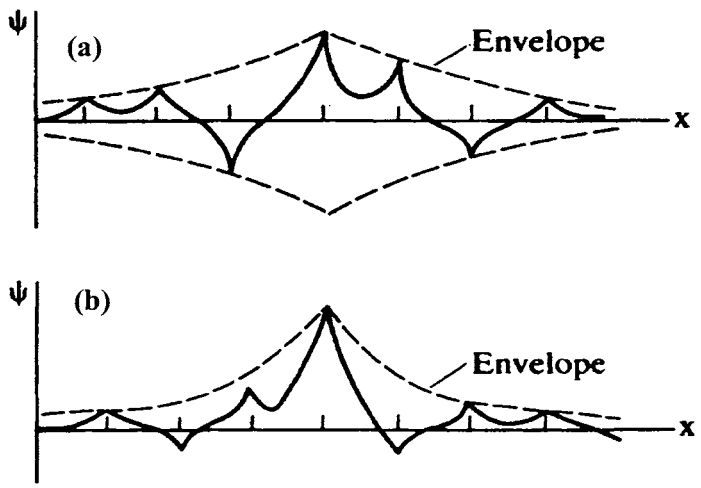

Figure 8.06: Schematic illustration of the form of the electron wave function in the Anderson model, (a) when states are just localized ($E \leq E_c$); (b) strongly localized (After Mott and Davis, 1979).

In one dimension, the extended nature of states is broken by the presence of any disorder irrespective of its magnitude and therefore, the states get localized. But in two and three dimensions a critical degree of disorder is needed in order to induce localization in the entire band. Anderson used a simple tight-binding hamiltonian, relevant for a periodic lattice to examine this problem. The hamiltonian has the form

$$H = \sum_i \langle i \mid E_i \mid i \rangle + \sum_{ij} \langle i \mid V \mid j \rangle \tag{8.08}$$

where $|i\rangle$ and $|j\rangle$ are wave functions. In this hamiltonian, the site energy, E_i, is considered as varying randomly, but the inter-site interaction, V, is

considered a constant. If E_i's are also of the same magnitude for all the sites, then it would lead to a energy band width B, as shown in Figure 8.07(a) (top). The corresponding schematic density of states is also shown in the figure on the left. The randomness is now introduced in terms of the

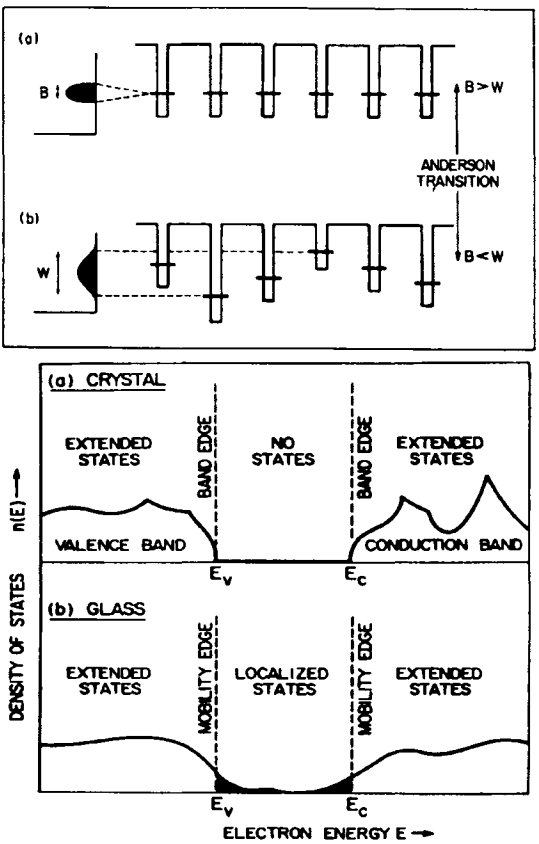

Figure 8.07: (top) One-electron tight-binding picture for Anderson transition. (a) Band width (left) and potential well structure in the absence of disorder. (b) Variation of band disorder in site energies. The horizontal marks are the energies E_is (schematic). When the width W of the disorder exceeds the overlap bandwidth B, disorder-induced localization takes place. (bottom) Schematic density-of-states diagram for a crystalline and an amorphous semiconductor, in the vicinity of the highest occupied and lowest empty states.

variation of the site energy (variation of the depth of the potential well at the periodic sites) as shown in Figure 8.07(b) (top). The extent of disorder in E_i is measured by the band width, W, over which E_i is distributed. The hamiltonian (equation 8.08) itself suggests that in the absence of the

second term, it gives rise to isolated localized states through the first term. The second term is responsible for producing extended Bloch states. For a given value of the magnitude of the disorder in site potentials, W, there are critical energies E_c and E_c', above and below which the states in the tails (of the conduction band, in this example) are localized. The remaining states in the centre of the band are delocalized or extended. As W increases, E_c and E_c' move towards each other and for a critical value of W all the states in the band get localized, a situation referred to as Anderson localization. Thus W/V serves as the quantitative criterion for Anderson localization. Usually W/zV where z is the coordination number takes care of the effect of coordination number on the magnitude of localization parameter. An alternate formulation due to Mott and Davis (1979) uses W/B, where B is the band-width for the same situation which is equal to $2zV$. For example critical value of W/V is 8.2 for a diamond cubic lattice.

The simple hamiltonian of the Anderson model has thus established that disordering of the site energies leads to localization of the states at the band edges. When the disorder is sufficiently large it can lead to localization of all states in the band. E_c and E_c' represent energy threshold for a transition from a localized to an extended state, often referred to as Anderson transition. Like in other classes of phase transitions (Stanley, 1971) a divergence of localization length, α^{-1}, has been observed. α^{-1} varies as $1/(E-E_c)^s$, as energy E decreases from band edge towards E_c. s is generally found to be of the order to 2/3.

E_c and E_c', are known as mobility edges and at T=0, electron mobilities on one side of the edge (localized side) is zero, while on the other side (extended states), it is finite; mobility changes discontinuously at critical values of energy in an Anderson transition. The localization of states close to the edges is a feature common to both valence and conduction bands. When we recognize that the Fermi energy lies somewhere in between the two bands and is flanked by localized states, we immediately realize that if E_F can be moved through E_c, it can cause an insulator to metal transition. A material is referred to as *Fermi glass* when its E_F lies in the region of localized states (see Figure 8.07 (b) (bottom)).

Minimum metallic conductivity

The localization described above refers to the consequence of introducing random disordering energies E_i on sites in a periodic lattice. Introduction of positional disorder as in a glass keeping $E_i \approx$ constant is

entirely equivalent and causes localization (Mott, 1977; Mott and Davis, 1979).

If the maximum width of the energy due to disorder is finite, W, the width of the localized tail states is also finite. If this disorder energy is much higher than the bandwidth, the entire band gets localized. Semiconducting glasses are often transparent because the tail states have a finite width and are localized. Also, the valence band tail states may not overlap with the conduction band tail states.

The magnitude of the conductivity can be evaluated assuming that σ arises only from extended states. It was shown by Thouless (1979) that

$$\sigma(\omega) = \frac{k_F^3 e^2 \tau}{3\pi^2 m \left(\frac{1}{1+\omega^2\tau^2}\right)} \tag{8.09}$$

Therefore, $\sigma_{dc} = \sigma(0)$ is given by,

$$\sigma_{dc} = \frac{k_F^2 e^2 l}{3\pi^2 \hbar} \tag{8.10}$$

The Fermi surface is assumed to be spherical. In the above equations, k_F is the Fermi wave vector, l is the electron mean free path, m is the electron mass and τ is the relaxation time. $\tau = ml/\hbar k_F$. As the disorder increases, more and more states get localized and E_c and E_c' move toward the centers of the respective bands. The mean free path (l) also decreases and in the limit, $l = a$ which is the lattice distance (Ioffe-Regel limit). The conductivity also reaches the limit and is $\approx e^2/(3\pi\hbar a)$, since $k_F l$ becomes approximately equal to 1. Introduction of any further disorder only broadens the band and does not affect l, it alters $N(E)$. The minimum metallic conductivity, σ_{min} (all σ values like σ_{min}, σ, $\sigma(0)$ etc. refer only to d.c. conductivities in this chapter; the subscript d.c. is dropped to make the notation less cumbersome. A.c. conductivities will be referred to as $\sigma(\omega)$), before the disorder localizes all the states and the conductivity drops to zero for the three dimensional problem may be approximated as

$$\sigma_{\min}(3D) \approx \frac{e^2}{(27\hbar a)} \tag{8.11}$$

When a is roughly equals to 3 Å (approximately the localization length), $\sigma_{min}(3D)$ is of the order of 300-600 S cm^{-1}. Although the mobility edge

suggests a sharp transition, the presence of potential fluctuations causes undulation of energy states at the mobility edges. Thus electrons reside in allowed energy states, which are themselves isolated by fluctuations. These superimposed potential undulations, however, merge at higher values of energies, slightly above E_c. Hence at higher energies above E_c, more and more of these regions become connected and electrons can percolate among the allowed states. σ behaves as a function of energy above E_c. Therefore conductivity may not be expected to exhibit a sharp transition and only increases less rapidly above E_c in a manner shown in Figure 8.08. In the figure, (i) represents a sharp transition, while (ii) is a

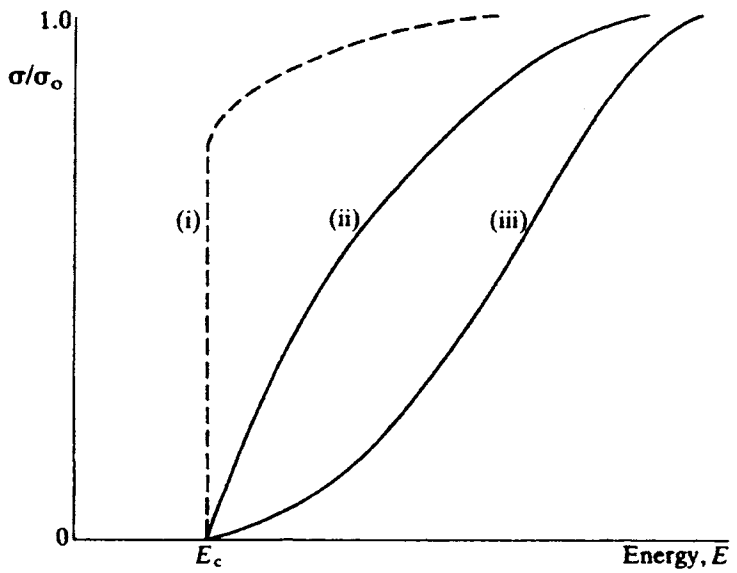

Figure 8.08. Behaviour of conductivity as a function of energy. Curve (i) is the sharp Mott mobility edge for homogeneous material, (ii) is the prediction of percolation theory and (iii) is the prediction of percolation theory for an inhomogeneous material (From Elliott, 1984).

percolative transition, which according to Fritzsche follows the power law,

$$\sigma = \sigma_0 (E - E_c)^{1.6} \tag{8.12}$$

where σ_0 is the energy independent value of conductivity in the extended states. It may be noted that minimum metallic conductivity was estimated by Mott as

$$\sigma_{min} = C\left(\frac{e^2}{\hbar a}\right) \tag{8.13}$$

where C is a constant with a value of 0.03, a is the minimum mean free path, which according to Ioffe-Regel rule cannot be less than the inter-atomic distance. Equation (8.13) also gives similar magnitude of minimum metallic conductivity, of 300 – 600 Scm^{-1}.

Conductivities

The semiconducting properties of the amorphous materials therefore, arises as a consequence of the existence of mobility edges, irrespective of whether there is a gap in the DOS or not. It is also likely that the gap consists of a variety of defect states as shown in Figure 8.09.

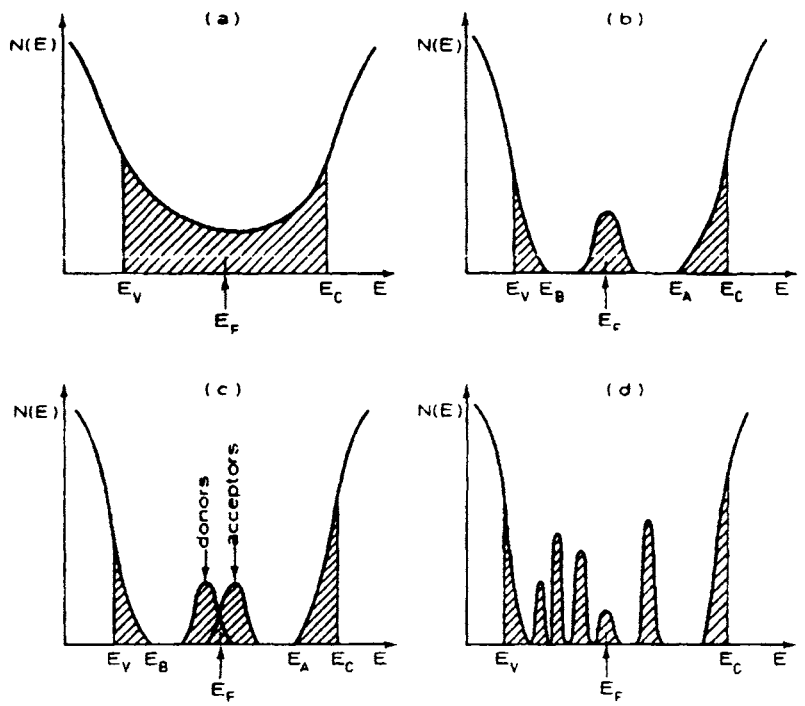

Figure 8.09. Density of states for amorphous semiconductors. (a) The CFO model, showing tailing of states causing overlap. (b) The Davis-Mott model, showing a band of compensated levels near the middle of the gap. (c) The Marshall-Owen model. (d) A "real" glass with defect states (After Nagels, 1979).

The total conductivity at finite temperature of an amorphous semiconductor is due to transport in both localized and extended regions, with the latter being obviously much higher than the former. The total conductivity, σ , is given by

$$\sigma = -\int \sigma_E \left(\frac{\partial f(E)}{\partial E} \right) dE \tag{8.14}$$

$$= e \int N(E).\mu(E).f(E)\{1 - f(E)\} dE \tag{8.15}$$

where $f(E)$ is the Fermi-Dirac distribution function and equal to $[1 + \exp((E - E_F)/kT)]^{-1}$ and $\sigma_E = e\, N(E)\mu(E)$ is the conductivity of electrons of energy E. The mobility of the electron in localized state may be taken as zero and neglected. Thus after integration

$$\sigma = \sigma_{ext} = eN(E_c)\mu_e kT \exp\left[-\frac{(E_c - E_F)}{kT} \right] \tag{8.16}$$

E_c is the mobility edge in the conduction band and before integration the function $(f(E)(1\text{-}f(E))$ has been approximated as $\exp[-(E\text{-}E_F)/kT]$. Thus

$$\sigma = \sigma_{min} \exp\left[-\frac{(E_c - E_F)}{kT} \right] \tag{8.17}$$

(in view of the earlier discussion on σ_{min}). Therefore, $\mu_e = \sigma_{min} / [ekTN(E_c)]$. If the mobility edges lie far from the center of the band ($W << B$) and if $N(E_c)$ is set roughly as $1/(B\, a^3)$, where a is approximately the localization length, using the expression $\sigma_{min} \equiv (\sigma_{min})_{3D} \approx e^2 / (27\, \hbar a)$, μ_e becomes,

$$\mu_e \approx \frac{ea^2 B}{27\hbar kT} \tag{8.18}$$

For reasonable values of parameters ($a \approx 3$Å, $B \approx 5$eV), μ_e becomes ≈ 9 $cm^2\ V^{-1}s^{-1}$. It should be remembered that although σ_{ext} is activated conductivity, $(E - E_F)$ is not equal to the observed E_{dc}, because the mobility gap itself is a function of temperature. Further several optical absorption and conductivity measurements have revealed that E_{dc} is less than or equal to half of $E_{optical}$, which indicates that Fermi level lies near

the center of the gap. Also value of E_F does not seem to vary by the introduction of a few shallow donors or acceptors and therefore, the Fermi energy may be considered as pinned in the mid-gap region.

Electron transport can also occur among localized states at non zero temperature and understandably only by thermally activated hopping between sites. The energy required for hopping is acquired by the exchange of energy with the thermal phonons in the system. Therefore it is the mobility μ_{hop}, that is activated for the case of hopping conduction and can be written as:

$$\mu_{hop} = \mu_0 \exp\left[-\frac{E_{hop}}{kT}\right] \tag{8.19}$$

where E_{hop} is the activation energy for hopping. An expression for μ_0 can be developed in the same manner as in the case of Brownian motion. If the mean free path is very short, $\mu_0 = eD/kT$, and $D = (1/6)\ \nu_0 R^2$; where R is the hopping distance and ν_0 is the attempt frequency corresponding to phonon frequency ($\approx 10^{13}$ s^{-1}). Therefore $\mu_0 = e.\nu_0 R^2 / (6\ kT)$. Using $R \approx 2$ Å and $E_{hop} \approx kT$, it gives μ_{hop} of roughly 10^{-2} $cm^2V^{-1}s^{-1}$ around 300 K, which is 3 orders of magnitude lower than the mobilities in extended states. This indeed justifies designating E_c and E_v as mobility edges. Thus there are distinct differences in the nature of conduction in amorphous and crystalline semiconductors.

On the basis of the fact that DOS in tail region varies rather sharply and that it follows a power law, Nagels (1979) derived an expression for hopping conductivity arising from localized states by assuming that hopping is confined to nearest neighbour sites,

$$\sigma_{hop} = \sigma^0_{hop}\left[\frac{kT}{(E_c - E_A)}\right]^s C\exp\left[-\frac{(E_A + E_F + \Delta)}{kT}\right] \tag{8.20}$$

where $\sigma^0_{hop} = ekTN(E_c)\mu_0$ and C is a constant dependent on temperature, s is the exponent and Δ is the mobility activation energy.

Variable Range Hopping

In highly defective amorphous semiconductor, there is a significant DOS in the gap and electron transport can also occur among such states.

Of course, it is necessary that electron transport occur by phonon assisted hopping from a filled to an empty state. Mott and Davis (1979) considered such a transport in the neighbourhood of E_F between two states separated by an energy Δ and a distance R. The hopping transition rate, ν, therefore depends on the carrier being able to find a phonon of energy, Δ. Electron transport is assumed to occur between two localized states with approximately equal localization length (α^{-1}). The attempt frequency is assumed to be ν_0. However, the electron transfer can also occur by tunneling between the two localized states and the probability for which is given by the overlap factor $\exp(-2\alpha R)$. Therefore the hopping transition rate ν is given by

$$\nu = \nu_0 \exp\left[-2\alpha R - \frac{\Delta}{kT}\right] \tag{8.21}$$

The conductivity is calculated using the relation, $\mu = eD/\mathrm{kT}$, where $D = (\nu R^2)/6$, so that

$$\sigma = \left(\frac{e^2}{6}\right) R^2 N(E_F) \nu_0 \exp\left(-2\alpha R - \frac{\Delta}{kT}\right) \tag{8.22}$$

where use is made of the fact that the DOS at the Fermi level contributing to conductivity is $\approx kT.N(E_F)$. At low temperatures, where the number and energy of phonons become very small, hopping to near neighbours becomes unfavourable because of the energy separation Δ. Tunneling term connecting distant sites becomes more favourable. Since such sites with similar energies are likely to be present at greater distances R (which is a variable range), Mott optimised the factor $2\alpha R + \Delta/kT$ using the criterion that there is at least one state of favourable energy range within a spatial distance R. That is in a sphere of volume $4\pi R^3/3$ and an energy range $N(E_F).\Delta$, there is at least one other state available for transport, thus, $1 = (4\pi/3).N(E_F).\Delta.R^3$ or $\Delta = 3/(4\pi\, N(E_F).\, R^3)$. Substituting this value for Δ in the exponent term $2\alpha R + \Delta/kT$, and optimising this function with respect to R by equating its differential to zero, the value of $R_{optimum}$ becomes

$$R_{optimum} = \left[\frac{9}{\{8\pi\alpha N(E_F) kT\}}\right]^{\frac{1}{4}} \tag{8.23}$$

Substituting this back into the previous expression for Δ, one gets $\Delta_{optimum}$. The two, $R_{optimum}$ and $\Delta_{optimum}$ can together be substituted in the expression for conductivity so that the expression for σ becomes

$$\sigma = \sigma_0 \exp\left(-\frac{A}{T^{1/4}}\right) \tag{8.24}$$

with $\sigma_0 = [e^2\ \nu_0/\ 2(8\pi)^{1/2}]\ [N(E_F)/\alpha kT]^{1/2}$ and $A = 2.1\ [\alpha^3/\ kN(E_F)]^{1/4}$. This is the celebrated Mott's $T^{1/4}$ law for variable range hopping, where it is assumed that DOS around E_F is constant. This expression has been used extensively in rationalizing the conductivity behaviour of amorphous materials at low temperatures. The expression suggests that from experimental plots of logσ vs $T^{-1/4}$, one can evaluate both $N(E_F)$ and α, using the values of σ_0 (intercept) and A (slope) but it needs to assume value of ν_0. The procedure gives $N(E_F)$ which is generally high and in the range of 10^{18} - 10^{19} /eV/cc. When α^{-1} is also assumed to be of the order of 10Å, the hopping distance is found to be in the range of 80 Å around 100 K. It may be noted that $N(E_F)$ and α can also be determined independently from an analysis of the high field behaviour of conductivities in the non-ohmic region.

Derivation of the $T^{-1/4}$ law, suggests that the spatial dimension of the amorphous sample should become important when one of the dimensions deceases to the level of R. In the study of thin film conductivities of Ge, it has been established that $T^{-1/4}$ dependence changes to $T^{-1/3}$ dependence, when the thickness of the film is reduced to less than ≈ 500 Å. (Knotek et al., 1974). As the temperature is lowered, we note that not only the magnitudes of the d.c. conductivity, but also the slopes, (the activation barriers) decrease. Thus the relevant activation barriers are (E_c - E_F) for band type conduction in extended states, and (E_A - E_F + Δ) for hopping conductivity in localized states. At still lower temperatures, the σ values dip further but becomes less sensitive to temperature in the region of variable range hopping. The variation of lnσ as a function of temperature can be linearised only when plotted as a function of $1/T^{1/4}$ and the slope gives A.

Thermoelectric power

Thermoelectric power is an important property essential for determining the sign of the charge carriers, in amorphous materials. When

a temperature gradient is applied across a sample, the sample develops a voltage. The constant of proportionality between voltage and temperature gradient for vanishing values of current through the sample, is known as Seebeck coefficient, S or the coefficient of thermoelectric power

$$S = \lim_{I \to 0}\left(\frac{\Delta V}{\Delta T}\right) \tag{8.25}$$

where ΔV is the voltage developed for an applied constant thermal gradient ΔT. S is related to the Peltier coefficient, Π as,

$$S = \frac{\Pi}{T} \tag{8.26}$$

The thermo power is given by the general expression:

$$S = -\frac{k}{(|e|\sigma)} \int \sigma_E \frac{(E - E_F)}{kT} \cdot \frac{\partial f(E)}{\partial E} . dE \tag{8.27}$$

Since $\sigma_E = eN(E)\mu(E)kT$, and also since $N(E)$ and $\mu(E)$ can be assumed as constant in the extended states, the above expression can be integrated so that,

$$S_{ext} = -\frac{k}{|e|}\left[\frac{(E_C - E_F)}{kT} + A\right] \tag{8.28}$$

(A.kT) represents the average energy of the transported electrons in the extended states. For conduction in extended states, $A \approx 1$ and since $(E_c - E_F)$ is temperature dependent, the above expression can be written as:

$$S_{ext} = -\frac{k}{|e|}\left[\left(\frac{\Delta E_{dc}}{kT}\right) - \frac{\gamma}{k} + 1\right] \tag{8.29}$$

where $E_{dc} = (E_c - E_F)$ at 0 K and γ is the coefficient of linear temperature variation of E_{dc}. Thus the slope of S vs $1/T$ plots gives $E_{dc}/|e|$. When the current is carried by hopping of carriers in localized tail states, where $N(E) \propto (E - E_A)^s$, a similar expression can be derived,

$$S_{ext} = \left(\frac{k}{|e|}\right)\left[\frac{(E_A - E_F + \Delta)}{kT} + K\right] \tag{8.30}$$

where K is a constant but different from A. Evidently the slope in S vs $1/T$ again gives the activation energy, which is different from that obtained from conductivity by a value Δ, which is the hopping energy. As the temperature is lowered in the measurement of S, the slope of S changes from (E_c - E_F) to (E_A - E_F), because the regime of electron transport changes from extended to localized states. It may be appropriate to note here that when transport is bipolar (i.e., both electrons and holes carry the current), S is weighted by the respective conductivities and is given by,

$$S = \frac{(S_e\sigma_e + S_h\sigma_h)}{(\sigma_e + \sigma_h)} \tag{8.31}$$

Hall coefficient

Hall effect is another important transport phenomenon and has been extensively studied in amorphous semiconductors. The Hall effect studies also assumed importance because of an anomaly observed between the sign of the charge carriers indicated by Hall coefficient and S in amorphous semiconductors. The Hall coefficient R_H is given by,

$$R_H = \frac{r}{ne} \tag{8.32}$$

where r is the scattering factor and n and e are carrier concentration and charge respectively. r is of the order of unity and is equal to ratio of hole and electron mobilities, $\mu_{hole}/\mu_{electrons}$. The sign of R_H corresponds to the sign of the charge carriers. Elliott (1984) has pointed out that the above equation is valid only, when the mean free path of the carrier is sufficiently long and therefore, Boltzmann transport theory is applicable. Since the mean free paths are short in amorphous materials, the above equation is strictly not applicable to amorphous semiconductors. In almost all cases of amorphous semiconductors, the sign of charge carriers indicated by R_H is opposite to that indicated by S and the origin of this observation is still not clearly understood. Since the mobilities of the carriers in localized states are very low, the observed Hall effect is generally assumed to arise only from extended states. Theoretical

formulation of Hall effect assumes that the carrier transport involves at least three sites perpendicular to the applied electric and magnetic fields. Friedman (1971) using random phase model, showed that the Hall mobility, μ_H is given by,

$$\mu_H \approx \left(\frac{4\pi}{3}\right)\frac{ea^5}{\hbar}.J.N(E_c)\left(\frac{\bar{z}}{z}\right) \tag{8.33}$$

In the above expression, a is the inter-site distance, $N(E_c)$ is the DOS at the mobility edge, J is the overlap integral (which determines B), z is the coordination number and $\bar{z}$ is the average number of closed three site paths around a given site. The above formulation suggest that the Hall mobility is temperature independent. Assuming that $\bar{z} \approx z$, a $\approx$ 3 Å and $J = B/2z \approx 1$ eV, μ_H is about 10^{-1} $cm^2V^{-1}s^{-1}$ which may be compared with electron mobilities from conductivity studies of about 10 $cm^2V^{-1}s^{-1}$. μ_H for hopping electrons in localized states turns out to be even smaller. $\mu_H^{hop} = 10^{-4}$ $cm^2V^{-1}s^{-1}$. It is generally argued that the sign of the Hall coefficient is related to the number of transfer integrals involved in closed loops. Even then the sign of Hall coefficient in chalcogenide glasses is invariably negative, while that of the Seebeck coefficient is positive, the reason for which still remains unclear.

Polaronic transport

The charge carriers (electrons and holes in the present context) invariably induce distortion or polarization in their surroundings. A localized carrier like electron, for example, induces dipole moment on its neighbours and gives rise to monopole-dipole interactions, which lowers its own energy. This is true of ions also in ionic transport. As a consequence of this polarization effect, the charge carrier has now become an entity known as *polaron*, the charge carrier plus its polarized environment. The charge transport itself is due to the motion of these entities and hence the description *polaronic conductivity*. If the distance over which the polarization occurs, is short, the entity is described as a small polaron and if it is long, it is described as a large polaron. Polaron formation may involve neutral molecules around a charge carrier, in which case it is described as a molecular polaron. In general, formation of a dipole and its interaction with carrier also involves distortion of the surroundings. The polaron formation energy, W_P, therefore, involves a deformation potential and the bulk modulus, which resists the distortion;

$$W_P = \frac{E_d^2}{2\kappa_T a^3} \tag{8.34}$$

where E_d is the deformation potential, κ_T is the isothermal bulk modulus and a^3 is a measure of the polaron size. Alternately W_P can also be calculated as,

$$W_P \approx \frac{e^2}{2\varepsilon_p a} \tag{8.35}$$

where

$$\frac{1}{\varepsilon_p} = \frac{1}{\varepsilon(\infty)} - \frac{1}{\varepsilon(0)} \tag{8.36}$$

During the polaron transport therefore, this polaron formation energy behaves as an additional barrier for hopping. Thus the polaronic conductivity, due to the carriers which are excited above the mobility edge, is given by,

$$\sigma = \sigma_0 \exp\left(-\frac{E_{dc} + W_H}{kT}\right) \tag{8.37}$$

where $W_H = W_P/2$ is the energy required to produce an equal number of oppositely charged carriers (electrons and holes) and E_{dc} is the activation barrier. The pre-exponential factor is given by,

$$\sigma_0 = \frac{Ne^2a^2\nu\ P}{kT} \tag{8.38}$$

where N is the charge carrier density and ν is the attempt frequency of the order of the lattice phonon frequency and P is the jump probability, which is itself a combination of two probabilities P_1 and P_2, where P_1 is a coincidence probability and P_2 is a charge transfer probability. $P_2 \approx 1$, while P_1 can be $\approx 10^{-1}$ - 10^{-2}. Hall mobility of the polarons μ_H (polarons) is lower than its conductivity mobility, μ_σ (polaron). μ_H (polaron) $\approx(1/3)\mu_\sigma$(polaron). Emin (1976) derived an expression for the

thermopower associated with small polaron transport (confined to extended states) as,

$$S_{ext} = -\frac{k}{|e|}\left(\frac{E_{dc}}{kT} + A\right) \tag{8.39}$$

where E_{dc} is the same as in the conductivity expression and A, which is the heat transport term, is generally expected to be of the order of 1-10.

Good examples of small polaron transport are the glasses containing transition metal ions in two valence states such as (V^{4+}, V^{5+}), (Fe^{2+}, Fe^{3+}), (Cu^{+}, Cu^{2+}) and (Mo^{5+}, Mo^{6+}). In all of them, when the electron jumps from the lower valent ion to the higher valent ion, the lattice distortion also moves along with the electron. Mott derived an expression for the polaronic d.c. electrical conductivity of glasses containing transition metal ions,

$$\sigma_{dc} = \sigma_0 \exp\left(-\frac{W}{kT}\right) \tag{8.40}$$

where $\sigma_0 = c\,(1\text{-}c)e^2\nu_{el}/(RkT)\exp[-2\alpha R]$, c is the concentration of one type of ions (for example V^{4+} in a glass containing V^{4+}:V^{5+} couple), R is the separation of carrier sites and α^{-1} is the localization length for the wave function. But W depends on temperature:

$$W = W_H + \frac{1}{2}W_D \quad \text{for } T > \frac{\theta_D}{2} \tag{8.41}$$

$$W = W_D \quad \text{for } T < \frac{\theta_D}{4} \tag{8.42}$$

W_D is a disorder energy, characterizing the distribution of the ions and θ_D is the Debye temperature. In transition metal oxide containing glasses, it has been noted that the activation energy decreases with decreasing temperature, an example of which is shown in Figure 8.10(a) and 8.10(b). Triberis and Friedman (1981) (TF) applied percolation theory to the high temperature transport considering that small polaron hopping is a multi-phonon assisted process. They derived as expression similar to Mott's $T^{1/4}$ law which is given by,

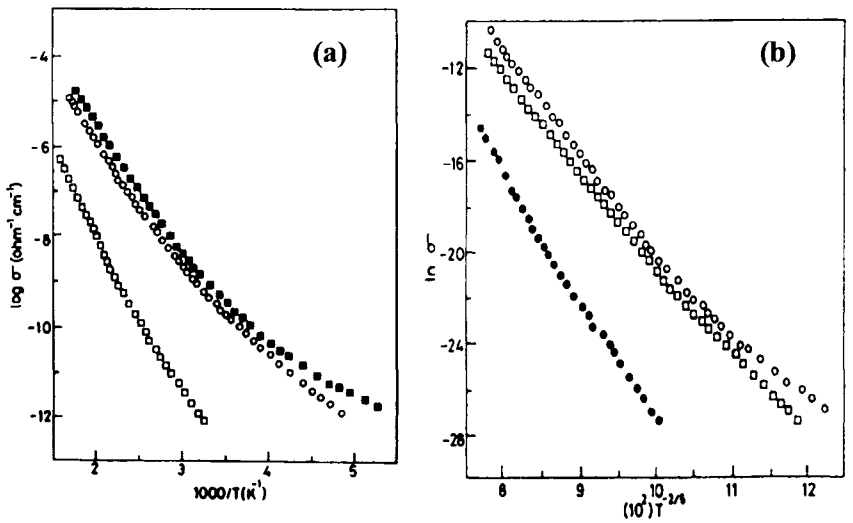

Figure 8.10. Plots of (a) logσ against 1000/T and (b) lnσ against $T^{-2/5}$, for xPbO-(80-x)MoO_3-20P_2O_5 glasses: ○, x=0; ■, x= 20; ◧, x=30 (After Selvaraj and Rao, 1988).

$$\sigma = \sigma_0 \exp\left[-\frac{A'}{T^{\frac{2}{5}}}\right] \tag{8.43}$$

where σ_0 and A' are constants and A' is equal to $[8.5N_s^{1/2}\alpha^{3/2}/(kN_0)]^{2/5}$. N_s and N_0 are the density of sites and density of localized states near E_F respectively. Selvaraj and Rao (1988) have used Triberis-Friedman (1981) analysis of conductivity for the case of phosphomolybdate and phosphotungstate glasses. Log σ vs $T^{-2/5}$ plots exhibit good linearity as shown in Figure 8.10(b). Further TF analysis also leads to the conclusion that the $2\alpha R$ term in the exponent of Mott expression for polaron conductivity becomes significant only at low values of R or higher concentrations of carrier centers. The continuous decrease in activation energy as the temperature is lowered, can also be explained on the basis of small polaron variable range hopping, because the activation energy for such hop should also continuously decrease with decreasing temperature.

A.c. conductivity

In a.c. fields the behaviour of conductivity of amorphous semiconductors as a function of ω follows the same universal behaviour as

in the case of glassy ionic conductors

$$\sigma(\omega) = \sigma(0) + A\omega^{s}$$

where $\sigma(0)$ is the non dispersive d.c. component of the conductivity. It has been pointed out (Elliott, 1993) that in identifying $\sigma(0)$ as σ_{dc}, there are conceptual difficulties, if the d.c. and a.c. transport mechanisms are not identical, as assumed in the above equality. In glasses like amorphous chalcogenides, such an assumption is not satisfactory, since a.c. and d.c. responses arise from different mechanisms. The exponent s in the above equation is generally less than unity and very often has a value of ~ 0.8. The relevant equations relating the complex susceptibility, dielectric constant and conductivity have already been discussed (chapter 7). We recast those relations slightly differently for facilitating the discussion to follow.

$$\varepsilon'(\omega) = 1 + \chi'(\omega) \tag{8.44}$$

$$\varepsilon''(\omega) = \chi''(\omega) \tag{8.45}$$

where χ' and χ'' are from the complex susceptibility. We recall that the components of complex conductivity can be written as,

$$\sigma'(\omega) = \omega\varepsilon_0\varepsilon''(\omega) \tag{8.46}$$

$$\sigma''(\omega) = \omega\varepsilon_0\varepsilon'(\omega) \tag{8.47}$$

The loss tangent is simply, $\tan\delta = \varepsilon''/\varepsilon'$. The real part of the a.c. conductivity, $\sigma'(\omega)$ is

$$\sigma'(\omega) = \int_0^{\infty} \alpha\, g(\tau) \left[\frac{\omega^2\tau}{(1+\omega^2\tau^2)} \right] d\tau \tag{8.48}$$

$g(\tau)$ is the distribution of relaxation times, α is the polarisability of a pair of sites connected in the transport event and assumed to be independent of τ. In general, evaluation of the frequency response of electron transport requires the loss terms to be calculated by considering the polarisability of an isolated pair of sites. There is no need for a continuous percolation

path. The basis of such calculation of a.c. loss term is known as 'pair approximation'. If $g(\tau)$ is assumed to be proportional to $1/\tau$, then the above integral can be written as

$$\sigma'(\omega) \propto \int \omega \frac{d(\omega\tau)}{1+\omega^2\tau^2} \tag{8.49}$$

Therefore,

$$\sigma'(\omega) \propto \omega \tag{8.50}$$

For $g(\tau)$ to be proportional to $1/\tau$, it requires the relaxation time to be an exponential function of some random variable ξ, such that $\tau = \tau_0 \exp(\xi)$, where ξ itself has a flat distribution. It means that $n(\xi)$ = constant, and $n(\tau) = n(\xi).\ (d\xi/d\tau) \propto \tau^{-1}$. If α, the polarisability, is also a function of ξ, then it can lead to a sub-linear frequency dependence of $\sigma'(\omega)$. The functional form given for the variation of τ can arise from two different relaxation mechanisms. The first is a classical barrier hopping, in which two energetically favourable sites like in a double well potential are separated by a barrier W and $\xi = W/kT$. The second mechanism is a phonon assisted quantum tunneling through a barrier, which separates two equilibrium positions, in which case $\xi = 2\alpha R$, where α^{-1} is the localization length and R is the separation between the sites. In the first case, by treating W as independent of R, it has been shown (Pollak and Pike, 1972) that

$$\sigma'(\omega) = \frac{\pi\omega\, e^2 R_0^2 NkT}{6\Delta_0 W_0} \tanh\left(\frac{\Delta_0}{2kT}\right) \tag{8.51}$$

where Δ_0 is the highest energy difference between the two sites, W_0 is the highest barrier among the connected sites and R_0 is the minimum distance between the sites. Important point to note is that this essentially atomic hopping model leads to linear dependence of $\sigma'(\omega)$ on ω. But assuming a quantum mechanical tunneling model, where the carrier tunnels through a barrier to a distance R, it has been shown that $\sigma'(\omega) \propto \omega^s$, where s is given by,

$$s = 1 - 4\ln^{-1}\left(\frac{1}{\omega\tau_0}\right) \tag{8.52}$$

For a value of ω equal to 10^4 s^{-1} and typical τ_0 of 2×10^{-13} seconds, s is equal to 0.8, which is the basis of the so-called $\omega^{0.8}$ law.

Austin and Mott (1969) derived an expression for the a.c. hopping conductivity using pair approximation and assuming that the dipoles which contribute most to σ are those for which $\omega\tau = 1$ (Drude's criterion). For electron hopping between two localized sites separated by a distance R and small energy, ΔE, the average hopping frequency $1/\tau$ is given by,

$$\frac{1}{\tau} = \nu_{phonon} \exp(-2\alpha R)\exp\left(-\frac{\Delta E}{kT}\right) \tag{8.53}$$

The mean hopping distance must depend on frequency because of Drude's condition. There are therefore, all the insignia of a variable range hopping, but with the hopping range determined by the a.c. frequency. Thus,

$$\sigma'(\omega) = Ce^2\alpha^{-5}g^2(E_F)kT\omega\left[\ln\left(\frac{\nu_{phonon}}{\omega}\right)\right]^4 \tag{8.54}$$

where $C = \pi^2/24\ln 2 \approx 0.3$ (but Pollack obtained C $\approx$ 1). Under quite general conditions such as $\omega << \nu_{phonon}$, it has been shown that the above equation gives $\sigma(\omega) = A\omega^s$.

Correlated Barrier Hopping

Tunneling model does not account for many experimental observations. Hence Pike (1972) and later Elliott (see Long, 1982 and Elliott, 1987) developed the model of *correlated barrier hopping*. The model is actually a combination of variable energy and variable range hopping models. Since in this model the height of the potential barrier is correlated to the intersite separation, it is known as correlated barrier hopping (CBH) model. CBH model allows for hopping of both single and pair of electrons, the later is referred to bipolaron hopping. The nature of hopping is represented in Figure 8.11, in which W_M represents the maximum barrier, experienced by a carrier, which is the difference in energy between E_c and the site energy. The dotted lines indicate the manner of variation of the potentials when the carrier is present in the two states, located at a distance R and Δ is the disorder energy. The variation of the effective barrier, W, is indicated by full line, which evidently tends

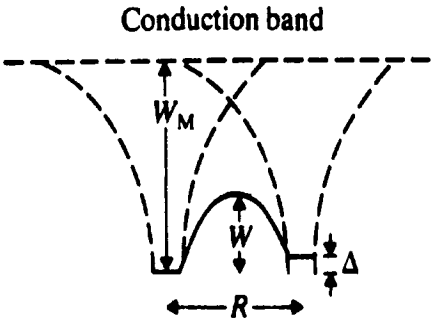

Figure 8.11. Diagram of the potentials experienced by carriers which are separated by a distance R in CBH model.

towards W_M as R increases. Functional dependence of W on R is given by,

$$W = W_M - \frac{ne^2}{\pi\varepsilon_0\varepsilon R} \tag{8.55}$$

where n is equal to 1, for single carrier hopping and 2 for a bipolaron hopping (see later). In the CBH model, both R and W are treated as frequency dependent. Hopping occurs preferentially when the activation energies for the sites is such that $\omega\tau = 1$. This leads to a relation between R_ω and W_ω (the ω - dependent hopping distance and ω - dependent energy) which is given by

$$R_\omega = \left(\frac{ne^2}{\pi\varepsilon\varepsilon_0}\right)\left[\frac{1}{(W_M - W_\omega)}\right] \tag{8.56}$$

The conductivity in the CBH model indicates that $\sigma(\omega) \propto R_\omega^6$. R_ω^6 is then expanded in terms of $(1/W_M^6)$ $(1/\omega\tau_0)^\beta$ in order to arrive at a frequency exponent of ω. The CBH model gives the exponent β which is $(1\text{-}s)$ as

$$\beta = \frac{6kT}{W_M} \tag{8.57}$$

Therefore the exponent s in the power law form is $[1\text{-}6kT/\ W_M]$ suggesting that s decreases with increase in temperature, which is the most commonly observed behaviour of s. Another implication from the CBH model is that

W_M is related to E_{dc}, the activation barrier in d.c. conductivity,

$$W_M = 2(E_0 - E_{dc}) \tag{8.58}$$

Since $E_{dc} \approx E_o/2$, where E_o is the optical gap, W_M is itself a measure of the optical gap.

In chalcogenide glasses (see later) charged defect pairs are formed and their transport is more appropriately described using a bipolaron mechanism. It is generally assumed that the defects are randomly distributed. But in glasses, this may not be the case because glasses are obtained by quenching from their molten states and the oppositely charged defects remain paired and frozen at T_g. This alters the spatial distribution function of defects. Instead of $P(R).dR = 4\pi NR^2 dR$ appropriate for random distribution, Elliott (1979) suggests the use of

$$P(R)dR = 4\pi NR^2 \exp\left(-\frac{4\pi NR^3}{3}\right)\exp\left(\frac{e^2}{4\pi\varepsilon\varepsilon_0 kT_g R}\right) \tag{8.59}$$

as the distribution function. The first exponential term in the above expression indicates that as pair distance, R increases, the probability decreases rapidly. The second exponential term produces the opposite effect due to Coulombic interactions. This feature affects the ω dependence significantly as a result of which $s = (1-\beta)$ changes to $s = (1 - \beta + \delta)$, where $\delta = T/8T_g$. Thus, in chalcogenide glasses, one would expect that if $W_M/6k \approx 8T_g$, then s will not only be unity but also temperature independent.

Long (1982) derived an expression for the real part of the a.c. conductivity for the same CBH model, which is given by,

$$\sigma'(\omega) = \left(\frac{1}{12}\right)\pi^3 g_0^2 (kT)^2 \varepsilon\varepsilon_0 \omega R_\omega^6 \tag{8.60}$$

where $g_0 = n/\Delta_0$. For the limiting value of Δ_0, the (largest) disorder energy, s has been shown to be

$$s = 1 - \frac{6kT}{W_M - kT\ln\left(\frac{1}{\omega\tau_0}\right)} \tag{8.61}$$

Similarly the temperature dependence of σ has been derived as $\sigma \propto T^a$, where $a = 1 - s \ln(1/(\omega\tau_0))$. In the case of small polarons there is a strong local polarization and an associated polaron formation energy, W_P. Due to the strongly localized nature of the distortions, there may not be any overlap between small polarons and the corresponding activation energy is simply $W_H \approx W_P/2$, which is independent of the inter-site separation R. The small polaron transport is therefore characterized by a modified s value, which is given by,

$$s = 1 - \frac{4}{\left[\ln\left(\frac{1}{\omega\tau_0}\right) - \frac{W_H}{kT}\right]} \tag{8.62}$$

However in the case of large polarons, the overlap of potential wells of neighbouring sites decrease the polaron formation energy which may be represented approximately as

$$W_H = W_{H0}\left(1 - \frac{r_0}{R}\right) \tag{8.63}$$

where W_{H0} is the polaron energy corresponding to zero overlap and r_0 is the polaron radius. Gilroy and Phillips (1981) considered the possibility of non-random distribution of barrier heights by postulating an exponential distribution and were able to show that s can surprisingly be super-linear and is given by

$$s = 1 + \frac{kT}{W_0} \tag{8.64}$$

W_0 is the maximum value of W - the barrier height – and is related to glass transition temperature. There has been much discussion in the literature about the functional dependence of exponent s on temperature and frequency. The various frequency dependencies of s values is shown schematically in Figure 8.12.

Chalcogenides of group IV and V elements form glasses, which constitute a major class of amorphous semiconductors. As a class of semiconductors, hydrogenated amorphous silicon and carbon constitute a

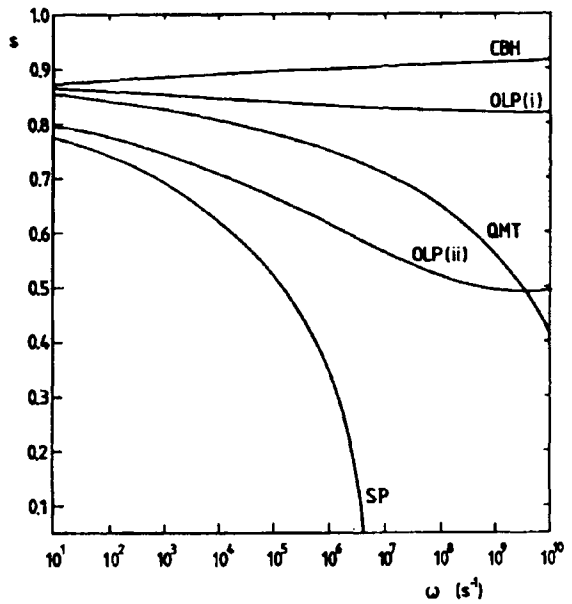

Figure 8.12. Frequency dependence of the frequency exponent s for various models: correlated-barrier hopping (CBH) ($W_M/kT=75$ has been assumed); small polaron (SP), quantum mechanical tunneling (QMT) and overlapping large polaron (OLP) tunneling. For OLP(i) the reduced polaron radius is $r_0'=20$ and for OLP(ii) $r_0'=2.5$. ($W_H/kT=10$ for SP and OLP) (After Elliott, 1987).

different category. Elliott (1987) has reviewed a.c. conduction in chalcogenide glasses. Notable features of the a.c. conductivity of chalcogenide glasses are: (1) a.c. conductivity increases monotonically with frequency almost up to 10^{10} Hz. (2) After subtracting the contribution from the d.c. conductivity, the a.c. conductivity alone can be fitted to $A\omega^s$ function. (3) At a given temperature, s is generally independent of frequency, but it is a function of temperature and usually increases towards unity as the temperature is decreased. (4) Value of s is generally slightly less than unity and only rarely exceeds unity. (5) The magnitude of the a.c. conductivity at a given frequency and temperature lies in a very narrow range (10^{-9} - 10^{-8} S cm^{-1}) for a variety of glassy chalcogenides as shown in Figure 8.13. (6) s increases with increasing band gap.

Charged defects

In the preceding discussion, we have assumed that there are extended and localized electron states, where the conduction is largely due

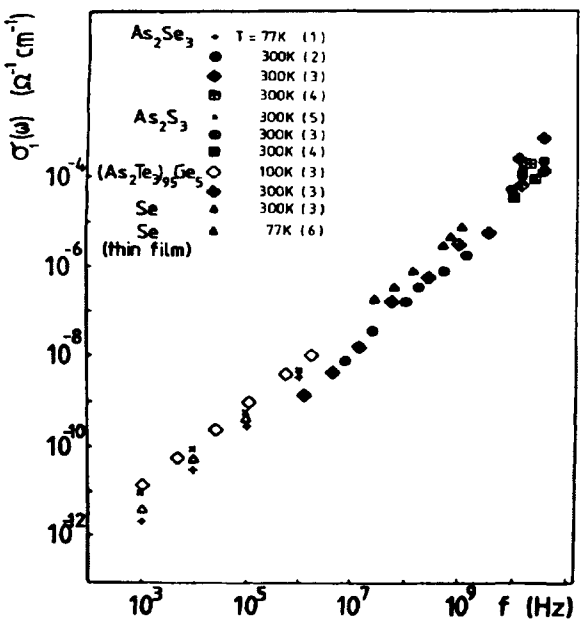

Figure 8.13. Frequency dependence of the real part of the a.c. conductivity for various chalcogenide glasses (After Le Cleac'h 1979 a,b).

to single electron transport. However, we also noted in the context of Mott and Davis model (Figure 8.09) that the center of the gap consists of small distribution of overlapping density of states, corresponding to single and paired states. When the state in the overlapping tail region originates from the valence band then the filled state appears to correspond to higher energy. We also noted in passing that transport can occur via bipolaron hopping which is due to the simultaneous transport of two electrons from one atomic site to another. We now concern ourselves with a discussion of the origin and manner of transport of such two electron states.

Covalent random networks conform to the (8-*n*) rule*. In these structures, a number of bonds are strained, either bent or over-stretched. Therefore, occasionally they get "broken". These broken bonds correspond to single electron carrying orbitals and are described as dangling bonds. In the case of a tetrahedral semiconductor, the nature of such states can be understood with the help of simple molecular orbital diagrams as shown in Figure 8.14. The bonding orbitals are the sp^3

* According to this rule an atom which has (8 - *n*) electrons can only form *n* covalent bonds – thus completing its stable octet of electrons in the valence shell.

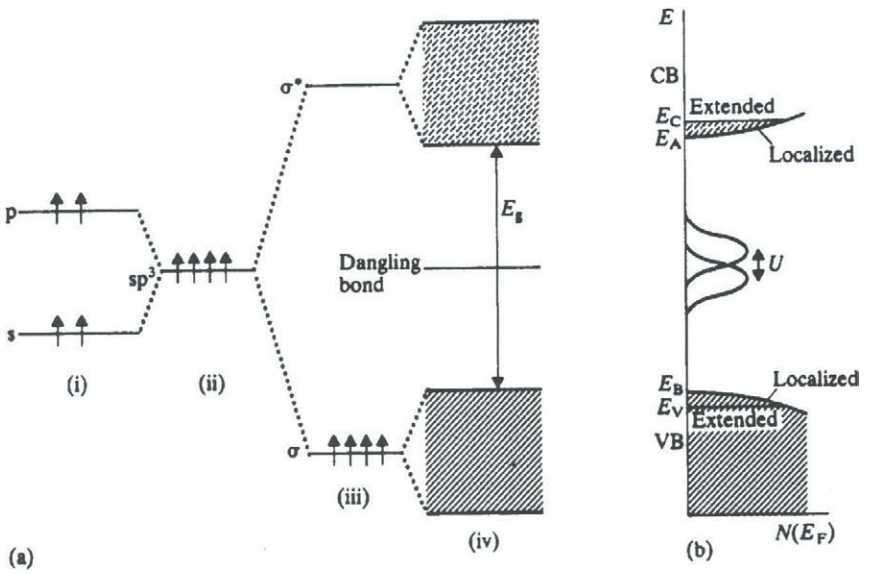

Figure 8.14. (a) Schematic representation of the origin of valence and conduction band states for a tetrahedrally bonded semiconductor (i) atomic *s*- and *p*- states; (ii) sp^3- hybrid states; (iii) bonding (σ) and anti-bonding (σ^*) states; (iv) broadening of σ- and σ^*- states into valence bands (VB) and conduction band (CB). (b) Density of states for such a band scheme, showing the localized band tail states. A dangling-bond band is also near mid-gap, together with the band for double occupancy higher by *U* in energy (for positive-*U* system) (From Elliott, 1984).

hybridised orbitals on Si or Ge. When they overlap in a tetrahedral coordination, they form four σ (bonding) and four σ^* (anti-bonding) orbitals. In solids, the σ and σ^* levels spread out into bands, as schematically represented in the figure. This may be compared with the now familiar DOS picture at the right extreme.

Dangling bond energies are in the middle of the gap because the corresponding orbitals have returned to their pre-bonding state after having been broken. These are shown in DOS diagram as two small bands. The peak energies are separated by *U*. The upper band in this corresponds to an addition of an electron to the singly occupied dangling bond orbital. Due to electron-electron correlation, which is positive, this band is shown displaced slightly upward in energy. The overlap of these little bands indicates that below the point of intersection of band, a few such doubly occupied states can exist. These are essentially lone pair states on the tetrahedral but three-coordinated atoms. The band corresponding to the doubly occupied states is like an acceptor band. The states in this band

carry a negative charge when filled. The band corresponding to singly occupied dangling bond is like a donor and is positively charged when empty and neutral when singly occupied, whereas the acceptor-like orbitals are neutral, when empty. U in Figure 8.14(b) is known as the Hubbard correlation energy, which is essentially coulombic and its expectation value is,

$$U = \left\langle \frac{e^2}{4\pi\varepsilon_0 \varepsilon\, r_{12}} \right\rangle \tag{8.65}$$

The DOS picture in Figure 8.14 depicts the model of Mott and Davis, who initially considered U as positive. An important consequence of this model was that it explained the transparency of amorphous tetrahedral semiconductors (for photon energies less than the mobility gap). We may recall that in the CFO model (Figure 8.09), it was considered that the gap region is filled completely by the overlapping of localized valence and conduction bands tail states. Since these states in the overlapping region are single electron states (dangling bonds), their overlapping effectively pins the E_F near the mid-gap. Mott-Davis model also accounts for pinning of E_F in a similar way. The overlap of conduction and valence band states in the middle region does not make the material a metal because the states are localized. The materials are indeed Fermi glasses as noted earlier. But then why would pairing occur if the energy of the resulting states is higher?

There are two important experimental observations in chalcogenide glasses which support pairing of electrons and which have led to new theoretical developments. They are the absence of ESR signals and the diamagnetic behaviour of the chalcogenide glasses (Agarwal, 1973). This is in contrast to the properties of tetrahedral semiconductors like *a*-Si and *a*-Ge. The absence of ESR signal can only be due to pairing of electrons in the otherwise single electron states. Anderson suggested that the stabilization of such doubly occupied states could be due to a strong electron-phonon coupling. In other words the coupling leads to a negative value of the effective correlation energy – negative Hubbard U. In the presence of electron-phonon coupling, U_{eff} at the electron pair site is given by

$$U_{eff} = U - \frac{2\lambda^2}{\hbar\omega} \tag{8.66}$$

where λ is the coupling constant and ω is the phonon frequency. Thus U_{eff} can be negative, when $2\lambda^2/\hbar\omega > U$. On comparison, one sees that both CFO and Anderson model postulate a continuous DOS in the gap, but the gap states in Anderson model are doubly occupied, while in CFO there can be singly occupied states as well. Since both of them allow for the presence of empty states just above E_F, if electrons are injected into such materials, they preferentially occupy states just above E_F without materially shifting it.

Creating a doubly occupied state out of the gap states, which originate from a dangling bond, is in effect creating a charged dangling bond. These charged dangling bonds have their counterparts in positively charged states, which are empty orbitals (donor orbital states). In chalcogenide glasses, there are two equivalent descriptions of the formation of these charged defects. Street and Mott (1975) designated these defects as D^0 (neutral dangling bond), D^+ and D^- which are respectively the positively and the negatively charged centers. D indicates that they are defects in an amorphous lattice. In a manner somewhat similar to Anderson's, Street and Mott (1975) suggested that formation of D^+ and D^- (charged pairs) from $2D^0$ states can be energetically favourable, because the coulombic interactions arising from the charged pair can give rise to local relaxations, which can decrease the otherwise positive Hubbard U into an effective negative Hubbard U as is schematically shown in Figure 8.15. Therefore the reaction $2D^0 \rightarrow D^+ + D^-$ is considered exothermic.

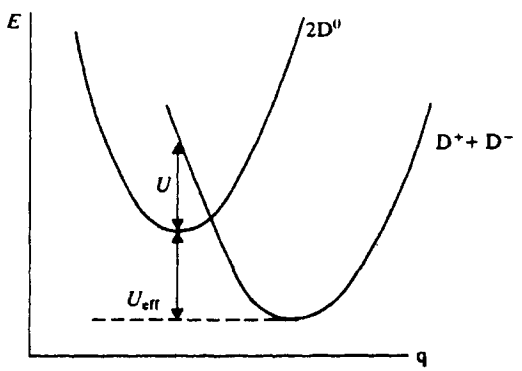

Figure 8.15. Configuration coordinate diagram for the formation of a D^+-D^- pair. Exchange of an electron between two D^0 centres to give a D^+-D^- pair at the *same* configuration costs the Hubbard energy U. The D^+-D^- centers subsequently relax to a different configuration and the overall energy is lowered by the effective correlation energy U_{eff}.

Kastner, Adler and Fritzsche (KAF) (1976) gave a simpler and more direct chemical explanation of pairing in their valence alternation model. Consider C as representing a chalcogen (ex: Se in selenium chains). Each C is coordinated to two other C atoms and carries zero charge. It can be designated as C_2^0 where superscript represents the charge and the subscript the bonded connectivity. When a C-C bond is broken, it corresponds to the formation of two C_1^0 atoms, C_1^0 being a singly covalently bonded neutral chalcogen. This represents the formation of dangling bonds. Two C_1^0s can react such that the electron from one is transferred to the other giving rise to a C_1^- and a C_1^+. C_1^+ is short of two electrons for the formation of stable valence level octet. Therefore C_1^+ can accept a lone pair from a neighbouring C_2^0 and form a covalent (dative) bond to C_1^+. The result is C_1^+ becomes C_2^0 and the C_2^0 responsible for the dative bond becomes C_3^+ since it now has three covalent bonds and a formal positive charge; formal because its own share of electrons falls short by one. The reactions may be summarized as

$$2C_2^0 \rightarrow C_1^0 + C_1^0 \qquad \text{(bond breaking)}$$
$$C_1^0 + C_1^0 \rightarrow C_1^+ + C_1^- \qquad \text{(electron transfer)}$$
$$C_1^+ + C_2^0 \rightarrow C_2^0 + C_3^+ \qquad \text{(dative bond formation)}$$

$$2C_2^0 \rightarrow C_1^- + C_3^+ \qquad \text{(net reaction)}$$

The net reaction is formation of a pair of coulombically charged centers. The important point to note is that the total number of covalent bonds are conserved in this reaction and an additional lone pair is created on one of the chalcogen atoms (C_1^-). In fact the first two reactions in effect corresponds to a single step heterolytic bond-breaking reaction quite familiar in chemistry. In elemental chalcogen glass like Se, it emphasizes the amphoteric nature of the reaction (Se behaves both an acceptor and a donor). The above reaction requires only a net energy expenditure of about 0.5–1.0 eV, which is the sum of lone pair formation energy, the coulombic stabilization energy due to the formation of charged centers and other lower order contributions to the energy. One can estimate the number of such defect pairs, present in a chalcogen glass assuming that they were at equilibrium just above T_g and were frozen at T_g. If the defects are randomly distributed then using the relation $n_d \approx n_0 \exp(-U/2kT)$, in the case of glassy Se, (T_g is $\approx$ 300K and n_0 is 10^{22}/cc), n_d is $\approx 10^{18}$/cc. This value seems to be in accordance with experimental estimates. If instead of being randomly distributed, the defects pair up in the molten stage such

that C_3^+ and C_1^- remain as nearest neighbours, their coulombic energies lower the formation energies still further and the number of such "intimate valence alternation pairs" (IVAP) can be much higher.

Defects of similar kind can form in pnictogen (As, Sb and Bi) containing glasses. D^+-D^- or C_3^+-C_1^- can be described as conjugate pairs of defects. Their formation in V group chalcogenide glasses like As_2Se_3 or As_2S_3 is easy to visualize. For example in As_2Se_3, there are only As-Se bonds and when an As-Se bond is broken, the higher electronegativity of Se dictates a heterolytic scission of the bond, leading directly to the formation of Se^- (C_1^- defect) in the structure. The positive charge bearing

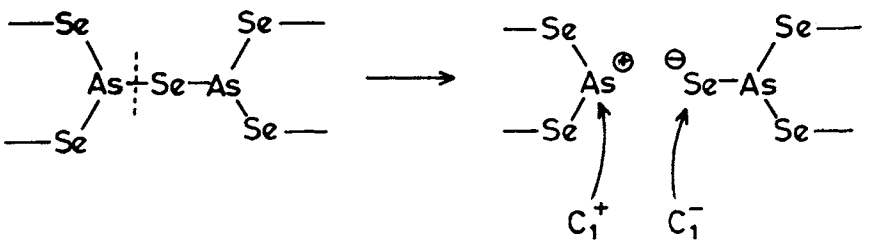

As^+ immediately bonds to the lone pair on a two-bonded Se (C_2^0) as shown below:

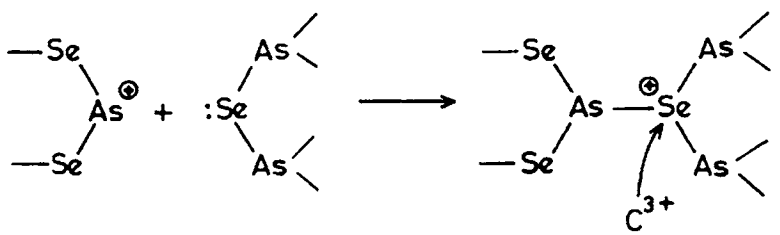

and creates the C_3^+ center. Thus, in a chalcogenide, both positively and negatively charged defects are formed by the more electronegative chalcogen atoms only.

Defect controlled properties

In complex chalcogenide glasses containing more than one chalcogen, such as in $As_2(Se,Te)_3$ it is intuitively obvious that the first heterolytic scission would occur on the weaker As-chalcogen bond so that C_1^- defect is formed on Te and recovery of the covalent bond would be by the coordination to Se. In this process, a relatively weaker As-Te bond is replaced by a stronger As-Se bond (see scheme below). The net energy

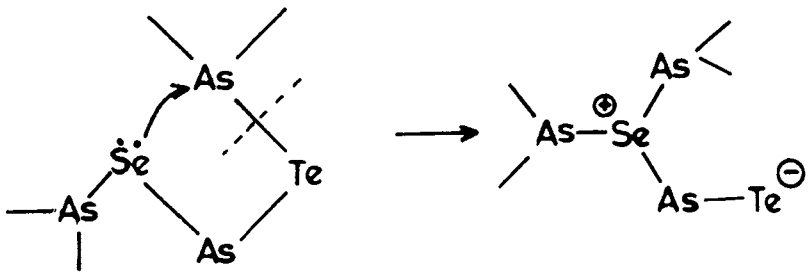

cost for the formation of the conjugate pairs in such situations can be written as, $U_{eff} \approx U_{lp} - \Delta$, where Δ is the difference in bond energies between As-Se and As-Te. Rao and Mohan (1981a) evaluated on the basis of this approach minimum energy required for the formation of conjugate pairs of defects in a variety of glasses using known values of bond energies, and assuming that the lone pair formation energy, U_{LP}, is approximately 1.0 eV.

The activation barriers for d.c. conductivity in defect controlled materials like chalcogenide glasses is the sum of the defect formation energy and the migration barriers. Since the migration barriers are generally very small, d.c. conductivity activation energies are expected to be equal to the defect formation energies. The experimental activation barriers for d.c. conductivities were found to be in good agreement with U_{eff} calculated in the above manner in several chalcogenide glasses as shown in Table 8.1. It is also possible to understand qualitatively the nearly universal positive sign of the Seebeck coefficient of chalcogenide glasses in the light of defect model (Rao and Mohan, 1981b). The mode of transport may be visualized as shown below in which positively charged defect can move in a more facile manner by bond switching compared to the motion of negative centers which need bond breaking.

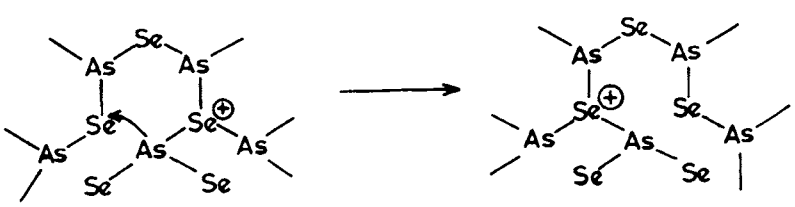

Another aspect of transport properties of chalcogenide glasses which needs to be understood is why Fermi level remains pinned in them. Adler and Yoffa (1976) calculated the Fermi level on the basis of the

existence of donor and acceptor like bands of small magnitude near the middle of the gap. Whenever U_{eff} is negative, the Fermi energy appears to remain constant, because the acceptor states are filled and the injected electrons only fill the narrow donor like bands which do not alter much the Fermi level which is why the Fermi level remains pinned.

Photoluminescence observed in amorphous chalcogenides (see chapter 11 for a discussion on photoluminescence) can also be understood on the basis of the presence of defect states. Photo-excitation of electrons occurs from states in the valence band to the states in conduction band. The electron energy thermalises and electron recombination with holes takes place in one of the deep-lying localized tail states which causes the

Table 8.1: Activation barriers for d.c. conductivity, bonds broken and formed along with defects pair.

Composition	Bond broken	Bond reformed	Conjugate pair of defects	U_{eff} eV	E_{dc} eV
$90(As_2Se_3)10Te$	–Te–Te–	$>Se^+$ –Te–	Se_3^+, Te_1^-	0.65	0.67
$Ge_{15}Sb_{10}Se_{75}$					0.92
$Ge_{20}Sb_{10}Se_{70}$	–Se–Se–	$>Se^+$ –Se–	Se_3^+, Se_1^-	1.0	0.99
$Ge_{22}Sb_{10}Se_{68}$					1.03
$Ge_{25}Sb_{10}Se_{65}$					1.09
$Ge_{30}Sb_{10}Se_{60}$	–Ge–Se–	$>Se^+$ –Ge–	Se_3^+, Se_1^-	1.0	1.02
$Ge_{32}Sb_{10}Se_{58}$					0.99
$50(As_2Se_3)50(Sb_2Se_3)$	>Sb–Se–	$>Se^+$ –Sb<	Se_3^+, As_2^-	0.71	0.72
$(As_2Se_3)_{0.9}(PbS)_{0.1}$					0.72
$(As_2Se_3)_{0.7}(PbS)_{0.3}$	>As–Se–	$>S^+$ –As<	S_3^+, Se_1^-	0.78	0.92
$(As_2Se_3)_{0.5}(PbS)_{0.5}$					0.88
$(As_2Se_3)Bi_{0.01}$					0.92
$(As_2Se_3)Bi_{0.02}$	>Bi–Se–	$>Se^+$ –Bi<	Se_3^+, Se_1^-	1.0	0.91
$(As_2Se_3)Bi_{0.1}$					0.89
$(As_2Se_3)Bi_{0.2}$					0.81
$As_{40}Se_{10}Te_{50}$					0.5
$As_{40}Se_{20}Te_{40}$	>As–Te–	$>Se^+$ –As<	Se_3^+, Te_1^-	0.73	0.53
$As_{40}Se_{30}Te_{30}$					0.61
$As_{40}Se_{40}Te_{20}$					0.66
$(Te_{35}Se_{65})_{0.99}Sb_{0.01}$					0.66
$Te_{35}Se_{60}b_5$					0.57
$Te_{45}Se_{50}Sb_5$	–Te–Te–	$>Se^+$ –Te–	Se_3^+, Te_1^-	0.65	0.53
$(Te_{35}Se_{65})_{0.97}Sb_{0.03}$					0.62
$(Te_{35}Se_{65})_{0.91}Sb_{0.09}$					0.48
$Pb_{0.12}Ge_{0.24}Se_{0.44}Te_{0.2}$	–Pb–Te–	$>Se^+$ –Pb–	Se_3^+, Te_1^-	0.5	0.47
$Sn_{0.12}Ge_{0.24}Se_{0.44}Te_{0.2}$	–Sn–Te–	$>Se^+$ –Sn–	Se_3^+, Te_1^-	0.5	0.45

Stokes shift. Another possibility is that the optical excitation occurs from a negatively charged (D^-) gap state to a D^0 gap state, where there is initial non-radiative loss of energy to a stable D^0 configuration. Photoluminescent emission takes place bringing the electron back to the D^- centre. This is illustrated in Figure 8.16 schematically. This type of

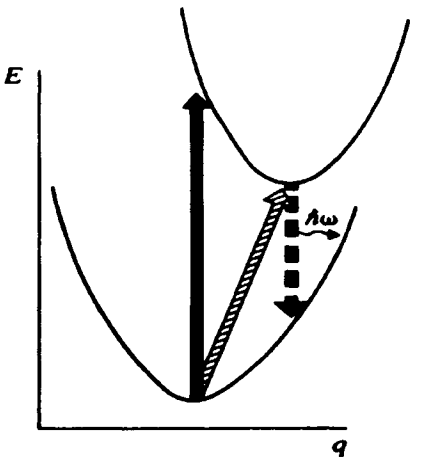

Figure 8.16. Configuration-coordinate diagram for excitation of D^- to D^0. Vertical arrows represent optical transitions; non-vertical arrow represents thermal transition.

Stokes shifted photoluminescence spectrum has been observed in arsenic chalcogenides. Luminescence can result from thermal excitations also which requires less energy as illustrated in the same figure by slanted arrow. The requirement of smaller energy in thermoluminescence is thought to, be due to the fact that the lattice has time to relax during the thermal transition and therefore, excitation occurs between potential minima.

Optical properties of amorphous semiconductors are in general consistent with the energy band structure modified in the light of defect formation as described above. Since the mobility gap is between 1-3 eV, inter-band transitions are observed for photon energies exceeding the band-gap. The absorption in this region is generally high and of the order of 10^5-10^6 Nepers/cm. For photon energies lower than the band-gap energy, the absorption does not fall off sharply. A typical and familiar plot of $(\alpha\hbar\omega)^{1/2}$ vs photon energy is shown in Figure 8.17. The absorption drops quite linearly till it reaches low energies. The extrapolation of the linear regions gives the optical band gap E_o, which is generally found to be about $2E_{dc}$. This behaviour directly follows from the dependence of the absorption coefficient on the photon energy,

$$\omega\,\alpha(\omega) \propto \omega^{2}\varepsilon''(\omega) \propto \left(\hbar\omega - E_{o}\right)^{2} \tag{8.67}$$

where $\alpha(\omega)$ is the absorption coefficient at the frequency ω. This expression has been derived using random phase approximation and its

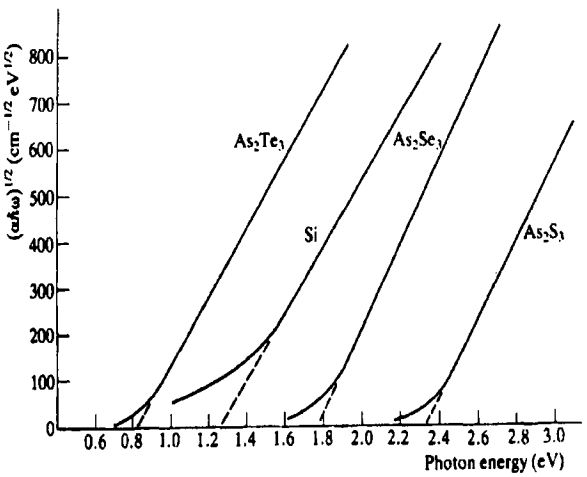

Figure 8.17. Examples of optical absorption edges of materials whose spectral dependence is given by $\alpha\hbar\omega=C(\hbar\omega - E_0)^2$ showing the extrapolation to give values for the optical gap E_0 (After Mott and Davis 1979).

observed validity is due to fact that the observed optical transition occur from extended state to extended state and involves little contribution from the localized states. However, the edge of the absorption in the above Figure is very clearly not sharp and E_0 is obtained by extrapolation of the linear region. The departure begins to occur at absorption coefficient values below 10^4 cm^{-1}. This is evident even more clearly in Figure 8.18, where absorption coefficient α is plotted against photon energy. The arrows in the figure correspond to $2E_{dc}$ and hence the optical gap E_0. The absorption coefficients extend well below these energies. α in this region seems to follow very accurately an exponential dependence on photon energy.

$$\alpha = \alpha_{0} \exp\left[-\Gamma(E_{e} - \hbar\omega)\right] \tag{8.68}$$

E_e is approximately equal to E_0 and Γ is a constant having a range of 10-25 eV^{-1}. Absorption edges which obey the above exponential equation are called 'Urbach edges'. There is as such no clear understanding of the origin

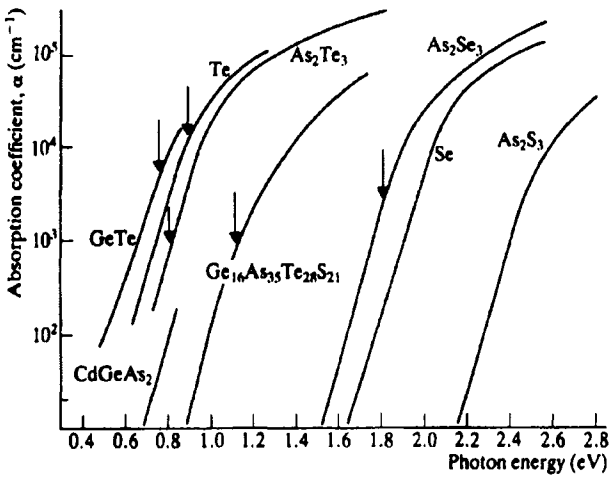

Figure 8.18. Optical absorption edges for a variety of amorphous semiconductors at room temperature showing Urbach behaviour. The arrows mark the value of $2E_{dc}$ for those materials for which the electrical conductivity is activated with E_{dc} (After Mott and Davis 1979).

of the Urbach edges. Dow and Redfield (1970) suggested that electric field broadening of the exciton* levels is responsible for the exponential edges. Excitons are formed from the optical excitations of localized gap states. By field ionisation of excitons, electrons can tunnel out of their quasi-bound states and as they enter into a deeper and wider potentials, they create local micro-fields. The micro-field induced potential is thought to be eventually responsible for the broadening of exciton absorption spectrum. An internal field of about 10^6 Vcm^{-1} appears to be sufficient to cause the observed exponential form of absorption. Both the optical gap E_o (E_o is also known as Tauc gap) and the Urbach energy, E_e are temperature independent at low temperatures but they change in opposite ways as the temperature is increased from 150 to 300 K; Urbach energy increases with temperature.

High field behaviour of chalcogenide glasses

An important feature, which stimulated great interest in amorphous chalcogenides is related to the high field electrical response. It was

* When an electron is excited from its bound state, the hole left behind and the excited electron form a coloumbicaliy interacting metastable pair, known as 'exciton'.

observed by Ovshinsky (1968) that thin films of complex telluride glasses exhibit reversible electrical switching - from a low conductivity "OFF" state to a high conductivity "ON" state - at a critical threshold voltage, V_{th}. The material switches suddenly from OFF to ON state, supporting a high value of current through it in the ON state, without passing through a negative resistance state. When the current through the film is decreased gradually, at some minimum holding current, I_h, it switches back to the high resistance "OFF" state. The behaviour is reversible and (Figure 8.19 (a)) is known as *threshold switching*. It is also referred to as *Ovishinsky switching*, after its inventor. In some amorphous chalcogenides it is also observed that the ON state sets in permanently and the current can be brought down to zero without affecting the behaviour of the ON state. This is represented in Figure 8.19 (b). However, the OFF state can be restored - reset - by passing a strong pulse of current. This behaviour is known as *memory switching*. Since the ON state is retained once it is switched to, it can be used to "write" or register information. Thus, memory switches are of technological importance in making ROM (Read Only Memory) panels.

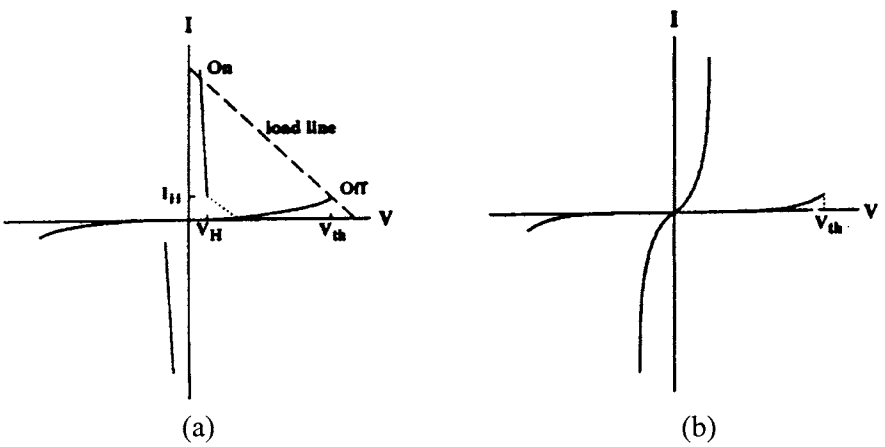

Figure 8.19: I-V characteristics of (a) threshold and (b) memory switching devices.

The structure of the memory switching materials in the ON state have been examined and found to be crystalline. The crystallized portions exhibit metallic conductivity or behave like small band gap semiconductors. Correspondingly, their optical properties like reflectivities are different in switched and unswitched (virgin, amorphous) states. Therefore, the memory state can be read optically, using laser

scanning. Threshold switching is of importance for fabricating binary logic (ON-OFF) elements. The switching times are long at V_{th} in Ovshinsky devices compared to the same in crystalline switching devices. However, when the applied voltages are increased 50 % above V_{th}, the switching times drop to nanoseconds or lower, making them competitive. Nevertheless, threshold switching has not been fully exploited due to inherent chemical instability problems and associated degradation of the devices, which restricts the number of possible switching cycles.

Memory switching is associated invariably with the formation of a conducting channel of crystallized products, some or all of which have much higher conductivity than the unswitched amorphous material at the same temperature. Often it is also found that the heavier elements such as Te in the glass tend to concentrate in the switched portions in complex chalcogenide glasses. Several compositions in Te-As-Ge-Si, Ge-Se-Tl, Ge-As-Te, Se-Sb-Bi etc. glassy systems have been found (Kotkata et al., 1994) to exhibit memory switching of the type shown in Figure 8.20. The

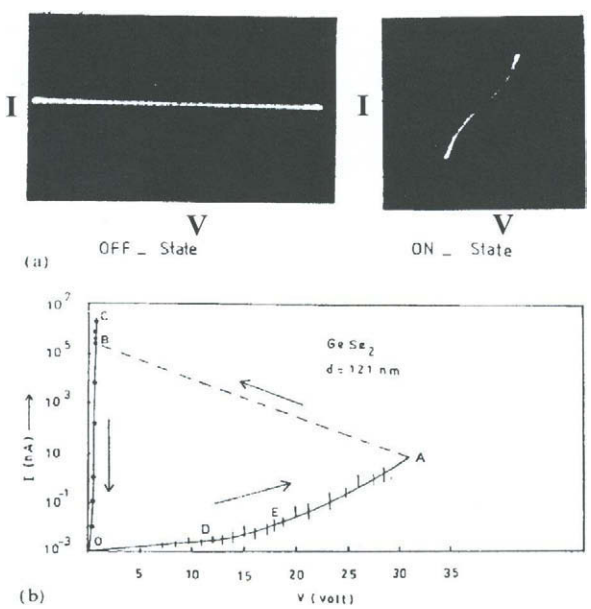

Figure 8.20: (a) I-V characteristics on voltage cycling (left, off state; right, on state) and (b) static *I-V* characteristic curves of a-$GeSe_2$ (After Kotkata et al., 1994).

I-V curve of the OFF state generally exhibits three different regions of resistance behaviour as the voltage increases. In the first portion, the behaviour is Ohmic, while in the second it exhibits Poole-Frenkel

behaviour (O'dwyer, 1973), where $I = I_0 \exp [(V/V_0)^{1/2}]$. The third portion is a more severe function of voltage (Poole like) where $I = I_0 \exp (V/V_0)$, where $V_0 = 4(kT)^2 d^2/\beta_{PF}$, where d is the film thickness and β_{PF} is the Poole-Frenkel coefficient $\beta_{PF} = 2e^{3/2}/\varepsilon^{1/2}$; where e and ε are the electronic charge and the low frequency dielectric constant ($\equiv\varepsilon(0)$) respectively. The threshold voltage V_{th} is generally found to be a function of temperature and fits the relation

$$V_{th} = V_0 \exp\left(\frac{E_s}{kT}\right) \tag{8.69}$$

where E_s is the activation energy for switching. It has also been observed that E_s is related to E_{dc} by the relation: $E_s/E_{dc} \approx 0.5$.

The switching mechanism may be either thermal, electro-thermal or purely electronic. In the thermal mechanism, it is assumed that heating occurs in the switched portions between the electrodes which results in a permanent transformation to the high conductivity material in those regions. The revival of the OFF state in memory switches which is achieved by passing a steady pulse of high current, appears to be due to local remelting of the crystalline region which restores the original amorphous state. Evidently the number of cycles for which this process can be carried out, depends both on the chemistry of the material and physical properties like inter diffusivity of the component atoms between glassy and crystalline regions. Kotkatta et al. (1994) set up heat balance equations and solved them assuming the electrical field to be uniform in the material. In a purely electronic mechanism, which is considered as relevant for threshold switching, thermal effect is ignored. The voltage drop across the device at V_{th} is of the order of 10^5-10^6 V cm^{-1}, which is quite high although lower than the dielectric breakdown voltages. In a device, therefore, both electrons and holes get injected from the electrodes, which fill the empty defect states in the band gap of the material. When the filling of states crosses the E_v and E_c, the mobility edges, a conducting plasma is created between the electrodes. The plasma is actually a degenerate electron and hole gas, and has a density of approximately 10^{18} cc^{-1}, which therefore manifests as sudden switching. The switching results in drop of potential across the device and therefore the holding voltage for the ON state is correspondingly small and only slightly higher than mobility gap. It is assumed in this double injection model that the carriers have very little cross-section for recombination for

a field of $\approx 10^3$ V cm^{-1} (around the holding voltage). If the mobility of the carriers is $\approx$ 10 cm^2 $V^{-1}s^{-1}$, the transit time for a 1μm thick device is only 10^{-8} seconds. Removal of the field restores the OFF state. However, in this model it is difficult to reconcile the decrease of V_{th} with temperature, which in some materials is known to decrease towards zero as the glass transition temperature is approached (DeNeufville et al., 1974).

The switching over to an ON state discontinuously is not a general feature of all chalcogenides but it appears, in general, that in high fields a super-linear variation of conductivity is observed even in simple chalcogenide films. The super-linear region can be almost vertical in the I-V plots. Typical I-V characteristics of $AsSe_x$ films are shown in Figure 8.21(a) for different temperatures. When the slope of super-linear region,

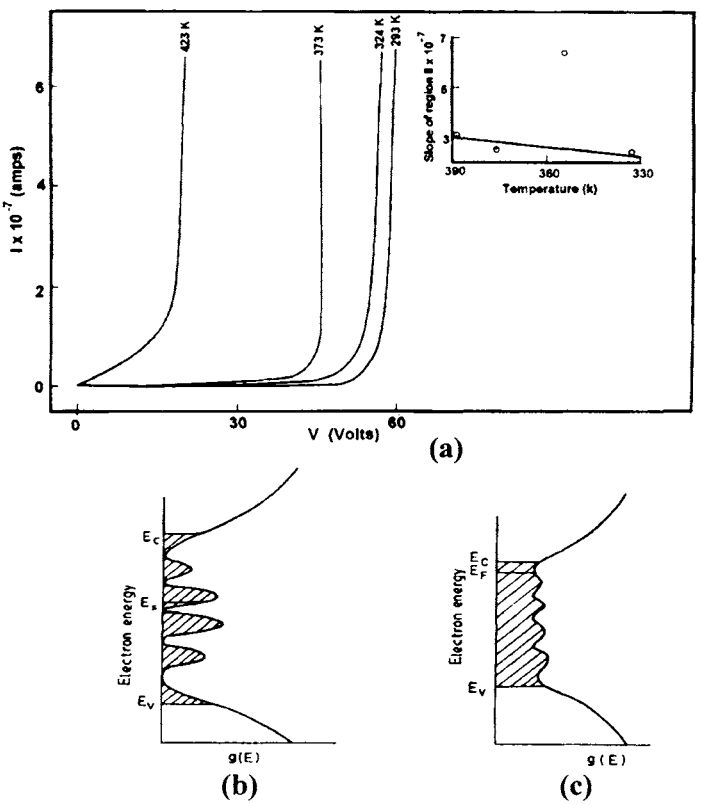

Figure 8.21. (a) *I-V* characteristics of an $AsSe_x$ film (thickness 1.1 μ) as a function of temperature. (b) Suggested density of states for $AsSe_x$ films and (c) variation of the same under the application of high electric fields (After Giridhar and Rao, 1979).

which represents the resistance, is plotted as a function of temperature (see inset), it is found to be metallic in this state. This behaviour can be understood with the reference to a plausible DOS diagram in Figure 8.21(b). A variety of defect states of minor magnitude are present in the gap region. The Fermi level lies in the gap states which presumably corresponds to single electron states. When a field is applied across the film, it alters the distribution of the DOS because of strong polarizing field, felt particularly by the single electron (dangling bond) states. The effect can be both dilation of bonds and distortion of bond angles. There can also be small localised structural rearrangements and realignments due to the field. It is visualized that a broadening of the gap states occur which cause extensive overlapping of DOS structures in the region. As a result the DOS in the gap get somewhat flattened and there is an upward shift of E_F which now gets closer to E_c. There is another effect which is more subtle and that is the alignment of the broken bonds and structural entities in the direction of the field. This has the effect of decreasing the disorder as a consequence of which E_c and E_v move towards the band gap. Therefore E_F and E_c can get closer to within kT. When electrons and holes are injected from the electrodes at this stage (V_{th}), the carriers find themselves in the extended states of much higher conductivity. This manifests in the super-linear I-V variations. Evidently in the superlinear region the material is metallic in character.

If the structural state arrived at V_{th} is a metastable structural state which is also metallic, it corresponds to threshold switching. But if at V_{th} the field induced rearrangement is such that the structure tumbles over into a deeper minimum corresponding to a crystalline state, it results in a permanent ON state. Superlinear state corresponds to an unstable structural state in this approach. The mechanism considers heating as incidental rather than as a cause for switching.

Application of high electrical fields can cause a few other types of switching. Notable are the transitions from OFF state to voltage controlled negative resistance (VCNR) state and from OFF state to current controlled negative resistance (CCNR) state. In a VCNR device, the material starts from a low resistance state and passes through a negative resistance region above a critical voltage V_t and eventually reaches a state of high resistance, as shown in Figure 8.22(a). The I-V characteristic is reversible in a simple (threshold) VCNR device.

But in a VCNR device with a memory, the low resistance state once reached is retained even when the voltage is reduced as shown in Figure 8.22(b). Amorphous oxides like Al_2O_3, Ta_2O_5, ZrO_2 etc. exhibit

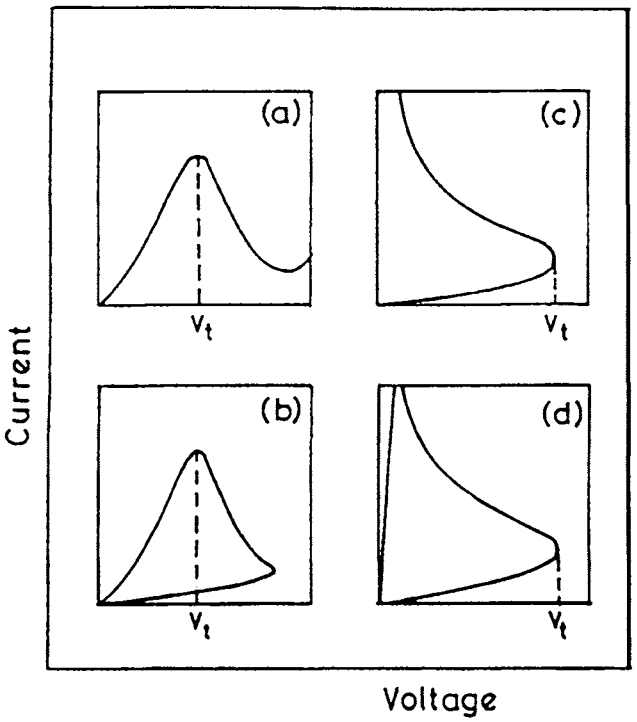

Figure 8.22. Four types of ohmic behaviour observed in amorphous materials: (a) VCNR; (b) VCNR with memory; (c) CCNR; (d) CCNR with memory (Fritzsche, 1974).

VCNR behaviour. CCNR devices exhibit I-V characteristics shown in Figure 8.22(c) and (d). At a threshold value of current I_{th}, with a corresponding threshold voltage V_{th}, voltage starts decreasing with increasing current and passes through a stable negative resistance region onto a low resistance state. While the I-V path is reversed in a simple CCNR device, it is set in low resistance state in a CCNR with memory. CCNR behaviour has been known to be exhibited by amorphous thin films, transition metal oxides like MoO_3, Nb_2O_5, V_2O_5 etc.

Photostructural changes in amorphous chalcogenides

Chalcogenide glasses respond to irradiation with optical or ultraviolet photons in a unique manner. They exhibit photostructural effects. Photostructural effects, in general, fall into two different categories. The first category is based on changes in scalar properties,

such as photodarkening and photoinduced refraction. The second category of photostructural effects are based on changes in vector properties, such as photo-induced anisotropy and photo-induced gyrotropy – i.e. circular dichroism and birefringence. The vectorial photo induced effects are due to the state of polarization of the inducing light. The scalar effects do not depend on the state of light polarization. These scalar and vectorial effects are again distinguished as reversible and irreversible. Reversible changes are observed in well annealed thin films and melt quenched glasses. The photo induced effects can be annealed out either by shining unpolarized light on them or by heating to higher temperatures, generally up to glass transition temperature. Irreversible changes occur very often in as-deposited evaporated thin films. The origin of these effects are not clearly understood and since they offer numerous possibilities of applications such as preparation of light-assisted wave guides, birefringent fibres, Bragg reflectors, micro lenses etc., they have been investigated very widely (Elliott and Tikhomirov, 1996; Lyubin and Tikhomirov, 1994).

Photo-darkening and light induced electron spin resonance (ESR) are typical examples of reversible photo-induced effects. Photo darkening occurs when the material is irradiated with band gap photons

$$E = \hbar\omega \geq E_c - E_v$$

The photo darkening effect is associated with decrease in band gaps and the absorption edges get red shifted. The shift is caused by increased distortions of the continuous random network structure of the amorphous chalcogenides. Photo-darkening is generally studied by irradiating thin films of a material cooled to low temperatures with light from a Hg-lamp to which a long wavelength cut off filter is attached. The optical band gap, E_o and $\sqrt{B}$ are determined by plotting $(\alpha h\nu)^{1/2}$ against $h\nu$. Since the Tauc relation is given by $(\alpha h\nu)^{1/2} = B^{1/2}\ (h\nu - E_o)$, where α is the absorption coefficient, the slope gives $\sqrt{B}$ and the intercept $\sqrt{B}\ E_o$. Observed band gap decrements are of the order of 50 meV, as in the case of $Ge_{37}S_{63}$ film. Since $1/\sqrt{B}$ is directly related to the disorder and also since $1/\sqrt{B}$ increases with decreasing $\sqrt{B}$, it is suggested that increased disorder is the origin of photo-darkening. Photo-darkening effects are suppressed by the presence of lone pair containing elements like Pb and Sn. The lone pairs on the atoms get excited there by preventing the chalcogenide from excitation of its electrons. Therefore, presence of Sn^{2+} or Pb^{2+} resists the photo structural changes. A large increase in ESR signal is observed in chalcogenide glasses upon irradiation even with sub-gap photons

($h\nu < E_0$). This can be attributed to the occurrence of the reaction $D^+ + D^- \rightarrow 2D^0$ or $C_3^+ + C_1^- \rightarrow 2C_2^0$ which increases the spin density in the material. The states involved are located within the band gap.

Vectorial effects like photo birefringence have been shown to be associated with irradiation with polarized sub-gap light. In the case of birefringence, the difference in the refractive indices, Δn, is considered to arise from variation in the higher order (cubic) susceptibility term, $\chi^{(3)}$ (see chapter 11). Thus Δn is a function of $\chi^{(3)}$ and N_s, where N_s is the number density of the dipoles. Dipoles which are in correct orientation interact with the electrical vector of the polarized light. Elliott and Tikhomirov (1996) have provided a visualization of the vectoral effects arising from photoexcitation of IVAP as shown in Figure 8.23. There is a photo induced reaction between C_3^+ and C_1^-. The reaction steps are visualized as $C_1^-C_3^+ + h\nu \rightarrow C_1^0C_3^0 \rightarrow C_3^+C_1^-$, and involves a charge transfer. The process is evidently most effective when the plane defined by the two

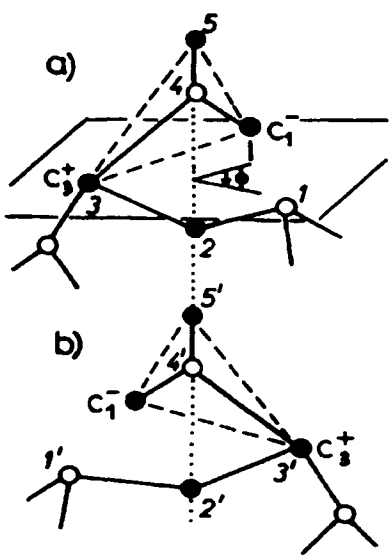

Figure 8.23. Schematic illustration of the center proposed to be responsible for anisotropic effects in pnictogen-chalcogenide systems (e.g. AsSe) before (a) and after (b) optical excitation. Open and solid circles denote pnictogens and chalcogens respectively, solid lines are bonds, and dashed lines delineate structural units. The extension of the bond involving the C center is exaggerated for clarity. Centers (a) and (b) are mirror images of one another in the plane shown by the dotted line. The numbers 1-2-3-4-5, 1′-2′-3′-4′-5′ denote helices of opposite handedness (After Elliott and Tikhomirov, 1996).

p-type lone pair orbitals of the C_1^- is parallel to the electrical vector of the (linearly) polarized (reaction inducing) light. The same mechanism, in principle, can account for circular dichroism and other vectorial phenomena. The highest magnitude of the photo induced birefringence is only of the order of 1 % or less compared to the value in the parent crystalline phase. For example in Se, As_2S_3 and As_2Se_3, photoinduced values of Δn in the glass and the parent crystalline phases are respectively, (-0.007, -0.8), (-0.002, -0.2) and (–0.008, -0.3) respectively (Tanaka et al., 1996).

The nature of the excitation centers involved in photo-structural changes have been investigated using Raman spectroscopy in the case of $Ge_xSb_{0.4-x}S_{0.6}$ glasses by Kotsalas et al. (1998). The different glasses were first irradiated with band gap photons (UV light from Hg lamp). It was found that photo-structural effects increase with increasing number of Ge-Ge bonds or decreasing Sb content. Coordination requirement of Ge being higher more and more Ge-Ge bonds are formed when Sb is substituted by Ge. Gladden et al. (1988) also arrived at a similar conclusion from EXAFS investigations. They found that presence of homopolar bonds as in $Ge_{40}Se_{60}$ and $As_{43}S_{57}$ (off stoichiometric compositions) lead to increased photo induced structural changes compared to stoichiometric $Ge_{33}Se_{67}$ and $As_{40}S_{60}$. In the off–stoichiometric compositions there are Ge-Ge and As-As bonds. EXAFS associated with K-edges of Ge, As and Se were used for the analysis.

Another remarkable photo structural effect is the giant photo expansion observed in As_2S_3 glass by Hisakuni and Tanaka (1994). When As_2S_3 films are irradiated with photons of energy $h\nu \geq E_o$, only about 0.5 % expansion is observed. But when photons of energy $h\nu < E_o$ are used, the observed expansion is 10 times higher (5 %). He-Ne laser ($h\nu$=2eV, E_o=2.4eV) was used for the experiments so that the photon energy corresponds to Urbach states. The expansion was found to saturate at around 10 Ws of photon energy for a 50μm thick As_2S_3 film. (Under similar irradiation conditions, amorphous SiO_2 film exhibits a contraction.) Small-angle X-ray scattering studies revealed that FSDP is located around 1.2 $Å^{-1}$ and it did not shift. FSDP intensity, however, was found to be enhanced on the lower Q-side (≈ 0.8 $Å^{-1}$) over a broad range. FSDP seems to arise from an inter layer distance of about 5Å and the change in intensity, $\Delta I(Q)$, over the range of FSDP, can account for a $\Delta V/V$, of $\approx(1\pm0.5)$% which is in good agreement with the observed 0.5% change in volume during irradiation with greater than band gap photons ($h\nu > E_o$) (Tanaka, 1998).

It is possible that the principal effect of irradiation involves creation of homopolar bonds at the expense of heteropolar bonds. Irradiation of amorphous chalcogenide films quite generally leads to volume increase as a photo structural effect except in $GeAs_4Se_5$. Some of the observed photo structural changes are summarized in Table 8.2, originally compiled by Tanaka (1998). Formation of homoatomic bonding during photo induced transformation can lead to nucleation of As in As_2S_3 films. This aspect has been examined by Dikova et al. (1994) who used conventional photographic development techniques and confirmed formation of As clusters.

Table 8.2: Volume changes in some chalcogenide glasses, oxide glasses, and crystals induced by radiation. Glass and crystal are abbreviated as g- and c- (After Tanaka, 1988).

Material	Excitation	ΔV/V (%)
g-As_2S_3	Light	+0.4
	Light	+0.7
g-As_2Se_3	Light	+0.7
g-GeS_2	Light	+0.5
g-SiO_2	E- beam	-3
	Neutron	-3
	γ-ray	-0.01
g-$Ge_1As_4Se_5$	Light	-0.2
g-SiO_2-Na_2O	Light	+
c-SiO_2	Neutron beam	+15
	E- beam	+10
c-KBr	X ray	+0.0001

Kolobov and Elliott (1995) observed another photo induced effect namely photo-amorphisation in crystalline $As_{50}Se_{50}$ after irradiation with band gap light. $As_{50}Se_{50}$ in its crystalline state is the As_4Se_4 molecular crystal with the realgar structure, shown in Figure 8.24(a). It appears that during irradiation, intra-molecular As-As bond (As-As bond length, 2.57 Å) breaks and forms inter-molecular As-As bonds (bond distance of 3.42 Å in realgar), resulting in the formation of a glass. The Raman spectra, shown in Figure 8.24(b) and (c) confirms the amorphisation.

Xerography: The high electrical resistivities and optical absorptivities of chalcogenides have lead to many important applications. One of the most remarkable applications is in xerography (dry writing). The principle involved is simply as follows: (i) Se film coated on an aluminium substrate is exposed to corona discharge in order to charge the selenium

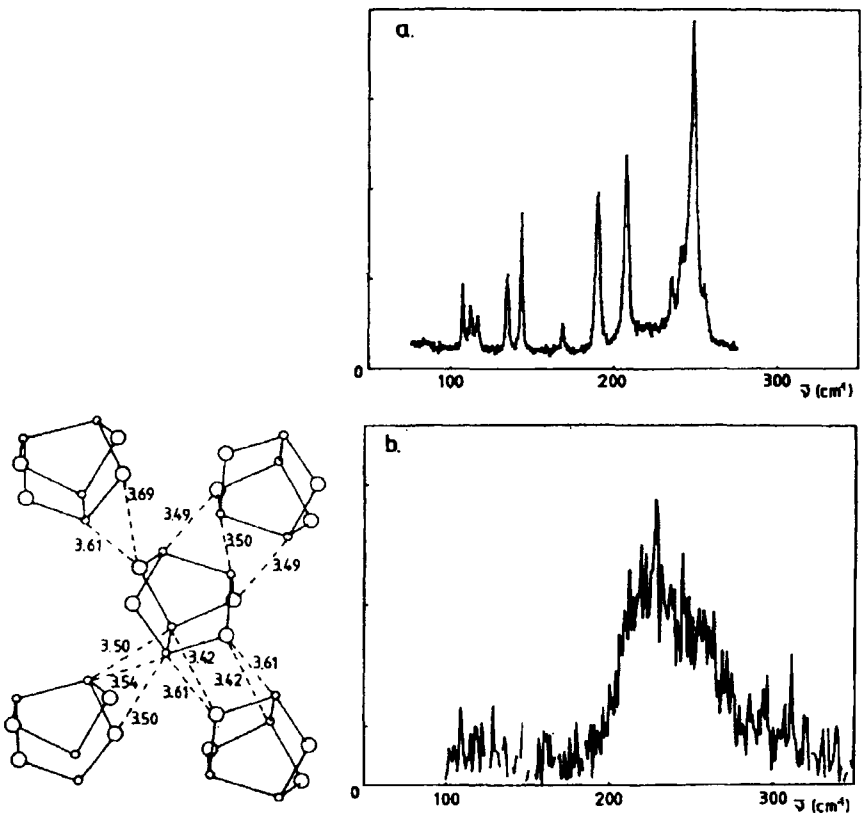

Figure 8.24: (a) Ralgar structure of As_4Se_4. Raman spectra of (b) low temperature c-$As_{50}Se_{50}$; (c) photo-amorphised film (After Kolobov and Elliott, 1995).

surface positive. (ii) Light (high intensity) is reflected from the surface of the document to be copied. The white (more reflective) portion of the document reflects light that generates electron hole pairs which drift in opposite directions. Electrons, which reach the surface of the film neutralize the positive charge in portions of the charged film which represent the white portions of the document. The holes drift and get discharged at the aluminium substrate. (iii) Surface is sprayed with toner particles (carbon particles of ~10μm size) which now stick to the undischarged portions (corresponding to the black (printed) portions in the document. (iv) A sheet of paper which is charged oppositely (electrons, negative charge) is made to contact the Se film. The former particles and hence the image of the print portions are now transferred on to the sheet of paper. (v) The sheet of paper is now heated to fix the image by melting carbon particles of the toner which are surrounded by a low-melting

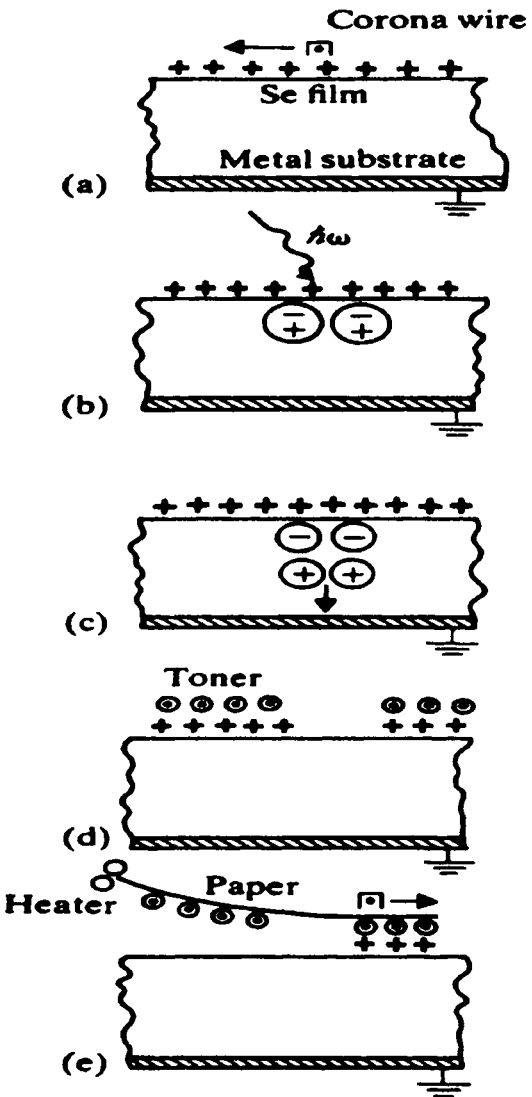

Figure 8.25. Schematic illustration of the Xerox process, using a-Se as the photo-receptor. (a) Positive charging of the surface by corona discharge. (b) Exposure of the photo-receptor by photons reflected from the document to be copied. (c) Discharge of the surface potential locally by the photo-generated electrons, the holes drifting across the thickness of the film. (d) Development of the latent image by means of negatively charged toner particles which are attracted to the remaining areas of positive surface charge. (e) Transfer of the image to paper by means of a second corona discharge and subsequent fixing by heating the paper to melt the toner particles into place (After Mott and Davis, 1979).

plastic. This completes the xeroxing process. The process is schematically shown in Figure 8.25. The two important aspects of xeroxing process is that the material should have a high quantum efficiency so that number of carriers generated per photon is high and the second is that the film material should be highly resistive so that the initial surface potential does not dissipate by diffusion of charges.

Chemically controlled carrier type reversal

The richness of phenomena associated with chalcogenide glasses is further exemplified by carrier type reversal transitions exhibited by them. Carrier type reversal in transport properties occur in germanium chalcogenide glass containing Bi or Pb (Tohge et al., 1979; Tohge et al., 1980). The concentration of Bi or Pb required to be present in these glasses in order to observe $p \rightarrow n$ transition is sufficiently high and belong to chemical modification regime rather than dopant regime. In both Bi and Pb containing chalcogenides, the Seebeck coefficient, S changes sign at a critical concentration of Bi or Pb atoms (around 8-9 % of Pb and around 7-8 % of Bi). Carrier sign reversal has been investigated in $Pb_xGe_{42-x}Se_{58}$, ($0 < x < 22$) glasses by Vaidynathan et al. (1997). The variation of the activation barrier for the electrical conductivity and the thermoelectric power at 100°C are shown in Figure 8.26. There is a clear break in the nature of the variation of activation barrier around 8 % Pb substitution, where $p \rightarrow n$ transition has been observed. The origin of the $p \rightarrow n$ transition is a consequence of the dominance of electron transport in Pb rich compositions.

The conductivity of the glasses evidently is due to both electron (n) and hole (p) transport. It was noted earlier that the chalcogenides are very generally p-type conductors. In simple Ge-Se glasses the defect pairs may be considered as located on Se atoms (see earlier sections) Since the number of covalent bonds are conserved during the defect pair formation in chalcogenides, the energy change is simply U_{LP}, which is the energy required for pairing of electrons in a p or a sp^n (hybridized) orbital. The pair formation energy is generally equal to the activation barrier for the d.c. conductivity arising from the motion of C_3^+ centers (the hole conduction). In the present glass system, the base glass $Ge_{42}Se_{58}$ has d.c. activation barrier $\approx$ 0.9 eV. The introduction of Pb into the glasses can be looked upon as creating more of C_1^- defects, because PbSe is ionic and a composition of a glass is written as $Pb_xGe_{42-x}Se_{58} \equiv x(PbSe) \cdot Ge_{42-x} \cdot Se_{58-x}$ and therefore the concentration of C_1^- can be calculated. The concentration

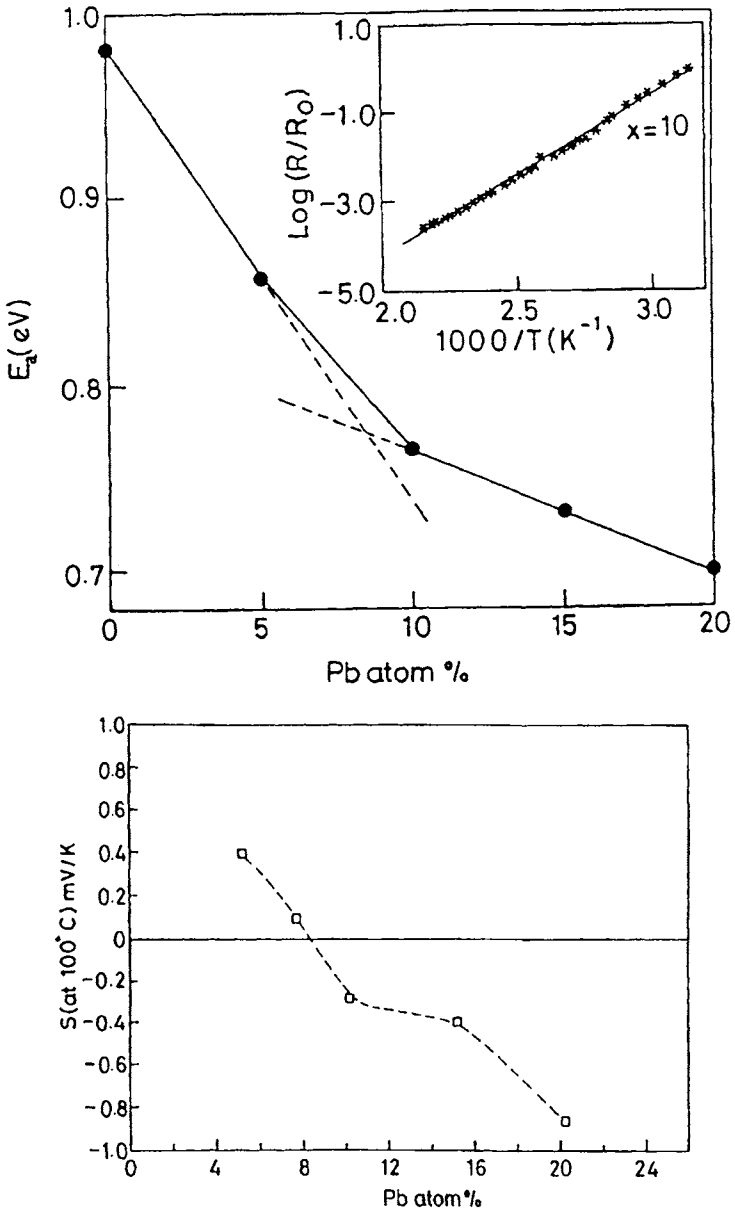

Figure 8.26. (top) Variation of conductivity activation energy (E_a) with Pb concentration in $Pb_xGe_{42-x}Se_{58}$ glasses. Inset shows a typical semi-logarithmic Arrhenius plot used for the determination of E_a; (bottom) Plot of thermoelectric power (S) at 100°C for $Pb_xGe_{42-x}Se_{58}$ glasses as a function of composition (After Vaidhyanathan et al., 1997).

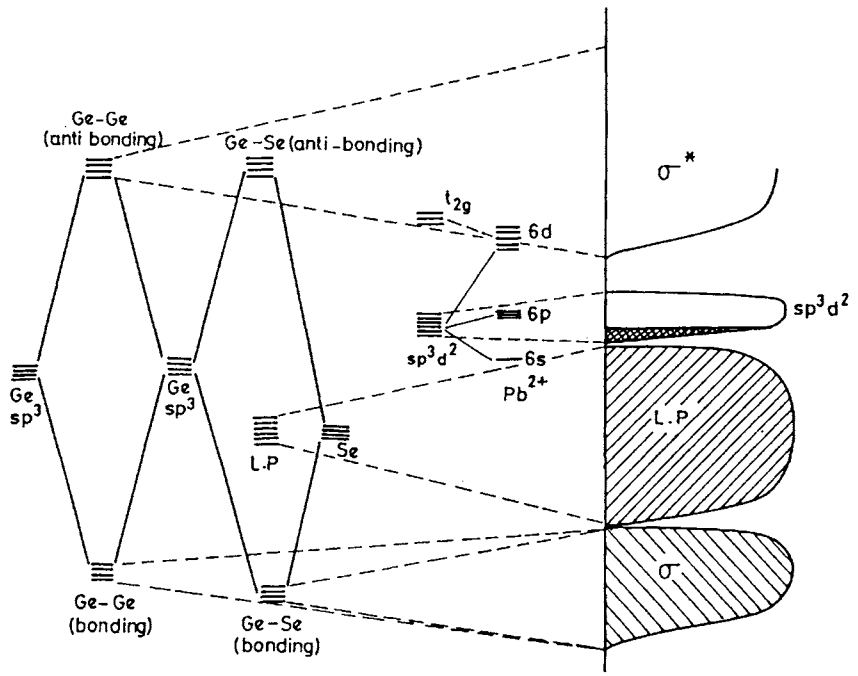

Figure 8.27: Molecular orbital scheme use for the formation of energy levels and schematic energy band diagram constructed for $Pb_xGe_{42-x}Se_{58}$ glasses (After Vaidhyanathan et al, 1997).

of C_1^- is much larger than the intrinsic concentration of C_1^- in the base Ge-Se glass itself. The manner of participation of C_1^- centers which give rise to electronic conduction has been discussed by Vaidhynathan et al. (1997) who have proposed a band energy diagram as shown in Figure 8.27. The diagram is based on experimental observations that Ge atoms are 4-coordinated and Pb^{2+} occupies octahedral positions. The required sp^3d^2 hybridisation of Pb orbitals give rise to a narrow sp^3d^2 band, located just above the lone pair bands arising from Se. The lone pair and sp^3d^2 bands are identified as valence and conduction bands respectively. Lone pair electrons from Pb in the sp^3d^2 bands are considered as localized. The width of sp^3d^2 band is assumed to be proportional to Pb concentration. The top of the valence band is constituted largely of the lone pairs arising from Se^- or C_1^- type of states. The conductivity is assumed to result from bipolaron transport which uses the empty sp^3d^2 states for the purpose. Electrons are excited from C_1^- state to the partially filled sp^3d^2 band before they are moved to another C_1^- center. Thus in order to account for the switching in

the nature of majority carriers, it is postulated that electronic conductivity arise from bipolaron hopping of C_1^- centers via sp^3d^2 band and hole conduction through bond switching involving C_3^+ center. The total conductivity σ is considered as $\sigma_h + \sigma_e$, and is given by

$$\sigma = \sigma_h + \sigma_e = n_h e \mu_h + n|e|\mu_e \tag{8.70}$$

and the total S as,

$$S = \frac{(\sigma_e S_e + \sigma_h S_h)}{(\sigma_e + \sigma_h)} \tag{8.71}$$

The activation barriers for transport of bipolarons (C_1^- centers) has to be the difference in the pairing energies in sp^3d^2 orbitals of Pb and in sp^3 orbitals of Se which is designated as ΔU_{LP}. Using plausible values of the various parameters (Table 8.3), the expected conductivities and thermo-

Table 8.3: Calculated electronic parameters of $Pb_xGe_{42-x}Se_{58}$ glasses (After Vaidhyanathan et al., 1997).

Composition	n_h cm^{-3} $\times 10^{10}$	n_e cm^{-3} $\times 10^{11}$	σ_h Scm^{-1} $\times 10^{-12}$	σ_e Scm^{-1} $\times 10^{-11}$	σ_{expt} Scm^{-1} $\times 10^{-12}$	σ_{model} Scm^{-1} $\times 10^{-12}$	ΔU_{LP} model (eV)	E_{dc} expt. (eV)
$Ge_{42}Se_{58}$	2.02	-	.0647	-	.0896	.0647	-	0.987
$Pb_5Ge_{37}Se_{58}$	26.3	1.00	.842	0.0321	5.52	1.16	0.61	0.856
$Pb_{10}Ge_{32}Se_{58}$	212	45.8	5.19	1.47	74.1	19.9	0.53	0.764
$Pb_{15}Ge_{27}Se_{58}$	314	477	10.0	1.53	177	163	0.48	0.730
$Pb_{20}Ge_{22}Se_{58}$	561	918	18.0	29.4	398	312	0.47	0.699

powers were calculated and the variations are shown as a function of Pb concentration in Figure 8.28. The p-n transition occurs around 8 % Pb in very good agreement with experimental observation. There is also good agreement in calculated conductivities. It should be recalled that E_{dc} is the activation barrier for hole motion, in the spirit of the point defect model and ΔU_{LP} is the activation barrier for bipolaron transport, where use is made of the narrow sp^3d^2 bands, provided by Pb. $p \rightarrow n$ transition appears to be possible only when Pb^{2+} (or Bi^{3+}) is present because of its tendency to occupy octahedral positions and form narrow sp^3d^2 band just above the lone pair band.

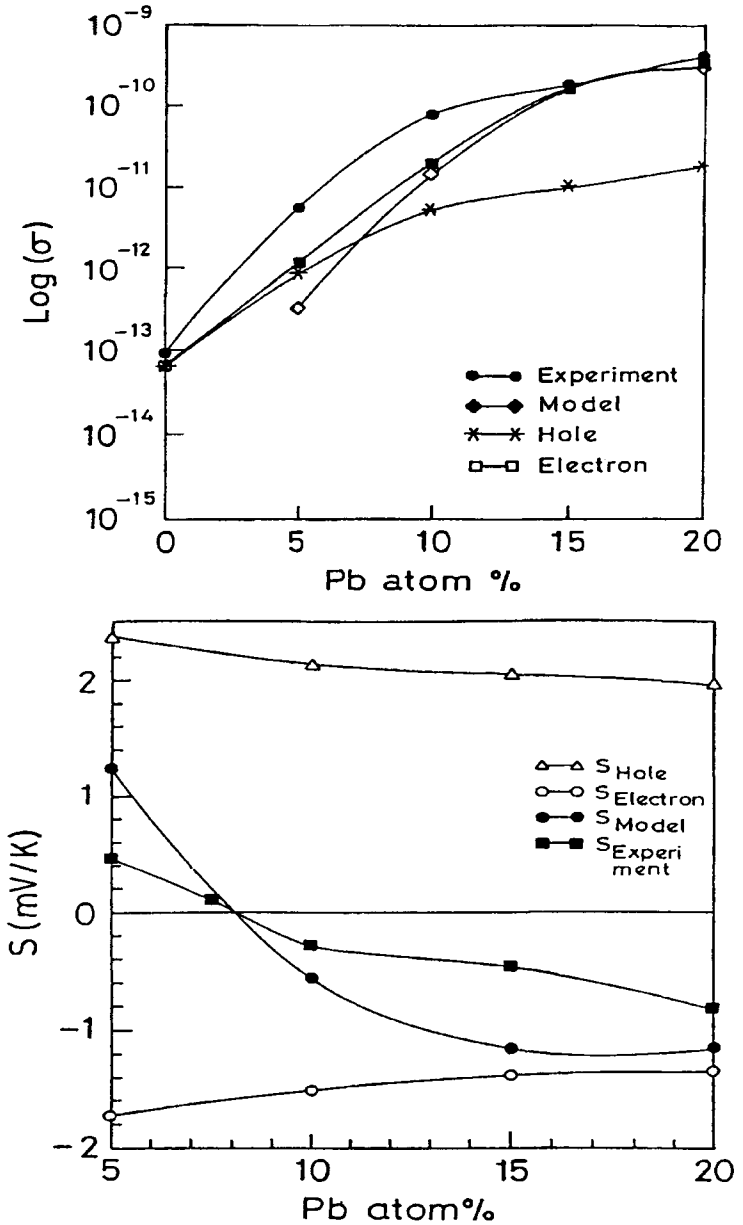

Figure 8.28. (top) The variation of hole conductivity, electronic conductivity and total conductivity of $Pb_xGe_{42-x}Se_{58}$ glasses calculated using the model as a function of Pb content. The experimentally observed conductivities are also plotted for comparison. (bottom) Variation of calculated and experimentally observed thermopower values of Pb-Ge-Se glasses as a function of Pb concentration (After Vaidhyanathan et al., 1997).

Amorphous silicon and carbon

An important difference between amorphous and crystalline semiconductors is with respect to the effect of doping, which dramatically alters the concentration of carriers. In crystalline Si for example doping is done with phosphorus and boron. P leads to injection of electrons into the conduction band and B leads to injection of holes into the valence band (donors and acceptors). This property arises from the fact that both phosphorus and boron are forced to occupy the position of Si in the crystalline lattice although they have valencies which, according to $(8 - n)$ rule, are different from silicon. Therefore, they either loose (as in phosphorus) or accept (as in boron) an electron in order to satisfy the bonding requirements at lattice positions of silicon. In glasses this requirement does not exist because of the absence of periodicity. The dopant atoms satisfy their own valence requirements locally. In fact, none of the glasses exhibits doping properties. However, it was discovered by Spear and Le Comber (1976) that amorphous silicon can be doped. Elemental semiconductors like Si and Ge cannot be quenched into glassy state from their melts. But silicon can be obtained in amorphous state by glow discharge decomposition of silane or by radio frequency sputtering from Si target in Ar/H_2 atmosphere. When sputtering is done in the absence of H_2, the resulting amorphous films contain a large DOS at E_F, arising from dangling bonds but in the presence of Ar/H_2 mixture in the ambient in both processes, significant quantity of hydrogen is taken up by the film, which saturates the dangling bonds. This has the effect of lowering the energy of the dangling bond, which therefore, gets merged with the valence band. In effect, H_2 cleans up the gap states and in the hydrogenated film designated *a*-Si:H, the DOS at E_F decreases to $\leq 10^{16}$ $cc^{-1}eV^{-1}$, from a value of $\geq 10^{20}$ $cc^{-1}eV^{-1}$ in the unhydrogenated films. Hydrogenated films however, often contain up to 10 times or more H_2 than is actually required to saturate all the dangling bonds. When these films are doped with boron or phosphorus, *p*- or *n*-type behaviour manifests with an enormous increase in conductivity as shown in Figure 8.29. In boron doping, diborane is used along with SiH_4 and PH_3 is used for phosphorus doping. In the case of boron doping, there is an initial drop in conductivity, because E_F is initially moved down in the gap. After this the conductivity rises rapidly and for doping levels of about 0.1 % as calculated from the ratios of the gases used for discharge. Conductivity rises by almost 10 orders of magnitude. In both p and n doping, the rate of increase of conductivity as a function of dopant concentration decreases

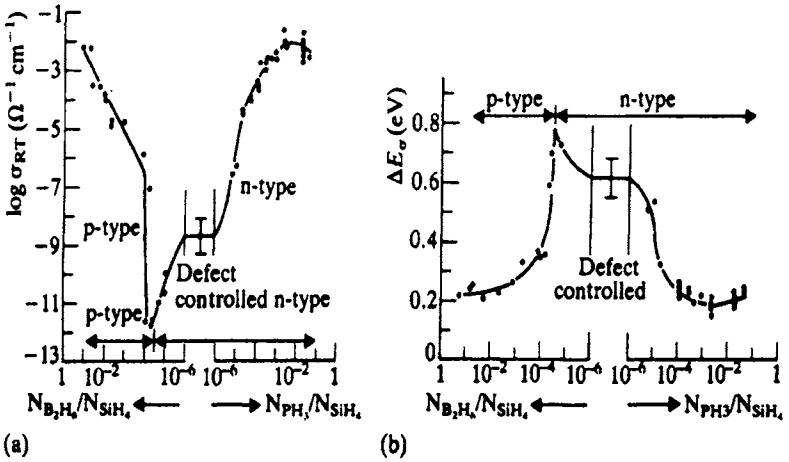

Figure 8.29. Substitutional doping in glow discharge *a*-Si:H (a) Changes in room temperature d.c. conductivity by doping with P and B. Intrinsic region is marked as 'defect-controlled'; (b) d.c. conductivity activation energy ΔE_σ ($\equiv E_{dc}$) is shown for the dopants (After Spear and Le Comber 1976).

because E_F passes through regions of increasing density of tail states.

Discovery of amorphous silicon and its dopability has already had a tremendous impact on industrial applications of amorphous materials. Amorphous Si is now used fairly extensively as a photovoltaic material. In photovoltaic applications, solar photons excite the electrons across the gap and the resulting electron-hole pairs, are driven towards the respective electrodes in order to prevent their recombination. Electron is driven through an external resistance to generate the electrical power. The efficiency of conversion of solar energy to electrical power is characterized by an efficiency factor, η, which is given by,

$$\eta = \frac{(V_{OC} I_{CC} f)}{P_{in}} \tag{8.72}$$

where V_{oc} and I_{cc} are the open circuit voltage and closed circuit current respectively and f is the fill factor, which is determined by the rectangularity of I_{cc} vs V_{oc} plot. P_{in} is the incident power density on the photovoltaic device. On a typical sunny day, when the Sun is in zenith (right above) and at sea level, P_{in} is ~100 mW cm^{-2}; this condition is termed as AM1 (Air Mass 1). At high altitudes in the atmosphere the value of P_{in} can go up to 135 mW cm^{-2}. Amorphous Si solar cells in large hetero junction configurations have already been found to give efficiencies of up

to 11 %. The ability to form *p-n*, *p-i-n*, etc. junctions puts amorphous Si on par with crystalline Si for device applications. Indeed almost all the devise possibilities have been realized with *a*-Si at least on a laboratory scale (Sakurai et al., 1993; Ovshinsky, 2000). Amorphous Si has also found applications in xerography.

One of the serious problem with amorphous Si films is that they get gradually degraded by long exposure to light. This is known as Staebler-Wronski effect (1977), which leads to the degradation of photovoltaic devices. It has been known that presence of highly electronegative atoms such as oxygen or groups such as NH in concentrations of $\geq 10^{19}$ cc^{-1} are responsible for this. Experiments have shown that this is due to the formation of structural defects other than silicon atom dangling bond. These effects are neutralized by annealing between 200 and 300 °C. Also the rate of defect generation is reduced by a factor of 3 when hydrogen is substituted by deuterium. The device quality of insulator-amorphous Si:H junctions decrease in direct proportion to the reduction in bonded hydrogen. On the strength of these observations, pathways for the defect formation, responsible for the Staebler-Wronski effect, has been suggested by Lucovski and Yang (1998), which is summarized in Figure 8.30 for the case of positively charged defects. Similar schemes have been worked out for negatively charged defects also and the energies, indicated in Figure 8.30 have been supported by *ab initio* calculations (Jing and Whitten, 1993; Jing et al., 1992).

The discovery of *a*-Si:H and realization of its dopability and device potential has spurred investigation of other amorphous hydrogenated tetrahedral semiconductors. An important development in recent times is the discovery of amorphous hydrogenated carbon. *a*-C:H in thin film form, is made by chemical vapour deposition technique from a C_2H_2 plasma. In plasma enhanced chemical vapour deposition technique, films with spin density $< 10^{18} cc^{-1}$ have been obtained. The deposition conditions greatly affect the ratio of sp^3 to sp^2 carbon atoms present in the resulting film. Carbon films in which non-interconnected sp^2 clusters remain embedded in a dielectric matrix of sp^3 carbons have a high potential for technological applications. The DOS of such a material is qualitatively sketched in Figure 8.31. The sp^2 clusters give rise to σ and σ^* bands, both of which constitute extended states. The π and π^* bands are located inside the gap of σ and σ^* bands and arise from spatially localized wave functions, of the sp^2 carbon cluster. The cluster size distribution, distortion of π bonds and the interaction due to cluster-cluster and cluster-sp^3 carbon lattice give rise to a spread of π and π^* bands, both of which are localized on either side of

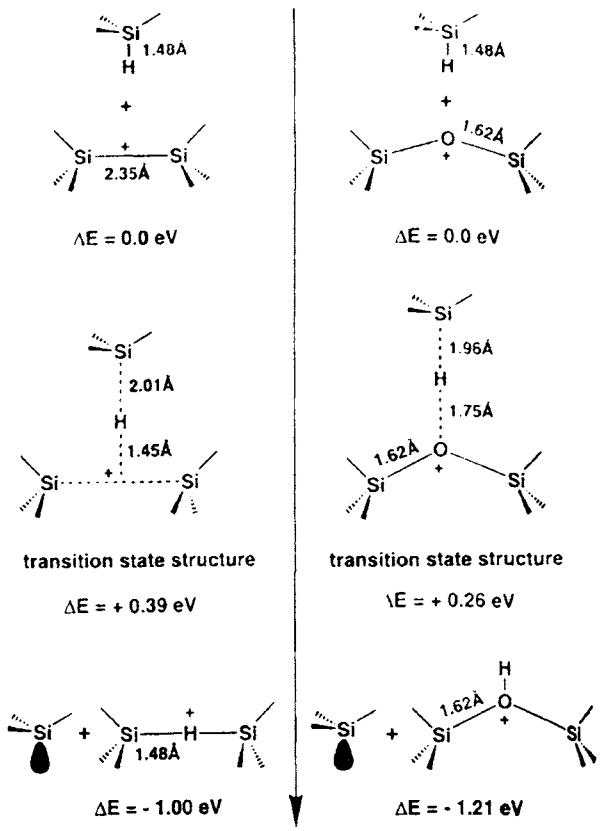

Figure 8.30: Pathways of Staebler-Wronski effect for positively charged defects by hole trapping (a) intrinsic and (b) extrinsic processes (After Lucovsky and Yang, 1998).

the Fermi level. Thus this situation gives rise to: (1) doubly occupied tail states of π character, (2) σ type dangling bonds, (3) isolated sp^2 dangling bonds and (4) π states due to sp^2 clusters, constituted by participation of odd number of atoms. These can be described as the defect states in the gap regions. In the study of photoluminescence behaviour, it appears that the above states control the non-radiative recombination processes of electrons and holes.

a-C:H is unique among Group IV semiconductors, because carbon atoms can exist with a range of coordinations depending upon the nature of hybridisation - tetrahedral (sp^3), planar (sp^2) and linear (sp). These are low mobility semiconductors with a band gap, which can vary from 1-4 eV. They give rise to room temperature photoluminescence and exhibit

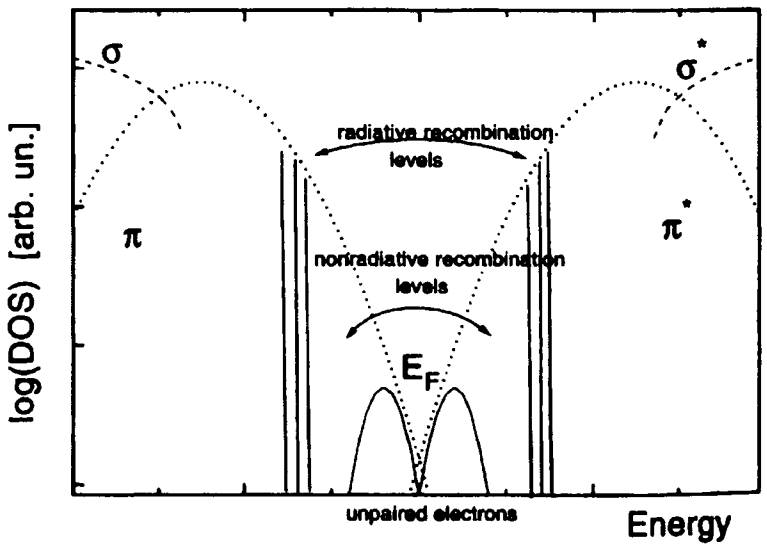

Figure 8.31: Schematic electronic density of states for *a*-C:H films (After Giorgis et al., 1998).

very low electron affinity. Unlike in *a*-Si:H, mobility gap in *a*-C:H is higher than the Tauc gap, E_o, which makes it unique for its potential as an opto-electronic material (Chen and Robertson, 1998). *a*-C:H, however, has not been successfully doped to obtain good *n* or *p* type conductivities, useful for device applications.

References:

Adler, D., and E.J. Yoffa, 1976, Phys. Rev. Lett., **36**, 1197.

Agarwal, S.C., 1973, Phys. Rev. B., **7**, 685.

Anderson, P.W., 1958, Phys. Rev., **109**, 1492.

Austin, I.G., and N.F. Mott, 1969, Adv. Phys., **18**, 41.

Chen, C.W., and J. Robertson, 1998, J. Non-Cryst. Sol., **227-230**, 602.

Cohen, M.H., H. Fritzsche and S.R. Ovshinsky, 1969, Phys. Rev. Lett., **22**, 1065.

DeNeufville, J.P., S.C. Moss and S.R. Ovshinsky, 1974, J. Non-Cryst. Sol., **13**, 191.

Dikova, J., N. Starbov and K. Starbova, 1994, J. Non-Cryst. Sol., **167**, 50.

Dow, J.D., and D. Redfield, 1970, Phys. Rev. B., **1**, 3358.

Elliott, S.R., 1984, Physics of Amorphous Materials (Longman, London).

Elliott, S.R., 1993, J. Non-Cryst. Sol., **160**, 29.

Elliott, S.R., 1979, Philos. Mag. B., **40**, 507.

Elliott, S.R., and V.K. Tikhomirov, 1996, J. Non-Cryst. Sol., **198-200**, 669.

Elliott, S.R., 1987, Adv. Phys., **36**, 135.

Emin, D., 1976, in Physics of Structurally disordered Solids, ed. S.S. Mitra (Plenum Press, New York).

Friedman, L., 1971, J. Non-Cryst. Sol., **6**, 329.

Fritzsche, H., 1974, in Amorphous and Liquid Semiconductors, ed. J. Tauc (Plenum Press, New York) p. 313.

Gilroy, K.S., and W.A. Phillips, 1981, Pjilos. Mag. B., **43**, 735.

Giorgis, F., F. Giuliani, C.F. Pirri, A. Tagliaferro and E. Tresso, 1998, J. Non-Cryst. Sol., **227-230**, 565.

Giridhar, A., and K.J. Rao, 1979, J. Non-Cryst. Sol., **33**, 177.

Gladden, L.F., S.R Elliott and G.N. Greaves, 1988, J. Non-Cryst. Sol., **106**, 189.

Husakuni, H., and K. Tanaka, 1994, Appl. Phys. Lett., **65**, 2925.

Jing, Z., J.L. Whitten, 1993, J. Chem. Phys., **89**, 7466.

Jing, Z., J.L. Whitten and G. Lucovsky, 1992, Phys. Rev. B., **45**, 13978.

Joannopoulos, J.D., and M.L. Cohen, 1976, Solid State Physics, Vol. 31, eds. H. Ehrenreich, F. Seitz and D. Turnbull (Academic Press, New York) p. 71.

Joannopoulos, J.D., 1979, J. Non-Cryst. Sol., **32**, 241.

Kastner, M., D. Adler and H. Fritzsche, 1976, Phys. Rev. Lett., **37**, 1504.

Kelly, M.J., 1980, in Solid State Physics, vol. 35, eds., H. Ehrenreich, F. Seitz and D.R Turnbull (Academic Press, Florida) p. 295.

Knotek, M.L., M. Pollak and T. M. Donovan, 1974, Proc. 5th Int. Conf. On Amorphous and Liquid Semiconductors, eds. J. Stuke and W. Brenig (Taylor and Francis, Hants) p. 225.

Kolobov, A.V., and S.R. Elliott, 1995, J. Non-Cryst. Sol., **189**, 297.

Kotkata, M.F., M.A. Afifi, H.H., Labib, N.A. Hegab and M.M. Abdel-Aziz, 1994, Thin Solid Films, **240**, 143.

Kotsalas, I.P., D. Papadimitriou, C. Raptis, M. Vlcek and M. Frumar, 1988, J. Non-Cryst. Sol., **226**, 85.

Le Cleac'h, X., 1979a, J. Phys., Paris, **40**, 27.

Le Cleac'h, X., 1979b, J. Phys., Paris, **40**, 417.

Ley, L., R.A. Pollak, S.P. Kowalczyk, F.R. McFeely and D.A. Shirley, 1973, Phys. Rev. B., **8**, 641.

Long, A.R., 1982, Adv. Phys., **31**, 553.

Lucovski, J., and H. Yang, 1998, J. Non-Cryst. Sol., **227-230**, 281.

Lyubin, V.M., and V.K. Tikhomirov, 1994, J. Non-Cryst. Sol., **171**, 87.

Mohan, R., and K.J. Rao, 1981b, Ind. J. Chem., **20A**, 864.

Mott, N.F., and E.A. Davis, 1979, Electronic Properties in Non-Crystalline Materials (Oxford University Press, New York).

Mott, N.F., 1977, Philos. Mag., **35**, 111.

Nagels, P., 1979, in Amorphous Semiconductor, ed. M.H. Brodsky (Springer_Verlag, Berlin) p. 117.

O'dwyer, J.J., 1973, The theory of Electrical Conduction and Breakdown in Solid Dielectrics (Clarendon Press, Oxford).

Ovshinsky, S.R., 1968, Phys. Rev. Lett., **21**, 1450.

Ovshinsky, S.R., 2000, in Insulating and Semiconducting Glasses, ed., P. Boolchand (World Scientific, Singapore) p. 729.

Pike, G.E., 1972, Phys. Rev. B., **6**, 1572.

Pollak, M., and G.E. Pike, 1972, Phys. Rev. Lett., **28**, 1449.

Pollard, W.B., and J.D. Joannopoulos, 1978, Phys. Rev. B., **17**, 1770.

Pollard, W.B., and J.D. Joannopoulos, 1978, Phys. Rev. B., **17**, 1778.

Rao, K.J., and R. Mohan, 1981a, Solid State Comm., **39**, 1065.

Sakurai, Y., Y. Hamakawa, T. Masumoto, K. Shirae and K. Suzuki, eds., 1993, Current Trends in Amorphous Materials Physics & Technology (North Holland, Amsterdam) p. 384-421.

Selvaraj, U., and K.J. Rao, 1988, Philos. Mag. **58**, 203.

Spear, W.E., and P.G. Le Comber, 1976, Philos. Mag. B., **33**, 935.

Staebler, D.L., and C.R. Wronski, 1977, Appl. Phys. Lett., **31**, 292.

Stanley, H.E., 1971, Introduction to Phase Transitions and Critical Phenomena (Academic Press, New York).

Street, R.A., and N.F. Mott, 1975, Phys. Rev. Lett., **35**, 1293.

Tanaka, K., K. Ishida and N. Yoshida, 1996, Phys. Rev. B., **54**, 9190.

Tanaka, K., 1998, Phys. Rev. B., **57**, 5163.

Thouless, D.J., 1979, *Ill*-Condensed Matter, eds. R. Balian, R. Maynard and G. Toulouse (North Holland, Amsterdam).

Tohge, N., Y. Yamamoto, M. Minami and M. Tanaka, 1979, Appl. Phys. Lett., **34**, 640.

Tohge, N., T. Minami, Y. Yamamoto and M. Tanaka, 1980, J. Appl. Phys., **51**, 1048.

Triberis, G.P., and L.R. Friedman, 1981, J. Phys. C., **14**, 4631.

Vaidhyanathan, B., S. Murugavel, S. Asokan and K.J. Rao, 1997, J. Phys. Chem. B, **101**, 9717.

Weaire, D., and M.F. Thorpe, 1971, Phys. Rev. B., **4**, 2508.

Weaire, D., M.F. Thorpe and V. Heine, 1972, J. Non-Cryst. Sol., **8-10**, 128.

Ziman, J.M., 1972, Principles of the theory of Solids (Cambridge University Press, Cambridge).

Nothing troubles me more than time and space; and yet
nothing troubles me less, as I never think about them.
- Charles Lamb

CHAPTER 9

RELAXATION PHENOMENA

In chapter 7, several aspects of conductivity and dielectric relaxation were discussed. Various other properties such as shear modulus, viscosity, refractive index, volume, enthalpy etc. also exhibit relaxational behaviour particularly in the glass transition region. In this chapter, few further aspects of relaxation are discussed. Relaxation of generalized stress or perturbation whether electrical, mechanical or any other form is typically non-exponential in nature. The associated property is a function of time. A variety of empirical functions, $\phi(t)$, have been used to describe the relaxation. Some of them have already been discussed in chapters 6 and 7. The most widely used function is the Kohlraush-Williams-Watts (KWW) function (Kohlraush, 1847; Williams and Watts, 1970; Williams et al., 1971). It is more commonly referred to as the stretched exponential function*. The decay or relaxation of the quantity $\phi(t)$ is given by,

$$\phi(t) = \phi_0 \exp\left[-\left(\frac{t}{\tau}\right)^{\beta}\right] \tag{9.01}$$

where β is called the stretching exponent and its value lies between 0 and 1. When $\beta = 1$, the function represents simple exponential decay, which is the Debye relaxation function with a characteristic time constant, τ_D.

Relaxation function $\phi(t)$ in equation (9.01) can be expressed equivalently through the use of relaxation functions in frequency domain –

---

* KWW expression is known as stretched exponential function and the reason is as follows. The simple exponential or Debye function is $\phi(t) = \phi_0 \exp[-(t/\tau_D)]$. Therefore, $\left(\frac{t}{\tau_D}\right) = \ln\left(\frac{\phi_0}{\phi}\right)_D$

similarly, $\left(\frac{t}{\tau_{KWW}}\right) = \left[\ln\left(\frac{\phi_0}{\phi}\right)\right]^{1/\beta}$. Hence, $\frac{\tau_{KWW}}{\tau_D} = \ln\left(\frac{\phi_0}{\phi}\right)_D \Big/ \left[\ln\left(\frac{\phi_0}{\phi}\right)\right]^{1/\beta}$. Since by definition relaxation time corresponds to (ϕ_0/ϕ) = e, $\frac{\tau_{KWW}}{\tau_D} = \frac{\ln e}{[\ln e]^{1/\beta}}$. For $0<\beta<1$, $\tau_{KWW} > \tau_D$. Therefore, τ_{KWW} is said to be "stretched".

a characteristic time, τ_0 manifests through a characteristic frequency ω_0, such that $\omega_0\,\tau_0 = 1$. Dielectric functions such as Cole-Cole, Davidson-Cole etc. (Cole and Cole, 1941; Davidson and Cole, 1958) are all functions in frequency domain. These functions can be derived as special forms of a general function which goes after the names, Havriliac and Negami, HN (Havriliac and Negami, 1966),

$$F(\omega) = \frac{F(0) - F(\infty)}{\left[1 + (i\omega\tau)^{1-\alpha}\right]^{\beta}} \tag{9.02}$$

With reference to dielectric relaxation[#], equation (9.02) can be written as,

$$\varepsilon^*(\omega) - \varepsilon(\infty) = \frac{\varepsilon(0) - \varepsilon(\infty)}{\left[1 + (i\omega\tau)^{1-\alpha}\right]^{\beta}} \tag{9.03}$$

When $\alpha = 0$ and $\beta = 1$, this gives rise to the Debye relaxation function, which gives rise to a semicircle, when ε'' is plotted against ε' [$\varepsilon^*(\omega) = \varepsilon'(\omega) - i\varepsilon''(\omega)$]. When α alone is zero,

$$\varepsilon^*(\omega) - \varepsilon(\infty) = \frac{\varepsilon(0) - \varepsilon(\infty)}{\left[1 + i\omega\tau\right]^{\beta}} \tag{9.04}$$

is the Davidson-Cole function, which gives a skewed semicircle in ε''vs ε' plots. When β alone is unity, it gives rise to Cole-Cole function, which gives semicircular arc in ε''vs ε'plots.

$$\varepsilon^*(\omega) - \varepsilon(\infty) = \frac{\varepsilon(0) - \varepsilon(\infty)}{\left[1 + (i\omega\tau)^{1-\alpha}\right]} \tag{9.05}$$

[#] The advantage of Havriliac and Negami function is that the experimental data can be represented with a fair degree of accuracy using this function. But equation (9.03) is a 5 parameter equation, only three of which may be readily interpreted in terms of molecular quantities. $\varepsilon(0)$ represents equilibrium behaviour, while $\varepsilon(\infty)$ represents instantaneous behaviour so that $\varepsilon(0) - \varepsilon(\infty)$ represents the effective moment of the orienting unit. Parameter τ is the jumping time associated with the jumping unit. However the exponents α and β are not well defined in molecular terms, while α describes the width of the dispersion, β describes the skewness of the dispersion: width increases as α varies from 0 to 1 and skewness decreases as β increases from 0 to 1.

The same designations of the functions hold good when instead of $\varepsilon^*(\omega)$, one has $Z^*(\omega)$, $M^*(\omega)$, $\chi^*(\omega)$ etc. Reference was made to Davidson-Cole function in the context of DCR model in chapter 7. The exponent β is generally designated as β_{CD} (subscript avoids the confusion with $\beta_{KWW} \equiv \beta$)

The value of β in equation (9.01) is determined by first introducing this into the expressions describing a relaxing property. For example, in the modulus description, we noted that (equation. 7.24) $M^*(\omega)$ is given by,

$$M^*(\omega) = M_s\left[1 - \int_0^\infty dt.\exp(i\omega t)\left(-\frac{d\phi(t)}{dt}\right)\right] \tag{9.06}$$

Equation (9.01) has to be substituted for $\phi(t)$ in eq. (9.06).

Stretched exponential function may characterize the relaxations of the imaginary parts of any of the quantities listed earlier. They all exhibit similar 'loss' peaks as functions of frequency. The corresponding full width at half maximum (FWHM) values are generally significantly greater than the Debye value and they are related to β. If FWHM is expressed as decades of width, Δ, then

$$\frac{1}{\beta} = -0.08984 + 0.96479\Delta - 0.004604\Delta^2 \tag{9.07}$$

for values $0.3<\beta<1$ and Δ value between 1.14 (Debye value) and 3.6 decades.

Secondary or β-relaxations

Secondary relaxations occur in the sub-glassy region and it is thought that it originates from localized motions of some parts of the glass structure. The β-relaxation[#] mode itself gets decoupled from the modes responsible for α-relaxation which is associated with the glass transition. β-relaxations are often associated with local ionic motions, particularly in

[#] The symbol, β, is in great demand in glass science. In the context of relaxation, in this book, $\beta \equiv \beta_{KWW}$. β used in HN equation for designating β-relaxation and for compressibility etc. have to be carefully noted in the respective contexts.

fast ionic conducting glasses. The decoupling index, R_τ, at T_g represents the relative magnitudes of the relaxation times at T_g of the α and β relaxations. ($R_\tau = \log(\langle \tau_s \rangle / \langle \tau_\sigma \rangle)$, where $\langle \tau_s \rangle$ is the structural relaxation time characterizing the glass transition and $\langle \tau_\sigma \rangle$ characterizes the electrical relaxation time at the glass transition). R_τ can be of the order of 12 or more. Therefore, to observe the secondary relaxation in dielectric studies, it may require very low temperatures or very high frequencies. The presence of β-relaxations was predicted in the potential energy surface approach to glass transition by Goldstein (1969) as a universal feature of all glasses. Thus small local rearrangements in organic glasses, are revealed in dielectric loss measurements. An early study of β-peaks in glasses by Johari and Goldstein (1971) is shown in Figure 9.01.

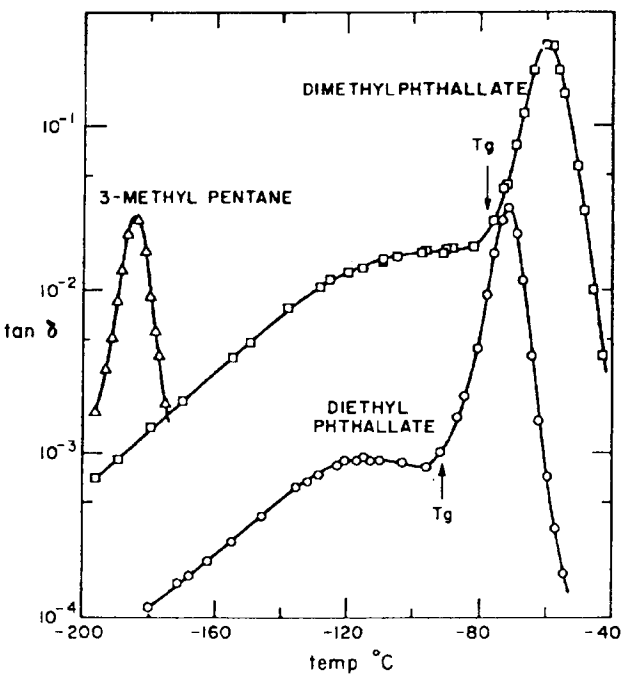

Figure 9.01: Temperature dependence of dielectric loss factor for dialkylphthallates and 3-methylpentane at 1 kHz. Scale for diethyl phthallate has been shifted downwards, and for 3-methylpentane upwards, by one logarithmic cycle (After Johari and Goldstein, 1971).

Secondary relaxation in sodium trisilicate glass has been observed in the measurements of electrical modulus (M') and shear modulus (G') as shown in Figure 9.02. It can be seen from the figure that behaviours of

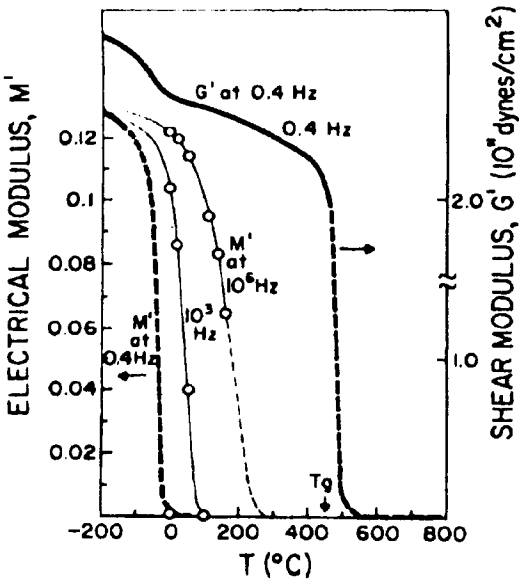

Figure 9.02: Shear modulus and electrical modulus for sodium trisilicate glass. Note the relaxation step in G' around ~ 0°C and that of M' at 0.4 Hz at ~ 0°C (After Angell, 1988).

M' and G' are very similar. More importantly G' also shows a second break in the same region where the secondary relaxation occurs (around 0°C). Although this observation of relaxation of mechanical modulus suggest that there is some local reorganization which contributes to modulus, no enthalpy relaxation associated with β processes has been reported. β processes generally exhibit Arrhenius behaviour over wide ranges of temperature in contrast to α processes which are non-Arrhenius. β-relaxations also follow KWW function. But the relaxation characteristics associated with β processes in electrical and mechanical properties can be different.

The many modes of relaxation in glasses

In the study of glasses, one realizes that a variety of relaxational stages are encountered as the temperature of the glass forming melt is lowered. The melting point, T_m, serves as a good starting point. The relaxation behaviour of CKN (Angell, 1991; Angell and Torell, 1983) is shown Figure 9.03. The relaxation data has been obtained from a variety

of experiments and covers 15 decades of data (which is almost the entire region of possible relaxation studies). The relaxation studies include

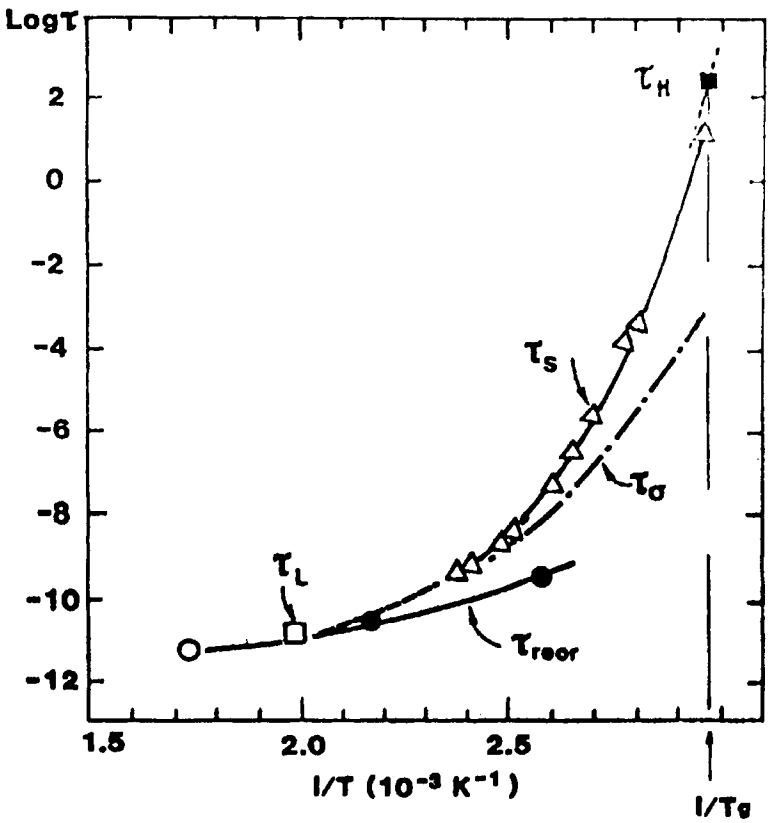

Figure 9.03: Arrhenius plot of the various relaxation times (After Angell, 1991).

τ_l (liquid structural relaxation–longitudinal) determined from Brillouin scattering, $\tau_{\text{reorientational}}$ obtained from vibrational spectroscopy, τ_σ determined from electrical conductivity, τ_s from viscosity and τ_H from differential scanning calorimetry. It is interesting to note the following from the figure, (1) The activation barriers for the relaxation times in the high temperature regime are remarkably low. Extrapolation of τ_l to $1/T = 0$ points to vibrational time scales, (2) there is strong dispersion in activation barriers in the low temperature region as T_g is approached, which obeys VTF equation (equation 3.02), (3) τ_σ in the glassy region has a lower activation barrier. (4) At some point close to T_g, τ_H branch manifests corresponding to enthalpy relaxation, which has a value ~ 100 s at T_g.

There are several "split off" or bifurcation points in the relaxation time graph. $\tau_{\text{reorientational}}$ splits off at high temperatures from τ_l (longitudinal), then τ_s splits off from τ_l, then τ_H splits off from τ_s. Thus there are a series of decouplings of relaxation times, which occur as the supercooled liquid approaches glass transition temperature. β-relaxation is one of these 'split off' branches, which survives in the glassy state still exhibiting Arrhenius behaviour. From the point of view of AG equation (3.09), those with the smallest $\Delta\mu$ (activation barrier) 'cut loose' from the slower modes. At cryogenic temperatures, there still waits the asymmetric double well potential (ADWP) structures, giving rise to yet another class of relaxation phenomena in glasses. Each stage of split off or decoupling marks the beginning of some 'mode', eventually falling out of equilibrium implying that there are several layers of metastability in a glass. When a melt is cooled, MCT (chapter 3) predicts the divergence of a structural (relaxation) mode at a temperature designated as T_C, a critical temperature, better known as cross over temperature. But T_C is still considerably above T_g at approximately $1.3T_g$. In the late 1960s (Boyer, 1966), presence of such a critical temperature was noted in many studies of liquid polymers and was designated as T_{LL}, as it was a liquid-liquid transition. The relation between T_g and T_{LL} is also known as Boyer's law, i.e., $T_{LL} = 1.2T_g$. $T_C \approx T_{LL}$ appears to be the same temperature, T^*, where the relaxation time spectrum splits off into α and β branches. The region between T^* and T_g is known as viscoelastic region and the behaviour of the α relaxation in the viscoelastic region is found to be governed by the VTF equation, $\tau = \tau_0 \exp[A/(T - T_0)]$. The T_0 of the VTF equation is, however, buried in the glassy region and inaccessible for relaxation time measurements. Between T_g and T^* ($T^* \approx T_{LL} \approx T_C$), the relaxation behaviour is found to be governed by many other functions. Notable are those suggested by Bassler ($\log\tau \sim B/T^2$) and by MCT ($\tau \sim (T\text{-}T_C)^{-\gamma}$). The β branch, however, continues to remain Arrhenius with a smaller activation energy. Rault (2000) found that between T_g and T^*, the time dependence of almost all properties of the system follow the stretched exponential or the KWW equation (see, Angell et al., 2000 for an excellent review on relaxation).

Scaling behaviour of relaxations

Relaxation behaviour is associated with two generic features - the scaling and the stretching phenomena. Scaling implies that the reduced relaxation properties, ($M''/M''(\max)$), ($\varepsilon''/\varepsilon''(\max)$), etc. measured as a

function of ω at different temperatures, T, may be made to collapse onto a single curve by scaling the ω axis with a temperature dependent characteristic frequency, ω_0. Correspondingly plots can be obtained using reduced quantities in time domain also. Stretching implies that the relaxation function, which describes the ω-dependence of the relaxing property is characterized by an exponent, β, ($0 < \beta < 1$) so that $\phi(t) = \exp\{-(t/\tau_0)^{\beta}\}$. The stretched exponential decay is frequently interpreted as an effective manifestation of a distribution of exponentially decaying relaxation times.

Glass transition is caused by the slowing down of α-relaxation. An aspect of interest in the α relaxation behaviour is that it almost always exhibits a time-temperature superposition principle. The chosen property (process) for study could be any susceptibility such as dynamic specific heat, or decay of the correlation functions, etc. Shown in Figure 9.04(a) is the variation of the density correlator, $\phi_Q(t)=S(Q,t)/S(Q)$ obtained from neutron spin echo spectroscopy (Mezei et al, 1987) for Q=1.7 Å^{-1}. $\phi_Q(t)$ for various temperatures can now be re-defined as $F(\tilde{t})$ where $\tilde{t} = t/\tau_\alpha(T)$. When this redefined function is plotted as a function of $t/\tau_\alpha(T)$, the various correlation functions fall on the same curve as shown in Figure 9.04(b), where $\tau_\alpha(T)$ is determined from the viscosity data (τ scales as η/T) Thus the change of temperature or other parameters like ρ merely change the scale of τ_α of the α process. Representation via $\tilde{t}$ gives the new function $F(\tilde{t})$ independent of temperature. These functions are referred to as "master functions". The plots are called as "master curves". The scaling law governing the observed α relaxation process is called the time-temperature superposition principle. Functions of frequency such as $\psi''(\omega)$ can be similarly modified using $\tilde{\omega}$, where $\tilde{\omega} = \omega/\omega_0(\alpha)$. In the glassy region also properties such as M'' or ε'' obey superposition principle for similarly chosen reduced frequencies (x-axis) (discussed in chapter 7). We may refer here to a scaling function, which has done very well in terms collapsing α relaxation data of several glass forming liquids over 13 decades of frequency *but it is not based on any known relaxation function.* The master curve is obtained by plotting $(1/W)$ log $(\varepsilon'' \nu_P/\nu\Delta\varepsilon)$ vs $(1/W)((1/W) + 1)$ log(ν/ν_P), where ν_P is the peak frequency, ε'' is the imaginary part of the dielectric constant and $\Delta\varepsilon = \varepsilon(0) - \varepsilon(\infty)$ and W is the reduced FWHM (ratio of FWHM divided by the Debye width, 1.144 decades). This scaling relaxation function of Dixon et al. (1990) not only covers the relaxation phenomena over 14 decades of frequency, but also

up to temperatures very close to T_g, which has been carried out on many fragile liquids like o-terphenyl, Dibutyl phthalate, etc. It was found that log ν_P vs $1/T$ plots did not approach an Arrhenius form at low temperatures, unlike in the case of viscosity data. α relaxations are

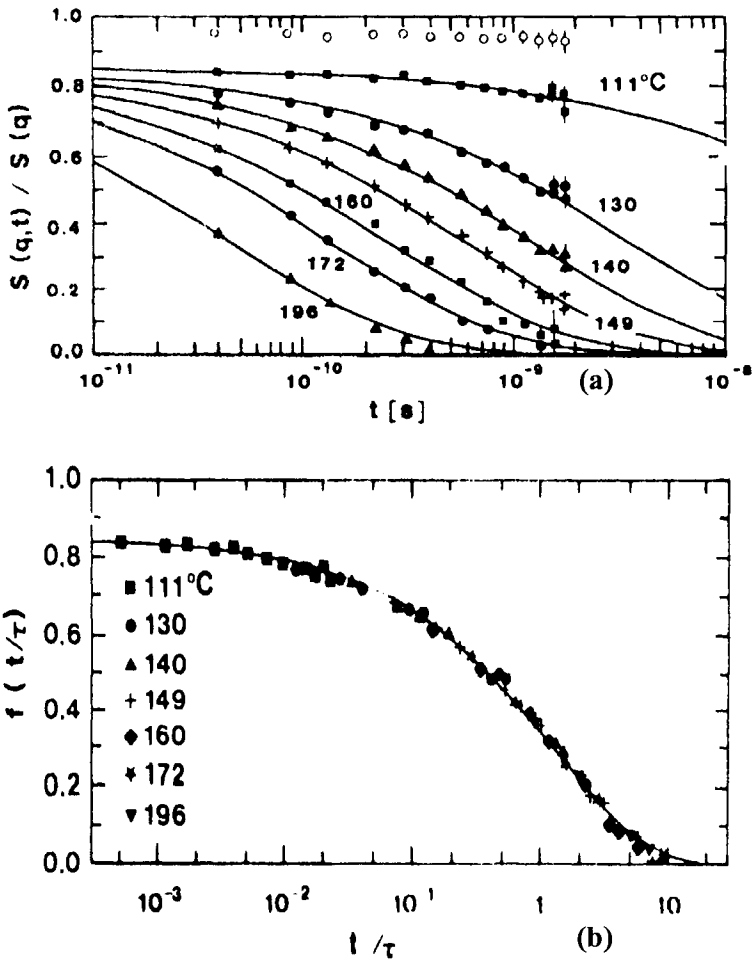

Figure 9.04: (a) The time-dependent dynamic structure factor of CKN ionic glass system at various temperatures. (b) The same data as in (a) plotted against the scaled time variable t/τ, ($\equiv t/\tau_\alpha$, discussed in the text) (After Mezei et al, 1987).

non-exponential and generally follow the stretched exponential (KWW) function, $\phi = \phi_0 \exp[-(t/\tau)^\beta]$. The factor ϕ_0 specifies the α peak area. This rather powerful function, referred so repeatedly in various contexts, plays

a very important role in the probability theory as a characteristic function of one-sided Lévy distributions (or stable distributions). They are used to describe a variety of phenomena in disordered systems. It was first used as an empirical fit formula in glass literature in the 1970s (Moynihan et al., 1976). The KWW behaviour of α relaxation was thought to be a consequence of the fractal distribution of free volumes. The Cohen-Grest description of glass transition, which has a percolation threshold character built into it gives rise to a fractal structure in space as T_g is approached. It envisages a fractal distribution of free volumes. But Cohen-Grest model (1979) requires that β has a lower bound of 0.5, and this is clearly violated in many polymers. Further the theory anticipates that α relaxation times (τ_α) are proportional to viscosity relaxation times (τ_η). This is also not borne out in simple systems like o-terphenyl and trinaphthyl benzene. Even the high frequency tail of the susceptibility variations has been found to be wrongly predicted by this theory. It may, however, be noted that KWW function does not account well for the α relaxation data at high frequencies as found in the studies on CKN, salol and several polymers (Moynihan, 1983).

KWW expression and Ngai's coupling model

The origin of the stretched exponential behaviour of the α - relaxations (applicable to other similar phenomena) has been examined in the Ngai's (1979) *coupling model.* In this model the relaxing units are visualized to be mutually interacting and therefore, influence each other's relaxations. The effect of interaction is assumed to be the slowing down of the net relaxation process. The interaction itself is characterized by coupling parameters which is as follows. To begin with, when there is no coupling, the relaxation function – the rate function – $W(T,t)$ has a time independent form designated as $W_0(T)$. When there is coupling, there is a resultant many-body interaction, which slows down the primitive rate $W_0(T)$. After a time $t_C = 1/\omega_C$ ($\omega_C\, t_C = 1$), the interaction causes effective relaxation rate $W(T,t)$ to become $W_0(T).(\omega_C\, t)^{-n}$, for $t > \omega_C^{-1}$. n is a fraction such that $0 < n < 1$. The structural relaxation function, $\phi(t)$ is obtained as a solution to the equation

$$\frac{d\phi}{dt} = -W(T,t)\cdot\phi \qquad (9.08)$$

Since $W(T,t)$ is equal to $W_0(T)$ for $\omega_c t < 1$, the relaxation function will be a simple exponential function for this time regime. For the region $\omega_c t > 1$, it is more complex. It has been shown by Ngai and co-workers (Nagai, 1979; Nagai et al., 1984) that KWW stretched exponential function, $\phi = \phi_0 \exp[-(t/\tau)^{\beta}]$, with $\beta = (1 - n)$, is a satisfactory solution to the above equation. When $\omega_c / W_0 >> 1$, the effective relaxation time τ^* and the primitive relaxation time $\tau_0 = 1/W_0$ are related as

$$\tau^*(t) = \left[(1-n)\omega_c \tau_0\right]^{1/1-n} \tag{9.09}$$

Thus the coupling model is characterized by two constants, $n = (1-\beta)$, which broadens the relaxation spectrum and τ_0, the primitive relaxation time, which escapes the influence of coupling. Both n, which represents the coupling strength and τ_0, are temperature dependent.

In most liquids and to a good approximation, $\beta = (1-n)$. Therefore n can be evaluated by evaluating β. β itself is given by the ratio W_d/W, where W_d and W are the Debye and actual widths of the relaxation spectrum. Even when loss curves (dielectric, mechanical or any other) are fitted to other standard analytical functions such as Cole-Cole (CC), Davidson-Cole (DC) or Haveriliac-Negami expressions, (see earlier section) one can determine β using the empirical relations

$\beta = 0.03 + 0.5\alpha_{CC} + 0.45\alpha^2_{CC}$ (Cole-Cole fit)
$\beta = 0.03 + 1.15\ \alpha_{DC} - 0.24\alpha^2_{DC}$ (Davidson-Cole fit)
$\beta = [\alpha_{CC}\alpha_{DC}]^{(1/1.23)}$ (Haveriliac-Negami fit)

(Note: The exponent in the HN equation is determined by α_{CC} and α_{DC}, which are the exponents of the Cole-Cole and the Davidson-Cole functions respectively and the constants in equation 9.02 have been redesignated as $(1 - \alpha) \equiv \alpha_{CC}$ and $\beta \equiv \alpha_{DC}$). β is temperature dependent and the values of β are identified as $\beta = 0$ at T_0 and $\beta = 1$ at T^*. The validity of this approach has been verified in a number of materials and a typical example given by Rault (2000) based on the measurements done in PIBMA (Poly isobutylene methacrylate) by Dhinojwala et al.(1992) using the data of the decay of chromophore orientation in a poled film is shown in Figure 9.05. In the region between T_0 and T^*, β is found to vary

generally linearly. There are, however, liquids like glycerol, propylene glycol, etc. which do not exhibit large variation of β and the behaviour of these liquids is, even otherwise, exceptional.[#]

β is also found to be sensitive to pressure and it decreases linearly so that $\beta = \beta_0 - \gamma P$, where $\beta = \beta_0$ at zero external pressure and γ is a constant of the order of unity, when pressure is expressed in GPa. This dependence arises from the fact that T_0, T_g and T^* are all pressure dependent. T_0 generally increases by about 10K per kbar. Thus, the stretched exponential function and the linear variation of the KWW exponent provides yet another approach to understand the empirical VTF law. Rault (2000) has proposed that below T^*, where the α- relaxation is characterized by a continuously increasing effective activation barrier, τ can be written as $\tau_0 \exp(E_\beta/\beta RT)$. That is the activation barrier for the cooperative motion is effectively increased to E_β/β. Referring to the VTF

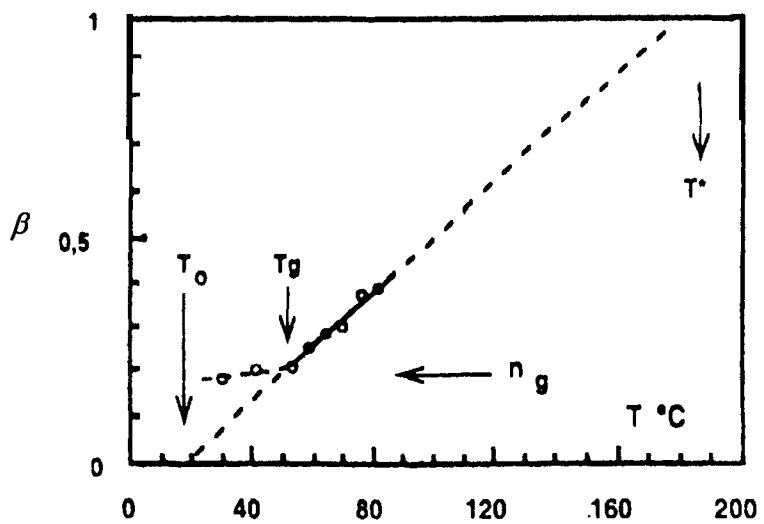

Figure 9.05: Direct method for determining the linear variations of the KWW exponent, β, with the temperature. (After Rault, 2000).

equation, the parameter B is now equal to $[(E_\beta/R)(T - T_0)/\beta T]$, which we may designate as B_R (R = Rault) so that the modified VTF equation is

[#] It may be noted that in many types of glasses, the creep compliance follows the well-known Andrade law; $J \approx \exp\{(t/\tau)^{0.3}\} \approx t^{0.3}$, which is the same as KWW with exponent $\beta = 0.3$.

$$\tau = \tau_0 \exp\left[\frac{B_R}{T - T_0}\right] \tag{9.10}$$

Since the exponent, β, is linearly dependent on temperature, $\beta(T)$ can be suitably reformulated;

$$\beta(T) = \frac{T - T_0}{T^* - T_0} \tag{9.11}$$

so that $\beta = 0$ at $T = T_0$ and $\beta = 1$ at $T = T^*$. The value of B in VTF equation becomes,

$$B = \frac{E_\beta (T^* - T_0)}{RT} \tag{9.12}$$

At T_g the value of $\beta_g T_g$ can be determined from the relation $\tau = \tau_0 \exp[B_R/(T - T_0)]$ by substituting the values of τ_0 ($\approx 10^{-14}$ s), τ_g ($\approx 10^2$ s) and B_R:

$$\beta_g T_g \approx \frac{E_\beta}{2.303 \times 16R} \tag{9.13}$$

This simple and approximate formula has been found to give reasonable estimates of β_g and it involves easily measurable parameters like T_g and E_β.

Thermodynamics in the region of glass transition

Since glasses are inherently in a non-equilibrium state around T_g, thermodynamic formulation relevant for this region has to include one important additional feature and that is a time scale. Even in laboratory time scales profound changes in properties can occur. It is the existence of this time scale, which led to the definition of a "fictive temperature" by Tool (Tool and Eichlin, 1931; Tool, 1946). If we call this reference or fictive temperature as T_f (which is more accurately written as $T_f(t)$ since it is time-dependent), then the Gibb's free energy of a glass can be described in terms of three parameters, T, P and T_f. Also the heat balance equation in

terms of entropy S, becomes

$$đQ = TdS_e + T_f dS_c' \tag{9.14}$$

S_e is the entropy of the equilibrium process and S_c' is the 'slow' part of the configurational entropy (not to be confused with the entropy of AG equation). This is the part of the entropy change involved in the annealing experiments. The configurational changes, which occur very fast, contribute to S_e itself. The slow relaxing part of entropy is described as the 'complexity' of the system. We recognize, therefore, that the observed entropy of the melt is the sum, $(S_c + S_c' + \Delta S_v)$, where ΔS_v is the excess vibrational entropy of the melt. It is now written as $(S_e + S_c')$ where $S_e = (S_c + \Delta S_v)$, S_c is the fast relaxing part of the configurational entropy. There is thus a need to define how slow is slow. All processes, which have a characteristic relaxation time τ_l less than $0.1\,\tau_{max}$ in the system are termed as slow in this treatment. In view of the inclusion of T_f and S_c', the first law of thermodynamics relevant to a glass may be written as

$$dU = TdS_e + T_f dS_c' - PdV \tag{9.15}$$

The Gibb's free energy is written as

$$G = U - TS_e - T_f S_c' + PV \tag{9.16}$$

In the differential form,

$$dG = -S_e dT - S_c' dT_f + VdP \tag{9.17}$$

Since total entropy S is equal to $S_e + S_c'$ and from the second law of thermodynamics, $TdS \geq dQ$, we have

$$(T_f - T)dS_c' \leq 0 \tag{9.18}$$

Since T_f is also a function of T and P, as both the entropy terms are, one can calculate the heat capacity of a glass in the region of glass transition as

$$C_P = C_1 + C_2\left(\frac{\partial T_f}{\partial T}\right)_P \tag{9.19}$$

where C_1 and C_2 (arising from S_c and S_c' respectively) are functions of temperature. Maxwell's relations also get modified for glasses due to the effect of T_f because T_f is itself now a function of T and P.

Nieuwenhuizen (2000) has shown that one of the Ehrenfest relations becomes

$$\Delta\alpha = \Delta\kappa\left(\frac{dP_G}{dT}\right) \tag{9.20}$$

where P_G refers to the pressure at the glass transition. The above Ehrenfest relation will correspondingly change the Prigogine-Defay ratio as

$$\begin{aligned}\Pi &= \frac{\Delta C_P}{TV\Delta\alpha\left(\frac{\partial P_G}{\partial T}\right)_V} \\ &= 1+\frac{1}{V\Delta\alpha}\left[1-\left(\frac{\partial T_f}{\partial T}\right)_P\right]\left(\frac{dS_c'}{dP}\right)\end{aligned} \tag{9.21}$$

$\partial P_G/\partial T$ determination requires performing cooling experiments at least at two pressures. $\partial P_G/\partial T$ can have a large range, which implies that Π itself depends on the particular set of experiments conducted and the values of Π can be even less than unity in cases where long time κ values are used. (Compare these terms with the terms derived without including T_f in chapter 2).

Two Level States and relaxation

A special feature of amorphous materials is the anomalous behaviour of several properties at very low temperatures, such as in the low temperature specific heats. Most of these anomalies are attributed to the presence of two-level states (TLS) separated by small barriers, which gives rise to tunneling excitations. These excitations are characterized by wide distribution of relaxation times and energies. Several ultrasonic and low temperature specific heat measurements have been performed to characterize the TLS but their physical nature such as their structures, etc. is far from having been understood. These are the ADWP states discussed earlier in Chapter 7 in some detail.

In brief, a double-well potential (Figure 7.07) with an asymmetry

in energy of Δ is characterized by eigen states

$$E = (\Delta^2 + \Delta_0^2)^{1/2} \tag{9.22}$$

Δ_0 is the coupling energy and is equal to $E_0.\exp[-\lambda]$, where λ is the tunneling parameter related to the height and the width of the barrier. E_0 is the zero-point energy. The transition from one well to the other occurs by emission or absorption of a phonon of energy $h\nu = E$. Thermodynamic quantities such as specific heat of this two level system can be calculated. The specific heat of glasses at low temperature is generally larger than the Debye value and the thermal conductivities are far lower. Below 1K specific heats are quasi linear in their temperature dependence, $C \propto T^{\alpha}$; α being of the order of 1.2 - 1.5. The thermal conductivity varies as T^2.

Another important manifestation of TLS is the time-dependent excess specific heat. This specific heat $C(t)$ has been shown to be given by the relation

$$C(t) = \frac{\pi^2}{12} g(E) \mathrm{k} T \log_{10}(4\gamma_{max} t) \tag{9.23}$$

where $g(E)$ is the density of states and γ_{max} is the maximum relaxation rate, which clearly indicates a time dependence of the specific heat. The log linear dependence of the heat capacity on time has been qualitatively verified.

The tunneling in two-level states takes place when both the barrier heights and the widths are very small and thus the barrier can be breached by heavy atoms, unlike in the case of electrons or protons, which involves only tunneling. It is not clear whether TLS is a distinct class of objects involved in relaxation or whether they are just the tail-end states of secondary relaxations with very broad distributions, which continue to be active down to cryogenic temperatures. Another remarkable feature of the low temperature specific heat is that its magnitude depends only weakly on chemical composition, implying that the TLS present in glasses is almost a universal feature.

Cohen and Grest (1979) have assigned on the basis of their modified free volume model that the tunneling states arise at very low temperatures ($T \ll T_g$) because the volume dependent free energies of the cell in their model (see Chapter 3) possess curvature, which lead to local free energy minima. These minima are separated by solid-like barriers of

the order of kT_g in size. T_g enters because it is near T_g that the system falls out of equilibrium and the potential variations are presumably frozen at this temperature. Far below T_g, this brings about a localization of the free volume within a few neighbouring cells. Atoms sharing this excess free volume are capable of changing their configurations by multi-particle tunneling. It has been shown that such centers are very few and of the order of 10^{-3}-10^{-5} times the number of atoms.

TLS have been probed effectively in ultrasonic experiments. An interesting strategy is used in these measurements. This is the so-called 'hole burning' technique. When the intensity of the acoustic pulse is sufficiently high, the two states in TLS become equally populated and therefore the absorption from the acoustic field becomes saturated. As a result, the subsequent pulse suffers a reduced attenuation. Thus the high intensity sound pulse has burnt a 'hole' in the occupation number at an energy, $E = \hbar\omega$ with a width $\Delta\omega$. This is illustrated in Figure 9.06 for the

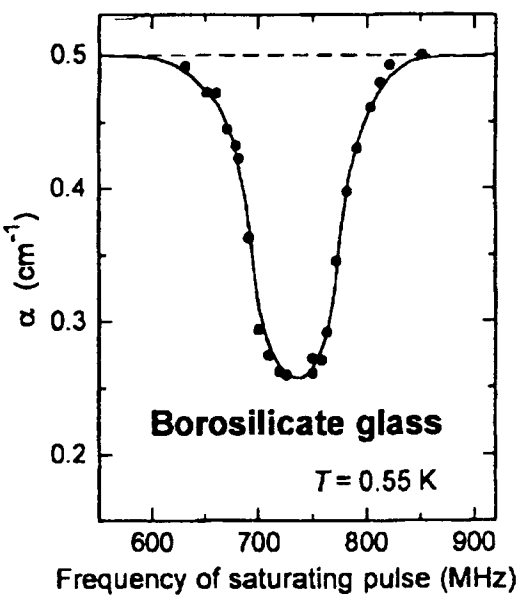

Figure 9.06: Resonant attenuation, α, of a weak probing pulse at 735 MHz as a function of the frequency of the intense saturating pulse (After Arnold and Hunklinger, 1975).

case of a borosilicate glass measured at 0.55 K and a probe pulse of 735 MHz. The breadth of the hole burnt is generally broad. This is because of the relaxational effects since the excitation involves a cooperative

rearrangement of the species responsible for TLS, which itself interacts with other TLS of similar nature in the excited state.

Enthalpy relaxation

Reference was made in chapter 2 to the characteristic humps (just above T_g) in the heat capacity plots and to the pre-transition endothermic and exothermic features. These features are typical manifestations of non-linear behaviour of glasses. Non-linear behaviour has been examined by the measurement of enthalpy relaxation characteristics. Enthalpy relaxation has been analyzed principally using two models - one generally referred to as Tool-Narayanaswamy-Moynihan, TNM model (Tool, 1946; Narayanaswamy, 1971; Moynihan et al., 1976) and the other as Scherrer and Hodge, SH model (Hodge, 1987; Scherrer, 1984). TNM model is used to analyse the variable temperature DSC scans, in which the system relaxation is treated as a superposition of isothermal relaxations. The latter are described using a combination of non-linear and non-exponential functions. SH model uses primarily AG expression and the non-linearity is related to the departure of the configurational entropy from the equilibrium value. Both analyses, however, yield similar results. Non-linear behaviour of the glasses is determined by the fictive temperatures. Therefore, the relaxation times are treated as functions of both, temperature, T and of the fictive temperature, T_f, which describe the state of the glass.

TNM expression for enthalpy relaxation is a result of introducing T_f into Arrhenius equation for τ and is given by,

$$\ln \tau(T, T_f) = \ln A + \frac{x\Delta H^*}{RT} + \frac{(1-x)\Delta H^*}{RT_f} \tag{9.24}$$

where T_f is the fictive temperature, τ the relaxation time, A and x are empirical constants and ΔH^* is the activation energy in the equilibrium state above T_g. The activation barrier is thus apportioned (using x) between the relaxations controlled by T and T_f. For $T \geq T_f$, $x = 0$. ΔH^* in this region is rather high particularly in fragile liquids (see Chapter 3); it is unclear if it can be considered as an activation barrier at all, although it is argued that it is high but shared by many atoms which are involved in cooperative motions (see section on fragility). In the SH model, T_f is introduced into AG equation. In the region of non-linearity, the excess entropy S_c is

determined by T_f rather than T. Since ΔC_p is often written as CT_0/T (hyperbolic variation), by integrating the heat capacity equation between the limits T_0 and T_f one arrives at the so-called Adam-Gibbs-Vogel (AGV) equation (Scherrer, 1984),

$$\tau = A\exp\left(\frac{B}{T(1-T_0/T_f)}\right) \tag{9.25}$$

The parameters of the TNM and AGV equations can be compared and the constants may be related as follows,

$$x = \left(1-\frac{T_0}{T_f}\right) \qquad \text{and} \quad \Delta H^* = \frac{BR}{\left(1-T_0/T_f\right)^2} = \frac{BR}{x^2} \tag{9.26}$$

Both TNM and AGV equations describe satisfactorily the non-linear variation of heat capacities observed in the case of atactic PMMA, shown as an example in Figure 9.07. Analysis of enthalpy relaxation in several

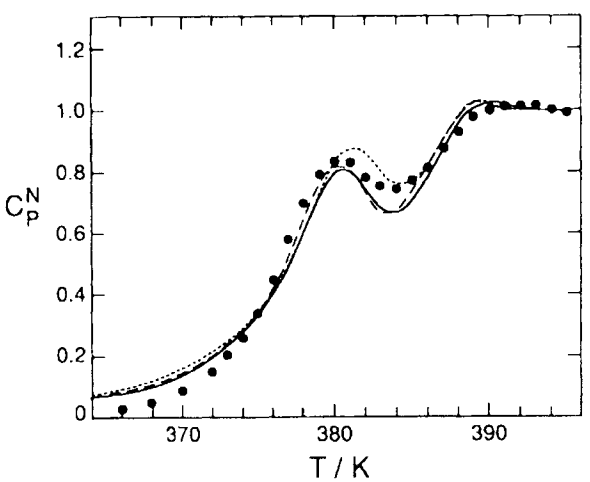

Figure 9.07: Fits using eqs. (9.24) (·····), (9.25) (———) and the experimental (•) data for atactic PMMA. History: cooling at 40 K min^{-1}, annealing for 17 hr. at 350 K, heating at 10 K min^{-1}; fit (— — —) is not discussed in this book (After Hodge, 1991).

glasses, molecular, polymeric and ionic, has revealed that strong liquids (which exhibit Arrhenius temperature dependence) possess small values of

ΔH^* near T_g and also small values of ΔC_p, whereas in fragile liquids these quantities have large values.

Enthalpy relaxation is one of the most widely studied in the context of both non-linearity and non-exponentiality of the measured glass properties. A convenient technique for these studies is scanning calorimetry. In simple cooling and heating experiments, heat capacity curves exhibit normal increase with characteristic hump of C_p above the glass transition as represented in Figure 9.08(A). The fictive temperature,

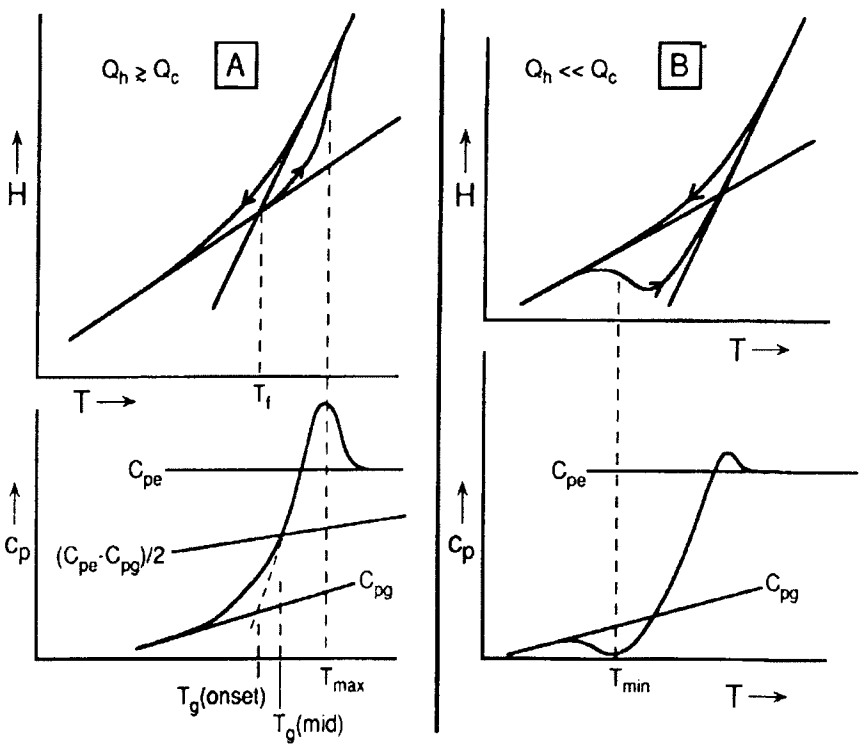

Figure 9.08: (A) Definition of onset and midpoint values of T_g and of T_f for a heating rate comparable with or greater than the cooling rate. (B) Illustration of exothermic excursion below T_g resulting from a heating rate that is much less than the cooling rate (After Hodge, 1994).

T_f and the various glass transition temperatures, such as T_g(onset), T_g(middle) etc. are also defined in Figure 9.08(A). The typical behaviour of both enthalpy and C_p are shown for a fast heating rate, where $Q_h >> Q_c$ at the bottom of the figure. Humps in heat capacity plots of the type shown in Figure 9.08(A) (bottom) occur when the heating rates are very much

higher than the cooling rates employed in forming the glasses.*

Figure 9.08(B) depicts the situation when heating rate is far lower than the cooling rate $Q_h << Q_c$. As the system approaches T_f during heating, a small exotherm is observed in the glass transition region and correspondingly a heat capacity dip is observed just below the glass transition temperature. The exotherm can be suppressed by decreasing the high initial values of T_f by annealing below T_g. The overshoot in the heat capacity curves is because the equilibrium condition $T = T_f$ is reached before any relaxation can occur. In many experimental studies, sub-T_g endotherms have also been observed when the glasses are annealed at temperatures 50 K (or more) below T_g. It is a common practice to anneal glasses around (T_g-20) K in which case sub-T_g endotherms merge with the T_g overshoot region. This has been widely noticed even in glassy alloys. The observation is generally rationalized using non-exponential functions with very broad distribution of relaxation times.

Enthalpy relaxation and a.c. heat capacities

The experimental glass transition is, therefore, associated with a relaxing property - the enthalpy. The enthalpy/specific heat modes, in principle, couple to all phenomena which occur in the glass transition region. Enthalpy relaxation can be studied by applying a sinusoidal temperature pulse, much like an alternating electric field, which is applied to study dielectric relaxation. The specific heat is therefore treated as a frequency (of thermal field) dependent property. The traditional adiabatic technique cannot be applied because the time required for heat diffusion across the sample has to be short compared to the measurement time and the former is determined by the thermal diffusivity, which is low for most solids and is of the order of 10^{-3} cm^2 s^{-1}.

Birge and Nagel (1985) overcame this problem by an ingeneous non-adiabatic method. They used one and same electrical resistor for both heating the sample and for measuring the temperature. The heater geometry is simply a thin metal film of resistance R, which was evaporated onto the glass substrate. The heater is immersed in a bath of the liquid sample, whose C_p behaviour is being probed. A sinusoidal current I, at a frequency ω /2, is passed through the heater. The power dissipated is I^2R, which has both, d.c. and a.c. components and the a.c. component appears at twice the frequency of the current oscillation

* T_f marks the quenching of melt structure equilibrated at T_f and does not mean that the structure of the resulting glass and that of the liquid at T_f are the same.

because of I^2 term. The d.c. component produces a constant temperature gradient in the sample cell, while the a.c. component emits diffusive thermal waves at frequency 2ω. The solution to the one dimensional diffusion equation, which is relevant to this problem requires that the temperature oscillations at the heater has a magnitude proportional to $(\omega C_p \kappa)^{-1/2}$ and also a phase lag of $\pi/4$ with respect to heat oscillations. C_p and κ are the specific heat and thermal conductivity of the material. The temperature is itself sensed by measuring the temperature dependent resistance of the metal heater. Since the resistance of the heater has a small component oscillating at a frequency, ω, which is proportional to the temperature oscillation, the voltage across the heater registers a large oscillating component at $\omega/2$ and a small component at $3\omega/2$. This is due to the current oscillation at $\omega/2$ being coupled to resistance oscillations at ω. The $\omega/2$ component is subtracted out by using a Wheatstone bridge circuit. The magnitude and phase of the $3\omega/2$ component is measured using a lock-in amplifier.

Birge and Nagel (1985) made measurements using this setup in the range $0.2 < \omega/2\pi < 6$ KHz. This method measures the product $C_p\kappa$ and not C_p. Since κ changes only very slowly near T_g, the observed behaviour of $C_p\kappa$ represents, essentially, the behaviour of C_p. Treating the frequency dependent $C_p\kappa$ as a complex quantity, one can write $(C_p\kappa)^* = (C_p\kappa)' + i(C_p\kappa)''$ and following the formalism discussed in chapter 7, the real and imaginary parts of $(C_p\kappa)^*$ can be determined. The measured values for the case of glycerol, both as a function of temperature at fixed frequency and as a function of frequency at fixed temperatures are shown in Figure 9.09 which reveals features very similar to those observed in electrical and mechanical relaxations. As the frequency increases, the glass transition is marked by steep fall in the real part of the thermal modulus. The loss peaks correspond to the dissipation of energy into the system. Thermodynamic laws require that there cannot be a net exchange of energy in one cycle of heat pulse between the sample and the surrounding bath, but the entropy of the bath can change during the cycle.

KWW function with a β of 0.65 ± 0.03 was found to fit well the imaginary parts of $C_p\kappa$ ($[C_p\kappa]''$) at all temperatures. The peak relaxation frequencies were found to follow VTF law with a T_0 of (128 ± 5) K, very close to the Kauzmann temperature of 134 K. Such specific heat spectroscopy measurements, as described above have great potential for use, where other relaxation spectroscopic methods are either difficult or inconceivable.

WLF equation

Historically, temperature dependence of mechanical and electrical relaxation times were first examined by Williams, Landel and Ferry

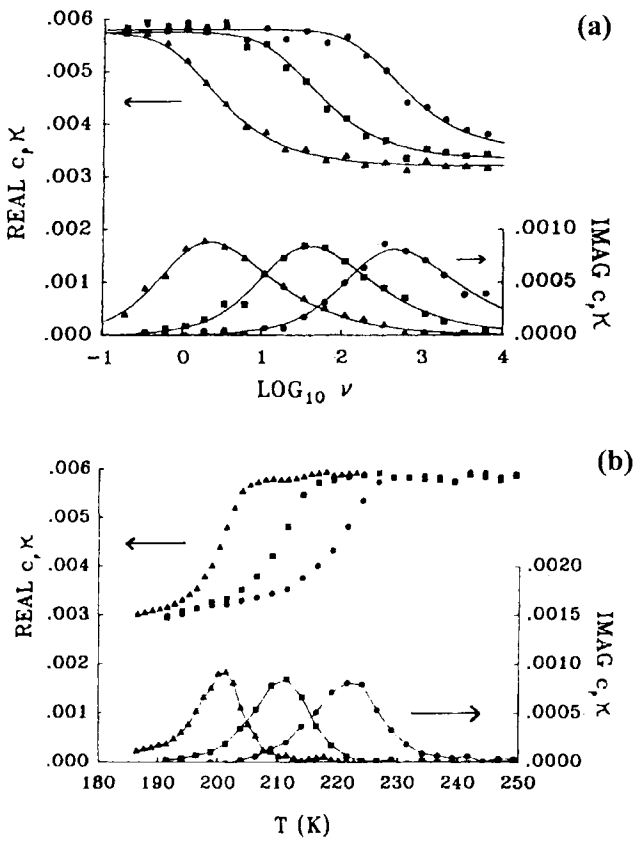

Figure 9.09: (a) The real and imaginary parts of $C_p\kappa^*$ glycerol as a function of frequency. (b) The real and imaginary parts of $C_p\kappa^*$ glycerol as a function of temperature. (After Birge and Nagel, 1985).

(1955) in a variety of polymers, polymer solutions, organic glass forming liquids and inorganic glasses. The empirical equation, which bears their names as WLF equation has been of seminal importance to glass science. If, a_T and b_T are mechanical and electrical relaxation times respectively at temperature T normalized with respect to their values at a suitably chosen temperature T_S, then WLF equation is written as

$$\log a_T = \log b_T = -\frac{8.86(T - T_s)}{10.16 + (T - T_s)} \tag{9.27}$$

The choice of T_S is based on the goodness of fit. WLF chose a T_S, which was ~ 50 ^{0}C above the T_g. They found that if T_g is itself chosen as the reference temperature, the numerical constants varied and the goodness of fit itself suffered although marginally. Shown in Figure 9.10 is a plot of log a_T or log b_T vs (T - T_S) for a variety of inorganic glasses.

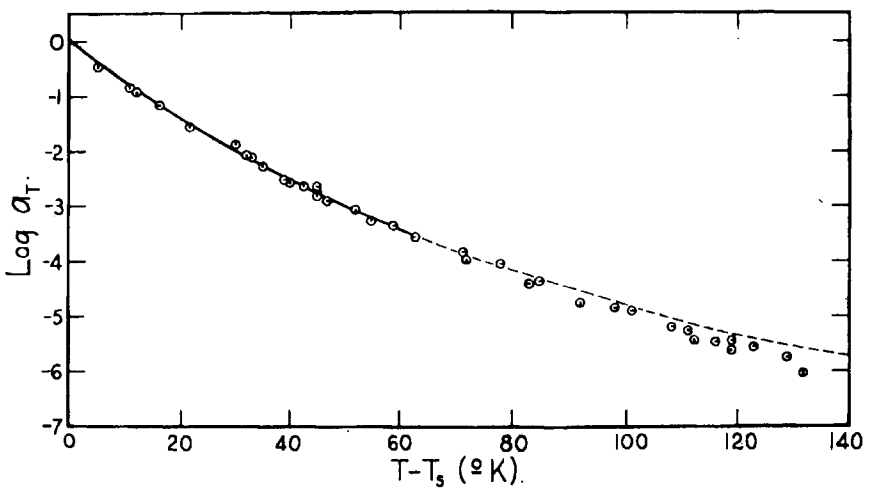

Figure 9.10: Log a_T plotted against (T – T$_s$) for some silicate and borate glasses. The lines are fits to equation (9.27). (After Williams et al., 1955).

There are several relaxation processes which occur in glasses and supercooled liquids. These are probed as responses to stresses, which can perturb the equilibrium states. The response to mechanical and thermal stresses has been fairly well fitted using WLF equation.

References:

Angell, C.A., 1988, J. Non-Cryst. Sol., **102**, 205.

Angell, C.A., and L.M. Torell, 1983, J. Chem. Phys., **72**, 937.

Angell, C. A., 1991, J. Non-Cryst. Sol., **131-133**, 13.

Angell, C.A., 1990, Chem. Rev., **90**, 523.

Angell, C.A., K.L. Ngai, G.B. McKenna, P.F. McMillan and S.W. Martin, 2000, J. Appl. Phys., **88**, 3113.

Arnold, W., and S. Hunklinger, 1975, Solid State Comm., **17**, 833.

Birge, N.O., and S.R. Nagel, 1985, Phys. Rev. Lett., **54**, 2674.

Boyer, J., 1966, J. Polym. Sci. C, **14**, 3.

Cohen, M.H., and G.S. Grest, 1979, Phys. Rev. B, **20**, 1077.

Cole, K.S., R.H. Cole, 1941, J. Chem. Phys., **9**, 341.

Davidson, D.W., and R.H. Cole, 1958, J. Chem. Phys., **19**, 1484.

Dhinojwala, A., G. Wong and J. Torkelson, 1992, Macromolecules, **25**, 7395.

Dixon, P.K., L. Wu, S.R. Nagel, B.D. Williams and J.P. Carini, 1990, Phys. Rev. Lett., **65**, 1108.

Goldstein, M., 1969, J. Chem. Phys., **51**, 3728.

Havriliak, S., and S. Negami, 1966, J. Polym. Sci. C, **14**, 99.

Hodge, I.M., 1983, Macromolecules, **16**, 898.

Hodge, I.M., 1991, J. Non-Cryst. Sol., **131-133**, 435.

Hodge, I.M., 1987, J. Am. Ceram. Soc., **20**, 2897.

Hodge, I.M., 1994, J. Non-Cryst. Sol., **169**, 211.

Johari, G.P., and M. Goldstein, 1971, J. Chem. Phys., **55**, 4245.

Kohlraush, R., 1847, Pogg. Ann. Phys., **12**, 393.

Mezei, F., W. Knaak and B. Farago, 1987, Phys. Rev. Lett., **58**, 571.

Moynihan, C.T., P.B. Macedo, C.J. Montrose, P.K. Gupta, M.A. DeBolt, J.F. Dill, B.E. Dom, P.W. Drake, A.J. Easteal, P.B. Elterman, R.P. Moeller, H. Sasabe and J.A. Wilder, 1976, Ann. N.Y. Acad. Sci., **279**, 15.

Ngai, K.L., 1979, Comments Solid State Phys., **9**, 127.

Ngai, K.L., A.K. Rajagopal, C.Y. Huang, 1984, J.Appl. Phys., **55**, 1714.

Narayanaswamy, O.S., 1971, J. Am. Ceram. Soc., **54**, 491.

Nieuwenhuizen, Th.M., 2000, J. Phys. Cond. Matter, **12**, 6543.

Rault, J., 2000, J. Non-Cryst. Sol., **271**, 177.

Scherer, G.W., 1984, J. Am. Ceram. Soc., **67**, 504.

Tool, A.Q., and C.G. Eichlin, 1931, J. Am. Ceram. Soc., **14**, 276.

Tool, A.Q., 1946, J. Am. Ceram. Soc., **29**, 240.

Williams, G., and D.C. Watts, 1970, Trans. Faraday Soc., **66**, 80.

Williams, G., D.C. Watts, S.B. Dev and A.M. North, 1971, Trans. Faraday Soc., **67**,1323.

Williams, M.L., R.F. Landel and D.J. Ferry, 1955, J. Am. Chem. Soc., **77**, 3701.

Science is a way of thinking, but it can only advance on the basis of a technique.
- Magnus Pyke.

CHAPTER 10

ELASTIC PROPERTIES AND PRESSURE EFFECTS

Elastic constants

In chapter 2 it was stated that glasses are isotropic solids. The isotropic behaviour is most evident in their elastic properties which are generally studied using macroscopic samples. We shall go through some definitions very briefly. When a small uniaxial stress is applied on a cubic piece of glass (Figure 10.01(a)) it deforms and this deformation almost instantaneously disappears when the stress is removed. The force applied can be a shearing force (parallel to one of the surfaces of, the cube, as in Figure 10.01 (b). Shear deformation also similarly disappears once the stress is removed. This behaviour of the glass constitutes its elastic

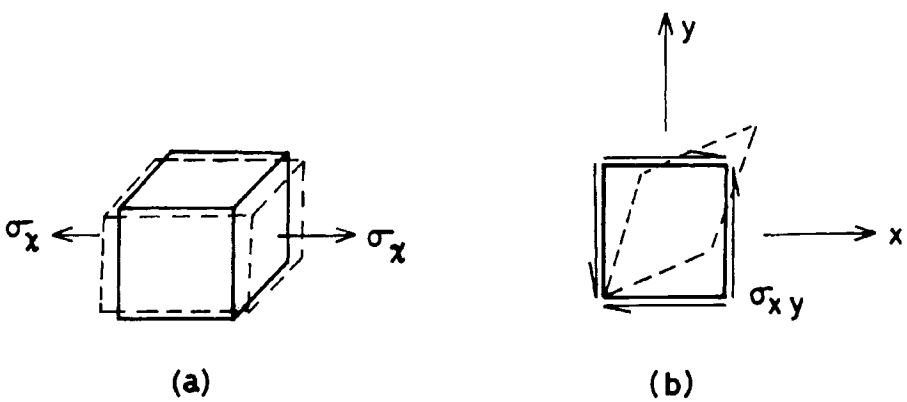

Figure 10.01: State of stress of a cubic glass body under (a) uniaxial stress,(b)pure shear.

response. Glasses in which there is no such quick and complete recovery of the shape after the stress is removed, reveal a permanent shape change known as plastic deformation. In such a case there is a stress induced flow in the glass as it happens in the region between annealing and softening temperatures. The applied stress generally decreases in magnitude as a

function of time and part of the stress is absorbed in causing a permanent deformation of the material. If the applied stress is a shear stress, it reduces to zero with time in liquids. This is the reason for which liquids find their own levels in containers - the stress is caused by the liquid's own weight.

Stress is defined as force per unit area. The elastic response of a solid consists of deformation which occurs in all the directions. Since force has three components in three (chosen) x, y and z directions and since the deformation also occurs in all three directions, stress, σ, is a tensor of the second rank having 9 components described by a (3 x 3) matrix $\{\sigma_{ij}\}_{i,\ j=1\ -\ 3}$. Alternately it may be easier to visualize why σ is a tensor of second rank if one recalls that area itself can be described by a vector perpendicular to the surface which has three components.

Deformation is measured by a quantity known as strain (strain is a relative extension or contraction of dimension). Strain is similarly a tensor of the second rank having nine components (3x3 matrix). The relation between stress and strain in the elastic regime is given by the classical Hooke's law. It is therefore obvious that the Hooke's proportionality constant, known as the elastic modulus, is a tensor of 4^{th} rank and is represented by a (9 x 9) matrix. Before further discussion we note the following. The stress tensor consists of 9 elements of which stability conditions require $\sigma_{xy}=\sigma_{yx}$, $\sigma_{xz}=\sigma_{zx}$ and $\sigma_{yz}=\sigma_{zy}$. Therefore the number of independent stress components in the symmetric stress matrix are only six. Similarly there are only six independent strain components. Therefore there can only be six stress and six strain components for an elastic body which has unequal elastic responses in *x, y* and *z* directions as in a completely anisotropic solid. The representation of elastic properties become simple by following the well known Einstein convention. The subscript *xx*, *yy*, *zz*, *yz*, *zx* and *xy* are respectively represented by 1, 2, 3, 4, 5 and 6. Therefore Hooke's law may now be written in a generalized form as,

$$\sigma_i = c_{ij} e_j \tag{10.01}$$

where c_{ij} is the elastic stiffness coefficient (moduli) and the indices i and j run from 1 to 6. The corresponding compliance (susceptance) relation is given by

$$e_i = s_{ij} \sigma_j \tag{10.02}$$

where s_{ij} are compliance coefficients and run from 1 to 6. It must be remembered that elastic stiffness coefficient c_{ij} and the compliance coefficient s_{ij} are tensors of the 4th rank represented by their compressed coefficient ij where both i and j themselves are the indices 11, 22 .. etc., as described above.

Thus one would expect from a (6x6) matrix of the elastic stiffness coefficients (c_{ij}) or compliance coefficients (s_{ij}) that there are 36 elastic constants*. By the application of thermodynamic equilibrium criteria, c_{ij} (or s_{ij}) matrix can be shown to be symmetrical ($c_{ij} = c_{ji}$ and $s_{ij}=s_{ji}$). Therefore there can be only 21 independent elastic constants for a completely anisotropic solid. These are known as first order elastic constants. For a crystalline material, periodicity brings in elements of symmetry. Therefore symmetry operation on a given crystal must be consistent with the representation of the elastic quantities. Thus for example in a cubic crystal the existence of $3C_4$ and $4C_3$ axes makes several of the elastic constants equal to each other or zero (zero when under symmetry operation c_{ij} becomes $-c_{ji}$). As a result, cubic crystal has only three independent elastic constants ($c_{11}= c_{22}=c_{33}$, $c_{44}= c_{55}= c_{66}$ and $c_{12}=c_{13}= c_{21}=c_{23}=c_{31}=c_{32}$). Cubic symmetry is the highest that can be attained in a crystalline solid but a glass is even more symmetrical in the sense that it is completely isotropic. Therefore the independent elastic constants reduce further to only two, because $c_{44}=(c_{11}- c_{12})/2$.

Conventionally elastic properties of solids are described using moduli called Young's modulus, E, shear modulus, G, bulk modulus, K and the Poisson's ratio, ν (due to the fact that mechanical properties were studied more extensively by engineers).Young's modulus is defined by the relation

$$\sigma_l = Ee_l \tag{10.03}$$

Thus E is the ratio of longitudinal stress, σ_l , to the longitudinal strain e_l. It may be noted that the convention is to represent tensile stress as positive and compressive stress as negative. G is the shear or rigidity modulus which relates the shear stress ($\sigma_{ij,\, i\neq j}$) to the shear strain ($e_{ij,\, i\neq j}$) through the relation

$$\sigma_{ij} = Ge_{ij} \tag{10.04}$$

* It is a historical awkwardness of symbols that compliances are denoted by s and the stiffness by c, an exchange of first letters.

When a solid is subjected to a tensile stress, it extends in the direction of the stress but contracts in the perpendicular direction. This is quantified by the Poissson's ratio which is the ratio of transverse strain to the longitudinal strain. This can be understood with reference to the application of a uniaxial stress as shown in Figure 10.01 (a) where the elongation in x-direction is associated with a shrinkage in y and z directions. Thus ν is defined by the transverse, $-e_t$ (e_t has a negative sign) and the longitudinal strain, e_l, as,

$$\nu = -\frac{e_t}{e_l} \tag{10.05}$$

($e_t = e_y \equiv e_{22}$; $e_3 = e_z \equiv e_{33}$ and $e_l = e_x \equiv e_{11}$)

The three quantities, the Young's modulus E, shear modulus G and the Poisson's ratio ν are related to each other for the case of an isotropic body like glass such that there are only two independent moduli λ and μ known as Lame constants:

$$\lambda = \frac{E\nu}{(1+\nu)(1-2\nu)} \tag{10.06}$$

$$\mu \equiv G = \frac{E}{2(1+\nu)} \tag{10.07}$$

Another important elastic modulus is the bulk modulus defined (see below) as the ratio of the hydrostatic pressure to the cubical compression and is given by

$$K = \frac{E}{3(1-2\nu)} \tag{10.08}$$

The off diagonal elements of stress tensor, namely σ_{12}, σ_{13} and σ_{23} describe the shear stress components. When a glass body is stressed, it is possible to give appropriate rotation and choose the axes such that the shear components vanish. The stressed phase is now completely described by the principal planes, the perpendiculars to which are the three chosen axes, known as the principal axes. Therefore the only three non-zero

stresses in the principal axes system are σ_{11}, σ_{22} and σ_{33} which in the compressed index notation are σ_1, σ_2 and σ_3 respectively. On the other hand by a further rotation of the axes by 45° the normal stress can be rendered zero and this gives the maximum values of the shear stresses, τ_i, which are the principal shears. Indeed τ_1, τ_2 and τ_3 are related to σ_1, σ_2 and σ_3 as

$$\tau_1 = \frac{(\sigma_2 - \sigma_3)}{2}; \quad \tau_2 = \frac{(\sigma_3 - \sigma_1)}{2}; \quad \tau_3 = \frac{(\sigma_1 - \sigma_2)}{2} \tag{10.09}$$

where τ_1, τ_2 and τ_3 are the principal shears. Failure of a glass generally occurs when the principal tensile stress exceeds a certain critical value and occurs along a plane known as fracture plane perpendicular to the direction of the principal tensile stress. This stress, σ_{eff}, is given by,

$$\sigma_{eff} = \left[\frac{(\sigma_1 - \sigma_2)^2}{2} + \frac{(\sigma_2 - \sigma_3)^2}{2} + \frac{(\sigma_1 - \sigma_3)^2}{2} \right] \tag{10.11}$$

In many experimental situations stress applied to a glass body can be considered as triaxial. The longitudinal strain in such cases is given by the relation,

$$e_l = \frac{1}{E}[\sigma_1 - \nu(\sigma_2 + \sigma_3)] \tag{10.12}$$

For the case where $\sigma_1 = \sigma_2 = \sigma_3$ which is known as hydrostatic stress (the situation when pressure is applied on a glass embedded in a material of low elastic constants – glass piece in steatite or in AgCl in a high pressure cell or simply embedded in a liquid) – then there are no shear strains. The hydrostatic stress is simply the pressure, P and the volumetric strain is e_m so that bulk modulus is also defined as

$$K = -\frac{P}{e_m} \tag{10.13}$$

Compressibility, β is defined as $1/K$. The quantities E, G, K and ν are

related among themselves as,

$$E = \frac{9KG}{3K + G} \tag{10.14}$$

$$G = \frac{E}{2(1+\nu)} \tag{10.15}$$

$$K = \frac{E}{3(1-2\nu)} \tag{10.16}$$

$$\nu = \left(\frac{E}{2G}\right) - 1 \tag{10.17}$$

Measurement of elastic moduli

Measurement of the elastic moduli such as E is made using rods of either circular or rectangular cross section and (generally) three or four point bending methods. The manner of putting the load on the sample is shown in Figure 10.02.

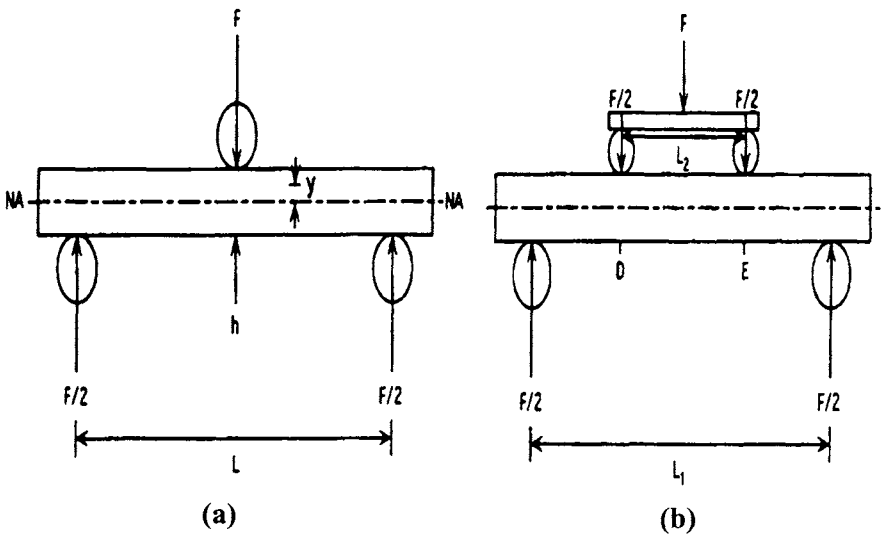

Figure 10.02 : (a) Scheme for three-point bending. (b) Scheme for four-point bending.

The experimental parameters are the load F applied on the sample at the central point of the distance between the edge supports and the physical dimensions of the solid. If the observed deflection at the point of loading is δ, then E is given by the relation,

$$E = \frac{FL^3}{48\, I\, \delta} \tag{10.18}$$

where I is the geometric moment of inertia equal to $\pi a^4/4$ for a cylindrical rod of radius a and $wh^3/12$ for a rod of rectangular cross-section where w is the width of the rectangular rod and n is its height ($w.h$ is the area of the cross section). In the case of four-point bend technique both the distances between the supporting edges and distance between the knife edges used for application of the load are important. E is given by,

$$E = \frac{F(L_1 - L_2)(2L_1^2 + 2L_1L_2^2 - L_2^2)}{96\, I\, \delta} \tag{10.19}$$

where L_1 and L_2 are the distances between the supports and load applying points respectively (Figure 10.02). The shear modulus, G is calculated by applying a twist at the other end of a rod whose one end is fixed rigidly. If the twist angle is θ for an applied torque, T, then

$$G = \frac{2TL}{\pi\theta\, a^4} \tag{10.20}$$

where L is the length of the rod between the rigid support and point at which the twist is measured. a is the radius. Direct measurement of bulk modulus is somewhat complicated and involves high pressure instrumentation. Liquid medium such as pentane, iso-pentane and even Hg are used to generate hydrostatic pressure. The volume decrease is measured by mercury displacement in an attached capillary. Obtaining large relative decrease in volume can affect the measurements because of the irreversible densification of several glasses, which do not permit repeat measurements on the same sample. The quantities necessary for the calculation of K are the change in volume, ΔV, and the change in pressure, ΔP. The volumetric strain is $\Delta V/V$ which gives e_m.

The most accurate method of measuring elastic constants is based on the use of ultrasonic sound velocity measurements. This is a dynamical

method and therefore enables measurements of attenuation and hence relaxation related parameters. Samples of small sizes, sometimes less than a cm in thickness in the form of a plate or disc is sufficient to measure the sound velocities (Figure 10.03).

Measurement consists of using quartz transducers for the generation of mechanical waves. Longitudinal and transverse waves are generated by using respectively X cut and Y cut transducers. (X cut is with faces perpendicular to X-axis and Y cut is with faces perpendicular to

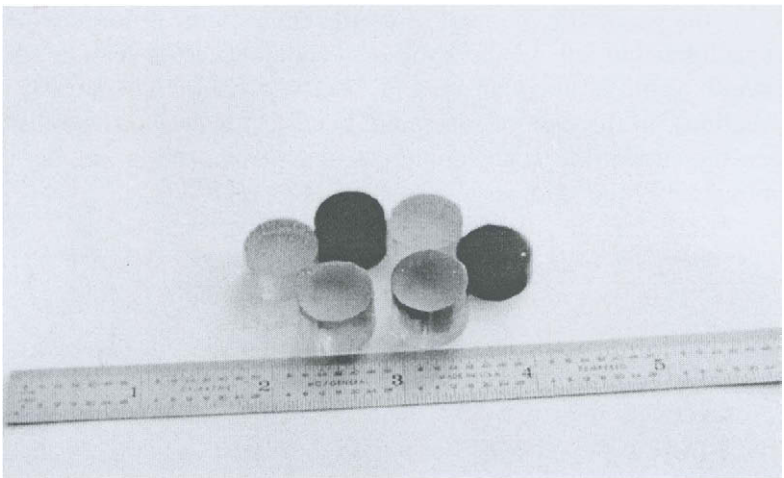

Figure 10.03: Photograph of the glass samples used in ultrasonic velocity measurements.

Y- axis; Y-axis is 90° rotated with respect to X-axis). The faces of the transducers are coated with gold (an open annular ring breaks the continuity of the gold coating on one side). The transducer used in the MHz range work by electrostriction and the vibrations generated are due to thickness modes. Therefore the transducers have to be very thin slices of quartz much less than a mm and are delicate. The sample preparation consists of polishing the surfaces to mirror finish and for the best results, to have the two surfaces highly parallel. Transducers are attached to one side of the sample and usually salol (phenyl silicilate) is used to fix the transducer (silicone grease can also be used). The experimental arrangement is shown in Figure 10.04.

The vibrational modes of the transducer are excited by an oscillator. The same transducer works both as the generator of mechanical waves and as the receiver of the reflected pulses in the so-called pulse

overlap (superposition) technique. Mechanical disturbance travels through the glass sample and is reflected back from its other surface. This happens several times with decreasing intensity because the sound waves get attenuated during its propagation in the glass sample. A part of the intensity is also lost due to transmission to surrounding gas medium generally air. The reflectivity coefficient depends on the differences in acoustic resistances of the two mediums in contact. At the glass-air interface (in most glasses), the reflectivity is reasonably high. One observes on the oscilloscope (which is triggered by same signal which switches on the field across the transducer), a train of echoes

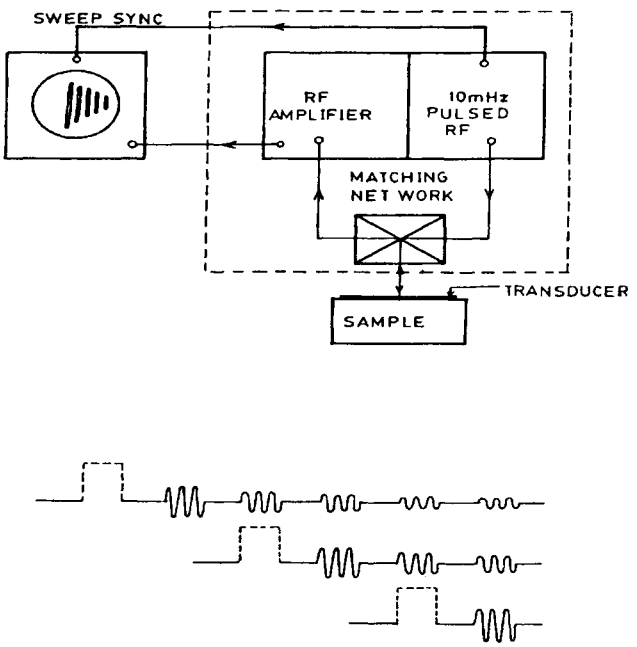

Figure 10.04: Schematic showing the ultrasonic pulse superposition set up (top) and the superposition of echoes (bottom).

corresponding to successive reflections from the free surface of the glass sample. The velocity of sound is given by the thickness divided by half the time between two echoes. There are several neat methods such as pulse overlap, phase matching etc. which will give very accurate sound velocities. The amplitude of the successive echoes decrease and the envelope of the echoes can be used to obtain the attenuation coefficient for sound propagation. In pulse echo experiment the pulse rate is so adjusted that a number of echoes may be seen between successive pulses. Poor

parallelism between surfaces result in distortion of successive echoes. The transverse velocities are generally half or less than half of the longitudinal velocities. The longitudinal and shear moduli are given by,

$$L = \rho \, v_L^2 \tag{10.21}$$

and

$$G = \rho \, v_T^2 \tag{10.22}$$

where v_L and v_T are the longitudinal and transverse velocities of sound and ρ is the macroscopic density of material. Poisson's ratio, ν, is given by

$$\nu = \frac{L - 2G}{2(L - G)} \tag{10.23}$$

Ultrasonic sound velocity measurements provide an easy method of determination of the elastic properties as a function of temperature by using a suitable variable temperature cell.

Mechanical relaxation experiments reveal that relaxation of shear moduli are similar to those of electrical moduli (chapter 7). In general mechanical relaxation spectra (G'' or E'') exhibit a higher value of FWHM compared to M'' (electrical relaxation spectra). The mechanical relaxation data can also be collapsed on to master plots, which suggests that they obey time temperature superposition principle. There is therefore a parallel theoretical basis for the phenomenon.

Ultrasonic and Brillouin scattering experiments are also used to evaluate elastic properties of glass using the following relations:

$$C_{11} = \lambda = \rho \, v_L^2 \tag{10.24}$$

$$C_{44} = \mu = \rho \, v_T^2 \tag{10.25}$$

$$Y = C_{44} \frac{(3C_{11} - 4C_{44})}{(C_{11} - C_{44})} \tag{10.26}$$

$$K = C_{11} - \left(\frac{4}{3}\right) C_{44} \tag{10.27}$$

Where μ, Y and K are the shear, Young's and Bulk moduli respectively. From Brillouin spectra one determines the velocity of the acoustic waves using the relations:

$$v = \frac{\lambda f}{2n\sin(\theta/2)} \tag{10.28}$$

where λ is the wavelength of incident light, n is the refractive index of the glass and θ is the scattering angle.

Structure of glasses and elastic constants

Elastic moduli are particularly helpful in correlating structural changes in glasses which are expected to occur as a function of composition. For example modification by alkali brings about a degradation of the structure which should generally decrease the shear modulus and it was observed to be so in the case of sodium silicate glasses. When modification occurs by Li_2O the tendency of Li^+ to coordinate to 4 oxygens almost simulates covalent cross linking which therefore may not decrease the shear modulus. The behaviour of PbO in silicates generally shows up uniquely because of its tendency to coordinate to 4 oxygens producing weak bonds. Sreeram et al. (1991) found a correlation between cross linking and Young's modulus in the complex Ge-Sb-As-Se-Te chalcogenide glasses. A decrease in Poisson's ratio with increasing average coordination number, m was also noted. Damodaran et al. (1989a) investigated a number of phosphomolybdate and phosphotungstate glasses (Damodaran et al., 1988) and also glasses with mixed alkali combinations (Damodaran et al., 1989b). A good correlation was found to exist between ring reformation in mixed alkali system and a variation in inter alkali ratios. Compressibility in general decreases with increase in temperature and pressure. There is the well known case of the anomalous behaviour of fused silica where at very low temperatures (up to 60 K) compressibility increases with temperature, thereby exhibiting an anomalous compressibility peak as shown in Figure 10.05. A similar anomalous behaviour is exhibited as a function of pressure and is shown in Figure 10.06; compressibility maxima is seen as a function of pressure around 30 kbar.

Although the origin of low temperature anomaly is unclear, the low pressure anomaly has been attributed to the presence of two different populations of Si-O-Si bond angles. The Si-O-Si bond angle distribution is

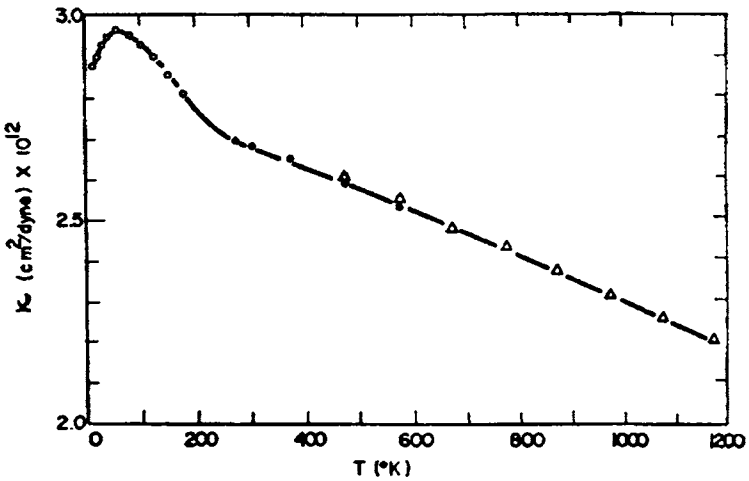

Figure 10.05: Temperature dependence of the compressibility, κ, of vitreous silica at zero pressure (After Vukcevich, 1972)

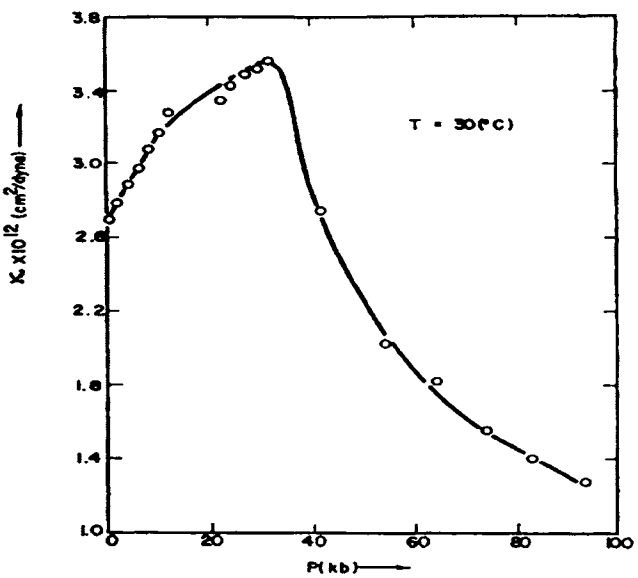

Figure 10.06: Room temperature compressibility, κ, of vitreous silica as a function of pressure. (κ is same as β, defined in the text) (After Vukcevich, 1972)

very broad and a peak is seen around 144°. A bimodal distribution of bond angles consisting of two peaks at 138° and 145° seems to provide a good agreement with both compressibility data and with the accurate bond angle distribution obtained by Mozzi and Warren (1969).

Elastic constants of solids can be related to the fundamental interaction energy terms. In fact it can be shown easily that the bulk modulus, K scales as the energy density, U/r^3 for an ionic material interacting through Born-Mayer potential (see later in this section). Thus the molar volume which increases with the presence of larger ions in glasses can be expected to cause a decrease in Young's modulus.

Theoretical estimates of the Young's modulus were made by Makeshima and Mackenzie (1973) using the formulae

$$E = 2V_t \sum_i g_i X_i \tag{10.29}$$

where

$$V_t = \frac{\rho}{M} \sum_i V_i X_i \tag{10.30}$$

In the above expression, g_i is the energy contribution of component oxide per unit volume, M is the effective molecular weight, ρ is density, X_i is mole fraction of component i and V_i is a packing factor of the component oxide A_mO_n, given by

$$V_i = N(mV_A + nV_O) \tag{10.31}$$

where V_A and V_O are the volume of the spherical A and O ions. It was found that the estimated values of Young's modulus were in excellent agreement with experiments. Model-based estimation of elastic constants require knowledge of individual force constants for the interacting pairs and also of the composition dependent variation of the bond angle distribution in covalently bonded glasses which are generally difficult to obtain. A semiempirical relation is found between packing density, V_t, dissociation energy per unit volume(D) and bulk modulus.

$$K = 2.4V_t^2 D \tag{10.32}$$

The relation is found to be valid in silicate and borate glass systems (Bhatti and Singh, 1988). In yet another approach, Yamane and Sakano (1974) have calculated Young's moduli from the composition, molar volume and melting point of the constituents and found good agreement with experimental values in network glasses like SiO_2, GeO_2 and P_2O_5.

However it should be recognized that these empirical relations do not give significant insight into the structural details of the glass, especially in complex glass forming systems. For this, a more detailed analysis of elastic properties in the light of the chemistry of the system is required. One of the early interesting observations of structure-elastic property relations is the polymerisation-depolymerisation process in alkali borate glasses (Bartnev, 1970). Sound velocity increases with increasing concentration of alkali oxide till 33 mole% due to the conversion of $[BO_{3/2}]$ units into $[BO_{4/2}]^-$ units while $[BO_{3/2}]$ gives rise to two dimensional network, $[BO_{4/2}]^-$ gives rise to a three dimensional network. With further addition of alkali oxide, non-bridging oxygens are created in the glass structure, dimensionality of the network decreases and sound velocity decreases. Similar behaviour has also been observed in Na_2O-GeO_2 (Kurkjian and Krause, 1966) and PbO-GeO_2 (Moynihan, 1972) glasses, where the coordination of Ge changes from 4 to 6 with increasing concentration of Na_2O or PbO.

Young's modulus of a large number of silicate glasses containing a variety of modifier oxides have been measured by Lowenstein (1961). It has been observed that the effect of a particular cation on the modulus depends on the structural role (whether it takes network forming or interstitial positions) and the nature of the cation-oxygen bond. In the case of cations taking only interstitial positions, a proportionality has been observed between the logarithm of cation field strength and Young's modulus. For cations which take network forming as well as interstitial positions, this relation seems to be not valid. A plot of Young's modulus vs electronegativity of the cation showed a maximum corresponding to the ionicity of cation-oxygen bond of 60%.

The relation between bulk modulus and volume has been widely investigated in both crystalline and glassy systems (Anderson and Soga, 1967; Osaka et al., 1985). From the Born-Meyer potential,

$$U = -\frac{Az_1z_2e^2}{r} + \frac{B}{r^n} \tag{10.33}$$

bulk modulus can be obtained as (Born and Huang, 1954)

$$K = Az_1z_2e^2(n-1)CV^{-\frac{4}{3}} \equiv \frac{U}{V} \tag{10.34}$$

where C is a structural constant. Generally in alkali halides and many

diatomic compounds (like sulphides, selenides) including oxides, the relation

$$K = aV^{-m} \tag{10.35}$$

(where a is now a constant as seen from equation (10.35)) is satisfied with $m \approx 1$. Interestingly, many covalent compounds also satisfy the relation with $m = 4/3$, though the potential is typical of ionic systems. Bulk modulus volume relationships in a variety of glass systems have been investigated by Soga (1981). The key factors affecting the modulus are, change in coulombic interaction of modifier cations, change in packing conditions or coordination number of network forming cations and change in excess volume in the glassy state. Variation in bulk modulus due to different alkali and alkaline earth ions in silicates follow the equation (10.34) with $m = 4/3$ as suggested by Born potential. Bulk modulus-volume relation shows $m = 4$ where packing conditions of network formers are involved. But in the case of mixed alkali silicate glasses (Matusita et al., 1974) log(K)-log(V) plots are not linear though volume changes with composition in a linear fashion. However, this correlation is not enough for a microscopic interpretation of the composition dependence of the bulk modulus.

Bridge et al. (1983) have interpreted the composition dependence of bulk modulus in a variety of glasses (SiO_2, GeO_2, As_2S_3, P_2O_5, B_2O_3) based on structure, dimensionality and interatomic force constants. Since glasses are isotropic, the response for isotropic compression of a three dimensional structure should mainly come from bond compression. In this bond compression model, bulk modulus, K_{bc} ,may be calculated by taking only the first order stretching force constants and it may be given as

$$K_{bc} = \frac{n_b r^2 f}{9} \tag{10.36}$$

where n_b is the number of bonds per unit volume. The ratio of K_{bc} to the measured bulk modulus gives a measure of the extent of bond-bending involved during compression. Bulk modulus and Poisson's ratio have also been correlated with atomic ring sizes and network connectivity in the system. With the interatomic force constants remaining constant, bulk modulus increases with reduction in ring size, since this would cause increase of bond density. Large rings will be more easily deformable

through bond bending. K is related to the bending force constants and average ring diameter by a power law of the form

$$K = (\text{constant}).f_b l^{-n} \tag{10.37}$$

where l is the average ring diameter and $n \approx 4$ and f_b the bending force constant. On this basis, Bridge et al. have interpreted the composition dependence of elastic properties in binary Co_3O_4-P_2O_5 and MoO_3-P_2O_5 glasses (Patel and Bridge, 1985; Higazy and Bridge, 1985; Higazy and Bridge, 1986). Elastic moduli in MoO_3-P_2O_5 show large discontinuities at 53 mol% and 63 mol% of MoO_3.

Elastic constants depend on pressure and temperature because of the anharmonicity of the interatomic potentials. From the dependence of bulk and shear moduli on hydrostatic and uniaxial pressure, third order elastic constants and Grüneisen parameters may be determined. Grüneisen parameter shows the effect of changing volume, V, on the phonon mode frequencies, ω.

$$\Gamma = -\frac{d\ln\omega}{d\ln V} \tag{10.38}$$

In the long wavelength limit, the longitudinal and shear mode gammas in isotropic systems may be obtained from the pressure derivatives as

$$\Gamma_l = \left(\frac{K}{2}\right)\left(\frac{d\ln(c_{11})}{dP}\right)_T - \frac{1}{6} \tag{10.39}$$

and

$$\Gamma_s = \frac{K}{2}\left(\frac{d\ln c_{12}}{dP}\right)_T - \frac{1}{6} \tag{10.40}$$

The mean Grüneisen parameter, Γ_m, is given by

$$\Gamma_m = \frac{\Gamma_l + 2\Gamma_s}{3} \tag{10.41}$$

Elastically normal glasses show positive pressure coefficient and negative

temperature coefficient of sound velocities and moduli. They exhibit negative third order elastic constants and positive Grüneisen parameters. Positive Grüneisen parameters imply stiffening (increase in frequency) of phonon modes with decreasing volume. Glasses like SiO_2, GeO_2 and BeF_2 have negative values for Grüneisen parameter which implies softening of modes with compression.

Effect of pressure on the bulk modulus of vitreous As_2S_3 has been studied by Girlich et al. (1979). It has been concluded that the main contribution towards the pressure dependence comes from the inter-layer compression and the contribution from intra-layer covalent bonds may be ignored. The pressure dependence of bulk modulus has been fitted to a potential having Lennard-Jones and Born-Mayer terms. Further, observed behaviour of the bulk modulus also suggests a pressure induced transition in the region $\approx$ 450 kbar. Pressure and temperature dependence of elastic properties have been studied in Ag-doped As_2S_3 and As_2Se_3 glasses (Kaga et al., 1978). The sound velocities increase markedly with small additions of silver. The pressure and temperature derivatives of sound velocities decrease with the addition of silver due to decrease in the anharmonicity of vibrations. Pressure dependence of elastic properties has been investigated in V_2O_5-P_2O_5 glasses with the addition of CuO and Na_2O by Drake et al (1983) and in TeO_2 glass by Lambson et al (1984). The open network structure of V_2O_5-P_2O_5 glasses causes a negative pressure derivative of shear moduli. The curious composition dependence of bulk modulus in these glasses has been explained by attributing a dual structural role for copper. At low concentrations (<5 mol%) copper enters the network substitutionally and in this region bulk modulus decreases. Between 5 and 10 mol%, Cu enters interstitial positions without expanding the network and bulk modulus increases in this region. At higher concentrations, Cu takes interstitial positions causing expansion of the network and hence bulk modulus decreases. In TeO_2 glass, pressure dependence of moduli suggests that bond bending motions of bridging atoms do not have any significant role to play and the positive Grüneisen parameter suggests stiffening of acoustic modes on compression.

Poisson's ratio depends on the dimensionality of the structure and cross link density. A three dimensional network structure has lower ν value than that of a two dimensional structure, which, in turn, is less than that of a one-dimensional structure since the number of bonds resisting a transverse deformation decreases in that order. However, in glasses which are isotropic, the definition of dimensionality becomes less rigorous. Typical three dimensional glasses like SiO_2 or GeO_2 have $\nu \approx 0.15$

whereas As_2S_3, B_2O_3, P_2O_5 glasses have $\nu \approx 0.3$ indicating a decrease in dimensionality. Addition of modifier oxides results in increase of ν due to creation of NBO and hence reduction in dimensionality.

Debye temperature are obtained from elastic data using the mean sound velocity and mean atomic volume in the relation

$$\Theta_D = \frac{\hbar}{k}\left[\frac{3N}{4\pi V}\right]^{1/3} v_m \tag{10.42}$$

$\hbar / k$ is the ratio of the Planck's constant to the Boltzmann constant, N is the Avogadro number, V is the mean atomic volume (molecular weight divided by density and the number of atoms per molecule) and v_m is the mean sound velocity, defined by the relation

$$\frac{3}{v_m^3} = \frac{1}{v_l^3} + \frac{2}{v_T^3} \tag{10.43}$$

Where v_l and v_T are the longitudinal and transverse velocities. A comparison of the elastic Debye temperature and calorimetric Debye temperature gives a measure of the contribution of the acoustic modes to heat capacity. Since no optic modes are excited at low temperatures, the elastic and calorimetric Debye temperatures are expected to be comparable which in the case of vitreous silica is not obeyed (see chapter 12).

Microhardness

A closely related mechanical property which has been used extensively in glass literature is the microhardness. 'Micro' in microhardness only indicates that the hardness measurements have been made on a micron scale. Microhardness actually measures only the scratch resistance of the material and thus a scale of microhardness is a scale of the scratch resistances – harder material can scratch the surface of the softer material. One of the widely used scales is Mohs scale of hardness calibrated with the hardness of the hardest material, namely diamond, marked with a value of 10 and with the hardness of the softest material, namely talc, marked with a value of 1. On this scale most oxide glasses register microhardnesses between 5 and 7. In scientific investigations two other scales are used, namely Knoop's hardness number (KHN) and

Vicker's hardness number (VHN). Hardness on Rockwell and Brinell scales are also reported for metals and alloys. In both KHN and VHN measurements, the approach is to make an indentation on the surface of the sample using a diamond micro-indenter. In the Vicker's method the indenter has the shape of a square pyramid, while in the Knoop's method it has the shape of an elongated pyramid. The indentation is generally of the order of few microns and a load of 5 to 1000 gm are used (in order to determine fracture toughness, it becomes necessary to use higher values of load (due to the necessity of initiating cracks)), VHN is given by,

$$\text{VHN} = \frac{18.19F}{D^2} \tag{10.44}$$

and KHN is given by,

$$\text{KHN} = \frac{139.60F}{L^2} \tag{10.45}$$

where D is the diameter of the indentation in Vicker's method and L is the length of the longer diagonal in Knoop's method. The process of indentation involves both compression and shear. If the load is such that these deformations are within the elastic limit, the shape is recovered after the removal of the load. Beyond the elastic limit there is both a permanent densification of the glass under the load of the indenter due to the hydrostatic stress component, and a plastic deformation caused by the shear component of excess stress. At even higher loads crack initiation takes place and measurements of the crack length can yield valuable information on fracture toughness. In the literature, variation of microhardnesses have been related to structural variations in glasses. For example, VHN of B_2O_3 increases as the modification increases and has been associated with formation of tetrahedral boron. Modified SiO_2 registers a decrease in microhardness (Bansal and Doremus, 1986) with increase in alkali content. In ionic glasses increased cohesive energy is associated with increased Vicker's hardness (Narasimham and Rao, 1978). It is easy to visualize why VHN reflects the structure because the indenter breaks the bonds in the structure.

Fracture of glasses

We noted in passing that when the tensile stress applied on a glass

body exceeds a critical limit, it breaks. Breaking represents mechanical failure. Failure is associated with creation of new surfaces. This may be contrasted with the behaviour of a metal piece subjected to similar stress. One generally observes, first the formation of a thinned down portion called 'neck' and the associated plastic deformation. Eventually at some point of stress it breaks apart indicating failure. This is indicated schematically in Figure 10.07 through the respective stress-strain behaviour. The modes of failure in materials like glass (Figure 10.07a) is known as brittle fracture while that in the metal as ductile failure (Figure 10.07b). There is generally no observable plastic deformation region in a glass. Although in micro-indentation experiments extremely small deformations are attributed to plastic flow. Plastic deformation in metals is

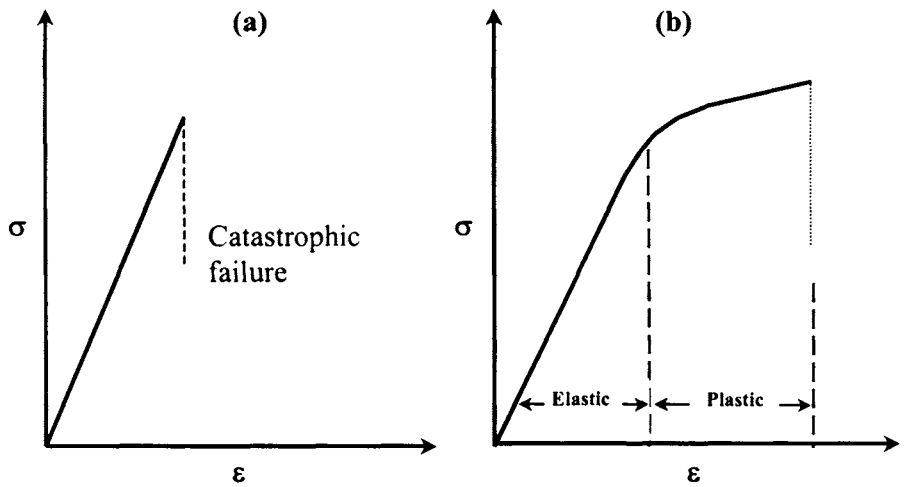

Figure 10.07: Schematic of (a) elastic and (b) plastic behaviour of solids.

attributed to the creation and movement of dislocations. Dislocations are linear defects which can move under applied stress without creating two new surfaces abruptly. Their movement involves only an activation barrier. A dislocation by its very definition is incompatible with a glass which is a disordered solid with no LRO. The stress required to bring about fracture and hence the failure is known as strength of the glass (having the same unit as stress, MPa). The strengths of glasses vary widely and the same material can exhibit very different values of strength depending on their physical conditions. This is because presence of flaws or defects which may be present on the glass surface. Flaws bring about wide variations in strengths since they act as stress intensifiers. Freshly drawn glass rods (alkali silicate composition) exhibit a strength of about

70-140 MPa, but when abraded their strength falls down to one fifth of this value. In wet conditions, this strength can go down by another factor of five. Freshly drawn glass fibers have a strength of about 0.7-2.1 GPa which may be compared with the strengths of best steels which fail at about 350 MPa. One can calculate the theoretical strength of a glass by considering that atoms at equilibrium distances are separated in order to create a new surface. When the atoms are pulled apart the energy required to separate them increases and passes through a maximum. Thus fracturing requires application of a stress equal to this maximum. If E is the Young's modulus and Δa is the separation needed to reach the maximum of the stress and a_0 is the distance over which the stress has to act (which is of atomic dimensions), then σ_m is given approximately by the equation

$$\sigma_m \approx \frac{E\,\Delta a}{a_0} \tag{10.46}$$

σ_m is associated with the creation of a new surface. Therefore the energy spent during the application of the stress must be equal to the energy of the surface created. Orowan (1934) showed that the theoretical strength of a perfectly brittle solid is given by

$$\sigma = \left[\frac{\gamma E}{a_0}\right]^{\frac{1}{2}} \tag{10.47}$$

where γ is the specific surface energy. With the substitution of the quantities in Orowan equation with reasonable values of the parameters (E=70 GPa, γ=3.5 J/m^2 and a_0 =0.2 nm), σ_m is found to be about 35 GPa which is about 50 % of the Young's modulus. But such high values are never exhibited by glasses. Therefore there must be other factors which operate which will make the effective stress involved in the creation of new surfaces much higher than the applied stress. Since flaws are known to be associated with easy fracture, flaws must be acting as stress intensifiers. Griffith (1921) showed that when there are flaws which have a certain critical length they propagate under the applied stress leading to a fracture. Therefore the fracture strength, σ_f, characterizing the brittle fracture is given by,

$$\sigma_f = \left[\frac{2\gamma E}{\pi c^*}\right]^{\frac{1}{2}} \tag{10.48}$$

where c^* is the critical length of the flaw. Griffith's equation (10.48) accounts for known observations in the failure of glass objects. Firstly the influence of wetness on σ_f. Since wetness is well known to decrease γ it brings down the value of critical failure stress. The other is the statistical nature of the values of fracture strengths, σ_f. This is clearly associated with the wide distribution in the sizes of flaws present on the surface. These are known as Griffith flaws and their influence far outweigh the influence of the glass compositions on σ_f. It is difficult to identify Griffith flaws which have very low depths. They are characterized using decoration techniques. Griffith's equation can be written alternatively as,

$$\sigma_f (\pi c^*)^{1/2} = (2\gamma E)^{1/2} \tag{10.49}$$

Compare this to $\sigma_m (a_0/2)^{1/2} = (2\gamma E)^{1/2}$. The quantity c^* is much greater than $a_0/2\pi$ which explains why the actual stress is highly intensified in the glass in the Griffith's analysis compared to the stress in an ideal flawless body. Thus $\sigma_f (\pi c^*)^{1/2}$ is known as the stress intensity factor K_C or the critical stress intensity factor. The crack propagation through a body is associated with moving away of two parts of the failed material. This has led to a consideration of three different modes of crack propagation in glass bodies. One of the modes for which investigations have been widely performed involves crack propagation direction being perpendicular to the direction of the applied stress. This is known as the first mode (I) and the corresponding failure stress is indicated by the critical stress intensity factor represented by K_{IC}.

It may be of interest to note here that the failure of glass exhibits a dependence on time. For example when a constant stress of the order of magnitude of K_{IC} is applied, the *time-to-failure* varies inversely as the applied stress. On the contrary if the applied stress is continuously increased such as to keep a constant strain rate, *stress-to-failure* varies directly as strain rate. These are manifestations of delayed failure which is due to the phenomenon of *fatigue*. Observations made under constant stress measures the *static fatigue* while the observations under constant strain rate conditions measure *dynamic fatigue*. The difference in

behaviour of the two types of fatigue can be understood when we consider the effect of stress on the flaws. Flaws grow under the application of stress. Since at higher stress value they grow faster, they also attain critical sizes faster and hence the time-to-failure decreases in the case of static fatigue. In the constant strain rate experiment, stress keeps increasing. Higher rates of increase of stress allows less and less time for the growth of flaws and therefore failure occurs at much higher value of the applied stress. Thus the growth rates of the sub-critical flaws are responsible for the observation of fatigue.

Hilling and Charles (1965) analysed sub-critical crack velocity, v under general conditions including the effect of chemical environment which can give rise to surface flaws. The velocity, v, of crack propagation is given by,

$$v = v_0 \exp\left[\frac{-\Delta E + \frac{\sigma \Delta V}{3} - \frac{V_m \gamma}{\rho}}{RT}\right] \tag{10.50}$$

where ΔE is the activation energy for the chemical reaction in the stress free conditions (only the chemical reaction or the corrosion is responsible for creation of flaws). ΔV is the activation volume, V_m is the molar volume and ρ is curvature of the crack tip, σ is the applied stress and γ is the surface energy. The problem of understanding stress corrosion cracking in glasses is not simple because it depends on the local chemistry in the glass in a complex manner. For example initiation of flaws through a reaction of acids and bases with the NBOs in silicate glass can be quite different depending on the composition. The topological disorder namely the ring statistics itself produces a variation in the sub-critical size of the flaws. Also the reactions of alkalies and acids at the crack tips are not similar.

Behaviour of glasses under high pressure

Because of the topological disorder in them, glasses exhibit very interesting response when subjected to pressure. Most glasses have lower density than parent crystalline materials. By adopting specific preparative conditions such as extremely slow rate of cooling or annealing the glass in a region close to its T_g, a glass can be made with density or specific volume close to its value in the crystalline state. Compressibility of such a glass can be determined reproducibly using low to moderate pressures

because in the elastic region the volume of the glass gets fully restored to the original value after removal of the pressure. But when the applied pressure is high some of the glasses like SiO_2 and B_2O_3 undergo permanent densification – permanent in the sense that when the pressure is released the density does not return to its original value at the same temperature. For example at a pressure of 10 GPa densities of SiO_2 can increase to the same value as that of α-quartz. Susman et al. (1990) achieved a 20 % increase in the density of fused silica at 16 GPa. Nevertheless several high pressure densified glasses recover their original densities slowly with time. The recovery of density in the case of B_2O_3 has been found to be fairly rapid. It is thought that irreversible densification is due to reorientations of polyhedral units in random network glasses, because of the possibility of rotation around single bonds in their structures. In modified glasses it is not improbable that bond switching can be induced by the applied pressure and bond reorganization can facilitate irreversible volume changes. But such mechanisms imply a change of topology of the structure and the glass recovered after high pressure is strictly structurally not the same – one of the polyamorphic phases induced by pressure. Most of the studies indicate however that when pressure densified glasses are reheated to their T_g, they recover their volumes.

In several chalcogenide and ionic salt based glasses, application of high pressure leads to crystallization. In chalcogenides crystallization, and onset of metallic conduction seems to coincide. Many germanium chalcogenides exhibit such behaviour (Gopal, 1992). The transition to the crystalline phase (with metallic conduction) can be gradual. Evidently in all such transitions a bond breaking and reorganization are involved and the fact that energy gap in the semi-conducting low pressure glass vanishes may itself trigger reorganization of the structure. The existence of structural defects such as charge defect pairs (C_3^+,C_1^-) (or equivalently (D^+,D^-) pairs) and their role in inducing crystallization reaction under pressure has also been discussed in the literature (Parthasarathy et al., 1984). Ionic glasses such as those in AgI-Ag_2MoO_4, AgI-Ag_2SeO_4 etc. systems also undergo crystallization when pressure of the order of a few GPa is applied. In all such glasses the mechanism of the crystallization is unclear but the recovered products are multiphasic and crystalline. In such glasses it appears that nuclei of the crystallised phases must have been present either prior to the application of the pressure or are formed at lower values of pressures. These nuclei grow when the pressure is increased resulting in complete crystallization. Since the crystalline phases

have lower free energies and also lower specific volumes the pressure favouring such a change is understandable from thermodynamic point of view (Le Chatelier's principle). But the actual mechanism of atomistic reorganization during conditions of decreasing available volume under pressure is not clear. Ionic glasses have been found to have higher specific volumes which approximately correspond to the rcp volumes of oxide ions or of the oxyanions. The density deficit in the rcp structures compared to crystalline close packing is, as noted earlier (chapter 2), quite high. Therefore it is tempting to attribute collapse of larger Bernal holes triggering a series of reorganizations leading to crystallization at some critical value of pressure. The pressure crystallization occurs in the manner of an irreversible transition.

In chapter 3, reference was made to variation of ionic conduction under pressure in simple ionic glasses and the initial increase of conductivity in such glasses are consistent with cluster-tissue texture of glasses. MRO (as in clusters), manifests in many phenomena like CRR, FSDP, Boson peaks etc. To these may be added the observation of small angle neutron scattering and small angle X-ray scattering peaks observed in several glasses such as those in silver iodide-silver borate systems (Swenson et al., 1997) etc. The pressure response of such systems, therefore, should be expected to reflect two regions, one corresponding to more compressible tissue and the other corresponding to the less compressible cluster.

In passing we may note that there is a converse behaviour exhibited by some tetrahedral crystalline solids (Sikka, 1991). This is the reversible pressure amorphisation. Examples are provided by crystalline SnI_4, SiO_2 and several others, all having tetrahedral structural units in the structure. Tetrahedral units do not fill space and the pressure is likely to force the extra volume out resulting in amorphous structure which reverts to the crystalline phase once the pressure is removed.

References:

Anderson, O. L., and N. Soga, 1967, J. Geophys. Res., **72**, 5754.

Angell, C. A., Chem. Rev., 1990, **90**, 523.

Bansal, N. P., and R. H. Doremus, 1986, Handbook of Glass Properties, (Academic Press, New York).

Bartnev, G. M., 1970, Structure and Mechanical Properties of Inorganic Glasses, (Wolters – Nordhoff, Groningen, The Netherlands).

Bhatti, S. S., and S. Singh, 1988, Acoustica, **65**, 247.

Born, M., and K. Huang, 1954, Dynamical Theory of Crystal Lattice, (Oxford Univ. Press, London).

Bridge, B., N. D. Patel and D. N. Waters, 1983, Phys. Stat. Solidi, **A77**, 655.

Damodaran, K.V., U.Selvaraj and K.J. Rao, 1988, Mater. Res. Bull., **23**, 1151.

Damodaran, K.V., and K.J. Rao,1989a, J. Mater. Sci., **24**, 2380.

Damodaran, K.V., and K.J. Rao,1989b, Phys. Chem. Glasses, **30**, 130.

Drake, C. F., B. W. James, H. Kheyrandish and B. Yates, 1983, J. Non-Cryst. Sol., **57**, 305.

Etienne, S., Y. Cavaille, J. Perez and G. P. Johari, 1985, Philos. Mag. B, **51**, L35.

Girlich, D., E. Litov and O. L. Anderson, 1979, Phys. Rev. B, **20**, 2529.

Gopal, E. S. R., 1992, in Proc. Of XIII AIRAPT Int. Conf. On High Pressure Tech., eds., A. K. Singh, (Oxford & IBH Publ. Co. Pvt. Lt., New Delhi) p. 298.

Griffith, A. A., 1921, Phil. Trans. Roy. Soc., **A221**, 163.

Higazy, A. A., and B. Bridge, 1985, J. Non-Cryst. Sol., **72**, 81.

Higazy, A. A., and B. Bridge, 1986, Phys. Chem. Glasses, **27**, 1.

Hilling, W. B., and R. J. Charles, 1965, in High Strength Materials, ed. V. F. Zackay, (J. Wiley, New York).

Kaga, H., S. Kashida and S. Umehara, 1978, J. Phys. Soc. Japan, **44**, 1208.

Kurkjian, K. L., and J. T. Krause, 1966, J. Am. Ceram. Soc., **49**, 134.

Lambson, E. P., G. A. Saunders, B. Bridge and R. A. El-Mallaway, 1984, J. Non-Cryst. Sol., **69**, 117.

Lowenstein, K. L., 1961, Phys. Chem. Glasses, **2**, 69.

Makishima, A., and J. D. Mackenzie, 1973, J. Noncryst. Solids, **12**, 35.

Matusita, K., S. Sakka, A. Osaka, N. Soga and M. Kunugi, 1974, J. Non-Cryst. Sol., **16**, 308.

Moynihan, C. T., 1972, J. Am. Ceram. Soc., **57**, 455.

Mozzi, R. L., and B. E. Warren, 1969, J. Appl. Crystallogr., **2**, 164.

Narasimham, P.S.L., and K.J. Rao, 1978, J. Non-Cryst. Sol., **27**, 225.

Orowan, E., 1934, Z. Krist., **A89**, 327.

Osaka, A., K. Takahasi and A. Ariyoshi, 1985, J. Noncryst. Solids, **70**, 243.

Parthasarathy, G., K. J. Rao and E. S. R. Gopal, 1984, Philos. Mag., **50**, 335.

Patel, N. D., and B. Bridge, 1985, J. Mat. Sci., **21**, 1187.

Sikka, S. K., 1992, in Proc. Of XIII AIRAPT Int. Conf. On High Pressure Tech., eds., A. K. Singh, (Oxford & IBH Publ. Co. Pvt. Lt., New Delhi) p. 254.

Soga, N., 1981, Bull. Inst. Chem. Res. Kyoto Univ., **59**, 147.

Sreeram, A. N., A. K. Varshneya and D. R. Swiler, 1991, J. Non-Cryst. Sol., **128**, 294.

Susman, S., K.J. Volin, R.C. Liebermann, G.D. Gwanmesia and Y. Wang, 1990, Phys. Chem. Glasses, **31**, 144.

Swenson, J., L. Börjesson, R. L. McGreevy and W. S. Howells, 1997, Phys. Rev. B, **55**, 236.

Vukcevich, M. R., 1972, J. Non-Cryst. Sol., **11**, 25.

Yamane, M., and T. Sakano, 1974, Glass. Tech., **15**, 134.

The quick harvest of applied science is the usable process, the medicine, the machine. The shy fruit of pure science is understanding.
- Lincoln Barnett.

CHAPTER 11

OPTICAL PROPERTIES

The most common applications of glasses are undoubtedly based on their optical properties. As we noted elsewhere in this book, use of glasses in making bulbs, sheets, bottles and a variety of chemical ware are all because of the transparency of oxide glasses in the visible region. Application of glasses for making optical instruments and lenses is based on properties like refractive index and its dispersion, which can be varied by varying chemical composition. One of the more important applications based on optical properties of glass today is in the field of information technology through the use of glass fibres. Although transparency is often associated with the visible region, several classes of glasses are highly transparent at other wavelengths of electromagnetic spectrum. In fact, this has led to the development of three important classes of glasses, namely, oxide, chalcogenide and halide glasses, which exhibit different windows of transparency. This is shown in Figure 11.01 as a plot transmission loss

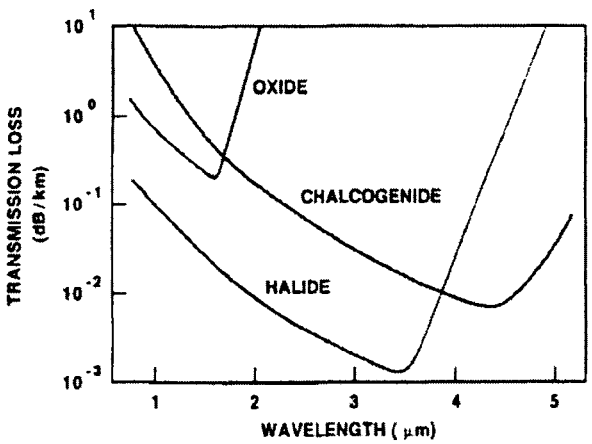

Figure 11.01: Regions of transparency for three general glass types (After Fleming, 1993).

(expressed as dB/km) versus wavelength (expressed in μm). The figure clearly shows that halide glasses (heavy metal fluoride glasses, which will

be discussed in chapter 14) exhibit much higher transparency than either oxide and chalcogenide glasses between 2.5 and 4.0 μm wavelength. Around 3.5 μm, halide fibres are very highly transparent and possess extraordinary potential for application in information technology. A few important materials exhibiting very high transparency are listed in Table 11.1 along with the wavelengths corresponding to minimum attenuation.

Table 11. 1: Predicted minimum absorption losses for a range of glasses and the wavelengths for maximum transmission (After, Lewis, 1989).

Material	Minimum loss (dB km^{-1})	Wavelength (μm)
As_2S_3	0.33	3.6
SiO_2	0.14	1.6
GeO_2	0.06	2.0
ZBLAN	0.013	2.5
BeF_2	0.005	2.1
$ZnCl_2$	0.0034	4.6

It is important to recognize at the outset that the optical properties of the glass have to remain time independent for their application. Although there are several relaxation processes associated with glasses, the sub-glassy relaxations have very little thermodynamic strength and well below the glass transition temperature, volume of the glass remains time independent which ensures that the refractive indices, which are functions of molar volumes, remain unaffected. In this chapter, some of the concepts related to the optical properties and to the formation of colours in glasses are presented. Coloured glasses have been important for both, artistic and technological applications.

Refraction, reflection and absorption of light

Light is electromagnetic wave propagation characterized by oscillating electric and magnetic fields in perpendicular directions, both of which are perpendicular to the direction of propagation of light. The speed of light propagation is 2.9979×10^8 ms^{-1} in vacuum. When light is incident on the surface of a glass, it is partly reflected and partly transmitted. The transmitted part undergoes refraction and it is characterized by the *refractive index* of the glass. The reflected part is quantified by the *reflectance*, R, at normal incidence and is a function of the refractive indices of both the medium (n_2) in which the light travels before it is

incident on the glass surface and the glass (n_1). Refractive index, n, is the ratio of the velocity of light in the medium to its velocity in vacuum. R is given by

$$R = \frac{(n_1 - n_2)^2}{(n_1 + n_2)^2} \tag{11.01}$$

Since the refractive index n_1 itself is a function of frequency, reflectance is also a function of the wavelength of radiation used. When one of the medium is vacuum or air (n_{vac} is 1.000 at 15°C and 760 mm pressure for the Na-D line - λ=589.3nm - and $\approx n_{air}$ which is 1.000275, under same conditions), reflectance can be written as $(n\text{-}1)^2/(n+1)^2$, where n is the refractive index of the medium.

The response of glass to the incident electromagnetic radiation of very high frequency is through coupling of electrons in the glass to the oscillating electric field. The refractive index is therefore related to the dielectric constant (ε) of the system (for the case of non-magnetic materials the response of the glass to the oscillating magnetic field is ignored). Dielectric constant itself is frequency dependent and as noted in chapters 5 and 6, is a complex quantity, which can be represented as

$$\varepsilon^*(\omega) = \varepsilon'(\omega) - i\varepsilon''(\omega) \tag{11.02}$$

From Maxwell's relations, it can be shown that at very high frequencies $\varepsilon^* = n^2$. Therefore, refractive index, n itself can be written as a complex quantity,

$$n^* = n' - i\kappa \tag{11.03}$$

For convenience (and to avoid confusion) we write n' as n. κ is known as the extinction coefficient and is responsible for attenuation of light in the same manner as ε'' is responsible for attenuation of electrical field causing dielectric loss.

The general expression for attenuation or the intrinsic loss of light intensity in a glass is given by,

$$L = A\exp\left(\frac{a}{\lambda}\right) + \frac{B}{\lambda^4} + C\exp\left(-\frac{c}{\lambda}\right) \tag{11.04}$$

where A, a, B, C and c are material constants. The first term represents loss due to electronic excitations and hence the UV absorption edge. The second term arises from Rayleigh scattering (chapter 4) while the third term represents multi-phonon processes arising in the infrared region. The variation of attenuation as a function of wavelength for a variety of glasses is shown in Figure 11.02. In fact, the amplitude of the electromagnetic

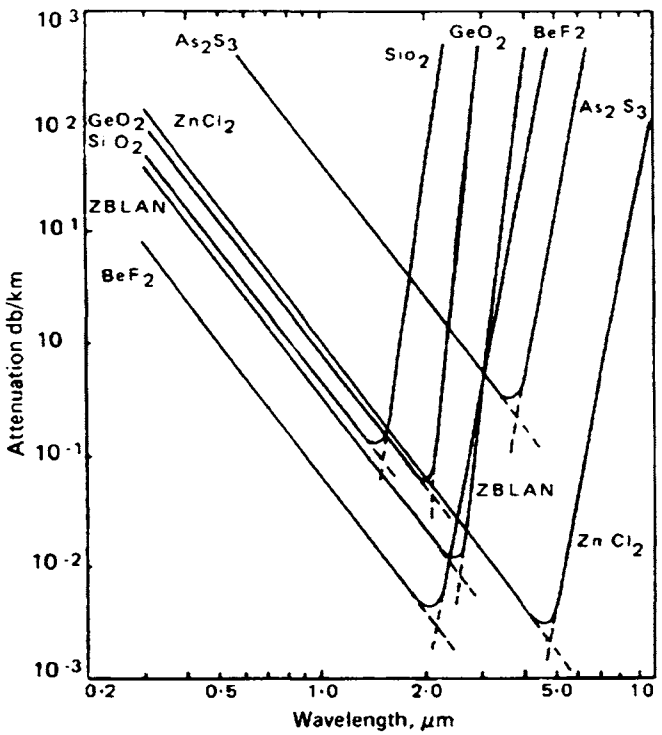

Figure 11.02: Absorption and scattering losses for a range of optical materials plotted on a log-log scale which gives straight lines for Rayleigh scattering but a slight curvature to the multiphonon edge (After France et al., 1986)

wave decreases by a factor, $\exp[-2\pi\kappa/n]$, for every λ. The decrease in intensity of the electromagnetic radiation passing through a glass medium is governed by Beer-Lambert's law,

$$I = I_0 \exp(-\in d) \tag{11.05}$$

where $\in$ is the absorption coefficient (extinction coefficient) and can be seen to be related to the real and imaginary parts of the refractive index as

$$\in = \frac{4\pi\kappa}{\lambda n} \tag{11.06}$$

where the distance term is taken as λ, which represents the wavelength of incident radiation in glass. Since $\lambda n = \lambda(\lambda_o/\lambda) = \lambda_o$,

$$\in = \frac{4\pi\kappa}{\lambda_0} \tag{11.07}$$

where λ_o is the wavelength of light in vacuum. When the glass is absorptive, the reflectance R at the vacuum-glass interface has to take into consideration the value of κ so that R can be written as

$$R = \frac{[(n-1)^2 + \kappa^2]}{[(n+1)^2 + \kappa^2]} \tag{11.08}$$

There is the extreme situation where the refractive index for the given frequency is dominated by κ so that R tends to unity as it happens in metals like in molten Ge. It may be noted that both amorphous and crystalline Ge have reflectances of ~38% at low frequencies, while it tends to 100% for molten Ge. This is attributed to the drastic changes in the local structure of Ge whereby the local coordination number changes from 4 in solid to 8 in the melt which is metallic.

Both dielectric constant and refractive index being complex quantities, the real and imaginary parts of them are related as follows: $\varepsilon^* = (n^*)^2 = (n^2 - \kappa^2) - 2in\kappa$ and $\varepsilon^* = \varepsilon' - i\varepsilon''$. Therefore,

$$\begin{aligned} \varepsilon' &= (n^2 - \kappa^2) \\ \varepsilon'' &= 2n\kappa \end{aligned} \tag{11.09}$$

It is useful to collect here a few more definitions normally used in the discussion of optical properties. One is the molar extinction coefficient $\in_M = \in/c$, where c is the concentration in moles/liter of the absorbing material which implies the assumption that the absorption of light is due to specific light absorbing species. Absorbance (A) and optical density (D) are the other two quantities. They are related as follows:

$$A = \ln(I_0 / I) = 2.303 \log(I_0 / I) = 2.303D \tag{11.10}$$

(absorbance is dimensionless but absorption coefficient $\in$ has units of cm^{-1} and an increase of $\in$ by 1 cm^{-1} is equal to a loss of 10^6 dB km^{-1}). Since refractive index is a function of wavelength, there have been several efforts in the literature to describe the functional dependence of n on λ. One of the widely used and successful relation is the Sellemeier relation, which gives n_λ, the refractive index at wavelength λ as

$$n^2(\lambda) - 1 = \sum_{i=1}^{n} \frac{A_i \lambda^2}{\lambda^2 - \lambda_i^2} \tag{11.11}$$

where A_i are oscillator strengths and λ_i are oscillator wavelengths (electrons in the glass are considered as oscillators with characteristic frequencies $\nu_i = c/\lambda_i$ where c is the velocity of light). It is found that only one or two terms ($n = 2$) are generally sufficient to describe the dispersion.

In the visible region, the dispersion of refractive index is often described by the *Abbe number*, ν_d is given by

$$\nu_d = \frac{(n_d - 1)}{(n_F - n_C)} \tag{11.12}$$

where the subscripts d, F and C refer to the wavelengths of light used; d refers to 587.6 nm yellow line from He spectrum; F refers to 486.1 nm of the blue line in H spectrum and C refers to 656.3 nm orange line of H spectrum. In optical applications of glasses, a map of the variation of refractive index as a function of Abbe number (dispersion) is used. In conventional maps, the designations of the glasses are given as 'Crown' and 'Flint', which is somewhat confusing. Figure 11.03, represents a refractive index map based on the chemistry of glasses. The dotted lines indicate the variation of the non-linear refractive indices (see later) of these materials.

The dielectric response of materials is governed by the Clausius-Mossotti relation which is

$$\left(\frac{\varepsilon - 1}{\varepsilon + 2}\right) = \frac{4\pi}{3} \sum n_i \alpha_i \tag{11.13}$$

where n_i is the number of i atoms present in unit volume having polarisability α_i which includes ionic polarisabilities also (but not the

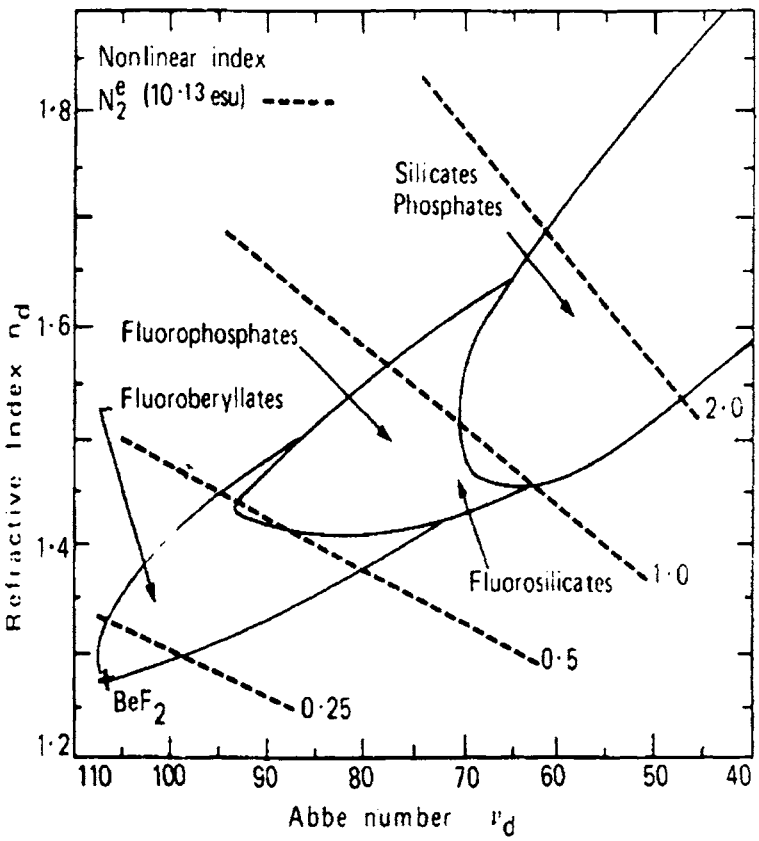

Figure 11.03: Plot of refractive index against dispersion for a range of optical glasses (After Baldwin et al., 1981)

dipolar contribution). The relation between polarisability at optical frequencies and the corresponding refractive indices can be written as

$$\left(\frac{n^2-1}{n^2+2}\right)=\frac{4\pi}{3}\sum n_i\alpha_i \qquad (11.14)$$

Multiply both the sides by M/ρ (Debye, 1929) where M is the molecular weight and ρ is the density of the glass. The right hand side now consists of $\sum\left(M/\rho\right)n_i\alpha_i=\sum V\,n_i\alpha_i=\sum N_i\alpha_i$, which is the total molar polarisability and it is a constant. Ni is the number of particles i in one

mole of the material. Therefore the equation (11.04) gives the molar polarisation, R_M, which may be written as,

$$R_M = \left(\frac{n^2 - 1}{n^2 + 2}\right)\frac{M}{\rho} = \frac{4\pi}{3}\sum N_i \alpha_i \qquad (11.15)$$

which is known as the Lorenz-Lorentz equation. This equation can be expressed slightly differently by using the definition of α, the polarisability. Electromagnetic radiation subjects the electrons to forced oscillations in the medium, and part of the energy of the radiation is dissipated as heat into the medium. The number of electrons subjected to such oscillations by the oscillating field of the radiation is large. Thus, the polarisability α can be expressed as

$$\alpha = \frac{e^2}{4\pi^2 m}\sum\left[\frac{f_i}{(\omega_i^2 - \omega^2)}\right] \qquad (11.16)$$

where ω is the frequency of the radiation and ω_i is the characteristic frequency of the ith electron and f_i is its oscillator strength. Therefore, by substituting this value of α, the Lorenz-Lorentz relation becomes

$$\left(\frac{n^2 - 1}{n^2 + 2}\right)\frac{M}{\rho} = \frac{Ne^2}{3\pi m}\sum\left[\frac{f_i}{(\omega_i^2 - \omega^2)}\right] \qquad (11.17)$$

Where N is the Avogadro number. Behaviour of n in glasses which are metallic is interesting. Electrons in metals are characterized by their plasma frequencies. Therefore, there is an anomalous dispersion of refractive index in the region of the plasma frequency. Refractive index increases and there is also an increased absorption of electromagnetic radiation as ω increases. But when ω crosses ω_p and correspondingly the dielectric constant becomes negative, the refractive index becomes largely imaginary. Hence there is no propagation of electromagnetic radiation through the medium and it gets reflected as mentioned earlier. The nature of the dispersion of the dielectric constant and the refractive indices as a function of frequencies is shown in Figure 11.04. The regions which correspond to pronounced transmission, absorption and reflection are also indicated.

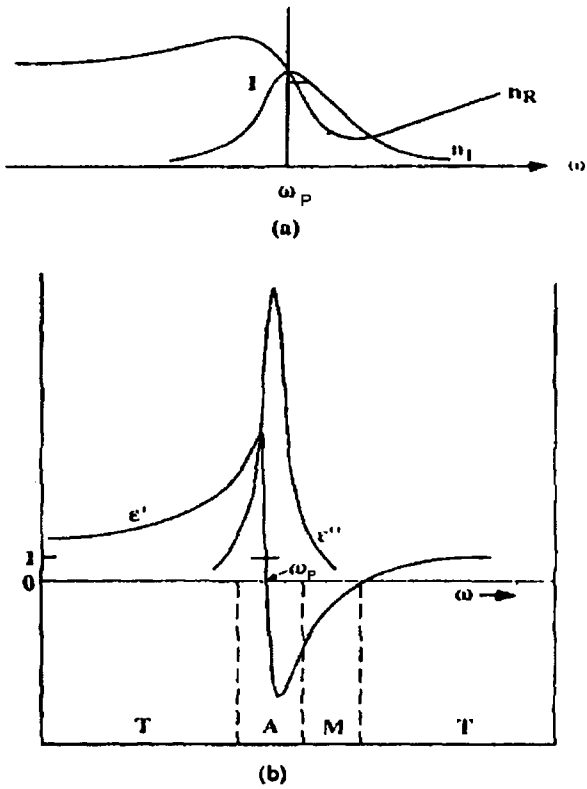

Figure 11.04: Angular frequency dependence of (a) the refractive index ($n_R \equiv n'$ is the real part; $n_I \equiv \kappa$ is the imaginary part) and (b) dielectric constant (ε' = real part; ε'' = imaginary part) for a dielectric. Regions of transmission, absorption and metallic reflection are marked T, A and M respectively (From Varshneya, 1994).

Measurement of optical constants

In the applications of glasses, refractive index plays a very important role. The value of n depends on the chemical composition and also on the thermal history of the glass, because, during annealing, glasses undergo increase in density and correspondingly n increases. Refractive index is easily measured to the 5^{th} decimal accuracy using a number of methods. Use of Abbe and Pulfrich refractometers is both simple and convenient. They enable measurements of refractive indices as a function of temperature also (over a limited range) by circulation of fluids around the samples and the prisms. Refractive index is also measured using reflection from the glass surface. This is based on the use of

Brewster's law. Reflected light in general is more polarised than the incident light and according to Brewster's law, the polarisation is maximum when $\hat{i} + \hat{r} = 90^0$ where $\hat{i}$ and $\hat{r}$ are the angles of incidence and refraction. There are several methods described in the literature such as those based on the use of prisms and fluid immersion (in fluids of known refractive indices) and index matching. The so-called Becke line technique for index matching uses observations under microscope.

When a glass sample cannot be obtained in simple geometrical shapes suitable for direct measurement of n and when it is highly absorbing (high κ values), both n and κ, in principle, can be determined using reflectance spectra obtained (necessarily) over a wide range of frequencies. The analysis is based on the use of Kramers-Kronig relation (Kittel, 1976). Since $R(\omega)$ is given by

$$R(\omega) = \frac{[(n-1)^2 + \kappa^2]}{[(n+1)^2 + \kappa^2]} \tag{11.18}$$

and also since $\varepsilon^*(\omega) = [n^*(\omega)]^2$, the quantities $(\varepsilon', \varepsilon'')$ and (n, κ) are related by the Kramers-Kronig relation.

$$n(\omega) = 1 + P\int_{-\infty}^{\infty} \frac{1}{\pi} \frac{\kappa(\omega')}{(\omega' - \omega)} d\omega' \tag{11.19}$$

$$\kappa(\omega) = 1 - P\int_{-\infty}^{\infty} \frac{1}{\pi} \frac{n(\omega') - 1}{(\omega' - \omega)} d\omega' \tag{11.20}$$

where P denotes the principal part of the integral. It is now easy to understand why R has to be measured over a wide range of frequencies. n and κ can be determined together and so are ε' and ε''. But Kramers-Kronig relations seem to have had limited utility since the procedure of collecting reflectance data over insufficient range leads to spurious values of n and κ.

Stress optical and non-linear optical constants

Glasses are isotropic in annealed state under the action of hydrostatic pressure. But they become anisotropic and exhibit birefringent behaviour when they are not properly annealed and when subjected to

non-hydrostatic pressure. By virtue of the birefringence, such glasses are characterized by two indices of refraction, one along the direction of applied or unannealed stress and the other perpendicular to it. Correspondingly, the unpolarised light gets resolved into two states of polarisation along these (pseudo optic) axes and travel with different velocities in the medium. In the unstressed direction, the propagating light is known as ordinary (o) ray and the one with the polarisation along the stress axis is known as the extraordinary (*e*) ray. The path difference, δ, between the *o*- and *e*- rays of a beam of light, resolved in this manner and passing through a distance d in a glass subjected to uniaxial stress, σ, may be written as

$$\delta = C\,\sigma\,d \tag{11.21}$$

where C is the stress-optic coefficient. C depends on the frequency of light since refractive index has a dispersion. If we define $n_{||}$ and $n_{\perp}$ as the refractive indices of the *e*- and the *o*-rays respectively and n as the refractive index of the unstressed glass, then it can be shown that

$$\begin{aligned} \Delta n_{||} &= n_{||} - n = n^2 \mathrm{Q}\sigma \\ \Delta n_{\perp} &= n_{\perp} - n = n^2 \mathrm{P}\sigma \end{aligned} \tag{11.22}$$

P and Q are also called as Neumann's constants and in turn they are related to Pockel's coefficients, which can be similarly defined. Stress optic coefficients are thus related to differences in refractive indices of *e*- and *o*- rays. Glasses containing PbO and such highly polarisable ions have been known to exhibit very low values of stress-optic coefficients. The stress optic coefficients have the units of inverse pressure and are of the order of 10^{-12} Pa^{-1} (known as Brewster) or 10^{-13} cm^2dyne^{-1} and generally vary between 2.5 – 4.0 Brewsters in glasses.

The stress optical behaviour of glasses is important in glass technology. Due to the different methods of their preparation, glass objects carry their own inherent thermal history. They often retain thermal stresses (more appropriately thermal strains), which have to be removed by subjecting them to annealing operation at temperatures close to T_g. Due to thermal stress they exhibit birefringence easily identified under crossed polars.

Refractive index is the most important property for the optical applications of glasses. Electronic polarisabilities of the constituent ions

determine the values of the refractive indices. By virtue of its low electronic polarisability, fluoride-containing glasses exhibit low refractive indices, but they generally also exhibit significantly high Abbe number. Glasses containing PbO exhibit high values of refractive index and low Abbe numbers (high dispersion). Depending upon a combination of these properties, practical glasses are often designated as Crown (K) and Flint (F).

When the intensities of the light passing through a glass is very high (the amplitude E of the electrical vector being very high) the refractive index becomes non-linear. This is because the polarisation brought about by the electrical field consists of contribution from the second and higher order susceptibilities. The second order non-linear susceptibility is however zero for the glasses as they are isotropic. Thus it is sufficient to use first and third order susceptibilities to describe the polarisation. It can be shown that if $\chi^{(3)}$ is the third order susceptibility, then the refractive index of the glass in high intensity light, is given by

$$n = n_0 + \left(\frac{12\pi\chi^{(3)}}{n_0}\right)E^2 = n_0 + n_2 I \tag{11.23}$$

where I is the average beam intensity, E^2 in watts per cm^2 and n_0 is the refractive index in low intensity light. Several non-linear optical devices are based on the non-linear refractive indices of glasses. The devices include non-directional couplers and optical Kerr shutters (Yamane and Asahara, 2000). Values of n_2 for some of the oxide glasses are listed in Table 11.2.

Table 11.2: Values of n_2 for some glasses (After Yamane and Asahara, 2000).

Glass type	n_2 (10^{-16} cm^2/W)
Fused silica	2.72
$40PbO{\cdot}35BiO_{1.5}{\cdot}25GaO_{1.5}$	125
$NbO_{2.5}{\cdot}TiO_2{\cdot}Na_2O{\cdot}SiO_2$	40.3
$Al_2O_3{\cdot}TeO_2$	174
$Na_2O{\cdot}TiO_2{\cdot}P_2O_5$ (35% TiO_2)	65.8
$PbO{\cdot}TiO_2{\cdot}SiO_2$	77.2
$Na_2O{\cdot}TiO_2{\cdot}P_2O_5$	48
$Na_2O{\cdot}TiO_2{\cdot}B_2O_3{\cdot}P_2O_5$	69
$Na_2O{\cdot}TiO_2{\cdot}SiO_2$	32

Colour of glasses

Another important optical property of a glass is its colour (we have so far discussed glasses without colour). Colour is imparted to glasses by several methods. One is by dissolving transition metal ions into glasses, which give rise to optical absorption due to the well-known *d-d* optical transitions. The other is to dissolve a material in the molten glass, which gets precipitated out as extremely fine particles, and scatter light of particular frequencies in the resulting glass, thus imparting colour to it. There are also glasses in which the absorption gets altered when the intensity of light falling on it changes so that the net light transmitted by the glass can be controlled. When the effect is reversible, the phenomenon is known is *photochromism*. Unlike in photochromic glasses, the incident light brings about permanent (irreversible) changes in the *photo-sensitive glasses*. In the latter, reactions similar to those occurring in photographic plates take place. We discuss in the following sections some salient features of colour and absorption of light in glasses.

Colour due to transition metal ions

Colour induced by the transition metal ions is due to *d-d* transitions. The basis of the use of transition metal ions to impart colour to a glass is briefly as follows. The transition metals, *3d* (Sc to Zn), *4d* (Y to Cd) and *5d* (Hf-Hg) are those which, in their valence state (≥2), contain incompletely filled *d* shells. The angular (l) and the spin (s) momenta of the electrons in such ions (d^1 to d^9) combine to form energy states which are represented by respective term symbols. For the 3*d* transition metals which are the most important for imparting colours to glasses, the combination of l and s momenta is governed by the Russell-Saunders coupling or the *L-S* coupling, where L has values equal to l_1+l_2, $(l_1+l_2-1)\ldots,|l_1-l_2|$ and S is $\sum s$. L represents the total angular momentum quantum number and it can have M_L values from $-L$ to $+L$ including 0 and the total angular momentum is $\hbar\sqrt{L(L+1)}$. Similarly S gives rise to $(2S+1)$ M_S values ranging from $-S$ to $+S$ including 0 and the total spin angular momentum is $\hbar\sqrt{S(S+1)}$. The total angular momentum (orbital + spin) is given by the vector sum of L and S and is designated as J. Therefore, in a transition metal ion the L and S values can have various combinations leading to different micro-states, subject to Pauli's exclusion principle (no two electrons can have the same set of l and s values). The

ground state (lowest energy state) is governed by the Hund's rule of maximum multiplicity, i.e., the ground state is the one having the largest value of S or a combination of highest L and S values when two states have the same multiplicity. These states have been calculated and listed for all the d ions starting from d^1 to d^9 (a filled shell is always in a singlet S state since both L and S are zero). We note here that the designation of a state, the energy term symbol, is by the value of L. $L=0,1,2,3$,etc. are referred to as S, P, D, F, etc. states. The left superscript on the energy term indicates the spin multiplicity which is equal to $2S+1$, and, the right subscript indicates J, whose values vary from $L+S$ to $L-S$. The *free ion* state energies or the energies corresponding to various terms have been determined in terms of Racah parameters, B and C (energy integrals). Some of the lower energy terms and their energies in terms of B and C are listed in Table 11.3. There is a symmetry in the terms arising as the number of electrons increase which is due to the equivalence of n electrons to (10-n) holes. Thus the Table indicates terms for d^1 which are identical to those of d^9 etc. It may also be noted that the ground state is

Table 11.3: Lower free ion term spacings (After Paul, 1982).

Configuration	State	Energy
$d^1 \equiv d^9$	^2D	0
	^3F	0
	^1D	5B+2C
$d^2 \equiv d^8$	^3P	15B
	^1G	12B+2C
	^1S	22B+7C
$d^3 \equiv d^7$	^4F	0
	^4P	15B
	^2G	4B+3C
	^2H	9B+3C
	^2P	9B+3C
$d^4 \equiv d^6$	^5D	0
	^3H	4B+4C
	$^3{}_aP$	$16B+5½C-1/2(912B^2-24BC+9C^2)^{1/2}$
	$^3{}_aF$	$16B+5½C-3/2(68B^2+4BC+C^2)^{1/2}$
	^3G	9B+4C
	^1I	6B+6C
d^5	^6S	0
	^4G	10B+5C
	^4P	7B+5C
	^4D	17B+5C
	^2I	11B+8C
	^4F	22B+7C

always taken to be at zero energy, although they have finite energy values. Secondly, the difference in energies between levels of same spin multiplicity generally require the use of only B and the difference in energy states of different multiplicity require the use of both B and C.

The transition between the energy states which produce colour in glasses is not from the free ions, because these ions are coordinated to other anions in the glass. In oxide and oxy-anion glasses, this coordination is provided by the oxide ions and the coordinations observed very widely, but not exclusively, either tetrahedral or octahedral. The simplest way of recognizing the influence of the coordination of oxygen ions is to treat them as point negative charges surrounding the transition metal ion in octahedral or tetrahedral symmetry – the basis of crystal field approach – which in most situations is enough to understand the spectroscopic features arising from transition metal ions. The five *d* orbitals on the transition metal ion, split into two set of orbitals in an octahedral field of negative charges, because one set of orbitals, $d_{x^2-y^2}$ and d_{z^2} are directed towards the oxygen ions (or the negative charges) in the octahedra, while the other set, d_{xy}, d_{yz} and d_{zx} orbitals project between the oxygen ions avoiding close interaction with the oxygen ions. If we imagine presence of electrons in the *d* orbitals, it is easy to visualize that while all orbitals are affected to a certain extent when oxygen ions of the octahedra are brought to their equilibrium position from infinity, the two sets of orbitals are affected to different extents. Because of the symmetry, the two groups of orbitals are designated as e_g and t_{2g} orbitals. In a transition metal ion with several electrons, the split levels can be imagined to be filled by these electrons subject to two considerations. (1) t_{2g} orbitals are first filled singly. (2) If the energy difference between e_g and t_{2g}, which is designated as 10Dq, is less than the pairing energy, Δ (the energy required to put a second electron in the same *d* orbital), then the e_g levels are filled. (3) But if Δ is greater than 10Dq, then the t_{2g} levels are doubly filled. It can be shown that in the range of energy splitting equal to 10Dq, t_{2g} levels are –4Dq (below) and the e_g levels are +6Dq (above) from a reference energy state (barycentre). Thus it can be verified that when there are 10 electrons (d^{10} case), the sum of the energies, $n_1(-4Dq) + n_2(+6Dq)$ is equal to zero. The energies calculated this way indicate whether there has been a net gain in energy due to crystal field splitting after taking into consideration, not only the 10Dq value but also the value of Δ. The resulting net energy is known as the crystal field stabilization energy (CFSE). When an electron from a t_{2g} is excited to an e_g level, the excitation energy corresponds to 10Dq and it is assumed in this description (crystal field

theory) that the spin of this electron remains unchanged. The net spin of the ion, however, can change in a situation like $(t_{2g}^6, e_g^0) \rightarrow (t_{2g}^5, e_g^1)$. Such a transition, in which there is a change in the net value of the spin, is forbidden. We may note that since these are transitions from one *d* state to the other ($\Delta l = 0$), they are also Laporte (wave function symmetry) forbidden.

The states connected by the transition and the spin allowedness of the transition is somewhat more elegantly understood by considering the transformation behaviour of the term symbols in an octahedral field using Group theory. The *s*, *p*, *d* and *f* orbitals, when brought into an octahedral field, remain either unaffected or split depending upon the inherent symmetry of the orbitals. While *s* and *p* orbitals remain unaffected in the octahedral field, *d* orbitals are split into two groups, which as we noted already, are designated as e_g and t_{2g} orbitals. *f* orbitals are split into three groups, which are designated as a_{2g}, t_{1g} and t_{2g}. This is because of the orbital shapes and their mutual dispositions in space, both being determined by the *l* quantum number. The orbital splitting in the multi-*d* electron systems is similarly based on *L*. The term symbols derived on the basis of total angular momentum quantum number *L*, splits into groups. Thus, for example, the energy terms are transformed into components as shown in Table 11.4. Therefore, we can immediately see how the energy

Table 11.4: Splitting of d^n terms in an octahedral field (After, Cotton, 1971).

Terms	Components in an octahedral field
S	A_{1g}
P	T_{1g}
D	E_g+T_{2g}
F	$A_{2g}+T_{1g}+T_{2g}$
G	$A_{1g}+ E_g+T_{1g}+T_{2g}$
H	$E_g+ T_{1g}+T_{1g}+T_{2g}$
I	$A_{1g}+ A_{2g}+ E_g+ T_{1g}+ T_{2g}+ T_{2g}$

levels of a particular ion in its ground state would split when subjected to an octahedral field. From Table 11.3, we observe that the ground states of the transition metal ions can only be *S*, *D* and *F*. However, the first excited energy state could be D, P, H or G states. Thus, for example, states in d^1 ion like Ti^{3+}, whose ground state is ^2D splits into ^2E_g and $^2T_{2g}$. Therefore we expect a single transition with a characteristic 10Dq. d^2 and d^7 ions like V^{3+} and Co^{2+} have a ^3F and ^4F ground states, which gets split into

$^3A_2/^4A_2$, $^3T_1/^4T_1$ and $^3T_2/^4T_2$ states. Therefore we expect two spin-allowed transitions, from $^3T_1 \rightarrow {}^3T_2$ and $^3T_1 \rightarrow {}^3A_2$ states. We may add here that for heavier transition metals like 4*d*, 5*d* and rare earths, the combination of L+S giving rise to J (right subscripts in the energy terms), also becomes important. Thus, the origin of the spectral absorption and hence the colour of the transition metal ion containing glasses is due to the transitions between levels resulting from the splitting of the energy terms in the respective crystal fields. It may be noted that there are alternate approaches to arrive at the origin of the energy absorption such as ligand field theory, but they are not discussed here.

It was observed in passing that the *d-d* transitions are Laporte forbidden and that transitions between different spin states are also forbidden. The spin selection rule often gets relaxed because of the spin-orbit interactions. Due to this interaction, the spin and orbital angular momenta get coupled. The spin and orbital wave functions are not strictly factorized and therefore spin-forbidden transitions such as singlet-triplet transitions do occur. Similarly, the *d-d* transitions, although strictly Laporte forbidden (because both the ground and excited state wave-functions are formed from the same symmetric *d* functions) become allowed since vibrational motions of the transition metal atoms in the structure invariably remove the symmetry and give rise to what is described as *vibronic coupling*. This enables transition between the ground and excited states. Transitions which are both spin and Laporte forbidden are generally very weak with extinction coefficients of the order of 0.1 cm^{-1}. The spin allowed but Laporte forbidden transitions have extinction coefficients of the order of 10 cm^{-1}. Absorption bands arising from transition metal ions in glasses are usually very broad and of the order of about 1000 cm^{-1}. One other aspect to be noted in connection with the TM ion spectra in glasses is the Jahn-Teller effect. For a TM ion in glass whose energy states are split by the crystal field, if the ground state is degenerate, the coordination geometry distorts itself in a manner which removes the degeneracy. d^1 and d^9 systems such as Ti^{3+} and Cu^{2+} in octahedral symmetry are candidate cases for the incidence of Jahn-Teller distortions.

Two examples of the study of transition metal ion spectra in glasses is shown in Figure 11.05 and 11.06. The first is the study of spectra in $ZnSO_4$-K_2SO_4 glass and the other in PbO-$NaPO_3$ glass. In the sulphate glass, the divalent transition metal ions, Fe^{2+}, Co^{2+}, Ni^{2+} and Cu^{2+} appear to be present in the octahedral positions surrounded by the oxygens of the sulphate ions. The assignments of the transitions, the 10Dq and the

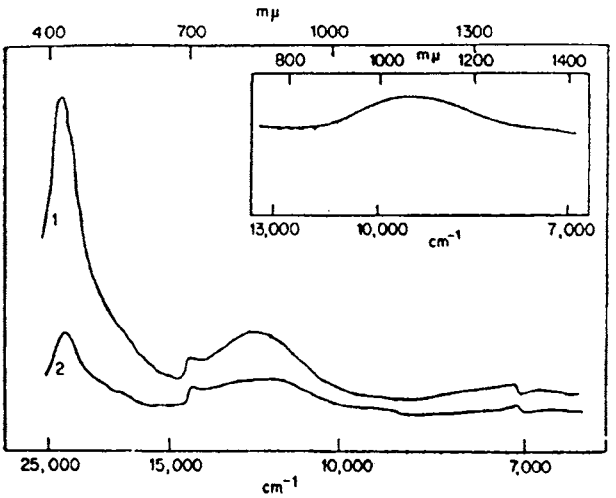

Figure 11.05: Spectra of Ni^{2+} in (1) 70:30 and (2) 20:80 K_2SO_4:$ZnSO_4$ glasses. Inset: spectrum of Fe^{2+} in 35 $K_2SO_4 \cdot 65ZnSO_4$ glass (After Narasimham and Rao, 1978)

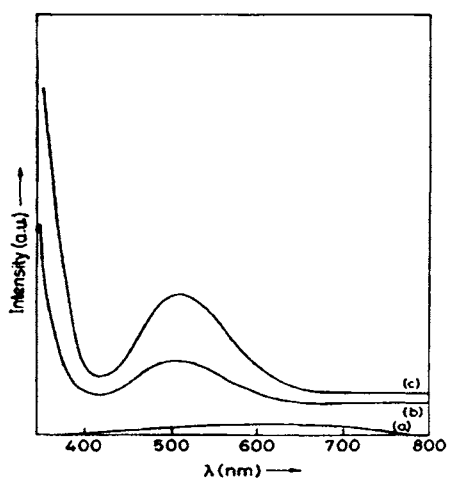

Figure 11.06: Room temperature optical absorption spectra of manganese ions (2 wt %) in: (a) microwave-prepared pure $NaPO_3$ glass; (b) microwave-prepared $70NaPO_3 \cdot 30PbO$ glass; (c) conventionally prepared $70NaPO_3 \cdot 30PbO$ glass (After Vaidhyanathan et al., 1997).

calculated Racah parameters for Co^{2+} and Ni^{2+} ions are given in Table 11.5. In fact, the Racah parameters are close to their free ion values which

Table 11.5: Assignment of transitions and energy parameters (After Rao, 1980).

Dopant ion	Observed transition cm^{-1}	Assignment	Calculated transition cm^{-1}	Ligand field splitting energy cm^{-1}	Racah parameter cm^{-1}
Fe^{2+}	9300	$^5D_5 \rightarrow {}^5D_3$	9300	9300	....
Co^{2+}	6870	$^4F_4 \rightarrow {}^4F_5$	6870	7490	720
	11040	$\rightarrow {}^4F_2$	13880	...	
	17360	$\rightarrow {}^4P_4$	16360	...	
Ni^{2+}	6800	$^3F_2 \rightarrow {}^3F_5$	6880	6880	880
	11700	$\rightarrow {}^3F_4$	11450	...	
	14290	$\rightarrow {}^1D_3$	14910	...	
	22730	$\rightarrow {}^3P_4$	22360	...	
Cu^{2+}	11150	$^2D_3 \rightarrow {}^2D_5$	11200	11200	

is consistent with the highly ionic nature of these glasses. The spectra of Mn^{2+}doped glasses shown Figure 11.06 is an example where the observed optical transition due to spin allowed $^5E_g \rightarrow {}^5T_{2g}$ transition of Mn^{3+} ions ($\approx$ 510 nm wavelength) is much more intense than the spin forbidden $^6A_{1g} \rightarrow {}^5T_{2g}$ transition ($\approx$ 650 nm wavelength) of Mn^{2+} ion. In the presence of PbO significant amount of Mn^{3+} is present in glasses. In pure $NaPO_3$ glass there is only Mn^{2+}. In conventional preparation, Mn^{2+} is more readily oxidised to Mn^{3+}. The spectrum of Mn^{2+} observed in alkali borate glasses reveals similar characteristics. Fe^{2+}, which is a d^6 ion, is generally present in octahedral positions in glasses and gives rise to two characteristic bands of moderate intensity around 9000 cm^{-1} and 5000 cm^{-1}. The former is attributed to $^5T_2 \rightarrow {}^5E$, while the 5000 cm^{-1} absorption is attributed to distortion splitting (Edward et al., 1972).

On the higher energy side of the visible region (towards the UV), transition metal ions can give rise to intense absorption due to charge transfer transitions. Charge transfer can occur from both metal to ligand and from ligand to metal. Glasses containing Fe are known to exhibit charge transfer bands arising from both Fe^{3+} and Fe^{2+} in the UV region. UV absorption due to Fe^{3+} appears to give rise to bands peaked around 40000 cm^{-1} in phosphate glasses, which shifts to around 45000 cm^{-1} in alkali silicate glasses. Similarly Cr^{6+} is also known to exhibit two charge transfer bands around 27000 cm^{-1} and 30000 cm^{-1}. The UV absorption leads to a high frequency cut off which is given by the relation λ_0 (nm) = $1240/E_g$(eV), where E_g is the (charge transfer) band gap energy.

Thus the absorption due to transition metal ions and the consequent

colouration of the resulting glasses is determined by the site symmetry in which the transition metal ion is present, the nature of the ligand and the resulting value of 10Dq. The colour imparted by several transition metal ions in oxide glasses is summarized in Table 11.6. Rare earth ions also

Table 11.6: Colours generated by transition-metal and rare earth ions in glass (After Varshneya, 1994).

Transition metal ions			Rare earth ions		
Configuration	Ion	Colour	Configuration	Ion	Colour
	Ti^{4+}	Colourless	$4f^0$	La^{3+}	None
d^0	V^{5+}	Faint yellow to colourless		Ce^{4+}	Weak yellow
	Cr^{6+}	Faint yellow to colourless	$4f^1$	Ce^{3+}	Weak yellow Green Violet-pink
			$4f^2$	Pr^{3+}	
			$4f^3$	Nd^{3+}	
d^1	Ti^{3+}	Violet-purple	$4f^4$	Pm^{3+}	None
	V^{4+}	Blue	$4f^5$	Sm^{3+}	None
	Mn^{6+}	Colourless	$4f^6$	Sm^{2+}	Green
				Eu^{3+}	None
d^2	V^{3+}	Yellow-green	$4f^7$	Eu^{2+}	Brown
				Gd^{3+}	None
d^3	Cr^{3+}	Green	$4f^8$	Tb^{3+}	None
d^4	Cr^{2+}	Faint blue	$4f^9$	Dy^{3+}	None
	Mn^{3+}	Purple			
d^5	Mn^{2+}	Light yellow	$4f^{10}$	Dy^{2+}	Brown
	Fe^{3+}	Faint yellow		Ho^{3+}	Yellow
d^6	Fe^{2+}	Blue-green	$4f^{11}$	Er^{3+}	Weak pink
	Co^{3+}	Faint yellow			
d^7	Co^{2+}	Blue-pink	$4f^{12}$	Tm^{3+}	None
d^8	Ni^{2+}	Brown-purple	$4f^{13}$	Tm^{2+}	None
d^9	Cu^{2+}	Blue-green		Yb^{3+}	None
d^{10}	Cu^{+}	Colourless	$4f^{14}$	Lu^{3+}	None

produce colours for precisely the same reasons as the transition metal ions (rare earths are also known as inner transition elements and the terms of rare earth ions are subject to splitting in crystalline fields. However, since the *f* orbitals are buried energetically deep inside, they are less sensitive to ligand surroundings compared to transition metal ions and are relatively less affected).

Fluorescence spectra

The ground state energy term, corresponds to the highest spin multiplicity. For ions like Mn^{2+} whose ground state is ^6S, only weak spin forbidden transitions occur. In such cases, the de-excitation is also forbidden and therefore do not occur readily. Also, we may recognize that both the excited and the ground states are characterized by slightly different potential energy profiles (with their own vibrational energy manifold) as schematically shown in Figure 11.07. The absorption of

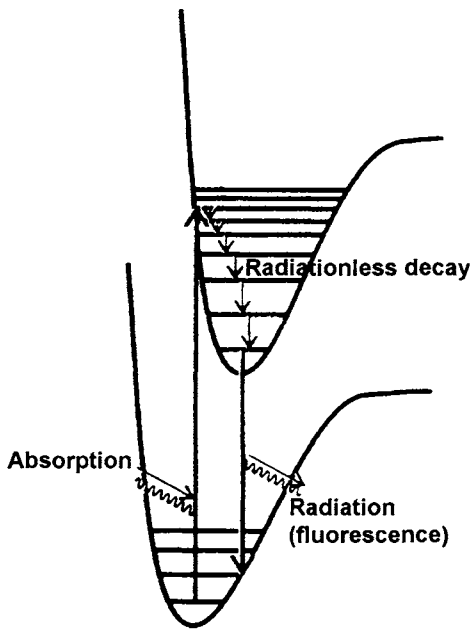

Figure 11.07: The sequence of steps leading to fluorescence.

radiation results in a vertical transition to one of the higher vibrational states. The excited state has now got time (because de-excitation is spin-forbidden) to relax through dissipation of part of the energy as phonons (heat); it descends to the lowest vibrational energy level of the excited state manifold and from there it undergoes a vertical de-excitation to one of the excited states of the ground vibrational state manifold. Therefore if the excited and ground states do not have the same spin multiplicity, the emitted radiation not only has lower energy, but also the emission persists even after the source of irradiation is removed. This constitutes

phosphorescence. But if the de-excitation stops within $\approx 10^{-8}$s after the exciting radiation is removed, the low energy emission is known as fluorescence (10^{-8}s is generally the excited state life time and is enough for $\sim 10^5$ vibrations to occur). A typical fluorescence emission spectra of Mn^{2+} doped in $PbO\text{-}NaPO_3$ glass is shown in Figure 11.08. Mn^{2+} occupies octahedral sites and its emission occurs at 595 nm, which is due to $^4T_{1g}(G) \rightarrow {}^6A_{1g}(S)$. The figure also reveals that the excitation spectra consists of peaks corresponding to all the spin-forbidden transitions to

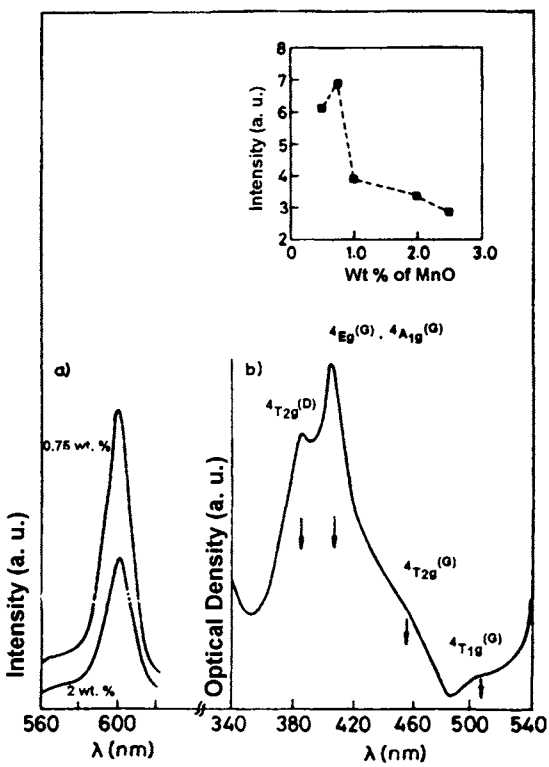

Figure 11.08: (a) Fluorescence emission spectra of Mn^{2+} ions in $NaPO_3$-PbO glasses at room temperature. (b) Excitation spectra of manganese ions in $NaPO_3$-PbO glasses. The inset shows the fluorescence emission intensity of Mn^{2+} ions as a function of MnO content. (After Vaidhyanathan et al., 1997)

quartet states. The emission intensity also decreases as the Mn concentration increases as shown in the inset. This is due to quenching of the fluorescence and in this case, self-quenching, whereby radiative transition becomes less likely than the non-radiative transitions. Similar excitation and emission spectra due to fluorescence occurs quite

commonly in glasses doped with rare-earths. An example of the study of Dy^{3+} excitation and emission spectra are shown in Figure 11.09 and 11.10 in typical NASICON glasses. The concentration dependent quenching of the fluorescence is also shown as an inset in Figure 11.10. The two emissions in Figure 11.10. correspond to the $^4F_{9/2} \rightarrow {}^6S_{13/2}$ (573 nm) and $^4F_{9/2} \rightarrow {}^6H_{15/2}$ (482 nm). Similar features are observed in the excitation-emission spectra of Tb^{3+} also and two prominent emissions occur at 543 nm and 487 nm respectively corresponding to $^5D_4 \rightarrow {}^7F_5$ and $^5D_4 \rightarrow {}^7F_6$.

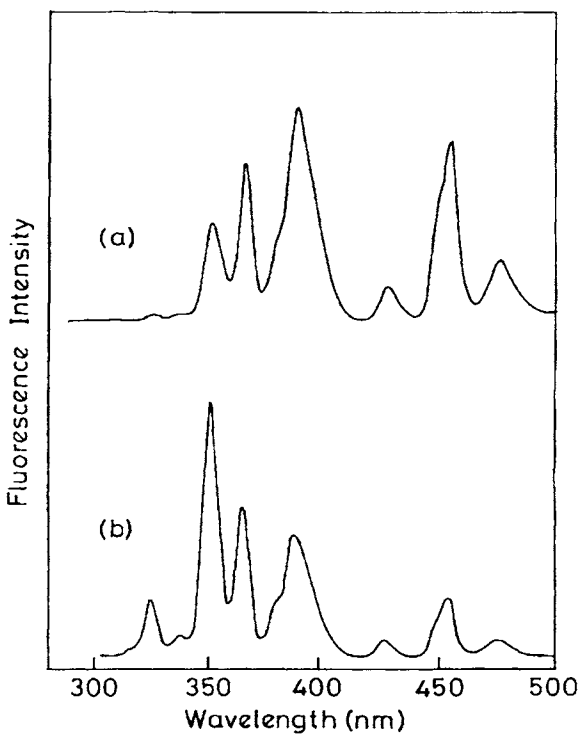

Figure 11.09: Excitation spectra of Dy^{3+} in (a) $Na_5Ti(PO_4)_3$ and (b) $Na_3Nb(PO_4)_3$ glasses (λ_{emm} = 573 nm). (After Sobha and Rao, 1996)

Another phenomenon which occurs when glasses are doped with two fluorescing ions is the energy transfer from one ion to the other during fluorescent emission. This is illustrated in Figure 11.11 for a NASICON glass. When doped with 1 wt% Dy^{3+} it shows the normal two peak emission (spectrum (a)). But when it is additionally doped with 1.2 wt% Tb^{3+}, emission peaks corresponding to Tb^{3+}, also begin to manifest as shown in spectrum (b) of Figure 11.11. This is due to an energy transfer

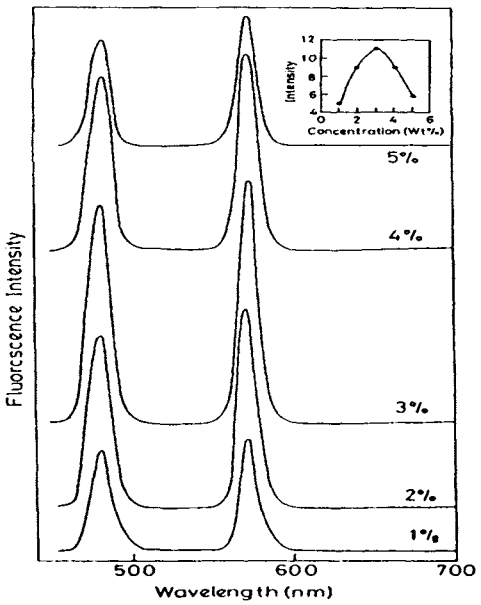

Figure 11.10: Emission spectra of Dy^{3+} in $Na_5Ti(PO_4)_3$ glass at various concentrations. (λ_{exc} = 389 nm). The inset shows the variation of fluorescence intensity with Dy^{3+} concentrations (After Sobha and Rao, 1996).

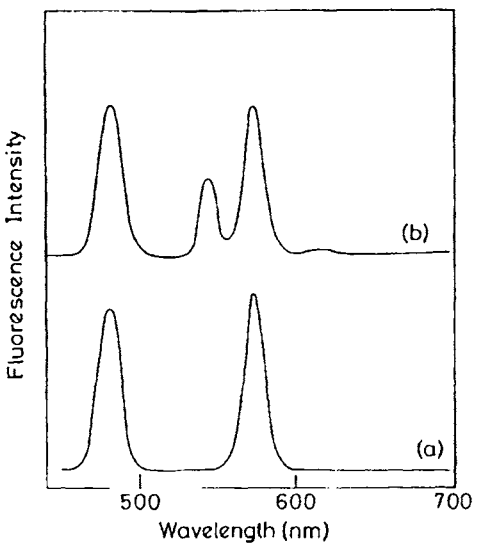

Figure 11.11: Emission spectra of $Na_3Nb(PO_4)_3$ glass doped with (a) 1.0% Dy^{3+} and (b) 1.0 wt % Dy^{3+} + 1.2 wt % Tb^{3+} (λ_{exc} = 389 nm) (After Sobha and Rao, 1996).

from Dy^{3+} to Tb^{3+}. The levels of Dy^{3+} and Tb^{3+} thus get coupled for energy transfer and the coupled levels have been identified as $^4F_{9/2}$ (482 nm) and $^5D_4$(487 nm) respectively. Several such inter-ionic energy transfers have been observed in rare-earth doped glasses.

Glass lasers

Delayed emission and shift in frequencies constitute basic features of lasers (which is an acronym for Light Amplification by Stimulated Emission of Radiation) also. Glasses are used as hosts for lasers and Nd laser in phosphate glass hosts has been in wide use (Snitzer, 1989). The principle of operation of Nd laser is shown in Figure 11.12 and typifies a

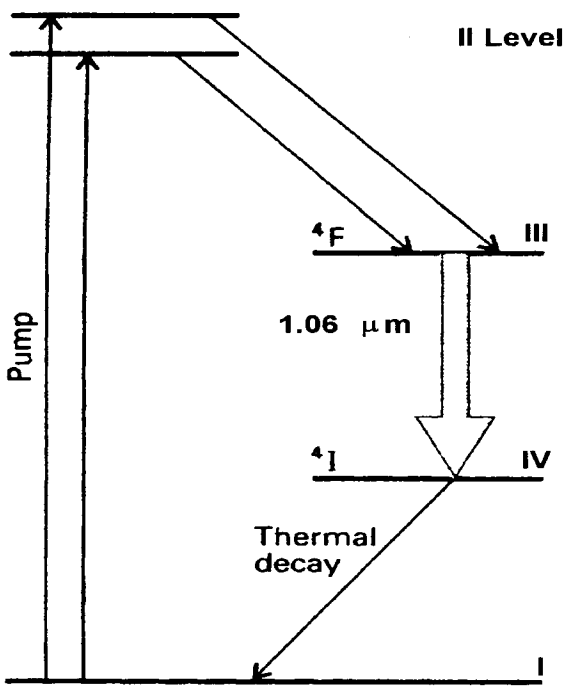

Figure 11.12: The transitions involved in the neodymium laser. The laser action takes place between two excited states, and the population inversion is easy to achieve.

four level laser. The principle of lasing action is as follows: (1) Using a suitable energy source (high intensity light or electrical discharge) electrons are pumped from the ground state (I level is $^4I_{9/2}$ for the case of Nd) to one or more excited states (II level). (2) The energy of the excited

electron decays (partly) non-radiatively to a lower excited state which is empty and from where the decay time is longer (by some forbiddenness). The excited state population thus builds up at this level (III level). (3) Any spontaneous emission from this level to level IV would trigger stimulated emission of electrons from level III to level IV (the coefficient for stimulated emission is the same as that for stimulated absorption). The stimulated emission from level III to level IV ($^4F_{3/2} \rightarrow {}^4I_{11/2}$) corresponds to 1.06$\mu$m. The electron from level IV decays thermally to the ground state. Many lasers operate only with three levels. The advantage of a four level laser is that level IV being empty, any concentration of electrons in level III always constitute an inversion in population and meets the most important requirement for stimulated emission. Phosphate (or for that matter any) glass has the disadvantage that it is a poor thermal conductor and Nd-YAG laser is superior for this reason. But this disadvantage is overcome by operating the laser in a pulsed mode. In this excitation of electrons from level I to level II (pumping) and the next stage of creating population inversion at elevel III are accomplished continuously but the stimulated emission from level III to level IV is interrupted by mechanisms such as Q-switching and mode locking, there by achieving a pulsed mode of operation.

Briefly, the laser medium is confined to a cavity (like Nd containing glass rod held between two mirrors). The cavity length is so adjusted that it corresponds to $N\lambda/2$, where λ is the desired wavelength of the laser light. The cavity therefore supports only these wavelengths. The (spontaneously) emitted radiation makes multiple passages in the glass rod and cause stimulated emission. The amplitude of the radiation corresponding to this wavelength builds up resulting in a powerful laser beam. Thus the Nd-glass laser is generally employed in a pulsed mode and is less suitable for making continuous wave lasers.

Several rare earth ions, besides Nd^{3+}, have been found suitable for making lasers such as Er^{3+}, Yb^{3+} and Ho^{3+}. The fluorescence life time, τ, for emission from level III to level IV, should be high for a good laser. The fluorescence width is between 20-40 nm in several glass media as observed in the case of Nd^{3+}. Concentrations of Nd^{3+} ions used in lasers correspond to about 1.5 to 3 wt% of Nd_2O_3. Some of these characteristics of Nd-based lasers are summarized in Table 11.7. Since extremely high levels of laser intensity can be achieved in pulsed (Q-switched) devices, Nd-laser can be used in non-linear optical devices to produce light of half the wavelength. The primary lasing ion is often referred to as an activator. It is possible to dope another ion which can absorb energy during the

pumping stage such as Cr^{3+} which absorbs energy at 450 nm and then transfer energy efficiently to Nd^{3+}. The fluorescence life times are seriously affected by the presence of ions like Fe^{2+}, Cu^{2+}, etc. which can quench the lasing action and therefore have to be avoided during the preparation of laser glasses. The effectiveness of a laser depends on its coherence length l_C, which is a measure of the distance over which the waves do not get de-phased. Evidently, l_C is related to $\Delta\lambda$ which is the range of wavelengths in the laser beam and is equal to $\lambda^2/2\Delta\lambda$.

Table 11.7: Properties of glasses used for Nd-laser applications (After Neuroth, 1987).

Glass type	Fluorescence		
	Lifetime τ (10^{-6}sec)	Maximum wavelength (nm)	Fluorescence width at half maximum (nm)
Silicate	300-1000	1060	30-40
Borate	50-400	1055	30-40
Borosilicate	200-800	1058	30
Phosphate	100-500	1054	20-30
Tellurite	140-240	1060	25-30
Fluorosilicoborate	300	1060	30
Fluorophosphate	350-500	1052	25-31
Fluoroberyllate	460-900	1048	18-28
Fluorozirconate	430-450	1049	26
Fluoroaluminate	400-600	1050	30-33
Chloride	180-220	1063	20
Chlorophosphate	290-300	1055	20-23
Sulphide	60-100	1076	21

Colour from particle scattering

One other well known method of colouring glasses is by inclusion of fine particles of metals like gold or oxides like Cr_2O_3, Cu_2O or cadmium sulpho-selenide. These are generally described as ruby glasses. Small percentages of the oxides or chalcogenides mentioned above are dissolved in the melt. They precipitate out when the glass forming melt is cooled. In case of the Cu-ruby, small amount of SnO is added as a reducing agent along with a cupric compound to the charge. Even as the melt is kept hot, the initial blue colour due to Cu^{2+} disappears and a pale yellow colour develops. The melt is then quenched to the glassy state. When this glass is re-heated for a reasonable length of time between T_g and softening temperature, red 'ruby' colour develops. This heat treatment

is known as *striking*. The extent to which the reduction occurs in the melt is critical for the ruby colour. Both, high degree of reduction of Cu^{2+} and retention of too much Cu^{2+} can result in failure to develop good ruby colour. It has been established through several careful experiments and thermodynamic analysis (Banarjee and Paul, 1974) that the colour is not due to metallic Cu, but is due to the formation of colloidal particles of Cu_2O during striking operation. These particles scatter light (Mie scattering) and are responsible for the ruby colour. Purely metallic particles of gold also produce ruby colour and gold is introduced simply as metallic powder. The colour is apparently due to absorption around 530 nm. Addition of CdS and Se in the ratio 1:2 also leads to development of deep red colour in glasses.

Window glass and other transparent glassware are made from glasses, which are only about 98+% transparent. The colour in such silicate glasses is largely due to the presence of iron. As pointed out, Fe^{3+} has an absorption in the near UV while Fe^{2+} absorbs in the near IR, both of which gives rise to a reduction in the transparency. Fe^{2+} imparts a bluish green colour, whereas Fe^{3+} imparts a straw yellow colour. A proper ratio of Fe^{3+} to Fe^{2+} can lead to decolourisation which is achieved by addition of small amounts of As_2O_3 to the glass batch. Decolourisation is also brought about by the addition of $NaNO_3$ or Ce compounds. Co^{2+} ions are particularly effective in imparting blue colour. Even in parts per million concentration, Co^{2+} imparts a blue tint while 1000 ppm of Co^{2+} gives intense blue colour characteristic of well-known cobalt-blue glasses. Unlike in the case of CuO where fine colloidal particles are present, the blue colour of CoO arises from uniform distribution of Co^{2+} ions.

Colours produced by transition metal ions are sensitive to anionic environment. For example, when small quantities of NaBr are dissolved in cobalt containing alkali-borate glasses, Br^- substitutes for the O^{2-} in the coordination of Co^{2+} (partially). This leads to profound change in the pink colour of the glass due to development of strongly absorbing bands in the region of 15000 cm^{-1} and 21000-26000 cm^{-1} (broad band). One of the industrially important coloured glasses is made by anionic substitution and that is the *amber glass*. Here, the glass is made by using impure sand containing significant quantities of Fe to which Na_2SO_4 and carbon are added. Na_2SO_4 is reduced to Na_2S by carbon. The resulting glass contains the Fe^{3+} which is coordinated to three oxide and one sulphide ions. The Fe^{3+} chromophore now gives two intense absorption bands around 23500 and 33900 cm^{-1}. The 23500 cm^{-1} band has an extinction coefficient of the order of 10^4 cm^{-1}. The production of the Amber glass therefore involves

both oxidation of Fe^{2+} to Fe^{3+} and reduction of Na_2SO_4 to Na_2S indicating that the partial pressure of oxygen and the temperature of the equilibrium glass melt are very critical for the formation of amber glasses. Na silicate glass ($30Na_2O \cdot 70SiO_2$) requires P_{O_2} of 10^{-8}-10^{-10} atm. at 1400°C for the best results. Use of Se in place of S gives rise to *Se-amber glass* which is black in colour. These colours are primarily due to charge transfer from chalcogen to iron.

Addition of P_2O_5, Sb_2O_5, As_2O_5, CeO_2, TiO_2 etc. oxides can give a milky white appearance to glasses, which are known as *opal glasses*. But opal glass is also formed by exposure of glasses containing Na_2O and Ca_2O to fluorine gas, due to the formation of fine crystalline precipitations of NaF and CaF_2. These fine crystallites produce the milky or opal appearance.

Photosensitive glasses

The incident light itself can bring about changes in the absorption characteristics of the glass. This is what characterizes a range of photo-sensitive behaviour observed in glasses. When a combination of ions are present in a glasses, both of which can undergo redox reactions, incident photons can bring about the redox reaction and change the colour of the glasses. When this occurs with the natural light, it is referred to as *solarization*. That is what happens when the redox couple is (Mn^{2+}, As^{5+}) or (Mn^{2+}, Fe^{3+}). The respective reactions may be represented as

$$\begin{aligned} 2Mn^{2+} + As^{5+} + h\nu &\rightarrow 2Mn^{3+} + As^{3+} \\ Mn^{2+} + Fe^{3+} + h\nu &\rightarrow Fe^{2+} + Mn^{3+} \end{aligned} \qquad (11.24)$$

Such photo-induced redox reactions can lead to loss of transparency or discolouration. When ions of the noble metals, Cu, Ag and Au are present in a glass, they may undergo photo induced reduction by exposure to light by the transfer of electrons from oxide ions to the metal ions. This results in the formation of neutral atoms. If the glass containing such neutral atoms is now heated, the neutral atoms agglomerate, and a coloured image is formed in much the same manner as in the photographic process. These are the *photosensitive* glasses. The reactions in photosensitive glasses are irreversible, those in solarization are not. The image in the photosensitive glass is coloured. But if the composition of the glass is made in such a way that when the glass is heated to sufficiently high temperature, the silicate composition around the nuclei of the metal particles crystallize, then the

image becomes turbid. These turbid regions can be etched away so as to obtain the image of the object used at the time of irradiation into a fine relief. The electon transfer reaction requires radiation of higher energy, preferably UV light. It is, therefore, necessary to avoid presence of oxides which have high UV absorption.

The widely used *photochromic* glasses, cut off light increasingly as the intensity of incident light increases. With an increase in incident light intensity, there is an increased optical density of the glass. The effect is completely reversible. Photochromism is initiated by the UV component in light, particularly between 320 and 420 nm. Glasses which exhibit this effect contain a distribution of Ag-halide crystals (having sizes of the order of 10 nm) in the same manner as in a photographic emulsion, the only difference being that the matrix in the glass, being rigid, does not allow ready diffusion of halogens away from their sites. Again as in the photographic process, electron transfer from halogen to silver leads to the formation of neutral Ag^0 and Cl^0 atoms. This process not only cuts off UV, but also leads to darkening of the glass increasing its optical density. When the source of light is removed there is a recombination of Ag^0 with Cl^0 which is present just in its vicinity and therefore it restores the transparency. A combination of Ag-halides with a small amount of Cu^+ ion exhibits similar photochromic property, except that the reduction of Ag^+ is attended with the oxidation of Cu^+ to $Cu^{2+}$and this reaction is also reversible and the darkening is attributed to Ag^0. Only small percentage (0.5%) of silver halide is necessary for the purpose and often a combination of the halides is used.

Fibre optics

Optical properties of glasses have made a change in the life of the whole world in the field of communication and that is through the introduction of fibre optics. Fibre optics is used in computers, in optical sensors and in biomedical devices. In the field of communication it is based on the possibility of transmitting acoustic signals which are first digitized and then used to modulate a light beam. The light beam is piped through an optical fibre no more than fraction of a mm in dia at the speed of light. Reversing the process at the other end, the acoustic signal is recovered. The process is diagrammatically indicated in Figure 11.13. Shown in the inset is the longitudinal section of a fibre, which acts as a light guide. The section of the fibre shows that the fibre consists of a core which is made of a glass of refractive index n_1 which is clad in another

glass of refractive index n_2, where $n_2 < n_1$. The two rays, A and B, which enter into the core are incident on the inner wall at angles ϕ and ϕ_C, where ϕ_C is the Brewster's critical angle. While a fraction of the intensity of A gets transmitted through the clad, all the intensity of B is internally reflected and passes on. Thus, for the beam which is incident for angles greater than or equal to ϕ_C, there is no loss of intensity by transmission to the clad. However, the light beam still suffers loss of intensity due to absorption by the core itself by several mechanisms. The essence of fibre optic communication is to device a glass for a given frequency of light which has an absolutely low absorption so that the beam is recovered at the other end of the fibre with minimum loss of intensity.

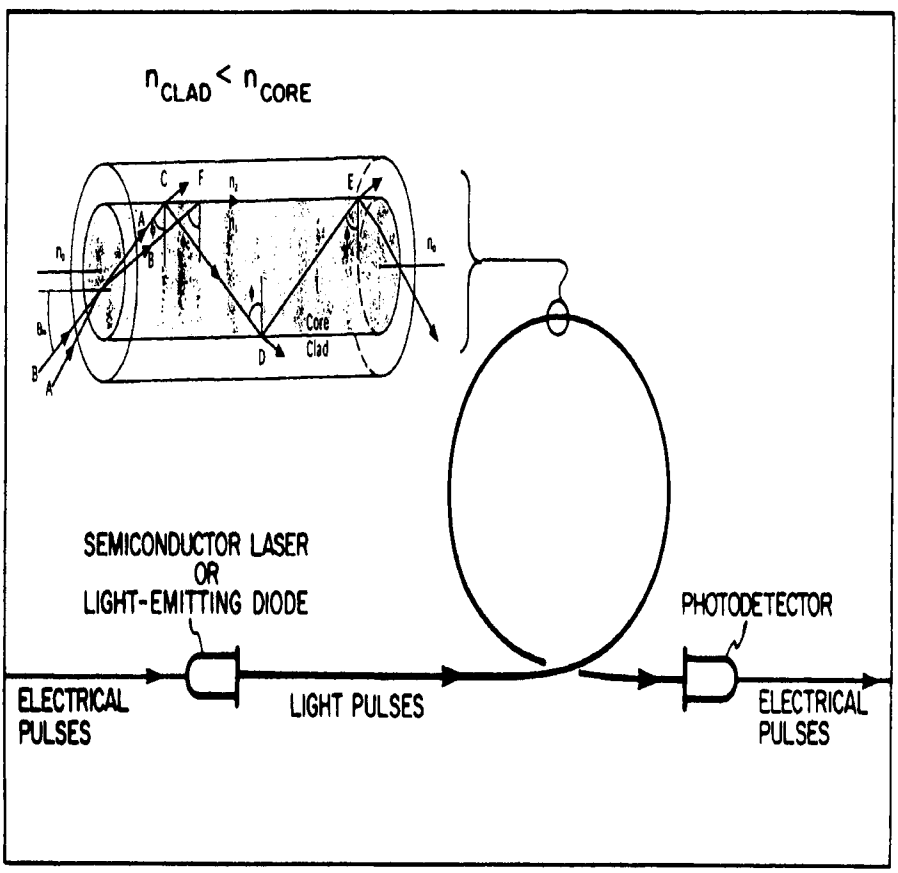

Figure 11.13: The use of ultratransparent glass fibres in telecommunications networks ($n_{clad} = n_2$ and $n_{core} = n_1$ in the text).

The propagation of a beam like B is restricted only to a discrete number of angles greater than or equal to ϕ_C, because, for other than such angles, interference eliminates the intensity. If we designate these angles as ϕ_M, it can be shown that

$$cos\phi_M = \frac{4rn_1}{m\lambda} \tag{11.25}$$

where m is the number of modes which can propagate and r is the radius of the core, n_1 is the refractive index and λ th wavelength of light. The total number of modes m can be approximated as

$$m = \left(\frac{2\pi^2 r^2}{\lambda^2}\right)\eta^2 \tag{11.26}$$

where η is the numerical aperture. By substituting proper values of r, η and λ it can be shown that a large number of modes are supported by optical fibres.

The attenuation of light or loss of intensity in the core arises from three sources (see equation 11.04). Rayleigh scattering causes a loss which varies as the inverse fourth power of λ. The intrinsic absorption arising from electronic excitations is rather limited, particularly when the light used is in the near IR region. However, multi-phonon absorptions (the last term in equation 11.04) give rise to significant losses. Several methods have been developed such as use of Modified Chemical Vapour Deposition (MCVD), Vapour Phase Axial Deposition (VAD) and Outside Vapour Phase deposition (OVD) based on the use of extremely pure metal halide vapours ($SiCl_4$, $GeCl_4$ or $POCl_3$), to make glasses which give rise to extremely low attenuations. SiO_2 fibres of high purity and homogeneity having very high transparencies for wavelengths of 1.5μ exhibit losses of less than 0.2 dB/km, and is currently used in making communication fibres. Heavy metal fluoride glasses exhibit even lower attenuations at somewhat higher wavelengths (see Figure 11.01) but the difficulty lies in making long fibres of halide glasses suitable for optical communication. We may note that in the Figure 11.13 only a step variation in the refractive index is shown as occurring at the core clad interface. Yet another configuration uses graded index (GRIN) fibres, which reduce path length differences of various modes. Generally multi-mode fibres have core diameter of 50 microns. Cores of 8-10 micron diameter allow the

propagation of only one mode (monomode fibres). The transmission is more efficient in single mode fibres. The GRIN fibres are drawn from GRIN rods, which are prepared generally by either ion exchange or molecular stuffing technique.

Fine particulates and nano-glasses

The fine particles of Cu_2O, Au etc. used in providing colours are colloidal particles which are nanometric in size ($\approx$ 10 nm in diameter). In addition to giving colours, these nanoparticles present in glasses give rise to non-linear susceptibility, photochromism etc. The size distribution of the nanoparticles is dependent on the thermal history of the glass. We will refer later (chapter 12) to the phase separation and crystallization of B_2O_3-rich borosilicate glass phase as fine crystalline particles, which are etched out in acids during preparation of SiO_2-rich products. These are also good examples of nanoparticles formed in glassy phases. Nanocrystalline materials are generally understood as consolidated products containing randomly orientated crystallites of particles whose sizes are ~10 nm and with well-defined surfaces. These surfaces actually constitute the grain boundaries in crystalline nanomaterials. A parallel situation in glasses can be visualized in which glass particles of nanometric size are similarly consolidated to make nanoglasses. There have been examples in the literature of studies on metallic nanoglasses like Pd-Fe-Si glass (Jing et al., 1989). Nanoparticles of Pd-Fe-Si were prepared by evaporation of the corresponding alloy in high pressure He gas and condensing the vapors onto cold fingers, held at liquid nitrogen temperature. Evidence was found in Mössbauer spectroscopy to suggest that interfacial and intraparticle structures in the nanoglasses are different. Si_3N_4 nanoglasses have been made (Pechenik et al., 1993) and consolidated under high pressures of 5 GPa; particles were $\approx$ 17 nm in diameter. On heating Si_3N_4 nanoglass compacts to around 1200^0C. A dramatic increase of Vicker's microhardness was noted, which was attributed to partial sintering of Si_3N_4 particles which were random close packed in the compact. Nanoglasses are a rapidly growing area of glass research.

References:

Baldwin, C. M., R. M. Almeida and J. D. Mackenzie, 1981, J. Non-Cryst. Sol., **43**, 309.

Banarjee, S., and A. Paul, 1974, J. Am. Ceram. Soc., **57**, 286.

Cotton, F.A., 1971, Chemical Applications of Group Theory (Wiley Interscience, New York).

Debye, P., 1929, Polar Molecules (Dover Publications, Inc., New York).

Edward, R. J., A. Paul and R. W. Douglas, 1972, Phys. Chem. Glasses, **13**, 137.

Fleming, J.W., 1993, in Experimental Techniques in Glass Science, eds. C.J. Simmons and O.H. El-Bayoumi (The American Ceramic Society, Ohio) p. 1.

France, P. W., S. F. Carter and J. M. Parker, 1986, Phys. Chem. Glasses, **27**, 32.

Jing, J., A. Kramer, R. Birringer, H. Gleiter and U. Gonser, 1989, J. Non-Cryst. Sol., **113**,167.

Kittel, C., 1976, Introduction to Solid State Physics (John Wiley & Sons, Inc., New York).

Lewis, M.H., 1989, Glasses and Glass Ceramics (Chapman and Hall, New York).

Narasimham, P. S. L., and K. J. Rao, 1978, Proc. Ind. Acd. Sci. (chem. Sci.), **87**, 275.

Neuroth, N., 1987, Opt. Eng., **26**, 96.

Paul, A., 1982, Chemistry of Glasses, (Chapman and Hall, London)

Pechenik, A., G. J. Piermarini and S. C. Danforth, 1993, Nanostrut. Mater., **2**, 479.

Rao, K. J., 1980, Bull. Mat. Sci., **2**, 357.

Snitzer, E., 1989, in Current Trends in the Science and Technology of Glass, eds., H. Jain, A.R.Cooper, K.J.Rao and D. Chakravorty (World Scientific, Singapore) p., 279.

Sobha, K.C., and K. J. Rao, 1996, J. Phys. Chem. Sol., **57**, 1263.

Vaidhyanathan, B., C. Prem Kumar, J. L. Rao and K. J. Rao, 1997, J. Phys. Chem. Sol., **59**, 121.

Varshenya, A. K., 1994, Fundamentals of Inorganic Glasses, (Academic Press, San Diego).

Yamane, M., and Y. Asahara, 2000, Glasses for Photonics, (Cambridge Univ. Press, UK).

A theory has only the alternative of being right
or wrong. A model has a third possibility
– it may be right but irrelevant.
- Manfred Eigen.

CHAPTER 12

OXIDE GLASSES

In this chapter some salient aspects of a variety of oxide glass systems will be summarized. Oxide glasses are historically the oldest and industrially the most exploited. Typical compositions and areas of application of the present day industrial glasses are given in Table 12.1. They are all silicate or alumino-borosilicate glasses containing a variety of monovalent and divalent oxides. Oxide glasses not containing silica are generally of limited volume in terms of consumption and used only in speciality applications. Therefore we begin with a discussion of silica and silicate glasses.

Table 12.1: Typical compositions of industrial glasses (After Wada, 1999).

Glass	SiO_2	Al_2O_3	B_2O_3	CaO	MgO	Na_2O	K_2O	PbO	Other
Sheet glass by float	72.6	1.8	-	7.9	3.8	12.2		-	0.7
Container glass	72.8	1.6		11.3		13.8		-	0.5
Crystal glass	56.9	-	-	-	-	2.8	13.6	26.0	0.3
Optical glass SF6	26.9	-	-	-	-	0.5	1.0	71.3	0.3
Optical glass BK7	66	-	12.4	-	-	8	12	-	1.6
Laboratory ware	80	2.25	13	-	-	3.5	1.15	-	0.9
Electric glass (stem)	57	1	-	-	-	3.5	9	29	0.5
TV panel glass	63.8	1.3	9.4 (SrO)	2.9	2.2 (BaO)	7.2	8.8	2.8	1.6
TV funnel	51	4	-	8[a]	-	6	7.5	23	0.5
TV neck	47	3.3	-	3.4[a]	-	3	10	33	0.3

Silica and silicate glasses

Silica is the archetypal tetrahedral glass. Silicon is coordinated to 4 oxygens and each oxygen is coordinated to 2 silicons so that the structure can be considered as a three-dimensional network of corner connected [$SiO_{4/2}$] tetrahedra. Since crystalline SiO_2 also contains the same [$SiO_{4/2}$] tetrahedra in its well known three phases namely quartz, crystobalite and trymidite, there have always been attempts to relate the structure of SiO_2 glass with the structure of one of the phases of crystalline SiO_2. In chapter 4, the radial distribution function (RDF) of SiO_2 glass determined experimentally using X-ray and neutron diffraction techniques were discussed. SiO_2 glass is made by allowing molten silica to cool at moderate rates of cooling. Its T_g is around 1200 ^{0}C. Therefore, the crystalline phase of SiO_2, whose structure is relevant for comparison is cristobalite. But the comparison has limited use because beyond suggesting that the same [$SiO_{4/2}$] tetrahedra constitute the building blocks in both crystalline and glassy phases, there is little else. The structure of silica glass has been understood satisfactorily on the basis of the CRN model of Zachariasen, which was discussed in chapter 2. The RDF of SiO_2 glass reveals that Si-O-Si bond angles have a broad distribution and the peak of the distribution occurs at 144°. This distribution of Si-O-Si bond angle is the primary factor in removing the three-dimensional periodicity of the crystalline form. Si-O bond lengths in the glassy and crystalline forms are comparable. The first peak in RDF is narrow and is consistent with the presence of tight SiO_4 units.

Si and O have electronegativities of 1.90 and 3.44 respectively which suggests that Si-O bond is almost 50 % ionic. Arguably this ionicity is sufficient to enable Si-O-Si angle to have the wide spread which it has. If in the glass oxygens are treated as oxygen ions with two negative charges and with the radius of 1.32Å, the tetrahedral void has a radius of 0.30Å, which is slightly smaller than the known radius of Si^{4+} ion (0.39Å). But the openness of the network (CRN) of silica also suggests that the directionality of Si-O bonds is quite strong. The Si-O-Si bond angle distribution, with its peak value of 144°, is possible only when oxygen orbitals are largely hybridised as *sp* (180°) and sp^2 (120°). As a result of this only one of the lone pairs of oxygen is present in the hybridised orbital. The other pair of electrons is present in a pure *p*-orbital, the *p*-electrons of the oxygen can give rise to back bonding to Si through $d\pi$-$p\pi$ interaction. This back bonding contributes not only to bond energy and the rigidity of the tetrahedra but to the shortening of the Si-O bond length

(less than the sum of the covalent radii). Quantum chemical Hartree-Fock (HF) calculation using the STO-3G* method (which includes 3*d* orbitals of Si in the calculations) has also revealed that the most stable structure corresponds to Si-O-Si bond angle of 144° (Lasaga and Gibbs, 1987).

MD simulations have been reported on SiO_2 and SiO_2-based glasses using a variety of potentials (Parker and Price, 1989; Damodaran et al., 1988; Verhoef and Hartog, 1992; Zirl and Garofalini, 1990; Soules, 1979; Soules and Busbey, 1981; Huang and Cormack, 1992; Abramo et al., 1992; Vessal et al., 1992; Elliott, 1992). Of particular interest is the use of Tsuneyuki et al. (1988; 1989; 1990) potentials, which have been constructed using fractional charges on Si and O, and which can reproduce the structure and compressibility of α-quartz. This potential gives the Si-O-Si bond angle distribution for fused quartz, which is in excellent agreement with experiments. The importance of this approach is that it emphasizes the need for using partial charges and adjusted two body potentials without requiring the use of three body potentials to restrict the range of any of the bond angles. These adjusted charges are generally lower than what one would use in a strictly ionic model with Born-Mayer-Huggins (BMH) potential. The actual charges on the atoms in a glass (for that matter in any solid) has always been difficult to assess since no material consisting of more than one type of atom can possess either perfect covalent linkages or are formed through complete charge transfer. Hetero-polar bonding always leads to only a partial charge flow from one atom to the other.

Reasonable estimate of the partial charges on atoms in a molecule or in a crystalline solid can be made using elaborate quantum chemical calculation. But in glasses, lacking in three-dimensional periodicity, such calculations are not only prohibitive but still insignificantly accurate. A thoughtful and conceptually sound method of estimating partial charges was developed by Sanderson (1983). In fact Sanderson's approach to bonding is quite helpful in understanding a variety of phenomena occurring in glasses. The basis of this procedure is that when a bond is formed between two atoms A and B with different electronegativities, there is an electron flow from less electronegative to more electronegative atom. The electron transfer ceases when the electronegativities become equal. This is because when electrons are accepted, the electronegativity of the acceptor atom decreases and when donated the electronegativity of the donor atom increases. Therefore, bond formation corresponds to a state of electronegativity equalization. This can be compared with metal-insulator or metal-semiconductor junctions, where electron flow stops

when the chemical potentials are equalized. Thus, electronegativity acts at the inter-atomic level in the same manner as free energy or chemical potential does in bulk materials. The assumption that electronegativities are equalized during bond formation has been shown to be correct by quantum chemical calculations (Parr, 1978). In practice, the calculation of partial charges involves the following stages. (1) When several atoms are involved in formation of a group of bonded atoms, it is assumed that all atoms possess the same average electronegativity, $\chi_{(average)}$, which is given by the geometric mean of the electronegativities of all the bonded atoms. (2) If an atom or a molecule or a group (structural entities) carry a charge which is assumed to be integral, the change in its electronegativity $\Delta\chi$, for a change of charge equal to unity is assumed to be given by

$$\Delta\chi = 1.56\sqrt{\chi} \tag{12.01}$$

Then the application of the electronegativity equalization principle can be illustrated as follows. Consider $Na_2Si_2O_5$, which consists of $[SiO_{3/2}O]^-$ units. Let us suppose that the electronegativity equalization has taken place and that the atoms in $[SiO_{3/2}O]^-$ group have effective electronegativity equal to χ_{eff}. Therefore, for the Si atom the change in electronegativity is $(\chi_{eff} - \chi_{Si})$. Similarly for the oxygen atom it is $(\chi_{eff} - \chi_O)$. As a result of this the atoms carry net charges – they are not any more neutral. If there is a change of unit positive charge on Si atom, its electronegativity would have changed by $1.56\sqrt{\chi_{Si}}$. Therefore the partial charge, Δ, on Si for which the electronegativity change is equal to $(\chi_{eff} - \chi_{Si})$ as a result of bonding is given by,

$$\Delta_{Si} = \frac{\chi_{eff} - \chi_{Si}}{1.56\sqrt{\chi_{Si}}} \tag{12.02}$$

Similarly for the case of oxygen atom also there is a partial charge on it which is given by,

$$\Delta_O = \frac{\chi_{eff} - \chi_O}{1.56\sqrt{\chi_O}} \tag{12.03}$$

Since there is one Si atom and 2.5 oxygen atoms in $[SiO_{3/2}O]^-$, the net

charge on it (-1) must be equal to the sum of the partial charges on the atoms:

$$1.0\Delta_{Si} + 2.5\Delta_O = -1 \tag{12.04}$$

There are three equations (12.02 to 12.04) and three unknowns (Δ_{Si}, Δ_O and χ_{eff}), which are readily solved. The partial charges work out to be Δ_{Si}= +0.116; Δ_O = -0.446. The net charge on Q_3 is $1.0\,\Delta_{Si} + 2.5\Delta_O = -1$. We will be making reference to this method of calculating partial charges in the discussion of several glasses discussed in this and later chapters.

Anomalous properties of silica glass

Although SiO_2 is a typical inorganic glass, it is also atypical in many ways. Several properties of vitreous silica are known to vary anomalously at low temperatures. Anomaly in the low temperature specific heat is the most notable and well investigated. This is reflected in serious disagreement between Debye temperatures calculated from thermal and acoustic measurements. θ_D (thermal) and θ_D (elastic) are respectively given by (Anderson and Dienes, 1960),

$$\theta_D \text{ (thermal)} = T\left(\frac{464.5n}{C_v}\right)^{\frac{1}{3}} \tag{12.05}$$

$$\theta_D \text{ (elastic)} = \frac{\hbar}{k}\left(\frac{3N}{4\pi V}\right)^{\frac{1}{3}} v_M \tag{12.06}$$

where T is the temperature of the measurement of C_v, n is the number of atoms in the unit of composition, $\hbar$ and k are the Planck and Boltzmann constants respectively, N is the Avagadro number, V is the mean molar volume (molar volume divided by n) and v_M is the mean sound velocity ($v_M^{-3} = v_L^{-3} + 2v_S^{-3}$, where v_L and v_S are longitudinal and sheer velocities). θ_D values calculated from both thermal and elastic data show a dip in the region of 10 to 15 K, but their extrapolation to 0 K indicates that θ_D (elastic) is 600 K compared to θ_D (thermal) of 450 K. This is attributed

to excess specific heat at very low temperatures arising from the presence of non-acoustic transverse mode of vibrations of the oxygen ion in SiO_2.

The behaviour of elastic moduli of vitreous silica is also anomalous. The Young's modulus seems to continuously increase in the region of 100 to 1000 K. This has been understood on the basis of the experimentally observed extremely low values of thermal expansivity of vitreous silica. The modulus, M, can be treated as a function of any two thermodynamic variables; $M \equiv M(V, T)$ or $M \equiv M(P, T)$. The temperature dependence of the modulus can therefore be written as,

$$\frac{dM}{dT} = \left(\frac{\partial M}{\partial V}\right)_T \left(\frac{\partial V}{\partial T}\right)_P + \left(\frac{\partial M}{\partial T}\right)_V = \alpha V \left(\frac{\partial M}{\partial V}\right)_T + \left(\frac{\partial M}{\partial T}\right)_V \qquad (12.07)$$

where α is the coefficient of thermal expansivity. Since α is very small, the sign of (dM/dT) is the same as that of $(\partial M/\partial T)_V$ and it has been shown that when α is very small, the sign of $(\partial M/\partial T)_V$ is positive at high temperatures, Although it can be negative at very low temperatures.

Similarly, the variation of refractive index with temperature of vitreous silica is found to be positive in contrast to the behaviour observed in other materials where it is negative. This is again a consequence of very low values of α. Even more anomalous is the variation of compressibility of vitreous silica with pressure, which was found to increase with pressure. This is also intimately connected with the negative expansivity coefficient of vitreous silica below 200 K, indicating that some of the vibrational modes must be characterized by negative Grüneisen constants (Grüneisen constant of a mode j is given by $\gamma_j = -(d \ln v_j / d \ln V)$). The contributions of these modes cause a decrease of the moduli with increasing pressure, which implies that the compressibility increases with pressure. The decrease in volumes also implies that the bent Si-O-Si bonds become even more bent at higher pressures, implying less and less participation of oxygen 2*s* orbital in bonding. This decreases the bond energy which qualitatively accounts for further bending of Si-O-Si becoming easier. Another explanation is based on assuming two different distributions of Si-O-Si bond angles (chapter 2). Similar anomalous variation of properties are exhibited by other tetrahedral glasses like GeO_2, BeF_2 and $Zn(PO_3)_2$ also.

Pure silica is perhaps the only single component glass which has a number of practical applications but the making of pure SiO_2 glass is very expensive because the working temperatures required for shaping pure

SiO_2 glass is around 2000 ^{0}C. Since extremely pure SiO_2 is needed for fibre optic applications, several organometallic vapour decomposition methods have been developed, which was discussed earlier in chapter 11. Sol-gel technique also provides a convenient route for making pure SiO_2 objects, but retention of hydroxyl groups in resulting glasses is a problem for its fibre optic applications. For several other applications, high SiO_2 glasses such as Vycor are required. Vycor glass is made by exploiting the phase separation properties of silicate and borosilicate glasses which we will discuss later in this chapter.

Crystalline SiO_2 (quartz) under pressure is known to undergo phase transition to stishovite (Baur and Khan, 1997) in which Si is 6-coordinated. 6-coordinated Si forms in binary silicophosphate glasses as a consequence of its chemistry (see later).

By the addition of alkali, silica glasses undergo modification as discussed in Chapter 2. The alkali ions locate themselves in the structure near the NBOs. It is generally assumed that the degradation of the network is systematic as the alkali concentration is increased. The modification results in the formation of meta, pyro and ortho-silicates in that order. $[SiO_{4/2}]^0, [SiO_{3/2}O]^-, [SiO_{2/2}O_2]^{2-}, [SiO_{1/2}O_3]^{3-}$ and $[SiO_4]^{4-}$, which are present in these glasses, are designated as Q_4, Q_3, Q_2, Q_1 and Q_0 respectively, where the subscripts indicate the number of BOs centered on the given Si atom through which it is connected to other Si atoms in the glass structure. One of the most powerful techniques, which has been used to identify and quantify these structural species is the HR MAS NMR of ^{29}Si. The Q_n species exhibit characteristic chemical shifts, δ. Since the chemical shifts are a consequence of partial charge on Si in its chemical state, one would expect a correlation between Si chemical shift δ and the partial charge on Si atom. Partial charges also give a measure of the de-shielding (or shielding) of the Si nucleus. The correlation is shown in Figure 12.01. Further, the hierarchy in the modification, namely $Q_4 \rightarrow Q_3 \rightarrow Q_2 \rightarrow Q_1 \rightarrow Q_0$ also appears to be not strictly followed. NMR experiments in $Na_2O{:}3SiO_2$ glass, indicates presence of both Q_2 and Q_4, in addition to Q_3 where as only Q_3 is expected to be present. This is possible only when there is a structural disproportionation of the type (Schramm et al., 1984; Prabakar et al., 1991)

$$2Q_3 \rightarrow Q_4 + Q_2 \qquad (12.08)$$

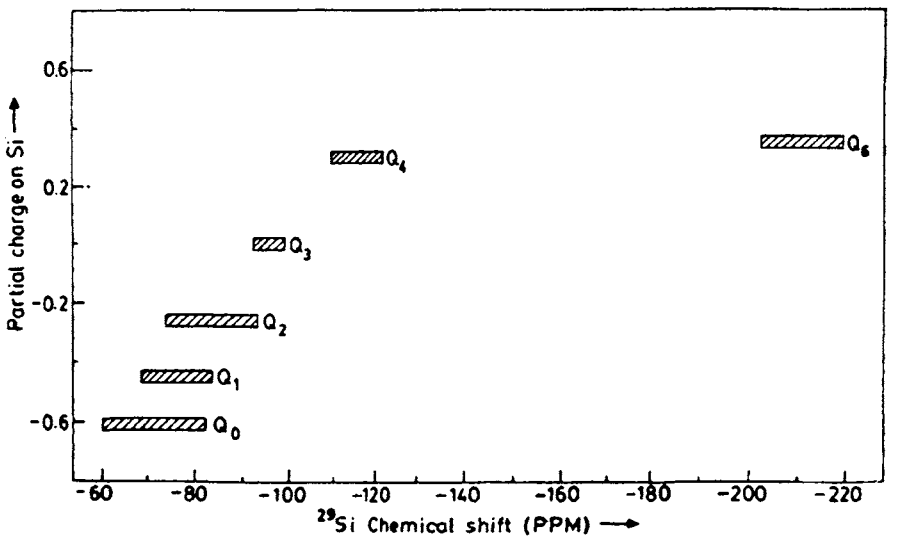

Figure 12.01. Plot of partial charges on Si against ^{29}Si chemical shifts (After Prabakar et al., 1991).

It is possible that such reactions tend to reduce the free energy of the system by increasing the entropy because although the total number of structural units (ΣQ_n) is conserved, introducing more types of species increases the configurational entropy. In Figure 12.01, the range of chemical shifts for the Q_n species which are generally used for identification purposes is shown. These chemical shifts are very sensitive to local structures around Si, their nearest and next nearest neighbours and to the various physico-chemical parameters, like molecular electronegativity, partial charges, basicities etc. *ab initio* molecular orbital calculations have led only to modest progress in this direction. Therefore efforts have been made to correlate the ^{29}Si chemical shifts in silicates to Si-O-T (T = Si or Al; see later) bond angles, state of hybridisation and the group electonegativities. The chemical shift data are available on a very wide range of materials including crystalline silicates and gels.

The chemical shift is determined by atleast three primary influences. One arising from the actual location – the connectivity - of the ^{29}Si atom (surrounded by a variety of other distinguishable Q_n species). Second, the chemical influence which is due to the nature of the cation present in the glass. Third, the electronegativity of the structural species in which the Si is located because, it determines the electron density in the species. The structural uniqueness arising from the connectivity in the

glass network can be quantified using graph theoretical techniques. For example, a Q_4 species surrounded by three Q_3 species and one Q_2 species is shown in Figure 12.02 using graphs (Prabakar et al., 1991). Such graphs

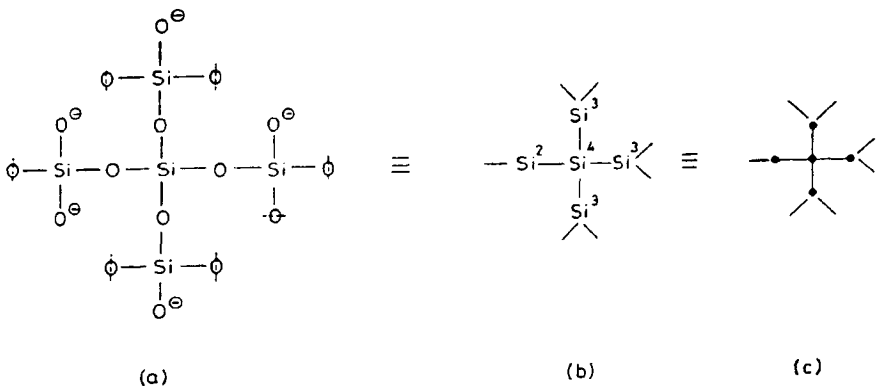

Figure 12.02. Graph representation; detailed (a) and oxygen suppressed (b & c) graphs for the species [$Q_4(3Q_3, Q_2)$] (After Prabakar et al., 1991).

as for a Q_4, uniquely define the structural environment of the species up to its second neighbour, and therefore enable an unambiguous identification of the ^{29}Si atom under consideration. It is assumed that the influence, beyond the second neighbour can be ignored in quantifying chemical shifts. Thus a characteristic quantity G_n of a Q_n species is suggested which is equal to $({}^1\zeta)^4/[{}^0\zeta.{}^2\zeta]$, where ${}^0\zeta$, ${}^1\zeta$, ${}^2\zeta$ are themselves given by

$$
\begin{aligned}
{}^0\zeta &= \sum_i (\delta_i)^{-1/2} \\
{}^1\zeta &= \sum_{i \neq j} (\delta_i \delta_j)^{-1/2} \\
{}^2\zeta &= \sum_{i \neq j,k} (\delta_i \delta_j \delta_k)^{-1/2}
\end{aligned}
\qquad (12.09)
$$

In the above equations, δ_i represents the "valence" or the number of connections which the *i*th Si atom makes with other Si atoms. The functional dependence of G_n on ${}^n\zeta$ has been defined empirically. The influence of the cation on the chemical shift is adequately described by Z^*/r (where Z^* is the unscreened nuclear charge and r is the radius of the modifier cation). The third term is governed by the effective electronegativity, χ_{eff} of the structural unit in which ^{29}Si is located. The

unscreened nuclear charge can be calculated using Slater's screening constants. It is now possible to define a quantity P, where

$$P = \left(\frac{Z^*}{r}\right)^{4-n} \left(\frac{1}{\chi_{eff}}\right) G_n \tag{12.10}$$

It has been shown that a plot of ^{29}Si chemical shifts (Figure 12.03 (a), (b) and (c)) in a variety of alkali-silicate glasses, crystalline silicates and gels

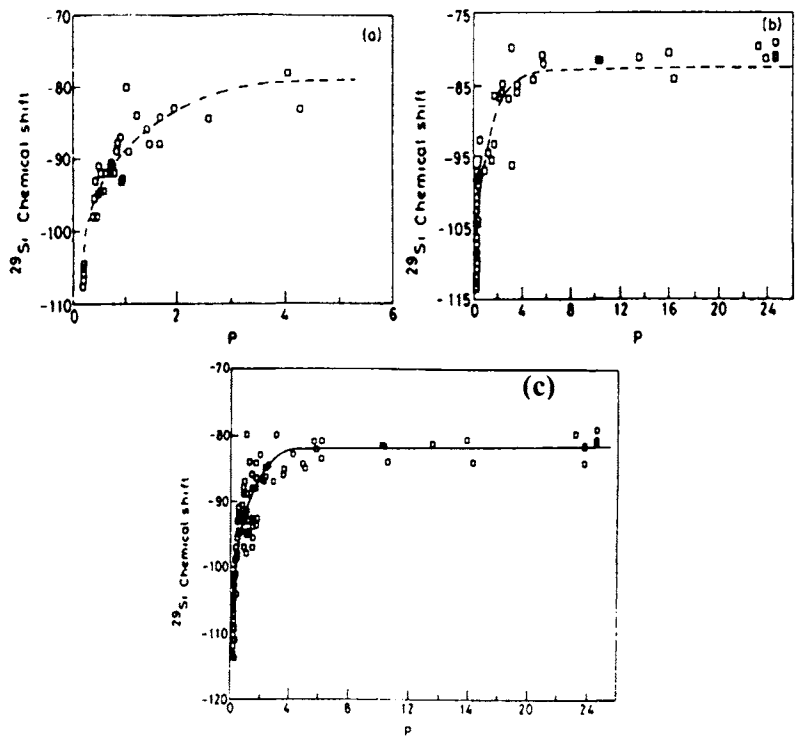

Figure 12.03. ^{29}Si chemical shifts versus the parameter P for (a) alkali silicate glasses, (b) other complex silicate glasses and (c) combined glasses, gels and crystalline silicates. Best fits are indicated by dashed lines (After Prabakar et al., 1991)

vary as a smooth function of P. The variation of δ in Figure 12.03 (a) can be described by the function,

$$\delta(\text{ppm}) = 28\{1 - \exp(-P)\} - 107 \tag{12.11}$$

For the cases of complex silicate glasses, gels and crystalline silicates, all combined, the behaviour of chemical shifts which range from –78 to –108 ppm (118 cases) as a function of P (range of 0.18 to 24.6) can be represented by the function (Figure 12.03 (c)),

$$\delta(\text{ppm}) = 28.4\{1 - \exp(-P)\} - 110.5 \qquad (12.12)$$

Phase separation and spinodal decomposition

A feature of immense practical interest in glass forming alkali silicate glasses is that several of them exhibit sub-liquidus immiscibilities in certain composition regions. This behaviour is exhibited by ternary alkali boro-silicates also. The metastable immiscibility for the case of Na_2O-SiO_2 is shown in Figure 12.04. There are two domes in the figure.

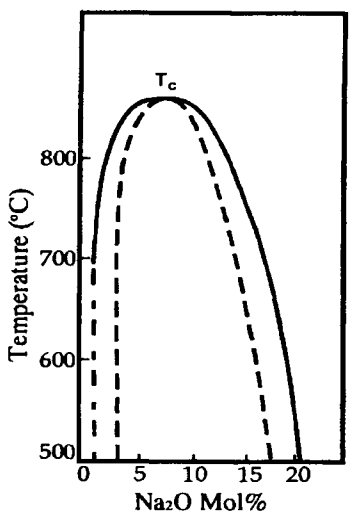

Figure 12.04. Immiscibility cupola for Na_2O-SiO_2 system. (After Filipovich, 1984).

The entire region enclosed by the outer dome represents immiscibility. The inner dome is known as the spinodal. The outer dome is known as the binodal. In the region of composition between the binodal and spinodal lines, phase separation occurs by the nucleation and growth mechanism and leads to the formation of dispersed micro-spherical glass particles in the matrix (see also Shelby, 1997). Spinodal decomposition which takes place inside the dotted region is a special type of phase separation. In order to understand this, consider two materials A and B, melts of which

are completely miscible above a certain temperature $T_1 > T_C$ in all compositions. The composition dependent free energy of such a system can be represented by the top line shown in the Figure 12.05. If the melt is cooled to temperature T_C, the free energy variation appears as in the central line in the figure. If the system is brought down to a temperature T_2, the free energy curve develops two minima at the compositions A_1B_1 and A_2B_2 as in the bottom line in the figure. But the

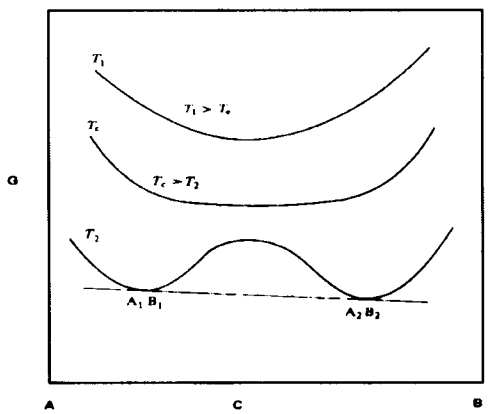

Figure 12.05: Effect of temperature on the free energy-composition behaviour (schematic); $T_1 < T_c < T_2$.

quenching can be performed such that the system is still homogeneous. We may now ask what happens to this system if there is a small fluctuation in composition – say ΔC around C_0? It can be answered by considering the free energy change which occurs due to such composition fluctuation. The free energy, $G(C_0)$ changes to $G(C_0 \pm \Delta C)$ when the composition fluctuates as $(C_0 \pm \Delta C)$. Hence the change in free energy is given by

$$\Delta G = G(C_0 + \Delta C) + G(C_0 - \Delta C) - 2G(C_0)$$

$$= G(C_0) + \Delta C.G'(C_0) + \frac{\Delta C^2}{2}.G''(C_0)$$

$$+ G(C_0) - \Delta C.G'(C_0) + \frac{\Delta C^2}{2}.G''(C_0) - 2G(C_0)$$

Hence,

$$\Delta G = \Delta C^2 . G''(C_0) \tag{12.13}$$

$G' \equiv (\partial\, \Delta G / \partial C)$ and $G'' \equiv (\partial^2 G / \partial C^2)$ are the first and second order partial derivatives at constant temperature and pressure. Therefore the free energy change depends on the sign of $G''(C_0)$. The sign of this is indicated in Figure 12.06 for the various regions. Thus, around the composition close

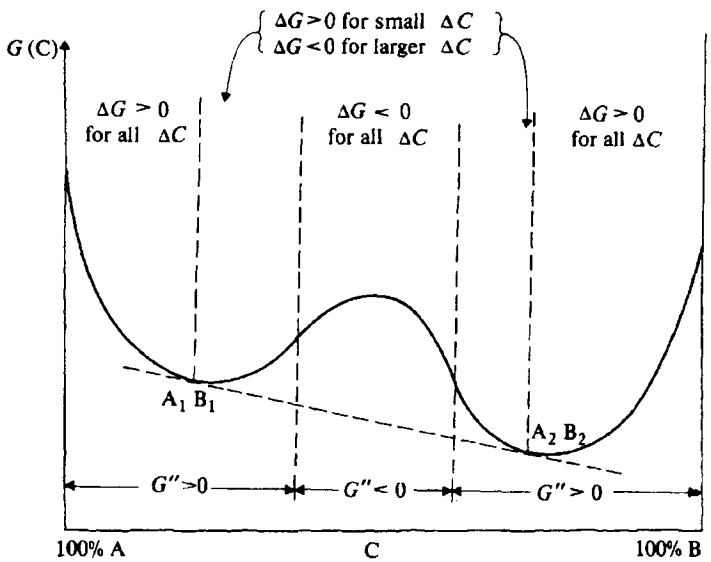

Figure 12.06: Free energy plot indicating the behaviour of ΔG for various fluctuations ΔC (After Shewman, 1969).

to A_1B_1 or A_2B_2, small fluctuations cause increase in ΔG. But in the central region, any fluctuation, small or big, decreases the free energy (ΔG is negative). This leads to gradual decomposition of the material into two phases, one rich in A, other in B. But around A_1B_1 and A_2B_2, large fluctuations are needed to render ΔG negative – the decomposition in this region occurs in a step-like fashion by nucleation and growth mechanism. The loci of the points corresponding to $G''(C_0) = 0$, and $G(A_1B_1)$ and $G(A_2B_2)$ are illustrated in Figure 12.04. They form two domes which touch each other at T_C. The inner dome is the spinodal in which the decomposition is gradual allowing all composition fluctuations. The region between the domes corresponds to compositions which decompose by nucleation and growth mechanism. The compositions between the outer

and the inner dome - between the spinodal and the bimodal - which phase separate by the nucleation and growth mechanism are inherently unstable as they belong to the region between the minima of free energies. An illustration of the phase separation which occurs in the binodal and spinodal regions is shown in Figure 12.07. Most important practical

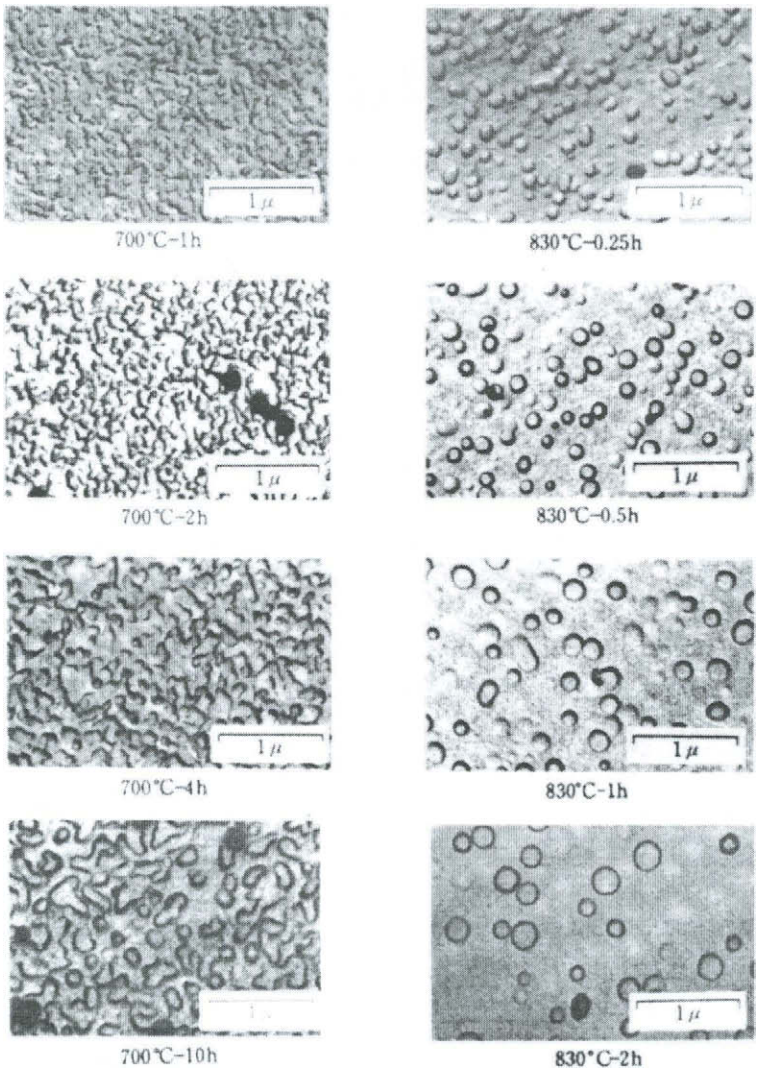

Figure 12.07. Electron micrographs of glasses phase separated by spinodal (left) and nucleation and growth (right) mechanisms. (After Yamane and Asahara, 2000).

application of phase separation of glasses is in making high SiO_2 glasses. Since the same phenomena is exhibited by borosilicate glasses, we cite the example of $8Na_2O{\cdot}20B_2O_3{\cdot}72SiO_2$ glass, which is heat treated between 500 and 800 ^{0}C, when it undergoes a phase separation, which is below its liquidus temperature of 1100 ^{0}C. The phase separation leads to formation of B_2O_3-rich (liquid) and SiO_2-rich (solid) phases, which is cooled to obtain a phase separated glass. The B_2O_3–rich glass is readily soluble in dilute HCl. Therefore, when B_2O_3–rich phase is leached out, a porous silica glass is formed. The glass can be used as such in applications like biological sieves or can be densified by heating to around 1200 ^{0}C when the pores disappear resulting in a SiO_2-rich glass known as *vycor glass*.

Alkaline earth oxides also cause similar modification on SiO_2 network, but alkaline earth oxide containing silicate melts exhibit liquid-liquid immiscibility above the liquidus temperature. Because of their enormous usefulness, a number of binary, ternary etc. silicate glass compositions have been developed and fully characterized. Design of glass ceramics (Beall, 1989; Lewis, 1989) is a technological outcome of controlled crystallization where heterogeneous nucleation is induced by nucleating agents like TiO_2, P_2O_5, ZrO_2, SnO_2, Cr_2O_3 etc. These are not discussed in this book.

SiO_x

SiO_2 is the stoichiometric and stable oxide of Si. But SiO_x ($1.0<x<2.0$) is neither stoichiometric nor stable but it forms as an amorphous material. It is a by-product in Si industry where large single crystalline rods of Si are grown from Si melts held in pure fused quartz containers under argon atmosphere. SiO_x forms as brownish scales in the containers. The structure of SiO_x has been debated (Temkin, 1975), because SiO_x may correspond to either a genuine random network of Si and O with Si-Si bonds or it may be a mixture of extremely fine particles of Si and SiO_2 in appropriate proportions. The NMR of these materials, however, reveal that SiO_x is built up of random network and consist of Si-Si linkages (Dupree and Pettifer, 1984; Ramesh and Rao, 1994). Figure 12.08 clearly shows that SiO_x consists of species like $[SiSi_{1/4}O_{3/2}]$ whose ^{29}Si MAS NMR peaks appear around $\delta = -76$ ppm, alongside the peak at –110 ppm due to $[SiO_{4/2}]$. ^{29}Si MAS NMR of a physical mixture of fine particles of SiO_2 and Si of the same average composition consists of a sharp peak of –81 ppm due to $[SiSi_{4/4}]$ units. Also, the carbothermal reduction and nitridation behaviour of the mixture and the amorphous

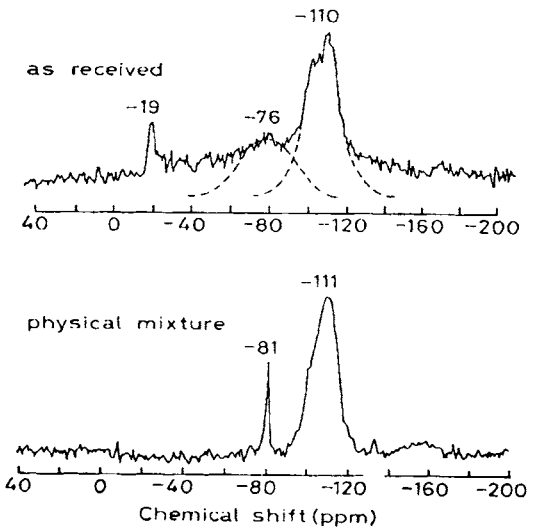

Figure 12.08. Figure at the top is ^{29}Si MASNMR of as received SiO_x. Figure at the bottom is ^{29}Si MASNMR spectrum of fine particle mixture of Si and SiO_2 with the average composition, $SiO_{1.7}$ (After Ramesh and Rao, 1994).

SiO_x powder have been found to be very different by Ramesh and Rao (1994), SiO_x (x=1.7) gives rise to Si_2N_2O, whereas the mixture of Si and SiO_2 gives rise to α-Si_3N_4.

B_2O_3 and borate glasses

B_2O_3 and borate glasses have been widely investigated, although their technological applications has been mostly in combination with SiO_2. B_2O_3 can be considered as having the highest glass formation tendency because molten B_2O_3 does not crystallize by itself even when cooled at the slowest rate. B_2O_3 crystallizes only under pressure. Boron is the first member of the Group III in the periodic table and the size of B^{3+} ion is very small. B^{3+} can fit into the trigonal void created by 3 oxide ions in mutual contact and form a $[BO_{3/2}]$unit. Nevertheless, B-O bond is even more covalent than the Si-O bond.$[BO_{3/2}]$units are the primary building blocks in all borate glasses. Since B in $[BO_{3/2}]$ is electron deficient (in covalently bonded $[BO_{3/2}]$unit, B has just 6 electrons in its outermost orbit) it can accept 2 more electrons in the form of a dative bond. This happens when an oxide ion is available in the glass composition for such

additional bonding. $[BO_{4/2}]^-$ units are thus readily formed in borate glass structures. $[BO_{4/2}]^-$ units are tetrahedral. From the known covalent radii of B and O, one would expect a B-O bond distance in $[BO_{3/2}]$ unit to be 1.53 Å, which is larger than its experimentally known B-O distance of 1.38 Å. This reduction in the observed distance suggests significant back bonding from the oxygen *p*-orbitals to the vacant *p* orbital on B (Balta and Balta, 1976). Several structural studies have been performed on B_2O_3 and it may be fair to say that there is no consensus as to how the building blocks $[BO_{3/2}]$ units are connected in the structure. It is considered that boroxol ring, which consists of $3[BO_{3/2}]$ units in hexagonal arrangement of six B-O bonds is a major constituent of glass structure. Boroxol* is particularly stable because of the possible delocalisation of the electrons among the π bonded *p*-orbitals of B and O perpendicular to the B-O-B plane as shown in Figure 12.09. On the basis of kinetic studies using XRD, the possible stabilisation energy of boroxol unit is found to be 11.8 kcal per boroxol (Balta and Balta, 1976). Glass structure is therefore considered as made up of significant proportions (80% B atoms or more) of boroxol units which are connected through simple BO_3 units. But the structural models of B_2O_3 glass, in general, fail to account for its observed low density (Gaskell, 1997). During modification by added ionic oxides,

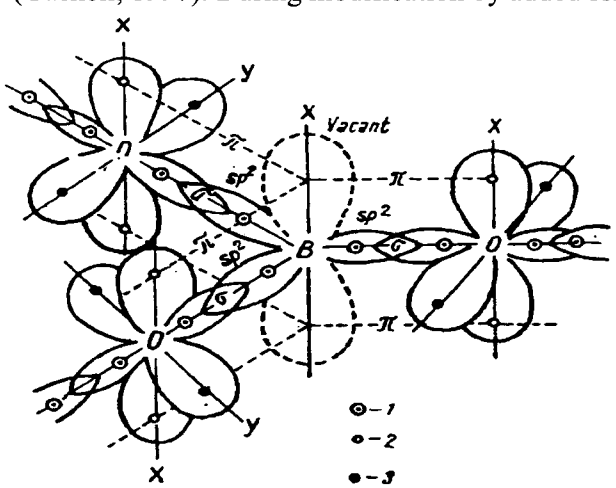

Figure 12.09. The superposition of orbitals in B_2O_3; (1) σ-electrons; (2) π-electrons; (3) lone pair electrons.

* Several authors prefer the name boroxyl to boroxol. In this book, boroxol is used as the nomenclature.

it is suggested that one of the $[BO_{3/2}]$ units in the boroxol structure is transformed into a tetrahedral $[BO_{4/2}]^-$ unit. This destroys the planarity of the boroxol and therefore it shifts the ring breathing vibration of boroxol at 790 cm^{-1} to 806 cm^{-1} in the Raman spectra.

Vibrational spectroscopy has been used with advantage to understand the structure of borate glasses. The classic work of Krogh-Moe (1965) indicated the possible presence of 5 different types of borate species in the glass structure (Figure 12.10). These are the species which

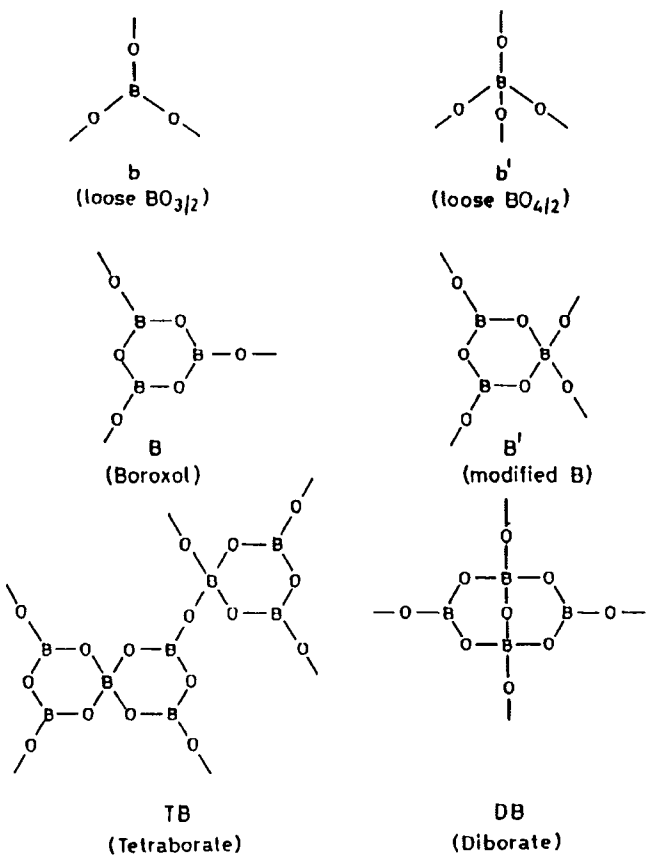

Figure 12.10. Different structural units present in alkali borate glasses.

form when B_2O_3 glass is modified by the addition of alkali or alkaline earth oxides. In the simplest binary alkali borate glasses, alkali oxide initially converts the trigonal borons ($[BO_{3/2}]$ units) to tetrahedral borons ($[BO_{4/2}]^-$ units) by the coordination of O^{2-} to two trigonal borons

$$2[BO_{3/2}]^0 + O^{2-} \rightarrow 2[BO_{4/2}]^-$$
$$2B_3 + O^{2-} \rightarrow 2B_4 \qquad (12.14)$$

The formation of B_4 proceeds till a maximum of 50 % B_3 are converted into B_4. When the modifier concentration increases further, the concentration of B_4 decreases rapidly. The composition in which B_3 and B_4 are equal is the diborate composition, and the corresponding mole fraction of the alkali oxide is 0.33. In Figure 12.11, the variation of

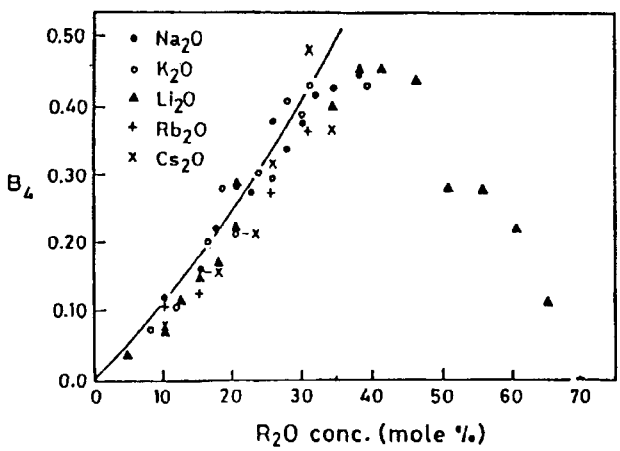

Figure 12.11. Variation of B_4 with R_2O concentration (After Zhong and Bray, 1989).

$N_4 (\equiv B_4 = B_4/(B_3 + B_4)$ in binary borate glasses) is shown as a function of alkali oxide in mole%. The maximum of N_4 is however, dependent on the size of the alkali also. Past the composition corresponding to maximum in Figure 12.11, the re- conversion of B_4 to B_3 starts and N_4 drops rapidly. This has consequences on various observed properties of borate glasses and the effect has been described as 'borate anomaly'. The tetrahedral $[BO_{4/2}]^-$ ion is not associated with an NBO, although the unit carries a negative charge. It only means that the negative charge is spread diffusely on the atoms of the BO_4 unit with a significant value on B itself. Except in the tight structure of diborate units, two B_4 units are not generally directly connected in borate glasses. In lithium containing glasses, even the diborate glass does not seem to favour B_4-B_4

connections (Selvaraj and Rao, 1984). The connectivity of the tetrahedra and the diffuse spread of the negative charge together give rise to open structure in borate glasses for alkali oxides mole fractions < 0.33. For alkali oxide mole fractions > 0.33, B_4 units breakdown and form $[BO_{1/2}O_2]^{2-}$ units,

$$\begin{aligned} 2[BO_{4/2}]^- + O^{2-} &\rightarrow 2[BO_{1/2}O_2]^{2-} \\ 2B_4 + O^{2-} &\rightarrow 2B_3^{2-} \end{aligned} \qquad (12.15)$$

As a consequence, there is a network collapse and better volume utilization. Therefore, rapid reversals occur in the variation of molar volume, refractive indices, T_g, thermal expansivity etc., as a function of alkali composition. All of these variations are directly or indirectly related to energy density and the observed variations are often referred as borate anomaly. An example of the variation of some of these properties is shown in Figure 12.12.

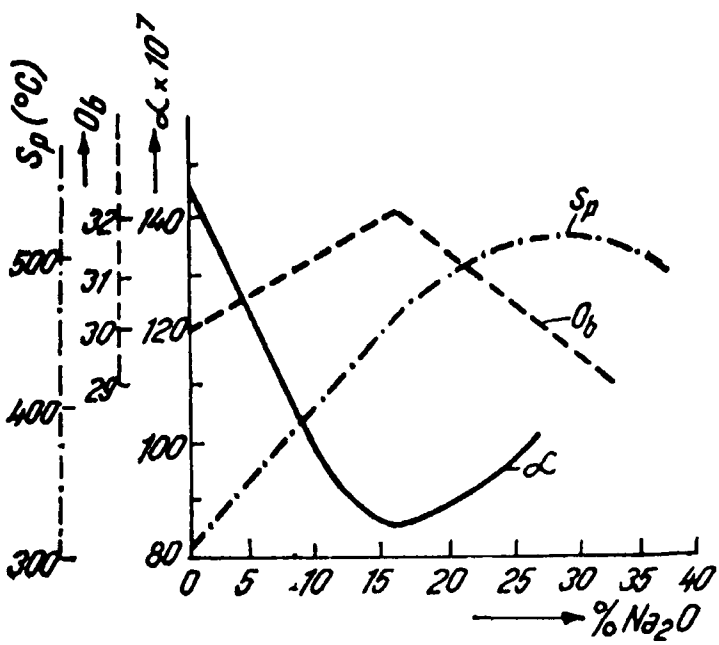

Figure 12.12: Variation in the number of bridging oxygen atoms (O_b), the coefficient of thermal expansion (α) and the softening temperature (S_P) as a function of alkali-oxide concentration in a B_2O_3 – containing binary glass (After Balta and Balta, 1976).

GeO_2 and germanate glasses

GeO_2 also can be quenched into a glass and GeO_2 glass is expected to be structurally very similar to SiO_2. Because of its high melting point and absence of large volume applications, investigations in GeO_2 glasses have been largely of academic interest. Modification of GeO_2 does not proceed the same simple way as in SiO_2. Oxide ions convert Ge initially to octahedrally coordinated Ge, increasing the cross-linking in the network. But above 15-20% alkali oxide, the octahedrally connected structure breaks down rapidly giving rise to various Q_n species, ($Q_n = [GeO_{n/2}O_m]^{m-}$ $(n+m) \leq 4$). This has consequences on a number of properties of alkali germanate glasses, which exhibit anomalous variations. This 'germanate anomaly' was first observed in infrared spectroscopic investigations by Murthy and Kirby (1964). The infrared frequency corresponding to one of the GeO_n stretching modes (880 cm^{-1}) tends to red-shift by about 100 cm^{-1} with increased alkali content. Above 20 mole% alkali, the octahedra appear to revert to tetrahedra with attendent formation of different Q_n species. The infrared spectra of several compositions are shown in Figure 12.13. Formation of octahedrally coordinated Ge is completely suppressed when Al_2O_3 is added to these glasses (Mundy and Jin, 1986). This is

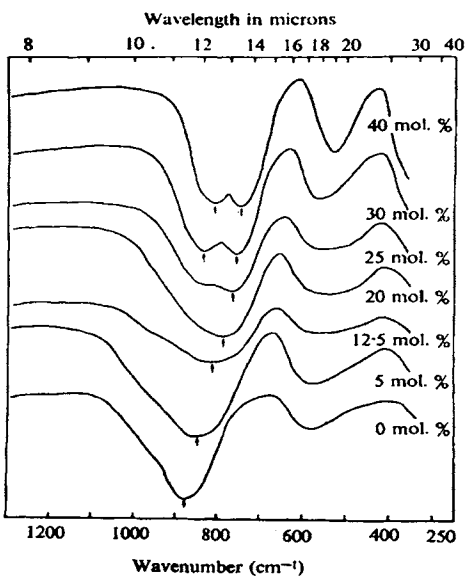

Figure 12.13. Infrared spectra of glasses in the system xK_2O-(100-x)GeO_2 (After Murthy and Kirby, 1964).

understandable because aluminium enters the network as $[AlO_{4/2}]^-$ for which it needs additional oxygen and therefore takes up all the O^{2-} from the alkalis. It is interesting that this anomaly is suppressed also by the addition of P_2O_5 to the glasses. The reason for this is evidently the high electronegativity of $[POO_{3/2}]^0$ groups. Available O^{2-} ions are preferentially taken up by the $[POO_{3/2}]^0$ groups to form $[POO_{2/2}O]^-$ units in the structure. The GeO_2 network remains unaffected by the alkali and hence the anomaly is suppressed (Kumar et al., 2001). However, when the P_2O_5 content is low so that it leaves exclusive GeO_2 regions in the network, part of the alkali enters these regions which results in the formation of $[GeO_{6/2}]^{2-}$. Formation of these units can be identified in infrared and Raman spectra by the appearance of unique spectroscopic features at 643 cm^{-1} (in Raman) and a well defined shoulder at 802 cm^{-1} (in infrared), both attributable to stretching vibrations (see also Kamitsos et al., 1996). It is worth noting that in Li_2O-GeO_2-P_2O_5 glasses, a composition corresponding to $10Li_2O{\cdot}50GeO_2{\cdot}40P_2O_5$ exhibits a T_g close to 870 K, which is one of the highest T_g for a germanate glass. Glasses in the system GeO_2-B_2O_3 have also been studied and at high percentages of B_2O_3, Ge is reported to acquire octahedral coordination (Margaryan and Piliavin, 1993).

P_2O_5 and phosphate glasses

P_2O_5 also forms a single component glass which however, can be made adopting very difficult preparative procedures (Hudgens and Martin, 1993). The pair correlation function obtained from neutron scattering seems to suggest that vitreous P_2O_5 contains P_4O_{10} molecular entities, although the possibility of the presence of corrugated sheets containing 6-membered rings of $[POO_{3/2}]^0$ units cannot be ruled out. Peaks in the structure factor, (S(Q)), suggest the presence of distances of 4.8 and 3.0 Å in RDF, which are likely to arise from P_4O_{10} molecular units. Modification of P_2O_5 glass by alkalis result in the formation of various Q_n species in the same manner as in silicates or germanates. The basic building block in phosphate glass is a 3-connected and 4-coordinated tetrahedral unit. One of the coordination arises from P=O, which has distinctly shorter bond distance compared to the other three bonds ($r_{P\text{-}O}$=1.581Å, $r_{P=O}$=1.432Å). *ab initio* quantum chemical calculations (Uchino and Ogata, 1995) have confirmed the dominant π-interaction between phosphorous and one of the oxygen atoms often referred to as the terminal oxygen. Structures of

phosphate glasses have been most profitably studied using ^{31}P HR MAS NMR. The free induction decay time of ^{31}P nucleus is significantly shorter than that of ^{29}Si, and therefore the collection of spectra is much easier (in studying the MAS NMR of silicates it is often necessary to add dopant levels of Mn^{2+} in order to reduce free induction decay time). But one of the disadvantages in the study of ^{31}P NMR spectra is the presence of high intensities of the side bands, particularly in glasses with low levels of modification. Although with increasing ratio of alkali oxide to P_2O_5, the structural species gradually change from Q_3 to Q_0 (ultra → meta → pyro → ortho) in alkali phosphate glasses, structural disproportionation referred to earlier in silicate glasses occurs in many phosphate glasses. For example, pyrophosphate glasses such as $Ag_4P_2O_7$ and $Pb_2P_2O_7$ consist of meta and ortho units, besides small amounts of ultraphosphate units (Ananthraj et al., 1986). It is again likely, that this is due to a gain in configurational entropy resulting from multiple speciation. Metaphosphates consist of long chains in the structure while pyrophosphates consist of discrete di-tetrahedral units. But in the glass structure it would be more appropriate to treat pyrophosphate as $[POO_{1/2}O_2]^{2-}$ units, which behave as chain terminators (they attach singly to other groups). Therefore their presence and concentration in the structure lead to a distribution of chain lengths. In phosphate glass, the presence and distribution of chain lengths was first established by van Wazer (1950, 1951) by chromatographic analysis (using aqueous extracts of the phosphate glasses – a unique advantage of these glasses is that their structures remain unaffected during dissolution). A more recent HPLC analysis of a number of phosphate glasses by Sales et al. (1998) is shown in Figure 12.14, where the average chain lengths have been indicated. Van Wazer explained the distribution of chain lengths based on Flory's theory, developed in the context of polymers. But it is important to note that the formation of glasses is easier in metaphosphates than in pyrophosphates. Infact, pyrophosphates appear to undergo structural disproportionation. This step can be visualized as involving the formation of $[POO_{2/2}O]^-$ and $[POO_3]^{3-}$ as the first step.

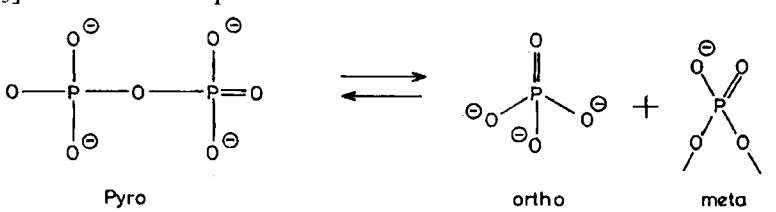

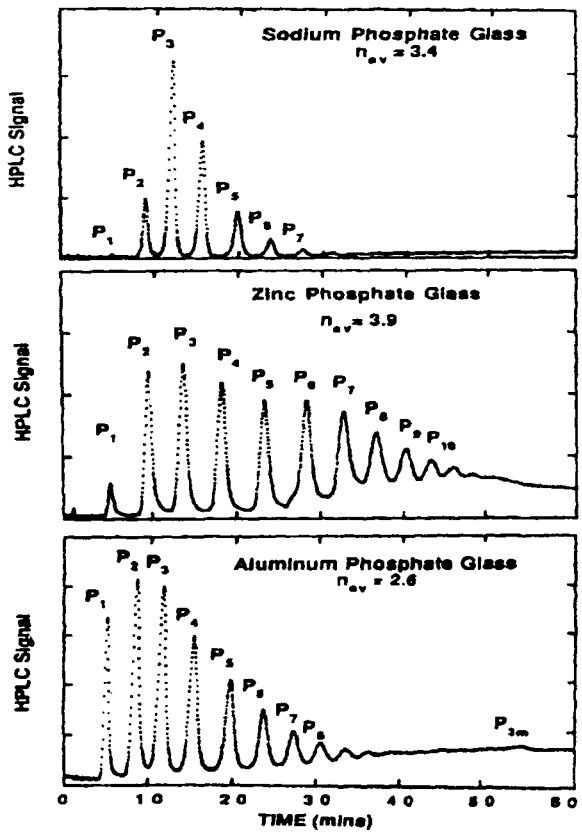

Figure 12.14. High-performance liquid chromatographs from Na- (top), Zn- (middle) and Al-polyphosphate glasses (bottom). Average chain lengths are indicated in each frame (After Brow, 2000).

The metaphosphate unit is like a 'synthon' which adds on to any chain and expands the chain length.

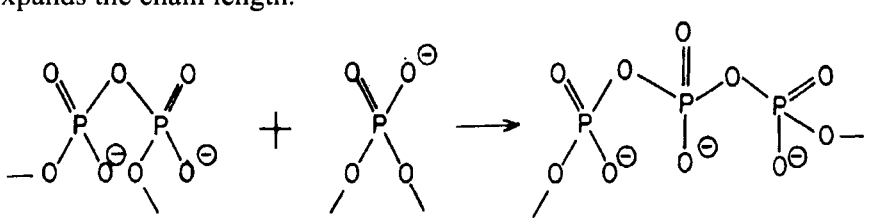

When the metaphosphate disproportionates, it forms ultra- and pyrophosphates. In Q_2 (metaphosphate) units, the P-O^- and P=O establish

resonance and as a consequence become indistinguishable. This indistinguishability manifests in the gradual disappearance of the P=O absorption in vibrational spectra in the region of 1200 – 1300 cm^{-1} (Brow et al., 1994; Brow, 2000) as the concentration of modifier oxide is increased. The range of chemical shifts of the Q_n species in phosphate systems, generally used for identification, is shown in Figure 12.15.

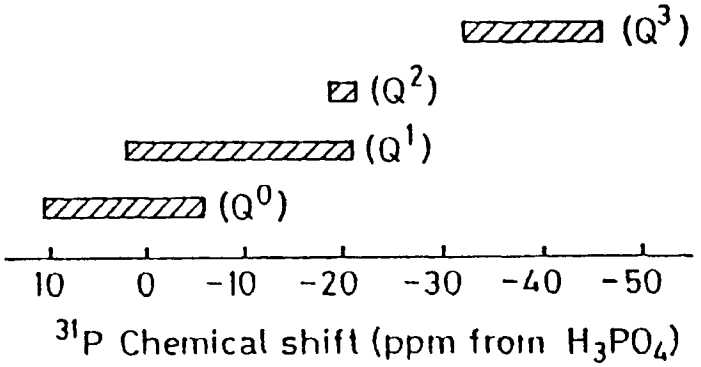

Figure 12.15: Range of ^{31}P MAS NMR chemical shift values for various phosphate groups (After Martin, 1991).

Bridging, non-bridging and terminal oxygens

In the above glass systems, the modification of the primary network in the glass results in the formation of chemically different types of oxygens in the network. For example, in silicates, there can be bridging oxygen (BO) and non-bridging oxygen (NBO) or an oxygen associated with an octahedrally coordinated Si (BO_6; see later). In phosphates, it can be a BO or an NBO or an oxygen double bonded to P, often called the terminal oxygen. In borates, it could be a BO attached to trigonal boron or a BO attached to tetrahedral B or an NBO associated only to trigonal borons. In germanate glasses, it could be a BO or an NBO or a BO associated with octahedrally coordinated Ge. These structurally and chemically different oxygens can be identified and quantified by using X-ray photoelectron spectroscopy. For example, in Figure 12.16, the BOs and NBOs, have been identified in the high resolution XPS of cobalt sodium silicate glasses of composition xCoO · 0.3 Na_2O · (0.7-x)SiO_2. The spectra clearly demonstrate increase of NBO with increasing concentration of CoO. The basis of this study is quite simple. Electron densities in the valence orbitals of oxygen vary for the various species. Valence orbital

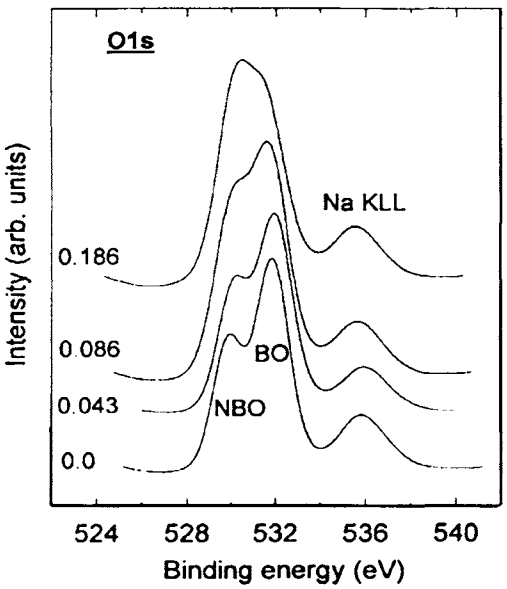

Figure 12.16. High resolution O1s transition for the analyzed glass sample (After Mekki et al., 1997).

wave functions penetrate the region of the core electron wave functions and therefore affect their binding energies. This enables PES to distinguish the nature of oxygen, whether it is BO or NBO or any other.

In chapter 4, we discussed how in the case of alumino-silicate glasses, BO and NBO are identified through O-1s binding energies, which are different for these two oxygens. In Figure 12.17, the O-1*s* spectra for four different silico-phosphate glasses are shown, which illustrates the formation of oxygen species which is in the coordination sphere of the octahedrally coordinated silicon (BO_6). The binding energy of the 1*s* electron in these three types of oxygens, BO, BO_6 and NBO give rise to peaks at 531, 532 and 533.5 eV respectively. Using the peak areas it is possible to quantify the manner of structural modification which occurs in siloco-phosphate glasses. Similar studies have been done in germanate and phosphate glasses also. (Lu et al., 1996; for phosphate glasses).

Complex oxide glasses

The silicophosphate glasses to which reference was made earlier are very interesting from a chemical point of view. It is very difficult to

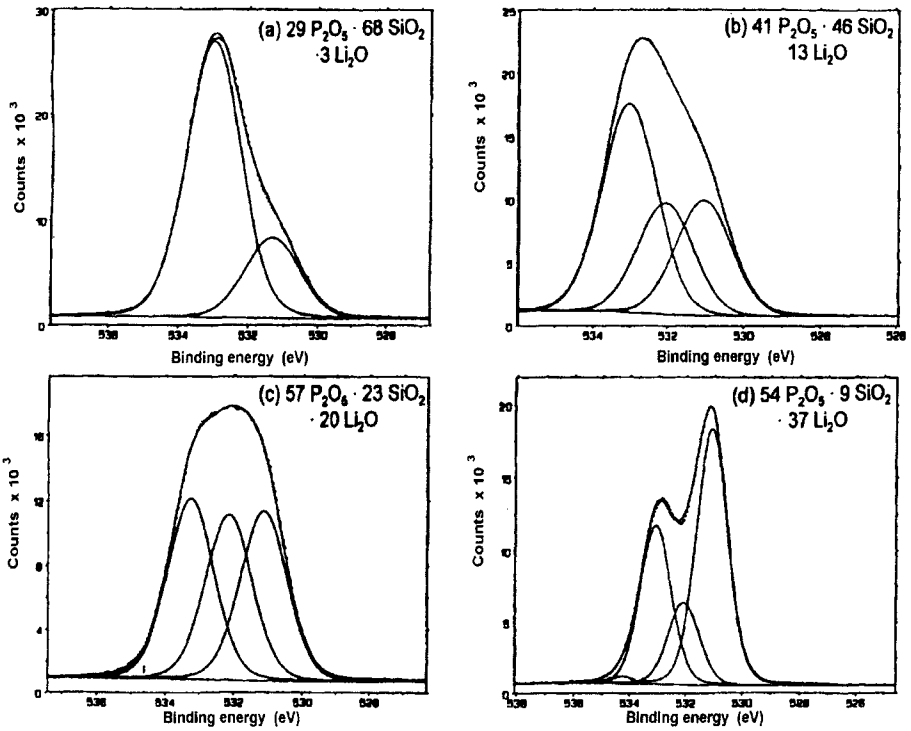

Figure 12.17. Shapes of oxygen 1s spectra of four different glasses including curve fitting by three Voigt functions related to three different types of oxygen BO, BO_6 and NBO. (After Peters et al., 1997).

prepare them by melt-quenching methods because, temperatures required are high, the difference in the melting points of the component oxides is large and P_2O_5 has an extremely high vapour pressure. It is easier to prepare them in the amorphous state by sol-gel route. Silica is introduced as tetra-ethoxy silane (TEOS) and P_2O_5 as phosphoric acid. Alkalis are introduced as nitrates. The xerogels obtained in the usual manner (chapter 2) are gradually heated to sufficiently high temperatures to obtain an amorphous powder of appropriate composition. They are melted (if necessary) and quenched as they do not pose the same problems as during direct melting of the components. It is easier to make lead silicophosphates by quenching melts obtained by heating PbO, SiO_2 and $(NH_4)_2PO_4$, together to temperatures between 1000-1300 °C. In these lead silicophosphate glasses also NMR spectra clearly reveal the presence of octahedrally coordinated silicon at a chemical shift value of -212 ppm. MAS NMR spectra of these glasses are shown in Figure 12.18. The

intensity of the Q_6 peak decreases with decrease of P_2O_5 and increase of PbO contents. This is because when PbO and P_2O_5 are present together, Pb acquires 4-coordination and enters into the network. The reaction can

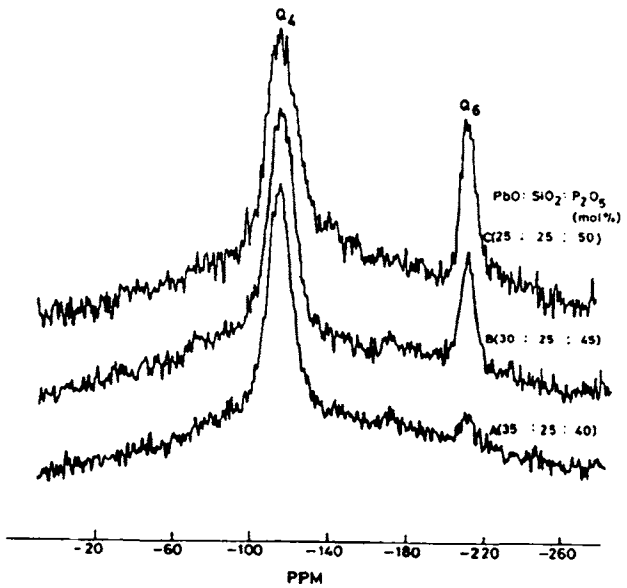

Figure 12.18. ^{29}Si MAS NMR spectra of lead phosphosilicate glasses (After Prabakar et al., 1991).

be represented as

$$2[POO_{3/2}]^0 + [PbO_{2/2}]^0 \rightarrow 2[PO_{4/2}]^+ + [PbO_{4/2}]^{2-} \qquad (12.16)$$

$2[POO_{3/2}]^0$ is the structural representation of P_2O_5 and $[PbO_{2/2}]^0$ of PbO. Thus PbO quantitatively converts $2[POO_{3/2}]^0$ units into $2[PO_{4/2}]^+$. In the process, the effective number of oxygens associated with P decreases and the electronegativity of the $[PbO_{4/2}]^+$ decreases. Thus presence of PbO only decreases the number of $[POO_{3/2}]^0$ units available for coordination to silicon through BOs. The formation of Q_6 requires silicon to become essentially ionic which is possible only when the electron density around silicon is pulled away by the coordinating phosphate groups. The silicon atoms in the glass network, which happen to be coordinated to maximum number (four) of $[POO_{3/2}]^0$ groups appear to be denuded of the electron density because of the high electronegativity of the $[POO_{3/2}]^0$ groups. Such

"ionic" silicon will either migrate or its surroundings rearrange so that it finds itself in an octahedral position with a coordination of six oxygens (not bonded covalently). This denudation or deshielding is responsible for the large negative chemical shift values associated with Q_6 (Q_6 is the same as BO_6 but in Q_6 the reference is to silicon and in BO_6, it is to the oxygen).

The behaviour of lead (Pb^{2+}) is also unique in oxide glasses. It plays a dual role. In some concentration regions it enters into the network structure when it is referred as a network former. In other concentration regions it stays as Pb^{2+} allowing the O^{2-} ion of PbO to break the oxygen bridges when it is described as a modifier. The composition at which the role of lead changes from that of a network former to a network modifier is associated with the changes in the trends of elastic properties. In fact it has been shown in lead phosphomolybdate glasses (Damodaran et al., 1988) that clear change in the trends of bulk moduli occur when the role of lead changes from one of a network former to that of a network modifier. The composition dependent role of lead is dependent on the availability of oxygen coordination that it can get from the host. In (binary) low-lead silicate glasses, conversion of $[PbO_{2/2}]^0$ to $[PbO_{4/2}]^{2-}$ is not possible since there are neither NBOs nor double bonded oxygens. Therefore, PbO acts as a modifier leading to the formation of Q_3. But as the concentration of Q_3 and other defects increase, formation of $[PbO_{4/2}]^{2-}$ becomes easier by coordinating to NBOs. The net reaction actually corresponds to

$$2PbO \rightarrow Pb^{2+} + [PbO_{4/2}]^{2-} \tag{12.17}$$

$[PbO_{4/2}]^{2-}$ does not prefer a tetrahedral structure because Pb^{2+} is an s^2 ion. It prefers pyramidal structure with its lone pair electrons projecting away from the plane of four oxygens. This lone pair, indeed, impedes the motion of alkali ions in alkali lead borate glasses (*stickiness* of the lone pair) (Ganguli et al., 1999) leading to rather low ionic conductivity in spite of the open network structures.

In alumino-silicate glasses, the structural disposition of Al is guided by the same considerations as that of Pb. In pure alumino-silicates, Al is found both in tetrahedral and in octahedral positions (Prabakar et al., 1991). The tetrahedral Al is in network positions, while octahedral Al is present as Al^{3+} and is surrounded by NBOs as confirmed in NMR experiments. This is because if both Al atoms in Al_2O_3 have to occupy tetrahedral positions, it requires four oxygens, $2[AlO_{4/2}]^-$, which it does not possess and $[SiO_{4/2}]^0$ cannot provide it. Therefore, Al_2O_3 behaves as if it has become,

$$2Al_2O_3 \rightarrow 3[AlO_{4/2}]^- + Al^{3+} \qquad (12.18)$$

Thus in the glass, part of Al_2O_3 integrates into the network as $[AlO_{4/2}]^-$ and part of it gives rise to Al^{3+} present in interstitial positions. Al^{3+} ions acquire octahedral coordination (Al^{3+} can be found in five coordinated positions also as it happens in gel-derived amorphous alumio-silicates (Prabakar et al., 1991)). If oxygen can be provided by the presence of modifier oxides, Al readily gets into the network positions and the ionic, octahedrally coordinated Al^{3+} disappears quantitatively. Thus, in $x Na_2O \cdot y Al_2O_3 \cdot (1\text{-}x\text{-}y)SiO_2$ glasses there are two ^{27}Al NMR signals ($\approx$ 1 ppm and $\approx$ 52 ppm) for all values of $y > x$. For $x \geq y$, only tetrahedral Al signals are observed. This is equivalent to stating that all the oxygen from modifier Na_2O is first taken up by Al to convert itself into tetrahedral Al (see also Tasker et al., 1985).

Another interesting observation in aluminosilicate glasses is that much like in crystalline aluminosilicates, the structure seems to disallow Al-O-Al connections in the network. This is the well known Lowenstein rule (Lowenstein, 1954) which is obeyed by zeolitic structures. Whether this is a consequence of the destabilization caused by the repulsion between $[AlO_{4/2}]^-$ units is not clear. A mechanism similar to the avoidance of corner-shared $[BO_{4/2}]^-$ may be operative with regard to $[AlO_{4/2}]^-$ also. Addition of modifier oxides to glass system containing two network formers raises the question of where in the network does modification occur (Rao et al., 1998). For example in silicophosphates, SiO_2 and P_2O_5 form an extensive random network of corner connected $[SiO_{4/2}]^0$ and $[POO_{3/2}]^0$ tetrahedra. Therefore, it consists of Si-O-P, Si-O-Si and P-O-P linkages. When a modifier oxide like Li_2O is added, O^{2-} can modify any one or all the three types of linkages. The result is the formation of pairs ($P\text{-}O^-$,$Si\text{-}O^-$), $2(Si\text{-}O^-)$ and $2(P\text{-}O^-)$ respectively containing NBOs. In order to determine if there is any order in the process of modification among the three types of linkages, an effective approach is based on estimating partial charges on the atoms in such links and examining the electronegativities of the groups. This can be accomplished satisfactorily by the Sanderson's procedure (Sanderson, 1983) discussed earlier. It is done by considering a unit like $\{[SiO_{4/2}]^0[POO_{3/2}]^0\}$ as a whole and calculating the partial charges on the Si, O and P atoms. Similarly, charges on the atoms in Si-O-Si and P-O-P links can also be calculated by considering $\{[SiO_{4/2}]^0[SiO_{4/2}]^0\}$ and $\{[POO_{3/2}]^0[POO_{3/2}]^0\}$ units. For example, in the silica-rich glass, where we do not expect P-O-P linkages to be present, the charges calculated in this manner for Si-O-Si and Si-O-P

links are as follows (given below each atom in the links).

$$\underset{0.463}{\text{Si}} - \underset{-0.232}{\text{O}} - \underset{0.463}{\text{Si}} \tag{12.19}$$

$$\underset{0.527}{\text{Si}} - \underset{-0.186}{\text{O}} - \underset{0.309}{\text{P}} \tag{12.20}$$

It is evident that the O^{2-} ion which approaches the bonding sites (linkages) experience lower coulombic repulsion and higher coulombic attraction with Si-O-P bonds than with the Si-O-Si bond. We should, therefore, expect that modification occurs on the Si-O-P linkage. The result of modification is formation of $[SiO_{3/2}O]^-$ and $[POO_{2/2}O]^-$. But the MAS NMR results suggest that $[SiO_{3/2}O]^-$ is not formed at all. The reason for this is quite readily provided again by the electronegativities of the resulting groups. In the network, $[SiO_{3/2}O]^-$ is expected to be connected to another $[POO_{3/2}]^0$ group (unless the concentration of P_2O_5 is very low) in the structure. This leads to a bond-switching reaction as a result of which $[SiO_{4/2}]^0$ and $[POO_{2/2}O]^-$ are formed. The reaction is dictated by a reduction of the electronegativity differences between the two connected groups. The reaction is shown below with the corresponding electronegativities given in parenthesis.

$$\underset{(2.11)}{[SiO_{3/2}O]^-} + \underset{(3.03)}{[POO_{3/2}]^0} \rightarrow \underset{(2.39)}{[SiO_{4/2}]^0} + \underset{(2.77)}{[POO_{2/2}O]^-} \tag{12.21}$$

The net result is that P_2O_5 in the glass grabs all the O^{2-} from the modifier. Thus modification in complex glass systems can be rationalized readily by a consideration of electronegativities and partial charges. An equivalent thermodynamic approach would be to find out which leads to greater free energy decrease and that is not easy. Yet another approach would be to find out which of the sites is more acidic so that the oxide ion preferentially approaches the site. Acid-base concept has been widely in use in glass science in the sense of describing oxides as acidic (P_2O_5), basic (CaO) or amphoteric (Al_2O_3). This is evidently based on their known reactivity towards acids and bases. Another approach to basicity has been to consider the electron donating or withdrawing ability of the oxides by studying their influence on the spectroscopic properties, particularly the UV absorption edges of cations like Tl^+, Pb^{2+} or Bi^{3+}, which are used as probe cations. This was discussed earlier in chapter 6. Some of the

calculated basicity values of oxides which are components of glasses are given in Table 12.2.

Table 12.2: Optical basicities of individual oxides and a few oxyanion glasses (Duffy and Ingram, 1971; Baucke and Duffy, 1991).

Oxide/Glass	Optical basicity
BaO	1.15
CaO	1.00
MgO	0.78
Li_2O	1.00
Na_2O	1.15
K_2O	1.40
Al_2O_3	0.60
SiO_2	0.48
B_2O_3	0.42
P_2O_5	0.40
$24.8Li_2O{\cdot}75.2B_2O_3$	0.51
$20Na_2O{\cdot}80B_2O_3$	0.56
$21.5K_2O{\cdot}78.5B_2O_3$	0.53
$50Na_2O{\cdot}50P_2O_5$	0.46
$15.4K_2O{\cdot}15.4Al_2O_3{\cdot}69.2B_2O_3$	0.49

In multi-component oxide glasses, the basicities have been calculated as $\Lambda = x_1\Lambda_1 + x_2\Lambda_2$..etc. where Λ_1 and Λ_2 are the basicities of the component oxides and x_1 and x_2 are their equivalent fractions (fraction of the total oxygen provided by the component oxide to the glass). In the context of modification, therefore, we may note the following: modifier oxides should be more basic than the glass forming oxides. When modifier oxides are added to glass-forming oxides, the resulting modification reaction is like an acid-base reaction in which the sites in the acidic (glass forming) oxide are approached by the oxide ion (of the modifier) in the order of decreasing acidities.

Glasses with dissolved salts

Network glasses such as phosphates and borates can often be prepared with addition of substantial quantities of salts such as sulphates and halides. The purpose of adding such salts is to increase the concentration of charge carrier ions. For example, Li_2SO_4 added to Li_2O-P_2O_5 glasses. In such glasses, the matrix is provided by the phosphate network, which generally lies in the composition regime of ultra to meta phosphates and the sulphate ions are randomly distributed between chains and sheet-like islands of ultra-phosphates. Thus the SO_4^{-2} ions, both by

virtue of their large size and negative charge, expand (open up) the anion matrix and creates easy routes for the passage of Li^+ ion in the structure. In fact, the Li^+ ion conductivities of sulpho-phosphate glasses are higher than in corresponding phosphate glasses prepared without the sulphate (Ganguli et al., 1999a). The activation barriers of sulphate containing glasses decrease and become independent of sulphate concentration above an optimum concentration supporting the view that the effect is primarily one of 'opening up' of the phosphate matrix. This is referred to as a 'plasticising effect'. Similar effect of the added Li_2SO_4 is observed in Li_2O-B_2O_3 glasses also. In boro-sulphate glasses, inter-anionic interaction is possible because sulphate ions can coordinate with a BO_3 group through its oxygen giving rise to sulpho-borate ions in the structure (Ganguli et al., 1999b). This has the consequence of increasing the concentration of tetrahedral boron, B_4, in the structure. This has been confirmed using MAS NMR as shown in the Figure 12.19 where N_4 is plotted against composition in the glass $x Li_2SO_4 \cdot y Li_2O \cdot z B_2O_3$.

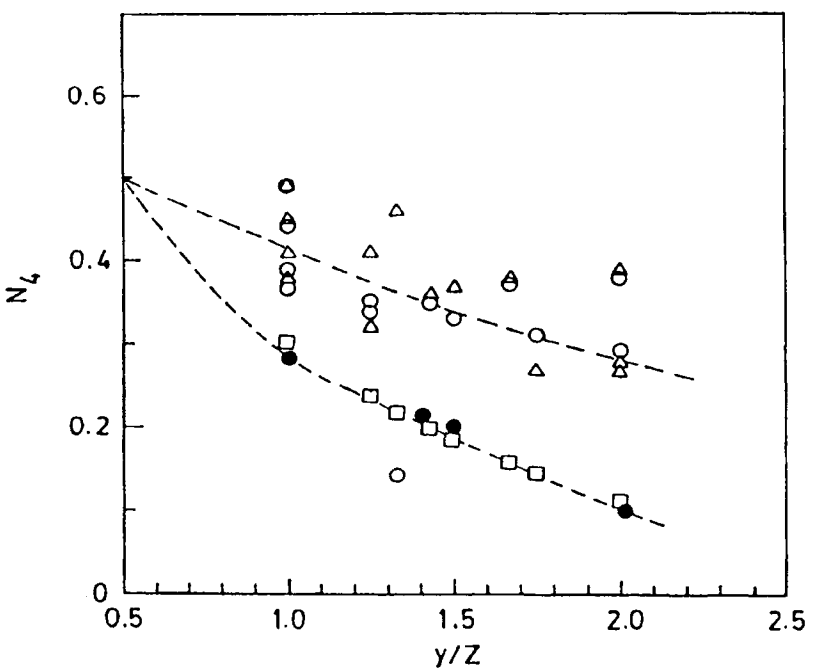

Figure 12.19. Variation of N_4 (NMR) (denoted by Δ), N_4 (IR) (denoted by ○) and (1/2)exp{1/(2-y/z)} (denoted by □) with y/z. (Experimental points are denoted by ●) (After Ganguli et al., 1999a).

Glasses containing transition metal oxides

MoO_3, WO_3, V_2O_5, TeO_2, etc. also form glasses, but generally in combination with other glass-forming oxides or sometimes simply in combination with some other oxides. One of the second components that ensures glass-formation with many such oxides is P_2O_5. Molybdo-phosphates and tungsto-phosphates are important systems which have been investigated in the glassy state (Muthupari and Rao, 1996; Selvaraj and Rao, 1988a,b). Mo and W are also transition metals capable of existing in multiple valence states. Both of them have stable valence states of +6 and +5. Mo-O and W-O bonds in their hexavalent oxides are significantly covalent (nearly as covalent as Si-O bond). Binary glasses containing P_2O_5 can be made over a wide range of composition with up to 80% MoO_3 or WO_3. Spectroscopic and other investigations have been used to characterize these glasses and it has been found that Mo and W are present in octahedral coordination. The glass structure consists of corner sharing $[MO_{6/2}]$ and $[WO_{6/2}]$ octahedra and $[POO_{3/2}]$ tetrahedra in the binary molybdophosphate and tungstophosphate glasses. Glasses containing 80 % of the two oxides are very prone to crystallization indicating that glasses containing only corner sharing octahedra may not be stable (see chapter 2 for Zachariasen's rules). Some of these glasses, particularly those rich in the hexavalent oxides are coloured (blue, green and often brown). These colours arise due to the presence of reduced forms of the oxides, Mo^{5+} and W^{5+} and their *d-d* transitions are responsible for their colour. Both, Mo^{5+} and W^{5+} are quite stable in octahedral configuration, although the octahedra are distorted due to Jahn-Teller effect. In these glasses, the effect of modification has interesting features, because, the structure consists of two types of tetrahedra and three types of linkages, namely M-O-M, M-O-P and P-O-P, where M is Mo or W. It is instructive to consider the origin of modification slightly differently from the one discussed above. First, we recognize that there is a clear hierarchy of energies, $E_{P\text{-}O\text{-}P} > E_{M\text{-}O\text{-}P} > E_{M\text{-}O\text{-}M}$. Because of this, the ease of bond-breaking follows the reverse order; M-O-M is broken more easily than M-O-P, which in turn is broken more easily than P-O-P. Therefore, when a modifier like K_2O is added, we must expect that the modification to occur first at the M-O-M linkage. The consequence of this is a chemical reaction like

$$2[MO_{6/2}]^0 + K_2O \rightarrow 2[MO_{5/2}O]^- + 2K^+ \qquad (12.22)$$

The same conclusion is arrived at by considering the partial charges on M, O and P by the procedure described earlier. The partial charges on the atoms in various linkages are shown below in Figure 12.20. Approach of O^{2-}, which is the key step in modification, is easy towards the M-O-M links and is less so towards the -P-O-P- links. In the next stage the product of modification of $[MO_{5/2}O]^-$ is $[MO_{4/2}O_2]^{2-}$. The structural entities $[MO_{5/2}O]^-$ and $[MO_{4/2}O_2]^{2-}$ may be designated as M_1 and M_2 respectively.

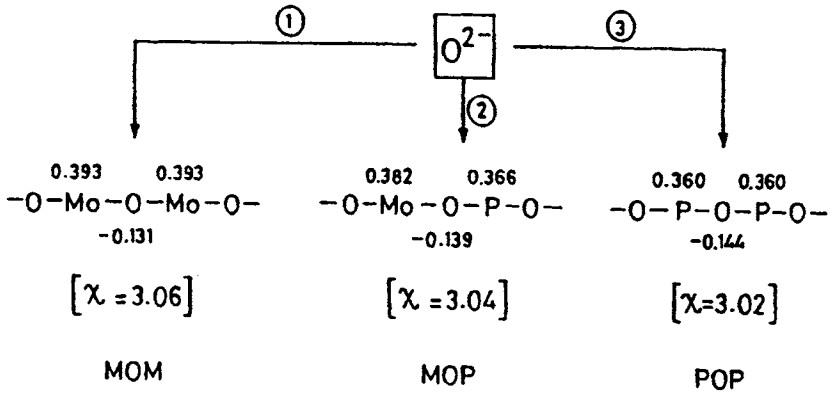

Figure 12.20: The partial charges on various atoms in the linkages and the group electronegativities (After Muthupari and Rao, 1996).

It is interesting to note here that M_2, which is an octahedra, has two NBOs attached to the central Mo or W. We should expect for reasons of coulombic repulsion that the two NBOs are posited at the opposite corners of the octahedron. The next stage of modification does not lead to the formation of $[MO_{3/2}O_3]^{3-}$. Indeed it does not occur at all in a chemical sense. Only $[MO_4]^{2-}$ is formed as a result of structural conversion of M_2. This is because the increased O^{2-} ion activity brought about by the higher concentration of K_2O, induces a structural rearrangement in $[MO_{4/2}O_2]^{2-}$ as

$$[MO_{4/2}O_2]^{2-} \xrightarrow{O^{2-}} [MO_4]^{2-} \qquad (12.23)$$

The formation of discrete MO_4^{2-} ($\equiv M_3$) shows up in the IR spectra and manifests in various properties of these glasses. Corresponding changes occur when M-O-P linkages are modified leading to the formation of Q_3,

Q_2, Q_1 and Q_0 species from $[POO_{3/2}]^0$ tetrahedra. Ultra, meta, pyro and ortho phosphate units are designated as Q_3, Q_2, Q_1 and Q_0 respectively as noted earlier in the context of phosphate NMR. These glasses have been investigated in detail and their chemistry in terms of the structural entities have been described using structural phase diagrams such as shown in Figure 12.21. (P_3, P_2 and P_1 in figure are identically Q_3, Q_2 and Q_1 respectively). In the figure, MM, MP and PP refer to paired units like $\{[MO_{6/2}]^0[MO_{6/2}]^0\}$,$\{[MO_{6/2}]^0[POO_{3/2}]^0\}$ and $\{[POO_{3/2}]^0[POO_{3/2}]^0\}$ respectively and they consist of M-O-M, M-O-P and P-O-P linkages. The dotted lines are the composition boundaries. These structural phase diagrams contain necessary information to anticipate the different structural species present in any given composition.

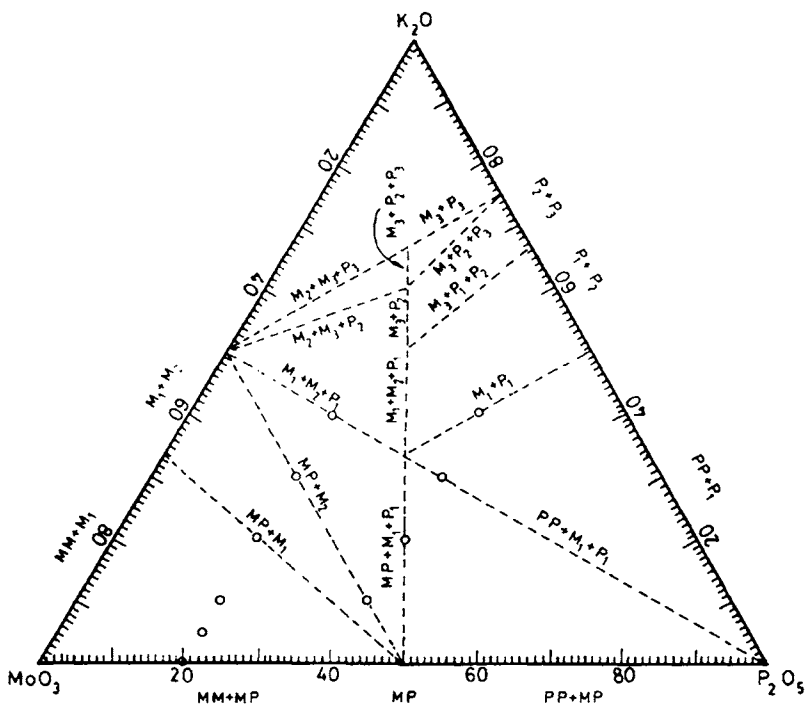

Figure 12.21: Structural phase diagram of K_2O-MoO_3-P_2O_5 glasses. Structural units present in each region are determined by the units indicated on boundaries (After Selvaraj and Rao, 1985).

If PbO is added instead of an alkali oxide to the molybdophosphate or tunstophosphate glasses, the modification becomes even more

interesting (Selvaraj and Rao, 1988a). As pointed out earlier, PbO, which is $[PbO_{2/2}]^0$, tends to become four-connected to oxygens as $[PbO_{4/2}]^{2-}$ by acquiring this additional coordination through the use of the double-bonded (terminal) oxygens in $[PO_{3/2}]^0$ groups. Therefore, in ternary compositions like xPbO · yMoO$_3$ · (1-x-y)P$_2$O$_5$, PbO gets incorporated into the network in the first stage till x = (1-x-y). Correspondingly, all of 2(1-x-y) of $[PO_{3/2}]^0$ units are converted into $[PO_{4/2}]^+$ units in the structure. But when the concentration of PbO increases above this level, it begins to act as a modifier and as a result Mo-O-Mo and Mo-O-P bonds are cleaved in succession. This change in the role of PbO manifests very clearly in the trends of elastic properties of the glasses as a function of PbO concentration. The bulk modulus and Poisson's ratio show greater rate of increase in the region of modification. This is due to rupture of weak Mo-O-Mo bonds followed by better packing. But, the shear and Young moduli do not exhibit any dispersion as shown in Figure 12.22. A concomitant effect of the changed role of Pb is on the concentration of Mo^{5+} in the glass.

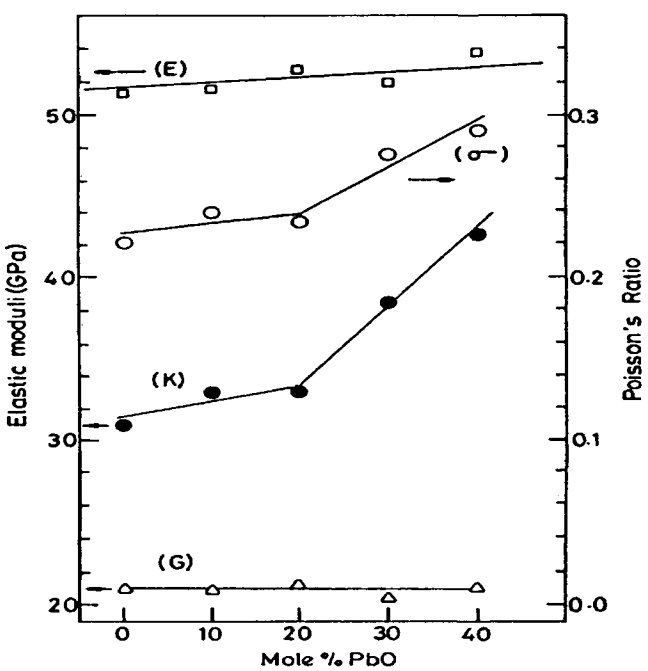

Figure 12.22. Variation of Young's (E), bulk (K), shear (G) moduli and poisson'sratio ($\sigma \equiv \nu$ as designated in the text) in xPbO·(80-x)MoO$_3$·20P$_2$O$_5$ glasses (After Damodaran et al., 1988).

Formation of Mo^{5+} is a consequence of a small degree oxygen loss during the preparation of these glasses. In the presence of modifier oxides, oxygen loss is suppressed and concentration is of Mo^{5+} is also suppressed. This is because of increased O^{2-} ion activity in the melt. The concentration of Mo^{5+} is excellently monitored using ESR of Mo^{5+}. By the method of double integration and use of appropriate ESR standards, Mo^{5+} concentration can be readily determined. The variation of Mo^{5+} concentration in two series of glasses, $xPbO \cdot (80\text{-}x)MoO_3 \cdot 20P_2O_5$ and $xPbO \cdot (60\text{-}x)MoO_3 \cdot 40P_2O_5$, are shown in Figure 12.23, which clearly reveals the cross over of structural role of PbO, which occurs precisely in the region where $x \approx (1\text{-}x\text{-}y)$.

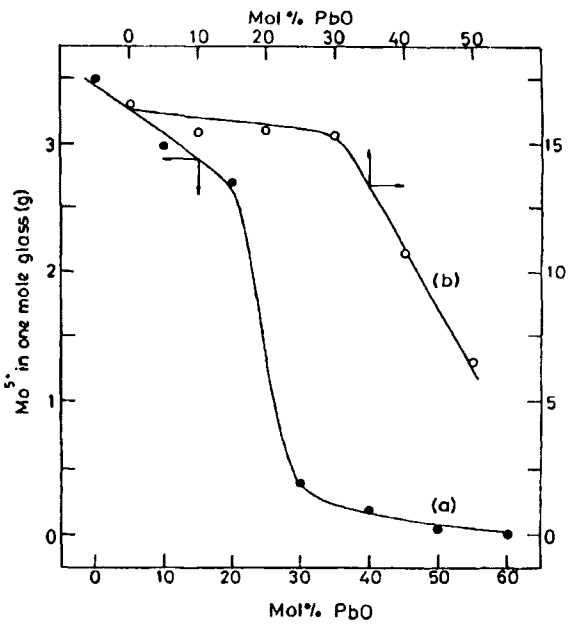

Figure 12.23. Variation of Mo^{5+} concentration with glass composition for: (a) $xPbO \cdot (80\text{-}x)MoO_3 \cdot 20P_2O_5$ and (b) $xPbO \cdot (60\text{-}x)MoO_3 \cdot 40P_2O_5$ (After Selvaraj and Rao, 1988b).

Another interesting transition metal oxide containing glass system is that of $Na_2O\text{-}B_2O_3\text{-}V_2O_5$. Alkali-borovanadate glasses such as $Na_2O\text{-}B_2O_3\text{-}V_2O_5$ are readily prepared over wide range of compositions by melt-quenching techniques. Like in molybdo-phosphate glasses, in this glass system also one of the constituents is a conditional glass former and that is V_2O_5. Indeed, in this glass system the T_g varies over a wide range of

300 degrees between 0 and 40 mol% V_2O_5 and the variation is closely associated with the concentration of V_2O_5. A structural model of this glass has been suggested by assuming that V_2O_5 is structurally analogous to P_2O_5 and therefore consists of $[VOO_{3/2}]^0$ units. $[VOO_{3/2}]^0$ and $[BO_{3/2}]^0$ are considered as forming a network which again leads to the existence of B-O-B, B-O-V and V-O-V linkages. Both units are three-connected because one of the oxygen atoms in $[VOO_{3/2}]^0$ is double bonded to V (terminal oxygen). IR spectra of V-rich glasses reveal the presence of V=O through its stretching vibration at 990 cm^{-1}. Interestingly $[VOO_{3/2}]^0$ and $[BO_{3/2}]^0$ have the same value of group electronegativities and hence the chemical affinities for the added modifier oxide ion is the same for both units. Therefore, the added modifier alkali distributes between the two types of groups in proportion to their concentrations. The random connectivities of $[VOO_{3/2}]^0$ and $[BO_{3/2}]^0$ units restrict the presence of two adjacent $[BO_{3/2}]^0$ units. It is not facile for the O^{2-} ions to create a bridge and give rise to two B_4 units in the absence of twinned $[BO_{3/2}]^0$ units in the structure. As a consequence, B_4/B_3 may not attain its limiting value of 1.0 as it does in simple alkali borate systems. It has been proposed that in alkali borovanadates bridging also occurs between B_3 and V_3 and between V_3 and V_3, in addition to B_3 and B_3 (B_3= $[BO_{3/2}]^0$), much like in alkali borates. Therefore, we should expect the formation of diborovanadates (like diborates), of the type shown in Figure 12.24. On the assumption that

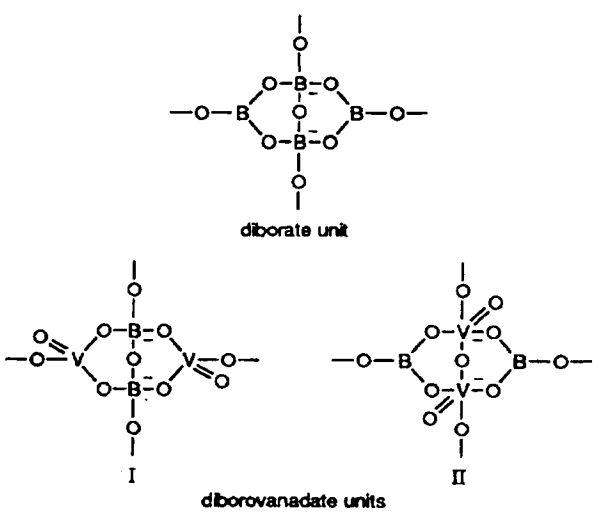

Figure 12.24. Structural units present in borovanadate glasses (After Muthupari et al., 1994).

alkali oxide is shared by B_2O_3 and V_2O_5 in the structure, the modification and consequent formation of various structural species have been evaluated. The ratio of B_4/B_3 (B_3 includes all boron atoms in trigonally connected species) has been calculated and compared with the experimentally determined B_4/B_3 using MAS NMR. The results are shown in Figure 12.25, which clearly supports the assumption. The presence of diborovanadates is also indicated by the presence of 1250 cm^{-1} band, in the alkali borovanadate glasses and this band is absent in binary borovanadate glasses.

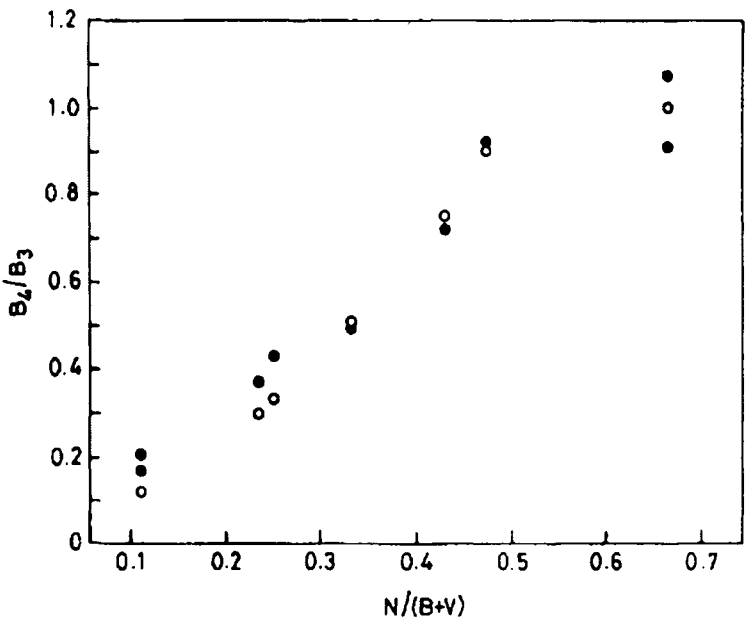

Figure 12.25. Variation of B_4/B_3 ratio of modifier oxide to the total amount of network formers. Solid circle denotes experiments while open circle indicates the calculated values from the model (After Muthupari et al., 1994).

Transition metal (TM) ions can be readily incorporated particularly into phosphate glasses. Since TM ions give rise to characteristic spectra in the region of near IR to near UV, their characterization is relatively easy. An example is the study of a series of glasses having chemical compositions of NASICONs. NASICON is an acronym for sodium super-ionic conductors of the general formula $A_nB_2(PO_4)_3$, where B is generally a TM ion or elements like Zr, Ge, Sn, etc. (or their combination) and A is an alkali metal, whose number n in the formula is dependent on the

valency of B. The crystalline structures of NASICONs are built by extensively connected networks of BO_6 octahedra and PO_4 tetrahedra, giving rise to R3 or $R\bar{3}C$ structures. Alkali ions are present in sites of higher coordination which are the connected interstices. The interstices form channels in the structure. This open structure of the crystalline NASICONs is rather insensitive to the change in volume of the alkali ions. Glasses can be made with the same composition of the NASICONs by melting together appropriate oxides and quenching them. In the glassy NASICONs such as $A_5Ti(PO_4)_3$, changing A ion from Li to K results in 12.7 cc/mol increase in volume, while in the crystalline $LiZr_2(PO_4)_3$, substitution of Li by K is attended with a volume change of only 2.08 cc/mol. Therefore, as expected, in glasses the open structures collapse and the alkali ions are intimately coordinated. In the glassy state, the composition of the NASICONs are better described in terms of the component oxides such as for example, $Li_5Ti(PO_4)_3$ is $50Li_2O{\cdot}20TiO_2{\cdot}30P_2O_5$. In this description it is possible to examine the nature of species expected to be present in the various glass compositions. A number of glasses examined in this way are shown in Table 12.3. The structural units expected to be present and the spectroscopic investigations used to confirm their presence are also indicated. It is evident that in most of the cases the B ions have lower valencies and higher coordinations indicating the presence of extensive phosphate network consisting of ultra or meta phosphate units. But higher valencies and lower coordination numbers like $[TiO_{4/2}]^0$ can lead to the presence of pyrophosphate units, which as we discussed earlier, are chain terminators (It appears a tough job for even $[POO_{3/2}]^0$ units to pull away oxygens from TiO_2 which, as we noted earlier it does in the case of SiO_2).

Crystalline NASICONs were developed in order to realize high ionic conductivities. Unfortunately NASICON glasses, due to reasons mentioned earlier (structural collapse), do not exhibit high ionic conductivities. But the study of a.c. conductivities of the NASICON glasses have provided some interesting insights, particularly with regard to the validity of the different forms of power laws, as noted in chapter 7.

Phosphate glasses containing Sn have been examined in the literature (Nover and Williamson, 1967; Ishikawa and Akagi, 1978; Bhat et al., 2001). SnO can be added to sodium metaphosphate ($NaPO_3$) glasses and in the pseudo-binary system ($SnO\text{-}NaPO_3$) glass formation occurs over a wide range of composition. Interesting feature of this glass system is that Sn establishes a redox equilibrium between Sn^{IV} and Sn^{II} states. The equilibrium ratio of $[Sn^{IV}]$ to $[Sn^{II}]$ seems to be constant for all melts

Table 12.3: Glass composition, spectroscopic investigation conducted and the structural units expected to be found in the glasses (After Rao et al., 2001).

Composition and designation	Spectroscopic investigation	Possible structural units (A=Li, Na or K)
$Li_3Fe_2P_3O_{12}$ $Na_3Fe_2P_3O_{12}$ $K_3Fe_2P_3O_{12}$	IR, FTIR	$3A^{1}+2[FeO_{4/2}]^{-}+2[POO_{3/2}]+1[POO_{2/2}O]^{-}$ $3A^{1}+2Fe^{3+}+3[PO_4]^{3-}$
$Na_3Ga_2P_3O_{12}$ $K_3Ga_2P_3O_{12}$	IR,FTIR,NMR IR, Raman, FTIR, NMR	$3A^{1}+2[GaO_{4/2}]^{-}+2[POO_{3/2}]+1[POO_{2/2}O]^{-}$
$Li_5TiP_3O_{12}$ $Na_5TiP_3O_{12}$ $K_5TiP_3O_{12}$	IR,Raman,FTIR,NMR IR,Raman,FTIR, NMR IR,FTIR,NMR	$5A^{1}+[TiO_{4/2}]^{0}+2[POO_{1/2}O_2]^{2}+1[POO_{2/2}O]^{-}$ $5A^{1}+[TiO_{5/2}]^{-}+[POO_{1/2}O_2]^{2}+2[POO_{2/2}O]^{-}$ $5A^{1}+[TiO_{6/2}]^{2-}+3[POO_{2/2}O]^{-}$
$Li_5GeP_3O_{12}$ $Na_5GeP_3O_{12}$ $K_5GeP_3O_{12}$	IR,FTIR,NMR IR,Raman,FTIR, NMR IR, FTIR	$5A^{1}+[GeO_{4/2}]^{0}+2[POO_{1/2}O_2]^{2-}+[POO_{2/2}O]^{-}$
$Na_4VP_3O_{12}$ $K_4VP_3O_{12}$	IR, FTIR,NMR IR	$4A^{1}+[VOO_{3/2}]^{0}+2[POO_{2/2}O]^{-}+[POO_{1/2}O]^{2-}$
$Na_4NbP_3O_{12}$ $K_4NbP_3O_{12}$	IR,Raman,FTIR, NMR IR,Raman,FTIR, NMR	$4A^{1}+[NbO_{6/2}]^{-}+3[POO_{2/2}O]^{-}$

equilibrated in air at 1000 ^{0}C. Because of the air ambience (P_{O2} = 0.2 atm), SnO oxidizes to SnO_2. The ratio [Sn^{IV}] to [Sn^{II}] is found to be essentially independent of composition. The ratio, [Sn^{IV}]/[Sn^{II}], has been determined using Mössbauer spectroscopy and is shown in Figure 12.26. The raw spectra is shown in Figure 12.26(a), an example of the deconvolution of the spectra used to determine the [Sn^{4+}] and [Sn^{2+}] concentrations is shown in Figure 12.26(b) and variation of the relative concentration of [Sn^{IV}] and [Sn^{II}] is shown in Figure 12.26(c). It appears that this oxidation involves first the dissolution of oxygen in the phosphate melts which then oxidises Sn^{2+} to Sn^{4+} with a resultant formation of O_2^{2-} in the melt. O_2^{2-} then decompose to O^{2-} and O, and eventually O atoms recombine to form O_2. The meta-phosphate picks up the O^{2-} resulting in modification of meta to

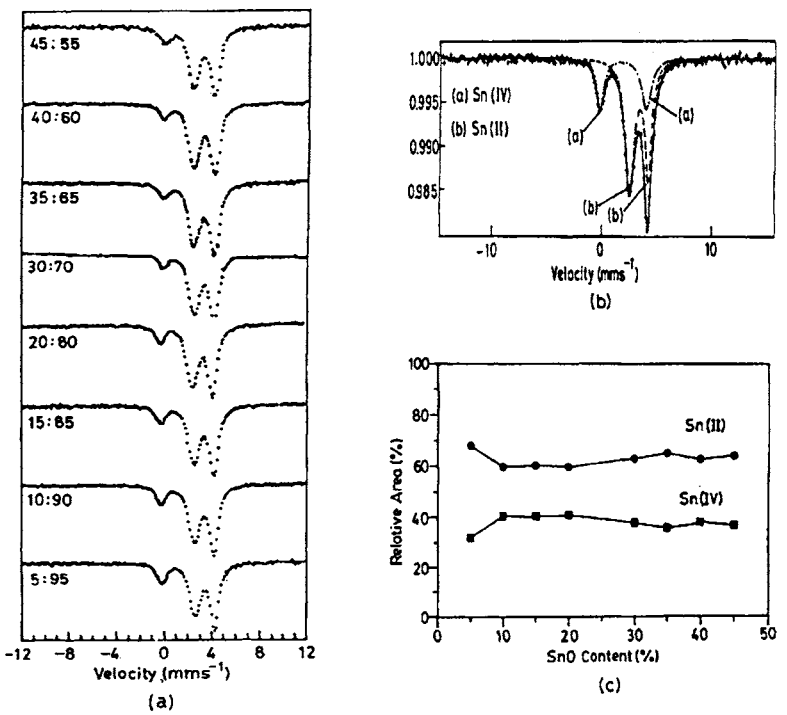

Figure 12.26: (a) ^{119}Sn Mössbauer spectra of SnO-NaPO3 glasses (b) Deconvoluted ^{119}Sn Mössbauer spectra of 05:95 glass and (c) variation of fractions of Sn^{4+} and Sn^{2+} as obtained from ^{119}Sn Mössbauer spectra (After Bhat et al., 2001).

pyrophosphate in the melt. Such a scheme involves the slow step of O_2^{2-} transferring O^{2-} to the phosphate matrix. This slow step determines the constancy of Sn^{IV} to Sn^{II} ratio. In addition to this, SnO plays the dual

structural role, first as a modifier upto 33 mole% of SnO and then as a network former above 33 mole %. Sn^{4+} also behaves like network former and is coordinated to 4 oxygens. The meta to pyro phosphate conversion stops above 33 mole % SnO. A reorganization of both meta and pyro-phosphate units and extensive reformation of the network occurs above 33 mole % SnO. The molar volumes and glass transition temperatures reflect this changed role of SnO very sensitively and the equilibrium of meta and pyro-phosphates examined using Raman spectroscopy also provides evidence for the change in the role of SnO. It is interesting to note here the network former – network modifier roles of Pb^{2+} and Sn^{2+} in phosphate matrices are opposite of each other: SnO acts as a modifier in lower concentration while PbO acts as a network former in lower concentration in phosphate matrices.

TeO_2 is one of the historically important compounds in glass science because it was predicted to form a glass on the basis of Sun's model (chapter 2) and indeed was shown later to be a glass former. It is generally considered as a conditional glass former. In tellurate glasses, Te exists in two different coordination geometries, namely, trigonal bypyramid (*tbp*) and trigonal pyramid (*tp*) and the corresponding structural units can be described as $[TeO_{4/2}]^0$ and $[TeOO_{2/2}]^0$ units. In both *tbp* and *tp* structures, Te bonds to oxygen through its sp^3d hybridised orbitals. In *tbp*, it involves hybridisation of 5*s*, 5*p* and d_{z^2} orbitals. As shown in Figure 12.27 the lone pair on Te is accommodated in an equitorial orbital in *tbp* and the other four orbital are used in bonding to BOs.

On the other hand, in the formation of *tp*, there is first the formation of sp^3 hybridised orbitals, of which one is used to accommodate the lone pair: two for bonding to BOs and the other one is bonded to an oxygen whose *p*-orbital overlaps with one of the *d*-orbitals of Te, forming a π-bond. This oxygen is therefore double bonded to Te (terminal oxygen) (Figure 12.27 (b)). It has been reported (Komatsu and Mohri, 1999) that modification of TeO_2 glass induces a preference for *tp* units, although both *tbp* and *tp* units are present in the structure. While *tp* units can only form chains, *tbp* units can give rise to 3-dimensional network structures. Thus *tp* and *tbp* units can make a big difference for the final glass structure. However, EXAFS studies have provided evidence for the presence of only *tbp* units (Neov et al., 1995; Osaka et al., 1992). The structural role of TeO_2 in sodium borate glasses has been examined recently in the pseudo-binary $LiBO_2$-TeO_2 glasses (Rao and Bhat, 2001). In pure $LiBO_2$, the ratio of the concentration of Li_2O to B_2O_3 is unity, and is well above the ratio of

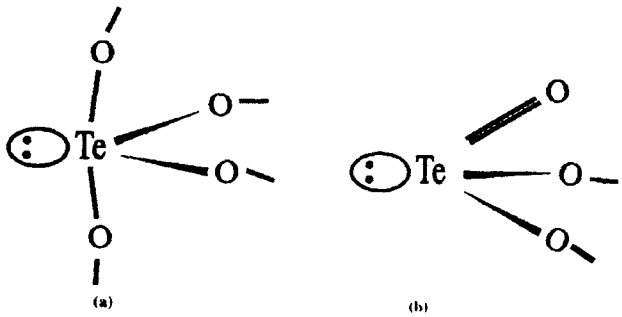

Figure 12.27: (a) trigonal bypyramid (*tbp*) and (b) trigonal pyramid (*tp*) structures of TeO_2.

0.5, for which $[B_4/(B_4 + B_3)] = N_4$, generally reaches the maximum of 0.5. Therefore, N_4 should be significantly lower than 0.5 in the present glasses. But contrary to the expectations, this ratio has been found to reach a high value of 0.65 in $LiBO_2$-TeO_2 glasses for $[LiBO_2]/([LiBO_2] + [TeO_2])$ equal to 0.8. This has been found to be due to stabilization of B_4 units in the structure by the intervention of the *tp* units. The alkali oxide present in $LiBO_2$-TeO_2 glasses is partly taken up by TeO_2 for its own modification as a result of which more and more *tbp* units are converted into charged *tp* units of the type $[TeOO_{1/2}O]^-$. Thus, there is both, a partial loss of Li_2O which decreases $[Li_2O]/[B_2O_3]$ ratio from its high value of 1.0 and the stabilization of B_4 by *tp* units in the structure (B_4 units as pointed out earlier in the chapter, are unstable when they have to share corners). Thus N_4 reaches very high values as shown in Figure 12.28. These glasses provide an excellent example of rather complex speciation ($[BO_{3/2}]$,

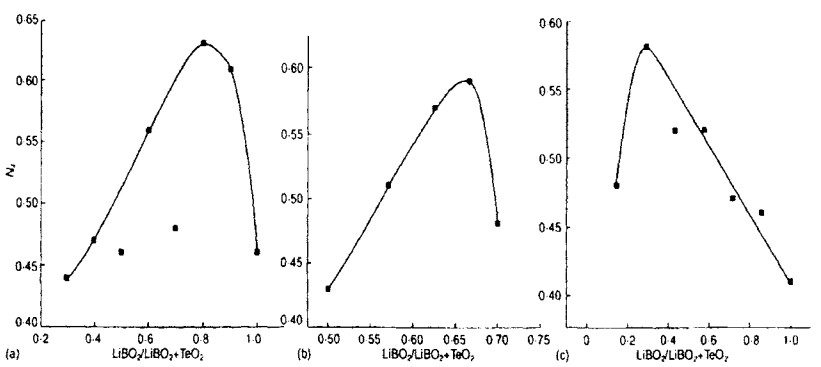

Figure 12.28: N_4 vs reduced $LiBO_2$ concentration (R) in three different series of of $LiBO_2$-TeO_2-LiCl glasse (After Rao and Bhat, 2001).

$[BO_{4/2}]^-$, $[BO_{2/2}O]^-$, *tbp*, *tp*, $[TeO_{2/2}O]^0$ etc.), presence of which has been confirmed by using infrared, Raman and MAS NMR spectroscopies.

References:

Abramo, M. C., C. Caccamo and G. Pizzimenti, 1992, J. Chem. Phys., **96**, 9083.

Ananthraj, S., K.B.R. Varma and K.J. Rao, 1986, Mat. Res. Bull., **21**, 1369.

Anderson, O.L., and G.J. Dienes, 1960, Non-Crystalline Solids, ed. V.D. Frechette (John Wiley, New York) p. 449.

Balta, P. and E. Balta, 1976, Introduction to the physical chemistry of the vitreous state, (Abacus, Kent).

Baucke, F. G. K. and J. A. Duffy, 1991, Phys. Chem. Glasses, **32**, 211.

Baur, W. H. and A. A. Khan, 1997, Acta. Cryst. **27**, 2133.

Beall, G.H., 1989, in Current Trends in the Science and Technology of Glass, eds., H. Jain, A.R.Cooper, K.J.Rao and D. Chakravorty (World Scientific, Singapore) p., 279.

Bhat, M. H., F. J. Berry, J. Z. Jiang and K. J. Rao, 2001, J. Non-Cryst. Sol., **291**, 93.

Brow, R. K., 2000, J. Non-Cryst. Sol., **263&264**, 1.

Brow, R. K., D. R. Tallant, J. J. Hudgens, S. W. Martin and A. D. Irwin, 1994, J. Non-Cryst. Sol., **177**, 221.

Damodaran, K. V. and K. J. Rao, 1988, Chem. Phys. Lett., **148**, 57.

Damodaran, K. V., V. S. Nagarajan and K. J. Rao, 1990, J. Non-Cryst. Sol., **124**, 233.

Damodaran, K. V., U. Selvaraj and K. J. Rao, 1988, Mat. Res. Bull., **23**, 1151.

Damodaran, K.V., U. Selvaraj and K.J. Rao, 1988, Mat. Res. Bull. **23**, 1151.

Duffy, J. A. and M. D. Ingram, 1976, J. Non-Cryst. Sol., **21**, 373.

Duffy, J. A., 1986, J. Non-Cryst. Sol., **86**, 149.

Duffy, J. A. and M. D. Ingram, 1971, J. Am. Chem. Soc., **93**, 6448.

Dupree, R. and R. F. Pettifer, 1984, Nature **308**, 523.

Elliott, S. R., 1992, Nature, **357**, 650.

Filipovich, V. N., 1984, Phase separation in glass, eds. O. V. Mazurin and E. A.

Pori-Koshits (Elsevier Science) p. 15.

Ganguli, M., M. H. Bhat and K. J. Rao, 1999, Mat. Res. Bull., **34**, 1757.

Ganguli, M. and K. J. Rao, 1999, J. Phys. Chem. B., **103**, 920.

Ganguli, M., M. H. Bhat and K. J. Rao, 1999a, Solid State Ionics, **122**, 23.

Ganguli, M., M.H. Bhat and K.J. Rao, 1999b, Phys. Chem. Glasses., **40**, 297.

Ganguli, M and K. J. Rao, 1999, J. Phys. Chem, 103, 920.

Gaskell, P. H., 1997, J. Non-Cryst. Sol., **222**, 1.

Huang, C. and A. N. Cormack, 1992, J. Mat. Chem., **2**, 281.

Hudgens, J. J. and S. W. Martin, 1993, J. Am. Ceram. Soc., **76**, 1691.

Hunter, C. C. and M. D. Ingram, 1984, Solid State Ionics, **14**, 31.

Ishikawa, T., and S. Akagi, 1978, Phys. Chem. Glasses, **19**, 108.

Kamitsos, E.I., Y.D. Yiannopoulos, M.A. Karakassides, G.D. Chryssikos and H. Jain, 1996, J. Phys. Chem., **100**, 11755.

Komatsu, T., and H. Mohri, 1999, Phys. Chem. Glasses, **40**, 257.

Krogh-Moe, J.,, 1965, Phys. Chem. Glasses, **6**, 30.

Kumar, S., S. Murugavel and K.J. Rao, 2001, J. Phys. Chem. B, **105**, 5862

Lasaga, A.C., and G.V. Gibbs, 1987, Phys. Chem. Minerals, **14**, 107.

Lewis, M.H., 1989, Glasses and Glass-Cramics (Chapman and Hall, New York).

Lowenstein, W., 1954, Am. Mineralogy, **39**, 92.

Lu, X., H. Jain and W. C. Huang, 1996, Phys. Chem. Glasses, **37**, 201.

Margaryan, A. and M. A. Piliavin, 1993, Germanate Glasses: Structure, Spectroscopy and Properties (Artech House, Boston).

Martin, S. W., 1991, Eur. J. Solid. State Chem., **28**, 163.

Mekki, A., D. Holland, Kh. Ziq and C.F. McConville, 1997, J. Non-Cryst. Sol., **220**, 267.

Mundy, J. N. and G. L. Jin, 1986, Solid State Ionics, **21**, 305.

Murthy, M. K. and E. M. Kirby, 1964, Phys. Chem. Glasses, **5**, 144.

Muthupari, S., S. Prabakar and K. J. Rao, 1994, J. Phys. Chem. **98**, 2646.

Muthupari, S., S. Prabakar and K. J. Rao, 1994, J. Phys. Chem., **98**, 2646.

Muthupari, S and K. J. Rao, 1996, J. Phys. Chem. Sol., **57**, 553.

Neov, S., I. Gerasimova, V. Kozukarov, P. Mikula and P. Lukas, 1995, J. Non-Cryst. Sol., **192&193**, 53.

Nover, J.C., and J. Williamson, 1967, Phys. Chem. Glasses, **8**, 164.

Osaka, A., Q. Gianwrong, T. Namba, J. Takada and Y. Miura, 1992, J. Non-Cryst. Sol., **142**, 81.

Parker, S. C. and G. D. Price, 1989, Advances in Solid State Chemistry, ed. C. R. A. Catlow (JAI Press, London).

Parr, R.G., 1978, J. Chem. Phys., **68**, 3801.

Peters, J., H. Jain, O. Kanert, R. Küchler and V. Blache, 1997, J. Non-Cryst. Sol., **222**, 113.

Prabakar, S., K. J. Rao and C. N. R. Rao, 1991, J. Mat. Res., **6**, 592.

Prabakar, S., K. J. Rao and C. N. R. Rao, 1991, Mat. Res. Bull., **26**, 285.

Prabakar, S., K.J. Rao and C.N.R. Rao, 1991, Chem. Phys. Lett., **183**, 176.

Ramesh, P. D. and K. J. Rao, 1994, J. Mat. Res., **9**, 2330.

Rao, K. J, and M. H. Bhat, 2001, Phys. Chem. Glasses, **42(3)**, 255.

Rao, K.J., K.C. Sobha and S. Kumar, 2001, Proc. Ind. Acad. Sci., (Chem. Sci) **113**, 497.

Rao, K.J., N. Baskaran, P.A. Ramakrishnan, B.G. Ravi and A. Karthikeyan, 1998, Chem. Mater., **10**, 3109.

Sales, B. C. and L. A. Boatner, and J. O. Ramey, 1998, J. Non-Cryst. Sol., **232-234**, 107.

Sanderson, R. T., 1983, Polar Covalence, (Academic Press, New York).

Schramm, C. M., B. H. W. S. de Jong and V. W. Parziable, 1984, J. Am. Chem. Soc., **106**, 4396.

Selvaraj, U. and K. J. Rao, 1988a, Chem. Phys., **123**, 141.

Selvaraj, U. and K. J. Rao, 1985, J. Non-Cryst. Sol., **72**, 315.

Selvaraj, U. and K. J. Rao, 1988b, J. Non-Cryst. Sol., **104**, 300.

Selvaraj, U., and K.J. Rao, 1984, Spectrochim. Acta, **40A**, 1081.

Shelby, J.E., 1997, Introduction to Glass Science and Technology (The Royal Society of Chemistry, Letchworth).

Shewman, P.G., 1969, Transformation in Metals (McGraw-Hill, New York), p.291.

Sobha, K. C. and K. J. Rao, 1995, Solid State Ionics, **81**, 145.

Soules, T. F., 1979, J. Chem. Phys., **71**, 4570.

Soules, T. F. and R. F. Busbey, 1981, J. Chem. Phys., **75**, 969.

Tasker, G. W., D. R. Uhlmann, P. I. K. Onorato, M. N. Alexander and C. W. Struck, 1985, J. Phys. (Paris), **C8**, 273.

Temkin, R. J., 1975, J. Non-Cryst. Sol., **17**, 215.

Tsuneyuki, S., M. Tsukada, H. Aoki and Y. Matsui, 1988, Phys. Rev. Lett., **61**, 869.

Tsuneyuki, S., H. Aoki, M. Tsukada and Y. Matsui, 1990, Phys. Rev. Lett., **64**, 776.

Tsuneyuki, S., Y. Matsui, H. Aoki and M. Tsukada, 1989, Nature, **339**, 209.

Uchino, T. and Y. Ogata, 1995, J. Non-Cryst. Sol., **181**, 175.

Van Wazer, J. R., 1950, J. Am. Chem. Soc., **72**, 644.

Van Wazer, J. R., 1951, Phosphorus and its compounds (I and II), (Interscience Publishers, New York).

Verhoef, A. H. and H. W. den Hartog, 1992, J. Non-Cryst. Sol., **146**, 267.

Vessal, B., G. N. Greaves, P. T. Marten, A. V. Chadwick, R. Mole and S. Houde-Walter, 1992, Nature, **356**, 504.

Wada, M., 1999, in Glass Engineering Handbook, eds. M. Yamane, I. Yasui, M. Wada, Y. Kokubu, K. Kondo and S. Ogawa (Asakura Shoten, Tokyo) p. 7.

Zhong, J. and P.J. Bray, 1989, J. Non-Cryst. Sol., **111**, 67.

Zirl, D. M. and S. H. Garofalini, 1990, J. Am. Ceram. Soc., **73**, 2848.

One sometimes finds what one is not looking for.
-Sir Alexander Fleming

CHAPTER 13

CHALCOGENIDE GLASSES

In their importance, chalcogenides are next only to oxide glasses. Chalcogenide glasses are widely used for infrared transmission. Region of infrared transparency for some of the chalcogenide glasses are listed in Table 13.1 (column under λ) along with some other relevant properties.

Table 13.1: Composition and properties of representative chalcogenide glasses (After Yamane and Asahara, 2000).

Glass	n	λ(μm)	T_f(°C)	α ($\times 10^7$ /°C)	ρ (Ω cm, 130°C)
As_2S_3	2.35	1.5 ~ 12	180	300	2.0×10^{12}
As_2Se_3		1 ~ 15	194		1.54×10^8
As_2Se_2Te					2.5×10^5
As_2SeTe_2					3.5×10^3
$As_{12}Ge_{33}Se_{55}$	2.49	1 ~ 16	474		
$As_{20}S_{20}Se_{60}$	2.53	1 ~ 13	218	200	
$As_{50}Te_{10}S_{20}Se_{20}$	2.51	1 ~ 13	195	270	
As_8Se_{92}	2.48	1 ~ 19	70	340	
$As_{20}Te_{70}Ge_{10}$	3.55	2 ~ 20	178	180	
$Ge_{30}P_{10}S_{60}$	2.15	2 ~ 8	520	150	
$Ge_{40}S_{60}$	2.30	0.9 ~ 12	420	140	
$Ge_{28}Sb_{12}Se_{60}$	2.62	1 ~ 15	326	150	
$Si_{25}As_{25}Te_{50}$	2.93	2 ~ 9	317	130	

n = refractive index; T_f = melting temperature; α = thermal expansivity; ρ = resistivity and λ = wavelength region of infrared transparency.

Shown in Figure 13.01 are the percent transmission of a few important chalcogenides, which are transparent in the infrared region. The three elements S, Se and Te of Group VI with a valence shell of ns^2 np^4 are known as chalcogens. Although oxygen is at the top of this group, there are great many differences in the behaviors of oxygen and chalcogens in their chemistry, particularly with reference to glass science. In their elemental states oxygen is only diatomic but, sulphur and selenium are constituted of octagonal rings (S_8 and Se_8). In the elemental Se glass, both rings and chains of various lengths have been identified. While S and Se

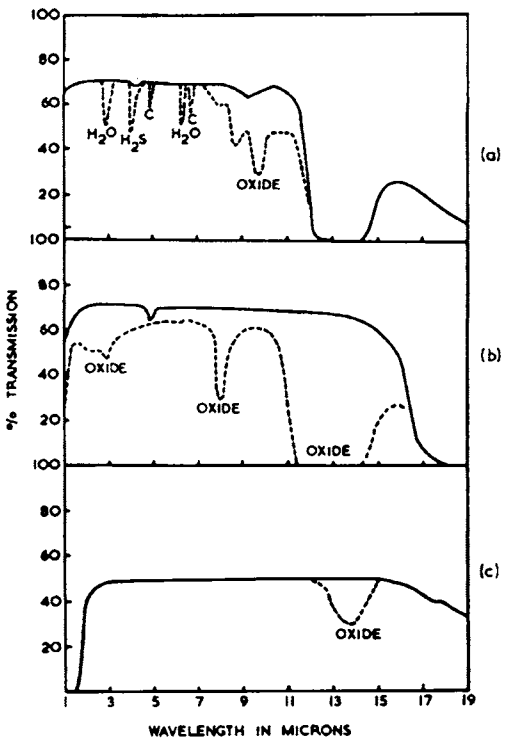

Figure 13.01: A comparison of the transmission ranges of Germanium Arsenic Sulphide (a), Selenide (b) and Telluride (c) (2 mm thick) glasses (After Savage, 1985).

are two coordinated, Te has been reported to be capable of 3-coordination (Cornet and Rossier, 1973) in tellurides. We have already referred to TeO_2 containing glasses in which Te can be both three and four coordinated to O. S-S, Se-Se and Te-Te links occur extensively in glasses, but O-O peroxy linkage is unknown in glasses. Since the electronegativity drops steeply as we go from O to S in the periodic table, the nature of bonding of chalcogens to other elements is far more covalent than the bonding of oxygens. Where as S and Se form glasses which are well-characterized, it has been found very difficult to quench O (and also Te) into glassy state. Since the valence state of O consists of only $2s$ and $2p$ orbitals, its bonding cannot involve any d orbital. But this is not a limitation with the chalcogens. Melting point of oxygen is very low and liquid oxygen has low viscosity at its melting point and therefore quenching oxygen into glassy state is extremely difficult. But vapor deposition onto cold thumbs give rise to amorphous oxygen deposits (Rawson, 1956). Te can be

quenched using severe conditions such as those employed for making metallic glasses. Crystalline S, Se and Te are semi-conductors with decreasing band gap in that order.

Chalcogen and inter-chalcogen glasses

S is easily quenched from its molten state. The viscosity behaviour of molten S is very unique. When the β form of S melts at 119°C, it gives a yellow, transparent liquid of low viscosity. When heated further, its color changes to brown and its viscosity increases rapidly above 160°C and reaches a maximum at ~200°C. The viscosity decreases thereafter, towards its boiling point and it becomes a dark red liquid close to its boiling point. Complex structural changes take place during heating alongside the viscosity changes. The rings open up and the chains gradually get degraded. Sulphur atoms at the chain terminations possess dangling bonds and therefore behave like free radicals. Their concentration can be as high as 6×10^{-3} mol/L at 300°C. In the region of maximum viscosity, S_n chains can consist of as many as $5\text{-}8\times10^5$ atoms and it may decrease to less than 1000 atoms/chain close to its boiling point. Thus, when molten S is quenched into glass, one should expect the glass to consist of interlaced chains and rings. However, the terminal sulphur atoms can interact giving rise to charged defects (intimate valence pairs) as discussed in chapter 8. In the so-called plastic region (plastic S), there is a tendency towards re-equilibration of chains and 8 membered rings.

Se is also a widely investigated glass whose T_g is around room temperature (30.2°C). Molten Se establishes an equilibrium of Se_8 rings and chains in the structure. Se-Se-Se bond angle is ~102° suggesting clearly an *s-p* hybridization of valence orbitals. It is unclear if the dihedral angles in the segments Se-Se-Se-Se have a well-defined value. There have been MD calculations to suggest that indeed there is no preference in the dihedral angle (Balasubramanian et al., 1992). In glassy Se also, like in glassy S, the chain lengths are quite high and the temperatures from where they are quenched generally determines the percentage of terminal Se atoms. Its magnitude can vary anywhere between 1-10% (Parthasarthy et al., 1981). The pair distribution function of glassy Se obtained from neutron diffraction studies is shown in Figure 13.02. Corresponding distance data obtained from X-ray diffraction studies (Wendo et al., 1982; Corb et al., 1982) are also marked by arrows at the top in the Figure. The MD simulation of Se was performed by using a combination of harmonic

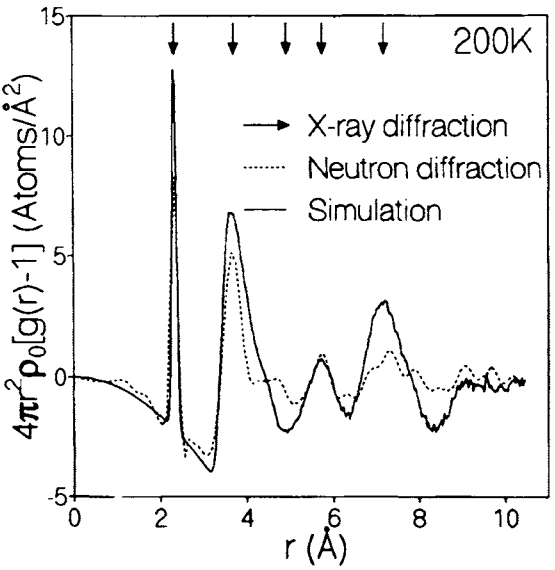

Figure 13.02: $4\pi r^2\rho_0[g(r) - 1]$ for *a*-Se at 200 K is compared with X-ray and neutron diffraction results of Hansen et al. (1975) (After Balasubramanian et al., 1992).

potentials (for intra-chain bonding) and L-J potential (for inter-chain interactions) and using only chain configurations. The pair distribution function G(r) obtained from simulations is also shown in the figure, which reproduces the observed distances fairly satisfactorily. Te, however, seems to form only helicoidal chains. The Te-Te-Te angles in tellurium glass and Te-rich tellurate glasses are generally large enough to allow a free rotation along the Te-Te bonds. The chain terminations in glassy Se are converted into charged defect pairs by the usual mechanism of transfer of charge from one terminal Se (radical) to another followed by the positively charged Se^+ coordinating itself to a normal two bonded Se in another chain. This results in the formation of C_3^+ (see chapter 8). The process of creation of charged defects results in reducing the concentration of terminal Se atoms and creating branched structures.

The presence and number of terminal Se atoms has important consequences particularly in $Se_{100-x}Te_x$ glasses. This is because when both Se and Te are present in the structure, (Se_3^+, Te_1^-) pair is energetically more stable than (Se_3^+, Se_1^-) pair. Therefore, in these glasses, as x increases, Te systematically substitutes Se chain terminations and forms Te^- centers till all the terminations are exhausted. Since these glasses are generally quenched from ~ 1100 K, it is estimated that they contain about

6 to 8 % Se chain terminations, which are substituted by Te^- centers. Above ~ 6 % Te, therefore, Te has to replace Se in the chains and rings. This change in the nature of substitution of Te manifests remarkably in their pressure-resistivity measurements. The behaviour of logarithmic resistivity as a function of pressure is shown for various compositions up to 6 % Te in Figure 13.03 and from 8 to 30 % Te in Figure 13.04. The

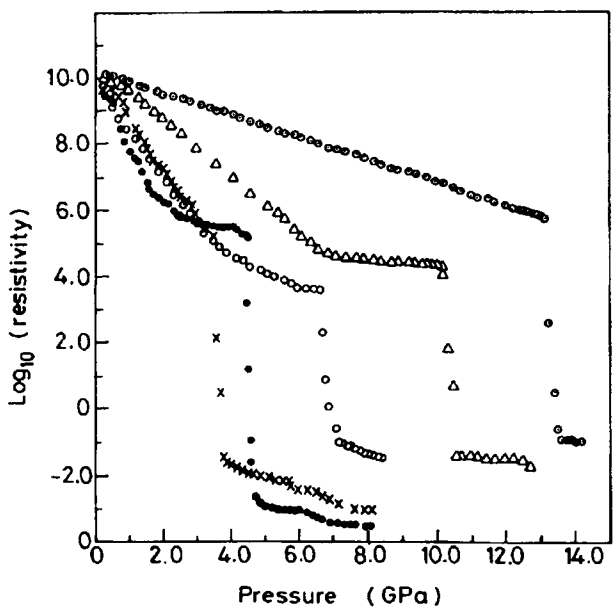

Figure 13.03: Variation of the electrical conductivity of bulk $Se_{100-x}Te_x$ glasses ($0 \leq x \leq 6$) with pressure (After Parthasarthy et al., 1984).

behaviour is remarkable because up to 6 % Te substitution there is a pressure induced transition to a low resistance state and in all cases the low resistance states were found to be crystalline. But the transitions in Figure 13.04 are continuous. The drop in the transition pressure with increase of Te is because the terminal Te^- being larger in size provides extra space around it, which is necessary for structural reorganizations required for the crystallization. Since Te gets randomly distributed in chains and rings at higher percentages, the crystallization begins to occur at different pressures depending on local Te concentration. Also, since the magnitude of the resistivity drop itself decreases around 6% Te, the variations of resistivity become increasingly continuous for $x > 6$. Because of distribution of Te and hence of the crystallization centers, several crystalline products are formed. The glass structure is largely

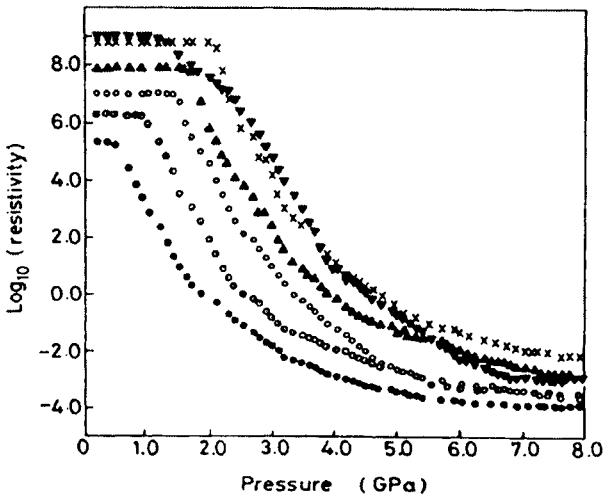

Figure 13.04: Variation of the electrical conductivity of bulk $Se_{100-x}Te_x$ glasses ($8 \leq x \leq 30$) with pressure (After Parthasarthy et al., 1984).

unaffected up to 6 % Te substitution, but above 6 % Te the inherent tendency of Te to be 3-coordinated gives rise to increased cross-linking. This is reflected in the behavior of T_g of these glasses, which remains unaffected till about 6 %, but increases as a function of x above 6 %.

Group V chalcogenides

The most widely studied chalcogenide glasses are those of P, As and Sb in Group V in addition to those of Si and Ge in Group IV of the periodic table. An incredibly large number of glasses have been synthesized using a combination of both chalcogens and other elements (Borisova, 1981). In the As-S system, glasses can be made with up to 43 % As, while in the As-Se system glasses can be formed with even up to 67 % As. In the As-Te system however, glass formation is difficult. In the As-S system, melts exhibit very high viscosity as percentage of As is increased towards the stiochiometric value of 40 % As. At 900 K, a clear maximum of viscosity of the order of 5-6 poises has been observed and it decreases sharply for higher As content. Activation barriers for viscosity exhibit a very sharp drop for additions of As in excess of stoichiometric compositions. Such a drop in viscosity has been attributed to the formation of molecular species like As_4S_4, realgar units, in As-excess compositions. In the case of As-Se system, realgar type molecular units are not as readily formed as in As-S system. In As_2Se_3, As forms three bonds and Se makes

two bonds and [$AsSe_{3/2}$] units constitute the building blocks of the glass structure. [$AsSe_{3/2}$] has the structure of a somewhat flattened pyramid with one corner being occupied by the lone pair of electrons of As. Thus, this glass is topologically similar to B_2O_3 but for the absence of MRO structures like boroxol. There is the critical requirement of planar units like [$BO_{3/2}$] for formation of boroxol-like units. The structure of As_2S_3 or As_2Se_3 glass is two dimensional, while the structure of elemental glasses like Se is one-dimensional.

Stoichiometric As_2S_3 and As_2Se_3 glasses exhibit the highest T_g in the respective glass systems. The variation of the T_g in As-Se glasses is shown as a function of composition in Figure 13.05. These T_gs could be

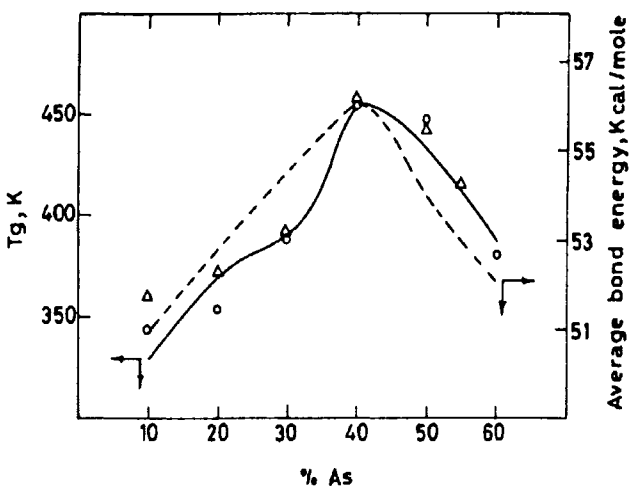

Figure 13.05: Variation of T_g with compositions: O and △ are experimental values. The variation of average bond energy is shown by the broken line and the corresponding scale is given on the right-side ordinate. The full line represents the T_g variation from bond-lattice calculations. (After Rao and Mohan, 1980).

rationalised on the basis of the bond-lattice model described earlier (chapter 3), in which the configurational heat capacities for various compositions were determined assuming plausible values of excitation enthalpies and entropies of the secondary bonds (interlayer bonds) in the structure. It was also assumed that As_2Se_3 structure is a chemically ordered network structure (see later). Several studies have been reported on As-Se glasses. In general, like all other chalcogenide glasses, they exhibit semi-conduction and the sign of the charge carriers is positive indicating dominant hole transport.

Chemical ordering

In a binary glass there can be three different bonds which are of two different types. For example, in As-S glasses, there are As-S bonds which are hetero-atom bonds and As-As and S-S bonds which are homo-atom bonds. Hetero-atom bonds are generally of higher energy because of the polar contribution, although it is not strictly correct in the case of As_2S_3. The question arises as to what types of bonds are formed in glasses, as they are quenched from their melts. In the stoichiometric composition like As_2S_3 or As_2Se_3, we would expect only hetero-atom bonds as in the parent crystalline compounds. We would expect homo-atom bonds in addition to hetero-atom bonds in the off-stoichiometric compositions; As-As bonds in As-rich compositions and S-S (or Se-Se) in S-rich (Se-rich) glasses. However, when a random network is constructed from a chemically stoichiometric As_2Se_3 (or As_2S_3) the bonding requirements can be completely met even when homo-atomic bonding is introduced randomly because for any introduction of As-As bond, it requires equivalent number of Se-Se (or an S-S) bonds to be introduced into the structure. In the stoichiometric compositions, the homoatomic bonds may be considered as wrong bonds. *A priori* probability of the wrong bond formation can be calculated. Their concentration is given by the product of such probabilities and the total number of possible bonds in the structure. A truly random network allows for the existence of both types of bonds in all binary glasses. Those As_xSe_y glasses, in which there is absence of Se-Se bonds in As-excess composition (where $x>2/3y$), of As-As bonds in Se-excess glasses (where $x<2/3y$) and of both in stoichiometric ($x=2/3y$) composition, are known as *chemically ordered* structures. With particular reference to chalcogenide glasses which form covalent networks, they are referred to as *chemically ordered networks* (CON). In the case of As-S glasses, the S-S bond energy (2.69 eV) is close to the energy of the hetero-atom As-S bond (2.48 eV). In the stoichiometric As_2S_3 glass, there is evidence for the existence of a small concentration of about 1% of homopolar bonds. Raman spectroscopic measurements (Even and Owen, 1980) have revealed the presence of As-As stretching frequency around 220 cm^{-1}. Even EXAFS studies of $As_2(S,Se)_3$ glasses have provided evidence for the presence of homo-atomic bonding (As-As and S-S) through the unusual spread of observed second neighbour distances of As (Parathasarthy et al., 1982). Therefore, glasses in the As-S system seem to violate chemical ordering. It is interesting to note here that As_2S_3 glass has a density which is about 10% lower than that of the crystalline As_2S_3 and

the openness of the structure can also be partly associated with significant homo-polar bonding.

Although in crystalline As_2Te_3, As sites are octahedrally coordinated by Te, in the glass they form only [$AsTe_{3/2}$] pyramidal units. In the glass, As-Te bond length is 2.5Å, and the Te-As-Te bond angle is 98°, As-Te-As bond angle lie in the range of 95°-98°. But the more interesting feature of this glass is that some of the Te atoms are found to be 3-coordinated. In As_2Se_3-As_2Te_3 glasses, evidence has been found from ^{129}I Mössbauer measurements (Wells and Boolchand, 1987) that the chemical ordering is violated and inter-chalcogen bonds are present. The presence of 3-coorindated Te is also evidenced in the EXAFS studies of the Te-rich $As_2(Se,Te)_3$ glasses (Parthasarathy et al., 1982).

Photoelectron spectroscopic studies have been used to determine the chemical shift variations of As, Se and Te in $As_2(Se,Te)_3$ glasses and the variations are shown in Figure 13.06. Arsenic shifts become more positive in intermediate compositions indicating that in these compositions the nature of bonding is more ionic. There is a remarkable variation in the

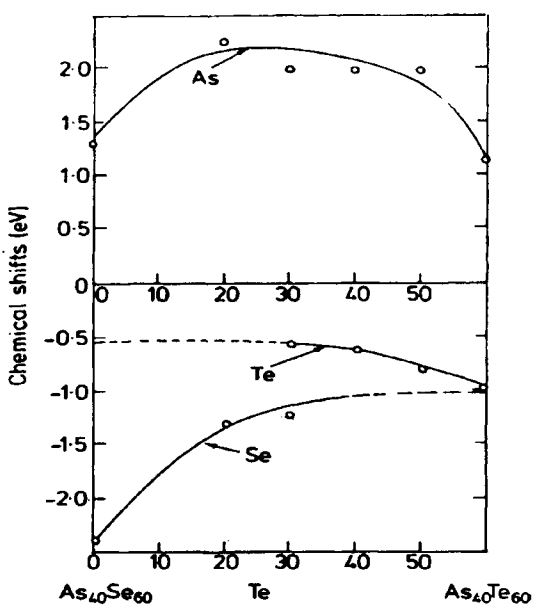

Figure 13.06: Variation with composition of chemical shifts of As, Se and Te obtained from X-ray absorption spectra (After Sarode et al., 1979).

chemical shifts of Se suggesting that in intermediate compositions Se is almost Se^-. Valence state of Te does not change much in these

compositions. In the As_2Te_3–rich glasses, one should expect manifestation of structural anomalies arising from the tendency of Te to be three-bonded and associated coordination changes of As from 3 to 4. Conductivity and thermoelectric power (TEP) measurements have been reported on these glasses (Mahadevan and Rao, 1979). It was found that TEP exhibits anomalous increase as shown in Figure 13.07. But no anomaly was observed in conductivities. The observations have been attributed to the emergence of small polaron conduction, which affects the temperature independent term in the expression for thermo-power. In turn, this is related to the structure because small polaron hopping depends on As-Te-As-Te connectivities. It is only in As_2Te_3-rich glasses that these connectivities exist over long distances.

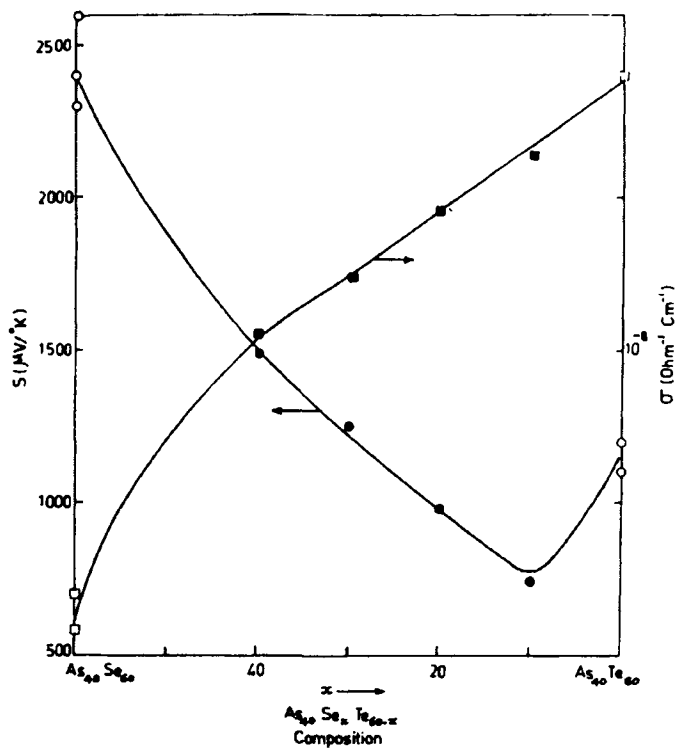

Figure 13.07: Variation of room temperature σ ($\equiv\sigma_{dc}$) and S with composition of glasses of the system As_2Se_3-As_2Te_3 (After Mahadevan and Rao, 1979).

Pressure also affects the conductivities in $As_2(Se,Te)_3$ glasses. The resistivities of these glasses decrease continuously with pressure (Ramani

et al., 1979). The variation of activation energy with pressure is shown for various compositions in Figure 13.08. The activation energy tends

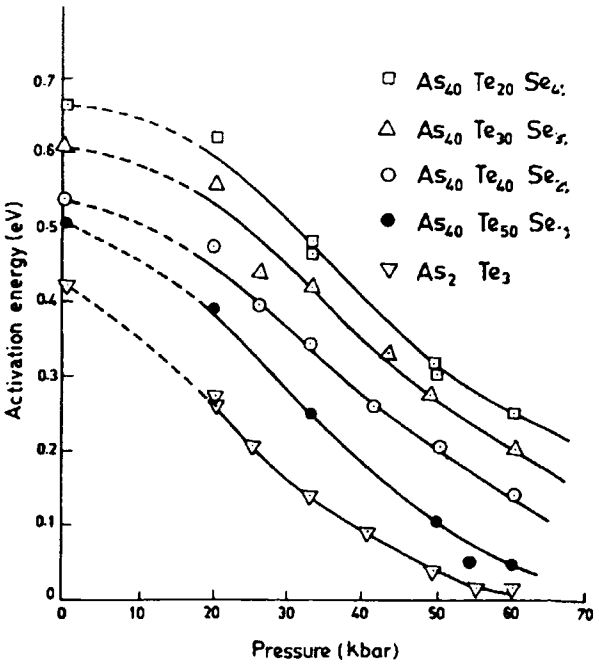

Figure 13.08: The variation of activation energy with pressure for $As_{40}Se_xTe_{60-x}$ (After Ramani et al., 1979).

towards zero in the case of Te-rich glasses around 100 Kbar pressure. This is attributed to the change of the coordinations of both As and Te, pushing the structure closer to that of crystalline As_2Te_3, which is known to become metallic (Sakai and Fritzsche, 1977). This is evidently due to participation of the lone pairs of both As and Te, which constitute the top of the valence band. The valence band moves towards the conduction band under pressure attended by a gradual decrease and vanishing of the mobility gap.

Phosphorous also forms chalcogenide glasses and they have been studied in considerable detail (Borisova, 1981; Elliott, 1991). Structurally these glasses are very interesting because molecular entities with the general formula P_4S_n and P_4Se_n (n=3-10) having cage-like structures are formed in glasses. It appears as if in the tetrahedral P_4 molecular structure, the P-P bonds are broken and a number of chalcogens are inserted. Symmetrical cages would result when 4 or 8 atoms are inserted and in the case of P_4S_3 and P_4Se_3 the cage is symmetrical but with insertion of the

chalcogen in only three of the P-P bonds. Attaching chalcogens to the apical P atom has been found to be less favorable. Phosphorous selenides, in general, are hygroscopic like phosphorous oxy compounds, although to a lesser extent. $P_{66.6}Se_{33.4}$ glass remains essentially unaffected even in humid air. Between P_4S_n and P_4Se_n alloys, P_4Se_n exhibits greater tendency towards glass formation. $P_xSe_{(1-x)}$ glasses are made by quenching from temperatures of around 700°C. There are two distinct glass-forming regimes in this system. The first one corresponds to $0< x <0.52$ and the second to $0.63< x <0.85$. Glasses in the intermediate composition region can be prepared but they are unstable and tend to crystallize. The stoichiometric composition of P_4Se_3 (x=0.57) lies at the center of the two glass-forming regimes. The variation of T_g and microhardness as a function of x in P-Se glasses is shown in Figure 13.09. Sharp and unusual breaks occur in both T_g and microhardness trends in the region between

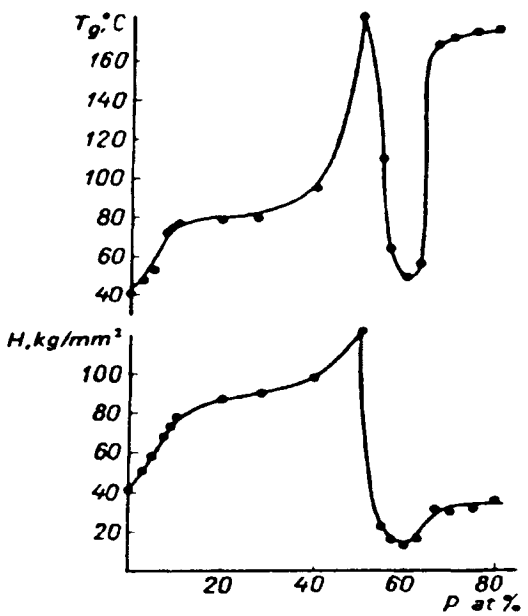

Figure13.09: Dependence of the microhardness (H) and T_g on the phosphorus content in glassy alloys of the P-Se system (After Borisova, 1981).

the two glass-forming regimes. In Se-rich glasses (regime1), some evidence has been reported for the presence of P_4Se_5 and P_4Se_3 molecules in the structure. Both Raman and MASNMR studies support the existence of P_4Se_n clusters. In the Se-rich regime, [$PSeSe_{3/2}$] (like [$POO_{3/2}$]) units are present where one of the Se is double bonded to P. ^{31}P HR MAS NMR

spectra of the Se-rich glasses are shown in Figure 13.10. The relative concentration of terminal Se is indicated by the growth of the peak corresponding to ~ 0 ppm (Eckert, 1989). In the P-rich glasses, the structure is built up of trigonal [$PSe_{3/2}$] units in addition to tetrahedral [$PSeSe_{3/2}$] units and at still higher concentrations of P, formation of homopolar P-P bonds (as in red P) has been reported.

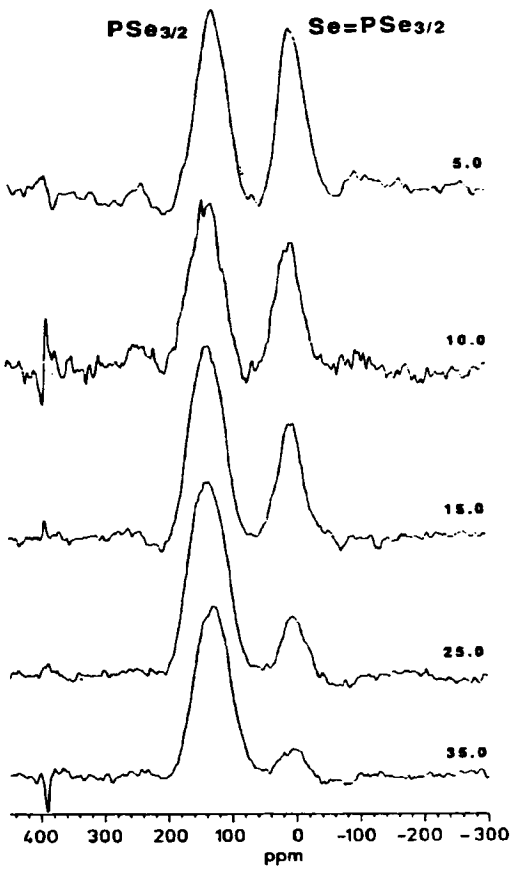

Figure 13.10: ^{31}P MAS NMR spectra of various P_xSe_{1-x} glasses (After Eckert, 1989).

Antimony, in Group V, also forms chalcogenide glasses although it requires relatively higher rate of quenching from the corresponding melts. Sb_2S_3 glass can be made only by roller-quenching (Cervinca and Hruby, 1982) and it consists of [$SbS_{3/2}$] pyramidal units in the structure. They give rise to characteristic Raman band around 290 cm^{-1}.

Group IV chalcogenides

Among the Group IV elements, chalcogenide glasses of Si and Ge have been widely studied. Both Si and Ge are generally present in tetrahedral coordination forming $[GeSe_{4/2}]$ or $[SiSe_{4/2}]$ units. But in chalcogenide glasses a unique feature, which is unlike their oxide counterparts, is that the tetrahedra share edges. Edge-sharing will decrease the dimensionality. In glassy GeS_2 and $GeSe_2$ presence of both edge shared and corner shared configurations seem to be present. Compared to GeS_2, Ge-rich compositions develop Ge-Ge bonds and in a glass of the composition Ge_2S_3, ethane like groupings ($Ge_2S_{6/2}$) have been identified. Using ^{119}Sn- Mössbauer studies of dopant Sn in these glasses, presence of two different Ge sites, one corresponding to $[GeS_{4/2}]$ and the other corresponding to $[GeS_{3/2}Ge_{1/4}]$ have been identified. In the chalcogen-rich compositions, S_n (Se_n) (where $n \geq 2$) linkages are present which bridge Ge atoms in the structure. In Ge-rich Ge-Se glasses, 3-coordinated Ge has been reported to be present as defects (Kawamura and Matsumura, 1979) along with 3-coordinated Se. These defects have been studied using Raman spectroscopy.

In SiS_2 and $SiSe_2$ glasses, it is very interesting to note that the structure consists of chains of edge-shared tetrahedra along with corner-connected tetrahedra. ^{29}Si-MAS NMR studies of SiS_2 and $SiSe_2$ glasses seem to suggest that almost 50% of the structure can be assigned to chain-like structures resulting from sharing of one edge (E^1) of the tetrahedra, while the remaining part consists of equal proportion of corner-shared (E^0) and double edge-shared (E^2) tetrahedra (Tenhover et al., 1988). This is neatly revealed in the ^{29}Si MAS NMR as shown in Figure 13.11. The presence of single and two-edge shared $[SiS_{4/2}]$ units in the structure of SiS_2 glass has been recently confirmed through *ab initio* molecular orbital calculations. These glasses give two Raman bands at 427 and 415 cm^{-1} and have been assigned to the breathing motions of S atoms present in the single edge and two edge-shared tetrahedral units respectively (Tokuda et al., 2001).

Thioborate glasses

Another important class of chalcogenide glasses is based on B_2S_3 (Menetrier et al., 1992). B_2S_3 glass itself consists of chains of edge-sharing $[BS_{3/2}]$ units as shown in Figure 13.12. The structure consists of small 4-membered rings connected via sulphur bridges and with pairs of

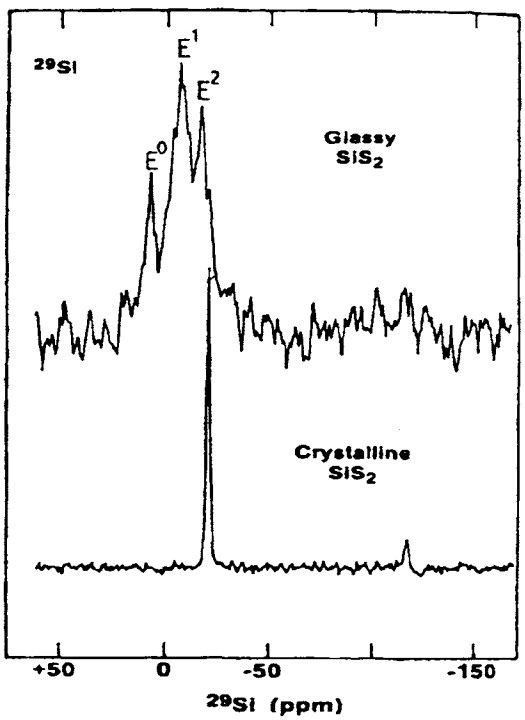

Figure 13.11: ^{29}Si MAS NMR of glassy and crystalline SiS_2 E^n corresponds to tetrahedra sharing n edges (After Tenhover et al., 1988).

thioboroxol rings having $3[BS_{3/2}]$ units interspersed in the chains like in crystalline B_2S_3 itself. The presence of these features in the structure has been confirmed through extensive NMR, neutron scattering and Raman spectroscopic work (Estournes et al., 1994; Menetrier et al., 1992; Haddad et al., 1992). Addition of Li_2S has the effect of modifying the structure by converting trigonal B_3 to tetrahedral B_4 (in complete analogy to oxides). For $[Li_2S]/[B_2S_3]$ ratio of 1.0, the ratio $[B_4]/\{[B_3]+[B_4]\}$ has been found to be as high as 0.35 and it decreases almost linearly to about 0.06-0.08, as the $[Li_2S]/[B_2S_3]$ ratio increases to 3.0. The modification produces linear segments and also tightly connected charged units containing B_4 as shown in Figure 13.13. But as the ratio of $[Li_2S]/[B_2S_3]$ increases towards 2 and 3, smaller units like pyro-thioborate, $[B_2S_5]^{4-}$ and ortho-thioborate, $[BS_3]^{3-}$ groups are also formed. Structural entities like $[BS_{4/2}]^-$ are similar to $[BO_{4/2}]^-$ observed in modified B_2O_3 glasses. The structure of glassy B_2S_3 has been examined using MD simulation. The potential function consisted of BMH coulombic interactions with reduced (partial) charges on B and S. A dipole interaction term dependent on the polarisabilities of the atom was

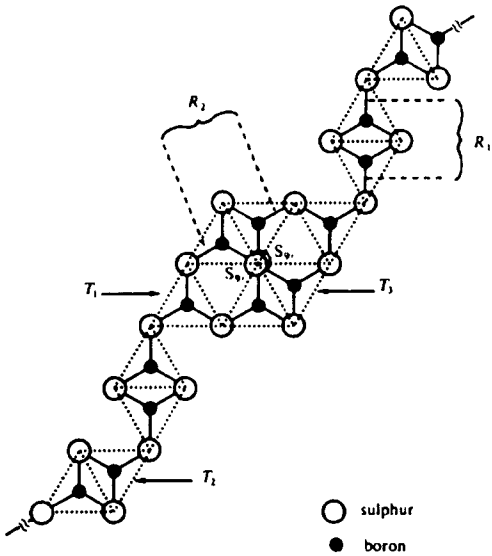

Figure 13.12: Structure of vitreous B_2S_3 (After Menetrier et al., 1992).

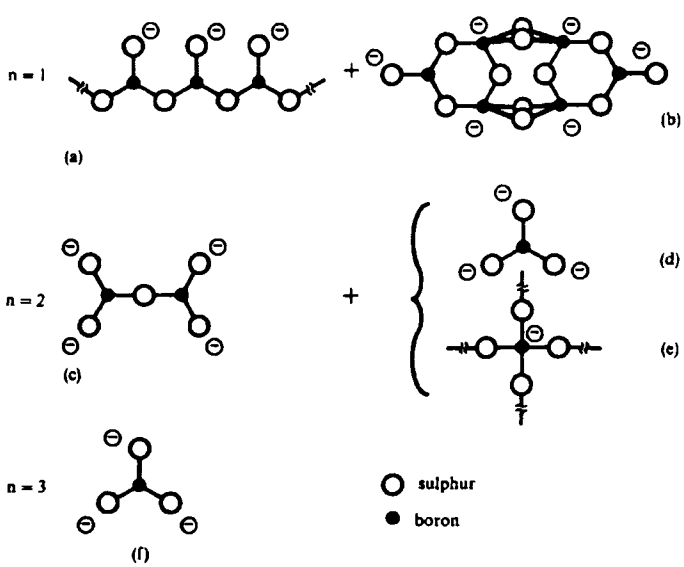

Figure 13.13: Structural entities suggested to be present in B_2S_3-nLi_2S glasses (After Menetrier et al., 1992).

also included. A three-body potential was introduced to account for the directional bonding (covalent) with two characteristic angles, S-B-S (=120°) and B-S-B (=60°) (Balasubramanian and Rao, 1994). Formation of long chains containing B_2S_2 small rings connected by S bridges was evident in the simulated structure. However, B_3S_3 rings, of the thioboroxol type, were not found to form, which is not fully consistent with the Raman spectroscopic results.

Raman spectroscopy has provided some important insights regarding the nature of modification in the Li^+ ion conducting $B_2S_3 \cdot nLi_2S$ systems. In the Raman spectrum of pure B_2S_3, (n = 0) (Figure 13.14) there are two major peaks at 780 cm^{-1} and 450 cm^{-1}. But as n is increased from 0 to 1, the Raman spectra undergo changes as shown in Fig 13.15. There

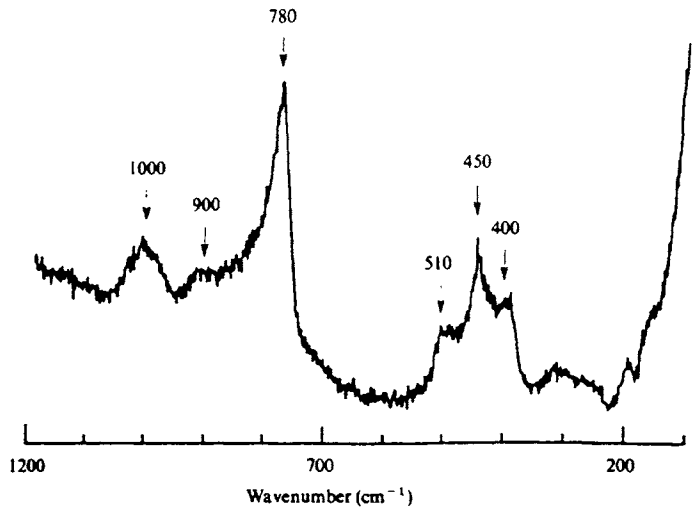

Figure 13.14: Raman spectrum of vitreous B_2S_3 (After Menetrier et al., 1992).

is clearly absence of high frequency lines, which are due to stretching of the 3-coordinated borons in $BS_{3/2}$ units, suggesting that the observed low frequency vibrations in the region of 450 - 500 cm^{-1} can only be attributed to modified R-type rings shown in Figure 13.12. These are essentially compact structures of several rings fused at the boron centers. Further modification leads to breaking down of the structure leading to pyro-thioborate and ortho-thioborate units. When n = 3, the dominant peak at 448 cm^{-1} which has nearly the same force constant as the $BS_{3/2}$ units, is attributed to $[BS_3]^{3-}$. This is a likely consequence of the additional electrons in $[BS_3]^{3-}$ filling the non-bonding levels in the molecular orbitals (Menetrier et al., 1992).

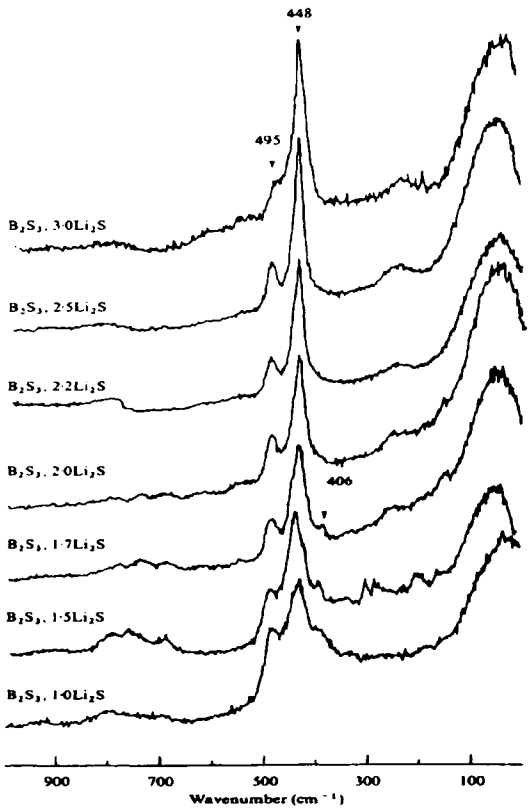

Figure 13.15: Raman spectrum of B_2S_3-nLi_2S glasses (After Menetrier et al., 1992).

A number of investigations have been reported on the preparation and properties of a variety of binary ternary and quaternary chalcogenides. Elements like Sb and Bi also exhibit tendency to be incorporated into chalcogenide network structures. As the number of elements introduced increase, there are two possibilities in the behaviour of the liquids. One is, they may develop tendency towards phase separation, which leads to the formation of inhomogeneous glasses. Secondly, the increased configurational entropy of the system expands the glass forming regime. An *a priori* prediction of this behaviour is difficult. However, several phase diagrams of the glass forming regions have been generated experimentally, some of which have been shown in Figure 13.16 as examples. It may be noted that while there is extensive glass formation in As-S-Se and As-Se-Te systems, in Ge-chalcogenide based systems, not only is the glass forming region limited but also there are two separated

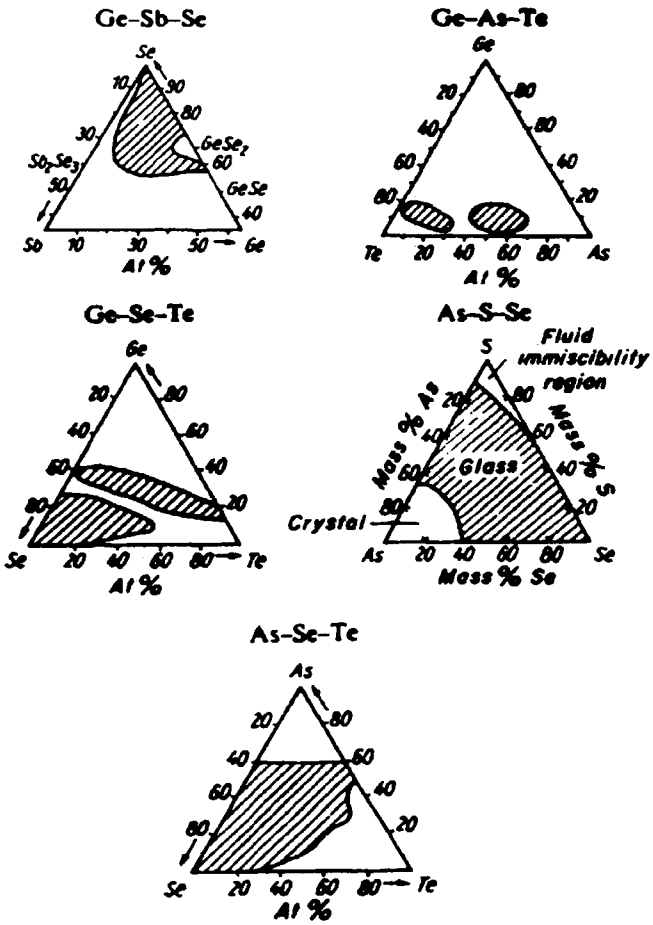

Figure 13.16: Ternary phase diagrams indicating glass formation regions involving Ge, Sb, S, Se and Te (After Vogel, 1985).

regions of glass formation.

Chalcogenide glasses containing halogens

Halogens, particularly iodine is readily incorporated at chain terminations in chalcogenide glasses (for example, As-Se-I glasses) (Borisova, 1981). This is consistent with the chemical nature of iodine because it has a valency of one. Incorporation of iodine brings down the T_g of the glass. Both, iodine and tellurium, as noted earlier in Chapter 8, are components of threshold and memory switching glasses. Iodine is also

introduced as I^- ions in several chalcogenide glasses. Li_2S modified chalcogenides give rise to extraordinarliy high Li^+ ion conductivities which is increased further by addition of LiI. Addition of salts like LiI increases the conductivities of thiosilicate glasses also. Iodide ions have the effect of expanding the structure and decreasing the activation barriers for Li^+ ion conduction. Like in oxide glasses (chapter 12), addition of lithium salts like Li_4GeO_4 or Li_3PO_4 into thiosilicate glasses leads to remarkably high Li^+ ion conductivities. Principles which govern their properties are understandably related to the dimensionality and the network connectivity of the constituent structural units. Increased proportions of chalcogens in glasses decrease the average coordination number making the structures more floppy. This manifests in decreased (mechanical) moduli and somewhat increased glass forming tendency. Of interest, in this context, is the more recent investigation of $Al_xTe_{(1-x)}$ ($17 \leq x \leq 30$) glasses (Murugavel and Asokan, 1998), which exhibit an unusual structural feature; Al is present both in tetrahedral and octahedral coordination as clearly evidenced in ^{27}Al-MAS NMR spectra shown in Figure 13.17. Octahedral Al in oxide glasses is well-known and is due to

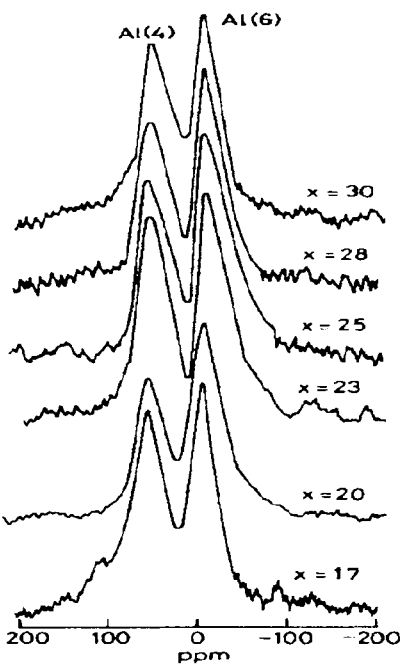

Figure 13.17: Compositional dependence of the ^{27}Al MAS NMR spectra in Al_xTe_{100-x} ($17 \leq x \leq 30$) glasses (After Murugavel and Asokan, 1998).

the presence of Al^{3+} ions in the structure. The glass transition temperatures increase almost linearly with Al concentration, which may possibly reflect network degradation of Te leading to better packing and greater cohesion.

The electronic conductivities of chalcogenide glasses are governed by the nature of the chalcogen because the top of the valence band is constituted of the lone pair states. Therefore, the energy gap tends to be lowest for the telluride glasses. Nevertheless, it is the mobility gap which is important in the context of conductivity and disorder determines the mobility gap (see Chapter 8). From the point of view of structures, sulphur and selenium in glasses remain 2-connected and only tellurium tends to be 3-connected (except in charged defects, C_3^+ and C_1^-). Therefore, much of the variety in structures of chalcogenide glasses seems to arise from the bonding tendencies of the other atoms present in the network.

References:

Balasubramanian, S., Damodaran, K. V. and K. J. Rao, 1992, Chem. Phys. **166**, 131.

Balasubramanian, S. and K. J. Rao, 1994, J. Phys. Chem., **98**, 9216.

Borisova, Z. U., 1981, Glassy Semiconductors (Plenum Press, New York), p. 76.

Cervinca, L. and A. Hruby, 1982, J. Non-Cryst. Sol., **48**, 231.

Corb, B. W., W. D. Wei and B. L. Averbach, 1982, J. Non-Cryst. Sol., **53**, 29.

Cornet, J. and D. Rossier, 1973, J. Non-Cryst. Sol., **12**, 85.

Eckert, H., 1989, Angew. Chem. Int. Ed. Engl. Ad. Mater., **28**, 1723.

Elliott, S. R., 1991, Materials Science and Technology: A Comprehensive Treatment, Vol. 9, eds. R.W. Cahn, P. Haasen and E.J. Kramer (Wiley-VCH, Weinheim) p. 375.

Estournes, C., A.P. Owens, M. Menetrier, A. Levasseur, K. J. Rao and S.R. Elliot, 1994, J. Non-Cryst. Sol., **171**, 80.

Even, P. J. S. and A. E. Owen, 1980, J. Non-Cryst. Sol., **36**, 1191.

Haddad, M., R.Berger, Y. Servant, M. Menetrier, A. Levasseur, and K. J. Rao, 1992, Phys. Chem. Glasses, **33**, 122.

Hansen, F. Y., T.S. Knudsen and K. Carneiro, 1975, J. Chem. Phys., **62**, 1556.

Kawamura, H. and M. Matsumura, 1979, Solid State Comm., **32** 83.

Mahadevan, S. and K. J. Rao, 1979, J. Non-Cryst. Sol., **34**, 53.

Menetrier, M., A. Hojjaji, A. Levasseur, M. Couzi and K. J. Rao, 1992, Phys. Chem. Glasses, **33**, 222.

Murugavel, S. and S. Asokan, 1998, Phys. Rev. B, **57**, 33.

Myers, M. B. and E. J. Felty, 1967, Mat. Res. Bull., **2**, 715.

Parathasarathy, R., K. J. Rao and C. N. R. Rao, 1982, J. Phys. C Solid State Phys., **15**, 3649.

Parathysarathy, R., K.J. Rao and C.N.R. Rao, 1982, J. Phys. C., **15**, 3649.

Parthasarthy, G., K. J. Rao and E. S. R. Gopal, 1984, Philos. Mag., **50**, 335.

Parthasarthy, R., P. R. Sarode and K. J. Rao, 1981, J. Mat. Sci. Lett., **16**, 3222.

Ramani, G., A. Giridghar, A. K. Singh and K. J. Rao, 1979, Philos. Mag., **39**, 385.

Rao, K. J. and R. Mohan, 1980, J. Phys. Chem., **84**, 1917.

Sakai, N. and H. Fritzsche, 1977, Phys. Rev. B, **15**, 973.

Sarode, P. R., K. J. Rao, M. S. Hegde and C. N. R. Rao, 1979, J. Phys. C Solid State Phys., **12**, 4119.

Savage, J. A., 1985, J. Non-Cryst. Sol., **47**, 101.

Tenhover, M., R. D. Boyer, R. S. Henderson, T. E. Hammond and G. A. Shreve, 1988, Solid State Comm., **65**, 1517.

Tokuda, Y., T. Uchino and T. Yoko, 2001, J. Non-Cryst. Sol., **282**, 256.

Vogel, W., 1985, Chemistry of Glass (Am. Cream. Soc.), p. 184.

Wells, J. and P. Boolchand, 1987, J. Non-Cryst.Sol., **89**, 31.

Wendo, W., B. W. Corb and B. L. Averbach, 1982, J. Non-Cryst. Sol., **53**, 19.

Yamane, M., and Y. Asahara, 2000, Glasses for Photonics, (Cambridge University Press, Cambridge).

Man masters nature not by force but by understanding.
- Jacob Bronowski.

CHAPTER 14

OTHER GLASSES

Halide glasses

Halide glasses like BeF_2 and $ZnCl_2$ have been known for a long time (Van Uitert and Wemple, 1978; Weber, 1986; Lucas, 1991). These glasses are obtained by simply quenching halides from their molten state. Structures of simple BeF_2 and $ZnCl_2$ seem to be based on tetrahedrally coordinated Be and Zn and with halogens forming bridges between tetrahedra. Therefore, their structures are similar to those of SiO_2 and GeO_2 or even more appropriately to that of amorphous water. Although F bridges are strong, the same cannot be said of other halogens. Therefore both these glasses are weak analogues of the covalently bonded tetrahedral SiO_2 glass. BeF_2 glasses doped with transition metal ions like Nd^{3+} are very good high-power laser materials because BeF_2 has very low linear and non-linear refractive indices. Reference was made earlier (Chapter 4) to the environment of Nd^{3+} in Nd-doped BeF_2 glasses. Nd^{3+} resides in NdF_7 polyhedra. The geometry of coordination polyhedron is that of a capped octahedron which can co-exist with and easily transform to a pentagonal bipyramid. Since F has the highest electronegativity, the bonding is highly ionic in fluoride glasses. Be-F bond is approximately 80% ionic (BeF_2 is extremely toxic, the threshold limit being 0.002 mg/m^3, which is 100 times lower than arsine). It has a T_g of 250 ^{0}C.

$ZnCl_2$ glass has been of much academic interest, although it has great potential to be used as an IR window in the 8-10μm range. $ZnCl_2$, like BeF_2 is hygroscopic, which is its chief limitation. $ZnCl_2$ glasses with $PbCl_2$, $CdCl_2$ and $CdBr_2$ have been found to be more resistant to attack by water (Yamane et al., 1985). Its tendency towards devitrification, however, improves by the addition of other halides like KBr and $PbBr_2$. Chloride bridges are much weaker than the fluoride bridges and the glasses are inherently unstable towards devitrification. Several other divalent metal halides are known to form glasses either by themselves or in combination. $ZnBr_2$ can be vitrified as a single component glass (Kadono et al., 1987), but its glass forming ability has been known to increase by the addition of KBr. $CdCl_2$ is like a conditional glass former which forms glass in combination with PbI_2 or $PbCl_2$. Similarly, melts of

mixtures of CdF_2, BaF_2 and NaCl have been obtained in the glassy state (Matecki et al., 1987). CdI_2 based systems such as CdI_2-KI, CdI_2-CsI have also been reported in the literature. The increased mass of the anion shifts the IR limit of transparency to almost 30μ in these systems (Cooper and Angell, 1983). But again, these glasses are inherently hygroscopic and have low T_g values, which diminish their utility. Glass forming ability in ionic halide system has often been related to the ratio of the field strength of cation, f_c, to that of the anion, f_a. Glass formation appears to be significant when this ratio, f_c/f_a is between 2.5 and 10.

There has been much interest in the investigation of fluoride glasses. The metal-fluorine (M-F) bond is unstable towards oxidation because M-O bond is inherently stronger. However fluoride glasses, particularly those based on heavy metal cations, hold very high promise for application as communication (optical) fibres due to their excellent optical properties. They are very highly transparent in the mid-IR region and multi-component heavy metal fluoride glasses have been developed with such applications in view. Fluorides of not-so-heavy elements such as AlF_3 and NaF are often added which improve the resistance of these glasses towards devitrification. This is a consequence of increased configurational entropy, which the multi-component glass-forming systems find difficult to eschew at ordinary rates of cooling. From the point of view of nucleation and growth of crystalline phases in multi-component melts, this is often referred to as *confusion principle.* Increasing LiF, NaF and AlF_3 content in halide glasses is known to decrease the refractive indices.

Trivalent halides like AlF_3, FeF_3, CrF_3 and GaF_3 (Jacoboni et al, 1983) are known to form glasses only in combination with divalent fluorides like ZnF_2, MnF_2 and PbF_2. Trivalent ions appear to be present in octahedral coordination of fluorines as MF_6.

Heavy metal fluoride glasses

It is the glass formation in tetraheral fluorides like ZrF_4 which created new interest in fluoride glasses in 1970s (Poulain et al., 1975; Poulain and Lucas, 1978; Poulain et al., 1977; Moynihan, 1989). Lucas and coworkers made the first heavy metal fluoride glasses with ZrF_4 as the major component. Neither ZrF_4 nor HfF_4 (nor ThF_4) can be vitrified as single-component glasses. But in combination with other fluorides like BaF_2 and LaF_3, which are di- and trivalent fluorides, they give rise to rather stable glasses, although over limited ranges of composition. A phase

diagram of ZrF_2-LaF_3-BaF_2 is shown in Figure 14.01 delineating the glass forming region. The multi-component heavy metal fluorides are very

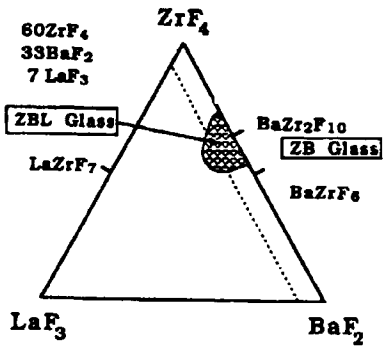

Figure 14.01: Glass forming domain in the ternary diagram ZrF_4·BaF_2·LaF_3 (After Lucas, 1991).

frequently represented by acronyms. The compositions and the acronyms of some of these glasses are given in Table 14.1. One of the widely used structural

Table 14.1: Compositions and acronyms of some of the heavy metal fluoride glasses.

Acronym	Composition
ZB	$64ZrF_4$·$36BaF_2$
ZT	$53ZrF_4$·$47ThF_4$
ZBN	$50ZrF_4$·$25BaF_2$·25NaF
ZBG	$63ZrF_4$·$33BaF_2$·$4GdF_3$
ZBL	$62ZrF_4$·$33BaF_2$·$5LaF_3$
HBL	$62HfF_4$·$33BaF_2$·$5LaF_3$
ZBT	$57.5ZrF_4$·$33.75BaF_2$·$8.755ThF_4$
HBT	$57.5HfF_4$·$33.75BaF_2$·$8.755ThF_4$
ZBU	$55ZrF_4$·$30BaF_2$·$15UF_4$
ZTY	$50ZrF_4$·$43ThF_4$·$7YF_3$
ZBLA	$57ZrF_4$·$36BaF_2$·$3LaF_3$·$4AlF_3$
ZBGA	$57ZrF_4$·$35BaF_2$·$5GdF_3$·$3AlF_3$
ZBYA	$45ZrF_4$·$36BaF_2$·$11YF_3$·$8AlF_3$
HBLA	$57HfF_4$·$36BaF_2$·$3LaF_3$·$4AlF_3$
YABC	$20YF_3$·$40AlF_3$·$20BaF_2$·$20CaF_2$
CLAP	$26.1CdF_2$·10LiF·$30.6AlF_3$·$33.3PbF_2$
ZBLAN	$56ZrF_4$·$19BaF_2$·$6LaF_3$·$4AlF_3$·15NaF

models for glasses like ZB assumes that Zr forms fluorine polyhedra which share the F corners and the polyhedra are of the type ZrF_7 and ZrF_8 as shown in Figure 14.02. Large Ba^{2+} ions occupy interstitial positions

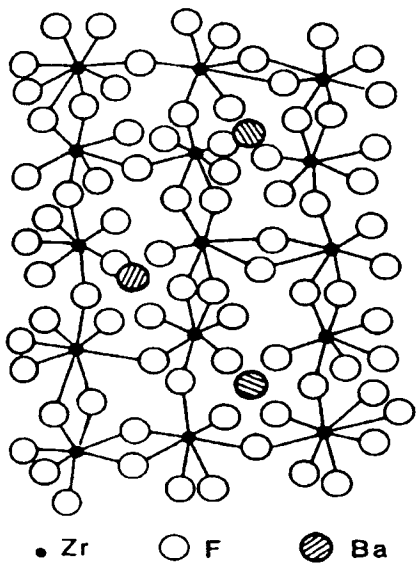

Figure 14.02. A structural model for the binary glass $2ZrF_4 \cdot 1BaF_2$. Elementary polyhedra ZrF_7 and ZrF_8 sharing corners and edges form a 3-D aperiodic framework. The large Ba^{2+} cations play the role of lattice modifiers (After Lucas, 1991).

surrounded mostly by non-bridging F. One can recognize a resemblance to the structures of modified oxide glasses if one were to treat ZrF_4 as $[ZrF_{8/2}]^0$ and $[ZrF_{6/2}F]^0$ and consider BaF_2 as a modifying fluoride. BaF_2 breaks the bridges and converts $[ZrF_{8/2}]^0$ to $[ZrF_{7/2}F]^-$ and $[ZrF_{6/2}F]^0$ to $[ZrF_{5/2}F_2]^-$. One can visualize the structure as having evolved from neutral units with different coordinations to the experimentally observed coordination polyhedra. In the Group IV fluorides of Zr, Th and Hf, the cations are coordinated to 8 fluorine atoms. It appears that the high anion coordination is a general feature, both in fluorides and oxides of these elements and is in conformity with the high ionicity of bonding which results with both F and O. The 8-coordination of Th in $0.33ThF_4 \cdot 0.6HfF_4 \cdot 0.07LaF_3$ glass has been examined using XANES and EXAFS associated with the L_{III} edge of Th, and compared with the XANES and EXAFS of crystalline ThF_4. The coordination numbers, distances and the spread in the distances (equivalent of Debye-Waller factor) are given in Table 14.2. The standard deviation from the EXAFS

Table 14.2: Structural parameters of $0.33ThF_4 \cdot 0.6HfF4 \cdot 0.07LaF_3$ glass from EXAFS analysis of L_{III} edge.

N(Å)	r(Å)	$\sigma^2(Å^2)$	Standard deviation of EXAFS fit
2.89	1.83	0.0092	
3.17	1.92	0.0065	7%
2.07	1.99	0.0005	

fit was found to be satisfactory. Therefore, the coordination number of Th remains almost unaltered in the glassy state. It is interesting to compare the XANES (Th-L_{III} edge) of ThF_4 in crystalline and glassy phases, which is shown in Figure.14.03. While the fluorine coordination of Th remains the same in crystal and glass, the white-line intensity in the glass is almost 12% higher. The white line intensity in general can be related to the bonding electron density on the metal ion itself and hence to the covalency of bonding. It is, therefore, suggestive of the metal-fluorine bonding being

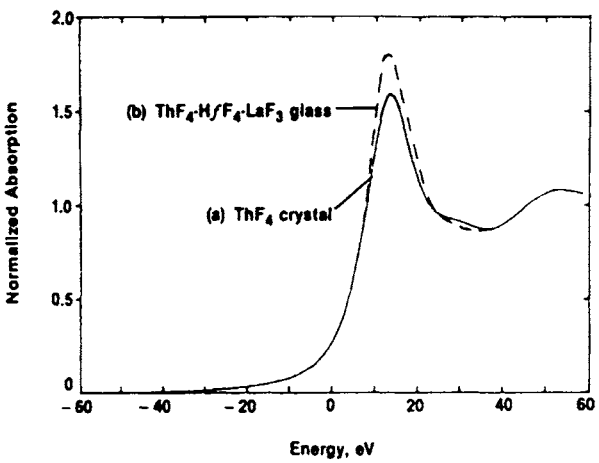

Figure 14.03: Normalized Th L_{III}-edge XANES in (a) crystalline ThF_4 and (b) 0.33 $THF_4 \cdot 0.6\ HfF_4 \cdot 0.07LaF_3$ glass (After Rao et al., 1984).

significantly more covalent than suggested by the Pauling ionicities in the glasses. In fact, this lends support to the network former-modifier description of these glasses implied in Figure 14.02.

It may be noted here that even a combination of just monovalent halides namely, AgCl-AgI-CsCl, AgBr-CsBr and AgI-CsI have been successfully vitrified (Angell and Zeigler, 1981; Angell et al., 1985).

Evidently in such multi-component glasses of simple halides, significant lowering of the eutectic temperatures and of course, the confusion principle, together assist formation of glasses.

There seems to be some pattern in the formation of glasses in the halide systems. In the quadrivalent halides, the quadrivalent element has a high coordination number of 7 or 8, bonding is reasonably covalent and glass formation region is expanded by former-modifier combinations. In glasses based on trivalent halides, the metal ion is generally octahedrally coordinated and is again reasonably covalent and combination with di and mono-valent halides assist glass formation. In divalent halides the structural unit is tetrahedral, the stabilities are dependent on the strength of the bridging halogen and the glasses are weak analogues of SiO_2. But when only a combination of monovalent halides are involved, it is the lowering of the liquidus temperatures by the increase of configurational entropy and the confusion principle which helps glass formation.

In the earlier chapters, reference was made to the importance of heavy metal fluoride glasses for applications based on their optical properties. The first important application is as hosts for high power lasers and the second, as infrared windows. Yet another application has been to use these glasses for making fibres for fibre-optic communication. Fluoride glasses, as noted in chapter 11, can give rise to extremely low attenuations of the order of 10^{-3}-10^{-2} dB/km, which raises the hope for repeater-less fibre-optic communication. Due to the low viscosity of heavy metal fluoride melts compared to oxide melts, drawing fibres and avoiding the formation of crystalline phases become extremely difficult (crystalline phases act as scattering centers and increase attenuation). In practice it has been difficult to achieve attenuations of less than 1dB/km.

Oxy-halide glasses

In the context of FIC glasses (chapter 6), we made references to glass systems like LiI-Li_2SO_4-$LiPO_3$. Alkali halide or silver halide can be added to such essentially oxide glass systems. The halide ions remain as such in the structure and these glasses may be considered as oxy-halide glasses, although oxygen and halogen are not present together in the primary coordination of the network-forming atom. From this point of view, lead oxy-halide glasses are very unique. In particular, PbO-PbF_2 and PbO-$PbCl_2$ are two systems in which glasses can be made over a wide range of compositions, with PbO ranging from 30-80% in PbO-PbF_2 and 40-90% in PbO-$PbCl_2$ (Rao et al., 1984; Damodaran and Rao, 1988; Rao

and Rao, 1984). These glasses exhibit T_g in the range of 460 K (30PbO-70PbF_2) to 600 K (90PbO-10$PbCl_2$). Increasing the halide content decreases the T_g. The components in these glass systems represent extremes in the nature of bonding. PbO is rather covalent and has a crystal structure (yellow PbO) consisting of $[PbO_{4/2}]^0$ pyramidal units, connected extensively in puckered layers. $PbCl_2$ and PbF_2 are highly ionic and the first neighbour shell of Pb consist of 9 halide ions in the structure. Therefore, the structures of the compositionally homogenous glasses, which PbO and PbF_2 (or $PbCl_2$) form are very interesting. RDFs obtained from an analysis of X-ray diffraction suggest the presence of a uniform structural motif in all compositions of the glasses. A model of the glass structure, consistent with the above observation requires that $[PbO_2X_4]$ (distorted) octahedral structural units be present in all of them. Oxygen plays a crucial role in connecting these octahedra and in the process it is coordinated to more than two (upto four) Pb atoms in the structure. In order to form octahedral units, Pb is sp^3d^2 hybridized (6*s*, 6*p* and 6*d* orbitals). The presence of $[PbO_2X_4]$ units was confirmed by several experiments; probe ion spectroscopy (ESR of $Mn^{2+}$and Fe^{3+} and fluorescence spectra of Mn^{2+}), EXAFS and XANES associated with Pb L edges and neutron diffraction. The XANES associated with L_I, L_{II} and L_{III} edges of Pb in PbO-PbF_2 glasses is shown in Figure 14.04. EXAFS analysis clearly indicated the constancy of the coordination number around Pb (Rao et al., 1988a). In the case of PbO-PbF_2 glasses, the XANES associated with L_{III} edge was analysed and it was found that the XANES was structured suggesting the presence of distinct energy states to which 2*p* electrons are excited. Such distinct final states are a consequence of the geometrical arrangement of two oxygens and four fluorines in the coordination polyhedra. The principal types of symmetries which can arise in $[PbO_2F_4]$ unit are shown in Figure 14.05. The symmetries evolve from $C_s \rightarrow D_{2v} \rightarrow D_{4h} \rightarrow O_h$ as the PbF_2 content in the glass increases. As seen in the figure, this evolution in symmetry is possible only when the O-Pb-O angle gradually increases from 90° in the pyramidal $[PbO_4]$ units present in parent PbO to 180° in $[PbO_2X_4]$. As the extent of the highly ionic PbF_2 increases in the glass, the PbO bond also becomes substantially ionic. The average bond ionicity is indeed reflected in the XANES (white line) intensities as may be seen from Figure 14.04, particularly in the white line intensities associated with L_I edge; it is significantly lower in PbF_2-rich glasses. The origin of the final states, responsible for the observed structure in the XANES can be visualized by constructing an appropriate molecular orbital (MO) diagram for bonding in the various $[PbO_2F_4]$ units

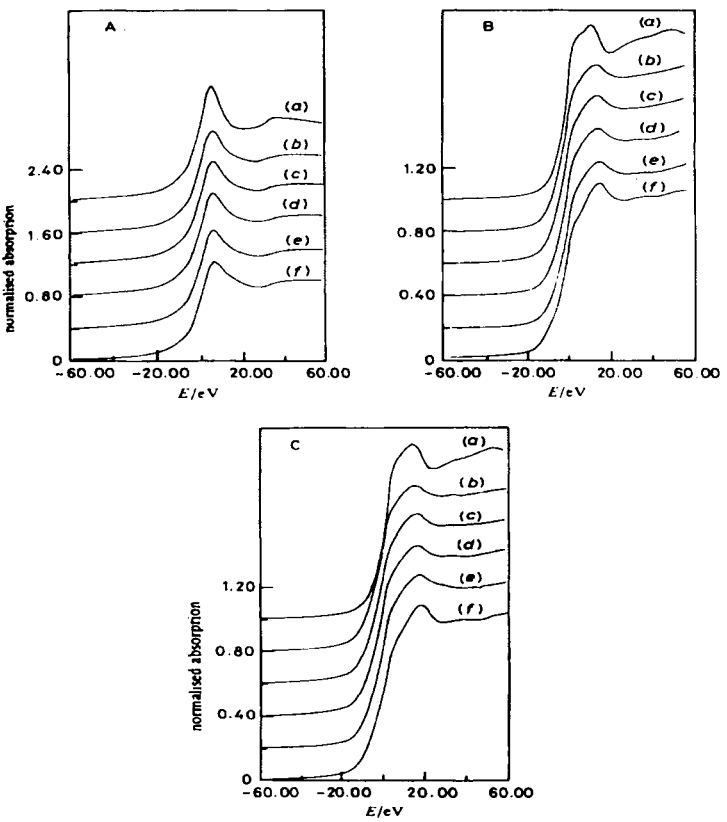

Figure 14.04. Normalized XANES spectra of the L_1 (A), L_2 (B) and L_3 (C) edges of Pb in PbO-PbF_2 glasses. % PbO = (a) 0, (b) 40, (c) 50, (d) 60, (e) 80 and (f) 100 (After Rao et al., 1988b).

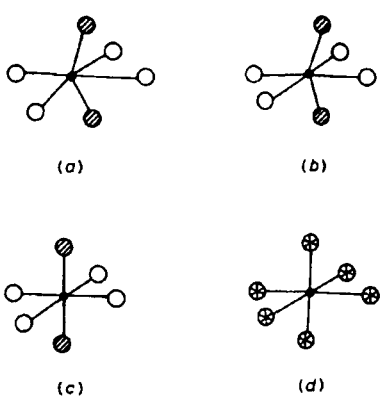

Figure 14.05. Geometry of six-coordinated Pb in PbO-PbF_2 glasses. •, Pb; O, F; ⊗, O/F (After Rao et al., 1988b).

shown in Figure 14.05. The MO diagrams have been drawn assuming a gradual evolution of symmetry in $[PbO_2F_4]$ units. It is found to consistently account for the observed features of the XANES spectra.

The glass structure depends crucially on the presence of oxygen bridges between Pb atoms. Therefore oxygen should be expected to be present in maximum coordination of Pb atoms in the glasses. MD simulation was performed on $PbO\text{-}PbF_2$ glasses of different compositions using BMH pair potentials and it was found that oxygen is always coordinated to 4 Pb atoms at a sharply defined distance of 2.2 Å. The pair distribution function (PDF) for the 4 compositions simulated using MD is shown in Figure 14.06.

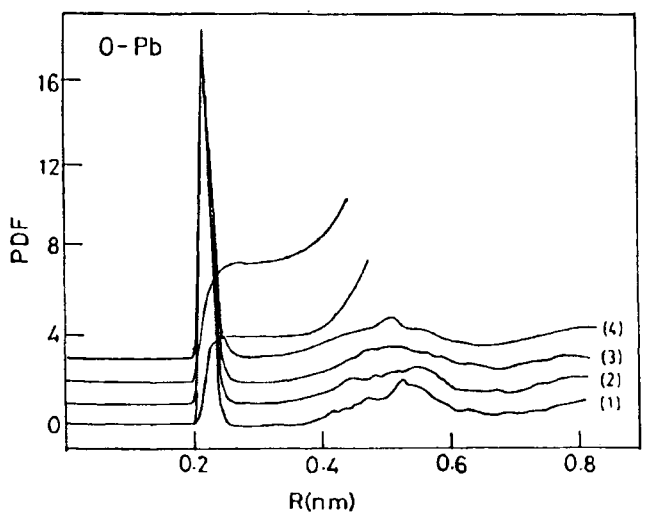

Figure 14.06. O-Pb pair distribution functions in $PbO{\cdot}PbF_2$ glasses. (1) $30PbO{\cdot}70PbF_2$, (2) $50PbO{\cdot}50PbF_2$, (3) $60PbO{\cdot}40PbF_2$ (4) $80PbO{\cdot}20PbF_2$. The running coordination number is also shown in cases (1) and (4) (Damodaran and Rao, 1988).

Therefore, lead oxyhalide glasses have unique features, which are different from both halide glasses and oxide glasses, discussed earlier. In the conventional oxide glasses like phosphates etc., when halides are introduced, halide ions remain as separate entities and do not seem to become part of the coordination polyhedra. There are very few examples, such as some borate glasses, where B_3 to B_4 conversion is brought about by the halide ion providing the additional coordination to boron atom (Minami et al., 1979). In $AgI\text{-}Ag_2MoO_4$ glasses also possibility of I^- being coordinated to Mo in the tetrahedral units, has been suggested (Hemalata

and Rao, 1983). But in PbO-PbX_2 glasses, extensive mixed oxygen-halogen coordination is observed. Unlike in heavy metal halide glasses, a purely halogen coordination of Pb with halogen bridges is not formed. The formation of $[PbO_2X_4]$ coordination polyhedra in the entire composition range is in itself very unique.

Glasses of mixed salts: discrete anion glasses

During the discussion on FIC glasses (chapter 6), several examples of mixed salt glasses were described such as AgI-Ag_2MoO_4 (Nambu and Tanaka, 1977; Borino et al., 1977, Magistris et al., 1976; Hemlata and Rao, 1983; Senapati et al., 1983), AgI-Ag_2SeO_4 (Tuller et al., 1980; Kunze, 1973)etc. The unique characteristic of these ionic glasses is that they contain small anions such as $[MoO_4]^{2-}$ and $[SeO_4]^{2-}$ in addition to I^- ions. There is a qualitative difference between these anions and the anionic entities present in modified glasses such as silicates and phosphates because anions in the latter case consists of chains or sheets of variable sizes in the glass forming regions. Metaphosphates and meta and pyrosilicate units in glasses are examples of this nature. In order that only simple SiO_4^{4-} and PO_4^{3-} ions be produced in the glasses, the extent of modification required is very high and in such compositions tendency towards devitrification is also extremely high. Therefore, anions carrying charges > 2- do not seem to be stable in the glassy state. Oxyanions of the Group VI elements such as SO_4^{2-}, SeO_4^{2-}, MoO_4^{2-}, WO_4^{2-} etc. are all found to be stable entities in glasses. In the Group V, NO_3^- is the only simple ion found in glasses. In a sense, these oxyanions of Group V and VI elements are small discrete anions, showing no tendency to reestablish network features – a cardinal feature of all oxide glasses. For example, PO_3^- or $Si_2O_5^{2-}$ are formally metaphosphate and metasilicate ions in glass structure; they do not exist as discrete anions but as $[POO_{3/2}]^-$ and $2[SiO_{3/2}O]^-$, both of which clearly suggest extensive polymerization and network formation. Therefore a class of ionic glasses, based on such small simple anions may be described as "discrete anion glasses".

Historically, nitrate glasses such as those formed in $Ca(NO_3)_2$-KNO_3 system (Thilo et al., 1964; Dietzel and Poegel, 1953; Moynihan et al., 1976) are among the oldest and most extensively investigated. The $40Ca(NO_3)_2 \cdot 60KNO_3$ glass, known as CKN (a convenient acronym particularly for non-chemists) has been studied extensively particularly with regard to its relaxation behaviour. Glass formation in nitrates takes place relatively easily when there is a combination of mono and divalent

cations. Divalent cations are coordinated to less number of NO_3^- than the monovalent ion except in the case of Li^+, which due to its high ionic potential (the charge to radius ratio) tends to acquire tetrahedral coordination. Lowering of the symmetry of NO_3^- ion in glasses is noticed in their infrared spectra, which can be attributed to its strong coordination to the divalent cation. Generally nitrate glasses have low T_g and most of the glasses are prepared in the laboratory by melting together the crystalline hydrates of the divalent metal nitrates with appropriate quantities of the monovalent nitrates in test tubes. The melts are dehydrated by bubbling dry N_2 and quenching in metal moulds or between polished metal plates. But the nitrate glasses are rather hygroscopic and unstable towards crystallization in the presence of moisture.

Formation of glasses in inorganic sulfates is indeed very similar to the glass formation in inorganic nitrates. Typical of these are $ZnSO_4$-K_2SO_4 glasses, which are prepared (Narasimham and Rao, 1978; Sundar and Rao, 1980) by melting together appropriate quantities of K_2SO_4 and $ZnSO_4.7H_2O$ and removing the water using bubbling dry N_2. It is possible to prepare glasses up to 80% $ZnSO_4$. Sulfate glasses are formed even more readily in ternary systems like $ZnSO_4$-Na_2SO_4-K_2SO_4. The glass formation region is shown in Figure 14.07.

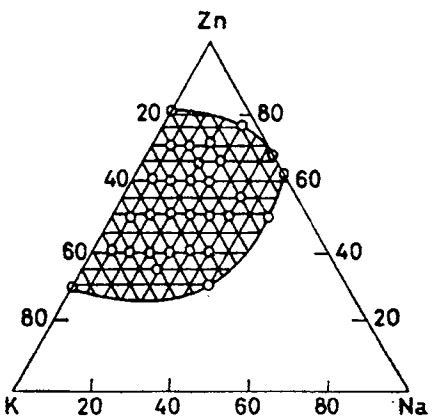

Figure 14.07. Glass formation region in the ternary sulphate system K_2SO_4·Na_2SO_4·$ZnSO_4$ (After Sundar and Rao, 1980).

From a structural point of view, sulfate glasses are excellent examples in which packing considerations dominate as in ionic crystals. Sulfate ions are tetrahedral but with a spherical envelope of rotation. The random close packing volume of SO_4^{2-} spheres with the radii of 2.65 Å is

73.7 cc, very close to the molar volume (72.5 cc) of the hypothetical K_2SO_4 glass (obtained from extrapolation of experimental glass molar volumes). Therefore, inserting two moles of K^+ ions into 1 mole of dense random close packed SO_4^{2-} ions appears to require no extra volume. This is so because sulfate ion itself can be looked upon as a tetrahedron of four oxide ions. The voids in the rcp of SO_4^{2-} ions are also tetrahedral. Therefore, there are four SO_4^{2-} ions surrounding a K^+ ion. The radius of O^{2-} in SO_4^{2-} ion is 1.32 Å, which is very close to the radius of K^+ (1.33 Å). We may visualize, a K^+ ion surrounded comfortably by 12 oxide ions originating from 4 SO_4^{2-} ions in an icosahedral geometry. This is entirely possible because 4 SO_4^{2-} ions in contact with each other in the rcp can be just tilted so that into an otherwise tetrahedral hole K^+ ion can be snugly fitted in. In fact, fitting an Na^+ ion into a similar hole can be accomplished by orienting 2 oxygens each from the 4 SO_4^{2-} ions in the tetrahedral hole of the same rcp assembly so that Na^+ ion gets a coordination of 8 O^{2-} ions. The radius ratio of Na^+ and O^{2-} ion (0.97:1.32 = 0.73) is the ideal ratio for body centered coordination. In fact, with appropriate volume corrections made for local rearrangements required for creating octahedral oxygen coordination for Zn^{2+} (Zn^{2+} is octahedrally coordinated in the glasses), molar volumes were found to be in excellent agreement with the experimental values, suggesting that the structure of discrete anionic glasses is dominated by packing considerations. Probe ion spectroscopy has been used to confirm octahedral coordination of Zn^{2+} and MD simulations, to confirm the coordinations of Zn^{2+}, Na^+ and K^+ ions. In Table 14.3, the coordination numbers found from MD simulations

Table 14.3: Composition and coordination numbers from MD simulation (After Rao et al., 1993).

Pair	Composition	Coordination number
Zn-O	$0Na_2SO_4 \cdot 50K_2SO_4 \cdot 50ZnSO_4$	6.1
	$50Na_2SO_4 \cdot 0K_2SO_4 \cdot 50ZnSO_4$	6.7
	$25Na_2SO_4 \cdot 25K_2SO_4 \cdot 25ZnSO_4$	6.3
K-O	$0Na_2SO_4 \cdot 50K_2SO_4 \cdot 50ZnSO_4$	12.0
	$25Na_2SO_4 \cdot 25K_2SO_4 \cdot 25ZnSO_4$	12.0
Na-O	$50Na_2SO_4 \cdot 0K_2SO_4 \cdot 50ZnSO_4$	8.0
	$25Na_2SO_4 \cdot 25K_2SO_4 \cdot 25ZnSO_4$	8.0

in various compositions have been listed. The activation barriers for d.c. conductivities, for the transport of Na^+ and K^+ ions are significantly higher than in other ionic glasses (greater then 1.0 eV), which can be attributed to the tightly packed structures.

Discrete anion glasses appear to minimize their energies through optimal packing. There is, however, an inherent instability towards crystallization of such glasses unless their configurational entropies are increased by adding different types of cations. In fact, in sulfate glasses, it has been shown by simple calculation that glass-formation in binary and ternary systems is confined to regions of maximum configurational entropy (Narasimham and Rao, 1978).

Oxynitride glasses

Oxynitride glasses are the oxide glasses in which O has been substituted by N to varying extents. In thioborate and thiosilicate glasses, where oxygen is substituted by chalcogen, we noted development of novel structural features such as edge sharing of structural units and lowering of dimensionality. Substitution of the O by N leads to enhanced cross-linking. This is because N being from Group V is capable of forming 3 covalent bonds. This substitution can be envisaged as three O in the structure being replaced by two Ns.

$$3 \quad -O- \quad \rightarrow \quad 2 \quad -N\begin{matrix}/\\ \\ \backslash\end{matrix}$$

Therefore, substitution by N in oxide glasses increases the network connectivity and dimensionality, which in some sense is the opposite of substitution by chalcogens. Also for a given oxide glass composition, substitution of oxygen by N leads to a weight loss. This in itself is a measure of N incorporation. It was reported early (Jack, 1977) that Mg- and Y-SiAlON systems (SiAlON, read as 'sialon', is acronym for the crystalline and amorphous products in the system, Si-Al-O-N) give rise to glasses containing up to 10 atom % N. N substituted glasses exhibit improved hardness, higher T_g, decreased thermal expansivity and increased refractive indices, all of which are of importance for various applications (Sakka et al., 1983; Homeny and McGarry, 1984; Hampshire et al., 19847). Therefore, a number of oxynitride glasses have been developed. They include M-Si-O-N, M-Si-Al-O-N, M-Si-B-O-N, M-P-O-N and M-O-N. The usual M atoms are alkali metals, alkaline earths or Group III elements like Al, Y and rare earths like La. In fact, many of the

M-SiAlON systems contain a combination of M atoms. Glass formation is found to be easier, more the types of atoms present in the nitrided glasses. Several simple silicates and phosphates which are 'nitrided' have provided much insight into the structure of oxynitride glasses.

There are three widely used procedures to prepare nitrided glasses. The first is melting together of appropriate network forming oxides along with a metal nitride. The second is nitridation using N_2, (which is generally not efficient) or NH_3. NH_3 is both reducing and nitriding. The third method is based on ammonolysis to obtain gels through which nitrogen is introduced into the structure. The most widely used nitrides in the first procedure are Li_3N, AlN, Si_3N_4, Mg_3N_2 and Ca_3N_2. Temperatures required can be as high as 1500 – 1700°C. It has been found that using carbonates in the charge material is undesirable because Si_3N_4 can react with CO_2 and thereby reduce the availability of nitrogen for nitridation (Wusirika, 1984).

$$Si_3N_4 + CO_2 \rightarrow 3SiO_2 + 6CO_2 + N_2 \qquad (\Delta G^0 = -733 kJ/mol \text{ at } 1650^\circ C)$$

Si_3N_4 is also unstable towards oxygen and gives rise to SiO and N_2 with a negative ΔG^0. SiO is formed in vapour state. High pressure N_2 atmosphere has been used to suppress the decomposition reaction leading to the formation of SiO and N_2. This procedure also increases the quantity of N_2 incorporated into the material. The preparations are generally done in N_2 or argon atmosphere and in Mo or graphite crucibles, often coated with BN. In La-Si-O-N glasses, it has been found possible to incorporate 36.8 equivalent % of nitrogen (Makishima et al, 1983).

In gel based preparation, a silicon containing gel, which has Si-OH groups is reacted with NH_3 so as to convert them to amine groups. These amines are later made to undergo condensation reaction at temperature around 400 ^{0}C or higher so that nitrogen is introduced into the network. It has been found possible to introduce even higher percentages of nitrogen into thin films of silica gel (Brow and Pantano, 1987) in which SiO_2 could be converted into Si_2N_2O. Solid state NMR, XPS and vibrational spectroscopy have proved to be exceedingly useful techniques in characterizing oxynitride glasses. In silicate glasses nitrogen is 3-coordinated. MAS NMR suggests the presence of groups like SiO_3N, SiO_2N_2 in nitrided silicate systems. Substitution of N (less electronegative) for O (more electronegative) leaves Si less de-shielded, making chemical shifts values less negative than in pure silicate glass (a downward shift of 9 to 15 ppm occurs for every substitution by N in the first coordination).

The resonance peaks also become much broader, requiring deconvolution of the resonance peaks for meaningful interpretation. In nitrided aluminosilicates, N appears to bridge preferentially to Si. We should expect no non-bridging N (nitrogen carrying a negative charge) because of the presence of the more electronegative O. Also in silicates, it is unlikely that N forms a double bond with Si. The nature of nitrided silicate structure is shown schematically in Figure 14.08(a). In vibrational spectra, N incorporation can be identified by the Si-N-Si linkages, which gives rise to vibrational bands around 850 cm^{-1}. The corresponding Si-O-Si linkages give rise to 1080 cm^{-1} band. The substitution by N is generally noticed as a gradual shift of the band position. Nitridation of phosphate glasses has also been studied extensively (Day, 1989). N substitutes both for bridging and terminal (double bonded O) in the phosphate structure. A schematic of such a structure is shown in Figure 14.08(b). Using a combination of XPS

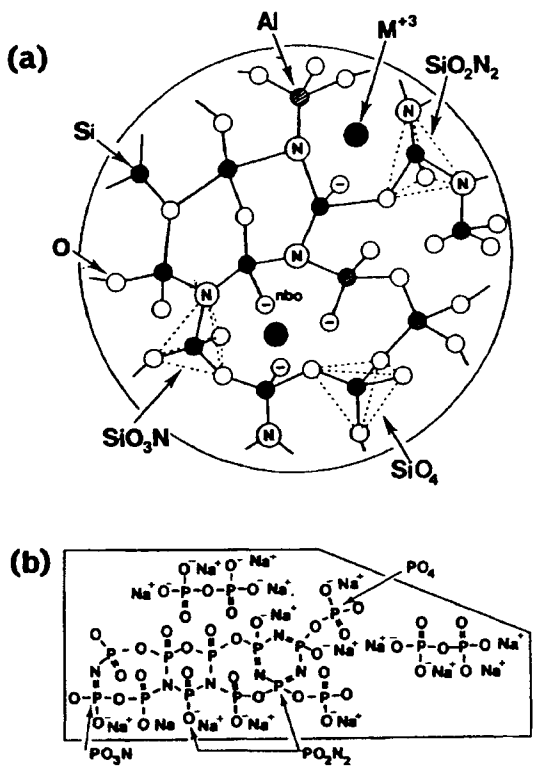

Figure 14.08: (a) Schematic structural representation of (a) M-Si-Al-O-N glass and (b) Na-P-O-N glass (After Bunker et al., 1987).

and NMR (both MAS and DQ - double quantum - techniques), it has been recently shown (Le Sauze et al., 2000) that N substitution is more likely to occur on a P atom, which is already attached to a N, which therefore leads to the formation of oxynitride micro-domains in the oxide matrix.

Nitridation in general is known to improve several properties. T_g has been found to uniformly increase in all nitrided systems (Hampshire et al, 1984). Variation of T_g by N substitution in phosphate glasses is shown in Figure 14.09. Nitrided glasses exhibit enhanced chemical durability.

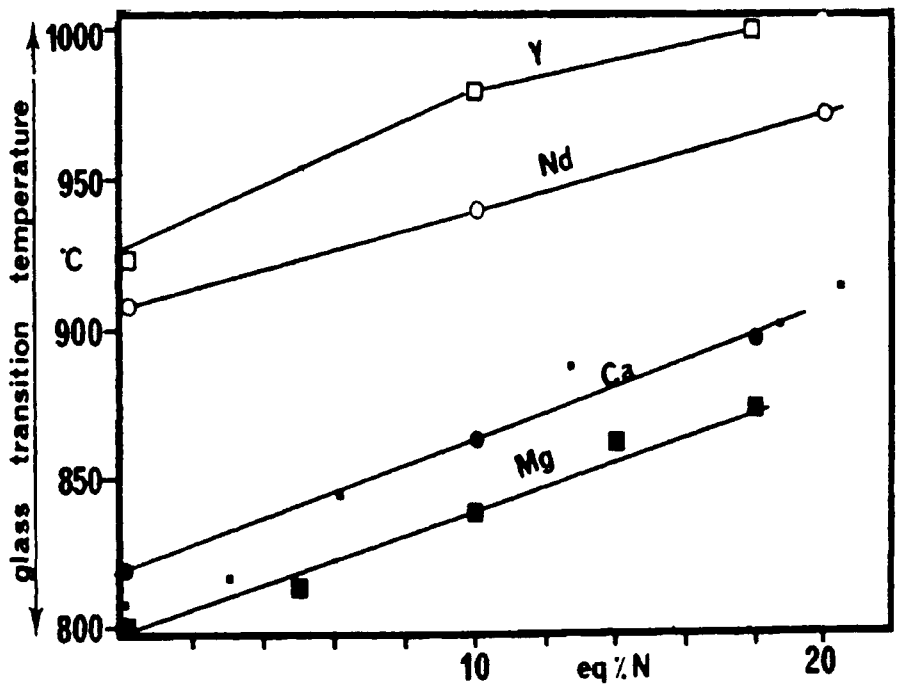

Figure 14.09: Variation of glass transition temperature in M-Si-Al-O-N glasses (M = Mg, Ca, Y, Nd) (After Hampshire et. al., 1984).

A complete substitution of O by N is equivalent to the preparation of pure nitride glasses. Glasses based on Li_3N-Ca_3N_2-P_3N_5 have been prepared by rapid quenching of melts, held under pressure of around 10 kbar and 1000°C (Grande et al., 1994). Phase diagram of this system indicating glass formation region is shown in Figure 14.10. These glasses exhibit remarkably improved properties such as refractive indices of 1.97 – 2.0. Their T_g values are higher than those of corresponding oxide glasses. Their structures appear to consist of PN_4 tetrahedra.

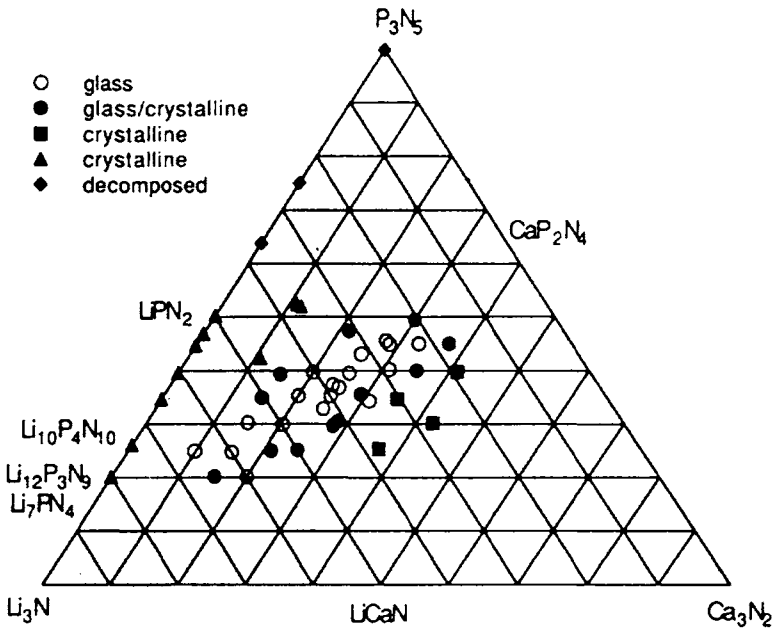

Figure 14.10: The glass-formation area in the ternary system Li_3N-Ca_3N_2-P_3N_5 at 8 kbar and 1400°C (After Grande et al., 1994).

Metallic glasses

It would be appropriate to make a brief reference to metallic glasses (see for an excellent overview, Cahn, 1991) although the focus in this book is on non-metallic inorganic glasses. Discovery of metallic glasses was a byproduct of the development of rapid quenching (RQ) methods (Duwez et al., 1960). RQ is employed to improve properties of alloys particularly by increasing solute concentrations in alloys. In general, metallic melts have a high propensity to crystallize and therefore, require very high rates of quenching of the order of 10^6 K per second (see chapter 2). Several experimental methods such as melt spinning, piston and anvil, twin roller etc. have been developed for the purpose (we may note that all metal alloys, and perhaps none singly, can be quenched into the glassy state by using vapor deposition techniques). There are principally two categories of metallic glasses. The first is referred to as metal-metalloid system, where the metal is either a transition or a noble metal. The best examples of this category are Au-Si, Pd-Si, Co-P, Fe-B, Fe-P-C, Fe-Ni-Pb, Mo-Ru-Si, Ni-B-Si etc. The metalloid (Si, B,

C or P) content is generally between 15 to 25 atom %. The second category of metallic glasses are formed by a combination of two transition metals, one early transition metal (like Sc, Ti, V in the 3*d* series and corresponding metals in the 4*d* and 5*d* series) and the other, a late transition metal (like Mn, Fe, Co, Ni or its followers down the periodic table). Typical examples are Zr-Ni, Y-Cu, Ti-Ni, Zr-Cu, Nb-Ni, Ta-Ni, Ta-Ir, W-Fe, Zr-Fe etc. In this category, one could include alloys of late transition elements and rare earths like Co-Gd and Ni-Gd. The range of compositions available is remarkably broad. For example, in Cu containing alloys, one could make glasses with 30 to 65 % Cu. The other categories of metallic glasses consist of a combination of elements from group I and II like Li and Mg in combination with group I b, II b, III b metals like Cu, Zn and Al. These glasses are typified by Mg-Zn, Ca-Mg etc. We may add to these, alloys of the type Ti-Be and Al-Y-Ni, which consist of a transition metal with lighter *p*-group metals. The first category of metal-metalloid glasses are the easiest to prepare. $Pd_{40}Ni_{40}P_{20}$ and $Pd_{77.5}Cu_6Si_{16.5}$ glasses can be obtained even at cooling rates of 1 K/s (Cahn, 1991).

The metal-metalloid glasses consist of small metalloid atoms dispersed in the matrix of larger transition metal atoms. Since rather good glasses are obtained with about 20 atom% of the metalloids, it was thought that the metalloid atoms stuff the Bernal holes in the rcp structure of the majority metal atoms. The stuffing was thought to prevent their easy crystallization. It chapter 2, we noted that there was a fairly successful comparison between the experimental differential correlation function of amorphous $Ni_{76}P_{24}$ and that of the corresponding rcp assembly of atoms. However, there have been alternate approaches to understand the structure of metallic glasses, like the one based on the packing of trigonal prisms of transition metals built around the metalloid atoms and with edge sharing arrangements (Gaskell, 1981). Several attempts have been made in the literature to investigate the criterion for glass formation in alloy systems (Rao, 1984). It appears that the mismatch in atomic size plays a very important role in determining the tendency towards glass formation. A simple criterion for glass formation in an alloy A-B is given by $C_B^{min}.(V_B-V_A) \approx 0.1$, where C_B^{min} is the minimum solute concentration and V_B and V_A are the atomic volumes. Another indication is that zero or negative change of specific volume on melting of a crystalline alloy generally favours glass formation. The critical quenching rates required in order to obtain the glass is related to T_g/T_m and it is lower for higher values of T_g/T_m. This variation is shown in Figure 14.11.

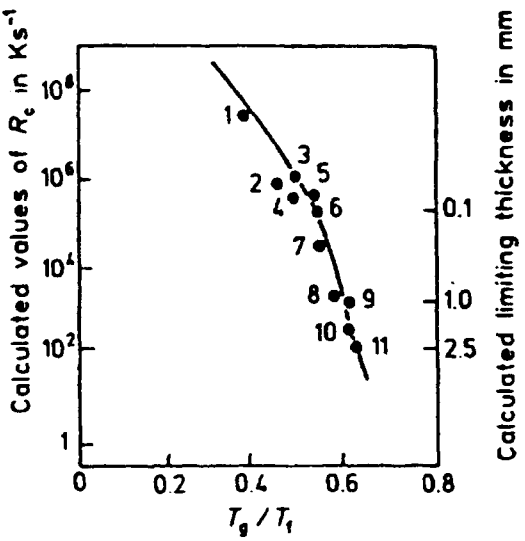

Figure 14.11. Calculated critical quenching rates, R_c, for glass formation, and examples of limiting ribbon thickness. (1) $Fe_{89}B_{11}$; (2) $Au_{78}Ge_{14}Si_8$; (3) $Fe_{83}B_{17}$; (4) $Fe_{41.5}Ni_{41.5}B_{17}$; (5) $Co_{75}Si_{15}B_{10}$; (6) $Fe_{79}Si_{10}B_{11}$; (7) $Fe_{80}P_{13}C_7$; (8) $Pd_{82}Si_{18}$; (9) $Ni_{63}Nb_{37}$; (10) $Pd_{77.5}Cu_6Si_{16.5}$; (11) $Pd_{40}Ni_{40}P_{20}$ (After Davies, 1978).

Since metallic glasses are generally quenched at very high rates, they are characterized by high fictive temperatures. Therefore, annealing leads to significant increase in densities and improved properties. Several metallic glasses exhibit a tendency towards crystallization even during annealing, perhaps due to facile heterogeneous and surface nucleation. But in systems such as $Fe_{40}Ni_{40}P_{14}B_6$ glass, it has been established that crystallization occurs through homogeneous nucleation.

Amorphous alloys like as $Ni_{90}P_{10}$ can also be obtained from electrolytic routes and by electroless deposition (Dietz, 1977). Even mechanical alloying has been used effectively to achieve amorphization (Lee et al., 1988). Glassy metals have been of importance particularly because of their special magnetic properties with low hysterisis and high values of magnetization. They are valuable in making transformer laminations (Schulz et al., 1988). Commercial Metglas 2605 SC ($Fe_{81}B_{13.5}Si_{3.5}C_2$) and Metglas 2605 S2 ($Fe_{78}B_{13}Si_9$) have been in use for quite some time. One of the recent advances is the use of metallic glasses in Ni-metal hydride batteries. The metal hydride (MH) is composed of a glassy metal, M, which is an alloy of V-Ti-Zr-Ni, capable of storing hydrogen at very densities. The electrochemical reaction involved is $2\ NiOOH + H_2\ (MH) \rightarrow 2\ Ni(OH)_2$ (Ovshinsky, 2000).

Glass-like carbon

Carbon, which is the first element of Group IV in the periodic table, is amorphous in some of its forms like soot. It can also be obtained in an industrially useful form known as vitreous or glass-like carbon. Vitreous carbon can be prepared in the same manner as amorphous Si and Ge using thin film techniques. It can be prepared in bulk form by other standard procedures to be described below. Glass-like carbon was first made from cellulose in 1957 (Davidson, 1957) and since then several methods have been developed for the preparation of vitreous carbon. Because of its potential and present applications in electrical, electronic and other industries, there have been several studies of the properties of vitreous carbon. We will adopt here the name glass-like carbon because it would be strictly inappropriate to call it 'vitreous carbon' since it is not prepared by the melt route (carbon begins to sublime at ordinary pressures and at high temperatures, and no liquid form of carbon has been characterized). Also, it may be preferable to reserve the description of amorphous carbon to the general category of carbons such as coke or soot.

Glass-like carbon is obtained from carbonization of solid carbonaceous materials (Davidson, 1957). Three generally used starting materials are cellulose, phenol resin and furfuryl alcohol resin (both of which are thermosetting resins). However, to prepare porous glass-like carbon, one can start with the same materials impregnated with resins, which can be removed at an intermediate stage before graphitisation. The procedure consists of first moulding and drying a slurry of cellulose or a thermosetting resin. The resin has to be hardened by using a hardener like benzoic peroxide. The molded material is pre-shaped by machining. These products are dehydrated slowly by heating under pressure at a low heating rate and then subjected to carbonization in inert atmosphere between 1000-1500°C. Finally, it is subjected to graphitisation at still higher temperatures (~2800°C). Glassy-carbon can be distinguished from soft carbons like coke by virtue of the variation of inter-layer distances identified by X-rays diffraction. For soft carbons it decreases as a function of graphitising temperature to a much greater extent (typically d_{002} is 4.8 Å at 500°C and decreases to 3.5 Å at 2800°C), while in glassy carbon the decrease is negligible (from 3.5 Å to 3.4 Å). From electron microscopic investigations, it has been found that graphitisation progresses from 1200°C to 2800°C. The structure consists of a random configuration of small crystallites in stacks of several layers of graphitic carbon (20-30 Å in thickness). They grow in size whereupon the stacks

thicken to 60-70 Å in size (stack size corresponding to about 10 layers). Based on these observations, there are two models of the structure of glass-like carbon – one due to Jenkins and Kawamura (1971) (also Jenkins et al., 1972) of interlaced ribbons forming a network of ribbon stacking (Figure 14.12(a)). It is quite complex and has earned the encomium 'Jenkins nightmare model'. On the strength of the argument that this model may not be consistent with the extremely low diffusivity of gases in glass-like carbon, an alternate model was proposed by Shiraishi (1984) (also see Otani and Oya, 1991) as shown in Figure 14.12(b). The most important chemical feature of the structure is that the carbons are almost exclusively sp^2 hybridized, except perhaps for those atoms at the branching positions.

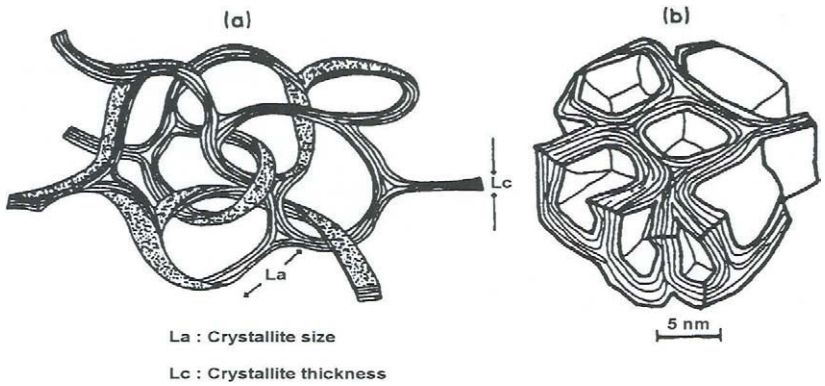

Figure 14.12: Two structural models of glass-like carbon heated to high temperature; (a) network of ribbon stacking model (After Jenkins and Kawamura, 1971) (b) alternate model. (After, Shiraishi, 1984).

Glass-like carbon has a low density of about 1.45 to 1.55 g/cc, much lower than that of both diamond (3.52 g/cc) and graphite (2.25 g/cc). Glass-like carbon is impermeable to gaseous diffusion and clearly suggests that the porosity responsible for low density is of the enclosed type. Gas permeabilities are generally of the order of 10^{-10} – 10^{-12} cm^2/s. They have high bending strengths of the order of 100 MPa, much higher than pyrex glasses (≈ 50 MPa). Compared to graphite, their thermal conductivities are very low (<10Watts/m/K; that of graphite is ~ 240 Watts/m/K). More importantly, their electrical resistivities are very low, although higher than graphite (about $40\times10^{-4}\Omega$cm). Glass-like carbon is chemically very inert and is not affected by H_2SO_4–HNO_3 mixtures, although it is unstable towards strong alkalis. Glass-like carbon and

graphite, both begin to get oxidized around the same temperature in air, but the oxidation proceeds at a far lower rate even at higher temperatures in glass-like carbon, which is intimately connected with its structure.

Based on the above properties, glass-like carbon has found applications as heating elements, as containers for chemical reactions and as containers for molten metals. They are also used as separators and electrodes in phosphoric acid fuel cells (Ovshinsky, 2000).

References:

Angell, C. A., C. Liu and H. G. K. Sundar, 1985, Mat. Sci. Forum, **5**, 189.

Angell, C. A. and D. C. Zeigler, 1981, Mat. Res. Bull., **16**, 279.

Borino, F., M. Lazzari, A. Leonardi, B. Rivotta and B. Scrosati, 1977, J. Solid State Chem., **20**, 315.

Brow, R. K. and C. G. Pantano, 1987, J. Am. Ceram. Soc., **70**, 9.

Bunker, B.C., G.W. Arnold, M. Rajaram and D.E. Day, 1987, J. Am. Cearm. Soc., **70**, 427.

Cahn, R. W., 1991, Materials Science and Technology: A Comprehensive Treatment, Vol. 9, eds. R.W. Cahn, P. Haasen and E.J. Kramer (Wiley-VCH, Weinheim) p. 493.

Cooper, E.I., and C.A. Angell, 1983, J. Non-Cryst. Sol., **56**, 75.

Damodaran, K. V. and K. J. Rao, 1988, Chem. Phys. Lett., **148**, 57.

Davidson, H. W., 1957, British Patent 860342.

Davies, H. A., 1978, Proc. 3rd Int. Conf. On Rapidly Quenched Metals (Rapidly Quenched Metals III), eds., B. Cantor, (Metal Society, London), p. 1.

Day, D. E., 1989, J. Non-Cryst. Sol., **112**, 7.

Dietz, G., 1977, J. Magn. & Magn. Mater., **6**, 47.

Dietzel, A., and H.J. Poegel, 1953, Proc. 3rd Int. Glass Congress, Venice, p. 219.

Duwez, P., R. H. Villain and W. Clement jr., 1960, J. Appl. Phys., **31**, 36.

Gaskell, P.H., 1981, Nature, **289**, 474.

Grande, T., J. R. Holloway, P. F. McMillan and C. A. Angell, 1994, Nature, **369**, 43.

Hampshire, S., R.A.L. Drew and K.H. Jack, 1984, J. Am. Ceram. Soc., **67**, C46.

Hemalata, S., and K.J. Rao, 1983, J. Non-Cryst. Sol., **54**, 313.

Hemlata, S., and K. J. Rao, 1983, J. Non-Cryst. Sol., **54**, 313.

Homeny, J., and D.L. McGarry, 1984, J. Am. Ceram. Soc., **67**, C225.

Jack, K. H., 1977, Nitrogen Ceramics, eds. F.L. Riley (Noordhoff International Publishers), p. 257.

Jacoboni, C., A. Le Bail and R. De Paape, 1983, Glass Technol., **24**, 164.

Jenkins. G.M., K. Kawamura and L.L. Ban, 1972, Proc. R. Soc. (London), **A327**, 501.

Jenkins, G. M. and K. Kawamura, 1971, Nature, **231**, 175.

Kadono, K., H. Nakamichi and M. Nogami, 1987, Mater. Sci. Forum, **19-20**, 63.

Kunze, D., 1973, Fast Ion Transport in Solids, eds. W. van Gool (North Holland, Amsterdam), p. 405.

Le Sauze, A., L. Montagne, G. Palavit, F. Fayon and R. Marchand, 2000, J. Non-Cryst. Sol., **263&264**, 139.

Lee, P.Y., J. Jang and C.C. Koch, 1988, J. Less-Common Metals, **140**, 73.

Lucas, J., 1991, in Materials Science and Technology: A Comprehensive Treatment, Vol. 9, eds. R.W. Cahn, P. Haasen and E.J. Kramer (Wiley-VCH, Weinheim) p. 455.

Magistris, A., G. Chiodelli and C. V. Campari, 1976, Z. Naturaf, **31a**, 974.

Makishima, A., M. I. N. Mitomo and M. Tsutsumi, 1983, J. Am Ceram. Soc., **66**, C55.

Matecki, M., M. Poulain and M. Poulain, 1987, Mat. Sci. Forum, **19-20,** 47.

Minami, T., T. Katsuda and M. Tanaka, 1979, J. Phys. Chem., 1306.

Moynihan, C. T., A. J. Easteal, M. A. Debolt and J. C. Tucker, 1976, J. Am. Ceram. Soc., **59**, 16.

Moynihan, C.T., 1989, in Current Trends in the Science and Technology of Glass, eds., H. Jain, A.R.Cooper, K.J.Rao and D. Chakravorty (World Scientific, Singapore) p., 279.

Nambu, T. M. H. and M. Tanaka, 1977, J. Am. Ceram. Soc., **60**, 283.

Narasimham, P.S.L., and K.J. Rao, 1978, J. Non-Cryst. Sol., **27**, 225.

Otani, S. and A. Oya, 1991, Materials Science and Technology: A Comprehensive Treatment, Vol. 9, eds. R.W. Cahn, P. Haasen and E.J. Kramer (Wiley-VCH, Weinheim) p.549

Ovshinsky, S.R., 2000, in Insulating and Semiconducting Glasses, Series on Directions in Condensed Matter Physics – Vol. 17, ed. P. Boolchand (World

Scientific, Singapore) p. 729.

Poulain, M., M. Poulain, J. Lucas and P. Brun, 1975, Mat. Res. Bull., **10**, 242.

Poulain, M. and J. Lucas, 1978, Verres. Refract., **32**, 505.

Poulain, M., J. Lucas, P. Brun and M. Drifford, 1977, Colloques Internationaux du CNRS, **255**, Paris, CNRS, p. 257.

Rao, B. G., K. J. Rao and J. Wong, 1988b, J. Chem. Soc. Faraday Trans. I **84**, 1773.

Rao, B. G. and K. J. Rao, 1984, Phys. Chem. Glasses, **25**, 11.

Rao, B. G., H. G. K. Sundar and K. J. Rao, 1984, J. Chem. Soc. Faraday I, **80**, 3491.

Rao, K.J., B.G. Rao and J. Wong, 1988a, J. Chem. Soc. Faraday Trans. I., **84**, 1779.

Rao, K. J., J. Wong and M. W. Shafer, 1984, J. Solid State Chem., **55**, 110.

Rao, K.J., S. Balasubramanian and K.V. Damodaran, 1993, J. Solid State Chem., **106**, 174.

Rao, P. R., 1984, Metallic glass: Production, properties and applications, eds.T. R. Anantharaman, (Transtech publication), p. 34.

Sakka, S., K. Kamiya and T. Yoko, 1983, J. Non-Cryst. Sol., **56**, 147.

Schulz, R., N. Chretien, N. Alexandrov, J. Aubin and R. Roberge, 1988, Mater. Sci. & Eng., **99**, 19.

Senapati, H., G. Parthasarathy, S. T. Lakshmikumar and K. J. Rao, 1983, Philos. Mag. B., **47**, 291.

Shiraishi, M., 1984, Tanso Zairyo Nyumon (Introduction to Carbon Materials, Revised Edition) (Kagakugijitsu-sha, Tokyo), p. 33.

Sundar, H. G. K. and K. J. Rao, 1980, J. Chem. Soc. Faraday Trans. I, **76**, 1617.

Thilo, E., C. Wiecker and W. Wiecker, 1964, Silikattechnik, **15,** 109.

Tuller, H. L., D. P. Button and D. R. Uhlmann, 1980, J. Non-Cryst. Sol., **40**, 93.

Van Uitert, L.G., and S.H. Wemple, 1978, Appl. Phys. Lett., 32, **403**.

Weber, M.J., 1986, in: Critical materials problems in Energy production. (Academic Press, New York) p. 261.

Wusirika, R.R., 1984, J. Am. Cearm. Soc., **67**, C232.

Yamane, M., H. Kawazoe, S. Inoue and K. Maeda, 1985, Mat. Res. Bull., **20**, 905.

Subject Index

1-Butene, 88
2-Methylpentane, 88
3-Methyl pentane, 87
Abbe number, 434, 440
Absorption coefficient, 153, 154, 155, 160, 173, 301, 347, 348, 356, 432, 434
Acidic oxides, 493, 494
Activation volume, 118, 238, 423
Adam-Gibbs theory, 51, 65, 89, 100
Adam-Gibbs-Vogel, 393
Ag_2O-B_2O_3, 237, 246
$Ag_2P_2O_7$ – $Li_4P_2O_7$, 130
Ag_2S-GeS_2, 293
$Ag_7I_4AsO_4$, 247
AgBr-Ag_2O-B_2O_3, 246
AgBr-CsBr, 539
AgCl-Ag_2O-B_2O_3, 246
AgCl-AgI-CsCl, 241, 539
AgI.Ag_2O-GeO_2, 246
AgI-Ag_2MoO_4, 17, 194, 237, 239, 241, 246, 247, 424, 543, 544
AgI-Ag_2MoO_4.$Ag_2Mo_2O_7$, 241
AgI-Ag_2O-B_2O_3, 241, 246
AgI-Ag_2O-P_2O_5, 241
AgI-Ag_2SeO_4, 246, 424, 544
AgI-$Ag_4P_2O_7$, 246
AgI-$AgBO_3$, 247
AgI-AgCl-CsCl, 247
AgI-CsI, 539
Al_2O_3, 22, 23, 37, 42, 71, 120, 235, 354, 440, 463, 483, 491, 492, 493, 494
Al_2O_3-TeO_2, 440
Alkali silicate glasses, 207, 212, 216, 226, 415, 447, 472, 473
AlTe, 532
Amber glass, 456
Amorphons, 105
Amorphous Ge, 187, 188
Amorphous germanium, 92, 310
Amphoteric, 343, 493
Amphoteric oxides, 343, 493
Anatase, 160
Anderson transition, 316, 317
Anderson-Stuart model, 208
Andrade law, 386
Anharmonicity, 106, 242, 416, 417
Annealing point, 53
Anomalous scattering, 102, 103, 153
Anti-bonding, 310, 339
Anti-Stokes, 170
As_2Se_3, 63, 83, 105, 110, 126, 130, 154, 343, 345, 346, 358, 359, 417, 513, 518, 519, 520, 521, 522
As_4Se_4, 359, 360
a-Si, 28, 29, 36, 341, 367, 368, 369, 371
As-Se-I, 531
As-Se-Te, 411, 523, 530
As-S-Se, 530
Atomic scattering factor, 140, 141, 144, 148, 153, 193
Attenuation, 125, 391, 408, 409, 430, 431, 432, 460, 540
Auger electron, 178, 179
Autocorrelation function, 193
B_2O_3, 14, 20, 30, 36, 42, 49, 55, 59, 67, 73, 85, 88, 103, 116, 126, 130, 148, 166, 218, 227, 230, 235, 241, 249, 277, 298, 415, 418, 424, 440, 461, 477-484, 494, 495, 500, 502, 506, 519, 527
B_2O_3-Li_2O, 289
B_2O_3-Li_2O-Cs_2O, 289
B_2O_3-Li_2O-K_2O, 289
B_2O_3-Li_2O-Na_2O, 289
B_2S_3, 22, 30, 210, 249, 251, 299, 300, 526, 527, 528, 529, 530
B_2S_3-Li_2S, 529
Back scattering, 156

Band theory, 307, 308
BaSF64, 111
Basic oxides, 227, 453, 484, 493, 494
Beer-Lambert's law, 432
BeF_2, 22, 36, 130, 158, 186, 417, 430, 468, 535
Eu^{3+}, 186
Bipolaron, 333, 334, 335, 338, 364, 365
Birefringence, 356, 357, 358, 439
Bloch functions, 307
Blocking electrode, 273
BNN relation, 264
BO, 25, 194, 206, 487, 488, 489
Bond angles, 23, 28, 29, 30, 36, 40, 42, 44, 64, 137, 139, 174, 185, 354, 411, 412, 464, 465, 468, 470
Bond energy, 37, 40, 464, 468, 519
Bond-switching, 493
Borate anomaly, 481, 482
Born-Mayer-Huggins, 190, 233, 465
Born-Openheimer, 196
Boroxol, 42, 44, 148, 479, 527
Boson factor, 112, 147
Boson peak, 91, 110, 112, 113, 425
Bragg reflection, 308
Brillouin, 119, 171, 173, 175, 237, 303, 308, 309, 380, 410, 411
Brinell hardness, 419
Bulk modulus, 328, 403, 404, 405, 407, 413, 414, 415, 417, 499
Butanethiol, 88
Butyronitrile, 130
Carrier type reversal, 362
CCl_4, 42
ccp, 31, 32
C-curve, 56, 57, 58
CdF_2-LiF-AlF_3-PbF_2, 537
CdI_2-CsI, 536
CdI_2-KI, 536
Chalcogen, 357, 513, 514, 518, 523, 532, 547
Characterization techniques
  EXAFS, 9, 153-160, 232, 358, 506, 520, 538, 539, 541
  NMR, 9, 161, 162, 166-170, 181, 182, 216, 226, 246, 282, 287, 469, 477, 485, 487, 489, 492, 493, 495, 498, 502, 504, 508, 525, 526, 527, 532, 548, 550
  Raman, 175, 230, 358, 506, 526, 529
  UVPES, 176, 312
  XANES, 9, 158, 159, 160, 538, 539, 541, 542, 543
  XPS, 9, 176, 177, 179, 180, 311, 312, 313, 487, 548
Chemical disorder, 30
Chemical ordering, 31, 520, 521
Chemical shift, 163, 164, 166, 169, 179, 469, 470, 471, 472, 473, 487, 489, 491, 521, 548
Chemical strengthening, 235
Chemically ordered networks, 520
cis -1,4-polyisoprene, 89
CKN, 49, 50, 51, 52, 123, 128, 130, 240, 271, 296, 297, 299, 300, 379, 383, 384, 544
CLAP glasses, 294
Clausius-Mossotti relation, 434
Cluster, 69, 100, 104, 105, 106, 108, 109, 196, 197, 216, 312, 369, 425
Cluster model, 105
Cluster-Bethe-Lattice, 311
Cluster-tissue, 216, 425
CNDO, 198
Co_3O_4-P_2O_5, 416
Cohen-Fritzsche and Ovshinsky, 313
Cole-Cole, 376, 385
Communal entropy, 81
Complex capacitance, 273
Complex impedance, 273
Complex moduli, 269
Complex permittivity, 265

Compliance coefficient, 403
Compressibility, 13, 46, 85, 377, 411, 412, 465, 468
Compton scattering, 143
Conductivity
  a.c., 230, 263-266, 276, 279, 287, 292-295, 299, 331, 335, 337
  d.c., 10, 246, 257, 264, 269, 271, 276, 278, 282, 286, 292, 293, 298, 335, 337, 344, 362, 368
  ionic, 10, 203, 216, 217, 226, 236, 239, 245, 263, 491, 503
Configurational entropy, 51, 62, 65, 82, 83, 86, 89, 90, 91, 96, 97, 99, 104, 127, 132, 388, 392, 470, 485, 530, 536, 540, 547
Confusion principle, 536, 540
Conjugate pair, 345
Constraint, 61-67, 95, 116
Cooling rate, 14, 45, 49, 52-61, 67, 70, 71, 98, 194, 394, 395, 552
Correlated barrier hopping, 333
Coupling model, 230, 275, 290, 293, 294, 384, 385
Covalency, 36, 40, 207, 539
crn, 26
Crown glasses, 434, 440
CRR, 101, 102, 127, 128, 132, 425
Crystal field, 159, 160, 443, 445
Current controlled negative resistance, 354
$d\pi$-$p\pi$, 44, 464
damping coefficient, 224
Damping constant, 114, 173, 175
Dangling bonds, 29, 197, 311, 315, 339-342, 367, 370, 515
Davidson-Cole, 278, 282, 287, 376, 377, 385
Deborah number, 52, 53, 61
Debye relaxation, 105, 274, 294, 297, 375, 376
Debye-Falkenhagen-Tomozawa, 281
Debye-Huckel, 281
Debye-Waller factor, 147, 538
Decoration technique, 30, 422
Decoupling index, 240, 243
Dense random packing, 33
Density functional, 127, 198
Density of states, 61, 112, 120, 147, 148, 176, 302, 309, 311, 313, 314, 316, 338, 353, 371, 390
Devitrification, 247, 535, 536, 544
Dibutyl phthalate, 383
Dielectric breakdown, 352
Dielectric loss, 216, 219, 223, 264, 266, 274, 278, 282, 292, 378, 431
Diethyl phthalate, 89
Differential correlation function, 35, 138, 552
Diffusion controlled relaxation, 277
Diffusion path model, 237, 245
Dispersion, 53, 153, 266, 268, 269, 272, 282, 302, 376, 380, 429, 434, 435, 436, 439, 440, 499
Domains, 101, 104, 110, 114, 550
Double-well potential, 285, 389
Drift velocity, 204
Ductile failure, 420
Dynamic specific heat, 382
Dynamically correlated domains, 105
Echo, 409
Ehrenfest relation, 389
Eigen functions, 307
Einstein convention, 402
Elastic, 113, 146, 171, 207, 208, 223, 280, 303, 401-407, 410-420, 424, 467, 468, 491, 499
Elasto-optic, 113
Electrodynamic coupling, 224, 226
Electron recombination, 345
Electron scattering factor, 148
Electronegativity, 36, 218, 243, 244, 343, 414, 465, 466, 470, 471, 484, 490, 493, 514, 535

Electron-phonon coupling, 341
Emission spectra, 452
Energy landscapes, 95, 96
Enthalpy relaxation, 392, 394, 395
Ergodicity breaking, 52
Ergodicity making, 52
Ethanol, 88
Ethylbenzene, 88
Excess entropy, 49, 392
Exciton, 349
Extinction coefficient, 173, 431, 432, 433, 445, 456
Fast ion conduction, 236, 238, 245
Fatigue, 220, 422
Fermi energy, 313, 317, 322, 345
Fiber optics, 458
Flint glasses, 434, 440
Fluorescence, 449, 452, 454, 541
Four point bending, 406
Fractal, 384
Fracture toughness, 419
Fragility, 6, 9, 31, 37, 50, 51, 87, 92, 95, 113, 116, 121-128, 132, 149, 150, 212, 229, 336, 341, 350, 354, 380, 383, 392, 393, 464, 535, 545, 555
Free induction decay, 168, 485
Free volume, 77-85, 92, 118, 238, 239, 247, 295, 384, 390
Frenkel defects, 203
Frozen entropy, 49, 82, 83, 85, 87
Frustration, 100, 103, 104, 110
Fused silica, 440
Gear predictor-correlator, 189
Ge-As-Te, 351
GeO_2, 14, 22, 23, 30, 39, 47, 55, 56, 71, 73, 105, 111, 120, 123, 126, 130, 194, 254, 283, 284, 298, 300, 413, 414, 415, 417, 430, 468, 483, 484, 535
GeO_2 –Na_2O, 111
GeO_2-B_2O_3, 484
Germanate glasses, 282, 283, 286, 483, 487
GeS_2-Li_2S-LiI, 241
Ge-Se-Tl, 351
$Ge_xS_{1-x-y}I_y$, 66
Giant photo expansion, 358
Glass blowing, 2
Glass former, 22, 23, 26, 36-38, 40, 42, 55, 118, 293, 500, 506, 535
Glass forming liquids, 9, 60, 73, 78, 83, 88, 121, 126, 382, 397
Glass forming tendencies, 36, 38
Glass lasers, 453
Glass transition, 9, 10, 13, 16, 44-53, 60, 61, 65, 77, 80-128, 193, 230, 231, 240, 241, 248, 258, 295, 336, 353, 356, 375, 377, 381, 382, 384, 387, 388, 389, 394, 395, 396, 430, 506, 533, 550
Glasses
  chalcogenide, 10, 355, 513, 531
  halide, 11, 246, 429, 430, 458, 460, 536, 540, 543
  metallic, 8, 11, 21, 33, 195, 515, 551, 552, 553
  natural, 1, 11
  oxyhalide, 11, 543
  oxynitride, 11, 548, 550
  tektites, 1
Glass-like carbon, 11, 554, 555, 556
Glaze, 2, 4
Glow discharge, 367, 368
Glycerol, 85, 88, 116, 130
Grüneisen parameter, 416, 417
$H_2Cr_2O_7$-H_2O, 258
H_2O, 17, 18, 57, 120, 130, 229, 258
$H_2SO_4.3H_2O$, 88
H_2ZnCl_4-H_2O, 258
$H_3Zn_2Cl_7$-H_2O, 258
$H_6B_9O_{18}Na_3$, 198
$H_6Si_2O_7$, 197
Hall coefficient, 326, 327
Hamiltonian, 166, 196, 310, 311

Hartree Fock, 196
Haven ratio, 229, 299
Havriliac-Negami function, 376
$HCl-H_2O$, 258
hcp, 31, 32
HDW, 130
Heat capacity, 13, 46, 49-53, 87, 90, 92, 93, 101, 122, 123, 125, 127, 247, 388, 390, 392-395, 418
$HfF_4-BaF_2-LaF_3$, 537
$HfF_4-BaF_2-LaF_3-AlF_3$, 537
$HfF_4-BaF_2-ThF_4$, 537
High field, 349
Hopping conductivity, 276
Hubbard U, 340, 341, 342
Hybridization, 42, 43, 311, 364, 370, 470, 506, 515
Hydrogen bonds, 93
Hydrogenated amorphous silicon, 28, 337, 367, 368, 369, 371
$HZn_2Cl_5-H_2O$, 258
$HZnCl_3-H2O$, 258
IML model, 214, 215, 227
INDO, 198
Infrared conductivity, 295, 301
Inherent structures, 97, 98
Internal friction, 219, 222
Interstitialcy, 214, 277
Ioffe-Regel limit, 318
Ion-exchange, 236
Ionic glasses, 34, 105, 219, 266, 296, 419, 425, 544, 547
Ionicity, 36, 37, 40, 128, 302, 414, 464, 538, 541
Isomorphous, 151
Isopentane glass, 186
Isotope, 151, 226, 227, 229, 230
Isoviscosity, 49
Jonscher regime, 290
$K_2O-MoO_3-P_2O_5$, 130, 498
$K_2O-WO_3-P_2O_5$, 130
$K_2S-B_2S_3$, 299, 300
$K_2SO_4-ZnSO_4$, 22, 35
Kauzmann paradox, 50, 104, 105
Kauzmann temperature, 60, 65, 91, 123, 396
Kerr shutters, 440
Kohlrausch-Williams-Watts, 275
Kramers-Kronig relation, 438
Lame constants, 404
Laporte forbidden transition, 445
Larmour, 161, 162
LaSF9, 111
La-Si-O-N, 548
Lennard-Jones, 34, 185, 190, 200, 417
Leyden jar, 275
$Li_2F_2-Li_2O-B_2O_3$, 286
$Li_2O-Al_2O_3-Nb_2O_5$, 256
$Li_2O-B_2O_3$, 130, 249, 495
$Li_2O-GeO_2-P_2O_5$, 130, 484
$Li_2O-K_2O-SiO_2$, 234
$Li_2O-P_2O_5$, 130, 494
Li_2O-TeO_2, 299
$Li_2O-TiO_2-P_2O_5$, 503
Li_2S-GeS_2, 246, 254
$Li_2S-GeS_2-LiBr-LiI$, 230
$Li_2SO_4-Li_2O-B_2O_3$, 130, 495
$Li_2SO_4-Li_2O-P_2O_5$, 130
Li_2S-SiS_2, 254, 257
$Li_2W_2O_7$, 251
$Li_3N-Ca_3N_2-P_3N_5$, 550
Li_3PO_4, 254, 532
$Li_3Zn_2Cl_7-H_2O$, 258
Li_4GeO_4, 257, 532
$Li_6W_4O_{15}$, 251
$LiBO_2-TeO_2$, 506, 507
$LiBr-Li_2O-B_2O_3$, 277
$LiCl-Li_2O-B_2O_3$, 246
$LiF-PbF_2-Al(PO_4)_3$, 230, 231
$LiI-Li_2S-B_2S_3$, 246, 250
$LiI-Li_2SO_4-LiPO_3$, 540
$LiI-Li_2S-P_2S_5$, 246, 249
Light scattering, 102
Lillie number, 53
Liquid-liquid transition, 120, 381

Lithium borate, 226, 286
Local density approximation, 198
Localized tail states, 318, 326, 345
Long range order, 9, 28, 174
Longitudinal modulus, 302
Loose random packing, 33
Lorch function, 144
Luminescence, 347
Mean free path, 113, 156, 180, 318, 320, 322, 326
Mechanical alloying, 553
Mechanical losses, 223
Mechanical relaxation, 302, 410
Medium range order, 28, 62, 112, 114
Melt spinning, 551
Metal-metalloid glasses, 552
Microcanonical, 195,233
Microhardness, 418, 419, 461, 524
Microwave heating, 16, 17
MINDO, 198
Minimum entropy, 85
Mixed alkali effect, 10, 194, 216, 219, 227, 233, 290
Mixed mobile ion effect, 230
Mixed oxides, 40, 218
Mobility edge, 313, 317, 319, 320, 321, 322, 352
Molecular orbitals, 197, 243, 339, 470, 526, 529, 541
Molybdo-phosphate glasses, 496
MoO_3, 22, 39, 130, 330, 355, 416, 496, 498, 499, 500
MoO_3-P_2O_5, 130, 416, 498
Mössbauer spectroscopy, 461, 505
Motional narrowing, 169, 287, 289
$Na_{1+x}Zr_{2-x/3}Si_xP_{3-x}O_{12-2x/3}$, 256, 257
Na_2O- SiO_2, 229, 473
$Na_2O{\cdot}B_2O_3$, 218
Na_2O-$3SiO_2$, 130
Na_2O-B_2O_3, 301
Na_2O-B_2O_3-SiO_2, 477
Na_2O-B_2O_3-V_2O_5, 500
Na_2O-GeO_2, 254, 414
Na_2O-TeO_2, 66
Na_2O-TiO_2-B_2O_3-P_2O_5, 440
Na_2O-TiO_2-P_2O_5, 440
Na_2O-TiO_2-SiO_2, 440
Na_2S-GeS_2, 254
$Na_2Si_2O_5$, 466
Na_2S-Li_2S-SiS_2, 230
Na_2S-P_2S_5, 254
$Na_3Fe_2(PO_4)_3$, 291
$Na_3Nb(PO_4)_3$, 451, 452
$Na_5Ti(PO_4)_3$, 451, 452
$NaPO_3$, 130, 445, 446, 447, 450, 503, 505
Na-P-O-N, 549
NASICON, 256, 502
NASIGLAS, 256, 257
Nb_2O_5, 355
NBO, 25, 181, 194, 206, 228, 277, 278, 280, 292, 418, 481, 487, 488, 489
$NbO_{2.5}$-TiO_2-Na_2O-SiO_2, 440
Nano glass, 53
Nernst-Einstein, 204, 221, 233, 241, 299
Neutron scattering, 64, 120, 144, 146, 147, 148, 151, 153, 195, 425, 484, 527
Newtonian, 189, 195
$Ni_{76}P_{24}$, 33, 35, 552
$Ni_{81}B_{19}$, 151, 152
Nitrided glasses, 548
Non-bridging oxygen, 25, 181, 194, 206, 228, 277, 278, 280, 292, 418, 481, 487, 488, 489
Non-radiative recombination, 370
Non-radiative transition, 450
n-Propanol, 85
Nuclear spin relaxation, 282
Nucleation and growth, 14, 54, 55, 57, 67, 74, 99, 104, 120, 473, 475, 476, 536
Opal glasses, 457

Optical basicity, 216, 494
Optical density, 433, 458
Optical gap, 335, 348, 349
Order parameter, 109
Orthophosphate, 255
Orthosilicate, 255
o-Terphenyl, 22, 88, 89, 90, 116, 117, 129, 131, 383, 384
OTP, 130
$p \rightarrow n$ transition, 362, 365
P_2O_5, 14, 20, 22, 24, 37, 39, 44, 67, 73, 130, 230, 413-418, 440, 457, 477, 484, 489-496, 499, 501
P_2O_5-Li_2O, 289
Pair approximation, 332, 333
Pair distribution function, 157, 193, 515, 516, 543
Partial charges, 465, 467, 470, 492, 493, 497
Partition function, 91, 97, 108
Pauling ionicity, 539
$Pb_2P_2O_7 - Li_4P_2O_7$, 130
PbGeSe, 362, 363, 364, 365, 366
PbO-BiO_5-$GaO_{1.5}$, 440
PbO-GeO_2, 414
PbO-Li_2O-B_2O_3, 130
PbO-MoO_3-P_2O_5, 499
PbO-$NaPO_3$, 445, 450
PbO-$PbCl_2$, 130, 540
PbO-PbF_2, 130, 540, 542, 543
PbO-TiO_2-SiO_2, 440
PbO-V_2O_5, 40, 41
Peltier coefficient, 325
Percolation, 64, 81, 102, 232, 292, 319, 329, 332, 384
PH_3, 367
Photo-amorphisation, 359
Photochromic glasses, 441, 458
Photochromism, 441, 461
Photodarkening, 356
Photoelectron, 177, 312
Photo-induced gyrotropy, 356
Photo-induced refraction, 356
Photoionization, 177
Photoluminescence, 345, 347, 370
Photo-sensitive glass, 441,457
Photostructural effect, 355
Photovoltaic, 368
Plastic deformation, 401, 419, 420
PMMA, 111, 393
Pnictide, 307
Polarizability, 44, 175, 198, 332, 434, 435, 436, 440
Polaron, 327-330, 336, 337, 522
Polyamorphic, 137, 424
Polyethyl methacrylate, 89
Polyisobutene, 85
Polyvinyl acetate, 85
Polyvinyl chloride, 85, 89
Poole-Frenkel, 351
Power law behaviour, 288
Pressure amorphization, 425
Prigogine-Defay ratio, 86, 389
Primary bonds, 94
Propylene Glycol, 130
Protonic conductors, 257
P-Se, 524
Pseudo atom, 62
Pseudo second order, 47
Pulsed NMR spectroscopy, 167
Quantum Chemical methods
Ab initio, 10, 196, 369, 470, 484, 526
Quantum efficiency, 362
Quantum mechanical tunneling, 263, 332, 337
Quasi-chemical equilibrium, 215
Quenching, 14,31, 51, 61, 74, 90, 96, 182, 186, 193, 247, 250, 335, 356, 367, 395, 450, 455, 474, 483, 489, 500, 503, 514, 524, 525, 535, 545, 550-553, 556
Racah parameter, 442, 446
Raman spectra, 91, 110, 112, 170, 172, 176, 359, 360, 480, 484, 529
Random potential energy, 275, 282

Random site model, 236, 237, 252, 253
Random walk, 204
Ravine and Souquet model, 214, 216
rcp, 31-35, 185, 425, 546, 552
RDF, 27-33, 99, 102, 137-139, 143, 149, 153, 158, 185, 186, 187, 193, 464, 484
Realgar, 359, 518
Reciprocal lattice, 33, 307, 309
Reflectance, 430, 431, 433, 438
Refractive index, 173, 301, 304, 375, 411, 429-440, 460, 468, 513
Reitveld, 187
Relaxation, 34, 48-55, 60, 82, 89, 94, 98-105, 114, 123, 124, 127, 168, 177, 185, 194, 222, 230, 235, 240, 242-248, 257, 266-283, 290-297, 302, 318, 332, 375-398, 408, 410, 430, 544
Relaxation times, 48-51, 82, 100, 104, 114, 223, 240, 243, 248, 266, 268, 275, 281, 290, 295, 332, 378, 380, 382, 384, 389, 392, 395, 397
Relaxed modulus, 247
Rheological properties, 42
Rigid lattice, 170, 226, 287, 289
Rockwell hardness, 419
Roller quenching, 7, 551
Ruby glasses, 455
Rutile, 160
Rydberg states, 159
Saddle point, 98, 206, 207, 209
Salol, 42, 86, 88, 105, 129, 130, 173, 384, 408
Sanderson method , 41, 76, 465, 492, 510
Sb_2O_3, 22, 36
Scaling, 36, 264, 295-299, 381, 382
Scattering intensity function, 141,
Schrödinger equation, 196
Second order transition, 47, 51, 60, 82, 83, 91, 94, 110
Secondary bonds, 92, 93, 519
Seebeck coefficient, 325, 345, 362
Selenium, 85, 88, 89
Se-Sb-Bi, 351
SF1, 111
Shear modulus, 48, 51, 53, 118, 208, 222, 268, 302, 375, 378, 403, 404, 407, 411
Shear stress, 18, 402, 403, 404
Si_2N_2O, 478, 548
Si_3N_4, 179, 461, 478, 548
SiAlON, 547
SiC, 179
SiH_4, 367
Silico-phosphate glasses, 488
Simulation
  molecular dynamics, 10, 98, 233
  Monte Carlo, 10, 185, 186, 187, 232, 253
SiO_2, 2, 14, 17-39, 42, 47, 63, 67, 71, 105, 111, 120, 123, 126, 130, 139, 147, 160, 179, 194, 195,212, 229, 235, 289, 358, 359, 413,415, 417, 419, 424, 425,430, 440, 460-469, 473, 477, 483, 487, 489,492, 494, 503, 535, 540, 548
$SiO_2.xH_2O$, 179
SiO_2-Li_2O, 289
SiO_2-Li_2O-Cs_2O, 289
SiO_2-Li_2O-K_2O, 289
SiO_2-Li_2O-Na_2O, 289
SiO_2-PbO-CaF_2-Na_2O-K_2O, 235
Si-O-Si, 17, 25, 28, 43, 192, 197, 411, 464, 465, 468, 492, 493, 549
Slater rule, 197, 244, 472
SnO-$NaPO_3$, 130, 503, 505
Sodium trisilicate, 290, 378, 379
Sol-gel, 17, 20, 75, 469
  aerogel, 19
  alcogel, 18
  hydrogel, 18

xerogel, 18
Sorbitol, 130
Sound waves, 113, 409
Spin echo method, 169
Spin flipping, 284
Spin-lattice relaxation, 167
Spinodal decomposition, 473
Spin-spin interaction, 167
Sputtering, 367
Staebler-Wronski effect, 369, 370
Stiffness coefficient, 402, 403
Stokes-Einstein, 73, 79, 112, 170, 175, 346, 347
Strain point, 53
Stress corrosion, 423
Stress intensifier, 420, 421
Stress intensity factor, 422
Stress-optic coefficient, 439
Strong electrolyte, 212
Structural relaxation, 55, 61, 95, 101, 104, 115, 243, 378, 380, 384
Structural unpinning, 218, 244, 245
Structure factor, 110, 114, 143, 147, 151, 152, 187, 188, 194, 383, 484
Sulpho-phosphate glasses, 495
Super-ionic conductor, 502
Switching, 350, 351, 352, 354, 531
Ta_2O_5, 354
Tauc gap, 349, 371
Taylor-Isard scaling, 264, 295
Te-As-Ge-Si, 351
TeO_2, 22, 36, 39, 66, 149, 417, 440, 496, 506, 507, 508, 514
TeO_2-V_2O_5-Na_2O, 257
Thermoelectric power, 325, 362, 363, 522
Thermometer, 235
Thioborate, 527
Thio-boroxol rings, 527
Three point bending, 406
Three-body interaction, 191, 192
Toluene, 88, 130
Tool-Narayanaswamy, 95, 392
Topological disorder, 30, 105, 311, 423
Total correlation function, 138
Transducer, 408
Transparency, 6, 8, 11, 340, 429, 430, 456, 457, 458, 513, 536
Transport number, 203, 254
Tri-α-napthylbenzene, 88, 384
T-T-T, 55, 56, 57, 58, 59
Tunneling coupling, 285
Tunneling splitting, 284, 292
Two-level states, 125, 389, 390
Two-state model, 92-98, 125, 169
Ultrasonic, 125, 302, 389, 391, 407,
Universal dielectric response, 274
V_2O_5, 22, 37-41, 355, 417, 496, 500, 502
Vacancy model, 209, 212, 279, 280
Valence band, 313, 339
van Hove correlation, 193, 194, 234
Variable range hopping, 323, 324, 330, 333
Verlet algorithm, 189, 190, 233
Vibronic coupling, 445
Voltage controlled negative resistance, 354
Voronoi polyhedra, 33, 78
VTF, 77, 79, 83, 95, 104, 116-127, 132, 295, 380, 386, 387, 396
Vycor glass, 469, 477
Weaire-Thorpe, 309, 310, 311, 313
Weak electrolyte, 212-216, 236, 237, 281
Wendt-Abraham ratio, 194
Wigner-Seitz cell, 33
Working point, 53
X cut, 408
Xerography, 359
Y cut, 408
YF_3-AlF_3-BaF_2-CaF_2, 537
Zeeman, 161, 165, 166
$ZnCl_2$, 22, 94, 130, 430, 535
$ZnSiO_3$, 179

$ZnSO_4$-K_2SO_4, 445, 545
$ZnSO_4$-Na_2SO_4-K_2SO_4, 545
ZrF_2-LaF_3-BaF_2, 537
ZrF_4-BaF_2, 302, 537
ZrF_4-BaF_2-GdF_3, 537
ZrF_4-BaF_2-GdF_3-AlF_3, 537
ZrF_4-BaF_2-LaF_3, 537
ZrF_4-BaF_2-LaF_3-AlF_3, 537
ZrF_4-BaF_2-LaF_3-AlF_3-NaF, 537
ZrF_4-BaF_2-NaF, 537
ZrF_4-BaF_2-ThF_4, 537
ZrF_4-BaF_2-UF_4, 537
ZrF_4-BaF_2-YF_3-AlF_3, 537
ZrF_4-ThF_4, 537
ZrF_4-ThF_4-YF_3, 537
ZrO_2, 39, 354, 477